(ISSN: 1411-9420 print / 2460-1578 online)

Indonesian Journal of Chemistry

Vol. 22, No. 4, August 2022

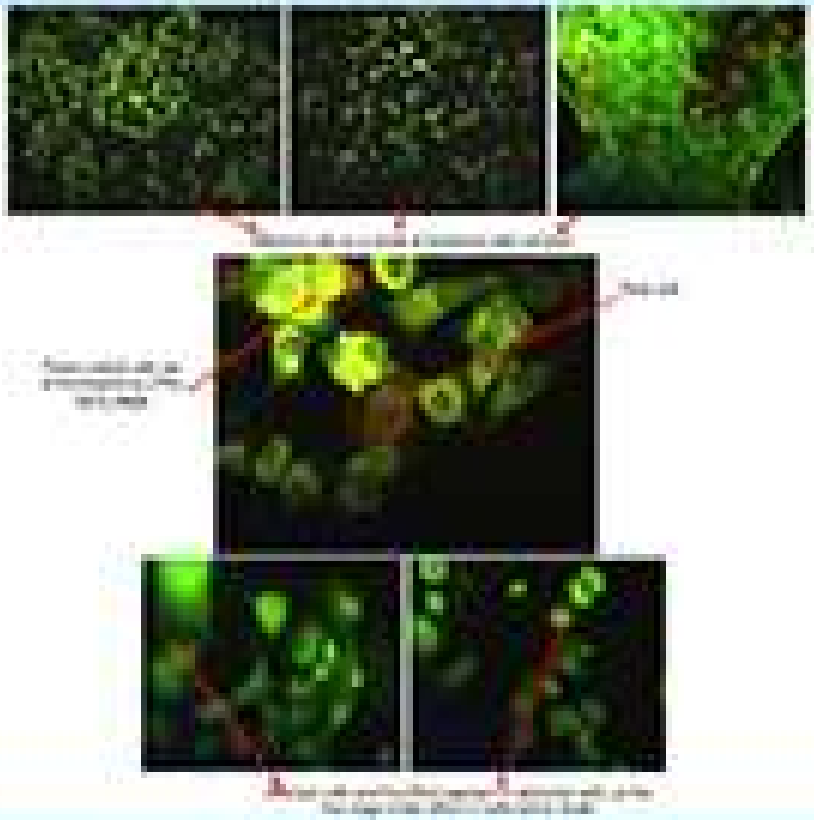

Accredited A (RISTEKDIKTI)
No. 30/E/KPT/2019

Indones. J. Chem | Vol. 22 | No. 4 | PP. 857-1162 | Yogyakarta August 2022 | (ISSN: 1411-9420 print / 2460-1578 online)

A Study on Factors Influencing the Hydrodistillation of *Triphasia trifolia* Essential Oil

Phuoc-Sang Huynh Ngo[1,2], Xuan-Cuong Luu[3], Minh-Thuan Huynh[4], Thien Hien Tran[5,6], Tan Phat Dao[5,6*], and Tien-Xuan Le[1,2]**

[1]*Department of Chemical Engineering, Ho Chi Minh City University of Technology (HCMUT), Ho Chi Minh City 700000, Vietnam*

[2]*Vietnam National University Ho Chi Minh City, Ho Chi Minh City 700000, Vietnam*

[3]*AOTA International Joint Stock Company, Ho Chi Minh City 700000, Vietnam*

[4]*Tan Ke High School, Ben Tre Province 86000, Vietnam*

[5]*Faculty of Food and Environmental Engineering, Nguyen Tat Thanh University, Ho Chi Minh City 700000, Vietnam*

[6]*Institute of Environmental Technology and Sustainable Development, Nguyen Tat Thanh University, Ho Chi Minh City 700000, Vietnam*

Corresponding author:

tel: 84-988889072[*]; +84-938369744[**]
email: dtphat@ntt.edu.vn[*]; tien.le@hcmut.edu.vn[**]

Received: November 22, 2021
Accepted: April 6, 2022

DOI: 10.22146/ijc.70646

Abstract: *The present study attempted to evaluate the suitable conditions for essential oil extraction from the fruit of* Triphasia trifolia *using hydrodistillation technique. The effect of various factors such as material size, solvent to solid ratio, heating temperature and distillation time, state of maturation, and fruit preservation on the oil yield was investigated. The physicochemical property, chemical composition, and biological properties were accessed. The highest yield of essential oil (7.9 mL/kg dry matter) from* T. trifolia *was obtained at optimal conditions such as fine particle size, solid to solvent ratio of 1:5, temperature oil bath of 140 °C, and distillation time of 3 h. The state of maturation of the fruits significantly affects the essential oil yield and insignificantly influences chemical composition based on the gas chromatography-mass spectrometry (GC-MS) analysis. It was found that the essential oil yield decreases significantly when ripened fruits are not kept in cool conditions before distillation. It implied that ripened fruits should be immediately processed or kept in cool storage to maintain the essential oil yield. Our findings will help produce high-quality essential oil from* T. trifolia *at a pilot or industrial scale.*

Keywords: Triphasia trifolia*; essential oil; hydrodistillation; GC-MS*

■ INTRODUCTION

Essential oil is a liquid containing volatile compounds extracted from leaves, peels, seeds, or other parts of plants and is widely used for various purposes [1-3]. Nowadays, essential oils are known as basic materials for food and pharmaceuticals worldwide. *Triphasia trifolia* (*T. trifolia*) has grown in many countries, including Vietnam. Its essential oil (EO) is a great source of antioxidants and medicinal properties such as vermicide and expectorant for diabetes [4-5].

T. trifolia fruit EO contains many medicinal compounds reported that immature fruit contains cryptoxanthin, α- and β-carotene that disappear on ripening [6]. In addition, fully ripe fruit contains pigments (e.g., triphasiaxanthin, semi-α-, semi-β- and β-carotenone). Rastogi et al. [7] reported that heraclenol, isomeranzing, and coumarins from *T. trifolia* have antimycobacterial activity against *M. kansaii* and *M. avium*. It was mentioned that essential oils from *T. trifolia* show comparable antioxidant potential as ascorbic acid. This EO has anti-inflammatory and anti-viral effects [8]. Moreover, at 0.2 μL/cm^2, the EO displayed repellency against *Tribolium castaneum* within 2-h exposure [9].

Hydrodistillation is the most common method to extract EO because of its simplicity in equipment and ease of operation [10]. The applicability of hydrodistillation can be done from laboratory to pilot scale and beyond to production scale, so this method is still being evaluated to this day [11-12]. Indeed, this method has been used to extract various aromatic plants such as lemongrass [13], lavender [14], mandarin [15], and grapefruit peels [16]. This method has been used to extract EO from the aerial parts of *T. trifolia* [9]. The results suggested many active compounds such as pinene, hexadecanoic acid, sabine, *p*-cymene, and *D*-limonene. Hydrodistillation was also used by Zoghbi et al. [17] to extract EO from *T. trifolia* stem, leaf, and fruit. Sabiene, β-pinene and γ-terpinene are considered the main components in all essential oils extracted from parts of *T. trifolia* cultivated in the State of Pará, Brazil.

To our best knowledge, the factors which affect the quality and yield of *T. trifolia* EO are not documented in the literature. Unique research related to *T. trifolia* EO from parts such as stem, leaf, and fruit in Brazil was reported [17]. However, the authors only analyzed the chemical composition, and the parameters related to the extraction process have not been mentioned. Therefore, this research aims to investigate these factors and evaluate the chemical composition of *T. trifolia* EO in Vietnam. Our results can help produce high-quality EO from *T. trifolia* fruits that forms the necessary database for extraction processes related to fruit *T. trifolia*.

■ EXPERIMENTAL SECTION

Materials

T. trifolia (Burm. f.) fruits were harvested in August 2018 from Ben Tre, Vietnam. A sample of fruits was selected, washed, and kept in a plastic bag in a cool room (15 °C). Anhydrous sodium sulfate (Na_2SO_4) was used to remove water from essential oils and purchased from Sigma Aldrich (US). Deionized water by Milli-Q purification system (Millipore) (Massachusetts, USA) was used as a solvent in the extraction process.

Instrumentation

Equipment used in the study included a distillation device with a volume of 1 L glass heat by thermal oil (110–160 °C). In addition, the unit was connected to a water-cooled condenser, Clevenger-type apparatus, and temperature sensor. The EOs were analyzed on a Shimadzu-QP2010 Plus system equipped with an Rtx 5MS fused capillary column (30 m × 0.25 mm; 0.25 μm film thickness). The brightness was determined through the Chromacolorimeter (NR60CP model) computer scanner.

Procedure

Essential oil distillation

Firstly, 1 kg of fruit in the ripe state was grounded into a flask with 600 mL of water and hydrodistilled using a Clevenger – type apparatus. The method of using thermal oil to transfer heat to the extraction process can accurately determine the temperature supplied to the system. The hydrodistillation operated at 155 °C until the amount of EO obtained was almost unchanged. The EO was obtained and dehydrated using anhydrous Na_2SO_4 of 5 g and subjected to GC-MS. The EO yield was expressed as mL/kg of the dry matter.

Determination of color change

The color change of the sample was determined using CIE Lab * color space as previously described by Nhi et al. [18]. The brightness was determined through the Chromacolorimeter (NR60CP model) computer scanner. Results are displayed in a numerical form via L* (lightness ranging from 0–100), a* (from green to red) and b* value (from blue to yellow).

Physicochemical properties of essential oils

The physicochemical properties of EOs, such as density, acid value, and saponification value, were carried out in the EO of a plant, which is used to determine the quality of essential oils extracted from plant parts [19].

GC-MS

The EOs were analyzed on a Shimadzu-QP2010 Plus system equipped with an Rtx 5MS fused capillary column. The following conditions were applied: helium as carrier gas with 36.5 cm/s of linear velocity, injector temperature of 250 °C, oven temperature program of 60–240 °C at 3 °C/min, electron energy of 70 eV, interface

temperature of 250 °C. Results were compared with MS library system NIST-98 and literature data [20].

■ RESULTS AND DISCUSSION

Effect of Material Size

The size of the materials is an important factor that affects the yield and quality of EO. In this experiment, *T. trifolia* fruits were grounded by different methods resulting in material sizes: fine, coarse, and raw material, as shown in Fig. 1.

As shown in Fig. 2, the material size influenced the extraction yield, which controls the mass transfer process. The most rapid extraction process was observed as coarse size (raw) materials were used. This may be explained by the difference in mass transfer capability and the possibility that some EO can be adsorbed on the fruit flesh. The smaller fruit size leads to a smaller intraparticle diffusion resistance due to shorter diffusion paths, thus enhancing the extraction rate [21]. However, when the particle size is reduced, the possibility that EO can bind to the fruit flesh increases, thus lowering the extraction rate. The fact that coarse size material is the most appropriate material for distillation results from the competition between two opposite trends as fruit size decreases. Hence, we chose coarse size as the optimized size for EO distillation, and this size is used in other experiments.

Effect of the Amount of Water Added

The amount of water added is considered an important factor in the extraction process. The more water was used for extraction, the greater the diffusivity of *T. trifolia* essential oil in the water achieved. If the amount of water is too large and the efficiency of EO collection increases insignificantly, it is inefficient, time-consuming, and has other energy costs. Therefore, it is necessary to determine the amount of water to be added appropriately for the most economical extraction process.

Various amounts of water were added to the system (0–600 mL/kg of fruit). It was observed from Fig. 3 that the amount of water added significantly affected the time

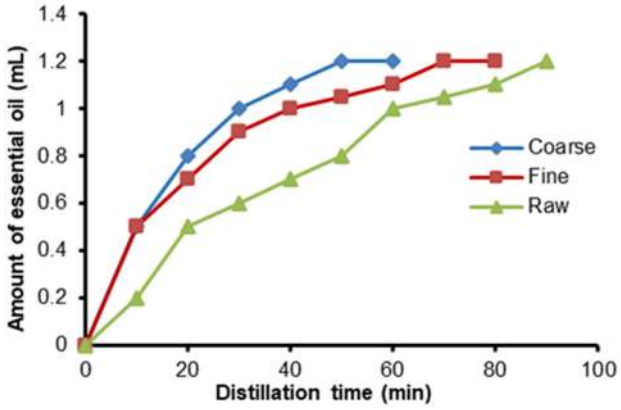

Fig 2. Effect of particle size on the EO yield

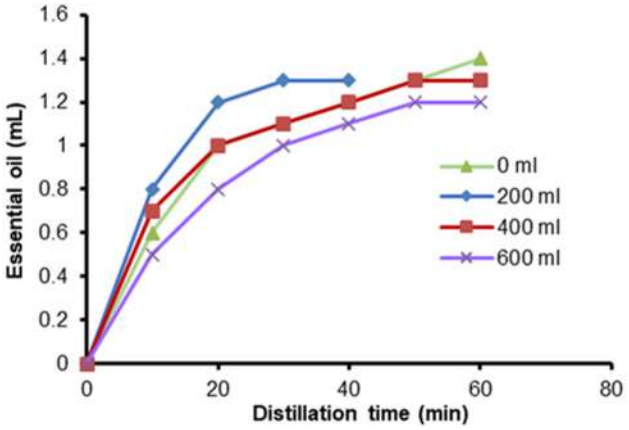

Fig 3. Effect of the amount of water added to the essential oil content

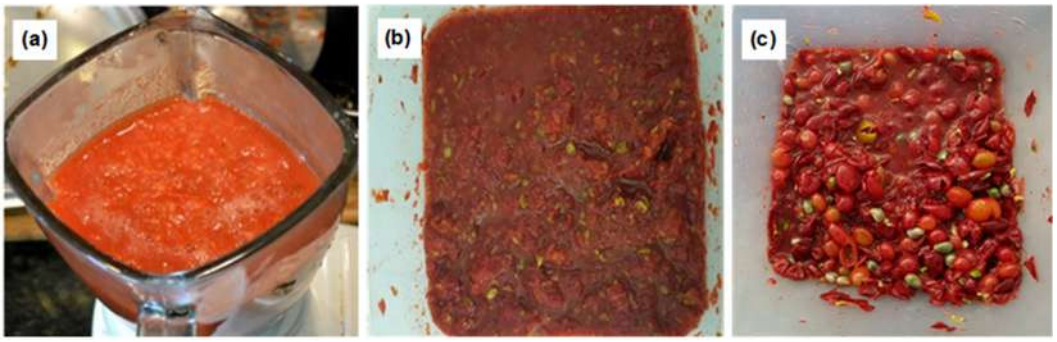

Fig 1. Various sample sizes were used in this experiment; (a) fine size; (b) coarse size; (c) raw material

of EO extraction process yet had little effect on the yield (Fig. 3). The highest amount of EO was obtained (1.4 mL/kg) when no water was added, followed by 1.2 mL/kg when 200 and 400 mL of water was added. In general, the yield of EO tended to decrease with the addition of more water, possibly due to the dissolution of the polar components in the essential oil. Besides, the hydrodistillation extraction process requires a covering of water to protect the raw materials exposed to high temperatures and limit thermal degradation [22]. Therefore, 200 mL of water was kept constant with the earlier problems while reducing extraction time by more than a third, which resulted in the highest energy costs for the extraction process. Based on the obtained results, 200 mL of water per kg of fruit was taken for the next experiment.

Effect of Oil Bath Temperature

Oil bath temperature has a significant effect on the yield. This factor is important since it affects the solubility, mass transfer rate of the solute in the material, and cavitation phenomenon. Fig. 4 demonstrates the influences of oil bath temperature on the EO yield. The amount of EO increased from 100 to 155 °C. At 100 °C, the lowest EO was obtained at 0.6 mL/kg. The temperature of 125 °C reached 1.2 mL/kg, and at the temperature of 140 °C obtained the maximum amount of 1.3 mL/kg. Indeed, low oil bath temperature would result in slight cavitation, thus minimizing the mass transfer. As a consequence, the obtained EO is negligible. As oil bath temperature increases, the effect of cavitation increases, together with the increased solubility of solutes in the solvent, leading to the rise in the amount of EO yield [20-21]. However, the excessive increase in oil bath temperature might enhance EO thermal degradation, which decreases the amount of obtained EO Besides, the short amount of extraction time can ensure the cost of the process and limit the oxidation of essential oils. Hence, 140 °C was chosen as the optimum temperature for hydrodistillation.

Effect of Fruit Ripening States

Various ripening stages of the fruits were considered. Fig. 5 shows the ripening stages of *T. trifolia* fruits. The fruits are characterized by measuring the color of the peels, and the values of L*, a*, and b* are shown in Table 1. We also presented the average weight of 20 species and the corresponding moisture content. The weight of the 20 species increases with the increase of the ripening stage. Therefore, the difference between the samples can be visually observed, and the Lab color value in Table 1 can make sample selection easy.

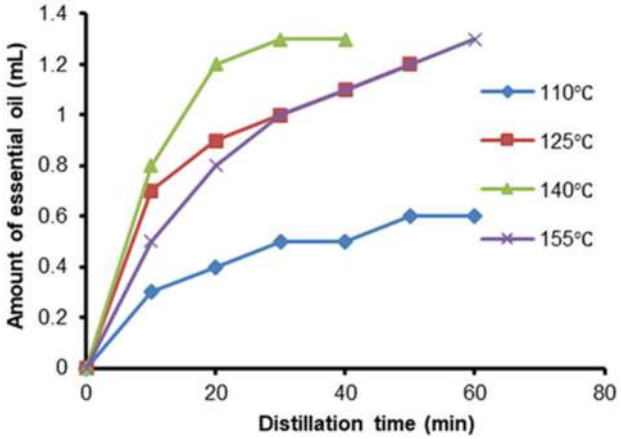

Fig 4. Variation of EO obtained as a function of time at various oil bath temperatures

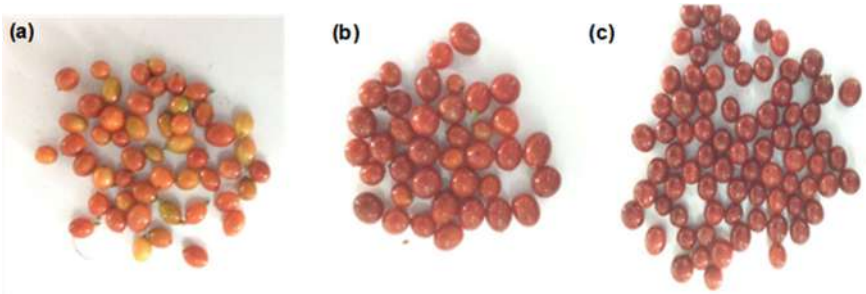

Fig 5. Image of *T. trifolia* fruits at different ripening stages. (a) Green stage, (b) Ripening stage, and (c) Fully ripened stage

Table 1. Color parameters of *T. trifolia* fruits at different ripening stages

	L*	a*	b*	Weight of 20 species (g)	Humidity (%)
Green stage	44.77	31.93	23.33	21.3246	83.63
	45.20	30.48	27.06		
	46.36	23.66	23.90		
	44.99	27.41	23.00		
	47.26	20.98	28.55		
Ripening state	39.48	29.17	18.27	24.3590	81.89
	37.44	26.67	12.33		
	37.31	29.46	14.53		
	37.25	26.49	12.36		
	39.28	29.17	15.22		
Ripe stage	31.24	21.29	7.33	36.3997	80.36
	31.66	22.06	7.41		
	31.02	21.06	6.60		
	32.23	21.49	7.81		
	32.24	21.12	7.92		

Based on Fig. 6, it can be seen that the amount of EO recovered gradually decreased with the maturity of *T. trifolia* fruits. In the samples of green, ripening, ripe fruits, the amount of EO obtained was 1.2, 1.3, and 1.5 mL/kg, respectively, and green fruit showed the highest value of essential oil. On the contrary, samples collected at maturities such as ripening and ripe fruits yielded lower EO This result is also reported in the study of Sedláková et al. [23], choosing the correct ripeness of the raw materials brings maximum economic efficiency.

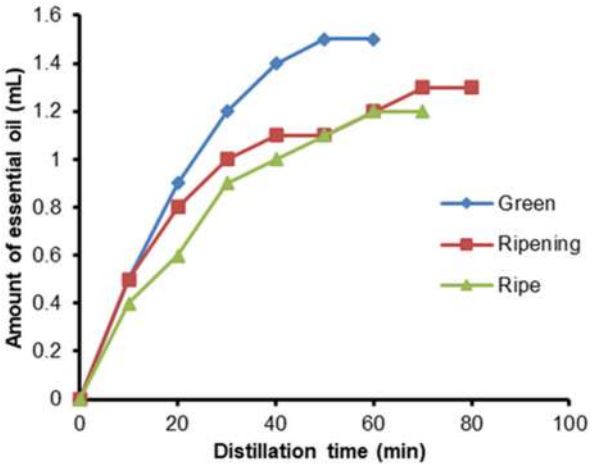

Fig 6. Effect of the ripening stage on the EO yield

Effect of Storage Time

Production of EO requires the storage of materials, and hence the condition of storage material plays a critical role in affecting EO's yield. The material was subjected to storage after collecting for 1, 2, and 3 days. As observed in Fig. 7, EO decreased from 1.2 to 0.8 mL/kg after 3 days of storage at 15 °C. It was shown that the EO yield ranked in order yield (1 day) > yield (2 days) > yield (3 days). This can be explained by the oil reservoir in the peels can be degraded and the volatile oil easily when exposed to the environment. Indeed, the fresh sample selected for evaluation was the best at all times. The same change was also found in the study of Zhang et al. [24]; the closest storage and harvesting time has a good effect on both the yield and quality of the EO.

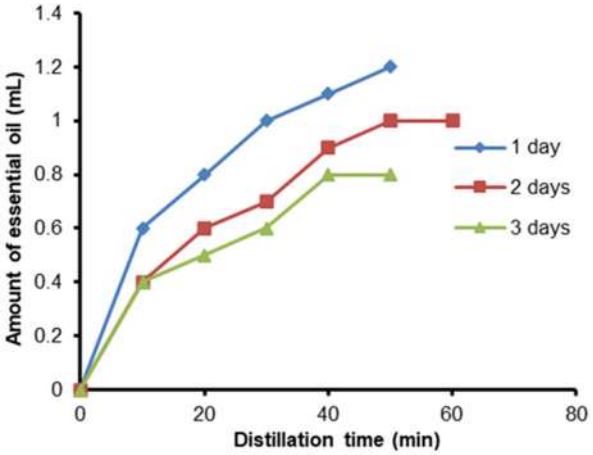

Fig 7. Yield of EO obtained at various storage conditions

Besides, extraction time is also considered an important criterion, and it was evaluated in parallel with the survey factors. Extraction time depends on many factors such as material size, amount of water added, and temperature. The longer the extraction time, the higher the recovered EO content. However, when the time is extended to a certain limit, the amount of EO obtained does not increase anymore and may adversely affect product quality [25]. On the other hand, the long extraction time consumes much energy for the heating process. Therefore, it is necessary to determine the appropriate extraction time.

Physicochemical Property and GC-MS Analysis

The EO sample was obtained at optimal conditions, such as green ripening, coarse size, 200 mL of water per kg of fresh fruit, and 140 °C, which was used to evaluate the physicochemical properties and GC-MS analysis of *T. trifolia* EOs.

The physicochemical characteristics of *T. trifolia* fruits EO such as density, acid value, and saponification value, were measured and presented in Table 2. These indexes depend on the extraction method and the freshness of the raw materials. With long-preserved raw materials, the acid index increases due to oxidation, the esters in EO are oxidized, and the ester in the EO is decomposed. The amount of free acid in the EO can be known from the acid number. A large soap index indicates that EOs have small molecular weight acids and vice versa. These results have not been compared because there are no official and published standardized reports on the characterization of *T. trifolia* fruits EO. For that reason, it is impossible to compare data on the density, acid value, and saponification value evaluated as EOs obtained by hydrodistillation in the southern region of Vietnam.

Eleven components were identified and quantitatively evaluated in the hydrodistillation extract from *T. Trifolia* fruits of different ripening states, representing more than 95% of the total EO (Table 3). Monoterpene hydrocarbons (more than 85%) predominated in all EO samples analyzed and reached maximum levels at full maturity. Oxygenated terpenoids were found to form from 7.166–7.750%, which was prominent in the green fruit stage and decreased equally in the other two states. Sesquiterpenes represent mainly in ripening fruit. The main components of *T. trifolia* fruits EO were found as sabinene (approximately 52.391–54.835%); D-limonene (5.534–8.342%), and γ-Terpinene (17.649–18.417%). The most found in the green fruit as sabinene (52.391%) and D-Limonene (8.342) were found the most.

Table 2. Physicochemical characteristics of *T. trifolia* fruits EO

Physicochemical characteristics	Results
Density at 25 °C (g/mL)	0.864–0.868
Acid value (mg KOH/g)	1.53
Saponification value (mg KOH/g)	30.70

Table 3. Chemical composition of the EO from *T. trifolia* obtained by hydrodistillation

Composition	Retention time (min)	Green (%)	Ripening (%)	Ripened (%)
a-Thujene	5.133	0.424	0.406	0.422
α-Pinene	5.377	2.371	2.463	2.596
Sabinene	6.568	52.391	55.372	54.835
α-Terpinene	7.774	1.992	1.608	1.875
p-Cymene	8.000	0.480	0.190	0.047
D-Limonene	8.197	8.342	7.464	5.534
γ-Terpinene	9.227	17.649	17.396	18.417
1-*p*-Menthene	10.210	1.985	1.870	2.029
Terpinen-4-ol	14.148	7.750	7.166	7.436
trans-α-Bergamotene	24.575	1.494	1.800	1.582
(E)-β-Farnesene	25.459	0.567	0.650	0.560

This result shows a slight similarity with the results reported by dos Santos et al. [26]; the chemical composition assessment was performed on both leaves and fruits of *T. trifolia*. The results showed that sabinene content accounted for the majority (37.2%), followed by β-pinene (23.95%) and γ-terpinene (16.3%) in the EO from the fruit, while the component in the leaves was sabinene (35.4%), and myrcene (34.1%). EOs of *T. trifolia* fruit and leaves have almost the same main composition and moderate antibacterial activity. In Brazil, Zoghbi et al. [17] analyzed volatile components of *T. trifolia* EO from plant parts by hydrodistillation extract. The EOs are characterized by high content of sabine (leaf: 31.1%, stem: 21.1%, fruit: 23.9%), and β-pinene (leaf: 40.8%, stem: 36.2%, fruit: 32.4%). It is worth mentioning that the chemical composition of a substance may vary with harvest time and geographical location [27].

Previously, sabinene exhibited strong to moderate antibacterial activity against gram-positive bacteria and anti-fungal activity against pathogenic fungi [28]. γ-Terpinene exhibits good antibacterial activity against many gram-negative and gram-positive bacteria [29]. Terpinen-4-ol has been previously reported to have potent antibacterial and anti-inflammatory properties. In addition, terpinen-4-ol was developed for the treatment of thrush in animals and for tissue healing applications [30].

■ CONCLUSION

This study considered various factors affecting *T. trifolia* EO obtained by hydrodistillation. It was found that the coarse size material, water to solid ratio of 200 mL/kg fresh fruit, and oil bath temperature at 140 °C were optimal values for EO distillation. The *T. trifolia* fruits should be used for distillation after harvesting. *T. trifolia* EO consists of many biologically active compounds such as sabinene, D-limonene, γ-terpinene, and terpinen-4-ol. Therefore, EOs have great potential to be applied in the food, pharmaceutical, and cosmetic fields because of their antioxidant properties equivalent to ascorbic acid.

■ ACKNOWLEDGMENTS

We acknowledge the support of time and facilities from Ho Chi Minh City University of Technology (HCMUT), VNU-HCM, and Notessen Co., LTD for this study.

■ AUTHOR CONTRIBUTIONS

Phuoc-Sang Huynh Ngo, Tien-Xuan Le conceived and designed the experiments; Xuan-Cuong Luu contributed reagents, materials, and analysis tools; Minh-Thuan Huynh, Thien Hien Tran, Tan Phat Dao analyzed and interpreted the data; Tan Phat Dao, Tien-Xuan Le revised the manuscript; Tan Phat Dao, Tien-Xuan Le wrote the paper, and Tan Phat Dao, Tien-Xuan Le performed the experiments. All authors agreed to the final version of this manuscript.

■ REFERENCES

[1] Dao, T.P., Do, H.T., Khoi, L.Q., Gia Phap, N.V.G., Cang, M.H., Pham, T.N., and Muoi, N.V., 2020, Evaluation of physico-chemical properties of lemongrass (*Cymbopogon citratus* L.) essential oil grown in Tien Giang Province, Vietnam, *Asian J. Chem.*, 32 (5), 1248-1250.

[2] Tran, T.H., Ha, L.K., Nguyen, D.C., Dao, T.P., Nhan, L.T.H., Nguyen, D.H., Nguyen, T.D., Vo, D.V.N., Tran, Q.T., and Bach, L.G., 2019, The study on extraction process and analysis of components in essential oils of black pepper (*Piper nigrum* L.) seeds harvested in Gia Lai Province, Vietnam, *Processes*, 7 (2), 56.

[3] Ngo, T.C.Q., Dao, T.P., Tran, T.H., Le, T.H.N., Pham, M.Q., Nguyen, N.H., and Tran, Q.T., 2020, Application of response surface methodology in the process of extracting essential oil from the calamondin (*Citrus microcarpa*) peels, *IOP Conf. Ser.: Mater. Sci. Eng.*, 736, 022062.

[4] Samoisy, A.K., and Mahomoodally, F., 2016, Ethnopharmacological appraisal of culturally important medicinal plants and polyherbal formulas used against communicable diseases in Rodrigues Island, *J. Ethnopharmacol.*, 194, 803–818.

[5] Gurib-Fakim, A., Sewraj, M., Gueho, J., and Dulloo, E., 1993, Medicalethnobotany of some weeds of Mauritius and Rodrigues, *J. Ethnopharmacol.*, 39 (3), 175–185.

[6] Yokoyama, H., and White, M.J., 1970, Carotenone formation in *Triphasia trifolia*, *Phytochemistry*, 9 (8), 1795–1797.

[7] Rastogi, N., Abaul, J., Goh, K., Devallois, A., Philogène, E., and Bourgeois, P., 1998, Antimycobacterial activity of chemically defined natural substances from the Caribbean flora in Guadeloupe, *FEMS Immunol. Med. Microbiol.*, 20 (4), 267–273.

[8] Curini, M., Cravotto, G., Epifano, F., and Giannone, G., 2006, Chemistry and biological activity of natural and synthetic prenyloxycoumarins, *Curr. Med. Chem.*, 13 (2), 199–222.

[9] Jaramillo Colorado, B.E., Martelo, I.P., and Duarte, E., 2012, Antioxidant and repellent activities of the essential oil from Colombian *Triphasia trifolia* (Burm. f.) P. Wilson, *J. Agric. Food Chem.*, 60 (25), 6364–6368.

[10] Zheljazkov, V.D., Astatkie, T., and Schlegel, V., 2014, Hydrodistillation extraction time effect on essential oil yield, composition, and bioactivity of coriander oil, *J. Oleo Sci.*, 63 (9), 857–865.

[11] Dao, P.T., Tran, N.Y.T., Tran, Q.N., Bach, G.L., and Lam, T.V., 2021, Kinetics of pilot-scale essential oil extraction from pomelo (*Citrus maxima*) peels: Comparison between linear and nonlinear models, *Alexandria Eng. J.*, 61 (3), 2564–2572.

[12] Tran, T.H., Ngo, T.T.Q., Tran, T.K.N., Lam, T.D., Dao, T.P., Linh, H.T.K., Ngoc, T.T.L., Quan, P.M., and Toan, T.Q., 2019, Manufacturing process for extracting essential oils from white pepper (*Piper nigrum* L.) by hydrodistillation technique, *Solid State Phenom.*, 298, 89-93.

[13] Mathialagan, R., Nour, A.H., Sulaiman, Z.A., Nour, A.H., and Raj, S.T., 2014, Comparison of essential oil of lemongrass (*Cymbopogon citratus*) extracted with microwave-assisted hydrodistillation (MAHD) and conventional hydrodistillation (HD) method, *Int. J. Chem. Eng. Appl.*, 5 (2), 104–108.

[14] Filly, A., Fabiano-Tixier, A.S., Louis, C., Fernandez, X., and Chemat, F., 2016, Water as a green solvent combined with different techniques for extraction of essential oil from lavender flowers, *C. R. Chim.*, 19 (6), 707–717.

[15] Dao, T.P., Quyen, N.T.C., Nhi, T.T.Y., Nguyen, C.C., Nguyen, T.T., and Le, X.T., 2021, Response surface methodology for optimization studies of hydrodistillation of essential oil from pixie mandarin (*Citrus reticulata* Blanco) peels, *Pol. J. Chem. Technol.*, 23 (4), 26–34.

[16] Manaila, E., Berechet, M.D., Stelescu, M., Craciun, G., Mihaiescu, D.E., Purcareanu, B., Calinescu, I., Fudulu, A., and Radu, M., 2016, Comparation between chemical compositions of some essential oils obtained by hydrodistillation from citrus peels, *Rev. Chim.*, 67 (1), 106–112.

[17] Zoghbi, M., and Andrade, E., 2009, Chemical composition of the leaf, stem and fruit essential oils from *Triphasia trifolia* (Burm. f.) P. Wilson cultivated in North of Brazil, *J. Essent. Oil Bear. Plants*, 12 (1), 81–86.

[18] Nhi, T.T.Y., Vu, N.D., Quyen, N.N., Thinh, P.V., Tho, N.T.M., and Truc, T.T., 2020, The effect of malt, pectin, and gelatin concentrations on elasticity, color and sensory evaluation of soursop (*Annona muricata* L.) jelly candy, *IOP Conf. Ser.: Mater. Sci. Eng.*, 991 (1), 012013.

[19] Hagos, Z., Mulugeta, A., Gopalakrishnan, V.K., Chaithanya K.K., and Nagaraju, B., 2017, Chemical composition and physicochemical properties of essential oil from *Myrtus communis*, *Int. J. Pharm. Clin. Res.*, 9 (6), 439–443.

[20] Dao, T.P., Do, H.T., Le, Q.K., Gia Phap, N.V., Bach, L.G., Muoi, N.V., Cang, M.H., 2020, Kinetic studies on extraction of essential oil from lemongrass leaves (*Cymbopogon citratus*) by steam distillation industrial scale, *Asian J. Chem.*, 32 (6), 1399–1403.

[21] Phat, D.T., Tuyen, K.C., Huynh, X.P., and Truc, T.T., 2020, Extraction process optimization and characterization of the pomelo (*Citrus grandis* L.) peel essential oils grown in Tien Giang Province, Vietnam, *Nat. Volatiles Essent. Oils*, 7 (4), 26–33.

[22] Dao, T.P., Tran, N.Q., Tran, T.T., and Lam, V.T., 2022, Assessing the kinetic model on extraction of essential oil and chemical composition from lemon peels (*Citrus aurantifolia*) by hydro-distillation process, *Mater. Today: Proc.*, 51 (1), 172–177.

[23] Sedláková, J., Kocourková, B., Lojková, L., and Kubáň, V., 2011, The essential oil content in caraway species (*Carum carvi* L.), *Hortic. Sci.*, 30 (2), 73-79.

[24] Zhang, T., Yang, H., Wen, S., Qiu, F., and Liu, X., 2019, Effects of harvest season and storage time on the essential oil of the linalool chemotype of *Cinnamomum camphora*, *J. Essent. Oil-Bear. Plants*, 22 (5), 1379-1385.

[25] Tran, T.H., Ngo, T.C.Q., Dao, T.P., Nguyen, P.T.N., Pham, T.N., Le, X.T., Vo, D.M.H., Minh, P.T.H., and Linh, H.T.K., 2020, Effect of microwaves energy on volatile compounds in pepper (*Piper nigrum* L.) leaves essential oil, *IOP Conf. Ser.: Mater. Sci. Eng.*, 736, 032013.

[26] dos Santos, R.P., Trevisan, M.T.S., Silveira, E.R., and Pessoa, O.D.L., and Melo, V.M.M., 2008, Composição química e atividade biológica das folhas e frutos de *Triphasia trifolia*, *Quim. Nova*, 31 (1), 53–58.

[27] Dao, T.P., Nguyen, T.V., Tran, T.Y.N., Le, X.T., An, T.N.T., Anh, N.H.T., and Bach, L.G., 2021, Central composite design, kinetic model, thermodynamics, and chemical composition of pomelo (*Citrus Maxima* (Burm.) Merr.) essential oil extraction by steam distillation, *Processes*, 9 (11), 2075.

[28] Arunkumar, R., Nair, S.A., Rameshumar, K.B., and Subramoniam, A., 2014, The essential oil constituents of *Zornia diphylla* (L.) Pers, and anti-inflammatory and antimicrobial activities of the oil, *Rec. Nat. Prod.*, 8 (4), 385–393.

[29] Anwar, S., Ahmed, N., Al Awwad, N., Ansari, S.Y., and Wagih, M.E., 2016, "Myrtle (*Myrtus communis* L.) Oils" in *Essential Oils in Food Preservation, Flavor and Safety*, Eds. Preedy, V.R., Academic Press, San Diego, US, 581-592.

[30] Ezzat, S.M., El Bishbishy, M.H., El Kersh, D.M., Zayed, A., Salem, M.A., and Salama, M.M., 2021, "Herbal Cosmeticology" in *Preparation of Phytopharmaceuticals for the Management of Disorders*, Eds. Egbuna, C., Mishra, A.P., and Goyal, M.R., Academic Press, San Diego, US, 129-168.

Performance of a Hybrid Catalyst from Amine Groups and Nickel Nanoparticles Immobilized on Lapindo Mud in Selective Production of Bio-hydrocarbons

Wega Trisunaryanti*, Salma Nur Azizah, Dyah Ayu Fatmawati, Triyono Triyono, and Novia Cahya Ningrum

Department of Chemistry, Faculty of Mathematics and Natural Sciences, Universitas Gadjah Mada, Sekip Utara, Yogyakarta 55281, Indonesia

* ***Corresponding author:***

email: wegats@ugm.ac.id

Received: November 23, 2021
Accepted: March 15, 2022

DOI: 10.22146/ijc.70667

Abstract: *In the present work, optimum conditions for hydrocracking of waste palm cooking oil (WPCO) over a Ni-NH_2/Lapindo mud catalyst were studied to obtain a high quantity and quality of biofuel. The utilized catalyst support material was Lapindo mud (LM) from Sidoarjo, Indonesia, which was only given physical treatment (i.e., washing, drying, grinding, and calcining). Ni/LM was prepared via wet impregnation in three different Ni weight loadings: 1, 5, and 10 wt.%, which were denoted as Ni(A)/LM, Ni(B)/LM, and Ni(C)/LM, respectively. As a result, the hydrocracking test of WPCO under the temperature of 470 °C and a feed/catalyst weight ratio of 50 showed that the Ni(A)/LM catalyst produced the highest liquid product reaching 46.65 wt.% among the other Ni-based catalysts. The liquid product can be increased drastically to 63.93 wt.% under a more optimum temperature at 550 °C. Functionalization of Ni(A)/LM as the best catalyst was carried out by grafting method with NH_2 groups from 3-APTMS, resulting in Ni(A)-NH_2/LM. This modification increased the liquid product to 68.17 wt.% under hydrocracking conditions using a weight ratio of 75. Moreover, the reusability of Ni(A)-NH_2/LM was found to be effective for three hydrocracking runs, constantly yielding an average biofuel of 80 wt.%.*

Keywords: *hydrocracking; Lapindo mud; nickel; 3-APTMS; waste palm cooking oil*

■ INTRODUCTION

The Lapindo mud (LM) flow disaster that occurred in 2006 in Porong, Sidoarjo, East Java, Indonesia, has not shown any improvement until now. One of the efforts to increase the use-value of LM is to convert it into a functional material. Based on research conducted by Kusumastuti et al. [1] stated that the LM consists of 49.24 wt.% Si, 19.30 wt.% Al, 14.06 wt.% Fe, and several elements in low quantities. This indicates that the LM is a potential source for the synthesis of silica-based materials. Among inorganic structures, silica (SiO_2) has been intensely studied for potential applications in catalysis, biological, biomedicine, etc., due to its abundance and simple synthesis method [2]. It is well-known that silica is intensively used in industry, indicating that it has low toxicity and is safe [3]. Some of the materials that have been successfully made using silica include Mobil Composition of Matter No. 41 (MCM-41), Santa Barbara Amorphous-15 (SBA-15), and mesoporous silica (MS). Mesoporous structures are characterized by having a large specific surface area and pores with diameters between 2 and 50 nm [4]. Mesoporous silica gained a raised interest, due to its extensive multi-functionality, based on its high specific surface area, uniform and tunable pore size, high pore volume, and facile functionalization [5]. Although mesoporous silica has advantages in terms of material characteristics and performance, synthesis methods involving many materials and complicated procedures limit its availability on an industrial scale [6]. Thus, we use the LM material directly as a natural catalyst support material without additional chemicals through easy initial preparation such as washing, drying, grinding, and calcining for removing volatile substances,

oxidizing a portion of the mass, or rendering them friable. This procedure has been done before by Trisunaryanti et al. [7], which utilizes beach sand with the main content of 43.09 wt.% Si, 12.91 wt.% Al, and 31.75 wt.% Fe as catalyst carrier materials. Although the material has a low specific surface area of 15.6 m^2/g, the overall catalyst is capable of producing 66.86 wt.% hydrocarbons, which is higher than using mesoporous silica as a catalyst carrier of 64.44 wt.%. This evidence allows that LM has tremendous potential as a catalyst support material as well as beach sand.

Supported nickel catalysts have attracted significant attention for their extensive applications in various industrial processes. During biomass conversion, nickel-based catalysts upgrade the composition of the liquid phase. Nickel metal has a relatively low price and a fairly high hydrogenation activity. In addition, the use of Ni metal as a catalyst can provide a high level of acidity from vacant p orbital [8]. This metal can increase catalytic activity and selectivity toward deoxygenated products [9]. The presence of incompleted orbitals in nickel metal can also play a good role in catalytic reactions and can homolytically break hydrogen gas in the hydrocracking process [1]. Jang et al. [10] have modified mesoporous silica with nickel-metal as a catalyst for hydrodeoxygenation and studied the effect of pore size and structure. The results of this study indicate that a high nickel content can reduce the surface area and pore volume of the silica support but does not affect the mesoporous structure. Paramesti et al. [11] have successfully tested the activity and selectivity of the Ni/MS catalyst against hydrocracking of waste cooking oil (WCO) into hydrocarbon compounds with variations in Ni concentration of 4%, 6%, and 8% (w/w). The results showed that the catalyst activity of Ni(4)/MS reached 80.57 wt.% and was more selective towards the formation of C_5-C_{12} chain hydrocarbon compounds of 54.22 wt.%.

The addition of the amine functional groups of 3-APTMS (3-Aminopropyltrimethoxysilane) to the surface of the silica support provides a Lewis base site derived from the electrons in the NH_2 groups [12]. This allows the groups to interact frequently with the acidic function in the feed compound, leading to more optimal free fatty acid (FFA) adsorption on the catalyst surface [13]. Interestingly, performing the reaction using a physical mixture of AP-MSN (AminoPropyl-Mesoporous Silica Nanoparticles) sorbent and Ni-MSN catalyst led to only 9 wt.% hydrocarbon yield compared to the 72 wt.% of hydrocarbons obtained using the hybrid AP-Ni-MSN as a catalyst [14]. The previous study also stated that the addition of amine groups to Ni-MS could increase the content of hydrocracking waste coconut oil from 47.7 to 68.8 wt.% and reduce FFA levels from 19.4 to 7.3 wt.%. This is due to the synergistic performance of the bifunctional adsorbent-catalytic nanoparticle material in converting FFA into hydrocarbons [8].

Today, the main energy source used in various countries is petroleum. Extensive and prolonged exploitation causes petroleum reserves to decrease. Among various refined petroleum products, gasoline and diesel are the fuels that are classified as the most widely used in transportation equipment [15]. Considering the importance of its use and availability, various efforts have been made to find alternative energy to replace these fuels. An alternative fuel that is currently very promising as a substitute for petroleum is palm oil [16]. But unfortunately, palm oil has the property of being easily oxidized because it contains fatty acids [17]. Direct use of palm oil can cause engine damage because the combustion products form deposits on the engine injector pipe and excess smoke [18]. In addition, palm oil also has a higher viscosity than petroleum [19]. From an economic point of view, direct use of palm oil is also less profitable because it will interfere with food security. Therefore, the conversion of waste palm cooking oil (WPCO) into biofuel is necessary so that it can be used as fuel without compromising food security. WPCO from the food industry and households is quite widely available in Indonesia. WPCO is harmful to health if reused for cooking because it contains a lot of FFA and radicals [20]. In addition, biofuels derived from vegetable oil are renewable fuels, easy to process, relatively stable in price, do not produce pollutants that are harmful to the environment (non-toxic), and are easily biodegradable [21].

The conversion of WPCO into biofuel is generally carried out through the hydrocracking method. This

method is a combination of thermal cracking and catalytic cracking involving the presence of hydrogen gas and catalyst material [22]. Activity, selectivity, stability, and product quality are the four keys to measuring the performance of hydrocracking catalysts [23]. Hydrocracking catalysts usually contain cracking sites from the support material such as silica, alumina, or zeolite, whereas hydrogenation sites are provided by the catalyst metal having d orbitals with unpaired electrons such as Pt, Pd, Co, Ni, Mo, etc. [24]. However, in this study, we involve the addition of amine groups that functions as an adsorption site of FFA in the feed so that the catalyst performance will be more optimal.

In this work, hydrocracking of WPCO will be carried out in the presence of a Ni-NH_2 catalyst prepared in LM as a support material. It is not only done to increase catalytic activity in producing hydrocarbon-based fuels but also on the use of natural sources to provide supporting materials with high availability and environmentally friendly. This LM will be used without any extraction process using chemicals that are harmful to the environment but only involve a simple physical process. Nickel metal deposited in the mud will be investigated through variations in loading weight where the most optimal loading weight in character and performance will be selected for functionalization using the amine groups of the 3-APTMS compound as represented in Fig. 1. The hydrocracking study on WPCO will be evaluated further through variations in the process temperature, feed/catalyst weight ratio, and reusability. Finally, the performance of each catalyst will be measured from the produced biofuel and their selectivity towards the gasoline and diesel fractions.

■ EXPERIMENTAL SECTION

Materials

The materials used in this study were Lapindo mud from Sidoarjo regency, East Java, Indonesia, as a source of catalyst support material, $NiCl_2{\cdot}6H_2O$ as Ni salt precursor (p.a) from Merck & Co, 3-APTMS (3-Aminopropyltrimethoxysilane, 97%) from Tokyo Chemical Industry, N_2 and H_2 gasses from PT. Samator Gas Industry, toluene (99.9%) and methanol (99.9%) from Merck & Co, distilled water, and waste palm cooking oil (WPCO) as feed in the hydrocracking reaction was collected from household waste.

Instrumentation

X-Ray Fluorescence spectrometer (XRF, analytical MiniPal 4) was used to determine the amount of metal/metal oxide in the material, X-Ray Diffractometer (XRD, Philips X'Pert MPD) was applied to identify the crystallinity of the material, Fourier-Transform Infrared Spectrometer (FT-IR, Shimadzu IRPrestige-21) was

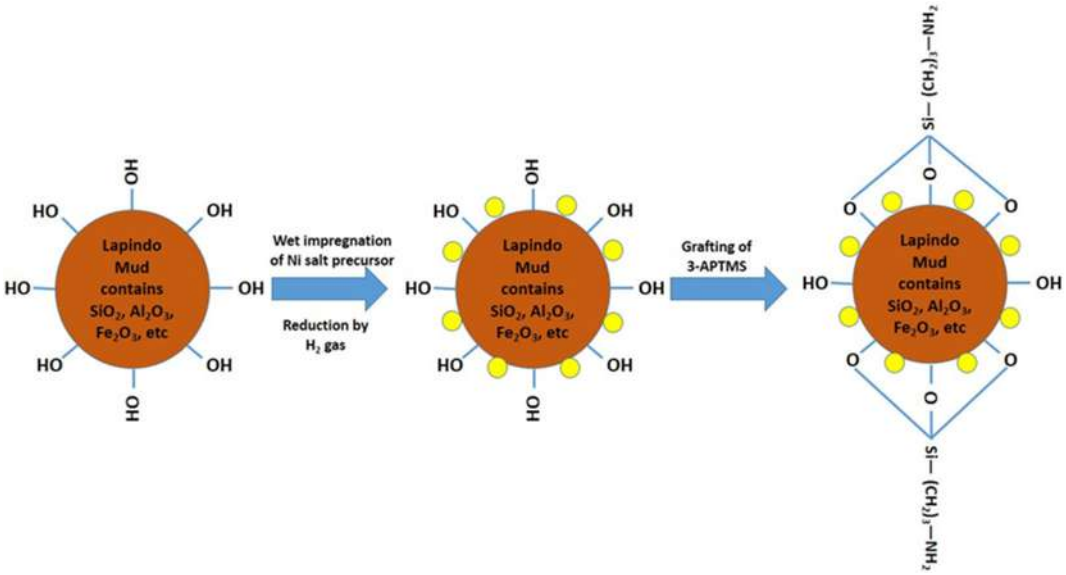

Fig 1. Diagrammatic representation of amine-grafted nickel/Lapindo mud material

utilized to analyze the characteristic functional groups in the material, Surface Area Analyzer (SAA, Quantachrome NOVAtouch 4LX) was used to observe the surface morphology of the material, and Transmission Electron Microscopy (JEOL JEM-1400 TEM) was utilized to characterize the nanostructure morphology of the material.

Procedure

Preparation of Lapindo mud as catalyst support material

First, Lapindo mud was washed with distilled water, then dried in an oven at 100 °C for 2 h. Next, the dried Lapindo mud was ground into fine particles until its size of 100 mesh. The sieved Lapindo mud was later called LM. After that, LM was calcined at a temperature of 500 °C, which is then called calcined Lapindo mud (CLM).

Preparation of Ni/Lapindo mud catalyst with various weight loadings of Ni metal

The nickel deposition process on the LM material was carried out by wet impregnation using $NiCl_2{\cdot}6H_2O$ as a salt precursor. First, 2 g of LM were put into a beaker and then suspended in 20 mL of distilled water. After that, Ni salt precursor with variations in Ni weight loading of 1, 5, and 10 wt.% to LM was added into the beaker. The mixture was stirred until homogeneous for 24 h at room temperature. The solution was directly evaporated and dried in an oven at 100 °C for 24 h. Afterward, the solid was calcined using N_2 gas at a flow rate of 20 mL/min at 500 °C for 3 h, followed by a reduction process using H_2 gas at the same condition to prepare zero valences of Ni metal. The resulting materials were then denoted as Ni(A)/LM, Ni(B)/LM, and Ni(C)/LM. Ni/LM catalyst with the highest total acidity value will be selected to be functionalized with NH_2 groups derived from 3-APTMS.

Functionalization of Ni/Lapindo mud with NH_2 groups originated from 3-APTMS

Modification of Ni/LM using 3-APTMS was carried out through the grafting method. Ni/LM was put into a flask and then injected with 3-APTMS until all surfaces became wet, then 20 mL of toluene was added. The mixture was refluxed for 6 h at 90 °C. The solids formed were separated from the solvent by centrifugation at 2000 rpm for 20 min. The sample was washed with methanol and then dried overnight at 80 °C.

Catalytic activity test through the hydrocracking process of waste palm cooking oil

Hydrocracking was applied by placing 0.1 g of each material as the catalyst and 5 g of waste palm cooking oil (WPCO) as feed in the column, then flowing hydrogen gas with a flow rate of 20 mL/min for 120 min at a temperature of 470 °C. The schematic illustration of the hydrocracking reactor can be seen in Fig. 2. The hydrocracking study was carried out through variations in process temperature, feed/catalyst weight ratio, and reusability test. The hydrocracking liquid product was then weighed to determine the activity of the catalyst. Meanwhile, Gas Chromatography-Mass Spectrometry (GC-MS, Shimadzu QP2010S) analysis was conducted to determine the selectivity of the catalyst to convert the feed into hydrocarbon compounds. The percentage conversion of hydrocracking products was estimated by the following calculations:

$$\text{Liquid (wt.\%)} = \frac{(\text{final flask weight} - \text{empty flask weight})}{\text{feed weight}} \times 100\% \quad (1)$$

$$\text{Coke (wt.\%)} = \frac{(\text{final catalyst container weight} - \text{initial catalyst container weight})}{\text{feed weight}} \times 100\% \quad (2)$$

$$\text{Residue (wt.\%)} = \frac{(\text{final feed container weight} - \text{empty container weight})}{\text{feed weight}} \times 100\% \quad (3)$$

$$\text{Gas (wt.\%)} = 100\% - (\text{Liquid} + \text{Coke} + \text{Residue}) \quad (4)$$

Based on the GC-MS analysis of the resulted hydrocracking liquid product, the selectivity of the catalyst was classified into four compound distributions, including gasoline (consisting of C_5-C_{12} chain hydrocarbon compounds), diesel (consisting of C_{13}-C_{20} chain hydrocarbon compounds), alcohol, and other oxygenates. The percentage of compound distributions in the liquid product can be determined by the following calculations:

$$\text{Gasoline (wt.\%)} = \frac{\text{GC area of C5} - \text{C12 compounds}}{\text{Total GC area}} \times \text{Liquid (wt.\%)} \quad (5)$$

$$\text{Diesel (wt.\%)} = \frac{\text{GC area of C13} - \text{C20 compounds}}{\text{Total GC area}} \times \text{Liquid (wt.\%)} \quad (6)$$

$$\text{Alcohol (wt.\%)} = \frac{\text{GC of alcohol compounds}}{\text{Total GC area}} \times \text{Liquid (wt.\%)} \quad (7)$$

$$\text{Others (wt.\%)} = \text{Liquid} - (\text{Gasoline} + \text{Diesel} + \text{Alcohol})\text{(wt.\%)} \quad (8)$$

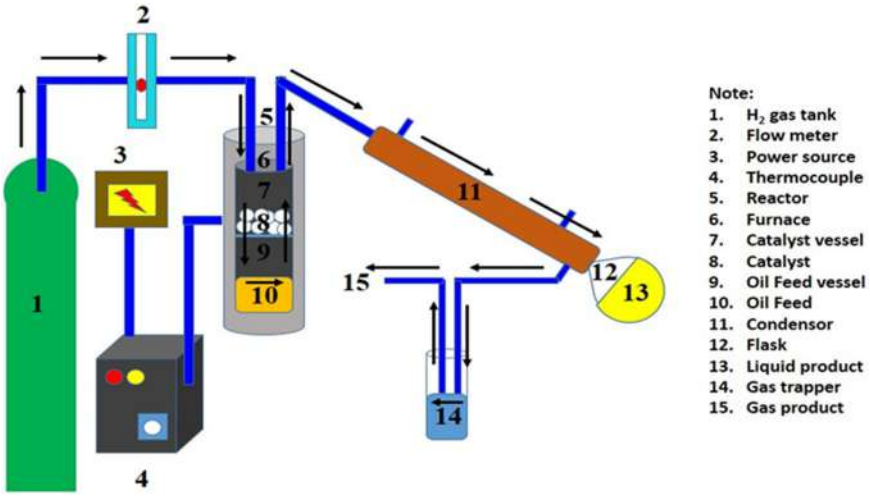

Fig 2. Schematic illustration of the hydrocracking reactor

■ RESULTS AND DISCUSSION

Catalysts Characterization

This research utilizes the catalyst carrier material in the form of mud from Porong, Sidoarjo. The XRF analysis results in Table 1 show the differences in the content of the main metal oxides between LM and CLM, namely silica, alumina, and iron oxides. According to Khoiri et al. [25], the silica and alumina contained in the mud can be used as catalyst support materials. From Table 1, it can be concluded that LM has more potential to be applied as a catalyst support material because it has a higher silica and alumina content than CLM. In addition, like other transition metals, the content of Fe_2O_3 also plays an important role in the hydrocracking process because the element Fe has a hydrogenation site as well as a Lewis acid site.

The impregnation of nickel-metal catalyst into the support material is carried out using the wet impregnation method with variations in the Ni weight loading on the LM support material by 1, 5, and 10 wt.%. The metal content itself plays an important role in the catalyst system because the presence of metal can contribute greatly to the Lewis acid site in the catalyst, where this active site affects the hydrocracking process. Based on the results of XRF analysis on the three catalysts, the nickel content of Ni(A)/LM, Ni(B)/LM, and Ni(C)/LM was 2.0, 6.9, and 17.5 wt.%, respectively. This difference in metal loading may be due to the oxidation state of Ni (x value) in the precursor salt $Ni(NO_3)_x{\cdot}6H_2O$ changes with storage time. Meanwhile, the calculation follows the x value listed on the packaging label.

Table 1. XRF analysis results on LM and CLM

Compound	wt.% content in LM	wt.% content in CLM
SiO_2	41.16	39.09
Fe_2O_3	18.24	19.24
Al_2O_3	12.84	12.22

The acidity test of the material was carried out using the gravimetric method, which compared the weight of the material before and after the adsorption of pyridine (C_5H_5N). This measurement is based on the amount of pyridine gas adsorbed by the material. Pyridine acts as a Lewis base having a lone pair of electrons on the N atom and as a Bronsted base accepting a proton to form a pyridinium ion ($C_5H_6N^+$).

Based on Table 2, it was found that the acidity of the mud decreased from 0.3533 to 0.2002 mmol/g after the calcination process. This is because the compounds that contribute to the acidity value are Al_2O_3, SiO_2, and Fe_2O_3. Looking back at the XRF results on the CLM, it revealed that the acidity value also decreased following the content of silica and alumina oxides. Here, because of the effect of high temperature on calcination, the iron oxide increases due to an increase in crystallinity. A 1% increase, on the other hand, indicates that the number has not changed considerably. This is the reason for choosing LM as a support material for the Ni catalyst in

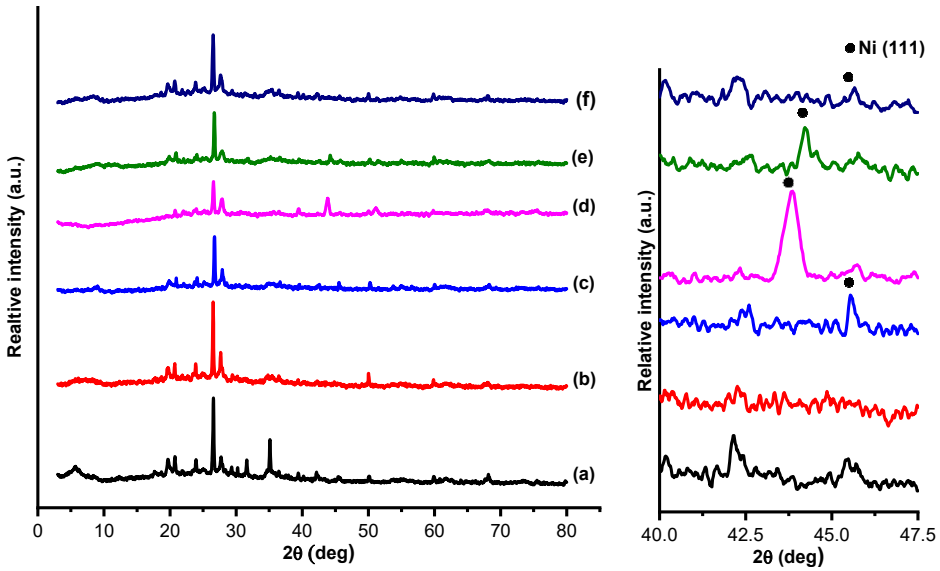

Fig 3. Diffractogram of (a) LM, (b) CLM, (c) Ni(A)/LM, (d) Ni(B)/LM, (e) Ni(C)/LM, (f) Ni(A)-NH_2/LM

Table 2. Acidity value of the materials

Material	Acidity (mmol/g)
LM	0.3533
CLM	0.2002
Ni(A)/LM	0.4087
Ni(B)/LM	0.0758
Ni(C)/LM	0.1517
Ni(A)-NH_2/LM	0.2289

Notes: acidity test was gravimetrically done to calculate the acid sites in the material using pyridine as a base adsorbate

the wet impregnation process.

The acidity test on this catalyst aims to see the contribution of the presence of nickel-metal that has been deposited on the LM material. Nickel metal is a transition metal group with an empty 4p electron orbital where this orbital acts as a Lewis acid site. Therefore, the presence of Lewis acid sites is expected to increase the acidity of the catalyst. Based on Table 2, Ni(A)/LM catalyst has the highest acidity compared to Ni(B)/LM and Ni(C)/LM catalysts. In fact, this is contrary to the theory that acidity increases with metal content. However, in another theory, the low metal content tends to make the nanoparticles evenly distributed on the surface of the supporting material. The non-closure of pores by nanoparticles also results in more optimal pyridine adsorption so that the acidity increases. According to Nugrahaningtya et al. [26], the presence of an increasing amount of metal loading makes the pores in the carrier material unable to adsorb due to steric resistance. In addition, an increase in Ni metal can cover the catalyst cavity, causing the Lewis acid site to be closed due to agglomeration. The agglomeration that occurs makes the acidity of the catalyst decrease, as happened in the Ni(B)/LM and Ni(C)/LM catalysts. But in this case, the higher acidity of catalyst Ni(C)/LM than Ni(B)/LM implies that the theory of the amount of metal content is stronger than the theory of metal distribution. Based on the acidity values of the three catalysts, Ni(A)/LM was chosen as the material to be grafted by the NH_2 groups of 3-APTMS. Meanwhile, after the acidity test was carried out on the material, the Ni(A)-NH_2/LM catalyst had a lower acidity than Ni(A)/LM. This is due to the presence of aminopropyl groups, which tend to be base.

XRD analysis was performed to evaluate the crystallinity character of the material. The type of compound or element can be seen from the peak that appears at the diffraction angle (2θ), while the crystallinity level of the catalyst can be seen from the peak intensity. The compilation of the diffractogram in Fig. 3 shows that all types of materials produce crystal peaks in the 2θ region between 20° to 40°. Similar results were obtained from other studies conducted by Kefaifi et al. [27]. In their research, it was revealed that these peaks are characteristic peaks of the element silicon in

the form of SiO_2 minerals. Meanwhile, the diffractogram of this study shows 2θ at 26.59° with an intensity of 100%, which is a type of quartz mineral SiO_2 with d-spacing 101 = 3.35 nm based on ICDD data 01-083-0539. In addition, the presence of alumina in the form of $AlPO_4$ (aluminum phosphate) in XRD spectra is shown at the peak of 2θ = 26.49°, which has an intensity of 100% with d-spacing 012 = 3.36 nm based on data on ICDD 01-084-0853. These peaks do not appear in the spectra because they are in a region similar to silica which allows overlapping. However, the presence of alumina compounds has been identified in the XRF data as well as silica.

Based on Fig. 3, it can be seen that after calcination, most of the crystalline peaks in LM experienced a decrease in intensity, as seen in the CLM, Ni(A)/LM, Ni(B)/LM, Ni(C)/LM, and Ni(A)-NH_2/LM spectra. In addition, the peak at 36.48° of the 110 crystal plane (based on data on ICDD 01-083-0539) in the LM disappeared after calcination. This is because the calcination process aims to form oxide compounds, rearrange the content of compounds in the material, and evaporate volatile compounds that can affect the structure of the material.

The presence of nickel-metal character in the diffractograms is indicated by crystal peaks that appear at 2θ of around 43–45° based on JCPDS no. 02-0850. The size of the Ni crystallite in the catalyst material can be calculated using the Scherrer equation as follows:

$$D = \frac{0.9\lambda}{\beta \cos\theta}$$

where D is the crystal size in nanoparticles (nm), β is full width at half maximum (FWHM, radian), θ is Braggs angle (radian), and λ is X-ray wavelength (λ = 1.54 nm for Cu Kα radiation). According to the equation, it is formulated that FWHM is inversely proportional to the crystallite size (D), so larger peaks result in smaller crystallite sizes. From the calculation results, the crystallite sizes for Ni(A)/LM, Ni(B)/LM, and Ni(C)/LM catalysts were 57.17, 18.15, and 33.65 nm, respectively. Meanwhile, the Ni(A)-NH_2/LM catalyst has a nickel crystallite size of 48.04 nm. This value is similar to that of the Ni(A)/LM catalyst, which indicates that the NH_2 grafting of 3-APTMS does not affect the crystallinity properties of the Ni(A)/LM catalyst. The large crystallite size is possible from a combination of smaller nanoparticles that agglomerate to form larger nanoparticles. Furthermore, although there is a trend, agglomeration is not always associated with high metal content. Agglomeration causes the nanoparticles to be unevenly distributed to the surface of the supporting material.

FTIR characterization aims to determine the presence of characteristic functional groups of material. Based on the results of the FTIR analysis in Fig. 4, it can be seen that there are characters of silica-alumina groups in all materials, which confirms the previous XRF and XRD results. These groups are represented by the symbol T as shown in Table 3. The presence of silica-alumina groups indicates that LM has the potential to be used as a catalyst carrier material. In addition, there is a left shift of the absorption peak in the T–O–T asymmetric stretching vibration in the CLM. This indicates the occurrence of dehydration on the surface of the silica-alumina, which makes the water release leaving alumina ions and then forming Lewis acid sites in the non-framework. Similar results also occurred in the study conducted by Dubey et al. [28]; there was a shift in the absorption peak from 1065 to 1080 cm^{-1} in MCM-41 before and after calcination. Meanwhile, the variation in the weight loading of the Ni on the LM did not significantly affect the vibration absorption produced. After the NH_2 grafting process on Ni(A)/LM

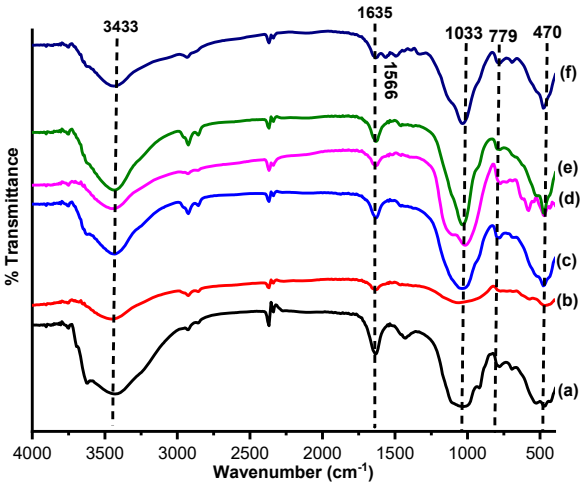

Fig 4. FTIR spectra of (a) LM, (b) CLM, (c) Ni(A)/LM, (d) Ni(B)/LM, (e) Ni(C)/LM, (f) Ni(A)-NH_2/LM

was carried out, a new characteristic functional group has emerged with low intensity namely $-NH_2$ at 1566 cm^{-1} derived from the 3-APTMS compound. This modification process was successful because there was a decrease in the intensity of the T–OH bending vibration due to the interaction between T–OH and 3-APTMS. These results are under the research conducted by Li et al. [29].

The nitrogen adsorption isotherm for the synthesized material is presented in Fig. 5. Several materials (except Ni(A)-NH_2/LM) exhibited a type IV isotherm corresponding to the characteristics of the mesoporous material, according to the IUPAC classification. This graph shows that metal impregnation does not damage the mesoporous properties of the support material. The process that occurs in this type of isotherm starts from adsorption at low pressure (< 0.02) for micropore filling, followed by monolayer and multilayer adsorption on the surface of the material, including mesopores, at medium relative pressure (0.2–0.5) the phenomenon of capillary condensation occurs in the mesopores. At this point, the amount of adsorbed gas increases sharply with a small pressure change due to the condensation of the molecules under the vapor

Table 3. Analysis result of FTIR spectra

Vibration type	Wavenumber (cm^{-1})					
	LM	CLM	Ni(A)/LM	Ni(B)/LM	Ni(C)/LM	Ni(A)-NH_2/LM
Bending of T–OH	1635	1635	1635	1635	1627	1635
Stretching of T–OH	3425	3448	3433	3448	3433	3433
Asymmetric stretching of T–O–T	1033	1064	1033	1018	1033	1033
Symmetric stretching of T–O–T	779	725	779	771	779	779
Bending of T–O–T	470	462	478	470	470	478
Bending of -NH_2	-	-	-	-	-	1566
Stretching of C–H	2924	2924	2924	2924	2924	2931

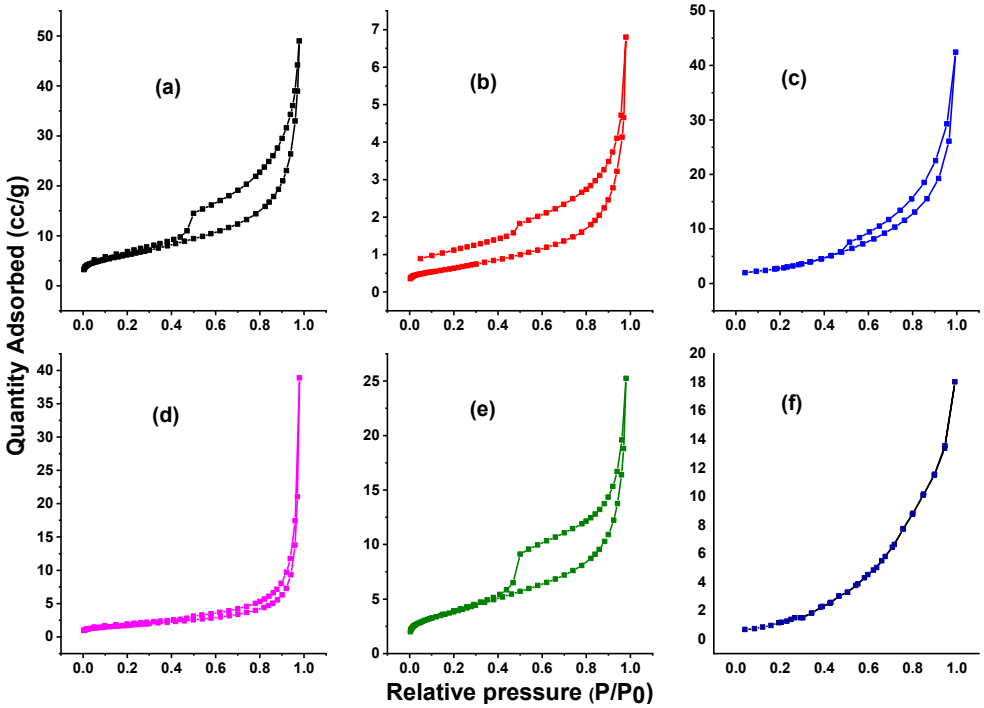

Fig 5. Nitrogen adsorption-desorption isotherm of (a) LM, (b) CLM, (c) Ni(A)/LM, (d) Ni(B)/LM, (e) Ni(C)/LM, (f) Ni(A)-NH_2/LM

pressure so that the liquid adsorbate fills the primary mesoporous. Thereafter, multilayer adsorption and/or condensation of liquids in the secondary mesopores occur at relatively high pressures (0.5–0.8) and finally at very high pressures (< 0.8), corresponding to the filling of voids between particles which can be considered as porosity [30]. The Ni(A)-NH_2/LM material shows a different type of isotherm from other materials. This material belongs to the type III category where there is no identifiable multilayer formation, meaning that there are relatively weak adsorbent–adsorbate interactions [31].

This typical mesoporous material is represented by the presence of a hysteresis loop at the isotherm. The type of hysteresis possessed by these materials follows the H3 pattern as described by IUPAC, where the desorption branch tends to be perpendicular to the adsorption branch in the closure region at lower relative pressures. In the hysteresis loop H3, the pores have a wedge or slit geometry, resulting from agglomerates of parallel plates-shaped particles [32]. The hysteresis loops never close in all these materials, even under very low pressure, as happened to CLM. This can be attributed to several reasons. First, the material is not a rigid structure and may deform, induced by adsorption or pore filling. Second, the trapped nitrogen cannot be released because of the affinity of nitrogen in the material caused by the heterogeneous property of the surface [33]; the adsorption potential of the pore wall traps the nitrogen molecules, which agrees with the observation that increasing temperature will deteriorate the hysteresis effect [34].

The pore distribution of the materials can be seen in Fig. 6. All pores in the material belong to the mesoporous class, where the diameter is between 2–50 nm. The pore diameter is taken from the highest point on each bar chart, representing the most frequent pore diameter based on the BJH desorption method. Meanwhile, the material surface area is calculated using the BET method. There was a drastic decrease in the surface area of LM after calcination from 22 to 2 m^2/g. This is because the silica and alumina content in LM decreases during the heating process [35], which is in line with the decrease in acidity value. Another decrease also occurred in LM loaded with Ni metal, where the surface area decreased following the increasing weight of metal loading. Among Ni catalysts, the smallest surface

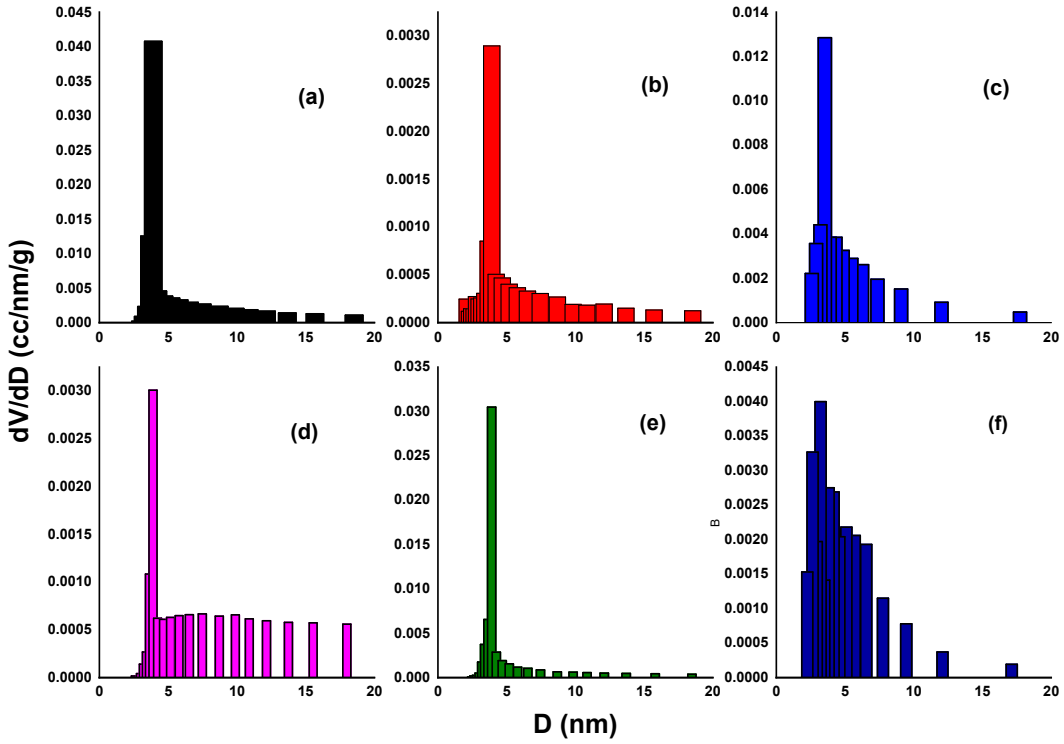

Fig 6. Pore size distribution of (a) LM, (b) CLM, (c) Ni(A)/LM, (d) Ni(B)/LM, (e) Ni(C)/LM, (f) Ni(A)-NH_2/LM

area is owned by Ni(B)/LM, which is possible due to the blockage of the pores of the material, strengthened by the lowest acidity value. The presence of 3-APTMS modification also contributed to the decrease in the surface area of Ni(A)/LM. Overall, the surface area of the material obtained is quite small, which is below 25 m^2/g. In theory, the high metal content and small particle size lead to a large surface area. This situation can be achieved if the nanoparticles are evenly distributed and do not block the pores of the supporting material [36]. The large nanoparticle size also contributes to the increase in surface area, although not as much as the small nanoparticles. However, in this case, we can only measure the metal content, but not the degree of distribution and pore-clogging. Data analysis of the textural properties of the material is presented in Table 4.

Study of Catalytic Activity and Selectivity

To evaluate the catalytic activity, all prepared catalysts were applied for the hydrocracking process of waste palm cooking oil (WPCO) at a temperature of 470 °C with a feed:catalyst weight ratio of 50. The catalyst that generates a liquid product with the highest level of hydrocarbons would be considered as the best catalyst and will be studied further to find the optimum conditions for the hydrocracking process.

The results of all the hydrocracking that have been shown by each catalyst are summarized in Table 5. Interestingly, the LM support material in the absence of Ni gave an excellent performance with a total liquid product of 56.30 wt.%. This provides a new point of view that natural material without chemical treatment has good catalytic activity, although its surface area is small (22.216 m^2/g) compared to other supports. Here, the calcination process in CLM shows its role in increasing the total liquid product up to 66.71 wt.%. As previously described, this process has several functions, including removing impurities. However, because of its low acidity value from the content of silica oxide and alumina as the main constituents, this material (31.1 wt.%) resulted in the hydrocarbon content being lower than LM (55.20 wt.%). Several reasons (high acidity, large surface area, and high hydrocarbon product) made LM chosen as a support material for Ni catalysts through a wet impregnation process.

Generally, the hydrocracking process consists of two

Table 4. Textural properties of materials

Material	Surface area (m^2/g) [a)]	Most frequent pore diameter (nm) [b)]	Total pore volume (cc/g) [c)]
LM	22.216	3.916	0.060
CLM	2.304	3.908	0.007
Ni(A)/LM	11.659	3.528	0.062
Ni(B)/LM	6.155	3.906	0.033
Ni(C)/LM	13.797	3.906	0.029
Ni(A)-NH_2/LM	5.953	3.225	0.028

Notes: [a)] based on BET calculation
[b)] based on BJH Desorption
[c)] at $P/P_0 = 0.99$

Table 5. Distribution of hydrocracking products based on the type of catalyst

Catalyst	Liquid (wt.%)					Gas (wt.%)	Coke (wt.%)	Residue (wt.%)
	Gasoline	Diesel	Alcohol	Others	Total			
LM	38.14	12.08	3.03	3.05	56.30	41.06	1.35	1.29
CLM	23.91	7.19	20.36	15.25	66.71	30.50	0.29	2.50
Ni(A)/LM	39.89	1.81	1.15	3.80	46.65	47.59	3.73	2.03
Ni(B)/LM	40.94	0.00	0.38	1.51	42.83	55.58	0.41	1.18
Ni(C)/LM	18.83	13.26	3.69	4.60	40.38	58.58	0.04	1.00

Notes: Temperature of 470 °C, feed/catalyst weight ratio of 50

reactions, namely hydrogenation and cracking. Hydrogenation involving the presence of hydrogen gas provides a role for further deoxygenation reactions, namely decarbonylation, decarboxylation, and hydrodeoxygenation. Both decarbonylation and decarboxylation release one C atom in the form of CO and CO_2, producing a hydrocarbon with one fewer carbon atom [2]. Meanwhile, hydrodeoxygenation only releases O atoms in the form of H_2O through a consecutive reduction process so that the hydrocarbon has a carbon length identical to the initial oxygenated compound as happened with CLM, which produces high alcohol products as a result of the final consecutive reduction.

In this case, all the catalysts used gave selectivity to the gasoline product, indicating that the deoxygenation reaction occurred to produce heavier hydrocarbons before being taken over by the cracking reaction to produce lighter hydrocarbons. With the advent of solar products, the reaction may stop only on deoxygenation. Ochoa-Hernández et al. [37] stated that an increase in acidity from Ni would cause the hydrotreatment process to run non-selectively towards the production of long-chain hydrocarbons through hydrodeoxygenation and decarboxylation. The addition of Ni makes the active site on the catalyst increase so that the catalyst becomes super active, which results in secondary cracking. Among the three Ni-based catalysts (Fig. 7), the Ni(A)/LM material provided the highest level of hydrocarbons (41.7 wt.%). This confirms that the acidity value is correlated with the hydrocarbon level. The higher diesel product at Ni(C)/LM compared to others is possible due to the blockage of the pores from agglomeration or deposition of the metal nanoparticles, causing a decrease in the number of accessible acid sites for the feed molecules. This pushes the deoxygenation reaction mechanism predominantly to produce heavier hydrocarbons and causes the splitting of larger molecules to become smaller in the cracking mechanism to be inhibited [38]. When compared with all the tested materials, LM produced the highest hydrocarbon products even without the addition of Ni metal. However, the aim of this study was not only to find the best catalyst in hydrocracking activity and selectivity but also to study the development of catalyst materials, in this case, LM as a natural-based catalyst support material without prior chemical treatment.

Despite producing good performance with a total liquid product and hydrocarbon content reaching 46.65 and 41.70 wt.%, the catalytic activity of the WPCO hydrocracking process using a Ni(A)/LM catalyst can still be improved by selecting the best temperature. This variation is carried out and observed to find the best conditions. As shown in Table 6, the highest conversion was obtained in hydrocracking at a temperature of 550 °C. At this temperature, the conversion level of WPCO increased to 63.93 wt.% compared to temperatures of 470 °C (46.65 wt.%) and 500 °C (53.09 wt.%). The increase in temperature may provide more energy in the system which will promote the adsorption force of the feed on the catalyst surface, causing the reaction rate to increase. According to Murachman et al. [22], the reaction rate constant is a function of temperature. This is because the

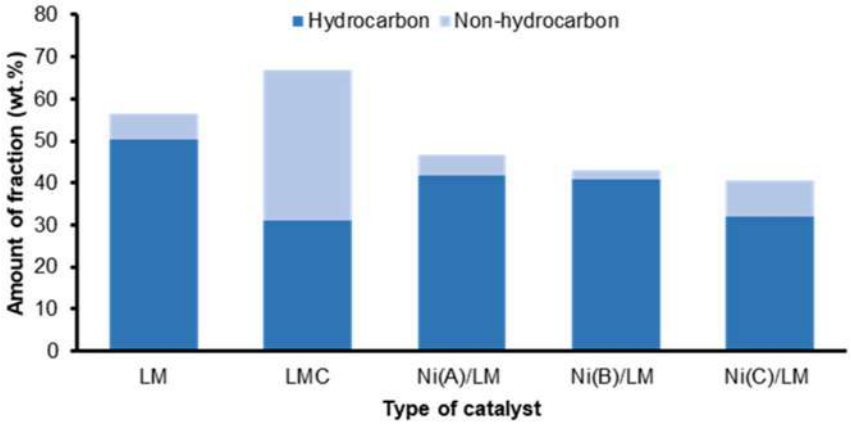

Fig 7. Effect of catalyst type on hydrocarbon and non-hydrocarbon

Table 6. Distribution of hydrocracking products based on various temperatures

Temperature (°C)	Liquid (wt.%)					Gas (wt.%)	Coke (wt.%)	Residue (wt.%)
	Gasoline	Diesel	Alcohol	Others	Total			
470	39.89	1.81	1.15	3.80	46.65	47.59	3.73	2.03
500	26.01	11.24	6.70	9.14	53.09	41.72	4.57	0.62
550	30.81	5.27	19.14	8.71	63.93	30.67	4.98	0.42

Notes: Ni(A)/LM catalyst, feed/catalyst ratio weight of 50

chance of collisions between molecules is getting bigger, which makes the average kinetic energy of the molecules increase. Not to mention, the optimum temperature also reduces feed residue to 0.42 wt.%.

As the previous results, in this condition, all temperatures provide selectivity for gasoline products (Fig. 8). Although 550 °C produces lower levels of hydrocarbons (36.08 wt.%) than at 500 °C (37.25 wt.%) and 470 °C (41.70 wt.%), its activity (amount of liquid product) shows the best performance. Moreover, it can be seen that this temperature gives a very high alcohol content of 19.14 wt.%. If it can be separated, this alcohol also provides benefits as a fuel mixture to increase the octane number [39]. A high octane number makes fuel efficiency increase so that it can cover its low energy density (when compared to gasoline or diesel), but the maximum content is only 10%. The presence of alcohol as a by-product suggests that this reaction mechanism follows hydrodeoxygenation which results in a step-by-step reduction of the carboxyl to aldehyde and ends to the alcohol. The decrease in selectivity is possible because the adsorption rate is too fast at high temperatures resulting in a less optimal reaction for converting oxygenated compounds into hydrocarbons.

In addition to Ni, secondary cracking also occurs because the catalyst support used is LM which naturally contains high levels of iron oxide. This Fe metal also provides Lewis acid sites which cause the catalyst to be super active so that the cracking becomes uncontrolled, causing the liquid phase produced to turn into a gas phase. The high gas product indicates that this process favors the production of the lightest hydrocarbon molecules due to the cleavage of the C–C or C–H bonds in the alkyl triglyceride or FFA chains.

In addition to the optimum temperature, the feed/catalyst weight ratio in hydrocracking also needs to be further investigated to obtain the best conditions to produce biofuels with high hydrocarbon content. In this study, a Ni(A)-NH_2/LM catalyst was also involved in determining the role of the NH_2 groups of the 3-APTMS compound on the surface of the LM. Based on Table 7, it can be seen that there is an increase in the conversion of Ni(A)/LM along with the weight ratio. However, the hydrocarbon selectivity decreased to only 4.47 wt.% at a ratio of 100. The grafting treatment on Ni(A)-NH_2/LM provided the Lewis base site from the lone pair of the nitrogen atom [40]. This makes the catalyst easier to capture and adsorb FFA in the feed, resulting in a higher

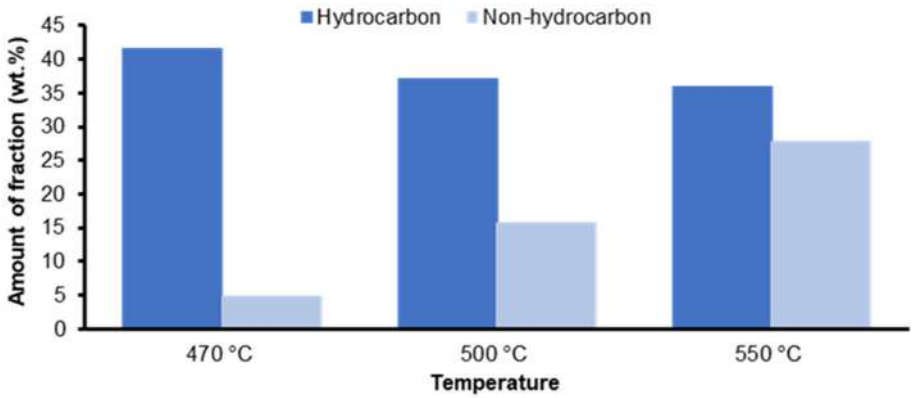

Fig 8. Effect of hydrocracking temperature on hydrocarbon and non-hydrocarbon

Table 7. Distribution of hydrocracking products based on a feed/catalyst weight ratio

Catalyst	Ratio	Liquid (wt.%)					Gas (wt.%)	Coke (wt.%)	Residue (wt.%)
		Gasoline	Diesel	Alcohol	Others	Total			
Ni(A)/LM	50	30.81	5.27	19.14	8.71	63.93	30.67	4.98	0.42
	75	12.99	18.14	29.77	7.12	68.02	26.36	2.96	2.66
	100	2.10	2.37	65.28	7.81	77.56	17.87	2.60	1.97
Ni(A)-NH_2/LM	50	26.91	4.31	16.11	17.70	65.03	32.81	1.17	0.99
	75	17.20	16.72	25.44	8.81	68.17	29.08	0.69	2.06
	100	8.03	9.56	28.21	4.04	49.84	48.73	0.94	0.49

Notes: Temperature of 550 °C

conversion than Ni(A)/LM at the same ratio. Although, in fact, at a ratio of 100, there was a decrease in biofuel up to 49.84 wt.%, possibly because too much feed was used, so the amount of catalyst could not accommodate the reaction optimally. The higher amount of feed will naturally enter the catalyst pores, inhibiting and slowing the feed flow, leaving a higher residue level. The presence of residue indicates that this process requires a longer reaction time. It could also be occurred due to polymerization to form heavier and larger molecules, which accumulate as residues. Pore filling during hydrocracking also results in carbon trapping, increasing overall coke deposition.

The synergistic action between Ni nanoparticles and NH_2 groups provides good catalyst selectivity toward hydrocarbon products. Meanwhile, the results at a ratio of 50 showed a 4.86% decrease in the hydrocarbon content from Ni(A) to Ni(A)-NH_2, which was possible under these conditions that were unfavorable for the catalyst. However, when viewed from the economic side, by using more feed oil (the ratio is higher), the catalyst containing NH_2 has better results. According to Fig. 9, the optimum ratio in converting WPCO to hydrocarbons (33.92 wt.%) using a Ni(A)-NH_2/LM catalyst is 75. The combination of NH_2 groups, acid sites, and hydrogenation sites causes this interaction to weaken the CO or C=O bonds, then intensifies the deoxygenation mechanism to produce hydrocarbons.

The use of Ni(A)-NH_2/LM catalyst is tested for durability after reuse, which is known as the catalyst reusability test. The age test was carried out using the same catalyst without being replaced and given any treatment after use. The reusability of Ni(A)-NH_2/LM in 3 runs of WPCO hydrocracking at 550 °C using a ratio of 75 was studied (Table 8). Interestingly, during these 3 runs, the catalyst was shown to produce an astonishing

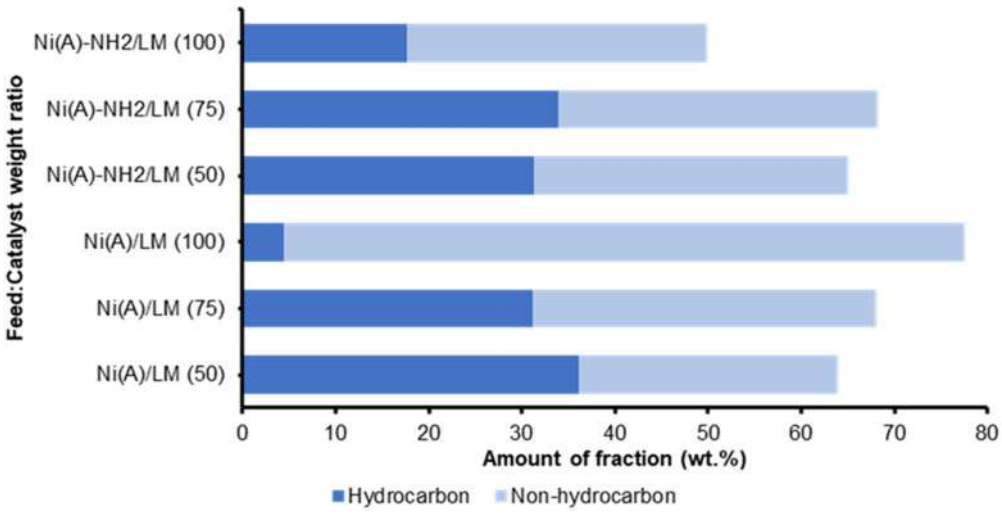

Fig 9. Effect of feed/catalyst weight ratio on hydrocarbon and non-hydrocarbon

result with a consistently high conversion level (~80 wt.%). The formation of coke is also seen to relatively occur at a controlled rate, indicating stability towards coke poisoning.

Despite the total liquid product increases, not all of the constituent compounds of this liquid product can be used as fuel. Selectivity studies cannot be carried out by looking at the percentage of liquid products because the trend always increases without showing a significant decrease. Therefore, this study will focus on the ability of the catalyst to direct the hydrocracking reaction to produce hydrocarbon products. Fig. 10 shows that the hydrocarbon level decreased drastically with the frequent use of the catalyst. This indicates that the active sites of catalysts such as NH_2 groups and Ni nanoparticles have started to decrease in performance due to repeated use. However, until the third use, the amount of hydrocarbons is still relatively high at 38.36 wt.%. This gives the view that this catalyst can still show good performance so that it can be used more than 3 times.

TEM analysis aims to see the morphology, structure, and pore regularity. The results of the TEM image presented in Fig. 11 imply the catalyst that has been used in the hydrocracking process experiences a

Table 8. Distribution of hydrocracking products based on reusability

Use	Liquid (wt.%)					Gas	Coke	Residue
	Gasoline	Diesel	Alcohol	Others	Total	(wt.%)	(wt.%)	(wt.%)
1	49.28	12.56	5.47	12.15	79.46	20.29	0	0.25
2	32.63	8.42	8.05	31.17	80.27	19.49	0	0.24
3	28.73	9.63	23.66	22.31	84.33	15.13	0	0.54

Notes: Ni(A)-NH_2/LM catalyst, Temperature of 550 °C, feed/catalyst ratio weight of 75

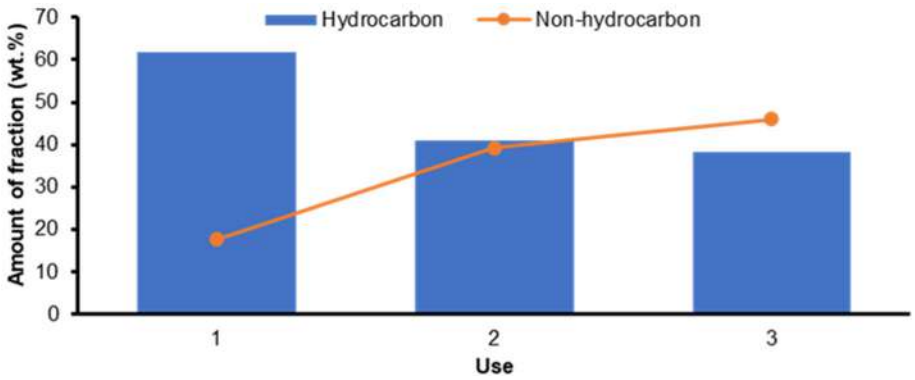

Fig 10. Effect of reusability on hydrocarbon and non-hydrocarbon products

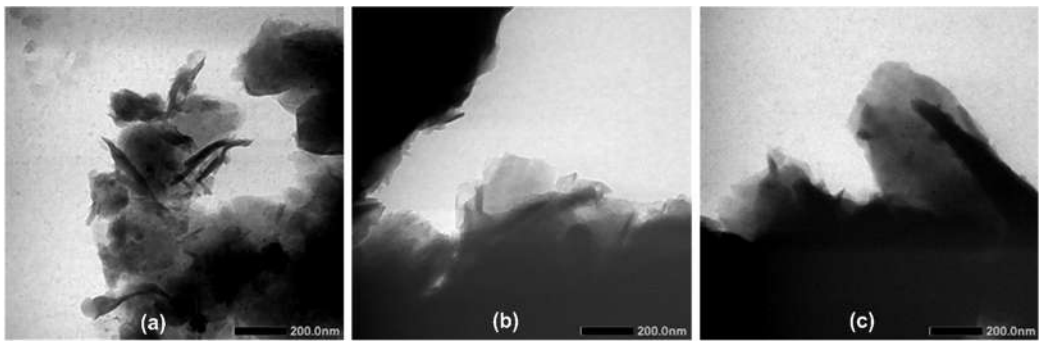

Fig 11. TEM images of (a) Ni(A)-NH_2/LM (75) before hydrocracking, (b) Ni(A)-NH_2/LM (75) after hydrocracking, (c) Ni(A)-NH_2/LM (100) after hydrocracking

darker color change due to the formation of coke deposition. The Ni(A)-NH_2/LM catalyst with a feed/catalyst ratio of 100 (Fig. 11(c)) looks very dark compared to Fig. 11(b), which explains that the pores of the catalyst have been closed due to the high interaction with the feed. This is evident from the coke production presented in Table 7 previously.

■ CONCLUSION

The hydrocracking study of waste palm cooking oil (WPCO) was prepared using natural catalyst support materials from Lapindo mud (LM), Sidoarjo, Indonesia, without any chemical treatment. This material is proven to have a high content of silica, alumina, and iron oxides. Even without the calcination process, this material has a higher acidity value which makes it effective as a Ni carrier. The weight of Ni loading on the LM at 1 wt.% gave the highest acidity value compared to 5 and 10 wt.%, following the obtained biofuel. This proves that a high weight loading does not always give a high catalytic activity as well because behavior like an agglomeration of the catalyst covering the support pores sometimes occurs in this situation. Interestingly, the small specific surface area of LM is capable of producing a high biofuel level of 56.30 wt.% with a hydrocarbon content of 50.22 wt.%. Process temperature and the weight ratio of feed/catalyst also affect the hydrocracking reaction. High temperatures will increase the reaction rate so that the kinetic energy between particles is getting bigger, causing more liquid products to be generated. Meanwhile, the obtained optimum ratio is at 75, where this ratio is increased more, the work of the catalyst will be harder, thereby reducing the quantity and quality of biofuels. The use of Ni(A)-NH_2/LM catalyst three times without a regeneration process was able to maintain the quantity of biofuel at around 80 wt.%, whereas the hydrocarbon level showed a decrease, but not less than 45% of the liquid product (wt.%). This is very reasonable because it is related to the formation of coke which leads to the deactivation of the catalyst. Overall, these results suggest good catalytic performance may offer an alternative pathway for the production of more environmentally friendly fuels in the future.

■ ACKNOWLEDGMENTS

The authors would like to thank the Ministry of Research, Technology, and Higher Education of Indonesia for the financial support under the scheme of PTUPT research grant 2021 (Contract Number: 2127/UN1/DITLIT/DIT-LIT/PT/2021) and also the Faculty of Mathematics and Natural Sciences, Universitas Gadjah Mada for the additional financial support under *Hibah Penelitian Dosen* 2021 (Contract Number: 148/J01.1.28/PL.06.02/2021).

■ REFERENCES

[1] Kusumastuti, H., Trisunaryanti, W., Falah, I.I., and Marsuki, M.F., 2018, Synthesis of mesoporous silica-alumina from lapindo mud as a support of Ni and Mo metals catalysts for hydrocracking of pyrolyzed α-cellulose, *Rasayan J. Chem.*, 11 (2), 522–530.

[2] Vazquez, N.I., Gonzalez, Z., Ferrari, B., and Castro, Y., 2017, Synthesis of mesoporous silica nanoparticles by sol-gel as nanocontainer for future drug delivery applications, *Bol. Soc. Esp. Ceram. Vidrio*, 56 (3), 139–145.

[3] Niculescu, V.C., 2020, Mesoporous silica nanoparticles for bio-applications, *Front. Mater.*, 7, 36.

[4] Rizzi, F., Castaldo, R., Latronico, T., Lasala, P., Gentile, G., Lavorgna, M., Striccoli, M., Agostiano, A., Comparelli, R., Depalo, N., Curri, M.L., and Fanizza, E., 2021, High surface area mesoporous silica nanoparticles with tunable size in the sub-micrometer regime: Insights on the size and porosity control mechanisms, *Molecules*, 26 (14), 4247.

[5] Lin, Y.S., Hurley, K.R., and Haynes, C.L., 2012, Critical considerations in the biomedical use of mesoporous silica nanoparticles, *J. Phys. Chem. Lett.*, 3 (3), 364–374.)

[6] Kumar, S., Malik, M.M., and Purohit, R., 2017, Synthesis methods of mesoporous silica materials, *Mater. Today: Proc.*, 4 (2), 350–357.

[7] Trisunaryanti, W., Larasati, S., Bahri, S., Ni'mah, Y.L., Efiyanti, L., Amri, K., Nuryanto, R., and

Sumbogo, S.D., 2020, Performance comparison of Ni-Fe loaded on NH_2-functionalized mesoporous silica and beach sand in the hydrotreatment of waste palm cooking oil, *J. Environ. Chem. Eng.*, 8 (6), 104477.

[8] Trisunaryanti, W., Triyono, Paramesti, C., Larasati, S., Santoso, N.R., and Fatmawati, D.A., 2020, Synthesis and characterization of Ni-NH_2/mesoporous silica catalyst from Lapindo mud for hydrocracking of waste cooking oil into biofuel, *Rasayan J. Chem.*, 13, 1386–1393.

[9] Li, G., Chen, L., Fan, R., Liu, D., Chen, S., Li, X., and Chung, K.H., 2019, Catalytic deoxygenation of C 18 fatty acid over supported metal Ni catalysts promoted by the basic sites of $ZnAl_2O_4$ spinel phase, *Catal. Sci. Technol.*, 9 (1), 213–222.

[10] Jang, M.S., Phan, T.N., Chung, I.S., Lee, I.G., Park, Y.K., and Ko, C.H., 2018, Metallic nickel supported on mesoporous silica as catalyst for hydrodeoxygenation: Effect of pore size and structure, *Res. Chem. Intermed.*, 44 (6), 3723–3735.

[11] Paramesti, C., Trisunaryanti, W., Sudiono, S., Triyono, T., Larasati, S., Santoso, N.R., and Fatmawati, D.A., 2021, The influence of metal loading amount on Ni/mesoporous silica extracted from Lapindo mud templated by CTAB for conversion of waste cooking oil into biofuel, *Bull. Chem. React. Eng. Catal.*, 16 (1), 22–30.

[12] Lu, H.T., 2013, Synthesis and characterization of amino-functionalized silica nanoparticles, *Colloid J.*, 75 (3), 311–318.

[13] Ma, Y., Wu, Y., Lee, J.G., He, L., Rother, G., Fameau, A.L., Shelton, W.A., and Bharti, B., 2020, Adsorption of fatty acid molecules on amine-functionalized silica nanoparticles: Surface organization and foam stability, *Langmuir*, 36 (14), 3703–3712.

[14] Kandel, K., Frederickson, C., Smith, E.A., Lee, Y.J., and Slowing, I.I., 2013, Bifunctional adsorbent-catalytic nanoparticles for the refining of renewable feedstocks, *ACS Catal.*, 3, 2750–2758.

[15] Chuah, L.F., Mohd Salleh, N.H., Osnin, N.A., Alcaide, J.I., Abdul Majid, M.H., Abdullah, A.A., Bokhari, A., A Jalil, E.E., and Klemeš, J.J., 2021, Profiling Malaysian ship registration and seafarers for streamlining future Malaysian shipping governance, *Aust. J. Marit. Ocean Aff.*, 13 (4), 225–261.

[16] Nanda, S., Rana, R., Hunter, H.N., Fang, Z., Dalai, A.K., and Kozinski, J.A., 2019, Hydrothermal catalytic processing of waste cooking oil for hydrogen-rich syngas production, *Chem. Eng. Sci.*, 195, 935–945.

[17] Ong, A.S.H., and Goh, S.H., 2002, Palm oil: A healthful and cost-effective dietary component, *Food Nutr. Bull.*, 23 (1), 11–22.

[18] Hartono, Z.A., and Cahyono, B., 2020, Effect of using B30 palm oil biodiesel to deposit forming and wear metal of diesel engine components, *Int. J. Mar. Eng. Innovation Res.*, 5 (1), 10–19.

[19] Ayetor, G.K., Sunnu, A., and Parbey, J., 2015, Effect of biodiesel production parameters on viscosity and yield of methyl esters: *Jatropha curcas*, *Elaeis guineensis* and *Cocos nucifera*, *Alexandria Eng. J.*, 54, 1285–1290.

[20] Goswami, G., Bora, R., and Rathore, M.S., 2016, Oxidation of cooking oils due to repeated frying and human health, *Int. J. Sci. Technol. Manage.*, 4 (1), 495–501.

[21] Huang, D., Zhou, H., and Lin, L., 2012, Biodiesel: An alternative to conventional fuel, *Energy Procedia*, 16, 1874–1885.

[22] Murachman, B., Deendarlianto, D., Nissaraly, H.F., and Hasyim, W., 2014, Experimental study on hydrocracking process of asbuton hydrocarbon based on the aromatic, and waxy residue based on paraffinic, by using Pt/Pd and γ-alumina catalyst in a fixed bed reactor, *ASEAN J. Chem. Eng.*, 14 (1), 59–75.

[23] Treese, S.A., Pujadó, P.R., and Jones, D.S.J., 2015, *Handbook of Petroleum Processing*, Springer, Cham, Switzerland.

[24] Alkhaldi, S., and Husein, M.M., 2014, Hydrocracking of heavy oil by means of in situ prepared ultradispersed nickel nanocatalyst, *Energy Fuels*, 28 (1), 643–649.

[25] Khoiri, H.M., Trisunaryanti, W., and Dewi, K., 2015, Synthesis of NH_2/MCM-41 catalysts using

silica of Sidoarjo mud and their characterization for palm oil transesterification, *IOSR J. Appl. Chem.*, 8 (8), 50–56.

[26] Nugrahaningtyas, K.D., Trisunaryanti, W., Triyono, T., Nuryono, N., Widjonarko, D.M., Yusnani, A., and Mulyani, M., 2009, Preparation and characterization the non-sulfided metal catalyst: Ni/USY and NiMo/USY, *Indones. J. Chem*., 9 (2), 177–183.

[27] Kefaifi, A., Sahraoui, T., Kheloufi, A., and Drouiche, N., 2018, Silica sand etching behavior during leaching process using design of experiments method (DOE), *Silicon*, 10 (3), 1187–1193.

[28] Dubey, R.S., Rajesh, Y.B.R.D., and More, M.A., 2015, Synthesis and characterization of SiO_2 nanoparticles via sol-gel method for industrial applications, *Mater. Today: Proc.*, 2 (4-5), 3575–3579.

[29] Li, X., Han, C., Zhu, W., Ma, W., Luo, Y., Zhou, Y., Yu, J., and Wei, K., 2014, Cr(VI) removal from aqueous by adsorption on amine-functionalized mesoporous silica prepared from silica fume, *J. Chem.*, 2014, 765856.

[30] Oliveira, D.M., and Andrada, A.S., 2019, Synthesis of ordered mesoporous silica MCM-41 with controlled morphology for potential application in controlled drug delivery systems, *Cerâmica*, 65, 170–179.

[31] Cychosz, K.A., and Thommes, M., 2018, Progress in the physisorption characterization of nanoporous gas storage materials, *Engineering*, 4 (4), 559–566.

[32] Thommes, M., Kaneko, K., Neimark, A.V., Olivier, J.P., Rodriguez-Reinoso, F., Rouquerol, J., and Sing, K.S.W., 2015, Physisorption of gases, with special reference to the evaluation of surface area and pore size distribution (IUPAC Technical Report), *Pure Appl. Chem.*, 87 (9-10), 1051–1069.

[33] Trisunaryanti, W., Wijaya, K., Triyono, T., Adriani, A.R., and Larasati, S., 2021, Green synthesis of hierarchical porous carbon prepared from coconut lumber sawdust as Ni-based catalyst support for hydrotreating Callophyllum inophyllum oil, *Results Eng.*, 11, 100258.

[34] Qi, L., Tang, X., Wang, Z., and Peng, X., 2017, Pore characterization of different types of coal from coal and gas outburst disaster sites using low temperature nitrogen adsorption approach, *Int. J. Min. Sci. Technol.*, 27 (2), 371–377.

[35] Junaidi, R., Hasan, A., and Zamhari, M., 2019, Influence the addition of Lapindo mud is calcined to the quality of cement podzoland by using electric furnace, *J. Phys.: Conf. Ser.*, 1167, 012043.

[36] Hu, H., Lu, S., Li, T., Zhang, Y., Guo, C., Zhu, H., Jin, Y., Du, M., and Zhang, W., 2021, Controlled growth of ultrafine metal nanoparticles mediated by solid supports, *Nanoscale Adv*., 3 (7), 1865–1886.

[37] Ochoa-Hernández, C., Yang, Y., Pizarro, P., de La Peña O'Shea, V.A., Coronado, J.M., and Serrano, D.P., 2013, Hydrocarbons production through hydrotreating of methyl esters over Ni and Co supported on SBA-15 and Al-SBA-15, *Catal. Today*, 210, 81–88.

[38] Auepattana-aumrung, C., Márquez, V., Wannakao, S., Jongsomjit, B., Panpranot, J., and Praserthdam, P., 2020, Role of Al in Na-ZSM-5 zeolite structure on catalyst stability in butene cracking reaction, *Sci. Rep.*, 10 (1), 13643.

[39] Anderson, J.E., Dicicco, D.M., Ginder, J.M., Kramer, U., Leone, T.G., Raney-Pablo, H.E., and Wallington, T.J., 2012, High octane number ethanol-gasoline blends: Quantifying the potential benefits in the United States, *Fuel*, 97, 585–594.

[40] Kubička, D., and Kaluža, L., 2010, Deoxygenation of vegetable oils over sulfided Ni, Mo and NiMo catalysts, *Appl. Catal., A*, 372 (2), 199–208.

Selective Identification for Glucose in the Presence of Fructose Using Imprinted Polyeugenol Modified Graphite Paste Electrode

Muhammad Cholid Djunaidi[1*], Gunawan Gunawan[1], Lutfia Cahyaningrum[1], Retno Ariadi Lusiana[1], and Miratul Khasanah[2]

[1]*Department of Chemistry, Faculty of Science and Mathematics, Diponegoro University, Jl. Prof. Soedharto SH, Tembalang, Semarang 50275, Indonesia*

[2]*Department of Chemistry, Faculty of Science and Technology, Universitas Airlangga, Campus C, Jl. Dr. Ir. H. Soekarno (MERR), Surabaya 60115, Indonesia*

* ***Corresponding author:***

email: choliddjunaidi@live.undip.ac.id

Received: December 6, 2021
Accepted: May 11, 2022

DOI: 10.22146/ijc.71013

Abstract: *High blood glucose levels indicate diabetes mellitus. The conventional way was carried out to determine glucose levels, but this method just shows the total reducing sugar levels. An electrode was developed to analyze glucose in the presence of fructose by potentiometry. The optimum graphite paste electrodes-Imprinted based on polyeugenol and Ethylene Glycol Dimethacrylate (EGDMA) as crosslinkers, had been used as a glucose sensor. Polyeugenol was made by the polymerization reaction with a BF_3 catalyst with a molecular weight of 6451.338 g/mol. A total of 2135.99 glucose was contacted with polyeugenol, and the result was crosslinked with EGDMA and 2,2'-Azobis(2-methylpropionitrile) (AIBN) initiator, then Molecularly Imprinted Polymer (MIP) was generated. The optimization of electrodes showed that the best composition of MIP: paraffin: graphite is 20:35:45 with the 19.16 mV/decade Nernstian Factor, which can measure samples at the range 10^{-5}–10^{-1} M with a detection limit of 1.0334×10^{-5} M, a response time of 6–15 s, a lifetime (use) of 19 times and has good selectivity on fructose sample with K_{ij} less than 1. Measurements using this electrode showed that honey contains 28.78% of glucose, not much different from the UV-Vis spectrophotometry, which is 29.68%, and HPLC is 30.42%.*

Keywords: *polyeugenol; imprinted; glucose; fructose; selective electrode*

■ INTRODUCTION

Diabetes mellitus is of chronic disease caused by the increase in glucose levels, or called hyperglycemia which makes the regulation of glucose homeostasis not work perfectly [1]. The values of blood glucose in the normal body are 60–100 mg/dL (6×10^{-3}–1×10^{-3} M), while in diabetics, blood glucose levels can increase to > 200 mg/dL or equivalent to 2×10^{-2} M. The conventional way was carried out to determine glucose levels, but this method just shows the form of total reducing sugar levels and cannot determine reducing sugar individually [2]. An alternative method that can be used to measure glucose levels is potentiometry. Potentiometry has two kinds of working electrodes there reference electrode and the working electrode. In potentiometry, a working electrode is used as a sensor to detect the analyzed compound. It is important to determine the type of sample because it can produce an accurate and selective analytical instrument sensor component. In a previous study, the synthesis of a polyeugenol-based Imprinted Polymer (IP) selective electrode with a Polyethylene glycol diglycidyl ether (PEGDE) crosslinker agent as a glucose sensor showed good performance as a glucose sensor [3].

Selective electrodes are made using eugenol derivative compounds because eugenol has a large abundance in Indonesia; and is found in almost 80% of plants in Indonesia. Eugenol can be used as a starting material for the synthesis because of the presence of three functional groups attached to it; there are allyl,

hydroxy, and methoxy groups; from this allyl group, eugenol can be polymerized into polyeugenol [4]. The working electrode is based on a molecularly imprinted polymer. The functional monomers, templates, initiators, solvents, and crosslinker agents will react around the template molecules through the polymerization process and produce a polymer called polyeugenol [5-6]. Compounds of Imprinted from polyeugenol have high selectivity because it only identifies the molecule template and also has good mechanical strength against organic solvents, bases, acids, high pressure, and temperature. Therefore, Molecularly Imprinted Polyeugenol (MIP) has great potential as a working electrode material for glucose sensors [7].

In this research, the synthesis of MIP was prepared with eugenol, BF_3 as a catalyst, EGDMA as a crosslinker, glucose as a MIP template, and a graphite electrode that had the ability to conduct the current from a sample. An electrode was made with various compositions and used to analyze glucose with varying concentrations and pH to get the optimum working electrode to enhance the performance of potentiometric sensors in glucose determination, such as Nernst factor, range of measurement, coefficient selectivity, response time, lifetime, and measurement glucose in the presence of fructose.

■ EXPERIMENTAL SECTION

Materials

Eugenol p.a, $BF_3(C_2H_5)_2$, Chloroform p.a, anhydrous Na_2SO_4, D-Glucose, L-Fructosa Ethylene glycol dimethacrylate (EGDMA), AIBN (2,2'-Azobis(2-methylpropionitrile), Paraffin, graphite, NaOH, Ethanol, HCl, KCl, Na_2HPO_4, NaH_2PO_4, CH_3COOH, CH_3COONa, Kaliumnatriumtartrat-Tetrahydrat were purchased from Merck-Sigma Aldrich (Jakarta, Indonesia), aqua demineralization was purchased from Bratachem (Semarang, Indonesia), 3,5-Dinitrosalicylic acid was purchased from HIMEDIA (Jakarta, Indonesia), and Randu Honey from Mabruuk (Semarang, Indonesia).

Instrumentation

The characterizations of the functional group were carried out using FTIR Shimadzu Prestige 21 (Semarang, Indonesia), for the surface morphology MIP, NIP, Electrode MIP (EMIP), and Electrode NIP (ENIP) were analyzed using SEM Phenom Pro X Desktop with EDX (Semarang, Indonesia), and Electrode performance that was synthesized before measured with Eutech PC510 potentiometer and Ag/AgCl reference electrode (Semarang, Indonesia).

Honey glucose levels containing fructose and glucose were measured by potentiometry. The result was then compared with UV-Vis Spectrophotometry LW-V-200-RS method using DNS complexing reagent (Semarang, Indonesia) and HPLC that consisted of a carbohydrate column at ambient temperature, a flow rate of 0.769 mL/min, and 80% acetonitrile eluent with a refractive index detector (Bogor, Indonesia).

Procedure

Polymerization of eugenol

In a three-necked flask, 5.8 g of eugenol was polymerized using BF_3-diethyl ether as a catalyst under stirring for 16 h. The polymerization then ended by adding methanol. The result was dissolved with chloroform and neutralized by adding water. Afterward, anhydrous Na_2SO_4 was used to remove the water completely and then filtered. The precipitate formed was dried, crushed, weighed, and analyzed by FTIR.

Synthesis of molecularly imprinted polyeugenol (MIP)

The synthesized polyeugenol was contacted with glucose by adding 0.5 g of polyeugenol with 10 mL glucose solution of 7500 ppm and stirred for 24 h. The product is then filtered, dried, and characterized by FTIR. A total of 0.222 g of polyeugenol-glucose was then crosslinked with 0.4 mL of EGDMA, 1.67 mL of chloroform, and 0.48 mL of AIBN as initiator. Then the mixture was refluxed at 60–70 °C for 30 min, and the results were dried in an oven and sieved with a 100 mesh sieve. Polyeugenol-glucose-EGDMA was then eluted with ethanol for 24 h. The contact and release of glucose were analyzed with a spectrophotometer UV-Vis. MIP is then characterized by FTIR and SEM-EDX.

Synthesis of non-imprinted polyeugenol (NIP)

NIP synthesis is done in the same way with MIP but without contacted polyeugenol with glucose, then characterized by FTIR and SEM-EDX.

Construct and characterization of electrode

The electrodes were made by filling the micropipette tube with sanded silver wire to connect the electrode to the potentiometer; as much as the micropipette was filled with melted paraffin, then the remaining tube was filled with pasta that forms by mixing the graphite solid paraffin and MIP. The filling of pasta in the tube is done by pressing to make it completely filled and then rubbed using *Houtvrij Schrijfpapier* (HVS) paper. This process is summed up in Fig. 1. The electrode is then used to determine the glucose level on the sample.

■ RESULTS AND DISCUSSION

Polymerization of Eugenol

Eugenol polymerization was carried out for 16 h through a cationic addition process because the allyl group in eugenol underwent an addition reaction. In eugenol polymerization, the initiation step uses a $BF_3(C_2H_5)_2$ catalyst so that the double in the allyl group of eugenol breaks up and produces a carbocation. Then at the propagation stage, a polymer chain will be formed, while at the termination stage, the polymer chain will end through the addition of methanol.

The resulting polyeugenol formed in a solid gel was then dissolved in chloroform and neutralized with aqua demineralization to remove the acid from the remaining catalyst. After neutral conditions, anhydrous Na_2SO_4 was added to bind the water. The result of polyeugenol has a reddish-brown with a molecular weight of 6451.338 g/mol and a yield of 89.9%. Eugenol and polyeugenol have been synthesized and analyzed using FTIR, and the result can be seen in Fig. 2.

At wavenumbers 994 cm^{-1} and 910 cm^{-1}, it appears that the polyeugenol has lost a vinyl group more than previously in eugenol, where there is a vinyl group. The vinyl group has been lost because it has been modified and binds to other eugenols to form polyeugenol. This is in accordance with the research before[3,8-9], so it can be concluded that the polymerization reaction was successfully carried out.

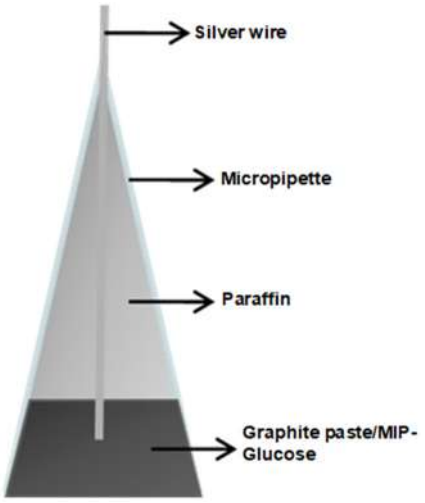

Fig 1. Electrode construction

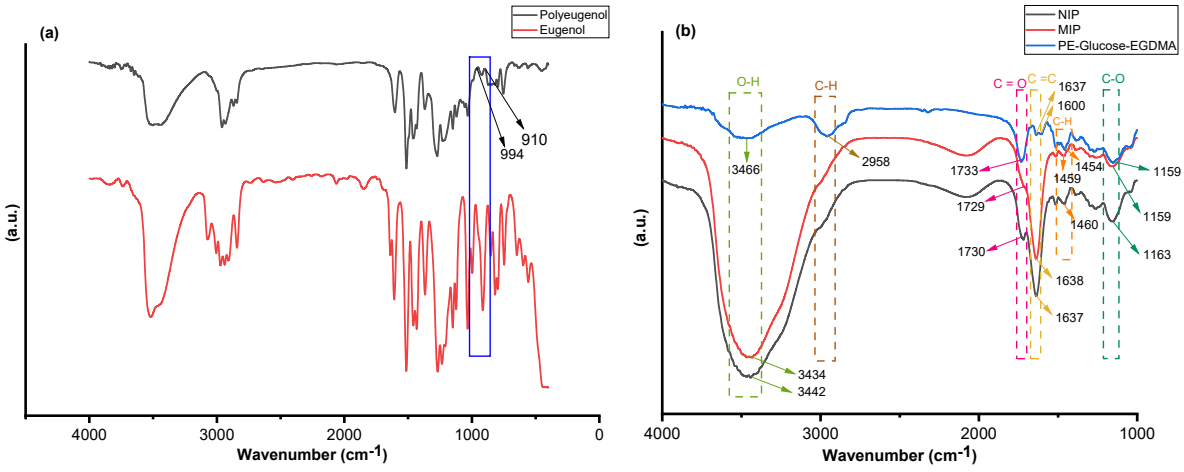

Fig 2. FTIR Comparison (a) Polyeugenol and eugenol (b) MIP, NIP, and polyeugenol (PE)-Glucose-EGDMA

Synthesis and Characterization of MIP and NIP

The amount of glucose in contact was analyzed by UV-Vis spectrophotometer and was obtained at 2135.99 ppm. The glucose released was 95.34%. The differences in functional groups and peaks that appear in NIP and MIP can be seen from the results of the FTIR spectra. A comparison of FTIR spectra between MIP, NIP, and PE-Glucose-EGDMA is shown in Table 1.

The presence of a CH group found in 2958 cm^{-1} PE-Glucose-EGDMA was not much different from the study before, which identified the presence of CH_3 vibrations in 2960 cm^{-1} EGDMA samples [10]. The MIP and NIP absorption were not clearly visible because they overlap with OH at 1600 cm^{-1}, which shows the presence of C=O aldehyde from glucose [11] which is found in PE-Glucose-EGDMA but not seen in MIP. It is because glucose has been released. The PE-Glucose-EGDMA spectra also showed a reduction in the intensity of the OH peak compared to the MIP due to the release of glucose with ethanol.

Subsequent analysis using SEM-EDX, which aims to see the surface morphology of MIP and NIP (Fig. 3) and to see the levels of C and O elements contained in MIP and NIP (Table 2). The SEM results in Fig. 3 show the surface morphology at 5000× magnification. It can be seen that the two samples have different surface morphology. The MIP sample has more pores, which is thought to be a mold of glucose compounds, while the NIP

Table 1. FTIR Comparison MIP, NIP, and PE-Glucose-EGDMA

Wavenumber (cm^{-1})	Functional group	NIP	MIP	PE-Glucose-EGDMAG
3400–3500	O–H	Presence	Presence	Presence
2954.5	C–H	Not Presence	Not Presence	Presence
1715–1730	C=O ester	Presence	Presence	Presence
1600	C=O stretching, aldehyde	Not Presence	Not Presence	Presence
1638–1648	C=C stretching	Presence	Presence	Presence
1450–1465	C–H bending, aromatic	Presence	Presence	Presence
1100	C–O stretching, ether	Presence	Presence	Presence

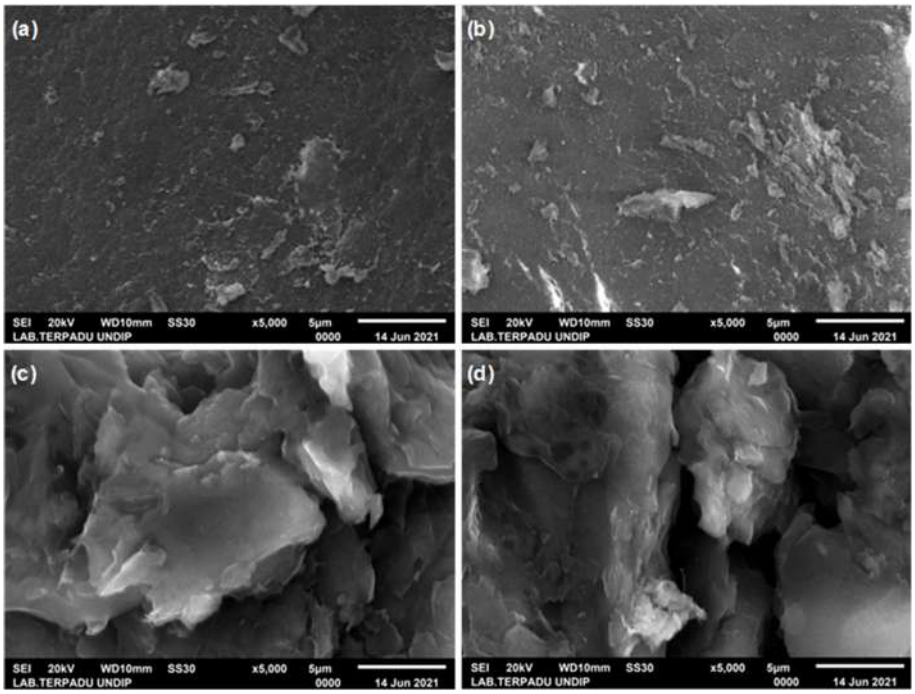

Fig 3. SEM result of (a) NIP (b) MIP (c) ENIP (d) EMIP

sample has a smoother surface. Both MIP and NIP used Image J software to show the amount of pore. The results of pore measurements using Image J are shown in Table 3.

Characterization of Graphite Paste/MIP-Glucose Electrodes (EMIP)

The synthesis of the electrode by mixing various compositions (% mass) of MIP, graphite, paraffin, and pH variations. Tables 4, 5, and 6 show the optimization results, with optimum pH being 7 with a Nernst factor of 19.16 mV/decade. E5 (EMIP) also shows a linearity value of 0.991, which is close to 1. So, E5 is an optimum electrode and suitable for analyzing glucose samples.

The ENIP was prepared with a composition such as E5 as control, and measurements were made in comparison to the E5 electrode (EMIP) (Table 7). The ENIP shows a Nernstian factor of 2.29 mV/decade. The result of this low Nernstian factor is that there is no

Table 2. Element mass percentage

Unsure	Mass (%)			
	MIP	NIP	EMIP	ENIP
C	71.82	72.72	94.51	96.06
O	27.76	26.79	4.67	3.87

Table 3. Pore measurements using Image J

	MIP	NIP	EMIP	ENIP
Count	185151	115917	51.91	44.60
Total area	130394	99909	1434799	1381.25
Area (%)	28.63	22.14	32.68	31.20

Table 4. Nernstian factor and measurement range in pH 3

Electrode	Composition (wt.%)			Nernstian factor	Measurement	Linearity
	MIP	Paraffin	Graphite	(mV/decade)	range (M)	(r)
E1	0	35	65	-14.84	10^{-8}–10^{-3}	0.95
E2	5	35	60	-9.99	10^{-8}–10^{-3}	0.92
E3	10	35	55	-8.11	10^{-7}–10^{-3}	0.98
E4	15	35	50	-5.88	10^{-7}–10^{-1}	0.92
E5	20	35	45	-3.33	10^{-7}–10^{-2}	0.83
E6	25	35	40	-4.64	10^{-8}–10^{-2}	0.96

Table 5. Nernstian factor and measurement range in pH 5

Electrode	Composition (wt.%)			Nernstian factor	Measurement	Linearity
	MIP	Paraffin	Graphite	(mV/decade)	range (M)	(r)
E1	0	35	65	-0.24	10^{-5}–10^{-2}	0.87
E2	5	35	60	-5.67	10^{-8}–10^{-1}	0.72
E3	10	35	55	1	10^{-7}–10^{-2}	0.75
E4	15	35	50	-2.57	10^{-5}–10^{-1}	0.93
E5	20	35	45	-1	10^{-4}–10^{-1}	0.83
E6	25	35	40	-1.1	10^{-4}–10^{-2}	0.89

Table 6. Nernstian factor and measurement range in pH 7

Electrode	Composition (wt.%)			Nernstian factor	Measurement	Linearity
	MIP	Paraffin	Graphite	(mV/decade)	range (M)	(r)
E1	0	35	65	0.68	10^{-5}–10^{-2}	0.98
E2	5	35	60	1.84	10^{-8}–10^{-1}	0.94
E3	10	35	55	1.28	10^{-7}–10^{-2}	0.89
E4	15	35	50	6.85	10^{-8}–10^{-4}	0.98
E5	20	35	45	19.16	10^{-5}–10^{-1}	0.99
E6	25	35	40	4.51	10^{-8}–10^{-2}	0.96

Table 7. Comparison of EMIP and ENIP performance

Electrode	Nernstian factor (mV/decade)	Measurement range (M)	Linearity (r)
EMIP (E5)	19.16	10^{-5}–10^{-1}	0.99
ENIP	2.29	10^{-5}–10^{-1}	0.88

imprinted molecule that is compatible with glucose.

Graphite paste from EMIP and ENIP was analyzed using SEM-EDX (Fig. 4). This analysis aims to see the surface morphology of MIP and NIP graphite paste which is a component of the electrode, and to see the levels of C and O (Table 2) elements contained in it. The SEM imaging results in Fig. 3 show the surface morphology at a magnification of 5000×.

EMIP and ENIP have a surface morphology that is not much different because both EMIP and ENIP have the same carbon composition of 45%, while the composition of MIP and NIP are 20% each, only the MIP surface has a more uneven surface. The results of pore measurements using Image J are shown in Table 3.

The result of the TGA/DTG analysis (Fig. 4) that was carried out with a temperature range of 10 to 1200 °C, the temperature increase of 10 °C/min, and using nitrogen flow rate showed the weight loss of graphite paste MIP and NIP. Both of them contained the same composition with a mass ratio of graphite:paraffin:MIP/NIP is 45:35:20 (wt.%) and have significant weight loss begins at 238 °C for MIP and 215 °C for NIP.

Limit of Detection

The lowest concentration of analyte in the sample can be reliably detected with a limit of detection [12]. In this study, the limit of detection is determined by the intersection between the linear and nonlinear lines of the standard curve [13]. The resulting linear line equation is $y = 19.16x + 251.4$ while the non-linear line $y = 7.4x^2 + 84.7x + 142.2$. The results of the measurement of the detection limit on EMIP are shown in Fig. 5. The EMIP detection limit is 1.0334×10^{-5} M so that the electrode can detect the presence of glucose theoretically up to 1.0334×10^{-5} M with the Nernst factor measured at 19.16 mV/decade. EMIP can be used to analyze the glucose level in the blood because the normal body has blood glucose levels at 60–100 mg/dL (6×10^{-3}–1×10^{-3} M), while people with diabetes mellitus have glucose levels of more than 200 mg/dL or equivalent, with 2×10^{-2} M [2]. The comparison of LOD results by our work and some previous research is reported in Table 8.

Response Time

Determination of the electrode response time is carried out to determine the time required for the electrode to respond to the analyte in solution. It can be seen (Table 9) that the greater concentration will give a faster response time. This is in accordance with the research [18] because the greater concentration will increase the molecular movements from the solution to the electrode.

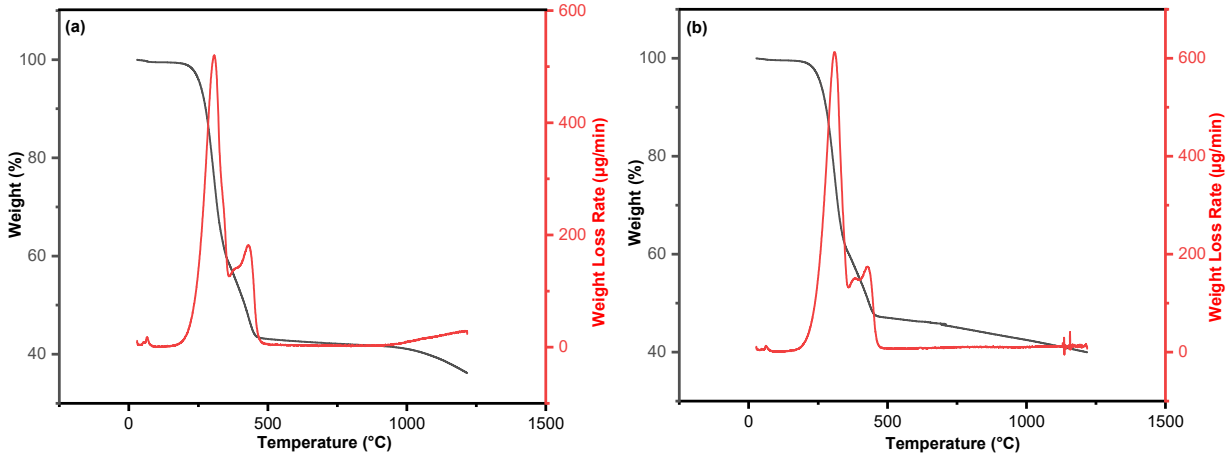

Fig 4. TGA/DTG of (a) MIP and (b) NIP

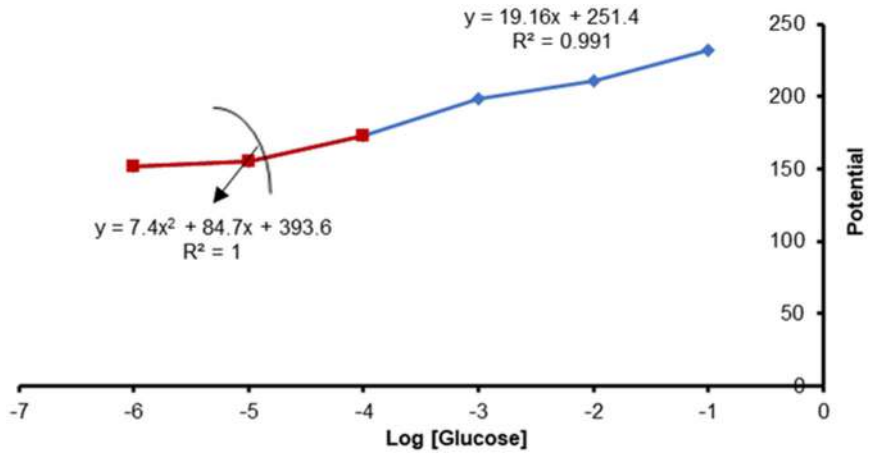

Fig 5. Detection limit measurement curve

Table 8. The comparison of the LOD result by our work and some previous research

Method	The material of the electrode	Linear range	LOD	Ref.
Amperometry	Carbon paste/GOx silica	5×10^{-4}–9×10^{-3} M	1.5×10^{-4} M	[14]
Amperometry	Carbon paste/selenium nanoparticle-mesoporous silica composite (MCM-41)	1×10^{-5}–2×10^{-3} M	1×10^{-4} M	[15]
Potentiometry	Poly (3-aminophenyl boronic acid-co-3-octylthiophene)	5×10^{-3}–5×10^{-2} M	5×10^{-4} M	[16]
Potentiometry	Carbon nanotube on gold printed	10^{-3}–10^{-1} M	1×10^{-4} M	[17]
Potentiometry	Carbon paste/IZ	10^{-4}–10^{-2} M	5.6×10^{-5} M	[13]
Potentiometry	Carbon paste/MIP Polyeugenol with crosslinker PEGDE	10^{-5}–10^{-1} M	8.363×10^{-5} M	[3]
Potentiometry	Carbon paste/MIP Polyeugenol with crosslinker EGDMA	10^{-5}–10^{-1} M	1.0334×10^{-5} M	This work

Table 9. Result of response time

Concentration (M)	Potential (mV)	Response time (sec)
10^{-5}	155.1	15
10^{-4}	173.2	12
10^{-3}	198.7	9
10^{-2}	211	8
10^{-1}	232	6

The Lifetime of the Electrode

Determination of the lifetime of the electrode aims to determine the time limit for using the electrode. Based on the measurement of the number of electrodes used, the Nernst factor results are produced as in Fig. 6. It shows that up to 19 times, the electrodes still show good performance. The weight of the electrode, after being used 25 times, was reduced by 0.12 g. Due to its weight loss, the amount of substance that functions as a mold was reduced, and the Nernstian Factor was also lowered.

Coefficient Selectivity

In this study, the potential match method (MPM) was used to determine the electrode selectivity for glucose analysis [19]. The value of the selectivity coefficient (K_{ij}) of the electrodes in a 10^{-5}–10^{-1} M fructose solution was 0.478, 0.266, 0.175, 0.219, 0.107, and 0.087. The fructose selectivity test was chosen because it has the most similar structure to glucose. From the K_{ij} value, fructose does not interfere with potentiometric glucose analysis using EMIP because the selectivity coefficient value is less than 1. The electrode will be selective for the analyte compared to the interfering compound if the

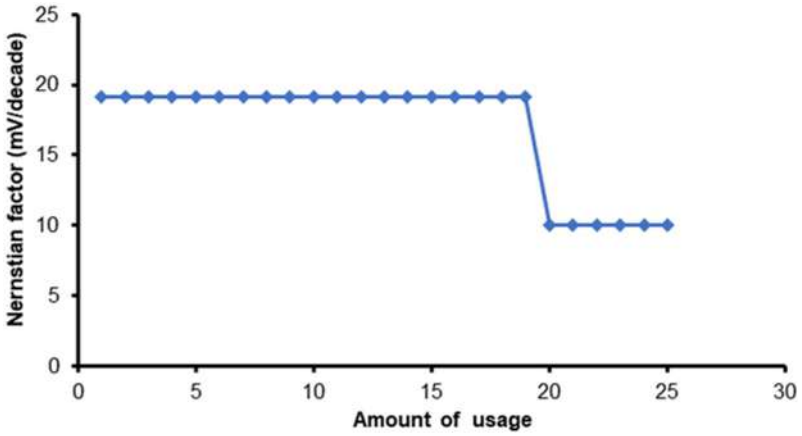

Fig 6. Lifetime electrode graph

value of $K_{ij} < 1$, otherwise the electrode will be selective for the interfering compound analyte if the value of $K_{ij} > 1$ and if the value of $K_{ij} = 0$, it means that the foreign compound does not interfere the analyte [20].

Measurement of Glucose on Honey Sample

Determination of glucose levels in honey was carried out to determine the ability of the hybrid electrodes to analyze glucose in samples containing reducing sugars (glucose and fructose). In this measurement, EMIP is used to measure the solution of raw honey. The measurement results showed that the glucose level in honey was 28.78%. Meanwhile, for measurements with UV-Vis spectrophotometry, glucose levels were 29.68%, then the measurement using HPLC where glucose and fructose are separated at retention times of 4.99 and 4.51 min, resulting in measurements for glucose of 30.42% and fructose of 38.38%.

■ CONCLUSION

The optimum composition electrode has a mass ratio of 45:35:20 (wt.%) by graphite:paraffin:MIP with an optimum pH of analyte is 7. Analysis of the performance of the electrode as a glucose sensor produces a Nernst factor of 19.16 mV/decade. The measurement range is 10^{-5}–10^{-1} M with a detection limit of 1.0334×10^{-5} M, a response time of 6–15 s, and a lifetime (use) of 19 times. It has good selectivity with a Kij of less than 1. The electrode can also measure glucose levels in honey samples and give a percentage result of glucose content is 28.78%, not much different from the measurement results on UV-Vis spectrophotometry, which is 29.68%, and HPLC, which is 30.42%. Based on this performance, the electrode is recommended as an alternative method to analyze glucose selectively on a blood sample.

■ ACKNOWLEDGMENTS

The authors would like to thank the Ministry of Education and Culture for the financial support of this study through Grant No 225-69/UN7.6.1/PP/2021.

■ AUTHOR CONTRIBUTIONS

M.C.D conducted the conceptualization, methodology, and validation, L.C. conducted the resources, and investigation, wrote and revised the manuscript, M.C.D., G.G., R.A.L., M.K. supervised the research. All authors agreed to the final version of the manuscript.

■ REFERENCES

[1] Ridwan, A., Astrian, R.T., and Barlian, A., 2012, Pengukuran efek antidiabetes polifenol (Polyphenon 60) berdasarkan kadar glukosa darah dan histologi pankreas mencit (Mus musculus L.) SW jantan yang dikondisikan diabetes mellitus, *JMS*, 17 (2), 78–82.

[2] McCuistion, L.E., DiMaggio, K.V., Winton, M.B., and Yeager, J.J., 2021, *Pharmacology-E-Book: A Patient-Centered Nursing Process Approach*, 10th Ed., Elsevier Health Sciences, St. Louis, US.

[3] Djunaidi, M.C., Afriani, M.D.R., Gunawan, G., and Khasanah, M., 2021, synthesis of graphite

paste/molecularly imprinted polymer (MIP) electrodes based on polyeugenol as a glucose sensor with potentiometric method, *Indones. J. Chem.*, 21 (4), 816–824.

[4] Djunaidi, M.C., Khabibi, K., and Ulumudin, I., 2017, Separation of Cu^{2+}, Cd^{2+} and Cr^{3+} in a mixture solution using a novel carrier poly(methyl thiazoleethyl eugenoxy acetate) with BLM (Bulk Liquid Membrane), *IOP Conf. Ser.: Mater. Sci. Eng.*, 172, 012032.

[5] BelBruno, J.J., 2018, Molecularly imprinted polymers, *Chem. Rev.*, 119 (1), 94–119.

[6] Saylan, Y., Akgönüllü, S., Yavuz, H., Ünal, S., and Denizli, A., 2019, Molecularly imprinted polymer based sensors for medical applications, *Sensors*, 19 (6), 1279.

[7] Djunaidi, M.C., 2019, Synthesis, caracterization and selectivity of moleculary imprinted polymer (MIP) glucose using polyeugenol as a functional polymer, *Rasayan J. Chem.*, 12 (2), 809–821.

[8] Djunaidi, M.C., Lusiana, R.A., and Kartikawati, N.G., 2010, Sintesis polieugenol dengan katalis BF_3 dietil eter dan H_2SO_4 untuk ekstraktan logam berat, *Prosiding Seminar Nasional Kimia dan Pendidikan Kimia 2010*, Badan Penerbit Universitas Diponegoro, 139–145.

[9] Djunaidi, M.C., Prasetya, N.B.A., Khoiriyah, A., Pardoyo, P., Haris, A., and Febriola, N.A., 2020, Polysulfone influence on Au selective adsorbent imprinted membrane synthesis with sulfonated polyeugenol as functional polymer, *Membranes*, 10 (12), 390.

[10] Shaipulizan, N.S., Md Jamil, S.N.A., Kamaruzaman, S., Subri, N.N.S., Adeyi, A.A., Abdullah, A.H., and Abdullah, L.C., 2020, Preparation of ethylene glycol dimethacrylate (EGDMA)-based terpolymer as potential sorbents for pharmaceuticals adsorption, *Polymers*, 12 (2), 423.

[11] Smith, B.C., 2017, The CO bond, Part I: Introduction and the infrared spectroscopy of alcohols, *Spectroscopy*, 32 (1), 14–21.

[12] Molina-Fernández, Í., Leuermann, J., Ortega-Moñux, A., Wangüemert-Pérez, J.G., and Halir, R., 2019, Fundamental limit of detection of photonic biosensors with coherent phase read-out, *Opt. Express*, 27 (9), 12616–12629.

[13] Khasanah, M., Widati, A.A., Handajani, U.S., Harsini, M., Ilmiah, B., and Oktavia, I.D., 2020, Imprinted zeolite modified carbon paste electrode as a selective sensor for blood glucose analysis by potentiometry, *Indones. J. Chem.*, 20 (6), 1301–1310.

[14] Park, S., Boo, H., and Chung, T.D., 2006, Electrochemical non-enzymatic glucose sensors, *Anal. Chim. Acta*, 556 (1), 46–57.

[15] Ahmed, J., Rashed, M.A., Faisal, M., Harraz, F.A., Jalalah, M., and Alsareii, S.A., 2021, Novel SWCNTs-mesoporous silicon nanocomposite as efficient non-enzymatic glucose biosensor, *Appl. Surf. Sci.*, 552, 149477.

[16] Kim, D.M., Cho, S.J., Cho, C.H., Kim, K.B., Kim, M.Y., and Shim, Y.B., 2016, Disposable all-solid-state pH and glucose sensors based on conductive polymer covered hierarchical AuZn oxide, *Biosens. Bioelectron.*, 79, 165–172.

[17] Alhans, R., Singh, A., Singhal, C., Narang, J., Wadhwa, S., and Mathur, A., 2018, Comparative analysis of single-walled and multi-walled carbon nanotubes for electrochemical sensing of glucose on gold printed circuit boards, *Mater. Sci. Eng., C*, 90, 273–279.

[18] Son, S.G., Park, H.J., Kim, Y.K., Cho, H.S., and Choi, B.G., 2019, Fabrication of low-cost and flexible potassium ion sensors based on screen printing and their electrochemical characteristics, *Appl. Chem. Eng.*, 30 (6), 737–741.

[19] Tohda, K., Dragoe, D., Shibata, M., and Umezawa, Y., 2001, Studies on the matched potential method for determining the selectivity coefficients of ion-selective electrodes based on neutral ionophores: Experimental and theoretical verification, *Anal. Sci.*, 17 (6), 733–743.

[20] Catrall, R.W., 1997, *Chemical Sensors*, Oxford University Press, United Kingdom.

Synthesis, Properties, and Function of Self-Healing Polymer-Based on Eugenol

Erwin Abdul Rahim*

Department of Chemistry, Tadulako University, Jl. Sukarno-Hatta Km 9, Palu 94148, Central Sulawesi, Indonesia

* ***Corresponding author:***

email: Erwin_abdulrahim@yahoo.com

Received: December 23, 2021
Accepted: April 4, 2022

DOI: 10.22146/ijc.71486

Abstract: *Eugenol-based self-healing polymers were synthesized in a very short time of 94–159 s. Polymerization of eugenol catalyzed by H_2SO_4-CH_3COOH yielded the corresponding self-healing polymers in quantitative yields in the range of molecular weight (5.18–15.10) × 10^5 g/mol. The polymer exhibited self-healing behavior at room temperature due to hydrogen bonds between the hydroxyl groups of polyeugenol and the hydroxyl groups of sulfuric acid. This material can function as a polyelectrolyte and a novel self-healing catalyst for biodiesel production.*

Keywords: *self-healing polymer; eugenol; catalyst; biodiesel production*

■ INTRODUCTION

Smart polymers are polymers that can only respond to small external stimuli. These small external stimuli include UV radiation, pH, temperature, magnetic field, etc. Self-healing smart polymers are a new class of smart materials that can repair themselves in the event of damage without the need for detection or repair by any kind of manual intervention. The increasing demand for fuel oil stocks used in the production of polymers and the need for polymer materials with improved performance in demanding applications further increases the need for durable materials. These challenges enable the synthesis of self-healing materials [1-5]. Compared to liquid electrolytes, solid electrolytes have higher safety and better thermal stability. In particular, the application of self-healing materials has led to intensive research on electronics, batteries, supercapacitors, solar cells, etc. Therefore, the practical demand for polyelectrolytes with self-healing properties will lead researchers to develop new self-healing materials [6-11].

In conjunction with world petroleum exhaustion, one improvement of renewable vitro sources is unique to selective fuel, especially vegetable oil as biodiesel. Biodiesel possess characteristics that matches diesel engine. These characteristics include being biodegradable, ecologically friendly, renewable, non-toxic and having high-thickness, high cetane number, and suitable sulphur content. The main disadvantage of commercialization of biodiesel is that it requires relatively expensive ingredients, i.e. beef oil with high quality and low free fatty acids, resulting in high manufacturing costs. One way to reduce the cost of biodiesel production is to use an inexpensive material with high free fatty acid content, for example, waste cooking oil (WCO). The preparation of waste cooking oil and methanol biodiesel involves an ester exchange reaction with a base catalyst and the formation of methyl ester and by-products in glycerol. However, the use of edible oils in this transesterification reaction resulted in very small transformation of biodiesel. This is because edible oil contains free fatty acids between 3–40%. Many researchers have developed a catalyst for the production of biodiesel made of skilled edible oil. One of them is a solid acid catalyst that replaces the liquid acid to eliminate corrosive and ecological problems [12]. An interesting topic regarding solid acid catalysts is green organic synthesis. Soluble polymer catalyst is one of the catalysts used for green organic synthesis. Some catalysts dissolved between them are polymeric based stimulation weakening catalysts. For instance, Sun et al. used polymer-based stimuli-responsive recyclable catalytic systems for organic synthesis [13], while Bergbreiter used soluble polymer as a tool in catalysis and also to recover catalysts and ligands [14]. However, until now, the use of self-healing polymer-based catalysts to produce biodiesel from waste used cooking oil has never been reported.

Indonesia is one of the world's major oil producers. In addition, Indonesia accounts for about half of the world's clove leaf oil consumption. The level of eugenol, also known as 3-(4-hydroxy-3-methoxyphenyl) propene, in oil is set at 80–90% by weight [15-18]. Furthermore, eugenol has the potential to be an excellent raw material for the creation of more valuable chemicals. To increase the price of eugenol, a number of tests were carried out. Eugenol-based optically active helical polyacetylene catalysts as a new smart material have been produced, according to a recent breakthrough. The intelligent material became motion-responsive, and gave birth to a new smart material [19].

This paper reports the synthesis, properties and function of eugenol-based self-healing polymers. The effects of catalyst concentration, reaction time, amount of methanol, and reaction temperature on the yield of biodiesel are investigated, as well.

■ EXPERIMENTAL SECTION

Materials

The materials used were eugenol (99.99% purity; obtained from Happy Green Co.), concentrated sulfuric acid, glacial acetic acid, methanol (p.a), ethanol 98%, chloroform, ethyl acetate, diethyl ether, *n*-hexane, benzene, anhydrous sodium sulfate (all were obtained from Sigma-Aldrich), and distilled water (obtained from Organic Laboratory, Palu, Central Sulawesi), WCO were collected from author`s university canteen.

Instrumentation

^{1}H spectra were recorded in chloroform-d ($CDCl_3$) on a JEOL EX-400 spectrometer. IR spectra were measured on a Bruker spectrophotometer. The tools used in this study were the melting point apparatus, pH meter, Ostwald viscometer, multimeter, analytical balance, stopwatch, separating funnel, hot plate, magnetic stirrer, aluminium foil, filter paper, and laboratory glassware.

Procedure

Synthesis of self-healing polymer-based on eugenol (SHPBE)

A 250 mL measuring cup was filled with up to 10 g of eugenol. Then, using a magnetic stirrer, 2.5 mL of catalyst (H_2SO_4-CH_3COOH; with a CH_3COOH percentage of 2, 4, 6%) was progressively added to the cup while being continually mixed (room temperature). The appearance of formed polymer and the release of concentrated white smoke indicated polymer formation. To stop the polymerization, 1 mL of methanol was introduced to the cup. After that, the polymer was allowed to settle for 24 h at room temperature before being identified. By dissolving SHPBE in ether and rinsing the catalyst away from the polymer with water, pure polyeugenol can be produced.

Determination of the molecular weight of SHPBE

One gram of SHPBE was dissolved in ethanol to 0.02 g/mL in a 50 mL volumetric flask. The polymer concentration was changed to 0.01500, 0.01000, 0.00500, 0.00250, and 0.00125 g/mL using ethanol dilution. The flow time of pure solvent, ethanol, and each concentration of polymer solution was measured using an Ostwald viscometer to give t0, t1, t2, t3, t4, t5, and t6. Using the Poisseuille equation, we get ηsp/C vs C. By projecting the curve to a concentration (C) of zero, we get [η]. The Mark-Houwink equation and the right parameters for K and a were used to calculate the polymer's molecular weight.

Self-healing properties

The support catalyst polymer was cut into small pieces and separated from the other parts. Then the polymer was left at room temperature for 24 h and observed for the process of self-healing.

Determination of ionic conductivity

Using ethanol as the solvent, the polymer was made into a solution with a thickness of 1 cm and a diameter of 6 cm for the electrodes. This investigation employed a frequency of 1–100 kHz and a voltage of 20 mV. To test the polymer's impedance, the material was clamped between two electrodes linked to the positive and negative poles of the LCR meter. Eq. (1) can be used to compute ionic conductivity.

$$\rho = RA/i;\ \sigma = 1/\rho \quad (1)$$

Biodiesel synthesis

A circular bottom flask with a magnetic stirrer was filled with 25 g of waste cooking oil. The catalyst was

then added in various concentrations of 1, 2, 3, 4, and 5%, and added with methanol at a 1:15 ratio (sample:methanol). To see the influence of reflux time on the yield of biodiesel produced, the catalyst concentration that provides the maximum biodiesel production was varied at 1, 2, 3, and 4 h at 60 °C. In the third step, the effect of raw material to methanol ratios of 1:11, 1:13, 1:15, 1:17, and 1:19 was examined (w:w). The experiment on the influence of temperature (40, 60, 80, 100, and 120 °C) was undertaken at the fourth stage. A Buchner funnel was used to filter the products. After that, 30 mL distilled water and 120 mL *n*-hexane were added to the filtrate. The mixture was placed in a separating funnel and left for 24 h to separate into two layers. Esters and *n*-hexane make up the top layer, while distilled water and the catalyst make up the bottom layer. Anhydrous Na_2SO_4 was transmitted through the top layer (esters and *n*-hexane). Then, using *n*-hexane, the esters were separated by rotating and measuring the volume. GC-MS was used to perform a quantitative analysis of FAME. The results were weighed and the biodiesel yield was calculated using Eq. (2).

$$\text{FAME yield} = \frac{\text{m actuacl}}{\text{m theoretical}} \times 100\% \quad (2)$$

The actual and theoretical masses of FAME in grams are denoted by m actual and m theoretical.

■ RESULTS AND DISCUSSION

Synthesis of SHPBE

The synthesis route for SHPBE is shown in Fig. 1. Eugenol was quantitatively converted into polymer electrolyte. ^{1}H-NMR (Fig. 3) and IR spectroscopy were used to identify the polymer electrolyte. The polymerization of eugenol using the H_2SO_4-CH_3COOH catalyst, which was found to be particularly effective for the polymerization of eugenol [12-19], produced excellent yields of the appropriate polymer (Table 1). According to FTIR analysis, the disappearance of absorption at wavenumbers 1637 and 995 cm^{-1}, which is indicative of vinyl group absorption, appeared in the IR spectrum of eugenol (Fig. 2(a)), but not in the spectrum of SHPBE (Fig. 2(b–d)). As a result, it pointed to the formation of SHPBE. SHPBE spectra in different concentrations of CH_3COOH were similar. The broad spectrum from –OH at wavenumber 3500 cm^{-1} suggested the establishment of hydrogen bonding in Fig. 2(b–d). Furthermore, ^{1}H-NMR research reveals that the vinyl group's proton resonance at 5 ppm was not detectable, indicating that polymerization had occurred (Fig. 3).

Self-healing and Motion Responsive Properties

Fig. 4 shows that the resulting polymer can undergo self-healing at room temperature. It was seen that the separate parts of the polymer coalesced after 24 h.

Ionic Conductivity of SHPBE

This SHPBE has an ionic conductivity of 3.6×10^{-1} $S.cm^{-1}$ and a semiconductor conductivity of $100–10^{-6}$ $S.cm^{-1}$. This SHPBE is a semiconductor polymer with

Table 1. Preparation of SHPBE

Run	Polymer			
	% CH_3COOH	Reaction time (s)	Yield (%)	M_w ($\times 10^5$) (g/mol)
1	2	159	94	5.18
2	4	129	99	15.10
3	6	94	98	5.52

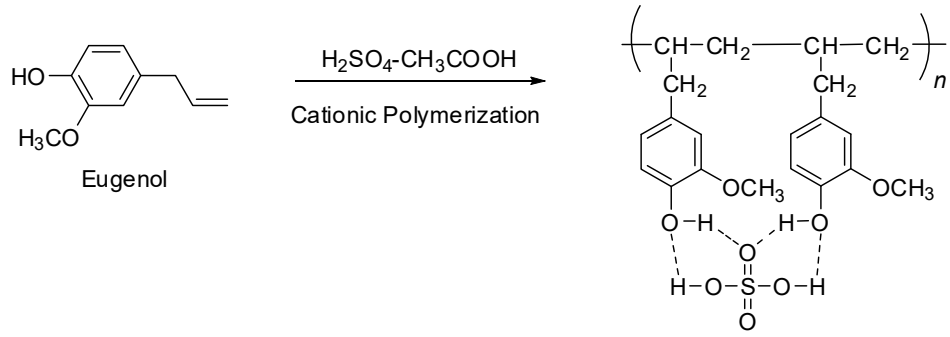

Fig 1. Schematic synthesis of SHPBE

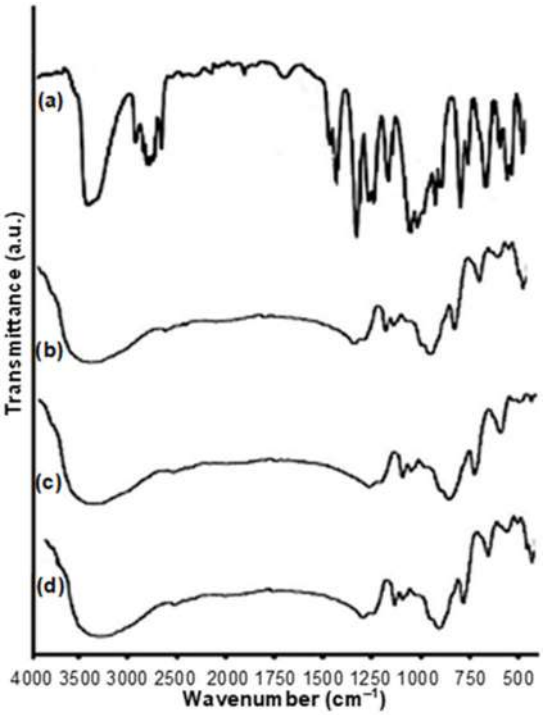

Fig 2. IR of SHPBE

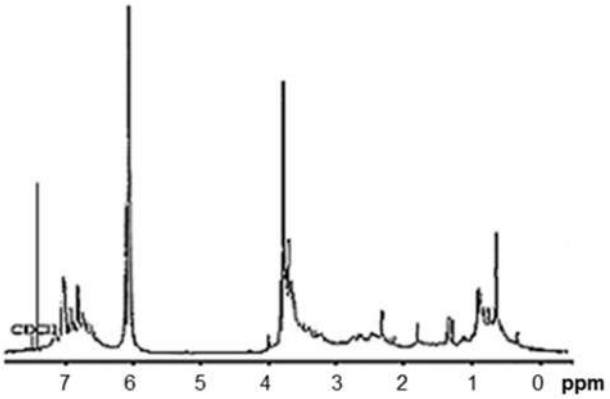

Fig 3. ^{1}H-NMR of SHPBE (Table 1, Run 2)

Fig 4. SHPBE at room temperature

Table 2. Comparison of the polymer properties with previous work

Sample	Properties	Ionic conductivity (S.cm^{-1})
This work	Self-Healing	3.6×10^{-1}
Xie et al. [2]	Self-Healing	$1.1 \times 10^{-4} - 1.78 \times 10^{-4}$
Evans et al. [7]	Self-Healing	3.5×10^{-4}
Nakamura et al. [20]	Not Self-Healing	$> 10^{-1}$

electrolytic characteristics. It can be utilized as a polymer electrolyte for Lithium-ion batteries because its conductivity is better than 10–5 S.cm^{-1} [8]. Table 2 compares the ionic conductivity achieved in this work to the ionic conductivity of the polymer electrolyte that was previously investigated. When compared to earlier studies, the sample size in this study is quite substantial. Membranes created by adding sulfuric acid (H_2SO_4) to cross-linked poly (4-vinyl pyridine) demonstrated ionic conductivity larger than 10^{-1} but no self-healing characteristics, according to Nakamura et al. [20]. This study's conductivity is the same as the previous one using the polymer/H_2SO_4 system.

Solubility of SHPBE

The solubility of this SHPBE was excellent. THF, benzene, toluene, CH_2Cl_2, $CHCl_3$, acetone, DMF, DMSO, can totally dissolve SHPBE in common solvents. The widespread use of homogeneous catalysts in synthesis, interest in green chemistry and sustainability, and the capacity to synthesize polymers with tailored specific features are all driving causes behind the growing interest in soluble polymers as catalysis tools [12].

SHPBE for Biodiesel Production from Waste Used Cooking Oil

From Fig. 5, it can be seen that at a catalyst concentration of 4%, the highest biodiesel yield was 56.98%, but the addition of 5% catalyst decreased the yield to 55.03%. At present, the reason for this finding is not clear. In this treatment, reflux time is carried out, which aims to see the highest yield. In Fig. 6, it can be seen that the higher the reflux time, the higher the yield of biodiesel produced, in which the highest yield was 57.79%.

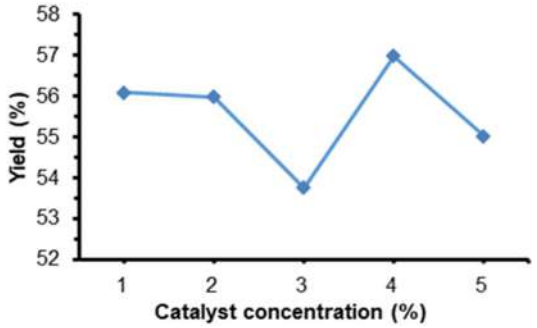

Fig 5. Effect of catalyst amount

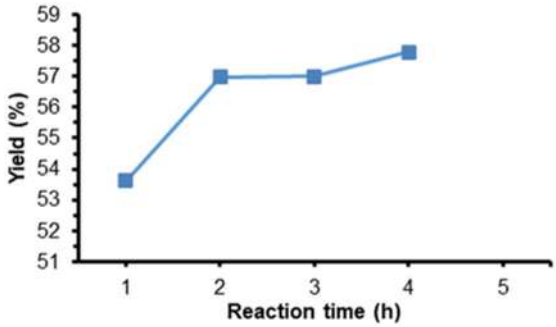

Fig 6. Effect of reaction time

Fig 7. Effect of methanol amount

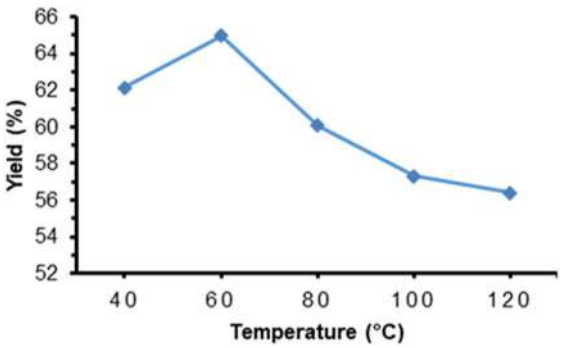

Fig 8. Effect of reaction temperature

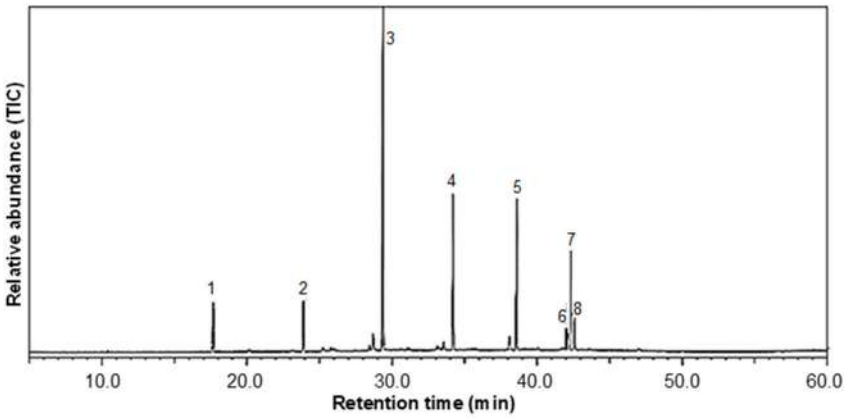

Fig 9. GC chromatogram of biodiesel using SHPBE

Table 3. Methyl ester compounds found in WCO

Peak	Retention peak (min)	Area (%)	Fatty acid methyl ester (FAME)
1	17.680	4.62	Methyl caprylate
2	23.913	5.02	Methyl caprate
3	29.407	38.59	Methyl laurate
4	34.234	17.40	Methyl myristate
5	38.616	16.62	Methyl stearate
6	42.025	3.01	Methyl linoleate
7	42.138	11.53	Methyl oleate
8	42.582	3.21	Methyl lignoserate

From Fig. 7, it can be seen the higher the oil: methanol ratio, the higher the yield of biodiesel. These results are in accordance with the research of Chuepeng [10], which states that an excessive amount of methanol must be added so that the reaction moves towards the product. From Fig. 8, it can be seen that the increase in biodiesel yield occurred from a temperature of 40 °C, namely 62.13, to 64.97% at 60 °C, and there was a significant decrease when the temperature was above 60 °C. At present, the reason for this finding is not clear. Fig. 9 shows the chromatogram of biodiesel, and Table 3 shows that methyl ester was found in WCO.

■ CONCLUSION

SHPBE with molecular weights ranging from (5.18–15.10) × 10^5 g/mol has been successfully synthesized. At room temperature, SHPBE has self-healing properties. This material also has a 3.6 × 10^{-1} S.cm^{-1} ion conductivity and is soluble in common organic solvents. The effects of operating factors such as catalyst amount, reaction time, methanol to WCO weight ratio, and temperature on FAME yields were examined and the maximum FAME yield obtained was 64.97%.

■ ACKNOWLEDGMENTS

EAR acknowledges the support of the Department of Chemistry, Faculty of Mathematics and Natural Science, Tadulako University.

■ REFERENCES

[1] Cheng, C., Li, J., Yang, F., Li, Y., Hu, Z., and Wang, J., 2018, Renewable eugenol-based functional polymers with self-healing and high temperature resistance properties, *J. Polym. Res.*, 25 (2), 67.

[2] Wang, H., Wang, P., Feng, Y., Liu, J., Wang, J., Hu, M., Wei, J., and Huang, Y., 2019, Recent advances on self-healing materials and batteries, *ChemElectroChem*, 6, 1605–1622.

[3] Liang, J.Y., Shin, S.R., Lee, S.H., and Lee, D.S., 2020, Self-healing and mechanical properties of thermoplastic polyurethane/eugenol-based phenoxy resin blends via exchange reactions, *Polymers*, 12 (5), 1011.

[4] Sumerlin, B.S., 2018, Next-generation self-healing materials, *Science*, 362 (6411), 150–151.

[5] Kumpfer, J.R., and Rowan, S.J., 2011, Thermo-, photo-, and chemo-responsive shape-memory properties from photo-cross linked metallo-supramolecular polymers, *J. Am. Chem. Soc.*, 133 (32), 12866–12874.

[6] Terryn, S., Roels, E., Brancart, J., Van Assche, G., and Vanderborght, B., 2020, Self-healing and high interfacial strength in multi-material soft pneumatic robots via reversible Diels–Alder bonds, *Actuators*, 9 (2), 34.

[7] Jing, B.B., and Evans, C.M., 2019, Catalyst-free dynamic networks for recyclable, self-healing solid polymer electrolytes, *J. Am. Chem. Soc.*, 141 (48), 18932–18937.

[8] Yao, P., Yu, H., Ding, Z., Liu, Y., Lu, J., Lavorgna, M., Wu, J., and Liu, X., 2019, Review on polymer-based composite electrolytes for lithium batteries, *Front. Chem.*, 7, 522.

[9] Jo, Y.H., Li, S., Zuo, C., Zhang, Y., Gan, H., Li, S., Yu, L., He, D., Xie, X., and Xue, Z., 2020, Self-healing solid polymer electrolyte facilitated by a dynamic cross-linked polymer matrix for lithium-ion batteries, *Macromolecules*, 53 (3), 1024–1032.

[10] Ngai, K.S., Ramesh, S., Ramesh, K., and Juan, J.C., 2016, A review of polymer electrolyte: fundamental, approaches and application, *Ionics*, 22 (8), 1259–1279.

[11] Choudhury, S., Stalin, S., Vu, D., Warren, A., Deng, Y., Biswal, P., and Archer, L.A., 2019, Solid state polymer electrolytes for high-performance lithium metal batteries, *Nat. Commun.*, 10 (1), 4398.

[12] Komintarachet, C., and Chuepeng, S., 2009, Solid acid catalyst for biodiesel production from waste used cooking oils, *Ind. Eng. Chem. Res.*, 48 (20), 9350–9353.

[13] Zhang, J., Zhang, M., Tang, K., Verpoort, F., and Sun, T., 2013, Polymer-based stimuli-responsive recyclable catalytic systems for organic synthesis, *Small*, 10 (1), 32–46.

[14] Bergbreiter, D.E., 2014, Soluble polymers as tools in

catalysis, *ACS Macro Lett.*, 3 (3), 260−265.

[15] Rahim, E.A, 2020, Synthesis of soluble novel polyecetylenes containing carbamate and eugenol moieties, *Indones. J. Chem.*, 20 (4), 818–824.

[16] Rahim, E.A., Sanda, F., and Masuda, T., 2004, Synthesis and properties of novel eugenol-based polymers, *Polym. Bull.*, 52 (2), 93–100.

[17] Rahim, E.A., Istiqomah, N., Almilda, G., Ridhay, A., Sumarni, N.K., and Indriani, 2020, Antibacterial and antioxidant activities of polyeugenol with high molecular weight, *Indones. J. Chem.*, 20 (3), 722–728.

[18] Rahim, E.A., Sanda, F., and Masuda, T., 2006, Synthesis and properties of optically active amino acid based polyacetylenes bearing eugenol and fluorene moieties, *J. Polym. Sci., Part A: Polym. Chem.*, 44 (2), 810–819.

[19] Rahim, E.A., 2018, Unique polymerization and new smart material of eugenol-based helical polymers, *Int. J. Sci. Res.*, 7 (11), 990–996.

[20] Kajita, T., Tanaka, H., Noro, A., Matsuhita, Y., and Nakamura, N., 2019, Acidic liquid-swollen polymer membranes exhibiting anhydrous proton conductivity higher than 100 mS cm^{-1} at around 100 °C, *J. Mater. Chem. A*, 7 (26), 15585–15592.

Impact of Anode Materials on Electrochemical Degradation of Carbamazepine: A Case Study of Producing the Main By-Product 10,11-Epoxycarbamazepine after Electrochemical Degradation of Carbamazepine

Zainab Haider Mussa[1] and Fouad Fadhil Al-Qaim[2,3,4*]

[1]*College of Pharmacy, University of Al-Ameed, PO Box 198, Karbala, Iraq*

[2]*Faculty of Medicine, University of Warith Al-Anbiyaa, Karbala, Iraq*

[3]*Department of Chemistry, Faculty of Science for Women, University of Babylon, PO Box 4, Hilla, Iraq*

[4]*School of Chemical Science and Food Technology, Faculty of Science and Technology, Universiti Kebangsaan Malaysia, UKM Bangi, Selangor Darul Ehsan, 43600, Malaysia*

** **Corresponding author:***

tel: +964-7821871620
email: fouad.fadhil@uobabylon.edu.iq

Received: January 6, 2022
Accepted: May 17, 2022

DOI: 10.22146/ijc.71976

Abstract: *Copper (Cu), nickel (Ni), platinum (Pt), and graphite (G)" have been applied to the electrochemical degradation of carbamazepine (CBZ) from its aqueous solution. The optimum results were observed with graphite anode as follows: fully complete removal of CBZ, 0.0758 min^{-1} rates constant, and 0.59 Wh/mg consumption energy under these conditions: 5 V, 0.5 g NaCl, and a graphite anode. Kinetics was also considered in the present study, in which rate constants ranged between 0.0023 and 0.0886 min^{-1}. It was observed that applied voltage affects consumption energy giving 0.34, 0.59, and 1.08 Wh/mg using 3, 5, and 7 V, respectively. Field emission scanning electron microscope (FESEM) and energy dispersive X-ray spectroscope (EDS) were used to characterize the organo-metallic precipitates which were formed using Ni and Cu anodes. The main by-product of 10,11-epoxycarbamazepine (EPX-CBZ) was elucidated and monitored using liquid chromatography-time of flight/mass spectrometry (LC-ToF/MS). Therefore, graphite is a promising electrode in that it performs well compared to other electrodes in removal and energy consumption.*

Keywords: *electrochemical degradation; carbamazepine; 10,11-epoxycarbamazepine; anode materials; graphite anode*

■ INTRODUCTION

Highly utilization of pharmaceuticals and personal care products resulted in increasing their presence in aquatic samples, then affecting organism life in water [1-2]. One of these pharmaceuticals is carbamazepine (CBZ) which is frequently used in the treatment of trigeminal neuralgia and psychiatric diseases [3]. It has been recognized as an emerging contaminant because of its ecological risk potential and chronic and synergistic effects.

It was reported that carbamazepine was one of the top most utilized pharmaceuticals in Malaysia [4] and worldwide, reaching up to 1014 tons per year [5]. Carbamazepine has been frequently detected in water bodies, which may be attributed to its high degradation resistance towards oxidation and biological treatment [6-7]. According to previous studies, several treatment processes have been applied for the elimination of carbamazepine.

It could be removed by a very basic technique of membrane filtration or adsorption. However, these methods may not be suitable because of their low efficiency and high cost. It could also be not preferred because producing secondary pollution means carbamazepine is merely transferred to another medium and is not destroyed. Nezhadali et al. applied polypyrrole-chitosan-Fe_3O_4 magnetic nanocomposite as a magnetic nano sorbent to remove carbamazepine. It was removed in 94.5% after 25 min of electrolysis treatment [8].

Esquerdo et al. investigated the hybrid treatment and sequence of treatment processes, including ozone and activated carbon, on the removal of carbamazepine. He noticed that using ozone treatment first and then activated carbon is better than using activated carbon and then ozone to achieve 90% carbamazepine removal [9]. Some reports explained that CBZ had not degraded well using biological treatment as it takes a long time, and the removal efficiency is very low. Moya-Llamas et al. combined a sludge blanket reactor with a membrane bioreactor to remove carbamazepine from wastewater and observed a CBZ percent removal of 49.5% after 193 days [10].

He noticed that an enzymatic membrane bioreactor equipped with ultrafiltration or nanofiltration has a good advantage for removing CBZ, reaching up to 65%. This removal efficiency decreased with increasing initial concentration. Furthermore, the hydraulic retention time in most biological treatments is long, reaching up to 6 days [11]. As carbamazepine is highly resistant to biological treatment, combined gamma radiation and biological treatment were applied for the removal of CBZ from wastewater. It was observed the removal of CBZ was 99%, but total organic carbon (TOC) was 26.5% using only gamma radiation, but after combination with biological degradation, TOC removal was increased to 79.3% [12].

Based on the findings from the literature, it is necessary to look for alternative technology that participates in developing cost-effective treatment methods. It is very well known that advanced oxidation approaches are effective and promising methods to oxidize carbamazepine which is attributed to the high potential of hydroxyl radical (E° = 2.7 V vs. Standard Hydrogen Electrode (SHE)) [13-14]. Hydroxyl radicals can react non-selectively with organic pollutants at ambient temperature and pressure [15-17]. Photocatalysis [18-19], electro-Fenton [20], UV/chlorine [21], electrochemical oxidation [22], and other techniques [23], have been used as effective options for the degradation of CBZ. The electrochemical oxidation process is one of the advanced oxidation methods that have high efficiency for the degradation of pollutants and good environmental compatibility, so it encourages a promising technology for the elimination of organic pollutants from water bodies [14].

In the electrochemical oxidation process, anodic oxidation could occur on the anode's surface and/or at the bulk solution, producing a very active oxidizing agent, active chlorine "ClO^-/HOCl" [24]. Removal of organic pollutants such as pharmaceuticals, dyes, pesticides, and so on depends strongly on the active chlorine when NaCl is present [25]. As reported in previous studies, graphite exhibited good results due to its long lifetime at specifically applied voltages, not too high, eco-friendly, and low evolving oxygen, which means at low current achieve high removal with low consumption energy. Using graphite is accompanied by releasing a very active oxidizing agent, "ClO_4^-" instead of hydroxyl radical. However, graphite has been used to remove different pharmaceuticals, as reported by Mussa et al. [26].

The aim of the present study is: (i) to optimize different anode materials for the removal of carbamazepine; (ii) to evaluate the electrochemical efficiency process for the elimination of carbamazepine, (iii) to determine the energy consumption and kinetic studies during the electrochemical oxidation process, (iv) to identify the 10,11-epoxycarbamazepine (EPX-CBZ) as the main by-product after electrochemical degradation process of CBZ.

■ EXPERIMENTAL SECTION

Materials

Carbamazepine standard compound (CAS no. 298-46-4) and 10,11-epoxycarbamazepine were provided from sigma-Aldrich (USA). The supporting electrolyte NaCl with high purity (99%) was bought from Merck (Germany). Acetonitrile, methanol, and formic acid were purchased from Merck (Germany). Other chemical reagents, such as tetrahydrofuran (Cas no. 109-99-9) and polyvinyl chloride, were purchased from Sigma Aldrich (USA). The stock solution of carbamazepine (1000 mg/L) has been prepared as follows: 0.01 g of standard reagent was dissolved in 10 mL of methanol and then preserved at −18 °C to minimize the degradation of the standard. Further dilutions of CBZ standard solutions were

provided in de-ionized water (DIW) and were kept at 4 °C.

Instrumentation

Analytical methods

A field emission scanning electron microscope (FESEM) instrument (brand: JEOL, model: JSM-7800F) was employed to characterize the precipitation after the electrochemical oxidation procedure at nickel and copper anodes.

Carbamazepine degradation was analyzed using an accurate instrument: LC-TOF/MS from a Dionex Ultimate 3000/LC 09115047 (USA). It is equipped with a vacuum degasser, a quaternary pump, and an auto-sampler. All separations were provided on a chromatographic column of Gemini 5 µm NX 110Å C18 column (2.1 mm × 250 mm, Phenomenex).

Carbamazepine degraded solution and its main by-product (EPX-CBZ) were analyzed in positive ionization mode. The binary mobile phase consisted of 0.1% formic acid in de-ionized water (DIW) (mobile phase A) and acetonitrile in methanol (3:1 v/v) (mobile phase B). The flow rate was 0.3 mL/min, and the elution program was carried out as follows: starting with 5% B at 0.0 min; 0–3 min, 60% B; 3–6 min, 97% B; 6–11 min, 97% B; 11–11.1 min, 5% B; 11.1–16.1 min, 5% B. Injection volume was 30 µL.

The structure of carbamazepine and 10,11-epoxycarbamazepine were elucidated after isolation of protonated molecular ions $[M+H]^+$ and $[M+Na]^+$, respectively, using ESI-TOF instrument (Bruker/ Germany). Furthermore, retention time (t_R) was considered an extra factor to confirm the identity of the EPX-CBZ by-product. Optimization of MS was obtained with the following settings: MS capillary voltages, 4000 [ESI (+)]; drying gas flow rate, 8.0 L/min; drying gas temperature, 190 °C; and nebulizer pressure, 4.0 bar. All analytes were acquired using an independent reference spray via the LockSpray interference to ensure accuracy and reproducibility.

Extraction of 10,11-epoxycarbamazepine

The main by-product (EPX-CBZ) was identified after electrochemical degradation of 200 µg/L of CBZ under the optimum conditions: 0.5 g NaCl and 5 V. Samples were subjected to an electrochemical degradation process for two hours, then it was monitored after each 20 min. The samples after that were treated with solid phase extraction (SPE) cartridges (Oasis HLB, 3cc) and then injected into LC-TOF/MS for further analysis and elucidation. Solid-phase extraction can be explained as follow: (i) all samples after the degradation process were filtered using 0.45 µm (Whatman filter paper); (ii) samples were loaded at a flow rate of 3 mL/min on SPE cartridges after the preconditioning step with 1 mL of methanol and 1 mL of DIW; (iii) drying of cartridges under vacuum for 5 min then elution of the intended 10,11-epoxycarbamazepine in a test tube using 5 mL of methanol as the best eluent for this purpose; (iv) gentle stream of N_2 was used for dryness the extract of EPX-CBZ then it was reconstituted with 1 mL of methanol-water (10:90, v/v); (v) finally, the extract was injected into LC-TOF/MS for analysis.

Procedure

Electrochemical procedure

The degradation of carbamazepine was provided in the laboratory in 50 mL glass beaker, and it was placed on a magnetic stirrer then, the solution was subjected to the rotation force to ensure all contents were mixed well under 500 rpm at normal conditions. The experimental setup used for this study is shown in Fig. 1.

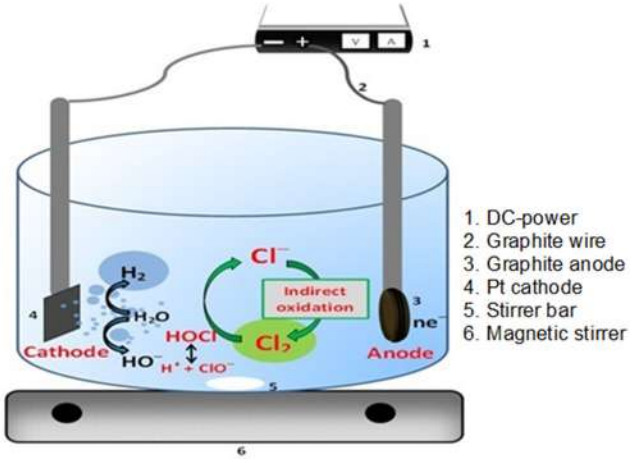

Fig 1. The schematic diagram of the real electrochemical process

Different anode materials have been used, namely: copper, nickel, platinum, and graphite. All have been applied and tested as anode electrodes, while the cathode electrode was fixed platinum in all experiments. The distance between anode and cathode was 4.0 cm to reduce the ohmic effect. Both electrodes assembly were connected to the DC power supply (CPX200 DUAL, 35 V 10 A PSU). All anode materials are plate sheets except for graphite powder. However, making graphite pellet was provided in steps, as explained in Fig. 2.

The influence of the electrochemical oxidation process factors such as applied voltage (3–7 V), processing time (0–80 min), and NaCl supporting electrolyte amount (0.1, 0.3, and 0.5 g) was examined at an initial concentration of carbamazepine 5 mg/L. During the electrochemical process, the electrode distance was maintained at 4 cm throughout the experiments.

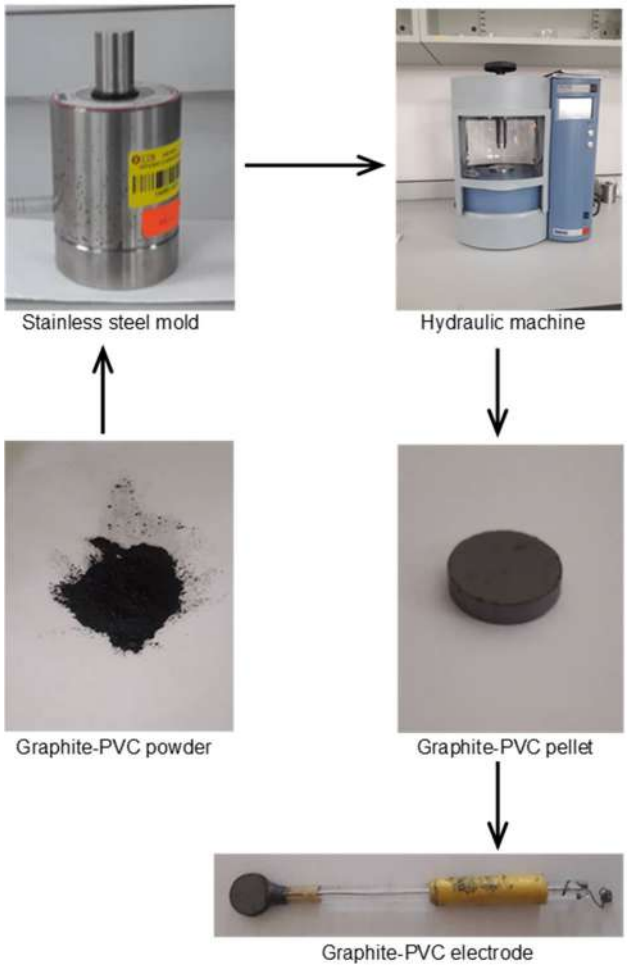

Fig 2. Steps of preparation of the graphite-PVC electrode

The consumption energy of electrochemical treatment of carbamazepine was also considered in the present study to confirm that the present study is preferred in terms of electric energy consumption.

■ RESULTS AND DISCUSSION

Effect of Anode Materials

In the electrochemical oxidation process, the anode is the electrode responsible for generating the electrons in solution to keep the oxidation-reduction process. The performance of the electrochemical oxidation process has been influenced by the type of anode material, as reported in previous studies [27-28]. In this study, four anode materials, namely: platinum (Pt), copper (Cu), nickel (Ni) plates, and graphite-PVC electrodes, were investigated for CBZ degradation. It is very well known that aluminum and iron anodes are common anodes used for this purpose, but they were not tested because these electrodes are only used for the electrocoagulation process, not the electrochemical oxidation process in which they produce a large volume of sludge, as reported by Nidheesh et al. [29].

Fig. 3(a) shows the effect of nature anode material on the degradation of carbamazepine at 0.5 g NaCl, 5 V, and 5 mg/L initial concentration of carbamazepine, and it was observed that graphite and platinum give the best percent removal of carbamazepine; contrarily for the two material anodes, Cu and Ni. This variation in percent removal depends on the mechanism of oxidation on the surface of the electrode. Nickel and copper prefer direct oxidation (i.e., producing hydroxyl radical as the main oxidizing agent) as the oxygen evolution potential is higher than Pt and graphite, while Pt and graphite prefer the indirect oxidation process, which means depending on the chlorine mediator in the solution. However, after 50 min, the removal was 96 and 93% of Pt and graphite, respectively, while it was 80 and 60% of Ni and Cu, respectively, under the same conditions of 5 V and 0.5 g NaCl. With increasing time, the removal was enhanced significantly in which it was complete at Pt, Ni and graphite except for copper, and it was 77%. It is well known that Pt as anode has good efficiency for removal of CBZ, but it is more expensive than graphite anode.

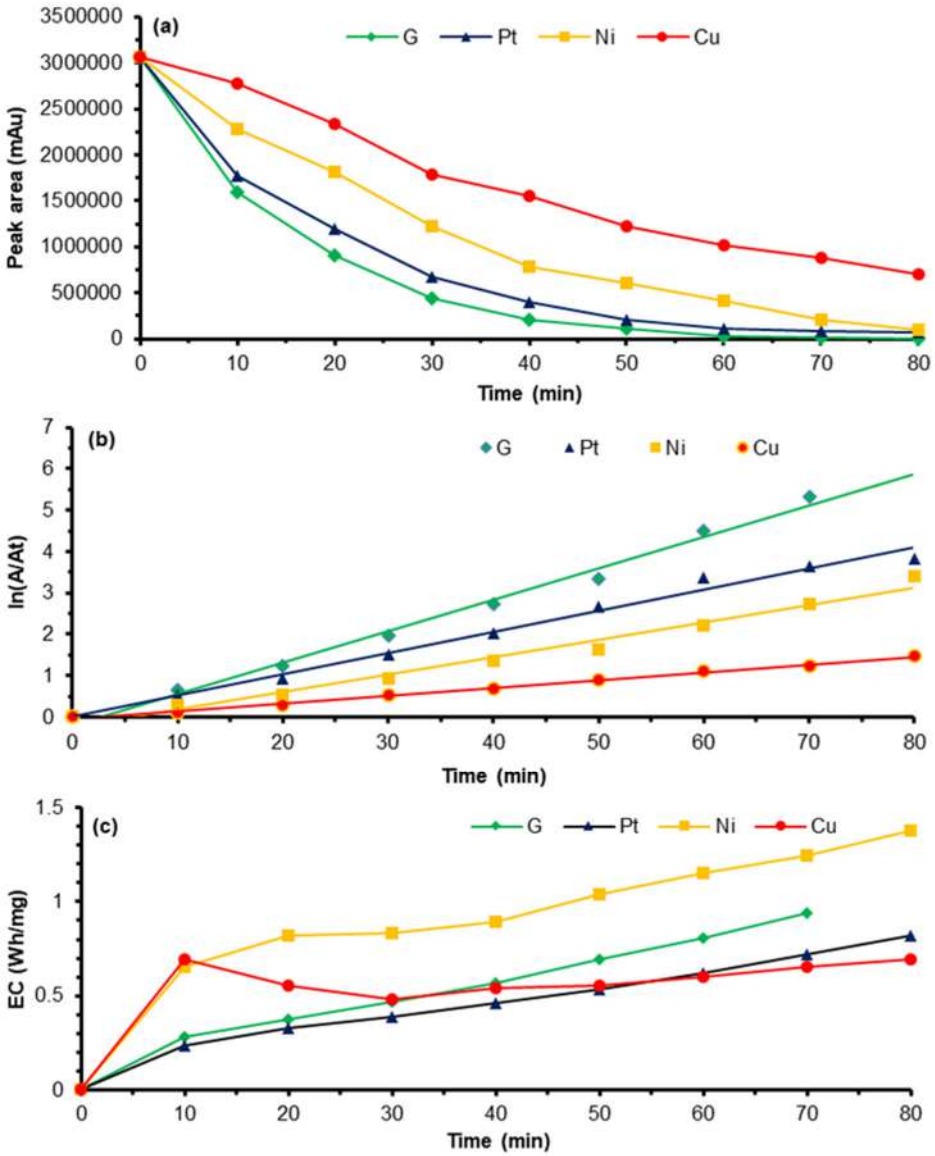

Fig 3. Effect of anode materials on (a) the removal of carbamazepine; (b) pseudo-first-order kinetic model; (c) consumption energy model during the electrochemical process under these conditions (5 mg/L CBZ; 0.5 g NaCl; 5 V)

In the present study, Ni and Cu electrodes were not suitable for the degradation of CBZ as their efficiency was insufficient. Both electrodes were corroded completely within one cycle of an electrochemical process, in agreement with that study reported by Nordin et al. He noticed that nickel and copper corroded after 120 and 95 min, respectively, after electrochemical degradation of dye [30].

Hypochlorite ions, as the main oxidizing agent, play an important role in the oxidation of carbamazepine. However, an excess concentration of ClO^- could not change more, so it remains constant through the electrochemical reaction. Based on this prospect, most of the indirect electrochemical oxidation reactions in the presence of chlorine obey the pseudo-first-order kinetics model [31-32]. The model could be presented in Eq. (1).

$$\frac{d[CBZ]_t}{dt} = -k_{obs}[CBZ]_t \quad (1)$$

where k_{obs} is the observed first-order rate coefficient; $[CBZ]_t$ is the total concentration of carbamazepine at the reaction time of t. After integrating Eq. (1) and rearranging it, Eq. (2) could be presented as follow:

$$\ln([CBZ]_t / [CBZ]_0) = -k_{obs}t \quad (2)$$

According to the equation, ln ($[CBZ]_t/[CBZ]_0$) was plotted versus electro-reaction time to generate a straight line, coefficient of determination (r2) ranged between 0.974 and 0.9958, with a slope of $-k_{obs}$ (Fig. 3(b)).

High-rate constants were observed with Pt and graphite of 0.0758 and 0.0513 min^{-1}. In contrast, the lowest rate constant was 0.019 min^{-1} for copper and nickel in the presence of 0.5 g NaCl and 5 V. These results may be attributed to the efficiency of anode materials in producing enough electrons in the solution.

According to the results reported in Table 1, it was observed that the degradation rate values were strongly influenced by the electrolytic anode materials. Based on the existing literature, nickel and copper are active electrodes that can be applied for direct electrochemical degradation because they produce hydroxyl radicals for the electrochemical degradation of organic pollutants [33]. It was found that the nickel electrode is inactive during the electrochemical process in the presence of supporting electrolytes such as Na_2SO_4 [34]. Graphite and Pt anode materials prefer an indirect electrochemical oxidation process, so supporting electrolytes' existence strongly enhances removal efficiency for carbamazepine [35]. The energy consumption was investigated and calculated according to Eq. (3) [36] during the electrochemical oxidation process of carbamazepine at all studied anode materials of Ni, Cu, Pt, and graphite.

$$EC = \frac{V.I.\Delta t}{\Delta[\text{reduced mass}]} \quad (3)$$

where EC (Wh/mg of carbamazepine) is the energy consumption required to degrade carbamazepine under certain conditions; V is the applied voltage; I (A) is the passed current in an electric cell; t (h) is the electrolysis time; Δ[reduced mass] is the reduced amount (mg) of carbamazepine. The energy consumption of carbamazepine is presented in Fig. 3(c), and it was observed that the energy consumption was very high in the case of nickel, while it was the lowest regarding copper anode. However, the percent removal was very low at both anodes. The consumption of energy was slightly different at platinum and graphite, and at the same time, the removal was also high for both electrodes. Consequently, graphite has been chosen for its availability and low price.

Effect of Applied Voltage

The applied voltage is influential in eliminating organic pollutants using the electrochemical treatment process. Some reported papers indicated that the decomposition of electrode materials, especially anodes might be attributed to the high applied voltage or oxygen evolution in some occurred reactions [37].

Different values of applied voltage have been investigated on the degradation of carbamazepine, and it was varied at 3, 5, and 7 V under these conditions: initial concentration of carbamazepine at 5 mg/L and supporting electrolyte amount NaCl of 0.5 g for all experiments. The results obtained are shown in Fig. 4(a).

Table 1. Pseudo-first-order rate constants for carbamazepine at different affecting parameters such as anode materials, sodium chloride amount, and applied voltage

Parameters	Quantity	No. points	Rate constant (min^{-1})	Coefficient of determination (r2)
Anode materials	Graphite-PVC	7	0.0758	0.9908
	Platinum	8	0.0513	0.9982
	Nickel	8	0.0418	0.9784
	Copper	8	0.019	0.9958
Sodium chloride (g)	0.1	8	0.0023	0.8565
	0.3	8	0.0274	0.9921
	0.5	7	0.0758	0.9908
Applied voltage (V)	3	8	0.0199	0.9864
	5	7	0.0758	0.9908
	7	4	0.0886	0.9875

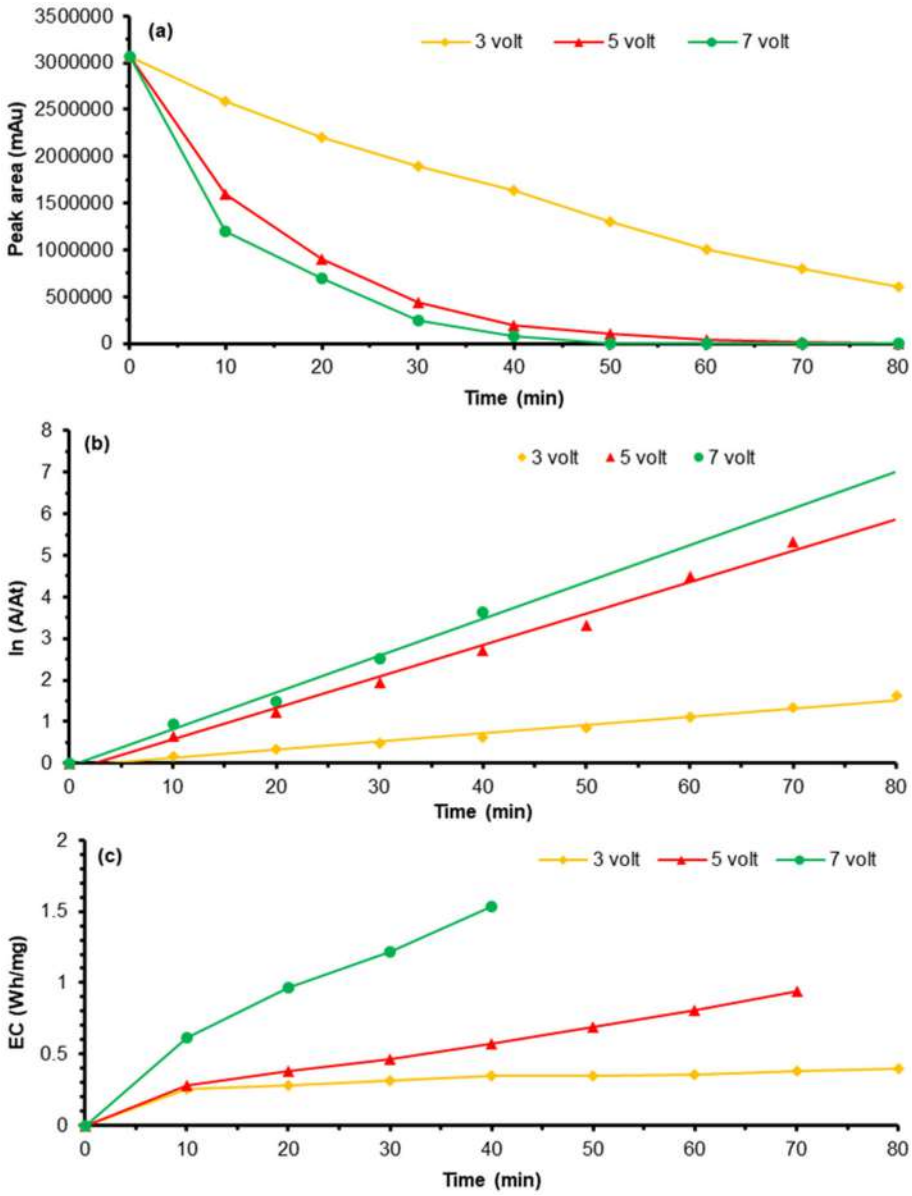

Fig 4. Effect of applied voltages on (a) the removal of carbamazepine; (b) pseudo-first-order kinetic model; (c) consumption energy model during the electrochemical process under these conditions (5 mg/L CBZ; 0.5 g NaCl; graphite as an anode)

It was observed that the removal of carbamazepine was 80.1% at 3 V after 80 min, while it was completely removed at 5 and 7 V after 80 and 50 min, respectively. This could be attributed to the high applied voltage producing more electrons that play an important role in forming active chlorine (Cl_2/HOCl) in bulk solution. However, high removal efficiency on the degradation of carbamazepine and high energy consumption was observed. It was noted that the removal rate was influenced highly by increasing applied voltage due to inducing oxygen evolution [38-39].

Electro-Fenton has been applied for the degradation of carbamazepine, and it was observed that increasing the current from 0.2 to 2 A resulted in decreasing the degradation process of carbamazepine from 68 to 53%. As the electro-Fenton requires ferrous ions, the current can be used for the oxidation-reduction process to form H_2O_2. High applied voltage resulted in

more energy consumption and shortened the life of the electrode [40]. At the same time, low applied voltage leads to slow degradation and waiting a long time to achieve some removal of carbamazepine. However, from the above findings, 5 V was chosen as the optimum applied voltage for further experiments.

Increasing of applied voltage resulted in producing more ClO^- which contributes strongly to the acceleration of electrochemical removal of carbamazepine. High k_{obs} of 0.0886 min^{-1} was observed at 7 V, which is slightly greater than k_{obs} at 5 V and eight times greater than k_{obs} at 3 V. However, all models fit pseudo-first-order kinetics as the coefficient of determination greater than 0.98 value as presented in Fig. 4(b) and Table 1.

Energy consumption steadily increased with time during the electrochemical process (Fig. 4(c)). It seems that high energy consumption was accompanied by 7 V of 1.5332 Wh/mg compared to 5 V of 0.9371 Wh/mg. However, the lowest consumption of energy was 0.4 Wh/mg with 3 V, but the percent removal was 80% after 80 min. It could be concluded that 5 V was the best selection for further experiments.

Effect of Supporting Electrolyte

In the electrochemical treatment process, the amount of supporting electrolyte is very effective when the indirect process is dominant.

As a general rule, keeping a low ohmic drop between the electrodes across the electrochemical cell requires high conductivity in solution to enhance the electrochemical efficiency [41]. NaCl as a supporting electrolyte has been chosen to increase the efficiency of the electrochemical treatment process for caffeine, compared to other electrolytes such as Na_2SO_4, which lead to a low efficient treatment process [36]. This can be attributed to increasing the electron transfer resulting in high electrical conductivity. The generation of chlorine, then the main oxidizing agent of hypochlorite ion OCl^- could be presented in Eq. (4-7).

$$2Cl^- \rightarrow Cl_2 + 2e^- \quad (4)$$

$$Cl_2 + H_2O \rightarrow H^+ + Cl^- + HOCl \quad (5)$$

$$HOCl \leftrightarrow H^+ + ClO^- \quad (6)$$

$$ClO^- + \text{organic pollutant} \rightarrow CO_2 + H_2O + Cl^- \quad (7)$$

Different electrolyte amounts of 0.1, 0.3, and 0.5 g NaCl have been applied to the electrochemical degradation of carbamazepine using graphite anode and 5 V (Fig. 5(a)).

The carbamazepine degradation efficiency increased significantly with the 0.3 and 0.5 g NaCl. After 80 min, the removal was complete, 97.7% of 0.5 and 0.3 g NaCl, respectively, while it was 77% of 0.1 g NaCl.

From Fig. 5(b) and Table 1, it was observed that k_{obs} of 0.0758 min^{-1} was the greatest at 0.5 g NaCl compared to 0.1 g and 0.3 g NaCl which was 0.0274 and 0.0023 min^{-1}, respectively. Gracia-Espinoza et al. reported that increasing sodium chloride using Nb/BDD as anode increased the rate constant, reaching 0.189 min [3]. The highest consumption energy of 2.8798 Wh/mg was achieved using 0.1 g NaCl at 5 V and 5 mg/L initial concentration of carbamazepine (Fig. 5c). At the same time, the percent removal is very low, accompanied by 0.1 g NaCl. For 0.3 and 0.5 g NaCl, the consumption energy was too close to 0.8889 and 0.937 Wh/mg, respectively. Finally, 0.5 g NaCl was selected for further experiments.

Characterization of Anode Materials

As we know, the selection of anode material is not only accompanied by the high efficiency of degradation for organic pollutants, but also it is related to some considerations such as: (i) the anode material must not be influenced by corrosion during the electrochemical oxidation process; (ii) the anode must be cheap, highly conductive, and produce fewer metal ions. However, Anglada et al. reported that using metal anodes might result in metal ions in the solution; thus, this approach needs a separation step to recover the metallic species, as explained in Eq. (8-15) [42]. Graphite reaction has not been reported here because it does not release ions to the solution like Ni and Cu electrodes to form precipitates. These precipitates may refer to the formation of organometallic compounds in the presence of Ni and Cu ions, as represented here:

$$Ni^0 \rightarrow Ni^{2+} + 2e^- \quad (8)$$

$$2Cl^- \rightarrow Cl_2 + 2e^- \quad (9)$$

$$Cl_2 + H_2O \rightarrow OCl^- + H^+ + HCl \quad (10)$$

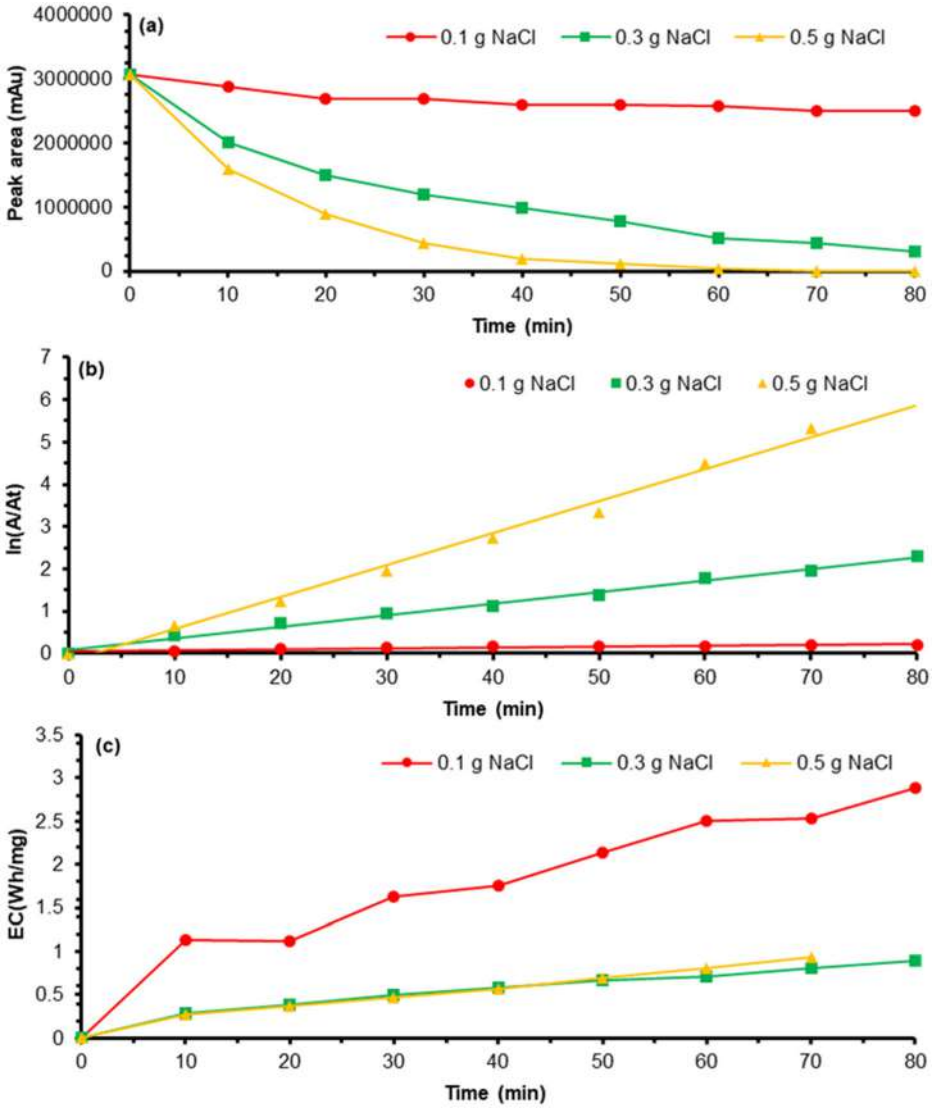

Fig 5. Effect of sodium chloride amounts on (a) the removal of carbamazepine; (b) pseudo-first-order kinetic model; (c) consumption energy model during the electrochemical process under these conditions (5 mg/L CBZ; 5 V; graphite as an anode)

$$Ni^{2+} + Cl_2 / H_2O + O-C \rightarrow Ni[O-C]_{ppt} + CO_2 + H_2O + Cl^- \quad (11)$$

$$Cu^0 \rightarrow Cu^{2+} + 2e^- \quad (12)$$

$$2Cl^- \rightarrow Cl_2 + 2e^- \quad (13)$$

$$Cl_2 + H_2O \rightarrow OCl^- + H^+ + HCl \quad (14)$$

$$Cu^{2+} + Cl_2 / H_2O + O-C \rightarrow Cu[O-C]_{ppt} + CO_2 + H_2O + Cl^- \quad (15)$$

where (O–C) is the organic compound.

It is well known that Ni^{2+} and Cu^{2+} ions were formed in the solution after the electrochemical oxidation process of nickel and copper anodes, respectively resulting in the generation of organometallic compounds. Graphite and platinum electrodes have not been discussed because they did not release ions in the solution. Therefore, the precipitates have not formed. The precipitates were only formed with nickel and copper electrodes and then washed in water. After that, they dried at room temperature for further characterization using EDX-FESEM. From Fig. 6, it could be observed that the intensities peaks for Ni and Cu (kα: 7.47 and kα: 8.04, respectively) are matched with energies listed in the energy table for EDX analysis. From EDX spectrum results, the elements on the surface of the precipitate

were C, O, Cl, Na, Ni, and Cu, using Ni and Cu as anode electrodes. Of course, C and O are from organic content, while Cl and Na are from the electrolyte salt (NaCl). However, Ni and Cu were from material anodes. Consequently, graphite-PVC was selected as the best anode for further experiments for these considerations: (i) efficient conductivity material; (ii) inert to side chemical reactions; (iii) available; (iv) no elements released to the solution compared to Ni and Cu; (v) high removal efficiency.

Stability of Graphite Electrode

Graphite has been selected as the best anode material compared to other materials, including Ni, Cu, and Pt. However, as we know, graphite is carbonaceous, which means it suffers from corrosion when used for a long time. Hence, its stability has been tested after ten cycles of the electrochemical treatment process using SEM. It was clear from Fig. 7, that the morphology of graphite before and after electrochemical treatment is different. The surface becomes more scraped, and small holes are observed during the electrolysis period after electrochemical treatment. The electrochemical stability experiments were studied under these conditions: 0.5 g NaCl, 5 V, 5 mg/L of carbamazepine, and 60 min. The percent removal of carbamazepine ranged between 88% and 99% after ten cycles indicating that graphite is able to overcome all these challenges when used for a long time.

It could be concluded that CBZ can be easily degraded by the graphite even after ten cycles which means three hours of the electrochemical oxidation process. Graphite-PVC composite exhibited good stability and excellent results in terms of electrochemical efficiency as it acted as an electron transfer catalyst thanks to its excellent electrical conductivity [43].

EPX-CBZ Identification during the Electrochemical Degradation Process

As discussed previously, the percent removal of carbamazepine was more than 99% within 80-min electrolysis by applying different anode materials. To explore the degradation pathway of carbamazepine, the

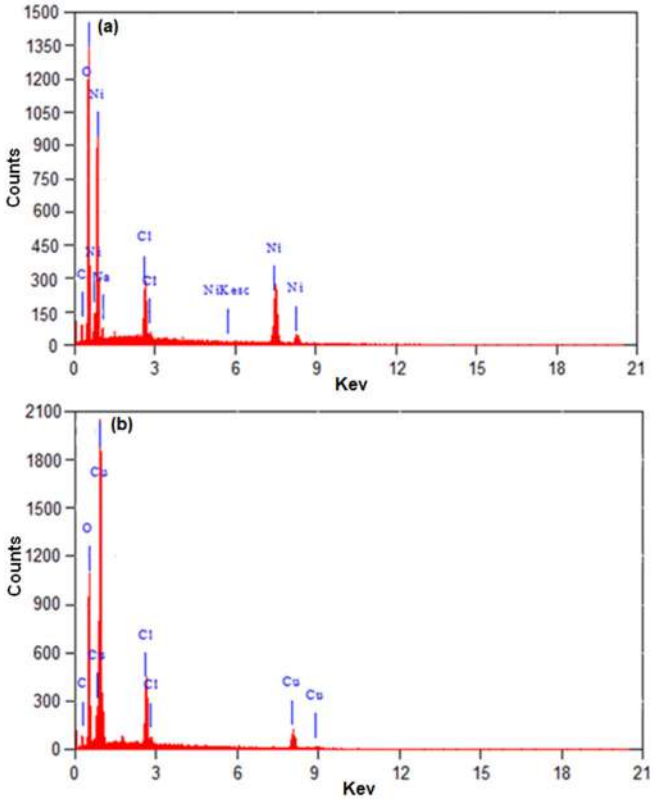

Fig 6. EDX-FESEM spectrums of (a) nickel and (b) copper after the electrochemical oxidation process of carbamazepine under these conditions: 5 mg/L CBZ; 5 V; 0.5 g NaCl

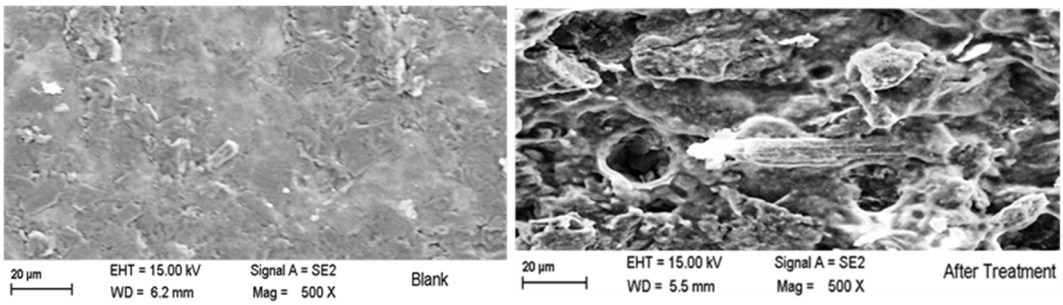

Fig 7. EDX mappings of graphite electrode before (left) and after ten cycles of electrolysis (right) under these conditions: 5 mg/L CBZ; 5 V; 0.5 g NaCl

formation of minor by-products during the synergetic process was detected by LC-TOF/MS analysis, and the results are shown in Table 2.

LC-TOF/MS is usually a crucial instrument in the electrochemical treatment process. This instrument was commonly used for qualitative and quantitative analysis after electrochemical degradation of the target compound. Further, it offers a rapid and accurate elucidation of the by-product structures in terms of the number of unsaturated bonds, number of rings, number of carbon, and so on. Due to the complexity of the detailed pathways, many intermediates, and the unavailability of standards, only the main by-product is illustrated and studied here. The determined EPX-CBZ and the proposed degradation process scheme of the electrochemical degradation of carbamazepine at 0.5 g NaCl, 5 V, and 200 µg/L spiked in 50 mL were provided.

To understand the oxidation behavior of carbamazepine on graphite and other material anodes, experiments were conducted in the presence of a standard compound of the main by-product EPX-CBZ.

It was observed that the intensity of EPX-CBZ is large enough using graphite and Pt anodes. In contracts, Cu and Ni anodes exhibited low intensity of EPX-CBZ. The main base peak was at *m/z* 275 and 7.621 min, which refers to $[M+Na]^+$ at all anode materials. It can be deduced that the main by-product 10,11-epoxycarbamazepine formed after hydroxylation of the olefinic double bond on the central heterocyclic ring of carbamazepine, generating an intermediate of carbocation that is responsible for forming the main by-product EPX-CBZ as shown in Scheme 1.

After identifying the optimized conditions for the formation of by-product EPX-CBZ through electrochemical degradation of carbamazepine and confirming no interference of EPX-CBZ, this method was validated using the external calibration curve standards of EPX-CBZ. Excellent linearity was obtained over the tested EPX-CBZ concentration ranges (10–1000 µg/L) of the linear equation "y = 481.5 × −4453". These results confirm the accuracy and reliability of using the oxidation products to quantify EPX-CBZ. The limit of quantification (LOQ, signal to noise (S/N) > 10) for the EPX-CBZ method was determined to be 0.109 µg/L.

In the electrochemical degradation process, 200 µg/L of carbamazepine was spiked in 50 mL of water and then electrochemically degraded. After that, every 10 min, the sample was withdrawn and then extracted using Oasis-HLB cartridges as described previously. Finally, all samples were injected into LC-TOF/MS for further analysis.

Table 2. Accurate mass measurements of the proposed by-products obtained by LC-TOF/MS after electrochemical of carbamazepine under these conditions: 5 V; 0.5 g NaCl; 200 µg/L of CBZ

Retention time (min)	Composition molecular ion	*m/z* ratio	Error (ppm)	S/N
7.621*	$C_{15}H_{12}N_2O_2$, $[M+Na]^+$	275.0821	1.1	340
8.216	$C_{15}H_{11}ClN_2O_2$, $[M+Na]^+$	309.0248	3.1	102
9.112	$C_{15}H_{14}N_2O$, $[M+Na]^+$	277.0700	1.7	114
10.485	$C_{15}H_{14}N_2O_3$, $[M+H]^+$	272.1480	0.4	84
11.012	$C_{15}H_{13}ClN_2O_3$, $[M+H]^+$	306.1082	−2.8	91

*EPX-CBZ is the main by-product

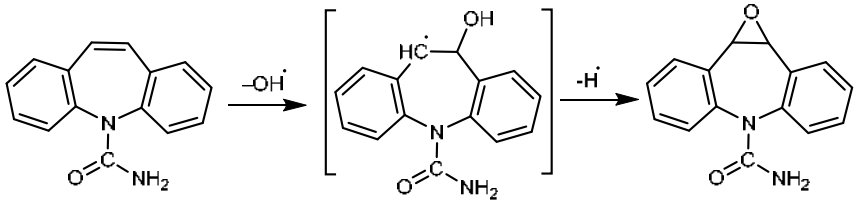

Scheme 1. proposed formation of 10,11-epoxycarbamazepine after electrochemical degradation of carbamazepine

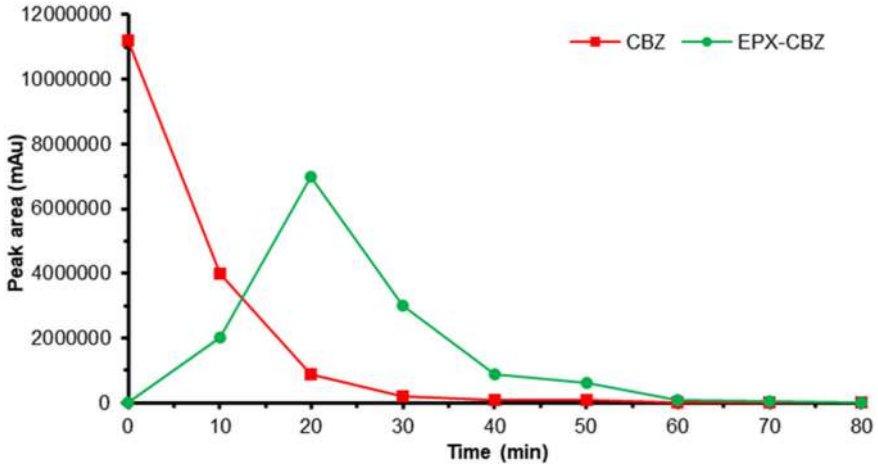

Fig 8. Monitoring 10,11-epoxycarbamazepine after electrochemical degradation of carbamazepine under these conditions: 5 volts; 0.5 g NaCl; 200 µg/L of CBZ

From Fig. 8, it could be observed that concentrations of EPX-BZ in the aqueous solution of treated carbamazepine differed from time to time due to appearance/disappearance reactions of EPX-CBZ in the solution. The lower EPX-CBZ concentration detected in the solution indicated a larger CBZ elimination. The varied detected concentrations of EPX-CBZ at different electrolysis times ranged from 13 to 142 µg/L. However, the highest concentration of EPX-CBZ was 142 µg/L at 20 min of electrolysis. The highest concentration of EPX-CBZ means the high consumption of CBZ at that time. It is important to note that at the far time of electrolysis, both EPX-CBZ and CBZ were almost eliminated and detected at the lowest concentration (below LOQ).

■ CONCLUSION

Electrochemical degradation of carbamazepine was carried out to optimize the influencing variables such as anode materials, applied voltage, and electrolyte amount was evaluated. The degradation efficiency of carbamazepine was achieved at more than 95% after 80 min electrolysis using graphite as anode under the optimal conditions with 0.5 g NaCl and 5 V. Copper and nickel as anode materials have shown minimum elimination of carbamazepine compared with graphite and platinum anodes. The supporting electrolyte sodium chloride was found to be effective for the elimination of carbamazepine, in which increasing of NaCl amount resulting high degradation rates from 0.0023 to 0.0758 min^{-1}. An increase in applied voltage resulted in increased degradation of carbamazepine accompanied by high consumption energy ranging from 0.4 to 1.5 Wh/mg. LC-TOF/MS analyzed and identified the main by-product 10,11-epoxycarbamazepine after different intervals using all selected anode materials. It was observed that the maximum yield was fooled by graphite anode compared to other anodes. EPX-CBZ was monitored for 80 min then after that, it was completely eliminated. The results obtained in this study show that electrochemical degradation is an efficient method for the degradation of carbamazepine and its main by-product 10,11-epoxycarbamazepine, in an aqueous medium. It could be concluded that graphite is the promising anode material electrode compared to copper, nickel, and platinum electrodes in terms of removal and consumption energy.

■ ACKNOWLEDGMENTS

The authors are very grateful for the financial support provided by Universiti of Al-Ameed (Karbala, Iraq). Many thanks to all staff at "Central Research for Instrumental Management, CRIM" for their continuous support.

■ AUTHOR CONTRIBUTIONS

Author (1) conducted full experimental work in terms of setting the electrochemical cell and collecting results. Author (2) has written the full paper and revised

it well in terms of organization and presentation. Author (1) analyzed sharing with the author (2) the main by-product after electrochemical degradation using LC-TOF/MS.

■ REFERENCES

[1] Pomati, F., Castiglioni, S., Zuccato, E., Fanelli, R., Vigetti, D., Rossetti, C., and Calamari, D., 2006, Effects of a complex mixture of therapeutic drugs at environmental levels on human embryonic cells, *Environ. Sci. Technol.*, 40 (7), 2442–2447.

[2] Wardhana, S.B., Kolb, M., Bahadir, M., Purwono, B., and Wahyuningsih, T.D., 2014, Method development for the analysis of pharmaceuticals with acethylcholinesterase activity in water using HPLC-DAD and solid phase extraction, *Indones. J. Chem.*, 14 (1), 22–31.

[3] García-Espinoza, J.D., Mijaylova-Nacheva, P., and Avilés-Flores, M., 2018, Electrochemical carbamazepine degradation: Effect of the generated active chlorine, transformation pathways and toxicity, *Chemosphere*, 192, 142–151

[4] Ministry of Health Malaysia, 2014, *Malaysian Statistics on Medicine*, Kuala Lumpur, Malaysia.

[5] Zhang, Y., Geißen, S.U., and Gal, C., 2008, carbamazepine and diclofenac: Removal in wastewater treatment plants and occurrence in water bodies, *Chemosphere*, 73 (8), 1151–1161.

[6] Lindberg, R.H., Östman, M., Olofsson, U., Grabic, R., and Fick, J., 2014, Occurrence and behaviour of 105 active pharmaceutical ingredients in sewage waters of a municipal sewer collection system, *Water Res.*, 58, 221–229.

[7] Al-Qaim, F.F., Mussa, Z.H., and Yuzir, A., 2018, Development and validation of a comprehensive solid-phase extraction method followed by LC-TOF/MS for the analysis of eighteen pharmaceuticals in influent and effluent of sewage treatment plants, *Anal. Bioanal. Chem.*, 410 (20), 4829–4846.

[8] Nezhadali, A., Koushali, S.E., and Divsar, F., 2021, Synthesis of polypyrrole–chitosan magnetic nanocomposite for the removal of carbamazepine from wastewater: Adsorption isotherm and kinetic study, *J. Environ. Chem. Eng.*, 9 (4), 105648.

[9] Esquerdo, A.A., Galvañ, P.J.V., Gadea, IS, and Rico, D.P., 2021, Carbamazepine and diclofenac removal double treatment: Oxidation and adsorption, *Int. J. Environ. Res. Public Health*, 18 (3), 7163.

[10] Moya-Llamas, M.J., Trapote, A., and Prats, D., 2021, Carbamazepine removal from low-strength municipal wastewater using a combined UASB-MBR treatment system, *Water Sci. Technol.*, 83 (8), 1920–1931.

[11] Calero-Díaz, G., Monteoliva-García, A., Leyva-Díaz, J.C., López-López, C., Martín-Pascual, J., Torres, J.C., and Poyatos, J.M., 2017, Impact of ciprofloxacin, carbamazepine and ibuprofen on a membrane bioreactor system: Kinetic study and biodegradation capacity, *J. Chem. Technol. Biotechnol.*, 92 (12), 2944–2951.

[12] Wang, S., and Wang, J., 2017, Carbamazepine degradation by gamma irradiation coupled to biological treatment, *J. Hazard. Mater.*, 321, 639–646.

[13] Gul, I., Sayed, M., Shah, N.S., Khan, J.A., Polychronopoulou, K., Iqbal, J., and Rehman, F., 2020, Solar light responsive bismuth doped titania with Ti^{3+} for efficient photocatalytic degradation of flumequine: Synergistic role of peroxymonosulfate, *Chem. Eng. J.*, 384,123255.

[14] Xu, L., Tang, S., Wang, K., Ma, X., and Niu, J., 2020, Insights into the degradation and detoxication mechanisms of aqueous capecitabine in electrochemical oxidation process, *Chemosphere*, 241, 125058.

[15] Iqbal, J., Shah, N.S., Sayed, M., Muhammad, N., Rehman, S., Khan, J.A., Haq Khan, Z.U., Howari, F.M., Nazzal, Y., Xavier, C., Arshad, S., Hussein, A., and Polychronopoulou, K., 2020, Deep eutectic solvent-mediated synthesis of ceria nanoparticles with the enhanced yield for photocatalytic degradation of flumequine under UV-C, *J. Water Process Eng.*, 33, 101012.

[16] Wang, Y., Zhou, C., Wu, J., and Niu, J., 2020, Insights into the electrochemical degradation of sulfamethoxazole and its metabolite by Ti/SnO_2-

Sb/Er-PbO_2 anode, *Chin. Chem. Lett.*, 31 (10), 2673–2677.

[17] Liang, H., Hua, P., Zhou, Y., Fu, Z., Tang, J., and Niu, J., 2019, Fabrication of Cu/rGO/MoS_2 nanohybrid with energetic visible-light response for degradation of rhodamine B, *Chin. Chem. Lett.*, 30 (12), 2245–2248.

[18] Xu, J., Li, L., Guo, C., Zhang Y., and Meng, W., 2013, Photocatalytic degradation of carbamazepine by tailored $BiPO_4$: Efficiency, intermediates and pathway, *Appl. Catal., B*, 130-131, 285–292.

[19] Rao, Y.F., Chu, W., and Wang, Y.R., 2013, Photocatalytic oxidation of carbamazepine in triclinic-WO_3 suspension: Role of alcohol and sulfate radicals in the degradation pathway, *Appl. Catal., A*, 468, 240–249.

[20] Komtchou, S., Dirany, A., Drogui, P., and Bermond, A., 2015, Removal of carbamazepine from spiked municipal wastewater using electro-Fenton process, *Environ. Sci. Pollut. Res.*, 22 (15), 11513–11525.

[21] Wang, W.L., Wu, Q.Y., Huang, N., Wang, T., and Hu, H.Y., 2016, Synergistic effect between UV and chlorine (UV/chlorine) on the degradation of carbamazepine: Influence factors and radical species, *Water Res.*, 98, 190–198.

[22] Gurung, K., Ncibi, M.C., Shestakova, M., and Sillanpää, M., 2018, Removal of carbamazepine from MBR effluent by electrochemical oxidation (EO) using a Ti/Ta_2O_5-SnO_2 electrode, *Appl. Catal., B*, 221, 329–338.

[23] Tran, N., Drogui, P., Brar, S.K., and De Coninck, A., 2017, Synergistic effects of ultrasounds in the sonoelectrochemical oxidation of pharmaceutical carbamazepine pollutant, *Ultrason. Sonochem.*, 34, 380–388.

[24] Bagastyo, A.Y., Batstone, D.J., Rabaey, K., and Radjenovic, J., 2013, Electrochemical oxidation of electrodialysed reverse osmosis concentrate on Ti/Pt–IrO_2, Ti/SnO_2–Sb and boron-doped diamond electrodes, *Water Res.*, 47 (1), 242–250.

[25] Moreira, F.C., Boaventura, R.A., Brillas, E., and Vilar, V.J.P., 2017, Electrochemical advanced oxidation processes: A review on their application to synthetic and real wastewaters, *Appl. Catal., B*, 202, 217–261.

[26] Mussa, Z.H., Al-Qaim, F.F., Alqaim, Z.H., and Latip, J., 2021, Electrochemical oxidation of different therapeutic classes of pharmaceuticals using graphite-PVC composite electrode, *Acta Chim. Slov.*, 68 (4), 811–820.

[27] dos Santos, A.J., Kronka, M.S., Fortunato, G.V., and Lanza, M.R., 2021, Recent advances in electrochemical water technologies for the treatment of antibiotics: A short review, *Curr. Opin. Electrochem.*, 26, 100674.

[28] Dirany, A., Sirés, I., Öturan, N., Ozcan, A., and Oturan, M.A., 2012, Electrochemical treatment of the antibiotic sulfachloropyridazine: Kinetics, reaction pathways, and toxicity evolution, *Environ. Sci. Technol.*, 46 (7), 4074–4082.

[29] Nidheesh, P.V., Kumar, A., Babu, D.S., Scaria, J., and Kumar, M.S., 2020, treatment of mixed industrial wastewater by electrocoagulation and indirect electrochemical oxidation, *Chemosphere*, 251, 126437.

[30] Nordin, N., Mohd Amir, S.F., Riyanto, R., and Othman, M.R., Mohamed, R.O., 2013, Textiles industries wastewater treatment by electrochemical oxidation technique using metal plate, *Int. J. Electrochem. Sci.*, 8, 11403–11415.

[31] Brillas, E., Garcia-Segura, S., Skoumal, M., and Arias, C., 2010, Electrochemical incineration of diclofenac in neutral aqueous medium by anodic oxidation using Pt and boron-doped diamond anodes, *Chemosphere*, 79, 605–612.

[32] Al-Qaim, F.F., Mussa, Z.H., Yuzir, A., Latip, J., and Othman, M.R., 2018, The fate of prazosin and levonorgestrel after electrochemical degradation process: Monitoring by-products using LC-TOF/MS, *J. Environ. Sci.*, 74, 134–146.

[33] Wang, Y.H., Chan, K.Y., Li, XY, and So, SK, 2006, Electrochemical degradation of 4-chlorophenol at nickel–antimony doped tin oxide electrode, *Chemosphere*, 65 (7), 1087–1093.

[34] Wu, T.N., 2007, Electrocatalytic oxidation of methyl tert-butyl ether (MTBE) in aqueous solution at a nickel electrode, *Chemosphere*, 69 (2), 271–278.

[35] Köktaş, İ.Y., and Gökkuş, Ö., 2022, removal of salicylic acid by electrochemical processes using stainless steel and platinum anodes, *Chemosphere*, 293, 133566.

[36] Al-Qaim, F.F., Mussa, Z.H., Othman, M.R., and Abdullah, M.P., 2015, removal of caffeine from aqueous solution by indirect electrochemical oxidation using a graphite-PVC composite electrode: A role of hypochlorite ion as an oxidizing agent, *J. Hazard. Mater.*, 300, 387–397.

[37] Marselli, B., Garcia-Gomez, J., Michaud, P.A., Rodrigo, M.A., and Comninellis, Ch., 2003, Electrogeneration of hydroxyl radicals on boron-doped diamond electrodes, *J. Electrochem. Soc.*, 150, D79.

[38] Liu, F., Zhao, J., Ma, Y., Liu, Z., Xu, Y., and Zhang, H., 2022, Removal of diesel from soil washing effluent by electro-enhanced Fe^{2+} activated persulfate process, *J. Electroanal. Chem.*, 906, 115995.

[39] Coria, G., Sirés, I., Brillas, E., and Nava, J.L., 2016, influence of the anode material on the degradation of naproxen by Fenton-based electrochemical processes, *Chem. Eng. J.*, 304, 817–825.

[40] Niu, J., Li, Y., Shang, E., Xu, Z., and Liu, J., 2016, Electrochemical oxidation of perfluorinated compounds in water, *Chemosphere*, 146, 526–538.

[41] Low, C.T.J., Pletcher, D., and Walsh, F.C., 2009, The electrodeposition of highly reflective lead dioxide coatings, *Electrochem. Commun.*, 11 (6), 1301.

[42] Anglada, A., Urtiaga, A., and Ortiz, I., 2009, Contributions of electrochemical oxidation to wastewater treatment: Fundamentals and review of applications, *J. Chem. Technol. Biotechnol.*, 84 (12), 1747–1755.

[43] Mussa, Z.H., Al-Qaim, F.F., Yuzir, A., and Shameli, K., 2020, Electrochemical degradation of metoprolol using graphite-PVC composite as anode: Elucidation and characterization of new by-products using LC-TOF/MS, *J. Mex. Chem. Soc.*, 64 (3), 165–180.

Antioxidant Flavonoid Glycoside from Leaves of Cacao Mistletoe (*Scurrula ferruginea* (Jack) Danser)

Mai Efdi[1*], Dara Pratama[1], Afrizal Itam[1], and Tia Okselni[2]

[1]*Department of Chemistry, Universitas Andalas, Kampus Limau Manis, Padang 25163, West Sumatra, Indonesia*

[2]*Research Center for Pharmaceutical Ingredients and Traditional Medicine, National Research and Innovation Agency, Jl. Raya Bogor Km 46, Cibinong, Bogor 16911, West Java, Indonesia*

* ***Corresponding author:***

email: maiefdi@sci.unand.ac.id

Received: January 11, 2022
Accepted: March 24, 2022

DOI: 10.22146/ijc.72133

Abstract: Scurrula ferruginea *(Jack) Danser is a folk medicine to treat several diseases.* S. ferruginea *is the mistletoe that lives by deriving nutrients from the host. Hence, the host has a significant effect on the biological activities and bioactive components of* S. ferruginea. *In this study, the leaves of* S. ferruginea *were macerated by methanol solvent to extract the chemical components and fractionated by hexane and ethyl acetate solvent, respectively, to separate organic compounds. The biological activity of crude extracts as the antioxidant was investigated by 2,2-diphenyl-1-picrylhydrazyl (DPPH) method. The result showed that the highest antioxidant activity was obtained from the ethyl acetate fraction with the* IC_{50} *of 10.88 ± 0.39 µg/mL. Furthermore, the trituration method used several solvents to isolate secondary metabolites from the initial crude methanol extract. This purification process produced a flavonoid compound of quercitrin. The antioxidant activity of quercitrin was also determined by the DPPH method. The result showed that this compound has stronger activity than the crude extracts with the* IC_{50} *of 5.95 ± 0.11 µg/mL. This study demonstrated that cacao mistletoe of* S. ferruginea *may have the potential activity to treat the diseases caused by the presence of free radicals.*

Keywords: Scurrula ferruginea *leaves; antioxidant; quercitrin*

■ INTRODUCTION

Plants are natural resources that have many benefits to human life. For instance, utilization of the part of the plant as a herbal medicine has been widely used in society since the ancient period. *Scurrula ferruginea* (Jack) Danser, known as "Dedalu Api Merah" in Indonesia, is mistletoe, a hemiparasitic plant from Santalales ordo and belongs to the family of Loranthaceae. The mistletoes have an interesting way to live, in which they grow and attach to the host. The mistletoes obtain nutrition by absorbing the water and mineral from the host plant and live with their photosynthesis [1-2].

S. ferruginea is a mistletoe that lives by deriving nutrients from the host. Hence the influence of the host in specific function as herbal medicine cannot be a negligible factor. The host species significantly affect the chemical constituents and biological activities of *S. ferruginea* [3-5]. The common host plants of the mistletoe of *S. ferruginea* are *Tabebuia pallida* and *Lagerstroemia speciosa* [6]. Traditionally, *S. ferruginea* has been used to treat wounds, snakebite, fever, beriberi, malaria, and postpartum [7]. Some previous studies have scientifically proved that *S. ferruginea* possesses pharmacological activity, such as cytotoxic effect on human cell lines of DU145 and U251 [7], human breast cancer cell MDA-MB-231 [8], antihypertensive activity [9], anti-inflammatory activity with the host of *Tecoma stans* [10], and antimicrobial activity against *Staphylococcus aureus* S261 and *Escherichia coli* E57 [11].

However, the studies about isolated compounds of *S. ferruginea* are not extensively reported. As far as our literature studies, only one exhibited the isolated compounds from the *S. ferruginea* plant: three flavonols, such as quercitrin, quercetin, and 4"-*O*-acetylquercitrin

from an unspecified host [12]. Another literature reported the chemical constituents of the crude extract based on the principal component analysis (PCA) method from ^{1}H-NMR data resulting in some identified compounds, such as quercitrin, 4''-*O*-acetylquercitrin, catechin, alanine, threonine, valine, leucine, isoleucine, histidine, formic acid, malic acid, succinic acid, citric acid, fumaric acid, acetic acid, gallic acid, chlorogenic acid, and choline [5].

Therefore, this study aims to isolate the metabolite compound from a specified host (cacao) of *S. ferruginea* and evaluate the biological activity as an antioxidant from the isolated compound and the crude extract of *S. ferruginea*.

■ EXPERIMENTAL SECTION

Materials

S. ferruginea leaves were obtained from Bayang, Pesisir Selatan Regency, West Sumatera, Indonesia. The sample was identified at the Herbarium Department of Biology, Faculty of Mathematics and Natural Sciences, Andalas University, with the official letter-number 163/K-ID/ANDA/IV/2017.

Instrumentation

Instruments used in this study were spectrophotometers of UV-1700/Shimadzu, FTIR-1600/Perkin Elmer, and NMR of JEOL JNM-ECZR 500 MHz.

Procedure

Extraction

Leaves of *S. ferruginea* were air-dried and milled. The powder of *S. ferruginea* leaves (1.3 kg) was macerated with methanol solvent three times at room temperature for 3 × 24 h for each extraction. The material-solvent ratio was maintained at approximately 1:2 (w/w) for each extraction. The crude methanol extract was concentrated by a rotary evaporator, yielding 55.65 g of crude methanol extract. After 24 h, a yellow solid was formed on the crude methanol extract. The crude methanol extract was re-dissolved with methanol solvent and fractionated with hexane solvent to separate the solid component and obtain the hexane extract. The polar fraction was further fractionated by ethyl acetate solvent. The rotary evaporator concentrated the extracts to evaporate the solvent and produced hexane, ethyl acetate, and methanol extracts.

Phytochemical screening

The extracts of *S. ferruginea* leaves were evaluated quantitatively to identify the chemical constituents in the extracts. The procedure was conducted based on the standard method of Harborne [13].

Purification and characterization

The isolated compound was purified using the trituration method with several solvents, such as hexane and ethyl acetate. The purification process produced 2.77 g of yellow powder from the isolated compound. The isolated compound was identified by ultraviolet (UV), infrared (IR), and nuclear magnetic resonance (NMR) spectra analysis compared to literature.

Antioxidant activity

The antioxidant activity was conducted with 2,2-diphenyl-1-picrylhydrazyl (DPPH) method [14] with slight modification. The tested sample was the isolated compound and the extract of hexane, ethyl acetate, and methanol. Ascorbic acid was used as a positive control. The DPPH solution with the concentration of 0.1 mmol/L was added into the tube containing 2 mL of the tested sample in various concentrations. The concentrations were varied for each tested sample, such as from 1.5625 to 25 μg/mL for the isolated compound, methanol, and ethyl acetate extracts, from 12.5 to 200 μg/mL for hexane extract, and from 0.625 to 10 μg/mL for ascorbic acid. The mixture of DPPH and sample was allowed to stand for 30 min at room temperature and unlighted. The absorbance was measured at the wavelength of 517 nm as the function of the DPPH solution. The varying of the sample was conducted to make the curve inhibition resulting and generate the IC_{50} value by the regression equation. The IC_{50} value means the required concentration to inhibit 50% of free radicals. The inhibition of free radical DPPH (I%) was calculated by the equation as follows:

$$I\% = \frac{A_{blank} - A_{sample}}{A_{blank}} \times 100\%$$

where A_{blank} is the absorbance of blank contained DPPH solution and A_{sample} is the absorbance of the tested sample. All of the tests were done in triplicate.

■ RESULTS AND DISCUSSION

Extraction

The fractionation process of the crude methanol extract of *S. ferruginea* leaves with several solvents, such as hexane and ethyl acetate, respectively, produced three different fractions with specific yields for each fraction (Table 1).

Secondary metabolite compounds generally exist in small amounts in plants. The suitable extraction method is a crucial factor to extract the organic compound from the plant material with a high yield and minimal change of the functional properties of the extract. The conventional extraction method is commonly performed through maceration in which the plant material is soaked with the solvent at room temperature to avoid degradation or functional group changing of the organic compounds. Hence, it is required to select the proper solvent based on sample matrix properties or chemical compound properties contained in plant material [15-18].

In this study, the methanol solvent was used initially to maximize the extraction of secondary metabolites from *S. ferruginea* since the methanol has good penetration properties to the cell-matrix of the plant. Then, the methanol crude extract was separated with hexane and ethyl acetate solvents, respectively, to obtain the crude fractions of *S. ferruginea* leave extract. The limitation of the yield percentage (Table 1) of the extract was assumed due to the less repetition in initial methanol extraction, which was only three times of maceration.

As shown in Table 1, there were three fractions with different polarities. Each fraction contained different chemical constituents, such as hexane fraction with non-polar compounds, ethyl acetate fraction with semi-polar compounds, and methanol fraction with polar compounds.

The fraction distribution of *S. ferruginea* leave extract is shown in Fig. 1. It revealed that the chemical constituents of the extract were dominated by polar compounds, in which the methanol fraction had the highest

Table 1. Fraction weight and yield of *S. ferruginea* leaves extract

No	Extract	Weight (g)	Yield (% w/w)*
1	Hexane	12.84	0.99
2	Ethyl acetate	3.32	0.26
3	Methanol	36.72	2.82

*Yield was the percentage value of crude extract weight compared to plant material weight

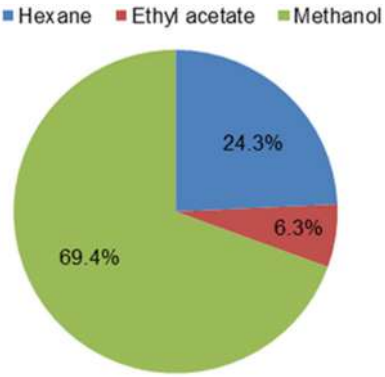

Fig 1. Fraction distribution of *S. ferruginea* extract

distribution percentage among the other fractions, with a value up to 69.4%. The quantity of the fraction is affected by the chemical composition and compound types. The chemical compounds of the extract will be distributed in the solvent according to their suitable polarity properties. Organic compounds with non-polar properties, such as terpenoid, steroid, and lipid, are dissolved properly in a non-polar solvent, such as hexane [19-20]. In contrast, organic compounds with polar properties, such as phenolic compounds, are highly distributed in the polar solvent [17].

Phytochemical Screening

The phytochemical screening of *S. ferruginea* extract exhibited the presence of secondary metabolite compounds such as steroids, flavonoids, and phenols, as shown in Table 2. Alkaloids were not detected in all extracts of *S. ferruginea,* whereas steroids were found in hexane and methanol extracts. The extracts of ethyl acetate and methanol had potential chemical constituents such as flavonoids and phenols. The phytochemical compound detection would be helpful information for future research, especially in pharmacological and medicinal topics. For example, steroids have been reported

Table 2. Phytochemical screening of *S. ferruginea* extract

Chemical constituent	Test type	Extract		
		Hexane	Ethyl acetate	Methanol
Alkaloids	Mayer	-	-	-
Steroids	Liebermann–Burchard	+	-	+
Flavonoids	Shinoda	-	+	+
Phenols	Ferric chloride	-	+	+

(+) indicated the presence of constituents, and (-) indicated the absence of the constituents

as antifungal, antidiabetic, antibacterial, and anti-inflammatory [21]. Flavonoids and phenols are also known to have highly ranging diverse biological activities, such as antioxidant, anti-inflammatory, and anticancer [22].

Purification and Characterization

The isolated compound was obtained from the initial crude methanol extract as a yellow powder. The solid shape of the compound was formed after obtaining the concentrated crude methanol extract. This yellow solid compound was purified with the simple trituration method with a gradient solvent system, such as hexane and ethyl acetate solvent, respectively. This method was carried out since the compound was already in solid form due to the high concentration of the compounds in the extract.

The purity of the isolated compound was determined by thin-layer chromatography (TLC) using various eluent ratios (Fig. 2). The mixture of the eluent with several ratios produces the solvent's different polarity, resulting in variation of the retention factor (Rf) value. The results showed a constant single spot on the TLC plate for all eluent ratios with the Rf value of 0.13, 0.31, 0.51, 0.67, and 0.70, respectively (Fig. 2(a-e)). It confirmed the purity of the isolated compound without the presence of impurities.

The purified compound was identified using UV, IR, and NMR data. All these analyses were combined to conclude the structure of the isolated compound. The compound was measured by a UV instrument combined with shift reagents to investigate the interaction of the compound against several shift reagents (Table 3).

Based on Table 3 shows that the UV spectrum of the compound gives two maximum absorption bands. Band II (240–280 nm) corresponds to A-ring with the benzoyl system and band I (300–380 nm) indicates to

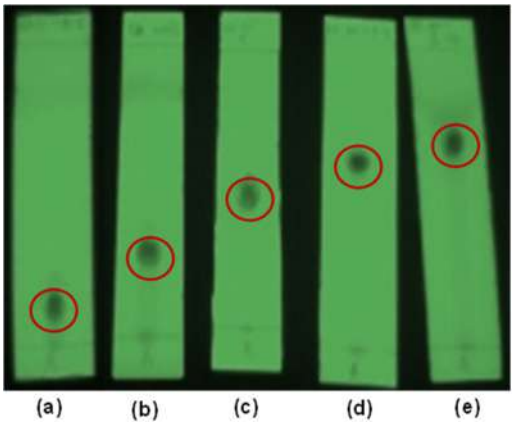

Fig 2. TLC of the isolated compound with various eluent ratios; (a) hexane:EtOAc (10:90), (b) EtOAc 100%, (c) EtOAc:MeOH (90:10), (d) EtOAc:MeOH (80:20), (e) EtOAc:MeOH (70:30)

Table 3. UV Analysis of Isolated Compound of *S. ferruginea*

Solvent/shift reagent	Band II (λ_{max}, nm)	Band I (λ_{max}, nm)	Shift Observed and Interpretation [23]
MeOH	256	350	Flavonol with 3-OR
MeOH+NaOH	272	398	Band I (+ 48 nm) → 4'-OH
		(Additional band, 326)	Additional band between 320-335 nm → 7-OH
MeOH+$AlCl_3$	275	429	Band I (+79 nm) → ortho position of OH at B-ring
MeOH+$AlCl_3$+HCl	272	401 (Additional band, 346)	Band I (+51 nm) → 5-OH
MeOH+NaOAc	266	393	Band II (+10 nm) → 7-OH
MeOH+NaOAc+H_3BO_3	263	374	Band I (+24 nm) → ortho position of OH at B-ring

B-ring with the cinnamoyl system [24]. This spectrum is affected significantly by the oxygenation pattern in the flavonoid structure. Generally, an increase in the oxygenation level will contribute to the shift of the absorption bands to the bathochromic system (longer wavelength). Shift reagents also give useful information to identify the flavonoid structure since each reagent will give a specific reaction with certain oxygenation positions [23]. Shift reagents used in this UV analysis were NaOH, $AlCl_3$, $AlCl_3$/HCl, NaOAc, and NaOAc/H_3BO_3. The result of the interpretation from UV data indicated that the isolated compound was a flavonol which had substituent "R" at oxygen atom in atom C-3 (C-OR) and hydroxyl (OH) substituent at atom carbon of 5, 7, 3', and 4' (Fig. 3).

The predicted structure from UV analysis was supported by IR data that confirmed the presence of the functional group of hydroxyl (OH, ν_{max} at 3237 cm^{-1}), C=C aromatic (ν_{max} at 1465 cm^{-1}), C-O ether/alcohol (ν_{max} at 1258 cm^{-1}), and an aliphatic C-H (ν_{max} at 2930 cm^{-1}).

The ^{13}C-NMR chemical shift of the isolated compound (Table 4) indicated the presence of 21 carbon atoms consisting of 12 aromatic carbon signals at δ 95.17–166.87 ppm, 1 carbonyl signal at δ 179.88 ppm, 2 ether alkene signals at δ 136.48 and 158.72 ppm, and 6 specific signals for glycoside with 4 signals at δ 72.22–74.84 ppm, 1 signal of C-1" of *O*-glycoside at δ 103.83 ppm, and 1 signal of C-6" of *C*-methylation at δ 17.96 ppm. Whereas the chemical shift of ^{1}H-NMR (Table 4) exhibited the appearance of 11 proton signals consisting of 5 aromatic proton signals at δ 6.19–7.34 ppm,

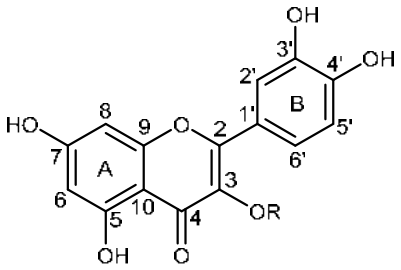

Fig 3. Predicted structure from UV analysis

Table 4. NMR chemical shift of isolated compound compared to literature

No	Carbon type	Isolated compound*			Literature [27]	
		δ_C (ppm)	δ_H (ppm) (multiplicity, *J*)	HMBC	δ_C (ppm)	δ_H (ppm) (multiplicity, *J*)
2	C	158.72			158.73	
3	C	136.48			136.08	
4	C	179.88			179.46	
5	C-OH	163.48			163.08	
6	CH	100.32	6.19 (d, *J* = 1.5 Hz)	C-8, C-10, C-5, C-7	100.63	6.19 (d, *J* = 1.4 Hz)
7	C-OH	166.87			168.26	
8	CH	95.17	6.36 (d, *J* = 2.5 Hz)	C-6, C-10, C-9, C-7	95.32	6.35 (d, *J* = 1.6 Hz)
9	C	159.39			159.09	
10	C	105.99			105.27	
1'	C	123.15			123.00	
2'	CH	117.21	7.34 (d, *J* = 2.0 Hz)	C-1', C-3', C-4', C-2	116.19	7.35 (d, *J* = 1.8 Hz)
3'	C-OH	146.60			146.52	
4'	C-OH	149.99			149.97	
5'	CH	116.67	6.92 (d, *J* = 8.5 Hz)	C-1', C-6', C-3', C-4'	116.42	6.93 (d, *J* = 8.3 Hz)
6'	CH	122.99	7.32 (dd, *J* = 2.0 and 8.5 Hz)	C-2', C-4', C-2	122.85	7.32 (dd, *J* = 1.9 and 8.3 Hz)
1"	CH	103.83	5.35 (d, *J* = 1.5 Hz)	C-2", C-3	103.55	5.36 (d, *J* = 1.2 Hz)
2"	CH	72.22	4.22 (brdd, *J* = 1.5 and 3.0 Hz)	C-4"	72.14	4.25 (d, *J* = 1.1 Hz)
3"	CH	72.71	3.76 (dd, *J* = 3.0 and 9.5 Hz)	C-4"	72.05	3.78 (dd, *J* = 3.3 and 3.3 Hz)
4"	CH	73.55	3.35 (d, *J* = 9.5 Hz)	C-6", C-2"	73.30	3.35 (d, *J* = 2.3 Hz)
5"	CH	74.84	3.44 (m)		71.94	3.43 (d, *J* = 6.0 Hz)
6"	CH3	17.96	0.95 (d, *J* = 6.0 Hz)	C-3"	17.67	0.96 (d, *J* = 6.1 Hz)

*The solvent was CD_3OD at 500 MHz for ^{1}H-NMR and 125 MHz for ^{13}C-NMR

1 proton signal of H-1" of 3-*O*-rhamnoside at δ 5.35 ppm, 1 proton signal of methyl (H-6") at δ 0.95 ppm, and 4 proton signals for sugar at δ 3.35–4.22 ppm.

The coupling constant (*J*) interpretation showed the presence of three signals of aromatic proton in the ABX spin system, in which the proton at δ 7.32 ppm (H-6') had the doublet of doublets multiplicity coupled at meta position with H-2' (δ 7.34 ppm) confirmed by the *J* value of 2.0 Hz and at ortho position with H-5' (δ 6.92 ppm) indicated by the J value of 8.5 Hz. This observation confirmed the presence of the substituent at C-3' and C-4'. An anomeric proton of the isolated compound was at δ 5.35 ppm (d, *J* = 1.5 Hz, H-1") correlated with carbon signal at δ 103.83 ppm in the HSQC spectrum. This coupling constant of 1.5 Hz confirmed the α-orientation of L-rhamnosyl moiety [25-27]. The constant coupling value of methyl proton of H-6" was 6.0 Hz, which this coupling constant was an identical value to Zhang et al. [26] and Gopi et al. [27].

HMBC analysis presented the correlation between protons and carbons separated by two or three and sometimes up to four bonds in the conjugated system. In the HMBC data (Table 4), the anomeric proton (δ 5.35 ppm, H-1") of the rhamnose was connected to the carbon signal at δ 136.48 ppm (C-3). It revealed that the rhamnose was attached at C-3 of the aglycone.

All spectroscopy data confirmed that the isolated compound was assigned as a flavonol of quercetin 3-*O*-α-L-rhamnoside, known as quercitrin, with the molecular formula of $C_{21}H_{20}O_{11}$ (Fig. 4). As additional information, this study was the first report that successfully isolated a quercitrin compound from *S. ferruginea* with the specified host of cacao. The isolated compound of *S. ferruginea* has not been extensively explored. Only three isolated compounds have been reported, such as 4"-*O*-acetylquercitrin, quercetin, and quercitrin [12]. Although quercitrin had been previously isolated from *S. ferruginea*, it was from an unspecified host. Quercitrin was also found from *Zanthoxylum bungeanum* [26], *Euphorbia hirta* [27], *Pistacia lentiscus* [28], and *Euphorbia characias* subsp. *wulfenii* [29].

Quercitrin was assumed to be the main chemical

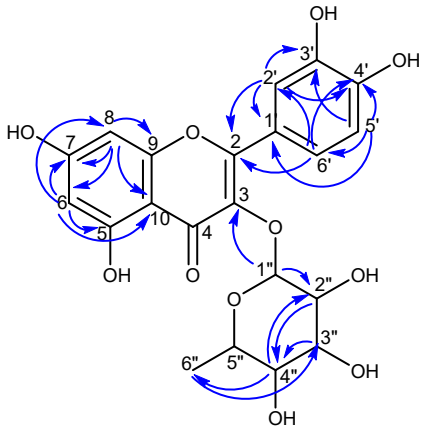

Fig 4. Quercitrin structure with key HMBC (H→C)

constituent in *S. ferruginea* from the cacao host. It was related to the amount of this isolated compound in which the percentage of the quercitrin was about 5.0% of the crude extract. Therefore, the quercitrin compound of *S. ferruginea* from the cacao host was simply isolated by the trituration method.

Antioxidant Activity

Plants are known to possess many bioactive compounds that can act as an antioxidant. Therefore, the evaluation of the antioxidant activity of several medicinal plants, including crude extract and isolated compounds, has attracted the interest of many researchers. The radical scavenging activity of the *S. ferruginea* extract and the isolated compound of quercitrin (Table 5) was investigated by the DPPH method. The principle of this method is based on the color-changing due to stabilizing of DPPH radical by the presence of an antioxidant agent.

As shown in Table 5, the extract of *S. ferruginea* leaves revealed intense antioxidant activity, in which the ethyl acetate extract had the highest activity with the IC_{50} of 10.88 ± 0.39 μg/mL. In contrast, hexane extract had the lowest antioxidant activity. This result was correlated to the active compound contained in each extract. The phytochemical screening of *S. ferruginea* extract (Table 2) had revealed that the ethyl acetate and methanol extracts were dominated by flavonoid and phenolic compounds. These compounds have been known to have potential antioxidant activity [30].

Table 5. Antioxidant activity of *S. ferruginea* extract and quercitrin

No	Sample	IC_{50} (μg/mL) ± SD
1	Hexane extract	102.72 ± 2.06
2	Ethyl acetate extract	10.88 ± 0.39
3	Methanol extract	18.36 ± 0.58
4	Quercitrin	5.95 ± 0.11
5	Ascorbic acid	2.83 ± 0.11

The values were presented as average ± standard deviation (n = 3)

This result was supported by the other works of literature that reported the antioxidant activity from the unspecified host of *S. ferruginea* with IC_{50} 27.81 μg/mL obtained from methanol extract of stem part [8] and IC_{50} higher than 30 μg/mL from acetone extract of the stem, leaves, and flower parts [31]. It revealed that *S. ferruginea* leaves extract from the cacao host had the strongest antioxidant activity among the others.

The isolated compound of *S. ferruginea* leaves, the quercitrin, also demonstrated strong antioxidant activity with the best IC_{50} of 5.95 ± 0.11 μg/mL compared to the crude extract. Quercitrin compound belongs to a phenolic compound that has an aromatic ring. The presence of an aromatic ring can stabilize the radical through the electron resonance effect in the ring system [32].

■ CONCLUSION

This study exhibited that the leaf extract of *S. ferruginea* growing on the cacao plant has the potential to be used as an antioxidant agent. This mistletoe also exhibited a high content of quercitrin compound that has stronger radical scavenging activity than the crude extract. Therefore, the cacao mistletoe of *S. ferruginea* may have the potential activity to treat the diseases caused by oxidative stress generated from free radicals.

■ AUTHOR CONTRIBUTIONS

Dara Pratama conducted the experiment, Afrizal supervised the experiment, Mai Efdi supervised and reviewed the experiment, Tia Okselni interpreted the data, wrote, and revised the manuscript. The authors agreed to the final version of this manuscript.

■ REFERENCES

[1] Lim, Y.C., Rajabalaya, R., Lee, S.H.F., Tennakoon, K.U., Le, Q.V., Idris, A., Zulkipli, I.N., Keasberry, N., and David, S.R., 2016, Parasitic mistletoes of the Genera *Scurrula* and *Viscum*: From bench to bedside, *Molecules*, 21 (8), 1048.

[2] Moghadamtousi, S.Z., Kamarudin, M.N.A., Chan, C.K., Goh, B.H., and Kadir, H.A., 2014, Phytochemistry and biology of *Loranthus parasiticus* Merr, a commonly used herbal medicine, *Am. J. Chin. Med.*, 42 (1), 23–35.

[3] Le, Q.V., Tennakoon, K.U., Metali, F., Lim, L.B.L., and Bolin, J.F., 2016, Ecophysiological responses of mistletoe *Dendrophthoe curvata* (Loranthaceae) to varying environmental parameters, *J. Trop. For. Sci.*, 28 (1), 59–67.

[4] Le, Q.V., Tennakoon, K.U., Metali, F., Lim, L.B.L., and Bolin, J.F., 2016, Host specific variation in photosynthesis of an obligate xylem-tapping mistletoe *Dendrophthoe curvata* in a Bornean heath forest, *Nord. J. Bot.*, 34 (2), 235–243.

[5] Hong, X., Mat Isa, N., Fakurazi, S., and Ismail, I.S., 2020, Phytochemical and anti-inflammatory properties of *Scurrula ferruginea* (Jack) Danser parasitising on three different host plants elucidated by NMR-based metabolomics, *Phytochem. Anal.*, 31 (1), 15–27.

[6] Rahmad, Z.B., Addo-Fordjour, P., Asyraf, M., and Nik Rosely, N.F., 2014, Mistletoe abundance, distribution and associations with trees along roadsides in Penang, Malaysia, *Trop. Ecol.*, 55 (2), 255–262.

[7] Lohézic-Le Dévéhat, F., Bakhtiar, A., Bézivin, C., Amoros, M., and Boustie, J., 2002, Antiviral and cytotoxic activities of some Indonesian plants, *Fitoterapia*, 73 (5), 400–405.

[8] Marvibaigi, M., Amini, N., Supriyanto, E., Abdul Majid, F.A., Jaganathan, S.K., Jamil, S., Almaki, J.H., and Nasiri, R., 2016, Antioxidant activity and ROS-dependent apoptotic effect of *Scurrula ferruginea* (Jack) Danser methanol extract in human breast cancer cell MDA-MB-231, *PLoS One*, 11 (7), e0158942.

[9] Ameer, O.Z., Salman, I.M., Quek, K.J., and Asmawi, M.Z., 2015, *Loranthus ferrugineus*: A mistletoe from

traditional uses to laboratory bench, *J. Pharmacopuncture*, 18 (1), 7–18.

[10] Hong, X., Ajat, M., Fakurazi, S., Noor, A.M., and Ismail, I.S., 2021, Anti-inflammatory evaluation of *Scurrula ferruginea* (Jack) Danser parasitizing on Tecoma stans (L.) H.B.K. in LPS/IFN-γ-induced RAW 264.7 macrophages, *J. Ethnopharmacol.*, 268, 113647.

[11] Justine, V.T., Mustafa, M., and Go, R., 2018, Effect of antimicrobial activities on the various solvents extracts of leaves of *Scurrula ferruginea* (Jack) Danser (Loranthaceae), *Pertanika J. Trop. Agric. Sci.*, 41 (2), 677–686.

[12] Lohézic-Le Dévéhat, F., Tomasi, S., Fontanel, D., and Boustie, J., 2002, Flavonols from *Scurrula ferruginea* Danser (Loranthaceae), *Z. Naturforsch., C: Biosci.*, 57 (11-12), 1092–1095.

[13] Harborne, J.B., 1984, *Phytochemical Methods - A Guide to Modern Techniques of Plant Analysis*, 2nd Ed., Chapman & Hall, London, UK.

[14] Okselni, T., Santoni, A., Dharma, A., and Efdi, M., 2018, Determination of antioxidant activity, total phenolic content, and total flavonoid content of roots, stem bark, and leaves of *Elaeocarpus mastersii* King, *Rasayan J. Chem.*, 11 (3), 1211–1216.

[15] Truong, D.H., Nguyen, D.H., Ta, N.T.A., Bui, A.V., Do, T.H., and Nguyen, H.C., 2019, Evaluation of the use of different solvents for phytochemical constituents, antioxidants, and *in vitro* anti-inflammatory activities of *Severinia buxifolia*, *J. Food Qual.*, 2019, 8178294.

[16] Ezez, D., and Tefera, M., 2021, Effects of solvents on total phenolic content and antioxidant activity of ginger extracts, *J. Chem.*, 2021, 6635199.

[17] Qasim, M., Aziz, I., Rasheed, M., Gul, B., and Ajmal Khan, M., 2016, Effect of extraction solvents on polyphenols and antioxidant activity of medicinal halophytes, *Pak. J. Bot.*, 48 (2), 621–627.

[18] Salamatullah, A.M., Hayat, K., Husain, F.M., Ahmed, M.A., Arzoo, S., Althbiti, M.M., Alzahrani, A., Al-Zaied, B.A.M., Alyahya, H.K., Albader, N., Nafidi, H.A., and Bourhia, M., 2022, Effects of different solvents extractions on total polyphenol content, HPLC analysis, antioxidant capacity, and antimicrobial properties of peppers (red, yellow, and green (*Capsicum annum* L.)), *Evidence-Based Complementary Altern. Med.*, 2022, 7372101.

[19] Jiang, Z., Kempinski, C., and Chappell, J., 2016, Extraction and analysis of terpenes/terpenoids, *Curr. Protoc. Plant Biol.*, 1 (2), 345–358.

[20] Ahmed, Y., Rahman, S., Akhtar, P., Islam, F., Rahman, M., and Yaakob, Z., 2013, Isolation of steroids from n-hexane extract of the leaves of *Saurauia roxburghii*, *Int. Food Res. J.*, 20 (5), 2939–2943.

[21] Zubair, M.S., Al-Footy, K.O., Ayyad, S.E.N., Al-Lihaibi, S.S., and Alarif, W.M., 2016, A review of steroids from *Sarcophyton* species, *Nat. Prod. Res.*, 30 (8), 869–879.

[22] Gutiérrez-Grijalva, E., Picos-Salas, M., Leyva-López, N., Criollo-Mendoza, M., Vazquez-Olivo, G., and Heredia, J., 2017, Flavonoids and phenolic acids from oregano: Occurrence, biological activity and health benefits, *Plants*, 7 (1), 2.

[23] Markham, K.R., 1989, "Flavones, Flavonols and Their Glycosides" in *Methods in Plant Biochemistry: Volume 1: Plant Phenolics*, 1st Ed., Eds. Harborne J.B., Academic Press, London, UK, 197–235.

[24] Mabry, T.J., Markham, K.R., and Thomas, M.B., 1970, "The Ultraviolet Spectra of Flavones and Flavonols" in *The Systematic Identification of Flavonoids*, Springer-Verlag, Berlin, Heidelberg, 41–164.

[25] Aisyah, L.S., Yun, Y.F., Herlina, T., Julaeha, E., Zainuddin, A., Nurfarida, I., Hidayat, A.T., Supratman, U., and Shiono, Y., 2017, Flavonoid compounds from the leaves of *Kalanchoe prolifera* and their cytotoxic activity against P-388 murine leukimia cells, *Nat. Prod. Sci.*, 23 (2), 139–145.

[26] Zhang, Y., Wang, D., Yang, L., Zhou, D., and Zhang, J., 2014, Purification and characterization of flavonoids from the leaves of *Zanthoxylum bungeanum* and correlation between their structure and antioxidant activity, *PLoS One*, 9 (8), e105725.

[27] Gopi, K., Anbarasu, K., Renu, K., Jayanthi, S., Vishwanath, B.S., and Jayaraman, G., 2016,

Quercetin-3-*O*-rhamnoside from *Euphorbia hirta* protects against snake venom induced toxicity, *Biochim. Biophys. Acta, Gen. Subj.*, 1860 (7), 1528–1540.

[28] Elloumi, W., Mahmoudi, A., Ortiz, S., Boutefnouchet, S., Chamkha, M., and Sayadi, S., 2022, Wound healing potential of quercetin-3-*O*-rhamnoside and myricetin-3-*O*-rhamnoside isolated from *Pistacia lentiscus* distilled leaves in rats model, *Biomed. Pharmacother.*, 146, 112574.

[29] Özbilgin, S., Acıkara, Ö.B., Akkol, E.K., Süntar, I., Keleş, H., and İşcan, G.S., 2018, *In vivo* wound-healing activity of *Euphorbia characias* subsp. *wulfenii*: Isolation and quantification of quercetin glycosides as bioactive compounds, *J. Ethnopharmacol.*, 224, 400–408.

[30] Kaurinovic, B., and Vastag, D., 2019, "Flavonoids and Phenolic Acids as Potential Natural Antioxidants" in *Antioxidants*, Eds. Shalaby, E., IntechOpen, Rijeka, Croatia.

[31] Marvibaigi, M., Amini, N., Supriyanto, E., Jamil, S., Abdul Majid, F.A., and Khangholi, S., 2014, Total phenolic content, antioxidant and antibacterial properties of *Scurrula ferruginea* extracts, *J. Teknol.*, 70 (5), 65–72.

[32] Velo-Gala, I., López-Peñalver, J.J., Sánchez-Polo, M., and Rivera-Utrilla, J., 2015, Role of activated carbon on micropollutants degradation by different radiation processes, *Mediterr. J. Chem.*, 4 (2), 68–80.

Adsorption of Methylene Blue on Nano-Crystal Cellulose of Oil Palm Trunk: Kinetic and Thermodynamic Studies

Mega Mustikaningrum[1,2*], Rochim Bakti Cahyono[2], and Ahmad Tawfiequrrahman Yuliansyah[2]

[1]*Department of Chemical Engineering, University of Muhammadiyah Gresik, Jl. Sumatera No. 101, Gresik 61121, East Java, Indonesia*

[2]*Department of Chemical Engineering, Faculty of Engineering, Universitas Gadjah Mada, Jl. Grafika No. 2, Yogyakarta 55284, Indonesia*

* ***Corresponding author:***

tel: +62-82136927311
email: megamustikaningrum@umg.ac.id

Received: January 11, 2022
Accepted: May 19, 2022

DOI: 10.22146/ijc.72156

Abstract: *The adsorption kinetic study of methylene blue using nano-crystal cellulose made from oil palm trunk was investigated. A sample of 0.08 g of nano-crystal cellulose was used to adsorb 300 mL of methylene blue solution, with a varied stirring speed at 100, 200, and 300 rpm. Meanwhile, the concentration of methylene blue was varied at 1, 2, and 3 mg/L. The experimental results showed that the range of adsorption rate constant was 0.0007–0.0130 m/min. For the thermodynamic study, adsorption temperature was varied at 303, 308, 313, and 318 K. The adsorption capacity values for such temperatures were 10.3389, 10.3802, 10.3614, and 10.3464 mg/g, respectively. It was found that ΔH° value of 0.00742 kJ/mol, ΔS° of 0.7758 kJ/mol K and ΔG° value of −242.81 kJ/mol. Based on the curve-fitting using the Henry, Langmuir, and Freundlich isotherm models, this adsorption tended to the Langmuir isotherm model, where the adsorption formed a monolayer covering the surface of the adsorbent. It was also found that the Langmuir affinity constant (K_L) value was 4.560 L/mg, and the maximum adsorption capacity (q_m) was 8.590 mg/g.*

Keywords: *nano-crystal cellulose; methylene blue; adsorption; oil palm trunk*

■ INTRODUCTION

The development of revolutionary technology 4.0 is the basis of the Indonesian government's thinking towards the "Making Indonesia 4.0" road map. One of the road maps is to develop several potential industrial sectors to develop the potential of Indonesia's industry, one of which is the textile industry [1].

The textile industry in Indonesia is integrated. Data from the central statistics agency shows that textile exports during January-August 2021 reached 160.854 tons, much higher than the same period in 2019 and 2020 of 152.474 tons and 147.982 tons, respectively. The development of the textile industry will be proportional to the increase in textile industry waste, especially liquid waste. Liquid waste that is difficult to process is textile dyes [2]. One of the dyes commonly used in the textile industry is methylene blue [3-4].

The existence of dye waste in the environment has become a significant world issue due to its damaging effect on aquatic life and ecosystems [5-6]. Disposal of dye waste without a prior degradation process can cause a health problem since dyes are toxic (or mutagenic) and carcinogenic [7-8]. Interestingly, the adsorption process is quite efficient in removing textile dyes from wastewater [9-12]. This study used nano-crystal cellulose as a biosorbent to adsorb methylene blue. The methylene blue is cationic, while nano-crystal cellulose is anionic, so there will be an electrostatic force between them. In this study, it is expected that nano-crystal cellulose has a larger surface area, increasing the adsorption sites of methylene blue [13].

Several studies have been done regarding the work function of nano-crystal cellulose as biosorbent for methylene blue, such as nano-crystal cellulose from oil palm empty fruit bunch (EFB) [9], from cotton [14],

from sawdust [15], poly(acrylic acid)/nano-crystal cellulose modification to nanocomposites hydrogel [16], and cross-linked nano-crystal cellulose aerogels [17]. This study used oil palm trunks as raw materials for making the adsorbents.

Oil palm trunks have a reasonably high cellulose content of 40%. In addition to the high cellulose content, the availability of oil palm trunks in Indonesia is also relatively abundant. Indonesia has an area of 11 million hectares of oil palm. Every year 4% of the rehabilitated land area will produce oil palm trunk waste of around 100 million cubic meters. Until nowadays, the use of oil palm trunks in Indonesia has been carried out by Jamal Balfas at the Research and Development Center for Forestry Engineering and Forest Product Management (Balitbang Hutan) as plywood and solid wood [18]. The cellulose content and the abundant availability of materials are the main reasons for choosing materials that allow the success of cellulose-based biosorbent products.

The adsorption process is when one or more gas or liquid components are adsorbed on a solid surface [19]. The most common adsorption type in nano-crystal cellulose is physical and chemical adsorption. The adsorption mechanism of methylene blue by nano-crystal cellulose covers hydrogen bonding, ion-dipole interaction, and electrostatic interaction [13]. The authors have carried out previous research on the adsorption of nano-crystal cellulose. The authors analyzed the differences in NaOH concentrations in the alkaline treatment process on the results of the impurity of nano-crystal cellulose produced [20] and the effect on the adsorption of methylene blue, then continued with the characterization of samples of nano-crystal cellulose made from palm trunks [21]. The study focuses on the effect of stirring and the initial concentration of methylene blue on the adsorption rate to achieve an equilibrium using a fitted kinetics study of Langmuir isotherm model, Freundlich isotherm, and distribution coefficient. The isotherm study aims to conclude whether the adsorption runs physically or chemically based on the adsorbent and adsorbate mechanisms. It checks the value of the maximum adsorption capacity quantitatively. The thermodynamic study aims to determine whether the adsorption properties are spontaneous by finding the values of ΔH° and ΔS° to get the value of ΔG° of methylene blue adsorption using nano-crystal cellulose.

The study of kinetics and thermodynamics, especially on the adsorption mechanism of nano-crystal cellulose made from oil palm stems, is still minimally studied. The results will be useful for optimizing products, operating conditions, and large-scale production processes.

■ FUNDAMENTALS

This subchapter explains the fundamental theory in detail in the proposed model used to describe the methylene blue adsorption process using nano-crystal cellulose.

Kinetics and Isotherm Studies

In methylene blue adsorption using nano-crystal cellulose, it can be assumed that the adsorbent granules are tiny, leading to fast diffusion of methylene blue from the adsorbent surface into the internal adsorbent pore. The concentration of methylene blue inside the pore is uniform; thus, the proposed mathematical model is as follows:

Mass balance of methylene blue in liquid materials

Rate of Mass in – Rate of Mass Out = Rate of Mass Accumulation

$$0 - k_c a(C_A - C_A^*)m = \frac{d}{dt}(VC_A) \quad (1)$$

$$\frac{dC_A}{dt} = -\frac{k_c am}{V}(C_A - C_A^*) \quad (2)$$

Mass balance of methylene blue in solid materials

Rate of Mass in – Rate of Mass Out = Rate of Mass Accumulation

$$k_c a(C_A - C_A^*)m - 0 = \frac{d}{dt}(m.X_A) \quad (3)$$

$$\frac{dX_A}{dt} = k_c a(C_A - C_A^*) \quad (4)$$

k_c is the rate of adsorption constant (m/min), a is the notation for the adsorbent specific surface area (m^2/g), m is the mass of the adsorbent used (g), V is the volume of solution (L), C_A^* is the adsorbate concentration in the liquid at equilibrium (mol/L), C_A is the concentration of

adsorbate in the liquid (mol/L), $\frac{dC_A}{dt}$ is the distribution of adsorbate concentration in the liquid (mol/min), and $\frac{dX_A}{dt}$ is the distribution of the adsorbate concentration in the adsorbent (mol/min).

C_A^* is a number that cannot be measured, so the value of C_A^* will be substituted with some basic equilibrium equations. Here are some of the equations used.

Distribution coefficient

$$X_A = K_d \times C_A^* \quad (5)$$

C_A^* is the adsorbate concentration in the liquid at equilibrium (mol/L) and X_A is the adsorbate concentration adsorbed on the surface of the adsorbent pore wall at equilibrium (mol/L), while K_d is the adsorption equilibrium constant.

Isotherm Langmuir

$$X_A = \frac{\beta C_A^*}{C_A^* + \alpha} \quad (6)$$

X_A is the concentration of adsorbate adsorbed on the surface of the adsorbent pore wall at equilibrium (mol/L), α is q_m (mg/g), β is a constant of the Langmuir equation × q_m (mg/g), while C_A^* is the concentration of adsorbate in liquid at equilibrium pressure (mol/L).

Langmuir modeling describes the monolayer adsorption on the adsorbent surface. This model assumes that the adsorption rate is the same as the desorption rate [22]. This modelling used three assumptions: The adsorption energy is constant at all sites due to a homogeneous surface. The adsorption occurs at a specific (localized) site, the adsorption energy at all sites is the same, and each active site accommodates one adsorbate molecule only [23].

Isotherm Freundlich

$$X_A = K_f C_A^{*\beta} \quad (7)$$

K_f is the Freundlich constant related to the adsorption capacity (mg/g) $(L/mg)^{-1/n}$, β is the Freundlich constant related to the heterogeneity factor or adsorption intensity, C_A^* is the concentration of adsorbate in the liquid at equilibrium (mol/L) and X_A is the concentration of adsorbate adsorbed on the surface of the adsorbent pore wall at equilibrium (mol/L). Freundlich modelling illustrates multilayer adsorption and heterogeneous adsorbent surfaces [23].

Thermodynamic Study

This study used the entropy factor and Gibbs free energy to determine whether the process occurred spontaneously. The parameters of enthalpy (ΔH°), Gibbs energy (ΔG°), and entropy (ΔS°) can be found using the adsorption kinetics equation tested at different temperatures [24].

$$\Delta G° = -RT \ln K_c \quad (8)$$

$$\Delta G° = \Delta H° - T\Delta S° \quad (9)$$

$$\ln K_c = \frac{\Delta S°}{R} - \frac{\Delta H°}{RT} \quad (10)$$

K_c is the adsorption equilibrium constant, T is the operating temperature (K), and R is the gas constant (8.314 J/mol K). The value of K_c is obtained from Eq. (11).

$$K_c = \frac{q_e}{C_e}\frac{m}{V} \quad (11)$$

The value of q_e can be formulated by the Eq. (12)

$$q_e = \frac{C_o - C_e}{m} V \quad (12)$$

■ EXPERIMENTAL SECTION

This research consists of four steps: preparation of nano-crystal cellulose, characterization of nano-crystal cellulose products, adsorption tests on methylene blue, and studies of kinetics and thermodynamics of the adsorption process, which refers to the previous research [25].

Materials

Nano-crystal cellulose, with oil palm trunk as raw material, has been prepared according to a method described in our previous research [20-21]. Briefly, the nano-crystal cellulose was synthesized by a sequential process of alkaline treatment, bleaching, hydrolysis, and sonication. Meanwhile, methylene blue (solid powder, Merck) was used as the parent material for the adsorbate solution in the adsorption test.

Instrumentation

The concentration of methylene blue on the adsorption test was measured using the PG Instruments

T60 UV-Vis Spectrophotometer at the wavelength 643 nm.

Procedure

Adsorption data were collected using a batch test. This test consists of two parts, kinetic studies, and thermodynamic studies.

Batch adsorption for kinetics studies

Firstly, adsorbent (0.08 g of nano-crystal cellulose) and methylene blue samples (300 mL of solution at concentrations 1, 2, and 3 mg/L) were prepared. The adsorbent was then put into an Erlenmeyer with methylene blue solution. The Erlenmeyer was stirred using a magnetic stirrer (varied at 100, 200, and 300 rpm). Every 20 min aliquot sample (5 mL) was taken to measure the value of the methylene blue concentration with a UV-Vis Spectrophotometer.

Batch adsorption for thermodynamic studies

For thermodynamic studies, 300 mL of 3 mg/L methylene blue solution was used as the liquid sample. A sample of nano-crystal cellulose (0.08 g) was used to adsorb the methylene blue. The adsorption was conducted for 2 h at varying temperatures (303, 308, 313, and 318 K). After adsorption, 5 mL of the sample was taken to analyze the final concentration of methylene blue using a UV-Vis Spectrophotometer.

■ RESULTS AND DISCUSSION

Result of Analysis and Characterization of Nano-Crystal Cellulose Product

Nano-crystal cellulose product as adsorbent has been characterized by several methods. Chesson analysis was used to determine its chemical composition. FTIR spectra have been conducted and it confirmed the loss and appearance of functional groups before and after adsorption. Meanwhile, SEM and TEM were carried out to analyze the morphology of the nano-crystal that have been made. The SEM and TEM results confirmed the shape of nano-crystal cellulose resembled needles. In addition, the XRD result indicated an increase in the degree of crystallization of the product. The BET method was used to determine the surface area with the result of the surface area is 77.369 m^2/g, and SAA confirm the size of the nano-crystal of cellulose that has been made with the size of the product ranging from 1.407 to 98.56 nm. These results have been discussed in our previous works [21,25].

Effects of Stirring Speed on Adsorption on Methylene Blue

The study adsorption was performed at room temperature, pH 9, with 300 mL solution and 0.08 g of adsorbent. The stirring variation was 100, 200, and 300 rpm. The stirring variation was also done at the variation of methylene blue of 1, 2, and 3 mg/L. The result of the adsorption process can be seen in Fig. 1.

The stirring can help the spread (mobility) of the adsorbent into the solution [26-28]. Thus, the faster the stirring, the higher the decolorization percentage in methylene blue. Besides, the faster the stirring, the smaller the resistance of the adsorbate to the adsorbent. Therefore, the faster the stirring, the smaller the final concentration [29].

Other factors that are dominant in the adsorption process are the internal surface area of the adsorbent, the distribution of pores, and the addition of active groups to the adsorbent [30]. Surface diffusivity is a function of surface loading [31]. The pore distribution will be proportional to the large surface area of the adsorbent. The greater the surface area, the greater the diffusivity of a compound and will increase the adsorption capacity. Specifically for cellulose nano-crystals, the dominant effect of an active group significantly affects the adsorption process, especially the addition of anionic groups to increase the electrostatic bond that occurs with methylene blue.

As shown in Fig. 1, there was a significant decrease in the methylene blue concentration for the first 20 min. However, it tends to stagnant from 40 to 120 min, indicating a decrease in the effectiveness of the adsorption process. A single layer of adsorbate may be formed on the adsorbent surface. Once this layer is formed, the adsorption rate decreases. This monolayer indicated that one active site could only be occupied by one molecule [32]. The lower adsorption rate is due to a decrease in the number of vacant active sites on the adsorbent. It also indicates a reduced availability of active sites for further adsorption until it reaches equilibrium [33]. The conclusion that a single or double

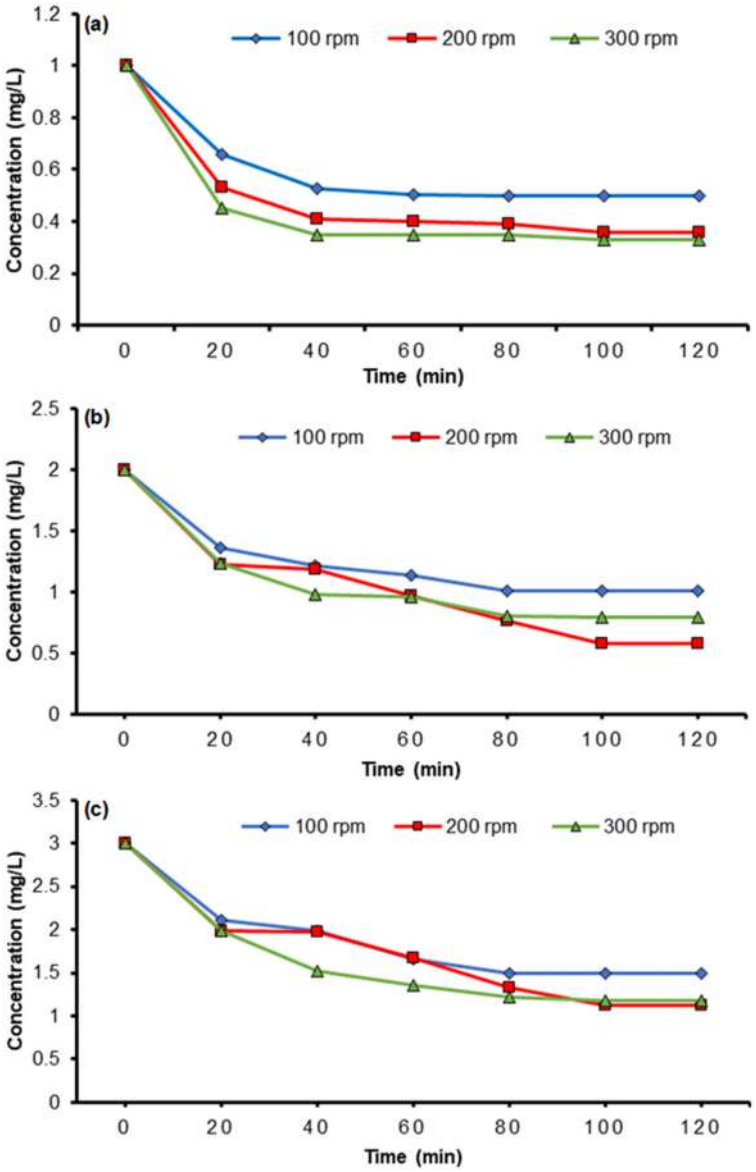

Fig 1. The study of adsorption of methylene blue at various concentrations (a) 1 mg/L, (b) 2 mg/L, and (c) 3 mg/L

layer is formed on the graph produced in the study whenever the short adsorption time produces a graphic pattern that reads saturated is possible to conclude that the layer on the adsorbent is a single layer. In contrast, for the double layer it can be concluded during the adsorption process experience a saturation point in an extended period.

Effects of Initial Concentration on the Adsorption of Methylene Blue

Besides the stirring factor, the initial concentration of methylene blue also affects the mass transfer of methylene blue adsorption to nano-crystal cellulose [34-35]. Research on the effect of the initial concentration of adsorbate on various adsorbents has yielded uniform conclusions. Deepak and co-workers in their study on the adsorption of methylene blue using activated carbon adsorbent from *Ficus carica* bast mentioned that an increase in efficiency of methylene blue removal is proportional to the increase in the initial concentration of methylene blue [36]. Hence, a higher initial concentration gave a higher driving force to resolve the solid-liquid mass transfer resistance. Meanwhile, at a very low concentration, there will be a vacant active site on the surface of the adsorbent that is not occupied by

the adsorbate molecule. It can be interpreted as a decrease in the adsorption capacity of the system. In addition, if an increase of initial concentration exceeds the optimum point, the active site on the surface of the adsorbent will decrease to slow down the adsorption process.

The graph of the methylene blue concentration variation on the adsorption capacity (mg/g) can be seen in Fig. 2. The figure shows the effect of the initial concentration of methylene blue with various stirring speeds on adsorption capacity. Generally, it can be concluded that the greater the initial concentration used, the higher the value of the adsorption capacity. This situation occurs with stirring speeds of 100, 200, and 300 rpm. The greater initial concentration gives a significant driving force to pass through the mass transfer resistance between the liquid (methylene blue) and the solid as nano-crystal cellulose [37]. At large concentrations of methylene blue, the amount of site nano-crystal cellulose may not be sufficient to absorb methylene blue molecules, causing a decrease in the percentage of color removal in the adsorption process.

The adsorption mechanism begins when methylene blue molecules reach the boundary layer and then diffuse to the adsorbent's surface. The molecules further diffuse to the interior of the adsorbent. As shown in Fig. 2, the phenomenon of methylene blue being adsorbed by the surface of the nano-crystal cellulose takes a relatively long time.

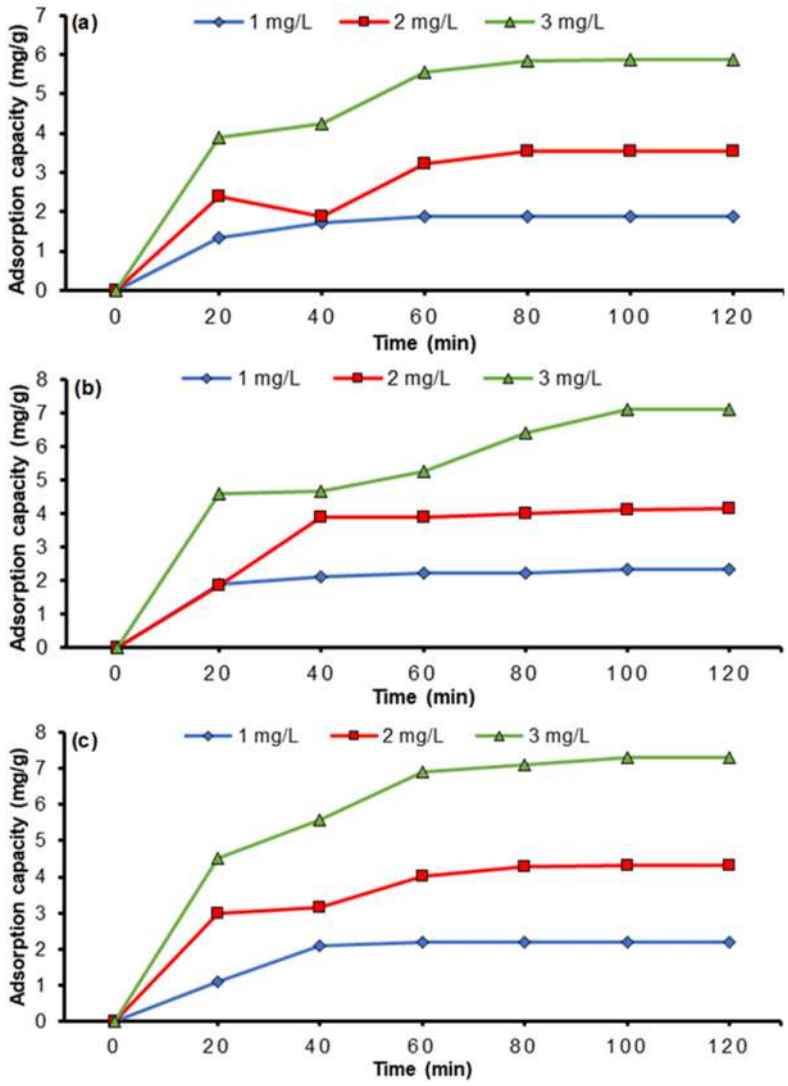

Fig 2. Adsorption capacity (a) 100 rpm, (b) 200 rpm, and (c) 300 rpm

Isotherms and Kinetics Studies

The kinetics study aims to identify the adsorption rate constant (k) value to achieve equilibrium [38]. The value of the adsorption rate constant (k_c) and the adsorption equilibrium constant was obtained using the Henry, Langmuir and Freundlich model equation approach. The results can be seen in Table 1. In addition, a comparison of simulation data of maximum adsorption capacity (q_m) and the experimental ones was presented in Table 2.

Table 1 indicates that stirring speed does not affect the value of the constant adsorption rate (k_c). The k_c value has no significant differences at 100, 200, and 300 rpm. This trend was observed for all three models. Furthermore, the proposed models have an SSE (sum square of errors) value of approximately 0. The three models can be considered suitable for the phenomenon of methylene blue adsorption using nano-crystal cellulose. Among the three models, The SSE value in the Freundlich model is the smallest. However, the q_m data of the Freundlich model (Table 2) were inconsistent with the experimental data. The Henry model's q_m data also differed significantly from the experimental ones. Overall, Table 2 suggested that the fittest model of the MB adsorption was the Langmuir model, in which the adsorption capacity tends to increase when the initial concentration of methylene blue is higher [33,39].

The Langmuir isotherm model is an adsorption kinetics model commonly used to describe complex adsorption mechanisms. This model adequately describes the adsorption of methylene blue by nano-crystal cellulose. The adsorption mechanism relies not only on the adsorbent's pores but on the presence of hydrogen bonds and Van der Waals interactions that occur to achieve stability. In this adsorption mechanism,

Table 1. Adsorption rate constants (k_c) at the stirring speeds of 100, 200, and 300 rpm on varied concentrations of methylene blue (1, 2 and 3 mg/L)

MB concentration	Stirring speed (rpm)	Henry model			Langmuir model			Freundlich model		
		k_c	K_d	SSE	k_c	K_L	SSE	k_c	K_f	SSE
1 mg/L	100	0.0013	4.4870	0.0040	0.0007	3.056	0.0206	0.0016	11.78	0.0006
	200	0.0019	8.3402	0.0009	0.0930	2.662	0.0419	0.0089	9.265	0.0432
	300	0.0028	7.8611	0.0036	0.0100	2.743	0.0174	0.0028	8.628	0.0036
2 mg/L	100	0.0012	4.2190	0.0117	0.0012	3.362	0.0139	0.0018	6.668	0.0106
	200	0.0026	6.2668	0.3127	0.0102	1.000	0.5250	0.0013	11.66	0.1444
	300	0.0029	4.9792	0.2157	0.0102	1.000	0.5250	0.0012	13.54	0.039
3 mg/L	100	0.0021	3.7576	0.0371	0.0009	2.782	0.1122	0.0007	8.122	0.018
	200	0.0015	4.3399	0.1850	0.0014	4.369	0.1791	0.0014	3.585	0.018
	300	0.0026	5.1870	0.2492	0.0130	4.560	0.0231	0.0016	6.446	0.018

Table 2. Maximum adsorption capacity data (q_m) at the stirring speeds of 100, 200, and 300 rpm on varied concentrations of methylene blue (1, 2 and 3 mg/L)

MB concentration	Stirring speed (rpm)	Henry model	Langmuir model	Freundlich model	Experimental data
1 mg/L	100	1.9163	7.8620	9.4240	7.0254
	200	2.6250	8.3540	7.4120	7.0438
	300	2.6250	8.3990	6.9024	7.0596
2 mg/L	100	6.3750	5.2130	5.3344	7.3914
	200	6.3750	8.9470	9.3280	7.7127
	300	6.3750	8.8760	10.8320	7.7258
3 mg/L	100	10.1250	7.6070	6.4976	7.8865
	200	10.1250	5.9100	2.8680	7.9418
	300	10.1250	8.5900	5.1568	8.0155

the hydrogen bond is characterized by the presence of hydrogen from the nano-crystal cellulose hydroxyl group, which binds the nitrogen element of methylene blue. The Van der Waals force is characterized by dipole ion interactions and electrostatic interactions.

The Langmuir isotherm model is a suitable model to describe the chemical adsorption mechanism. It is indicated by the visible adsorption mechanism, namely the monolayer [40]. This monolayer surface illustrates that the adsorption is carried out by an active site, and one active site can be occupied by one molecule only [41].

The Langmuir isotherm model for the methylene blue adsorption process using nano-crystal cellulose was also confirmed in several studies, such as the adsorption of methylene blue from nano-crystal cellulose made by the TEMPO [42] method. In addition, the model was also appropriate for the adsorption of nano-crystal cellulose on various organic dyes, such as methylene blue, methyl orange, rhodamine B, and crystal violet. The adsorption of methylene blue adsorption using nano-crystal cellulose-alginate hydrogel on a fixed-bed column also followed the model [43].

Based on the isotherm study, the layer of nano-crystal cellulose produced is a monolayer. To maximize the removal of methylene blue from a solution by using cellulose nano-crystal based on the layer formed, another

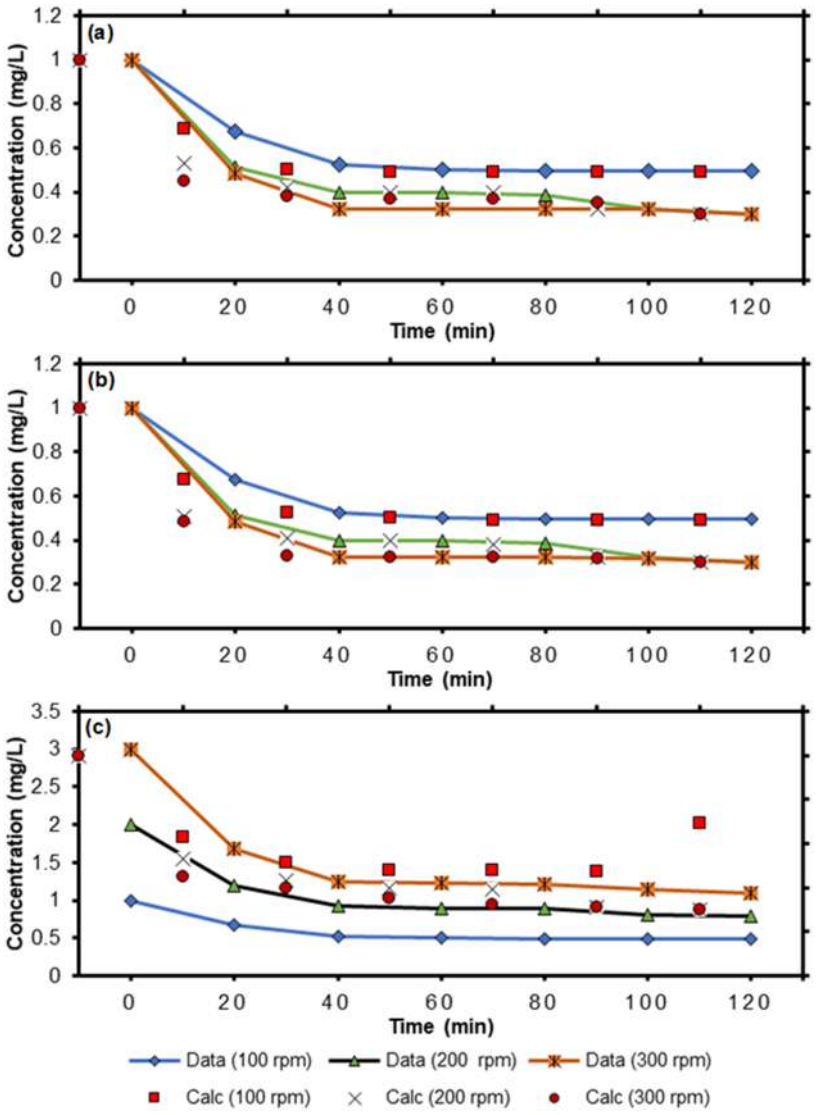

Fig 3. Fitting results (a) Henry model, (b) Langmuir model, (c) Freundlich model

active group, which is anionic, can help the binding of methylene blue (which is cationic). In chemical adsorption, the k value on surface interactions tends to be low. It indicates that the limiting step in the methylene blue adsorption mechanism using nano-crystal cellulose does not depend on diffusion but on surface interactions. The results of fitting each model to the sample with the lowest SSE can be seen in Fig. 3.

Thermodynamic Study

The parameters used for thermodynamic studies are changes in standard enthalpy (ΔH°), entropy (ΔS°), and standard free energy (ΔG°) resulting from the transfer of moles of solute from solution to the solid-liquid surface. Thermodynamic studies were carried out on 3 mg/L of methylene blue with a stirring speed of 300 rpm at a pH of 9.

The thermodynamic study was tested at various temperatures to determine the value of Gibbs energy produced by the adsorption process, and the results can be seen in Table 3.

The study was conducted at 303, 308, 313, and 318 K and presented in Table 3. The increased temperature from 303 to 308 K indicates an increase in the adsorption capacity from 10.3389 mg/g to 10.3802 mg/g. Based on the data presented, the temperature increase causes an increase in the adsorption capacity due to the swelling of the internal structure of the nano-crystal cellulose, which allows methylene blue to penetrate further [44]. However, when the temperature was increased to 313 and 318 K, there was a slight decrease in the adsorption capacity. An increase in temperature can reduce the surface area value of nano-crystal cellulose [45]. Decreasing the adsorbent area reduces the adsorption site for methylene blue. According to Tang et al. [46], the greater operating temperature of the adsorption test can reduce the pore width and decrease the diffusion of methylene blue tested on flakes-shaped nano-crystal cellulose. Besides, the hydroxyl groups in the cellulose crystal nanostructures are bound in hydrogen bonds at higher temperatures due to the larger capillary force so that the cellulose crystal nano molecules are close to each other.

The higher the temperature, the lower the final absorbed concentration of methylene blue. The lower the final adsorbed methylene blue concentration, the higher the adsorption capacity (mg/g). It indicates that the nature of the adsorption process is endothermic. A higher operating temperature causes an increase in the adsorption capacity by diffusing the intraparticle of methylene blue molecules into the adsorbent pores. Based on the Table 3, when the temperature was increased to 313 and 318 K, the value of the adsorption capacity decreased as a result of the weakening of the hydrogen and hydroxyl bonds in nano-crystals cellulose due to increased molecular motion. Exothermic conditions by increasing the operating temperature in this study are quite possible to optimize the adsorption process. However, the operating temperature must be controlled to avoid the agglomeration of nano-crystal cellulose, leading to an increase in nano-crystalline cellulose's particle size. The obtained data became the basis for creating the graph with ln K_c as the y-axis and 1/T as the x-axis (see Fig. 4).

Based on the calculation, the value of ΔH° is 0.00742 kJ/mol. It confirms that the adsorption process is endothermic. The value of ΔS° is 0.7758 kJ/mol K, and based on the enthalpy and entropy values, the ΔG° value reaches −242.81 kJ/mol. It shows the feasibility of the

Table 3. Calculation of thermodynamic studies

Temperature (K)	C_e (mg/L)	q_e (mg/g)	K_c
303	0.311	10.3389	5.541
308	0.300	10.3802	5.767
313	0.305	10.3614	5.661
318	0.309	10.3464	1.724

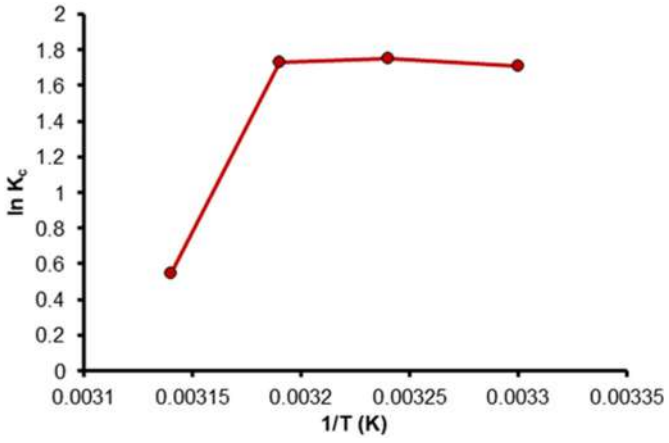

Fig 4. Graph ln K_c vs 1/T

process and the spontaneous process of methylene blue adsorption by nano-crystal cellulose [47].

Based on the experimental results, an important parameter that can maximize the adsorption of methylene blue in a solution is to set the agitator rotation at a higher rpm, and operate at a temperature of 313 K. Raising the temperature above the standard temperature, in this case, can help stretch the internal structure of nano-crystal cellulose. Conditions can be optimized by increasing the surface area of the adsorbent by reducing the size of the cellulose nano-crystals produced. The larger the surface area of the adsorbent, the more adsorbate can be adsorbed on the pore structure, and also attached to the nano-crystal cellulose bonds, which have more active functional groups.

■ CONCLUSION

The kinetic study showed that the surface interaction was the limiting step in the methylene blue adsorption mechanism. Meanwhile, the thermodynamic study concluded that the adsorption process was spontaneous and endothermic. The appropriate model for the adsorption is the Langmuir isotherm model. Overall, methylene blue adsorption using nano-crystal cellulose followed the chemical adsorption type.

■ ACKNOWLEDGMENTS

This research was funded by Universitas Gadjah Mada through a research grant of "*Rekognisi Tugas Akhir 2020*" (Contract No. 2488/UN1.P.III/DIT-LIT/PT/2020).

■ AUTHOR CONTRIBUTIONS

The first author and also as the corresponding author served as a researcher and carried out data collection. The second and third authors served as writers, conducting revisions and final assessments of the data and written reports.

■ REFERENCES

[1] Kemenperin, 2018, Kebijakan Sektor Industri Kimia dan Tekstil dalam Rangka Implementasi Roadmap Industri 4.0, *Indonesia Industrial Summit 2018: Implementasi Industri 4.0 dalam rangka Transformasi Lanskap Industri Nasional menuju Top 10 Ekonomi Dunia 2030*, Ministry of Industry of Republic of Indonesia, Jakarta, Indonesia.

[2] Badan Pusat Statistik, 2021, *Statistik Indonesia Tahun 2010*, Statistics Indonesia (BPS), Jakarta, Indonesia.

[3] Shanmugarajah, B., Chew, I.M.L., Mubarak, N.M., Choong, T.S.Y., Yoo, C.K., and Tan, K.W., 2019, Valorization of palm oil agro-waste into cellulose biosorbents for highly effective textile effluent remediation, *J. Cleaner Prod.*, 210, 697–709.

[4] Umoren, S.A., Etim, U.J., and Israel, A.U., 2013, Adsorption of methylene blue from industrial effluent using poly (vinyl alcohol), *J. Mater. Environ. Sci.*, 4 (1), 75–86.

[5] Rafatullah, M., Sulaiman, O., Hashim, R., and Ahmad, A., 2010, Adsorption of methylene blue on low-cost adsorbents: A review, *J. Hazard. Mater.*, 177 (1-3), 70–80.

[6] Lellis, B., Fávaro-Polonio, C.Z., Pamphile, J.A., and Polonio, J.C., 2019, Effects of textile dyes on health and the environment and bioremediation potential of living organisms, *Biotechnol. Res. Innovation*, 3 (2), 275–290.

[7] Hassaan, M.A., and El Nemr, A., 2017, Health and environmental impacts of dyes: Mini review, *Am. J. Environ. Sci. Eng.*, 1 (3), 64–67.

[8] Ismail, M., Akhtar, K., Khan, M.I., Kamal, T., Khan, M.A., Asiri, M.A., Seo, J., and Khan, S.B., 2019, Pollution toxicity and carcinogenicity of organic dyes and their catalytic bio-remediation, *Curr. Pharm. Des.*, 25 (34), 3653–3671.

[9] Jadhav, A.C., and Jadhav, N.C., 2021, "Treatment of textile wastewater using adsorption and adsorbents" in *Sustainable Technologies for Textile Wastewater Treatments*, Eds. Muthu, S.S., Woodhead Publishing, Cambridge, UK, 235–273.

[10] Katheresan, V., Kansedo, J., and Lau, S.Y., 2018, Efficiency of various recent wastewater dye removal methods: A review, *J. Environ. Chem. Eng.*, 6 (4), 4676–4697.

[11] Brião, G.V., Jahn, S.L., Foletto, E.L., and Dotto, G.L., 2017, Adsorption of crystal violet dye onto a mesoporous ZSM-5 zeolite synthetized using chitin as template, *J. Colloid Interface Sci.*, 508, 313–322.

[12] Ince, M., and Ince, O.K., 2017, An overview of adsorption technique for heavy metal removal from water/wastewater: A critical review, *Int. J. Pure Appl. Sci. Technol.*, 3, 10–19.

[13] An, V.N., Van, T.T.T., Nhan, C.H.T., and Heu, V.L., 2020, Investigating methylene blue adsorption and photocatalytic activity of ZnO/CNC nanohybrids, *J. Nanomaterials*., 2020, 6185876.

[14] Ibrahim, I., Al-Obaidi, Y.M., and Hussin, S.M., 2015, Removal of methylene blue using cellulose nanocrystal synthesized from cotton by ultrasonic technique, *Chem. Sci. Int. J.*, 9 (3), 1–7.

[15] Oyewo, O.A., Adeniyi, A., Sithole, B.B., and Onyango, M.S., 2020, Sawdust-based cellulose nanocrystals incorporated with ZnO nanoparticles as efficient adsorption media in the removal of methylene blue dye, *ACS Omega*, 5 (30), 18798–18807.

[16] Safavi-Mirmahalleh, S.A., Salami-Kalajahi, M., and Roghani-Mamaqani, H., 2019, Effect of surface chemistry and content of nanocrystalline cellulose on removal of methylene blue from wastewater by poly (acrylic acid)/nanocrystalline cellulose nanocomposite hydrogels, *Cellulose*, 26 (9), 5603–5619.

[17] Liang, L., Zhang, S., Goenaga, G.A., Meng, X., Zawodzinksi, T.A., and Ragauskas, A.J., 2020, Chemically cross-linked cellulose nanocrystal aerogels for effective removal of cation dye, *Front. Chem.*, 8, 570.

[18] Susanto, I., 2013, *Batang Sawit Bernilai Tinggi*, https://regional.kompas.com/read/2013/05/23/02481574/batang.sawit.bernilai.tinggi, accessed on 29 September 2019.

[19] Holman, J., 1981, *Heat Transfer*, McGraw Hill International Book Co. Inc., New York, US.

[20] Mustikaningrum, M., Cahyono, R.B., and Yuliansyah, A.T., 2021, Effect of NaOH concentration in alkaline treatment process for producing nano crystal cellulose-based biosorbent for methylene blue, *IOP Conf. Ser.: Mater. Sci. Eng.*, 1053, 012005.

[21] Miranda, F.F., Putri, A.S., Mustikaningrum, M., and Yuliansyah, A.T., 2021, Preparation and characterization of nano crystal cellulose from oil palm trunk for adsorption of methylene blue, *AIP Conf. Proc.*, 2338, 040008.

[22] Ayawei, N., Ebelegi, A.N., and Wankasi, D., 2017, Modelling and interpretation of adsorption isotherms, *J. Chem.*, 2017, 3039817.

[23] Saadi, R., Saadi, Z., Fazaeli, R., and Fard, N.E., 2015, Monolayer and multilayer adsorption isotherm models for sorption from aqueous media, *Korean J. Chem. Eng.*, 32 (5), 787–799.

[24] Smith, J.M., Van Ness, H.C., and Abbott, M.M., 2001, *Introduction to Chemical Engineering Thermodynamics*, 6th Ed., McGraw Hill International Book Co. Inc., New York, US.

[25] Mustikaningrum, M., 2021, Peningkatan fungsi limbah batang kelapa sawit untuk biosorben sebagai dye removal dengan variasi konsentrasi NaOH pada ektraksi dan waktu sonikasi, *Thesis*, Universitas Gadjah Mada, Yogyakarta.

[26] Darmadi, D., Choong, T.S.Y., Chuah, T.G., Yunus, R., and Taufik Yap, Y.H., 2008, Adsorption of methylene blue from aqueous solutions on carbon coated monolith, *AJChE*, 8 (1), 27–38.

[27] Fil, B.A., and Ozmetin, C., 2012, Adsorption of cationic dye from aqueous solution by clay as an adsorbent: Thermodynamic and kinetic studies, *J. Chem. Soc. Pak.*, 34 (4), 896–906.

[28] Yousef, R.I., El-Eswed, B., and Al-Muhtaseb, A.H., 2011, Adsorption characteristics of natural zeolites as solid adsorbents for phenol removal from aqueous solutions: Kinetics, mechanism, and thermodynamics studies, *Chem. Eng. J.*, 171 (3), 1143–1149.

[29] Altaher, H., Khalil, T.E., and Abubeah, R., 2014, The effect of dye chemical structure on adsorption on activated carbon: A comparative study, *Color. Technol.*, 130 (3), 205–214.

[30] Müller, B.R., 2010, Effect of particle size and surface area on the adsorption of albumin-bonded bilirubin on activated carbon, *Carbon*, 48 (12), 3607–3615.

[31] Krishna, R.A., 1993, A unified approach to the modelling intraparticle diffusion in adsorption processes, *Gas Sep. Purif.*, 7 (2), 91–104.

[32] Banerjee, S., and Chattopadhyaya, M.C., 2017, Adsorption characteristics for the removal of a toxic dye, tartrazine from aqueous solutions by a low cost agricultural by-product, *Arabian J. Chem.*, 10, S1629–S1638.

[33] Jain, N., Dwivedi, M.K., and Waskle, A., 2016, Adsorption of methylene blue dye from industrial effluents using coal fly ash, *Int. J. Adv. Eng. Res. Sci.*, 3 (4), 9–16.

[34] Geng, Y., Zhang, J., Zhou, J., and Lei J., 2018, Study on adsorption of methylene blue by a novel composite material of TiO_2 and alum sludge, *RSC Adv.*, 8 (57), 32799–32807.

[35] Banerjee, S., Chattopadhyaya, M.C., Uma, U., and Sharma, Y.C., 2014, Adsorption characteristics of modified wheat husk for the removal of a toxic dye, methylene blue, from aqueous solutions, *J. Hazard., Toxic Radioact. Waste*, 18 (1), 56–63.

[36] Pathania, D., Sharma, S., and Singh, P., 2017, Removal of methylene blue by adsorption onto activated carbon developed from *Ficus carica* bast, *Arabian J. Chem.*, 10, S1445–S1451.

[37] Al-Ghouti, A.M., and Al-Absi, R.M., 2020, Mechanistic understanding of the adsorption and thermodynamic aspects of cationic methylene blue dye onto cellulosic olive stones biomass from wastewater, *Sci. Rep.*, 10 (1), 15928.

[38] Hameed, B.H., Krishni, R.R., and Sata, S.A., 2009, A novel agricultural waste adsorbent for the removal of cationic dye from aqueous solutions, *J. Hazard. Mater.*, 162 (1), 305–311.

[39] Khuluk, R.H., Rahmat, A., Buhani, B., and Suharso, S., 2019, Removal of methylene blue by adsorption onto activated carbon from coconut shell (*Cocos nucifera* L.), *IJoST*, 4 (2), 229–240.

[40] Wang, J., and Guo, X., 2020, Adsorption isotherm models: Classification, physical meaning, application and solving method, *Chemosphere.,* 258, 127279.

[41] Hasan, R., Ying, W.J., Cheng, C.C., Jaafar, N.F., Jusoh, R., Jalil, A.A., and Setiabudi, H.D., 2020, Methylene blue adsorption onto cockle shells-treated banana pith: Optimization, isotherm, kinetic, and thermodynamic studies, *Indones. J. Chem.*, 20 (2), 368–378.

[42] Mohammed, N., Grishkewich, N., Waeijen, H.A., Berry, R.M., and Tam, K.C., 2016, Continuous flow adsorption od methylene blue by cellulose nanocrystal-alginate hydrogel beads in fixed bed columns, *Carbohydr. Polym.*, 136, 1194–1202.

[43] Batmaz, R., Mohammed, N., Zaman, M., Minhas, G., Berry, R.M., and Tam, K.C., 2014, Cellulose nano-crystals as promising adsorbents for the removal of cationic dyes, *Cellulose*, 21 (3), 1655–1665.

[44] Hu, X.S., Liang, R., and Sun, G., 2018, Super-adsorbent hydrogel for removal of methylene blue dye from aqueous solution, *J. Mater. Chem. A.*, 6 (36), 17612–17624.

[45] Tan, K.B., Reza, A.K., Abdullah, A.Z., Horri, B.A., and Salamatinia, B., 2018, Development of self-assembled nanocrystalline cellulose as a promising practical adsorbent for methylene blue removal, *Carbohydr. Polym.*, 199, 92–101.

[46] Tang, Y., Yang, M., Dong, W., Tan, L., Zhang, X., Zhao, P., Peng, C., and Wang, G., 2015, Temperature difference effect induced self-assembly method for Ag/SBA-15 nanostructures and their catalytic properties for epoxidation of styrene, *Microporous Mesoporous Mater.*, 215, 199–205.

[47] Lesbani, A., Palapa, N.R., Sayeri, R.J., Taher, T., and Hidayati, N., 2021, High reusability of NiAl LDH/biochar composite in the removal methylene blue from aqueous solution, *Indones. J. Chem.*, 21 (2), 421–434.

Surface Complexes of Cr(VI) by Eucalyptus Barks

Hind Khalil[1*], Fatima Ezzahra Maarouf[1], Mariam Khalil[1], Sanaa Saoiabi[1], Saidati Bouhlassa[1], Ahmed Saoiabi[1], Mhamed Hmamou[1], and Khalil Azzaoui[2]

[1]*Laboratory of Applied Chemistry of Materials (LCAM), Department of Chemistry, Faculty of Sciences, Mohammed V University, 4 Ibn Batouta Avenue in Rabat 1014, Morocco*

[2]*Laboratory of Applied Chemistry and Environment (LCAE), Department of Chemistry, Faculty of Sciences, University Mohamed I, P.O. Box 717, Oujda 60000, Morocco*

* ***Corresponding author:***

tel: +212-661-293957
email: hindkhalil8@gmail.com

Received: January 19, 2022
Accepted: May 19, 2022

DOI: 10.22146/ijc.72358

Abstract: *The sorption mechanism of hexavalent chromium sorption on eucalyptus barks was evaluated as a function of solution pH for different adsorbent dosages, surface coverage, and the amount of adsorbent. The chromium retention was evaluated based on the distribution coefficient (D), and this retention is attributed to $HCrO_4^-$ species, which is predominant between pH 1 and 6.5. The biosorption of Cr(VI) ions onto barks achieved at pH 2.0 in the highest sorbet conditions corresponding to [Cr(VI)] = 10^{-5} mol (V = 100 mL) is examined for various surface coverage. The surface complexes formed between chromate and eucalyptus barks were found to be > S ($HCrO_4$) and > S (CrO_4). Logarithmic stability for log K_{1-1} and the log K_{10} values of the complexes were measured and found to be -5.93 in acidic medium and -0.76 in alkaline medium, respectively. Pointed out that the adsorption of Cr(VI) on eucalyptus bark was greater than 90% in all cases, Cr(VI) recovery is strongly acidic dependent and shows maximum retention, for various sorbent amounts, at pH around 2, and this retention is attributed to $HCrO_4^-$ species, which is predominant between pH 1 and 6.5, the morphological surface of eucalyptus barks were examined by Scanning Electron Microscope (SEM) connected to a micro analyzer EDS.*

Keywords: *chromium(VI); eucalyptus barks; surface complexes; adsorption; surface charge*

■ INTRODUCTION

Heavy metals (HM) are among the most toxic elements introduced into aquatic systems as a result of natural or industrial processes. The rising use of HM, which are soluble, persistent, and non-biodegradable, is associated with environmental pollution through effluents. Chromium is significantly introduced into the aquatic medium from various industrial activities, including alloying, plating, corrosion inhibition, tanning, and pigments [1-3]. Trivalent chromium (Cr(III)) and hexavalent chromium (Cr(VI)) are the most preponderant in soils and aquatic environments [4-5].

Generally, Cr(III) is reported to be not harmful, insoluble $Cr(OH)_3$ at pH typical of groundwater and complexed by organic matter. On the other hand, Cr(VI) is more toxic, highly mobile in soil and groundwater, persistent, and non-biodegradable. This species prevails in the form of chromate (CrO_4^{2-}) and dichromate ($Cr_2O_7^{2-}$) can precipitate with divalent cations. Hexavalent chromium is ranked among the metals of public health concern; hence, it is severely controlled in environmental management. Usually, Cr(VI) anion species are badly sorbed by the negatively charged soil particles and, consequently, can be transferred to the aqueous environments [6-8]. Therefore, total chromium in drinking water with a maximum contamination level of 50 µg/L was taken into account when adjusting Cr(VI) discharged into the environment. Consequently, the presence of this species in drinking water is regulated through the total chromium, whose maximum

contaminant Level is 50 μg/L. Cr(VI) recommended maximal permissible limit (MPL) in the surface water is regulated to 2 mg/L and to 0.1 mg/L in drinking water [9-13]. Naturally occurring Cr(VI) is found in ground and surface waters at values above 50 μg/L [6,14]. To meet these environmental standards/regulations, effluents and metal-polluted water must be treated prior to discharge into freshwater. The elimination of Hexavalent chromium ions from wastewater becomes an absolute necessity. The conventional methods used for this purpose are precipitation, coagulation, electroplating, ion exchange, adsorption, liquid-liquid extraction, and ion exchange processes. The adsorption route is an efficient method for hexavalent chromium removal due to its simplicity, availability of various adsorbents, and convenience for lower heavy metals contamination [15-17]. Efficient sorbents such as granular activated carbon show low chromium uptake due to their anionic nature associated with strong hydration.

However, the biosorption process appears as a potential alternative for detoxification and metal recovery from industrial wastewater. This technique achieved by different biosorbents has received considerable interest in water treatment for the uptake of trace metals, in particular, hexavalent chromium. Biosorption has emerged as a potential technique and promising alternative to a conventional method for environmental clean-up using waste biomass. These advantages include availability, regeneration, short operation time, and no chemical sludge [4,18-21]. One can note that more than one process is implicated in the sorption operation, which is performed by combining adsorption, ion exchange, and micro precipitation process. Thus, complex interactions are involved in biosorption, and optimal physicochemical parameters are determined using numerical calculations combining mathematical and statistical models [15,22]. As suggested, understanding the sorption mechanisms requires the distribution of functional groups of binding sites, depending on time and pH suspensions. In this case, global sorptions combining various reactions make the overall kinetic model more complicated to evaluate [23]. To avoid this dilemma, the sorption phenomenon is studied at even time intervals over the process duration [24].

Biomass materials have strong metal binding power due to various surface functional groups, such as hydroxyl, alkyl, carbonyl, sulfhydryl, amino, and phosphate groups. Bark, as a lingo cellulosic residue, is predominantly utilized in thermal energy production [24]. For this material, uronic acid units with both carbonyl and carboxylic acid functional groups and phenolic groups are the active sites involved in metal sorption, mainly governed by surface complexation [23,25]. Indeed, it is reported that the eucalyptus barks exhibit a caves-like, rough, and irregular surface morphology with active groups that are mainly composed of carboxylic acid (–COOH), followed by Hydroxyl (–OH) and amine groups ($–NH_2$). The carboxyl and hydroxyl groups are H^+ exchangers, while the other groups are OH^- exchangers [26-28].

Mechanisms of Cr(VI) sorption is rather complex process, including chemisorption and ion exchange. Removal of this metal with various biosorbents is found to be dependent on pH solution. As a result, the sorption of anion species is controlled mainly by surface exchange reactions. Further insertions occurring in the unavailability of active sites are considered to be due to diffusion into the biomass system. In addition, unidentified mechanisms may also be involved in biosorption, and which definition is suggested to require, firstly, the characterization of the functional groups. Generally, the rate of hexavalent chromium sorption is strongly pH-dependent and rises with a decrease in medium acidity. The optimum pH for sorption of Cr(VI) ranges from 1 to 3 [29]. Indeed, the biosorption process of Cr(VI) is strongly dependent on the suspension acidity and is more dependent on pH. Optimal uptake conditions are achieved at pH ranging from 1 to 3. From the distribution diagram of chromium, acid chromate ($HCrO_4^-$) is the prevailing species in these optimal sorption conditions. As a result, this sorption technique is more convenient for acid effluent clean-up [9,18,30-33].

Nevertheless, some studies report maximum Cr(VI)

biosorption at relatively higher pH ranging from 5.5 to 6.2 [34-35]. The adsorption mechanisms occurring between Cr(VI) anions and biosorbents are due to predominantly the electrostatic interactions and exchange of proton ions with biosorbent surface [9,36]. Several biomasses are used to remove metals from an aqueous solution, including bacteria, algae, fungi, olive waste, cassia, and neem barks. While various kinetic models are successfully used to fit biosorbent sorption, the chemical reaction mechanism is nevertheless required for the whole description of this process [9,20]. For bark sorbents, extensive studies are mainly dealing with the kinetic removals of cationic metals whose maximum uptake is rapidly occurring within the first 5–10 min. For Cr(VI), this maximum is reached at a minimum duration explored of 30 min [4,25]. Assessment of the most suitable sorption equilibrium model needs optimization of the various physicochemical parameters such as initial Cr(VI) concentration, adsorbent dose, contact time, and pH. For this purpose, mathematical and statistical models are developed to evaluate the main influent parameters on this process involving complex interactions [37]. Comparing these models with mass transfer rate is often found to best fit with Freundlich and Langmuir models [38].

The regeneration of biosorbent is a primordial operation for the successful use of biosorption technology. Therefore, total metal elution is more required for biomass reutilization in biosorption cycles. After seven adsorption-desorption cycles, full regeneration is achieved with 0.1 M HCl, and Cr(VI) adsorption capacity remains similar to the initial value. Thus, the main objective of the present study is to investigate the sorption mechanism of Cr(VI) sorption on eucalyptus barks using column mode. For this purpose, Cr(VI) removal is performed to examine the effect of contact time and biomass dosage.

■ EXPERIMENTAL SECTION

Materials

All reagents are of analytical grade obtained from Sigma Aldrich and used without further purification. Stock metal solutions of Cr(VI) (10^{-4} M) were prepared by dissolving suitable amounts of potassium bichromate ($K_2Cr_2O_7$, 99%). Chemicals used were sodium hydroxide (NaOH, 99%), nitric acid (HNO_3, 99%), hydrochloric acid (37%), sodium chloride (NaCl, 99%), phosphatic acid solution (H_3PO_4, 85%), and all chemicals were used without further purification. The acidity of this suspension is adjusted using a 0.1 M solution of HNO_3 or NaOH for all experiments, we used High quality of distilled water.

Instrumentation

Morphological surface features were examined by applying Jeol JSM-IT100 In TouchScopeTM Scanning Electron Microscope (SEM) connected to a microanalyzer EDS [39]. Analysis of the dosage of chromium(VI) is carried out in the aqueous phases before and after adsorption by a (EPA 7196A) UV-Visible spectrophotometer.

Procedure

Preparation of biosorbent

The eucalyptus barks are washed, air dried, milled, and then crushed between 40 and 60 mesh. To avoid coloration release, the biosorbent is suspended successively in a 2 M caustic solution and 1.4 M phosphoric acid for 4 h at 80 °C. The adsorption studies are conducted with a fixed-bed process. A given amount of adsorbent is placed in a glass column with an internal diameter of 8 mm and a length of 40 cm. Fig. 1 shows the biosorbent appearance before and after initial preparation.

The effect of pH is investigated in the elute medium for biomass suspension of 1.0, 1.5, and 2.0 g/L. The acidity of this suspension is adjusted using a 0.1 M solution of HNO_3 or NaOH. An aliquot of 5.0 mL of the supernatants is filtered, and the chromium concentration is determined using the 1,5-diphenylcarbazide (EPA 7196A) spectrophotometry method. The distribution coefficient (D), which is the ratio of Cr(VI) concentrations in solid and aqueous phases, is evaluated chromium retention. One can note that the eluted solution is discarded for successive volumes of 10 mL. The Adsorption of Cr(VI) ions by the biosorbent, eucalyptus barks, is examined according to the pH, the contact time,

Fig 1. Raw eucalyptus barks material before and after initial preparation

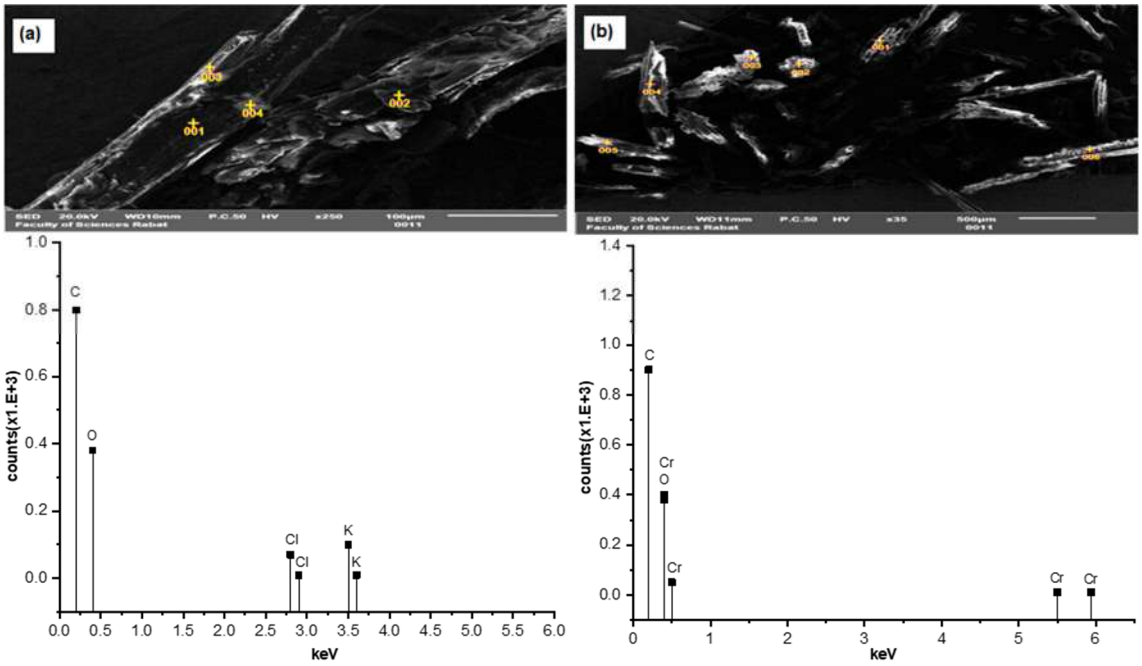

Fig 2. Surface images and EDX analysis of eucalyptus bark obtained by SEM (a) sample extracted with water only (b) eucalyptus bark in the presence of Cr(VI)

the suspension, and the mass of the biosorbent. The effect of pH on the partition of Cr(VI) between the solution and the solid phase is examined for various contact times [40].

Adsorption studies are carried out at room temperature as a function of pH and adsorbent dosage (m). Potassium dichromate solution (1×10^{-4} M) is channeled into the column at a flow rate of 5 mL/min, corresponding to 5×10^{-7} mol/min of Cr(VI).

■ RESULTS AND DISCUSSION

Surface Morphology of Eucalyptus Barks

The surface morphology of eucalyptus bark samples is studied by the scanning electron microscopy (SEM) technique. Fig. 2 shows the SEM micrograph and its energy-dispersive X-ray spectroscopy (EDX) images obtained with 1000× magnification and a scale bar of 20 µm. SEM images of the eucalyptus barks before and after Cr(VI) sorption are shown in Fig. 2; a comparison of these micrographs before and after Cr(VI) sorption shows that the adsorption of Cr(VI) occurs on the surface of the eucalyptus barks.

To examine the morphology of eucalyptus barks, SEM was applied, and the image is shown in Fig. 2; it is shown that the eucalyptus bark surface is porous and composed of (a), (b).

EDX analysis results of the eucalyptus barks with water only and in the presence of chromium(VI). As evident in Table 1 and Table 2.

Table 1. EDX results of the eucalyptus barks

Elements symbol	Mass%	Atom%
C	51.97	59.98
O	44.85	38.86
Cl	0.97	0.38
K	2.20	0.78

Table 2. EDX results of the eucalyptus barks in the presence of chromium(VI)

Elements symbol	Mass%	Atom%
C	56.19	63.21
O	40.91	34.24
Cr	2.53	0.79

Effect of pH on Chromium Adsorption

The effect of pH on chromium uptake was examined for different adsorbent dosages. As can be seen from Fig. 3 that the logarithmic variations of D decrease with increasing equilibrium pH. As found previously, Cr(VI) recovery is strongly acidic dependent and shows maximum retention, for various sorbent amounts, at pH around 2. As a consequence, this retention is attributed to $HCrO_4^-$ species that are predominant between pH 1 and 6.5 [40].

As shown, log D in the function of pH variations are best fitted (R^2 > 95%) with second-order equations that are typical of anionic adsorption behavior, with a decreasing distribution coefficient when the pH is increased. The decrease in anionic adsorption by increasing pH was suggested to be due to competitive –OH uptake and electrostatic repulsion [41]. Generally, it is assumed that the uptake of the weak acid is optimal at a pH value around its dissociation constant or near the Point of Zero Charge (PZC) of surface sorbent materials. For eucalyptus barks, PZC is found to be equal to 5.5 [42].

Therefore, electrostatic attraction of Cr(VI) to positively charged adsorbent sites prevails in the acidic medium of pH lower than. The variation in the removal efficiency with pH is linked, essentially, to hydrogen chromate ($HCrO_4^-$) species, predominating in an aqueous medium of pH lower than pKa2 = 6.5. The value of $y = \frac{\delta \log D}{\delta pH}$ which ranges between 0.0 and -0.3, means that both electrostatic and chemical sorption mechanisms are occurring.

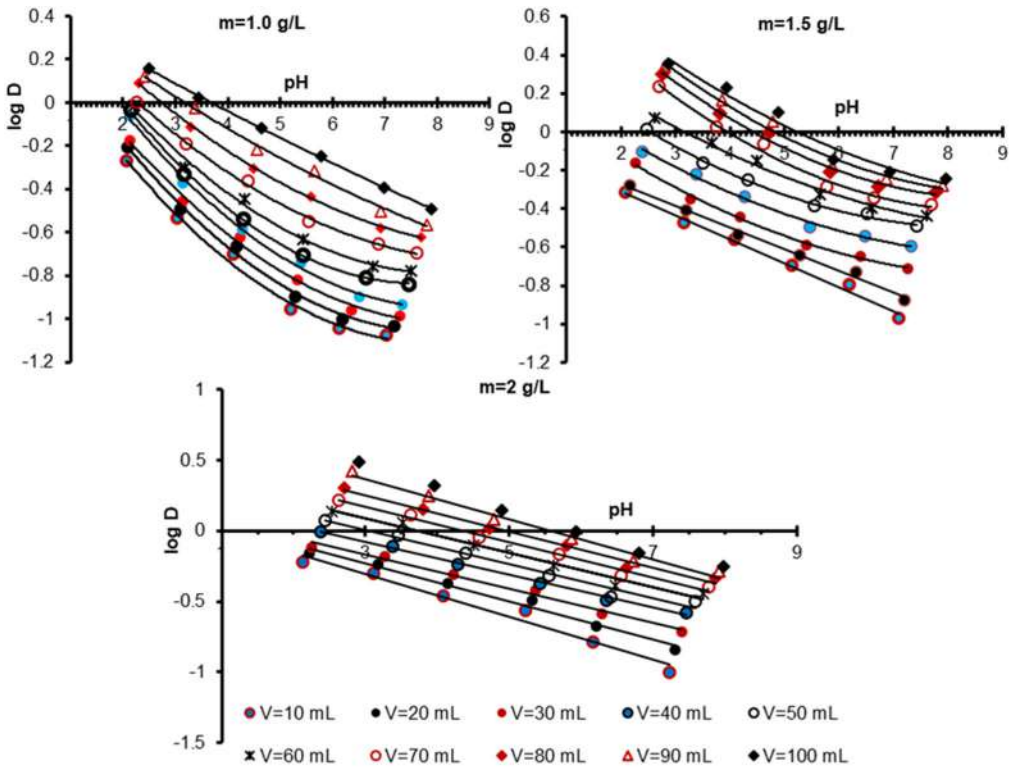

Fig 3. Variations of log D in the function of pH were obtained for various volumes of 1.0×10^{-4} M Cr(VI) solutions at sorbent m = 1.0, 1.5, and 2.0 g/L. The flow rate is 5×10^{-7} mol/min of Cr(VI), which corresponds to 5 mL/min

The reuse of the bisorbent is tested in optimal conditions by regenerating the barks in 0.1 M NaOH solution. The results obtained show that the recovered adsorbent is reusable over more than seven cycles. Generally, it is assumed not possible to differentiate between these mechanisms [43]. The adsorption is highly dependent on the pH of the aqueous suspension; the Cr(VI) retention is maximal at low pH values. As a result, the eucalyptus barks are more suitable for Cr(VI) removal from acidic mediums such as chromium plating effluent, tannery effluent, and electroplating effluent, whose pH range between 1.0 and 2.2 [44]. Fig. 4 shows log D = f(n) obtained for various suspension amounts.

Experiment results show that the adsorption increases with the increasing sorbent mass. The lower slope value of about 0.2 of the obtained straight line reveals that the sorption of about 20% of Cr(VI) is carried out through the chemisorptions process. As shown previously, the predominant physical adsorption occurs by strong electrostatic interactions and Van Der Waals forces between the metal anion and the positively charged active sorption sites [46-47].

The slopes $\frac{\delta \log D}{\delta n}$ are varying between 5.8×10^{-8} and 9.3×10^{-8}. At a lower "n" (the mol chromium in eluate) value, adsorption efficiency increases slightly with sorbent amount. As discussed before, the biosorption of the oxyanion depends on the surface coverage (biosorbent dosage or sorbet/sorbent ratio). Indeed, a more pronounced effect of biosorbent dosage is observed at higher chromium coverage [45].

The biosorption of hexavalent chromium ions onto barks was achieved at pH 2.0 in the highest sorbet conditions corresponding to $n = 10^{-5}$ mol (V = 100 mL) is examined for various surface coverage. The results are shown in Fig. 5.

Fig. 6 shows the variations of the pH corresponding to 50% ($pH_{50\%}$) of chromium adsorption carried out with various surface coverage (n/m).

Obtained results show that the slopes of $pH_{50\%}$ in the function of $(\frac{n}{m})$ curves are rising with sorbent amounts. At given "m" (sorbent amount), $pH_{50\%}$ increases with surface coverage to reach maximal value $(pH_{50\%})$ max, which decreases as $(\frac{n}{m})$ continue to rise. Indeed, $(pH_{50\%})$ max of about 4, 5, and 6 are reached at surface coverage of 1.0×10^{-5}, 6.7×10^{-6}, and 5.0×10^{-6}, respectively.

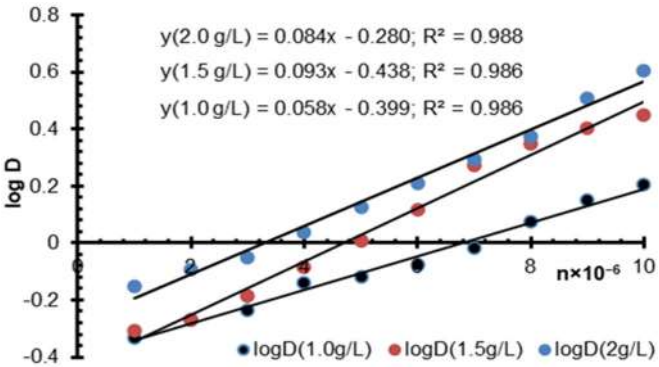

Fig 4. Variations of log D in the function of n obtained at pH = 2.0 for suspension mass of 1.0, 1.5, and 2.0 g/L at a flow rate of 5×10^{-7} mol/min of Cr(VI), which corresponds to 5 mL/min

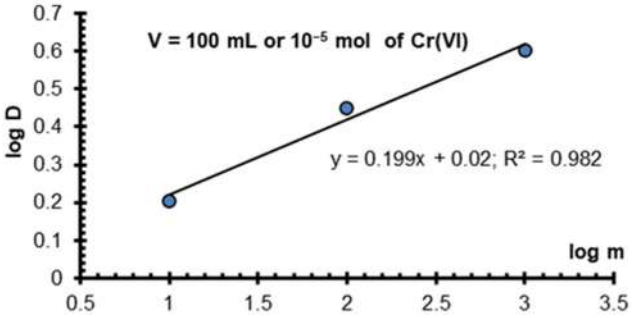

Fig 5. Variations of log D in the function of log m obtained at pH 2.0 at a flow rate of 5×10^{-7} mol/min of Cr(VI), which corresponds to 5 mL/min

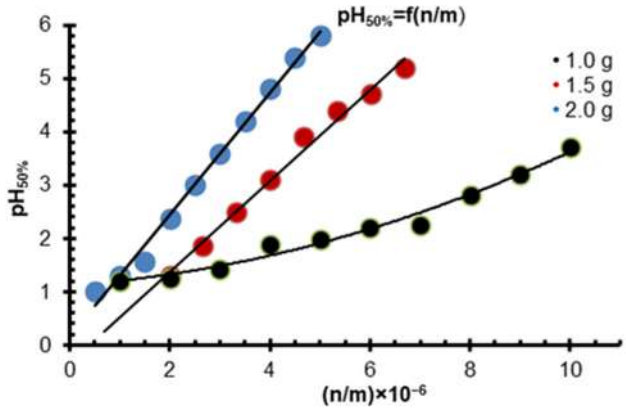

Fig 6. Variations of $pH_{50\%}$ in the function of $(\frac{n}{m})$

Chromium(VI) Adsorption Reactions

The distribution of chromium between sorbate and sorbent phases is expressed as a Cr(VI) biosorption

isotherms. These isotherms are often used to define the relationship between the mass of the sorbate and the mass of the sorbent. Several isotherm models are successfully used to analyze data of Cr(VI) biosorption. Nevertheless, the adsorption reactions are slightly, or not described. Recently, it has been shown that these reactions could be quantified from the logarithmic variation of the D, with equilibrium pH [48].

The variation in the sorption efficiency with the pH of the solution is correlated with the protonation and deprotonation reactions of both $HCrO_4^-$ anion and surface groups ($\overline{>SOH}$).

These reactions can be expressed in Eq. (1) and (2):

$$\overline{>SOH} + H^+ \leftrightarrow \overline{>SOH_2^+};\ K^+ \quad (1)$$

$$\overline{>SOH} \leftrightarrow \overline{>SO^-} + H^+;\quad K^- \quad (2)$$

Considering that surface complexes are monodentate and taking into account that $y = \frac{\delta \log D}{\delta pH}$ was varying between -0.3 and 0, the adsorption reaction of hexavalent chromium on barks is expressed in Eq. (3):

$$\overline{>SOH} + HCrO_4^- \leftrightarrow \overline{>SOH(HCrO_4)H_{-y}^{(-y-1)+}} + yH^+ - 1 \le y \le 0;\ K_y \quad (3)$$

H_{-1} and H_1 designate H^+ and OH^-, respectively.

This notation allows to write:

$$H_{-1} + H_1 \leftrightarrow H_2O; \quad (4)$$

The surface complexation constant can be expressed in Eq. (5):

$$K_y = \frac{\overline{[>SOH(HCrO_4^-)H_{-y}]}[H^+]^y}{\overline{[>SOH]}[HCrO_4^-]}; \quad (5)$$

To simplify, the surface charge is omitted.

The distribution coefficient is expressed in Eq. (6):

$$D = \frac{\overline{[>SOH(HCrO_4^-)H_{-y}]}}{[HCrO_4^-]}; \quad (6)$$

The used sorbent concentration is considered to be $[\overline{>SOH}] = m$ (g/L) that it is obtained:

$$\log D = \log K_y + \log m + y pH; \quad (7)$$

Surface Complexes

The slope analysis method of $\log D = f(pH)$ variations was used to define the nature of the surface complex noted as $C_y \equiv \overline{>SOH(HCrO_4)H_{-y}}$; Fig. 7 shows $|y| = [(\frac{\delta \log D}{\delta pH})_m] = f(pH)$ graphs achieved for various sorbent mass and sorbet/sorbent ratio.

As it is indicated in Fig. 7, chromium ions, sorption exhibited differences in shape and surface complexes. Slopes different from zero were achieved at low surface coverage corresponding to m = 1.0 and 1.5 g/L, while for

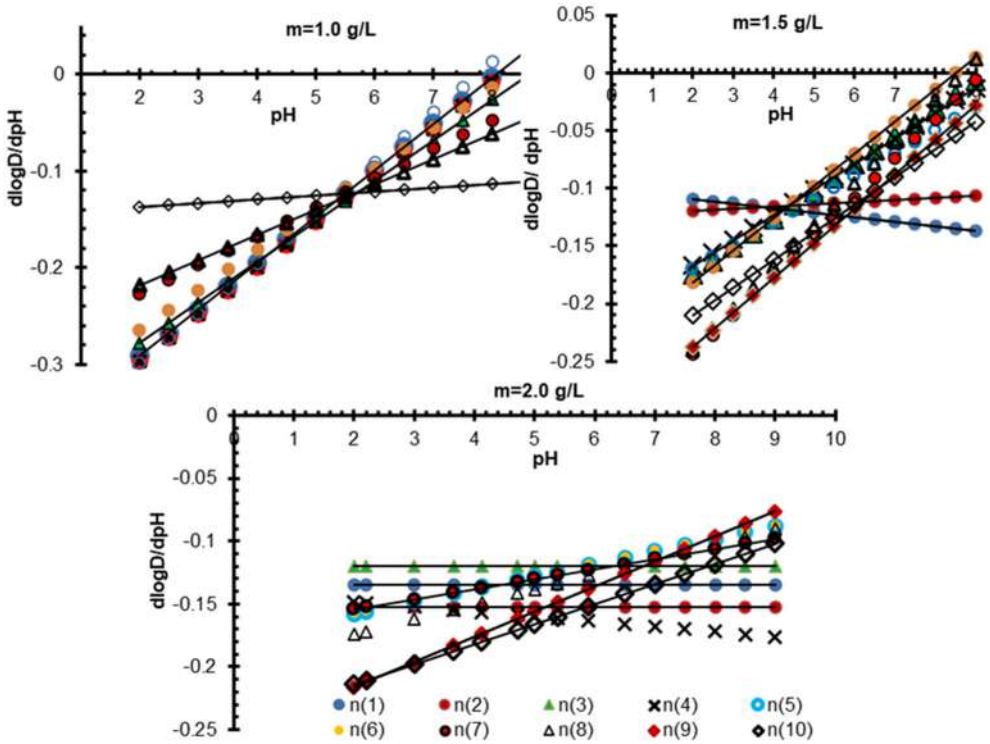

Fig 7. Variations of $y = (\frac{\delta \log D}{\delta pH})_m$ in the function of pH obtained at various amounts (n(i)) of Cr(VI); $n(i) = i \times 10^{-6}$ mol

m = 2.0 g/L. This result was observed for n(i) greater than 4×10^{-6} mol. The decimal value of H_3O^+ (y) stoichiometry coefficient is due to a partial exchange reaction which is combined with physisorption retention [25].

Indeed, at pH around 2, no more than 25% of chromium uptake is found to be occurring through a chemical exchange process. These results agreed with the previous study, suggesting that adsorption equilibrium associated with eucalyptus barks sorbents was mainly controlled by mass transfer and intraparticle diffusion processes. The common intersection point observed for a low sorbent mass of 1.0 g/L corresponds to the PZC found previously and which is 5.5. For this bark concentration, the retention mechanism of spontaneous nature occurring at pH 5.5 is more convenient for rapid chromium adsorption, as found before [42].

I taking this result into account, log D can be expressed in general as:

$$\log D = \log K_y + \log m + y\,pH \quad (7)$$

It is important to note that at pH 2, similar values of about 0.2 are obtained for $\left|\left(\frac{\delta \log D}{\delta pH}\right)_m\right|$ and $\left(\frac{\delta \log D}{\delta \log m}\right)_{pH}$. This would suggest that two sorption processes corresponding to y = 0 and -1 may contribute to the overall Cr(VI) retention. Therefore, we can conclude that chromium adsorption onto eucalyptus barks consists of physisorption and chemical adsorption due to the prevailing surface complexes described according to the following reactions:

$$\overline{>SOH} + HCrO_4^- \leftrightarrow \overline{>SCrO_4^-} + H_2O; y = 0; K_0 \quad (8a)$$

$$\overline{>SOH} + HCrO_4^- + H^+ \leftrightarrow \overline{>SOH(HCrO_4)H_1} \leftrightarrow \overline{>S(HCrO_4)} + H_2O;\ y = -1 \quad (9a)$$

These equilibria could also be expressed in Eq. (8b):

$$\overline{>\mathbf{SOH_2^+}} + \mathbf{HCrO_4^-} \leftrightarrow \overline{>\mathbf{SOH_2^+, HCrO_4^-}};\ \mathbf{y = 0} \quad (8b)$$

$$\overline{>SOH} + HCrO_4^- \leftrightarrow \overline{>SOH_2^+, CrO_4^=}$$

$$\overline{>\mathbf{SOH}} + \mathbf{HCrO_4^-} \leftrightarrow \overline{>\mathbf{S(HCrO_4)}} + \mathbf{OH^-};\ \mathbf{y = -1};\ \mathbf{K_{-1}} \quad (9b)$$

Considering |y| also the fraction 1OH^- (Hydroxyl ion) exchange reactions, the partition equilibrium is:

$$(1\text{-}|y|)(\overline{>\mathbf{SOH}} + \mathbf{HCrO_4^-} \leftrightarrow \overline{>\mathbf{(SCrO_4)^-}} + \mathbf{H_2O};\ \mathbf{K_0}) \quad (10)$$

$$(|y|)(\overline{>\mathbf{SOH}} + \mathbf{HCrO_4^-} \leftrightarrow \overline{>\mathbf{SHCrO_4}} + \mathbf{OH^-};\ \mathbf{K_{-1}}) \quad (11)$$

The global adsorption reaction was:

$$\overline{>SOH} + HCrO_4^- \leftrightarrow \overline{>SOH(HCrO_4)H_{-y}^{(-y-1)+}} + yH^+ \equiv \overline{>S(H_{-y}CrO_4)^{y-1}} - yOH^- + (1+y)H_2O;\ y = 0, -1;\ K_y) \quad (12)$$

The apparent constants (K_y) is given by Eq. (13) and (14):

$$K_y = K_0^{(1-x)} K_1^x \quad (13)$$

$$\log K_y = (1-x)\log K_0 + x \log K_1 \quad (14)$$

Equilibrium Constants

The log (D) in the function of pH variations (Fig. 3) could also be shaped (R^2 > 95%) with straight lines showing, for m = 1.0 g/L, slopes ranging from -0.2 to -0.06. From the obtained results, it can be shown that the plots of log K_y in the function of y shown in Fig. 8 are linear in all examined conditions. The effect of pH and mass of sorbent on Cr(VI) sorption is described by Eq. (7):

$$\log D = \log K_y + \log m + y\,pH \quad (7)$$

The apparent constant (K_{ap}) of the overall equilibrium is given in the following equations in Eq. (15) and (16):

$$K_{ap} = (K_0)^{(1-|y|)}(K_{-1})^{|y|} \quad (15)$$

$$\log K_{ap} = (1-|y|)\log K_0 + |y| \log K_{-1} \quad (16)$$

$$\log K_{ap} = \log K_0 + |y|(\log K_{-1} - \log K_0)$$

$$\log K_0 = -0.76;\ \log K_{-1} - \log K_0 = -5.17;\ \log K_{-1} = -5.93$$

K_{ap} value could be obtained experimentally and is variable, depending on the pH and the surface charge. As a result, the constants K_0 and K_{-1} are the intersect and the slope of the linear plots of log K_{ap} in the function of y, respectively. For y = -1, which corresponds to OH^- release, Eq. (17) is obtained:

$$\log K_{ap} = \log K_{-1} \quad (17)$$

The constants K_0 and K_{-1} are respectively obtained from the intercept and the gradient of the linear plot of log K_{ap} versus 'y'. The logarithmic values are log K_0 = -0.76 ± 0.13 and log K_{-1} = -5.93 ± 0.13.

The changes of log K_{ap} in the function of y have to do with the contribution of the electrostatic effect K_{col}, which is related to surface potential [49].

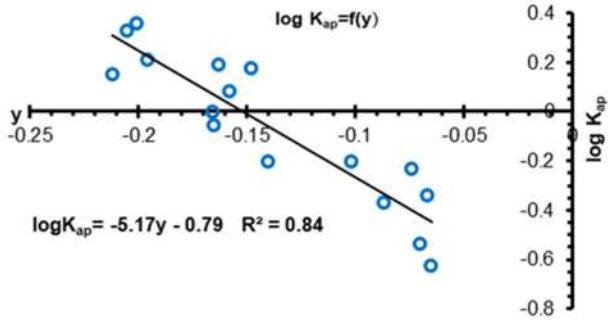

Fig 8. Variations of log K_{ap} in the function of y obtained at m = 1.0 g/L

According to Eq. (18):

$$\mathrm{LnK}_{col} = -\frac{|y|\,\mathrm{F}\Psi_0}{\mathrm{RT}} \quad (18)$$

Ψ_0 is the surface potential, and R (8.314), T (273 + 20), and F (96500) are the gas constant, absolute temperature, and Faraday constant, respectively.

The intrinsic adsorption reaction which was predominating in an acidic medium is of electrostatic nature (8b). As a consequence, the coulombic effect is determined by using the following equation obtained for y = −1:

$$\mathrm{LnK}_{col} = \mathrm{LnK}_0 = -\frac{\mathrm{F}\Psi_0}{\mathrm{RT}} \rightarrow \Psi_0 = -\frac{\mathrm{RT}}{\mathrm{F}}\mathrm{LnK}_0 = 0.025165\mathrm{x}0.76\mathrm{V} = 0.0191\mathrm{V}$$

$$\Psi_0 = 19.1\mathrm{mV} \quad (19)$$

Weak Van der Waals forces contribute to physical adsorption, and its activation energy is not higher than the chemical sorption.

$$\mathrm{K_{ap}} = \mathrm{K_0}\,(\mathrm{K_{col}})^{-1} \quad (20)$$

For x = 1 we obtain:

$$\mathrm{K_{-1}} = \mathrm{K_{10}}\,(\mathrm{K_{col}})^{-1} \rightarrow \mathrm{logK_{-1}} = \mathrm{logK_0} - \mathrm{LnK_{col}} \rightarrow \mathrm{LnK_{col}} = \mathrm{logK_0} - \mathrm{logK_{-1}} = -0.76 + 5.93 = 5.17$$

Moreover, Cr(VI) removal using modified biomaterials such as activated carbon from tamarind wood and coconut shell, phosphate-treated sawdust, coconut husk, palm pressed fibers, oil palm endocarp, and *Leucaena leucocephala* waste sawdust was documented [35]. However, many of these readily available adsorbents showed a limit of adsorption capacity and could not be reused (Table 3). Therefore, it is always interesting to search for new low-cost adsorbents suitable for practical application in a large-scale operation.

Response Surface Analysis

The mathematical models for the chrome, Cr(VI), surface complexes with eucalyptus barks were used to build response surfaces and determine the process's optimal conditions. 3D response surfaces plots for the significant interaction.

Fig. 9 presents the For the chrome, Cr(VI), surface complexes with eucalyptus barks, the most significant interactions were the m, pH, V, and log (D). Fig. 9(a) indicates that the chrome number increased with the increase of activation D and m ratio with decreased pH; Fig. 9(b) shows that the chrome number increased with the increase of the impregnation ratio and decrease of activation time when the volume is fixed at 90 mL. The most significant interaction for the V 90 mL index was log D and activation pH. From Fig. 9(b), it can be observed that the chrome index increased with the increase of the activation log D and the pH. The maximal chrome index response was obtained at the volume of 10 mL.

For the V 10 mL index, the same significant interactions are found in the insertion of chrome, including log D and pH. From Fig. 9(c), it can be observed that the chrome insertion increased with the increase of the m and log D. The maximal chrome responses were obtained at a volume of 10 mL. Fig. 9(c) shows that the sodium increased with decreased log D and decreased pH in case the volume is fixed at 10 mL.

Table 3. The adsorption capacity of eucalyptus barks to the other published low-cost adsorbents for Cr(VI) removal

Adsorbent	Maximum Cr(VI) concentration (mg/L)	pH	Adsorption capacity (mg/g)	Reference
Eucalyptus barks	200	2	3.940	This study for Cr(VI)
Mixed waste tea	250	2	94.34	[50]
Coffee ground	250	2	87.72	[50]
Peanut shell	100	4	8.31	[51]
Coconut shell charcoal	25	4	10.38	[51]
Treated waste newspaper	50	3	59.88	[52]
Walnut shell	100	2	40.83	[53]
Fertilizer industry waste	100	4	15.24	[54]
Rice husk	100	2	13.1	[55]
Tamarind hull-based	50	2	81	[56]

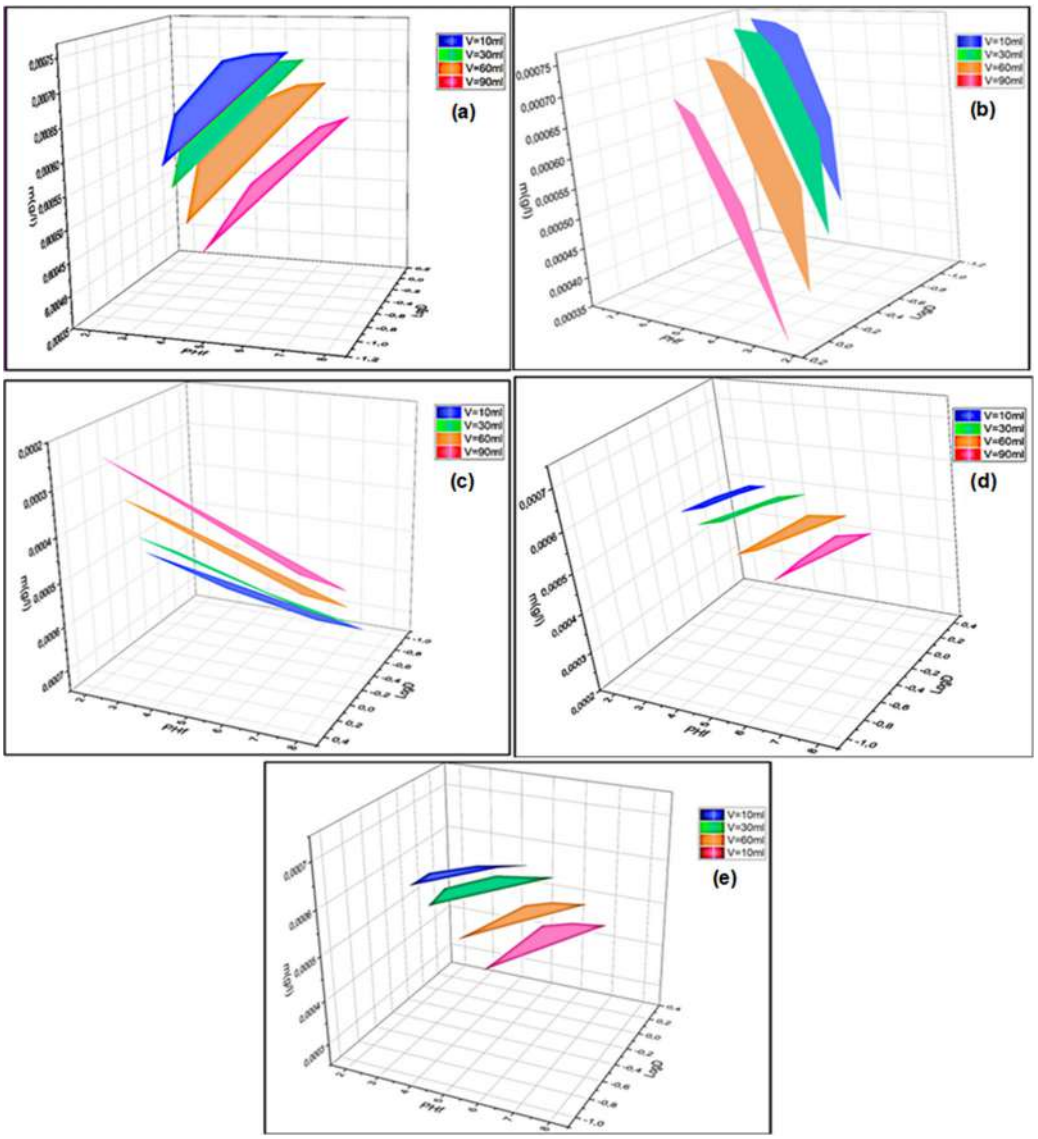

Fig 9. Surface response plots for the chrome, Cr(VI) surface complexes with eucalyptus bark surface response plots

■ CONCLUSION

Thorough research was done on the adsorption of hexavalent chromium Cr(VI) on eucalyptus barks. The sorption mechanism was evaluated as a function of solution pH for different adsorbent dosages, surface coverage, and the amount of adsorbent. The chromium retention is evaluated by the distribution coefficient D. It is obviously seen from obtained variations at a given suspension mass (m) that Cr(VI) adsorption is strongly volume-dependent and increases with an increase in n. The slopes $\frac{\delta \log D}{\delta n}$ are varying between 5.8×10^{-8} and 9.3×10^{-8}. At a lower n value, adsorption efficiency increases slightly with sorbent amount. As discussed before, the biosorption of the oxyanion is dependent on the surface coverage. The study of log D = f(pH) experimental data, the Cr(VI) retention is maximal at low pH values. As a consequence, this retention is attributed to $HCrO_4^-$ species which are predominant between pH 1 and 6.5. Therefore, eucalyptus bark exhibited high adsorption capacity for Cr(VI).

■ ACKNOWLEDGMENTS

The authors would like to thank Mohammed V University in Rabat for executing this research work in the Applied Chemistry Laboratory Materials. It has

provided us with all the necessary chemical products and measurement equipment.

■ REFERENCES

[1] Oliveira, H., 2012, Chromium as an environmental pollutant: Insights on induced plant toxicity, *J. Bot.*, 2012, 375843.

[2] Economou-Eliopoulos, M., Antivachi, D., Vasilatos, Ch., and Megremi, I., 2012, Evaluation of the Cr(VI) and other toxic element contamination and their potential sources: The case of the Thiva basin (Greece), *Geosci. Front.*, 3 (4), 523–539.

[3] Filote, C., Roşca, M., Hlihor, R.M., Cozma, P., Simion, I.M., Apostol, M., and Gavrilescu, M., 2021, Sustainable application of biosorption and bioaccumulation of persistent pollutants in wastewater treatment: Current practice, *Processes*, 9 (10), 1696.

[4] Koutahzadeh, N., Daneshvar, E., Kousha, M., Sohrabi, M.S., and Bhatnagar, A., 2013, Biosorption of hexavalent chromium from aqueous solution by six brown macroalgae, *Desalin. Water Treat.*, 51 (31-33), 6021–6030.

[5] Gezahegn, A.M., Feyessa, F.F., Tekeste, E.A., and Beyene, E.M., 2021, Chromium laden soil, water, and vegetables nearby tanning industries: Speciation and spatial distribution, *J. Chem.*, 2021, 5531349.

[6] Tchounwou, P.B., Yedjou, C.G., Patlolla, A.K., and Sutton, D.J., 2012, "Heavy Metals Toxicity and the Environment" in *Molecular, Clinical and Environmental Toxicology: Volume 3: Environmental Toxicology*, Eds. Luch, A., Springer Basel, Switzerland, 133–164.

[7] Mondal, N.K., and Chakraborty, S., 2020, Adsorption of Cr(VI) from aqueous solution on graphene oxide (GO) prepared from graphite: Equilibrium, kinetic and thermodynamic studies, *Appl. Water Sci.*, 10 (2), 61.

[8] Kokab, T., Ashraf, H.S., Shakoor, M.B., Jilani, A., Ahmad, S.R., Majid, M., Ali, S., Farid, N., Alghamdi, R.A., Al-Quwaie, D.A.H., and Hakeem, K.R. 2021, Effective removal of Cr(VI) from wastewater using biochar derived from walnut shell, *Int. J. Environ. Res. Public Health*, 18 (18), 9670.

[9] Tefera, Y., and Prasad, D., 2014, Biosorption of hexavalent chromium using bark of *Cassia spectabilis*, *Sci. Technol. Art Res. J.*, 3 (2), 83–87.

[10] Khan, M.M.R., Mitra, T., and Sahoo, D., 2020, Metal oxide QD based ultrasensitive microsphere fluorescent sensor for copper, chromium and iron ions in water, *RSC Adv.*, 10 (16), 9512–9524.

[11] European Commission, 2002, Heavy Metals in Waste, *Final Report*, DG ENV. E3, Project ENV.E3/ETU/2000/0058.

[12] WHO, 2003, *Chromium in drinking-water. Background document for development of WHO Guidelines for drinking-water quality*, World Health Organization, Geneva.

[13] Prajapati, A.K., Verma, P., Singh, S., and Mondal, M.K., 2022, Adsorption-desorption surface bindings, kinetics, and mass transfer behavior of thermally and chemically treated great millet husk towards Cr(VI) removal from synthetic wastewater, *Adsorpt. Sci. Technol.*, 2022, 3956977.

[14] Yu, Y., Ali, J., Yang, Y., Kuang, P., Zhang, W., Lu, Y., and Li, Y., 2022, Synchronous Cr(VI) remediation and energy production using microbial fuel cell from a subsurface environment: A review, *Energies*, 15 (6), 1989.

[15] Sugashini, S., and Sheriffa Begum, K.M.M., 2013, Column adsorption studies for the removal of Cr(VI) ions by ethylamine modified chitosan carbonized rice husk composite beads with modelling and optimization, *J. Chem.*, 2013, 460971.

[16] Qi, H., Niu, X., Wu, H., Liu, X., and Chen, Y., 2021, Adsorption of chromium(VI) by Cu(I)-MOF in water: Optimization, kinetics, and thermodynamics, *J. Chem.*, 2021, 4413095.

[17] Giri, D.D., Shah, M., Srivastava, N., Hashem, A., Abd_Allah, E.E., and Pal, D.B., 2021, Sustainable chromium recovery from wastewater using mango and jackfruit seed kernel bio-adsorbents, *Front. Microbiol.*, 12, 717848.

[18] Qaiser, S., Saleemi, A.R., and Umar, M., 2009, Biosorption of lead(II) and chromium(VI) on groundnut hull: Equilibrium, kinetics and

thermodynamics study, *Electron. J. Biotechnol.*, 12 (4), 3–4.

[19] Quintelas, C., Fernandes, B., Castro, J., Figueiredo, H., and Tavares, T., 2008, Biosorption of Cr(VI) by three different bacterial species supported on granular activated carbon–A comparative study, *J. Hazard. Mater.*, 153 (1-2), 799–809.

[20] Salman, M., Rehman, R., Farooq, U., Tahir, A., and Mitu, L., 2020, Biosorptive removal of cadmium(II) and copper(II) using microwave-assisted thiourea-modified *Sorghum bicolor* agrowaste, *J. Chem.*, 2020, 8269643.

[21] Samrot, A.V., Sahithya, C.S., Selvarani A.J., Pachiyappan, S., and Kumar, S.S., 2019, Surface-engineered super-paramagnetic iron oxide nanoparticles for chromium removal, *Int. J. Nanomed.*, 14, 8105–8119.

[22] Kucuker, M.A., Wieczorek, N., Kuchta, K., and Copty, N.K., 2017, Biosorption of neodymium on *Chlorella vulgaris* in aqueous solution obtained from hard disk drive magnets, *PLoS One*, 12 (4), e0175255.

[23] Javanbakht, V., Alavi, S.A., and Zilouei, H., 2014, Mechanisms of heavy metal removal using microorganisms as biosorbent, *Water Sci. Technol.*, 69 (9), 1775–1787.

[24] Loukidou, M.X., Karapantsios, T.D., Zouboulis, A.I., and Matis, K.A., 2004, Diffusion kinetic study of chromium(VI) biosorption by *Aeromonas caviae*, *Ind. Eng. Chem. Res.*, 43 (7), 1748–1755.

[25] Su, P., Granholm, K., Pranovich, A., Harju, L., Holmbom, B., and Ivaska, A., 2013, Sorption of metal ions from aqueous solution to spruce bark, *Wood Sci. Technol.*, 47 (5), 1083–1097.

[26] Şen, A., Pereira, H., Olivella, M.A., and Villaescusa, I., 2015, Heavy metals removal in aqueous environments using bark as a biosorbent, *Int. J. Environ. Sci. Technol.*, 12 (1), 391–404.

[27] Yao, S., Gao, C., Nie, S., Niu, F., Wang, S., and Qin, C., 2017, Effects of formaldehyde modification of eucalyptus bark on Cr(VI) adsorption, *BioResources*, 12 (4), 8986–9000.

[28] Pertile, E., Dvorský, T., Václavík, V., and Heviánková, S., 2021, Use of different types of biosorbents to remove Cr(VI) from aqueous solution, *Life*, 11 (3), 240.

[29] Labied, R., Benturki, O., Hamitouche, A.E., and Donnot, A., 2018, Adsorption of hexavalent chromium by activated carbon obtained from a waste lignocellulosic material (*Ziziphus jujuba* cores): Kinetic, equilibrium, and thermodynamic study, *Adsorpt. Sci. Technol.*, 36 (3-4), 1066–1099.

[30] Overah, L.C., 2011, Biosorption of Cr (III) from aqueous solution by the leaf biomass of *Calotropis procera* - 'bom bom' and cited references, *J. Appl. Sci. Environ. Manage.*, 15 (1), 87–95.

[31] Imandi, S.B., Chinthala, R., Saka, S., Vechalapu, R.R., and Nalla, K.K., 2014, Optimization of chromium biosorption in aqueous solution by marine yeast biomass of *Yarrowia lipolytica* using Doehler experimental design, *Afr. J. Biotechnol.*, 13 (12), 1413–1422.

[32] Samuel, M.S., Abigail, M.E.A., and Ramalingam, C., 2014, Biosorption of Cr(VI) by *Ceratocystis paradoxa* MSR2 using isotherm modelling, kinetic study and optimization of batch parameters using response surface methodology, *PLoS One*, 10 (3), e0118999.

[33] Netzahuatl-Muñoz, A.R., Cristiani-Urbina, M.C., and Cristiani-Urbina, E., 2015, Chromium biosorption from Cr(VI) aqueous solutions by *Cupressus lusitanica* bark: Kinetics, equilibrium and thermodynamic studies, *PLoS One*, 10 (9), 0137086.

[34] Shukla, D., Vankar, P.S., and Srivastava, S.K., 2012, Bioremediation of hexavalent chromium by a cyanobacterial mat, *Appl. Water Sci.*, 2 (4), 245–251.

[35] Malwade, K., Lataye, D., Mhaisalkar, V., Kurwadkar, S., and Ramirez, D., 2016, Adsorption of hexavalent chromium onto activated carbon derived from *Leucaena leucocephala* waste sawdust: Kinetics, equilibrium and thermodynamics, *Int. J. Environ. Sci. Technol.*, 13 (9), 2107–2116.

[36] Marandi, R., 2011, Biosorption of hexavalent chromium from aqueous solution by dead fungal biomass of *Phanerochaete crysosporium*: Batch and fixed bed studies, *Can. J. Chem. Eng. Technol.*, 2 (2), 8–22.

[37] Vasudevan, M., Ajithkumar, P.S., Singh, R.P., and Natarajan, N., 2016, Mass transfer kinetics using two-site interface model for removal of Cr(VI) from aqueous solution with cassava peel and rubber tree bark as adsorbents, *Environ. Eng. Res.*, 21 (2), 152–163.

[38] Rzig, B., Guesmi, F., Sillanpää, M., and Hamrouni, B., 2021, Modelling and optimization of hexavalent chromium removal from aqueous solution by adsorption on low-cost agricultural waste biomass using response surface methodological approach, *Water Sci. Technol.*, 84 (3), 552–575.

[39] Maarouf, F.Z., Saoiabi, S., Azzaoui, K., Chrika, C., Khalil, H., Elkaouni, S., Lhmir, S., Boubker, O., Hammouti, B., and Jodeh, S., 2021, Statistical optimization of amorphous iron phosphate: Inorganic sol-gel synthesis-sodium potential insertion, *BMC Chem.*, 15 (1), 48.

[40] Hmamou, M., Maarouf, F.Z., Ammary, B., and Bellaouchou, A., 2021, Surface complexation of chromium(VI) on iron(III) hydroxide: Mechanisms and stability constants of surfaces complexes, *Indones. J. Chem.*, 21 (3), 679–689.

[41] John, Y., David, V.E., and Mmereki, D., 2018, A Comparative Study on Removal of Hazardous Anions from Water by Adsorption: A Review, *Int. J. Chem. Eng.*, 2018, 3975948.

[42] Bjijou, W., El Yahyaoui, A., Bouhlassa, S., and El Belghiti, M.A., 2016, Determination of zero charge point of a biosorbent which origin is vegetable, *Pharma Chem.*, 8 (13), 258–261.

[43] Silva, J.P., de Senna, L.F., do Lago, D.C.B., da Silva, P.F., Dias, E.G., de Figueiredo, M.A.G., and Chiaro, S.S.X., 2007, Characterization of commercial ceramic adsorbents and its application on naphthenic acids removal of petroleum distillates, *Mater. Res.*, 10 (2), 219–225.

[44] Maheshwari, U., and Gupta, S., 2015, Removal of Cr(VI) from wastewater using activated neem bark in a fixed-bed column: Interference of other ions and kinetic modelling studies, *Desalin. Water Treat.*, 57 (18), 8514–8525.

[45] Uzoamaka, I.E.M., Chibuike, O., and Onyewuchi, V., 2019, Tri-carboxylic acid red onion (*Allium cepa*) skin extract resin for the removal of chromium (VI) ion from aqueous solution, *Mod. Chem. Appl.*, 7 (1), 266.

[46] Fabre, E., Vale, C., Pereira, E., and Silva, C.M., 2019, Experimental measurement and modeling of Hg(II) removal from aqueous solutions using *Eucalyptus globulus* bark: Effect of pH, salinity and biosorbent dosage, *Int. J. Mol. Sci.*, 20 (23), 5973.

[47] Yang, K., Xing, J., Xu, P., Chang, J., Zhang, Q., and Usman, K.M., 2020, Activated carbon microsphere from sodium lignosulfonate for Cr(VI) adsorption evaluation in wastewater treatment, *Polymers*, 12 (1), 236.

[48] Elyahyaoui, A., Ellouzi, K., Al Zabadi, H., Razzouki, B., Bouhlassa, S., Azzaoui, K., Mejdoubi, E.M., Hamed, O., Jodeh, S., and Lamhamdi, A., 2017, Adsorption of chromium (VI) on calcium phosphate: Mechanisms and stability constants of surface complexes, *Appl. Sci.*, 7 (3), 222.

[49] Kim, J.W., 2005, The Modeling of Arsenic Removal from Contaminated Water Using Coagulation and Sorption, *Dissertation*, Texas A&M University, US.

[50] Cherdchoo, W., Nithettham, S., and Charoenpanich, J., 2019, Removal of Cr(VI) from synthetic wastewater by adsorption onto coffee ground and mixed waste tea, *Chemosphere*, 221, 758–767.

[51] AL-Othman, Z.A., Ali, R., and Naushad, M., 2012, Hexavalent chromium removal from aqueous medium by activated carbon prepared from peanut shell: Adsorption kinetics, equilibrium and thermodynamic studies, *Chem. Eng. J.*, 184, 238–247.

[52] Dehghani, M.H., Sanaei, D., Ali, I., and Bhatnagar, A., 2016, Removal of chromium(VI) from aqueous solution using treated waste newspaper as a low-cost adsorbent: Kinetic modeling and isotherm studies, *J. Mol. Liq.*, 215, 671–679.

[53] Ghasemi, S., Gholami, R.M., and Yazdanian, M., 2017, Biosorption of heavy metal from cadmium rich aqueous solutions by tea waste as a low cost bio-adsorbent, *Jundishapur J. Health Sci.*, 9 (1), e37301.

[54] Gupta, V.K., Rastogi, A., and Nayak, A., 2010, Adsorption studies on the removal of hexavalent chromium from aqueous solution using a low cost

fertilizer industry waste material, *J. Colloid Interface Sci.*, 342 (1), 135–141.

[55] Sugashini, S., and Sheriffa Begum, K.M.M., 2015, Preparation of activated carbon from carbonized rice husk by ozone activation for Cr(VI) removal, *New Carbon Mater.*, 30 (3), 252–261.

[56] Verma, A., Chakraborty, S., and Basu, J.K., 2006, Adsorption study of hexavalent chromium using tamarind hull-based adsorbents, *Sep. Purif. Technol.*, 50 (3), 336–341.

Synthesis, Antimicrobial, Antioxidant, Toxicity and Anticancer Activity of a New Azetidinone, Thiazolidinone and Selenazolidinone Derivatives Based on Sulfonamide

Zainab Kadhim Al-Khazragie, Bushra Kamel Al-Salami, and Adnan Jassim Mohammed Al-Fartosy*

Department of Chemistry, College of Science, University of Basrah, Basrah, Iraq, PO BOX 781, Basrah, Iraq

** **Corresponding author:***

tel: +964-7704051812
email: zezit1993aa@yahoo.com

Received: January 21, 2022
Accepted: April 1, 2022

DOI: 10.22146/ijc.72454

Abstract: *A new series of azetidinone (Z_2a-Z_2e, Z_2g), thiazolidinone and selenazolidinone derivatives (Z_2B, Z_2E, Z_2B', Z_2E') based on sulfonamide have been synthesized and characterized by different instrumental techniques, such as elemental analyses, FTIR, multinuclear NMR (^{1}H, ^{13}C) and mass spectrometry. The tested compound containing selenium (Z_2E') was less toxic than its analogs containing sulfur (Z_2E) based on the LD_{50} value determined by Dixon's up and down method. All compounds showed antibacterial properties, however, Z_2E' was more active against Gram-negative bacteria:* Escherichia coli *and* Pseudomonas aeruginosa *than Gram-positive ones:* Streptococcus aureus *and* Bacillus*, with the lowest MIC value of 5 mg/mL. All compounds showed good antioxidant activity at a lower rate than the standard compound BHT (82%). More precisely, Z_2b was the main compound that possess strong activity as an antioxidant (73%). MTT viability assay showed that all tested compounds had cytotoxic effects on MCF-7 cells after 72 h of treatment. Our results revealed that Z_2E' and Z_2E compounds possessed strong activity (IC_{50} = 24.8 and 90.9 µg/mL, respectively) against MCF-7 cells at a higher rate than the standard compound 5-FU (IC_{50} = 97.47 µg/mL). Our results indicated that Z_2E' had a promising bioactive scaffold of great medicinal interest due to their numerous pharmacological and biological activities.*

Keywords: *2-azetidinone; 4-thiazolidinone; 4-selenazolidinone; sulfonamide; biochemical activities*

■ INTRODUCTION

Sulfonamides are the first effective chemotherapeutic agents used for bacterial disease in humans. They are widely used for prophylaxis and treatment of bacterial infections although they are bacteriostatic rather than bactericidal. Their value lies in the ability to slow down or prevent growth in wounds or infected organs without appreciable toxicity to normal tissues [1]. A large number of sulfonamide derivatives have been synthesized, which made it possible to establish a correlation between specific structural characteristics and the antimicrobial activity of newly synthesized molecules. A free aromatic NH_2 group in the para position, relative to the sulfonamide group, is essential for the activity of sulfonamides [2]. The presence of the additional substituent in the ortho and meta position of the benzene ring reduces the sulfonamide activity. On the other hand, the *N*1-monosubstituted derivatives of sulfanilamide produce active compounds. The activity degree of such compounds increased by introducing heteroaromatic substituents. The introduction of various substituents resulted in the products with different physicochemical, pharmacokinetic (a degree of protein binding, metabolism, excretion), and pharmacodynamic properties [3]. Recent studies demonstrated that sulfonamides are active to prevent cancerous cells [4]. 2-Azetidinones (β-lactams) are saturated four-membered ring heterocyclic compounds containing three carbon atoms, a nitrogen atom, and a carbonyl group [5]. The name "β-Lactam" is given to cyclic amides because the nitrogen atom is associated with the β-carbon atom relative to the carbonyl group.

2-Azetidinones, a structural unit found in the most widely used antibiotics [6], have occupied a basic

position in medicinal chemistry for almost a century now. The microbe's basic position in medicinal chemistry for almost a century now. With the microbes responding to the traditional antibiotics through β-lactamases, the need for novel antibiotics prevails, making the synthesis of newer β-lactams ever more important. In addition to their use as antibiotics, 2-azetidinones are increasingly being used as synthons for other biologically important molecules [7-10]. 2-Azetidinones have been found to act as cholesterol acyl transferase inhibitors, thrombin inhibitors, human cytomegalovirus protease inhibitors, matrix metalloprotease inhibitors, cysteine protease, and apoptosis inductors [6]. The biological activity is usually associated with the nature of the groups linked to *N*-1, *C*-3, and *C*-4 of the 2-azetidinone molecules [11]. 2-Azetidinone derivatives containing β-lactam nucleus have a wide range of pharmaceutical activity and have become an integral part of the chemotherapeutic arsenal available to today's medical practitioners [12].

Thiazolidinones (or selenazolidinones) are thiazolidine (or selenazolidine) derivatives and have an atom of sulfur (or selenium) at position 1, an atom of nitrogen at position 3 and a carbonyl group at position 4 [13-14]. However, thiazolidinone derivatives belong to the most frequently studied moieties and its presence in penicillin was the first recognition of its occurrence in nature [15]. Thiazo- and selenazolidine-4-ones are an important class of compounds in organic and medicinal chemistry [16-17]. The 4-thiazolidinone or 4-selenazolidinone ring system is a core structure in various synthetic pharmaceutical agents, displaying a broad spectrum of biological activities such as antitubercular, antibacterial, anti-inflammatory, antioxidant agents, antiviral agents, especially as anti-HIV agents, and their use as anticancer drugs [13,18-20]. They received considerable attention during the last two decades as they are gifted with a variety of activities and have a wide range of therapeutic properties [16-17].

In the present work, we synthesized a new series of 2-azetidinone, 4-thiazolidinone and 4-selenazolidinone derivatives through cycloaddition reaction of imines with ketene, thioglycolic acid and 2-selenoglycolic acid, respectively. The compounds were studied *in vivo* acute toxicity, antioxidant, antibacterial, and anticancer activity.

■ EXPERIMENTAL SECTION

Materials

All the chemicals and solvents used were of analytical grade supplied from BDH, Fluka, USP, Merck, MOLBASE and Aldrich. 2-Chloroquinoline-3-carbaldehyde, *p*-toluenesulphonic acid (PTSA), 2-amino-4-chlorobenzenesulfonamide, sulfamerazine, sulfisoxazole, sulfamethazine, sulfathiazole, sulfanilamide, chloroacetylchloride, thioglycolic acid, and zinc chloride ($ZnCl_2$) as well as butylated hydroxyl toluene (BHT) were obtained from Sigma-Aldrich. 2-Seleno-glycolic acid and β-carotene were supplied from MOLBASE and USP respectively. Tween-20 (Polyoxyethylene (20) sorbitan monolaurate), linoleic acid, 1,4-dioxane and dimethylformamide were obtained from Fluka. Sodium azide, triethylamine, Na_2SO_4 and $NaHCO_3$ from Merck. Sulfuric acid, ethanol, acetone, methanol, and chloroform were obtained from BDH. Thin-layer chromatography (TLC) was carried out by using an aluminium sheet coated with silica gel $60F_{254}$ (Merck), iodine and ultraviolet (UV) light was used for visualized TLC plates.

Instrumentation

The FTIR spectra as KBr discs were recorded in the range 4000–400 cm^{-1} using a Shimadzu FT-IR model 8400s instrument. The experimental values of ^{1}H and ^{13}C-NMR spectra for the studied compounds were obtained in a Brucker spectrophotometer (400 and 75 MHz, respectively) and using DMSO-d_6 as a solvent and TMS as an internal standard (Central Laboratory, University of Tehran, Iran). The mass spectra were measured by the EI technique at 70 eV using an Agilent Technologies 5975C spectrometer. Elemental analysis (C,H,N,S) was calculated using CHNS-932 LECO apparatus. Melting points were determined with a Bauchi 510 melting point apparatus and are uncorrected.

Synthesis

The compound tetrazolo[1,5-a]quinoline-4-carbaldehyde (**2**) was prepared and characterized as

previously described in the literature [21]. This compound gave satisfactory elemental analysis and spectroscopic data, and they are not reported. The synthetic procedure for the preparation of compound **(2)** is presented in Scheme 1.

Synthesis of sulfonamide imines (2a-2e, 2g)

The following general method was used to prepare compounds **2a**-**2e** and **2g** according to the literature method [21]. An equimolar quantity of sulfonamide derivatives (2-amino-4-chlorobenzenesulfonamide (5 mmol, 1.03 g), sulfamerazine (5 mmol, 1.32 g), sulfisoxazole (5 mmol, 1.34 g), sulfamethazine (5 mmol, 1.4 g), sulfathiazole (5 mmol, 1.3 g) sulfanilamide (5 mmol, 0.861 g) and tetrazolo[1,5-a]quinoline-4-carbaldehyde (**2**) (5 mmol, 0.99 g) were dissolved in a 25 mL of ethanol, then a catalytic amount of concentrated H_2SO_4 (2 drops) was added and the reaction mixture refluxed for about 6–10 h, the progress of the reaction was

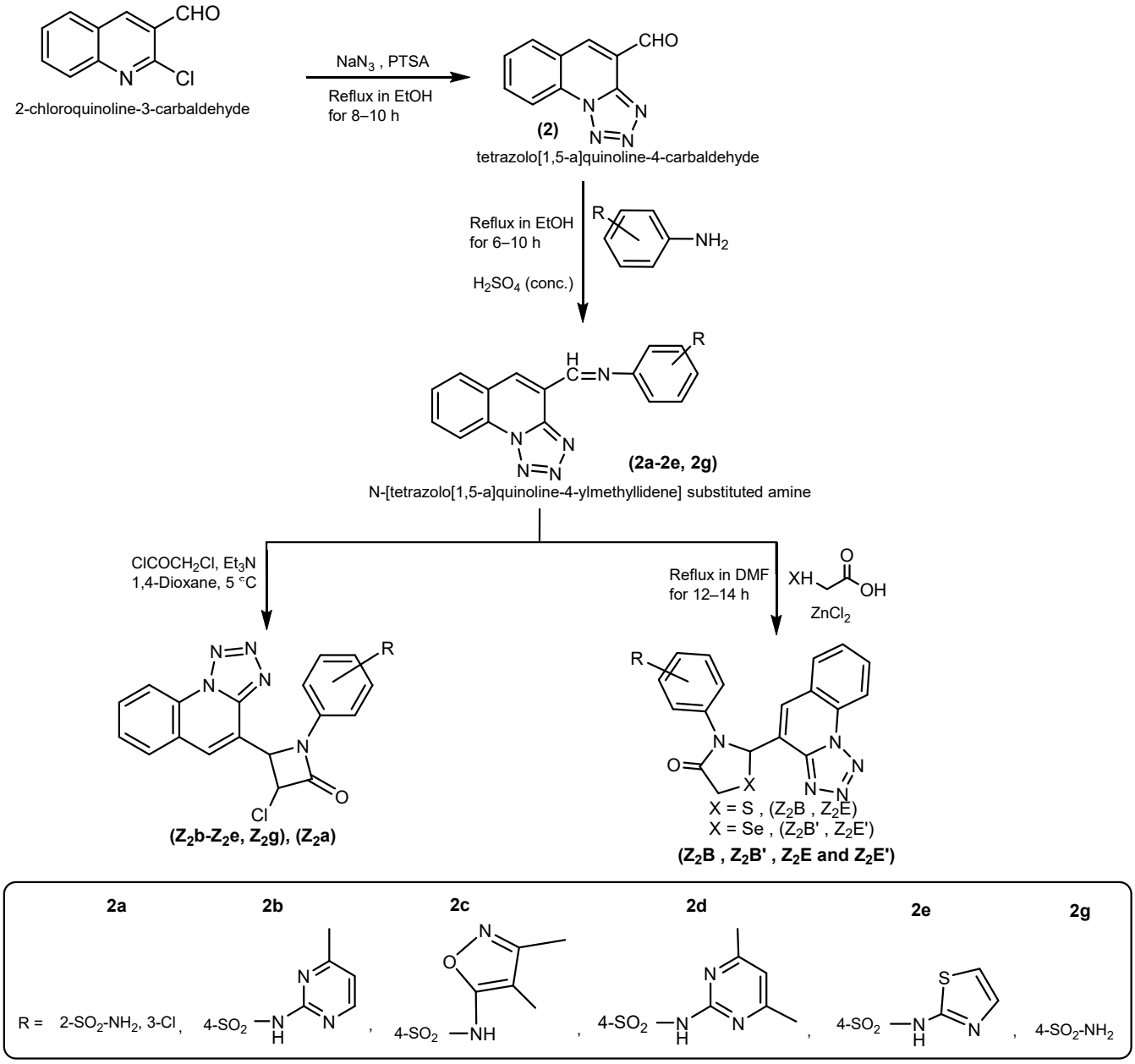

Scheme 1. Synthesis of 2-azetidinones, 4-thiazolidinones and 4-selenazolidinones

monitored by TLC using ethyl acetate/*n*-hexane (v/v 2:8) as eluent and UV light as appearance, the resulted compounds were obtained by pouring the reaction mixture onto crushed ice. The precipitated solids were filtered off from the reaction mixture and washed with cold water, dried, followed by recrystallized in ethanol to get the target compounds. The synthetic procedures for the preparation of compounds (**2a**-**2e** and **2g**) are presented in Scheme 1.

4-Chloro-2-((tetrazolo[1,5-a]quinolin-4-ylmethylene) amino)benzenesulfonamide (2a). Pale yellow powder; yield: 63%; Rf: 0.90; m.p: 218–222 °C; Elemental analysis for $C_{16}H_{11}ClN_6O_2S$ (386.82 g/mol); Calcd: C, 49.68; H, 2.87; N, 21.73; S, 8.29. Found: C, 49.71; H, 2.89; N, 21.69; S, 8.24. IR (KBr) cm^{-1}: 3344 $\nu_{str.}(NH_2$, asymmetrical), 3178 $\nu_{str.}(NH_2$, symmetrical), 1654 ν(C=N, tetrazole ring), 1600 ν(CH=N), 1500–1473 ν(C=C), 1323 $\nu_{str.}(SO_2$, asymmetrical), 1168 $\nu_{str.}(SO_2$, symmetrical), 1249 ν(N-N=N, tetrazole ring), 952 ν(S-N), 860 ν(C-Cl), 632 $\nu_{str.}$(C-S, sulfonamide); ^{1}H-NMR (400 MHz, DMSO-d_6) (δ/ppm): 8.68 (d, 1H, *J* = 12 Hz, Ar-H), 8.58 (s, 1H, CH=N), 8.35 (s, 1H, pyridine-H), 8.08 (t, 1H, J_1 = 8, J_2 = 12 Hz, Ar-H), 8.01 (s, 1H, Ar-H), 7.88 (t, 1H, $J_1 = J_2$ = 12 Hz, Ar-H), 7.66 (d, 1H, *J* = 12 Hz, Ar-H), 7.07 (s, 2H, NH_2), 6.89 (d, 1H, *J* = 16 Hz, Ar-H), 6.60 (d, 1H, *J* = 16 Hz, Ar-H).

***N*-(4-Methylpyrimidin-2-yl)-4-((tetrazolo[1,5-a]quino line-4-ylmethylene)amino)benzenesulfonamide (2b).** Yellow powder; yield: 91%; Rf: 0.86; m.p: 232–234 °C; Elemental analysis for $C_{21}H_{16}N_8O_2S$ (444.47 g/mol); Calcd: C, 56.75; H, 3.63; N, 25.21; S, 7.21. Found: C, 56.72; H, 3.59; N, 25.25; S, 7.18. IR (KBr) cm^{-1}: 3225 ν(N-H), 1631 ν(C=N, tetrazole, pyrimidine ring), 1589 ν(CH=N), 1465–1496 ν(C=C), 1323 $\nu_{str.}(SO_2$, asymmetrical), 1153 $\nu_{str.}(SO_2$, symmetrical), 1278 ν(N-N=N, tetrazole ring), 979 ν(S-N), 678 $\nu_{str.}$(C-S, sulfonamide); ^{1}H-NMR (400 MHz, DMSO-d_6) (δ/ppm): 12.06 (s, 1H, NH), 8.60 (s, 1H, CH=N), 8.54 (t, 1H, $J_1 = J_2$ = 4 Hz, Ar-H), 8.40 (d, 1H, *J* = 4 Hz, pyrimidine-H), 8.30 (d, 1H, *J* = 12 Hz, Ar-H), 8.08 (s, 1H, pyridine-H), 7.97 (t, 1H, J_1 = 8, J_2 = 12 Hz, Ar-H), 7.83 (d, 2H, *J* = 12 Hz, Ar-H), 7.23 (d, 2H, *J* = 4 Hz, Ar-H), 7.08 (t, 1H, $J_1 = J_2$ = 8 Hz, Ar-H), 6.67 (d, 1H, *J* = 20 Hz, pyrimidine-H), 2.10 (s, 3H, CH_3).

***N*-(3,4-Dimethylisoxazol-5-yl)-4-((tetrazolo[1,5-a]qui nolin-4-ylmethylene)amino)benzenesulfonamide (2c).** Yellow crystals; yield: 60%; Rf: 0.91; m.p: 190–193 °C; Elemental analysis for $C_{21}H_{17}N_7O_3S$ (447.47 g/mol); Calcd: C, 56.37; H, 3.83; N, 21.91; S, 7.17. Found: C, 56.41; H, 3.86; N, 21.88; S, 7.19. IR (KBr) cm^{-1}: 3383 ν(N-H), 2924 ν(CH, asymmetrical, aliph.), 2854 ν(CH, symmetrical, aliph.), 1651 ν(C=N, tetrazole, isoxazole ring), 1597 ν(CH=N), 1462–1531 ν(C=C), 1338 $\nu_{str.}(SO_2$, asymmetrical), 1161 $\nu_{str.}(SO_2$, symmetrical), 1253 ν(N-N=N, tetrazole ring), 875 ν(S-N), 671 $\nu_{str.}$(C-S, sulfonamide); ^{1}H-NMR (400 MHz, DMSO-d_6) (δ/ppm): 12.25 (s, 1H, NH), 9.02 (s, 1H, CH=N), 8.86 (s, 1H, pyridine-H), 8.69 (d, 1H, *J* = 8 Hz, Ar-H), 8.47 (d, 1H, *J* = 8 Hz, Ar-H), 8.15 (t, 1H, J_1 = 8, J_2 = 12 Hz, Ar-H), 7.92 (t, 1H, J_1 = 12, J_2 = 8 Hz, Ar-H), 7.60 (d, 2H, *J* = 8 Hz, Ar-H), 7.45 (d, 2H, *J* = 12 Hz, Ar-H), 2.10 (s, 3H, CH_3), 1.58 (s, 3H, CH_3).

***N*-(4,6-Dimethylpyrimidin-2-yl)-4-((tetrazolo[1,5-a] 4uinoline-4-ylmethylene)amino)benzenesulfonami de (2d).** Pale orange powder; yield: 59%; Rf: 0.67; m.p: 276–278 °C; Elemental analysis for $C_{22}H_{18}N_8O_2S$ (458.50 g/mol); Calcd: C, 57.63; H, 3.96; N, 24.44; S, 6.99. Found: C, 57.59; H, 3.98; N, 24.41; S, 7.03. IR (KBr) cm^{-1}: 3352 ν(N-H), 1662, 1643 ν(C=N, tetrazole, pyrimidine ring), 1593 ν(CH=N), 1469–1500 ν(C=C), 1338 $\nu_{str.}(SO_2$, asymmetrical), 1149 $\nu_{str.}(SO_2$, symmetrical), 1253 ν(N-N=N, tetrazole ring), 914 ν(S-N), 678 $\nu_{str.}$(C-S, sulfonamide); ^{1}H-NMR (400 MHz, DMSO-d_6) (δ/ppm): 10.68 (s, 1H, NH), 9.01 (s, 1H, CH=N), 7.92 (d, 1H, *J* = 10 Hz, Ar-H), 7.68 (s, 1H, pyridine-H),7.44 (t, 1H, $J_1 = J_2$ = 5 Hz, Ar-H), 7.25 (dd, 2H, *J* = 20 Hz, Ar-H), 7.18 (t, 1H, $J_1 = J_2$ = 5 Hz, Ar-H), 6.86 (d, 1H, *J* = 5 Hz, Ar-H), 6.75 (dd, 2H, *J* = 10 Hz, Ar-H), 6.60 (s, 1H, pyrimidine-H), 3.03 (s, 6H, $2CH_3$).

4-((Tetrazolo[1,5-a]quinolin-4-ylmethylene)amino)-*N*-(thiazol-2-yl)benzenesulfonamide (2e). Dark yellow crystals; yield: 90%; Rf: 0.91; m.p: 204–205 °C; Elemental analysis for $C_{19}H_{13}N_7O_2S_2$ (435.48 g/mol); Calcd: C, 52.40; H, 3.01; N, 22.51; S, 14.73. Found: C, 52.38; H, 2.98; N, 22.54; S, 14.71. IR (KBr) cm^{-1}: 3379 ν(N-H), 2920 ν(CH, asymmetrical, aliph.), 2850 ν(CH, symmetrical, aliph.), 1651 ν(C=N, tetrazole, thiazole

ring), 1608 ν(CH=N), 1419–1462 ν(C=C), 1330 $\nu_{str.}(SO_2$, asymmetrical), 1168 $\nu_{str.}(SO_2$, symmetrical), 1284 ν(N-N=N, tetrazole ring), 925 ν(S-N), 636 $\nu_{str.}$(C-S, sulfonamide); ^{1}H-NMR (400 MHz, DMSO-d_6) (δ/ppm): 12.86 (s, 1H, NH), 9.07 (s, 1H, CH=N), 7.97 (d, 1H, *J* = 12 Hz, Ar-H), 7.83 (d, 1H, *J* = 12 Hz, Ar-H), 7.70 (d, 2H, *J* = 12 Hz, Ar-H), 7.50 (t, 1H, J_1 = 4, J_2 = 8 Hz, Ar-H), 7.31 (s, 1H, pyridine-H), 7.23 (d, 2H, *J* = 4 Hz, Ar-H), 7.08 (d, 1H, *J* = 12 Hz, thiazole-H), 6.90 (d, 1H, *J* = 8 Hz, thiazole-H), 6.79 (t, 1H, J_1 = 8, J_2 = 12 Hz, Ar-H).

4-((Tetrazolo[1,5-a]quinoline-4-ylmethylene)amino) benzenesulfonamide (2g). Maroon crystals; yield: 93%; Rf: 0.89; m.p: 192–194 °C; Elemental analysis for $C_{16}H_{12}N_6O_2S$ (352.37 g/mol); Calcd: C, 54.54; H, 3.43; N, 23.85; S, 9.10. Found: C, 54.57; H, 3.42; N, 23.89; S, 9.07. IR (KBr) cm^{-1}: 3448 $\nu_{str.}(NH_2$, asymmetrical), 3417 $\nu_{str.}(NH_2$, symmetrical), 2924 ν(CH, asymmetrical, aliph.), 2854 ν(CH, symmetrical, aliph.), 1651 ν(C=N, tetrazole ring), 1608 ν(CH=N), 1550–1446 ν(C=C), 1334 $\nu_{str.}(SO_2$, asymmetrical), 1153 $\nu_{str.}(SO_2$, symmetrical), 1242 ν(N-N=N, tetrazole ring), 918 ν(S-N), 690 $\nu_{str.}$(C-S, sulfonamide); ^{1}H-NMR (400 MHz, DMSO-d_6) (δ/ppm): 8.89 (s, 1H, CH=N), 8.31 (d, 1H, *J* = 10 Hz, Ar-H), 8.03 (s, 1H, pyridine-H), 7.89 (d, 1H, *J* = 5 Hz, Ar-H), 7.71 (dd, 2H, *J* = 10 Hz, Ar-H), 7.47 (t, 1H, J_1 = 10, J_2 = 15 Hz, Ar-H), 7.36 (t, 1H, $J_1 = J_2$ = 10 Hz, Ar-H), 7.10 (dd, 2H, *J* = 10 Hz, Ar-H), 6.97 (s, 2H, NH_2).

Synthesis of 2-azetidinone derivatives (Z_2a-Z_2e, Z_2g)

A mixture of imine **2a** (2 mmol, 0.77 g), **2b** (2 mmol, 0.89 g), **2c** (2 mmol, 0.895 g), **2d** (2 mmol, 0.92 g), **2e** (2 mmol, 0.87 g), **2g** (2 mmol, 0.7g), respectively and triethyl amine (4 mmol, 0.40 g) were dissolved in dry 1,4-dioxane (25 mL), cooled at 5 °C and stirred. To this well-stirred cooled solution, a solution of chloroacetyl chloride (4 mmol, 0.45 g) in dry 1,4-dioxane (25 mL) was added dropwise within a period of 20 min, at 5 °C with constant stirring. The reaction mixture was then stirred for an additional 8 h and left at room temperature for 48 h, and the solution was filtered to separate the white triethylamine hydrochloride salt. The filtrate was concentrated to half of its initial volume and then poured onto crushed ice. The progress of the reaction was monitored by TLC. The precipitated products were filtered, washed with cold ethanol absolute several times, dried in air, and recrystallized from ethanol to get the purified 2-azetidinones [22-23]. The Rf values of 2-azetidinones were determined by using ethyl acetate:benzene (3:7) as solvent system. The synthetic procedures for preparing compounds (**Z_2a**-**Z_2e** and **Z_2g**) are presented in Scheme 1.

4-Chloro-2-(3-chloro-2-oxo-4-(tetrazolo[1,5-a]quinolin-4-yl)azetidin-1-yl)benzenesulfonamide (Z_2a). White powder; yield: 54%; Rf: 0.74; m.p: 202–203 °C; Elemental analysis for $C_{18}H_{12}C_{l2}N_6O_3S$ (463.30 g/mol); Calcd: C, 46.66; H, 2.61; N, 18.14; S, 6.92. Found: C, 46.70; H, 2.63; N, 18.11; S, 6.99. IR (KBr) cm^{-1}: 3344 $\nu_{str.}(NH_2$, asymmetrical), 3136 $\nu_{str.}(NH_2$, symmetrical), 2924 ν(CH, asymmetrical, aliph.), 2854 ν(CH, symmetrical, aliph.), 1701 ν(C=O, azetidin-2-one ring), 1535 ν(C-N, azetidin-2-one ring), 1654 ν(C=N, tetrazole ring), 1500–1469 ν(C=C), 1319 $\nu_{str.}(SO_2$, asymmetrical), 1168 $\nu_{str.}(SO_2$, symmetrical), 1226 ν(N-N=N, tetrazole ring), 914 ν(S-N), 860 ν(C-Cl), 636 $\nu_{str.}$(C-S, sulfonamide); ^{1}H-NMR (300 MHz, DMSO-d_6) (δ/ppm): 8.68 (d, 1H, *J* = 6 Hz, Ar-H), 8.55 (s, 1H, pyridine-H), 8.34 (d, 1H, *J* = 6 Hz, Ar-H), 8.00 (s, 1H, Ar-H), 7.87 (t, 1H, $J_1 = J_2$ = 9 Hz, Ar-H), 7.62 (d, 1H, *J* = 9 Hz, Ar-H), 7.04 (s, 2H, NH_2), 6.88 (t, 1H, $J_1 = J_2$ = 21 Hz, Ar-H), 6.56 (d, 1H, *J* = 9 Hz, Ar-H), 6.05 (d, 1H, *J* = 12 Hz, CH-Cl, 2-azetidinone ring), 4.17 (dd, 1H, *J* = 20 Hz, CH-N, 2-azetidinone ring); ^{13}C-NMR (300 MHz, DMSO-d_6) (δ/ppm): 168.72, 148.33, 140.25, 138.42, 132.36, 131.53, 130.09, 129.81, 128.23, 125.65, 123.92, 123.14, 120.03, 119.74, 118.83, 115.93, 60.53, 55.37; The EI-MS m/z (%): 463 $[M]^+$ (3.5), 431 $[C_{18}H_{16}ClN_6O_3S]^+$ (2.5), 373 $[C_{18}H_{14}C_{l2}N_4O]^{\bullet+}$ (3.3), 314 $[C_{18}H_{12}N_5O]^+$ (5.2), 194 $[C_9H_7ClN_2O]^{\bullet+}$ (65.3), 148 $[C_9H_{10}NO]^+$ (100).

4-(3-Chloro-2-oxo-4-(tetrazolo[1,5-a]quinolin-4-yl) azetidin-1-yl)-*N*-(4-methylpyrimidin-2-yl)benzene sulfonamide (Z_2b). Dark brown powder; yield: 68%; Rf: 0.48; m.p: 240–242 °C; Elemental analysis for $C_{23}H_{17}ClN_8O_3S$ (520.95 g/mol); Calcd: C, 53.03; H, 3.29; N, 21.51; S, 6.16. Found: C, 53.10; H, 3.28; N, 21.57; S, 6.21. IR (KBr) cm^{-1}: 3483 ν(N-H), 2920 ν(CH, asymmetrical, aliph.), 2854 ν(CH, symmetrical, aliph.), 1697 ν(C=O, azetidin-2-one ring), 1519 ν(C-N, azetidin-

2-one ring), 1573 ν(C=N, tetrazole ring), 1481–1435 ν(C=C), 1334 $\nu_{str.}(SO_2$, asymmetrical), 1161 $\nu_{str.}(SO_2$, symmetrical), 1257 ν(N-N=N, tetrazole ring), 922 ν(S-N), 821 ν(C-Cl), 663 $\nu_{str.}$(C-S, sulfonamide); ^{1}H-NMR (300 MHz, DMSO-d_6) (δ/ppm): 10.69 (s, 1H, NH), 8.31 (s, 1H, pyridine-H), 8.00 (d, 1H, *J* = 9 Hz, pyrimidine ring), 7.78 (d, 1H, *J* = 9 Hz, Ar-H), 7.69 (d, 2H, *J* = 9 Hz, Ar-H), 7.53 (t, 1H, $J_1 = J_2$ = 9 Hz, Ar-H), 6.96 (d, 1H, *J* = 6 Hz, Ar-H), 6.83 (d, 2H, *J* = 12 Hz, Ar-H), 6.77 (t, 1H, $J_1 = J_2$ = 9 Hz, Ar-H), 6.57 (d, 1H, *J* = 9 Hz, pyrimidine ring), 4.26 (d, 1H, *J* = 6 Hz, CH-Cl, 2-azetidinone ring), 3.02 (d, 1H, *J* = 15 Hz, CH-N, 2-azetidinone ring), 1.18 (s, 3H, CH_3); ^{13}C-NMR (300 MHz, DMSO-d_6) (δ/ppm): 170.13, 158.07, 151.98, 148.68, 144.76, 141.96, 135.82, 132.30, 130.22, 129.90, 128.98, 126.23, 125.38, 120.68, 119.92, 119.42, 116.73, 113.17, 61.48, 58.47, 26.72; The EI-MS m/z (%): 522 $[M]^+$ (1.7), 365 $[C_{18}H_{14}ClN_6O]^+$ (2), 225 $[C_9H_9N_2O_3S]^+$ (3.4), 195 $[C_9H_8ClN_2O]^+$ (6.2), 148 $[C_9H_{10}NO]^+$ (100).

4-(3-Chloro-2-oxo-4-(tetrazolo[1,5-a]quinolin-4-yl)azetidin-1-yl)-*N*-(3,4-dimethylisoxazol-5-yl)benzenesulfonamide (Z_2c). Dark brown powder; yield: 42%; Rf: 0.77; m.p: 140–142 °C; Elemental analysis for $C_{23}H_{18}ClN_7O_4S$ (523.95 g/mol); Calcd: C, 52.72; H, 3.46; N, 18.71; S, 6.12. Found: C, 52.80; H, 3.51; N, 18.69; S, 6.17. IR (KBr) cm^{-1}: 3448 ν(N-H), 2974 ν(CH, asymmetrical, aliph.), 2870 ν(CH, symmetrical, aliph.), 1705 ν(C=O, azetidin-2-one ring), 1570 ν(C-N, azetidin-2-one ring), 1651, 1616 ν(C=N, tetrazole, Isoxazole ring), 1462–1427 ν(C=C), 1338 $\nu_{str.}(SO_2$, asymmetrical), 1161 $\nu_{str.}(SO_2$, symmetrical), 1284 ν(N-N=N, tetrazole ring), 922 ν(S-N), 763 ν(C-Cl), 690 $\nu_{str.}$(C-S, sulfonamide); ^{1}H-NMR (300 MHz, DMSO-d_6) (δ/ppm): 10.80 (s, 1H, NH), 7.93 (d, 1H, *J* = 9 Hz, Ar-H), 7.82 (s, 1H, pyridine-H), 7.77 (d, 2H, *J* = 15 Hz, Ar-H), 7.69 (t, 1H, $J_1 = J_2$ = 6 Hz, Ar-H), 7.34 (t, 1H, J_1 = 6, J_2 = 9 Hz, Ar-H), 6.78 (d, 1H, *J* = 12 Hz, Ar-H), 6.59 (d, 2H, *J* = 9 Hz, Ar-H), 4.30 (d, 1H, *J* = 15 Hz, CH-Cl, 2-azetidinone ring), 3.56 (d, 1H, *J* = 3 Hz, CH-N, 2-azetidinone ring), 2.07 (s, 3H, CH_3), 1.61 (s, 3H, CH_3); ^{13}C-NMR (300 MHz, DMSO-d_6) (δ/ppm): 172.15, 157.00, 151.90, 149.54, 140.64, 139.62, 131.89, 131.38, 129.07, 127.05, 123.30, 122.90, 119.45, 118.96, 118.17, 113.59, 110.36, 65.44, 61.23, 17.24, 12.58; The EI-MS m/z (%): 523 $[M]^+$ (1), 413 $[C_{18}H_{12}ClN_5O_3S]^{\bullet+}$ (1), 253 $[C_{11}H_{13}N_2O_3S]^+$ (35.8), 181 $[C_9H_8ClNO]^{\bullet+}$ (43.8), 161 $[C_9H_{11}N_3]^{\bullet+}$ (100), 135 $[C_8H_9NO]^{\bullet+}$ (86.9), 104 $[C_3H_3ClNO]^+$ (23.4).

4-(3-Chloro-2-oxo-4-(tetrazolo[1,5-a]quinolin-4-yl)azetidin-1-yl)-*N*-(4,6-dimethylpyrimidin-2-yl)benzenesulfonamide (Z_2d). Pale yellow powder; yield: 47%; Rf: 0.56; m.p: 230–233 °C; Elemental analysis for $C_{24}H_{19}ClN_8O_3S$ (534.98 g/mol); Calcd: C, 53.88; H, 3.58; N, 20.95; S, 5.99. Found: C, 53.91; H, 3.54; N, 20.98; S, 6.03. IR (KBr) cm^{-1}: 3383 ν(N-H), 2924 ν(CH, asymmetrical, aliph.), 2854 ν(CH, symmetrical, aliph.), 1712 ν(C=O, azetidin-2-one ring), 1531 ν(C-N, azetidin-2-one ring), 1658,1585 ν(C=N, tetrazole, pyrimidine ring), 1465–1427 ν(C=C), 1334 $\nu_{str.}(SO_2$, asymmetrical), 1153 $\nu_{str.}(SO_2$, symmetrical), 1257 ν(N-N=N, tetrazole ring), 979 ν(S-N), 871 ν(C-Cl), 663 $\nu_{str.}$(C-S, sulfonamide); ^{1}H-NMR (300 MHz, DMSO-d_6) (δ/ppm): 12.06 (s, 1H, NH), 8.48 (d, 1H, *J* = 30 Hz, Ar-H), 8.28 (s, 1H, pyridine-H), 7.97 (d, 2H, *J* = 27 Hz, Ar-H), 7.79 (d, 1H, *J* = 6 Hz, Ar-H), 7.51 (d, 2H, *J* = 9 Hz, Ar-H), 7.19 (t, 1H, J_1 = 39, J_2 = 30 Hz, Ar-H), 6.87 (s, 1H, pyrimidine ring), 6.69 (t, 1H, $J_1 = J_2$ = 9 Hz, Ar-H), 4.22 (d, 1H, *J* = 9 Hz, CH-Cl, 2-azetidinone ring), 3.40 (s, 1H, CH-N, 2-azetidinone ring), 2.35 (s, 6H, $2CH_3$); ^{13}C-NMR (300 MHz, DMSO-d_6) (δ/ppm): 169.63, 153.86, 148.05, 140.94, 138.71, 132.43, 130.75, 129.38, 127.91, 127.65, 124.81, 124.57, 120.13, 119.82, 118.65, 116.83, 113.74, 61.53, 58.41, 25.32; The EI-MS m/z (%): 536 $[M]^+$ (2.2), 428 $[C_{18}H_{13}ClN_6O_3S]^{\bullet+}$ (1.8), 331 $[C_{15}H_{15}N_4O_3S]^+$ (2.3), 274 $[C_{16}H_{12}N_5]^+$ (51.2), 160 $[C_9H_{10}N_3]^+$ (34.4), 148 $[C_9H_{10}NO]^+$ (100), 93 $[C_6H_7N]^{\bullet+}$ (71.6).

4-(3-Chloro-2-oxo-4-(tetrazolo[1,5-a]quinolin-4-yl)azetidin-1-yl)-*N*-(thiazol-2-yl)benzenesulfonamide (Z_2e). Pale brown powder; yield: 77%; Rf: 0.92; m.p: 130–133 °C; Elemental analysis for $C_{21}H_{14}ClN_7O_3S_2$ (511.96 g/mol); Calcd: C, 49.27; H, 2.76; N, 19.15; S, 12.53. Found: C, 49.22; H, 2.80; N, 19.10; S, 12.56. IR (KBr) cm^{-1}: 3375 ν(N-H), 2924 ν(CH, asymmetrical, aliph.), 2854 ν(CH, symmetrical, aliph.), 1701 ν(C=O, azetidin-2-one ring), 1527 ν(C-N, azetidin-2-one ring), 1651,1600 ν(C=N, tetrazole, thiazole ring), 1455–1400 ν(C=C), 1327 $\nu_{str.}(SO_2$, asymmetrical), 1138 $\nu_{str.}(SO_2$, symmetrical), 1276 ν(N-N=N, tetrazole ring), 929 ν(S-N), 848 ν(C-Cl), 636 $\nu_{str.}$(C-S, sulfonamide); ^{1}H-NMR

(400 MHz, DMSO-d_6) (δ/ppm): 10.68 (s, 1H, NH), 7.92 (d, 1H, *J* = 4 Hz, Ar-H), 7.84 (s, 1H, 1H, pyridine-H), 7.73 (d, 2H, *J* = 8 Hz, Ar-H), 7.67 (d, 1H, *J* = 8 Hz, Ar-H), 7.44 (t, 1H, $J_1 = J_2 = 4$ Hz, Ar-H), 7.18 (t, 1H, $J_1 = J_2 = 4$ Hz, Ar-H), 6.77 (d, 2H, *J* = 8 Hz, Ar-H), 6.74 (d, 1H, *J* = 4 Hz, thiazole ring), 6.60 (d, 1H, *J* = 4 Hz, thiazole ring), 4.28 (d, 1H, *J* = 4 Hz, CH-Cl, 2-azetidinone ring), 3.20 (d, 1H, *J* = 20 Hz, CH-N, 2-azetidinone ring); ^{13}C-NMR (300 MHz, DMSO-d_6) (δ/ppm): 168.48, 163.03, 152.50, 151.50, 149.72, 147.99, 142.14, 139.31, 132.03, 128.34, 128.19, 127.53, 124.75, 119.41, 118.51, 113.02, 111.51, 68.98, 62.47; The EI-MS m/z (%): 513 $[M]^+$ (2.3), 309 $[C_{12}H_{11}N_3O_3S_2]^{\bullet+}$ (2.8), 279 $[C_{12}H_{10}ClN_3OS]^{\bullet+}$ (2.8), 256 $[C_9H_{10}N_3O_2S_2]^+$ (3.4), 239 $[C_9H_7N_2O_2S_2]^+$ (3.4), 105 $[C_7H_7N]^{\bullet+}$ (100).

4-(3-Chloro-2-oxo-4-(tetrazolo[1,5-a]quinolin-4-yl)azetidin-1-yl)benzenesulfonamide (Z_2g). Pale gray powder; yield: 81%; Rf: 0.63; m.p: 208–210 °C; Elemental analysis for $C_{18}H_{13}ClN_6O_3S$ (428.85 g/mol); Calcd: C, 50.41; H, 3.06; N, 19.60; S, 7.48. Found: C, 50.49; H, 3.01; N, 19.63; S, 7.41. IR (KBr) cm^{-1}: 3448 $\nu_{str.}$(NH_2, asymmetrical), 3417 $\nu_{str.}$(NH_2, symmetrical), 2974, 2935 ν(CH, asymmetrical, aliph.), 1743 ν(C=O, azetidin-2-one ring), 1546 ν(C-N, azetidin-2-one ring), 1647 ν(C=N, tetrazole ring), 1477–1442 ν(C=C), 1338 $\nu_{str.}$(SO_2, asymmetrical), 1157 $\nu_{str.}$(SO_2, symmetrical), 1260 ν(N-N=N, tetrazole ring), 914 ν(S-N), 817 ν(C-Cl), 690 $\nu_{str.}$(C-S, sulfonamide); ^{1}H-NMR (300 MHz, DMSO-d_6) (δ/ppm): 8.02 (s, 1H, pyridine-H), 7.95 (d, 1H, *J* = 9 Hz, Ar-H), 7.69 (d, 2H, *J* = 9 Hz, Ar-H), 7.50 (t, 1H, $J_1 = 9$, $J_2 = 6$ Hz, Ar-H), 7.00 (t, 1H, $J_1 = J_2 = 9$ Hz, Ar-H), 6.99 (s, 2H, NH_2), 6.79 (d, 1H, *J* = 9 Hz, Ar-H), 6.67 (d, 2H, *J* = 9 Hz, Ar-H), 4.30 (d, 1H, *J* = 6 Hz, CH-Cl, 2-azetidinone ring), 3.23 (s, 1H, CH-N, 2-azetidinone ring); ^{13}C-NMR (300 MHz, DMSO-d_6) (δ/ppm): 169.05, 154.64, 151.12, 142.74, 142.50, 137.64, 137.10, 134.03, 132.01, 127.84, 127.61, 124.93, 120.49, 111.52, 56.46, 45.71; The EI-MS m/z (%): 429 $[M]^+$ (1), 351 $[C_{18}H_{14}ClN_5O]^{\bullet+}$ (1.1), 225 $[C_9H_9N_2O_3S]^+$ (1.2), 197 $[C_9H_{10}ClN_2O]^+$ (1.4), 149 $[C_9H_{11}NO]^{\bullet+}$ (2.8), 86 $[C_4H_8NO]^+$ (100).

Synthesis of 4-thiazolidinone or 4-selenazolidinone (Z_2B, Z_2E, Z_2B', Z_2E')

A mixture of Schiff base **2b** (10 mmol, 4.4 g), **2e** (10 mmol 4.35 g) and a catalytic amount of zinc chloride (0.05 g) in DMF (10 mL) was reacted with thioglycolic acid (20 mmol, 1.84 g) or 2-seleno-glycolic acid (20 mmol, 2.78 g) in DMF (10 mL). The mixture was refluxed for 12–14 h. The reaction mixture was then poured into crushed ice. The separated solid was neutralized by sodium bicarbonate to remove excess thioglycolic acid. Solid compounds obtained were filtered, washed several times with water and recrystallized from ethanol. The completion of the reaction and the purity of the products were confirmed by the TLC using methanol:carbon tetrachloride (2:8) [21]. The synthetic procedures for the preparation of compounds (**Z_2B**, **Z_2E**, **Z_2B'** and **Z_2E'**) are presented in Scheme 1.

***N*-(4-Methylpyrimidin-2-yl)-4-(4-oxo-2-(tetrazolo[1,5-a]quinolin-4-yl)thiazolidin-3-yl)benzenesulfonamide (Z_2B).** Reddish orange powder; yield: 72%; Rf: 0.81; m.p: 138–140 °C; Elemental analysis for $C_{23}H_{18}N_8O_3S_2$ (518.57 g/mol); Calcd: C, 53.27; H, 3.50; N, 21.61; S, 12.37. Found: C, 53.31; H, 3.55; N, 21.57; S, 12.44. IR (KBr) cm^{-1}: 3225 ν(N-H), 2924 ν(CH, asymmetrical, aliph.), 2854 ν(CH, symmetrical, aliph.), 1691 ν(C=O, thiazolidinone ring), 1519 ν(C-N, thiazolidinone ring), 1627,1573 ν(C=N, tetrazole, pyrimidine ring), 1481–1438 ν(C=C), 1338 $\nu_{str.}$(SO_2, asymmetrical), 1157 $\nu_{str.}$(SO_2, symmetrical), 1273 ν(N-N=N, tetrazole ring), 976 ν(S-N), 725 $\nu_{str.}$(C-S-C, asymmetrical), 678 $\nu_{str.}$(C-S-C, symmetrical), 624 $\nu_{str.}$(C-S, sulfonamide); ^{1}H-NMR (300 MHz, DMSO-d_6) (δ/ppm): 11.24 (s, 1H, NH), 8.33 (d, 1H, *J* = 6 Hz, Ar-H), 8.00 (d, 1H, *J* = 9 Hz, pyrimidine-H), 7.70 (t, 1H, $J_1 = 9$, $J_2 = 3$ Hz, Ar-H), 7.52 (d, 2H, *J* = 9 Hz, Ar-H), 6.96 (d, 1H, *J* = 6 Hz, Ar-H), 6.85 (s, 1H, pyridine-H), 6.77 (t, 1H, $J_1 = J_2 = 9$ Hz, Ar-H), 6.76 (d, 2H, *J* = 9 Hz, Ar-H), 6.59 (d, 1H, *J* = 9 Hz, pyrimidine-H), 6.00 (s, 1H, CH-N, thiazolidinone ring), 3.67 (s, 2H, CH-CO, thiazolidinone ring), 2.98 (s, 3H, CH_3); ^{13}C-NMR (300 MHz, DMSO-d_6) (δ/ppm): 167.87, 156.07, 151.62, 147.28, 140.36, 132.83, 130.75, 130.12, 129.87, 128.74, 126.63, 124.71, 124.11, 122.37, 119.43, 118.55, 115.73, 111.96, 57.25, 33.82, 22.18; The EI-MS m/z (%): 518 $[M]^+$ (1.6), 364 $[C_{15}H_{16}N_4O_3S_2]^{\bullet+}$ (1.2), 272 $[C_{12}H_{10}N_5OS]^+$ (6.2), 250 $[C_{10}H_{10}N_4O_2S]^{\bullet+}$ (30.3), 147 $[C_5H_{11}N_2OS]^+$ (3.5), 105 $[C_3H_7NOS]^{\bullet+}$ (100).

***N*-(4-Methylpyrimidin-2-yl)-4-(4-oxo-2-(tetrazolo[1,5-a]quinolin-4-yl)-1,3-selenazolidin-3-yl)benzenesulfonamide (Z_2B').** Maroon powder; yield: 51%; Rf: 0.51; m.p: 194–196 °C; Elemental analysis for $C_{23}H_{18}N_8O_3SSe$ (565.47 g/mol); Calcd: C, 48.85; H, 3.21; N, 19.82; S, 5.67. Found: C, 48.89; H, 3.18; N, 19.79; S, 5.63. IR (KBr) cm^{-1}: 3360 ν(N-H), 2920 ν(CH, asymmetrical, aliph.), 2854 ν(CH, symmetrical, aliph.), 1701 ν(C=O, thiazolidinone ring), 1519 ν(C-N, thiazolidinone ring), 1597,1570 ν(C=N, tetrazole, pyrimidine ring), 1481-1438 ν(C=C), 1330 $\nu_{str.}(SO_2$, asymmetrical), 1157 $\nu_{str.}(SO_2$, symmetrical), 1273 ν(N-N=N, tetrazole ring), 972 ν(S-N), 574 $\nu_{str.}$(C-Se); ^{1}H-NMR (300 MHz, DMSO-d_6) (δ/ppm): 10.58 (s, 1H, NH), 8.32 (s, 1H, pyridine-H), 7.98 (d, 1H, *J* = 9 Hz, Ar-H), 7.77 (d, 1H, *J* = 6 Hz, pyrimidine-H), 7.69 (d, 2H, *J* = 9 Hz, Ar-H), 7.52 (d, 1H, *J* = 9 Hz, Ar-H), 6.95 (t, 1H, J_1 = 9, J_2 = 6 Hz, Ar-H), 6.82 (d, 2H, *J* = 18 Hz, Ar-H), 6.77 (t, 1H, J_1 = 9, J_2 = 6 Hz, Ar-H), 6.59 (d, 1H, *J* = 9 Hz, pyrimidine-H), 6.03 (s, 1H, CH-N, thiazolidinone ring), 3.25 (s, 2H, CH-CO, thiazolidinone ring), 2.73 (s, 3H, CH_3); ^{13}C-NMR (300 MHz, DMSO-d_6) (δ/ppm): 167.86, 162.78, 157.38, 153.35, 151.60, 142.13, 138.23, 132.18, 130.29, 129.88, 129.68, 129.35, 125.76, 123.28, 120.36, 118.94, 115.90, 112.53, 56.19, 31.22, 29.83; The EI-MS m/z (%): 566 $[M]^+$ (1.2), 407 $[C_{18}H_{13}N_6OSe]^+$ (0.8), 303 $[C_9H_9N_2O_3SSe]^+$ (1.3), 227 $[C_9H_{10}NOSe]^+$ (30.7), 199 $[C_{10}H_9N_5]^{\bullet+}$ (51.4), 134 $[C_8H_8NO]^+$ (100).

4-(4-Oxo-2-(tetrazolo[1,5-a]quinolin-4-yl)thiazolidin-3-yl)-*N*-(thiazol-2-yl)benzenesulfonamide (Z_2E). Brown powder; yield: 67%; Rf: 0.75; m.p: 160–162 °C; Elemental analysis for $C_{21}H_{15}N_7O_3S_3$ (509.58 g/mol); Calcd: C, 49.50; H, 2.97; N, 19.24; S, 18.88. Found: C, 49.56; H, 3.01; N, 19.28; S, 18.82. IR (KBr) cm^{-1}: 3363 ν(N-H), 2920 ν(CH, asymmetrical, aliph.), 2854 ν(CH, symmetrical, aliph.), 1693 ν(C=O, thiazolidinone ring), 1535 ν(C-N, thiazolidinone ring), 1597 ν(C=N, tetrazole, thiazole ring), 1420 ν(C=C), 1369 $\nu_{str.}(SO_2$, asymmetrical), 1138 $\nu_{str.}(SO_2$, symmetrical), 1280 ν(N-N=N, tetrazole ring), 929 ν(S-N), 748 $\nu_{str.}$(C-S-C, asymmetrical), 686 $\nu_{str.}$(C-S-C, symmetrical), 628 $\nu_{str.}$(C-S, sulfonamide); ^{1}H-NMR (300 MHz, DMSO-d_6) (δ/ppm): 10.55 (s, 1H, NH), 8.90 (d, 1H, *J* = 9 Hz, thiazole-H), 8.32 (d, 1H, *J* = 6 Hz, Ar-H), 7.95 (s, 1H, pyridine-H), 7.73 (d, 2H, *J* = 9 Hz, Ar-H), 7.44 (d, 1H, *J* = 9 Hz, Ar-H), 7.34 (t, 1H, J_1 = 9, J_2 = 12 Hz, Ar-H), 7.11 (t, 1H, J_1 = 6, J_2 = 18 Hz, Ar-H), 7.10 (d, 2H, *J* = 6 Hz, Ar-H), 6.75 (d, 1H, *J* = 6 Hz, thiazole-H), 6.03 (s, 1H, CH-N, thiazolidinone ring), 3.03 (s, 2H, CH-CO, thiazolidinone ring); ^{13}C-NMR (300 MHz, DMSO-d_6) (δ/ppm): 170.68, 157.20, 147.03, 141.75, 134.23, 131.93, 130.83, 130.37, 129.86, 129.69, 123.67, 122.12, 120.30, 119.18, 115.29, 110.44, 109.16, 56.17, 32.45; The EI-MS m/z (%): 509 $[M]^+$ (1.4), 267 $[C_{10}H_9N_3O_2S_2]^{\bullet+}$ (1.8), 239 $[C_9H_7N_2O_2S_2]^+$ (2.2), 195 $[C_{10}H_5N_5]^{\bullet+}$ (5.0), 177 $[C_9H_9N_2S]^+$ (2.8), 86 $[C_3H_4NS]^+$ (64), 64 $[O_2S]^+$ (100).

4-(4-oxo-2-(tetrazolo[1,5-a]quinolin-4-yl)-1,3-selenazolidin-3-yl)-*N*-(thiazol-2-yl)benzenesulfonamide (Z_2E'). Yellowish brown powder; yield: 58%; Rf: 0.61; m.p: 178–180 °C; Elemental analysis for $C_{21}H_{15}N_7O_3S_2Se$ (556.48 g/mol); Calcd: C, 45.33; H, 2.72; N, 17.62; S, 11.52. Found: C, 45.31; H, 2.69; N, 17.66; S, 11.48. IR (KBr) cm^{-1}: 3367 ν(N-H), 2920 ν(CH, asymmetrical, aliph.), 2854 ν(CH, symmetrical, aliph.), 1689 ν(C=O, thiazolidinone ring), 1523 ν(C-N, thiazolidinone ring), 1600 ν(C=N, tetrazole, thiazole ring), 1431–1408 ν(C=C), 1365 $\nu_{str.}(SO_2$, asymmetrical), 1138 $\nu_{str.}(SO_2$, symmetrical), 1276 ν(N-N=N, tetrazole ring), 933 ν(S-N), 555 $\nu_{str.}$(C-Se); ^{1}H-NMR (300 MHz, DMSO-d_6) (δ/ppm): 10.52 (s, 1H, NH), 8.32 (d, 1H, *J* = 5 Hz, Ar-H), 7.70 (s, 1H, pyridine-H), 7.37 (d, 2H, *J* = 10 Hz, Ar-H), 7.29 (t, 1H, J_1 = 10, J_2 = 5 Hz, Ar-H), 7.24 (d, 1H, *J* = 10 Hz, Ar-H), 7.06 (t, 1H, J_1 = 10, J_2 = 5 Hz, Ar-H), 6.70 (d, 2H, *J* = 5 Hz, Ar-H), 6.56 (d, 1H, *J* = 10 Hz, thiazole-H), 6.54 (d, 1H, *J* = 5 Hz, thiazole-H), 4.92 (s, 1H, CH-N, thiazolidinone ring), 3.74 (s, 2H, CH-CO, thiazolidinone ring); ^{13}C-NMR (300 MHz, DMSO-d_6) (δ/ppm): 173.82, 166.23, 148.68, 144.76, 135.82, 132.30, 130.22, 129.90, 128.98, 128.71, 125.38, 124.96, 122.86, 120.68, 119.92, 116.73, 113.17, 58.47, 35.66; The EI-MS m/z (%): 557 $[M]^+$ (1.2), 435 $[C_{19}H_{13}N_7O_2S_2]^{\bullet+}$ (2.5), 320 $[C_{12}H_{10}N_5OSe]^+$ (1.2), 279 $[C_{10}H_9N_5Se]^{\bullet+}$ (31.7), 239 $[C_9H_7N_2O_2S_2]^+$ (2.8), 174 $[C_{10}H_{12}N_3]^+$ (60.1), 64 $[O_2S]^+$ (100).

Biological Activity

Acute toxicity (LD_{50})

Healthy albino mice of either sex (male and female),

aged from 7 to 9 weeks and whose body weight ranged between 23–33 g, were used to study the acute toxicity of 4-thiazolidinone (**Z_2E**) and 4-selenazolidinone (**Z_2E'**) derivatives. The animals were injected intraperitoneally with the first dose of 500 mg/kg. The result was read death X or life O after 24 h and increases or decreases the amount of dose was constant 50 mg/kg and repeat dosing up or down for 4 mice after changing the result death to life and versa. LD_{50} was calculated based on the diagram and equation of Dixon

$$LD_{50} = Xf + Kd$$

where Xf: the last dose, K: the interval between dose levels, d: the tabulated value, Table 1 [24].

Antibacterial activity

The compounds (**Z_2B**, **Z_2E**, **Z_2B'** and **Z_2E'**) were screened *in vitro* for antibacterial properties. The panel of pathogens involved *Staphylococcus aureus* and *Bacillus* as a Gram-positive bacterium, *Escherichia coli* and *Pseudomonas aeruginosa* as a Gram-negative bacterium, using the agar diffusion method. The antibiotic tetracycline was used to calibrate and compare with the antibacterial stuff. 0.2 mL of bacterial inoculums were uniformly spread using a sterile cotton swab on a sterile petri dish Mueller Hinton Agar (MHA). The tested compounds and tetracycline drug was dissolved in DMSO with concentrations including 1, 5, 25,125, 250, and 500 mg/mL for each compound. 50 µL from 1–500 mg/mL concentrations of tested compounds and tetracycline were added to every well (7 mm diameter holes cut within the agar gel, 20 mm aside from one another). The plates were incubated for 24 h at 36 °C ± 1 °C, under aerobic conditions. After incubation, confluent bacterial growth was observed. Inhibition of the bacterial growth was measured in mm [25]. Furthermore, values of minimum inhibitory concentration (MIC) of those compounds [26]. The MIC was recorded because of the lowest concentration at which no visible growth was observed.

Table 1. The tabulated Dixon values

	O	OO	OOO	OOOO	
XOOO	0.157-	0.154-	0.154-	0.154-	OXXX
XOOX	0.878-	0.861-	0.860-	0.860-	OXXO
XOXO	0.701	0.747	0.741	0.741	OXOX
XOXX	0.084	0.169	0.181	0.182	OXOO
XXOO	0.305	0.372	0.380	0.381	OOXX
XXOX	0.305-	0.169	0.144-	0.142-	OOXO
XXXO	1.288	1.500	1.544	1.549-	OOOX
XXXX	0.555	0.0897	0.985	1.000	OOOO
	X	XX	XXX	XXXX	

K represented serial tests started with: -

Antioxidant activity

The antioxidant activity of the azetidin-2-one (**Z_2a**-**Z_2e**, **Z_2g**), 4-thiazolidinone (**Z_2B**, **Z_2E**) and 4-selenazolidinone (**Z_2B'**, **Z_2E'**) were determined according to the β-carotene bleaching method [27]. The β-carotene bleaching method is based on the loss of the yellow color of β-carotene because of its reaction with radicals formed by linoleic acid oxidation in an emulsion and according to previous methods [28]. A solution of β-carotene was prepared by dissolving 0.01 g of β-carotene in 50 mL of chloroform. As much as 1 mL of this solution was then pipetted into a round-bottom rotary flask containing 0.02 mL of linoleic acid and 0.2 mL of Tween-20. After removing the chloroform by vacuum evaporation using a rotary evaporator at room temperature, 50 mL of distilled water was added to the flask with manual shaking as the first stage. The emulsion (3.8 mL) was added to tubes containing 0.2 mL of the prepared compounds and the reference (BHT) compound which was prepared by dissolving 0.01 g of these compounds in 0.2 mL of DMSO. The absorbance was read at 470 nm, and the samples were then subjected to thermal autoxidation at 45°C in a water bath for 2 h. Absorbance was measured every 15 min [27]. Antioxidant activity (AA) was calculated as the percent of inhibition relative to the control using the equation

$$\%AA = 1 - [(Ai - At) / (Ai^* - At^*)] \times 100$$

where, Ai: is the measured absorbance value of the sample at zero time. At: is the measured absorbance value of the sample after incubation 105 min at 45 °C. Ai*: is the measured absorbance value of control at zero time, At*: is the measured absorbance value of control after incubation 105 min at 45 °C.

Anti-breast cancer activity

In vitro *MTT cellular viability assay*. The cytotoxicity of samples on the MCF-7 cell line was determined by the 3-(4,5-dimethyl-2-thiazolyl)-2,5-diphenyl tetrazolium

bromide (MTT) cell viability assay [29]. Cells at a density of 1 × 10^4 cells/mL (100 µL/well) were seeded in 96-well plates and incubated overnight under 5% CO_2 at 37 °C, followed by exposure to a series of concentrations (6.25, 12.5, 25, 50, 75, and 100 µg/mL) of the tested compounds (**Z_2E** and **Z_2E'**) and 5-Fluorouracil as reference drug. At the same time, a group only containing culture medium was set as blank control. Each group had three biological repeats. After dosing for 72 h, the cells were washed, and then fresh medium (100 µL) supplemented with 28 µL of 2 mg/mL solution of MTT was added to each well. After incubated in the dark for 2 h at 37 °C, removing the MTT solution and the crystals remaining in the wells were solubilized by adding 100 µL of DMSO followed by 37 °C incubation for 15 min with shaking [30]. The optical density at 620 (OD620) of each well was measured by a plate reader (Synergy H4: Bio-Tek, Winooski, VT, USA). The results are presented as mean ± standard deviation (SD). The survival rate of control cells treated without the tested compounds was 100%. Cell viability was calculated using the following equation

$$\text{Cell viability}(\%) = \frac{\text{dosing cell OD} - \text{blank OD}}{\text{control cell OD} - \text{blank OD}} \times 100$$

Acridine orange/Ethidium bromide staining. Morphological apoptosis of MCF-7 cells treated with different concentrations of the newly prepared compounds (**Z_2E** and **Z_2E'**) and standard (5-Fluorouracil) were assessed using an acridine orange/ethidium bromide (AO/EB) staining kit (Solarbio, Beijing, China, Cat No. CA1140). The density of 1 × 10^4 MCF-7 cells/mL was plated in 6-well plates (1 mL/well) and incubated overnight. The medium was replaced with the tested compounds-containing 6.25, 12.5, 25, 50, 75, and 100 µg/mL medium and incubated for 48 h under the same conditions mentioned before. Cells were washed with PBS and stained with AO/EB solution (20 µL AO/EB freshly mixed solution of equal volume in 1 mL PBS) for 2–3 min in the dark. After the successive washes, the fluorescent images were taken with an inverted fluorescence microscope (Olympus Corporation, Beijing, China) [31].

■ RESULTS AND DISCUSSION

The 2-azetidinone (**Z_2a**-**Z_2e**, **Z_2g**), 4-thiazolidinone (**Z_2B**, **Z_2E**) and 4-selenazolidinone (**Z_2B'**, **Z_2E'**) compounds were prepared via reaction of imines with ketene, thioglycolic acid, and 2-selenoglycolic acid, respectively. The prepared thiazolidin-4-ones and selenazolidine-4-one are obtained as solid compounds, often melting with decomposition but the attachment of an alkyl group to the nitrogen lowered its melting point compared to the β-Lactam compounds. 2-Azetidinones, 1,3-thiazolidin-4-ones and 1,3-selenazolidine-4-ones are stable in air, and they are soluble in most polar solvents. The suggested mechanisms for preparing a 2-azetidinone and thiazo- or selenazolidin-4-one ring are shown in Scheme 2. Also, the existence of interactive unsaturated ketone group in 2-azetidinones and thiazo- or selenazolidin-4-one are accountable for their biological activities [32]. The elemental analysis results C, H, N, and S of the studied compounds are in agreement with the theoretical values.

Spectroscopic Analysis

Infrared spectra (FTIR)

All the infrared spectra of the compounds were characterized by a medium to a weak band at 1226–1284 cm^{-1} which corresponds to the ν(N-N=N) stretching vibration for tetrazole ring [33]. Also, the IR spectra of all the prepared compounds show featured bands in the range 1319–1369 and 1138–1168 cm^{-1}, which are assigned to asymmetrical and symmetrical stretching vibration, respectively, of SO_2 group [34]. The compounds (**2a**, **2g**, **Z_2a** and **Z_2g**) show two bands within the range 3136–3448 cm^{-1}, which is attributed to asymmetric and symmetric stretching of ν(NH_2) groups. In addition, the medium to weak bands at 3225–3448 cm^{-1} can correspond to the ν(N-H) stretching vibration. IR spectra of the Schiff bases **2a**-**2e**, **2g** showed the absence of band at 1681 cm^{-1} which attribute to carbonyl ν(C=O) stretching vibration which was apparent in the tetrazolo[1,5-a]quinoline-4-carbaldehyde compound (**2**) and instead, the appearance of a strong new band at 1589–1608 cm^{-1} that assigned to the imine ν(CH=N) linkage, which indicates the reaction between the amino and aldehyde moieties of the starting reagents which are no more existed and have been

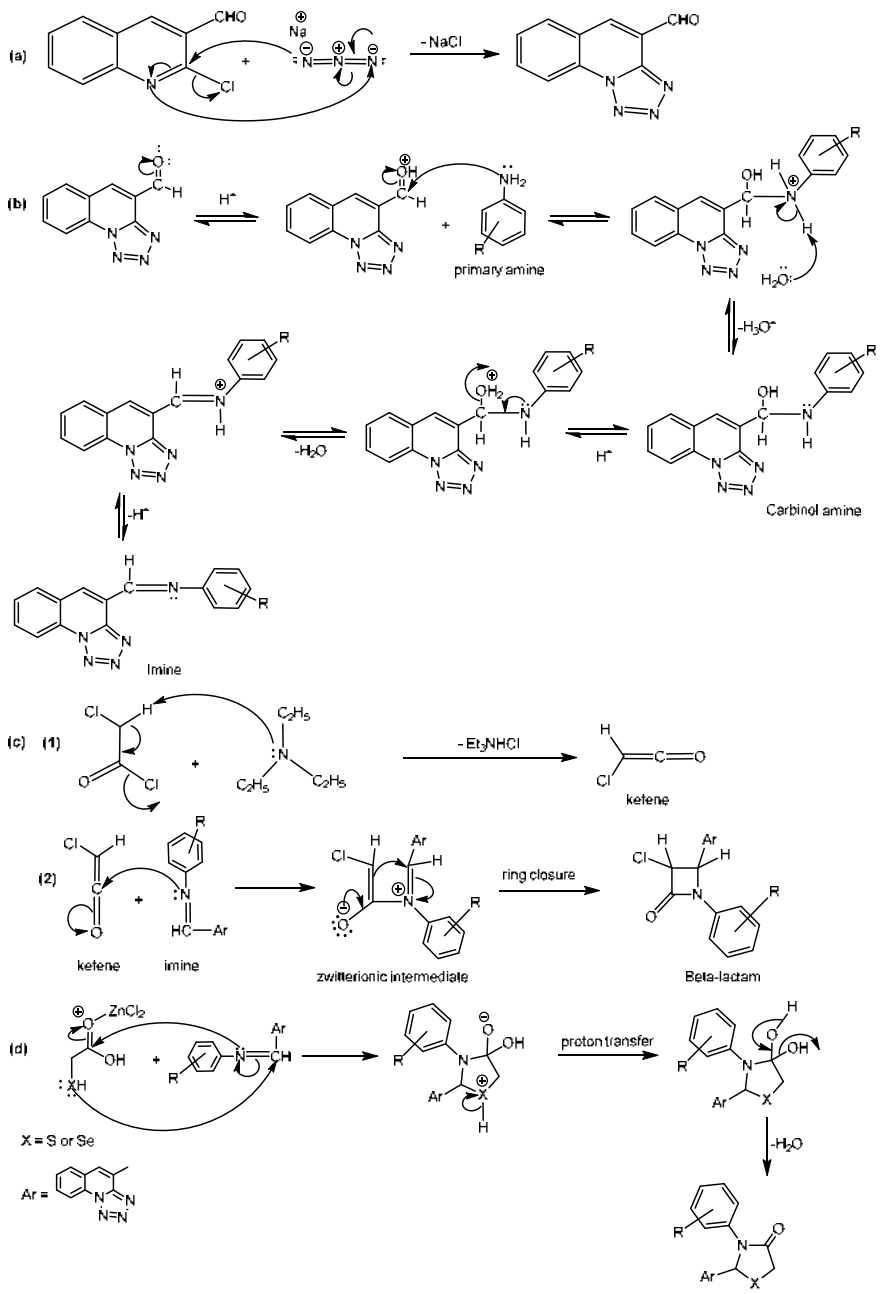

Scheme 2. The suggested mechanisms of (a) Tetrazole ring, (b) Schiff bases, (c) β-Lactam compounds and (d) 4-thiazolidinone or 4-selenazolidinone compounds), respectively

converted into the respective Schiff base linkages [4,21].

The structure of 2-azetidinones (i.e., compounds **Z_2a**-**Z_2e** and **Z_2g**) was established by IR spectroscopy which showed the disappearance of CH=N bands in the region 1589–1608 cm^{-1} combined with the appearance of absorption bands at 1697–1743 and 1519–1546 cm^{-1} due to ν(C=O) and ν(C-N), respectively [21-22]. Ring closure in 4-thiazolidinones and 4-selenazolidinones can be observed by the appearance of strong bands at 1689–1701 and 1519–1535 cm^{-1} which attributed to the stretching vibration of the carbonyl group ν(C=O) and ν(C-N), respectively [20-21]. The spectrum was distinguished by the appearance of distinct absorption bands for ν(C-S-C) at the range 725–748 and 678–686 cm^{-1}, which assigned to asymmetrical and symmetrical stretching vibration respectively for the 1,3-thiazolidin-4-ones

(**Z_2B** and **Z_2E**) [12,34]. Furthermore, the strong to medium bands which appeared in the range 555–574 cm^{-1} are attributed to the ν(C-Se) stretching vibration for the 4-selenazolidinones (**Z_2B'** and **Z_2E'**) [35]. All the prepared compounds show strong to medium bands in the range 914–979 and at 624–690 cm^{-1} in IR spectrum can be related to stretching of ν(S-N) and ν(C-S), respectively [4].

^{1}H-NMR and ^{13}C-NMR spectra

The ^{1}H-NMR spectra of the prepared compounds show a singlet signal at the range δ 10.52–12.86 ppm, which is attributed to the N-H protons. Furthermore, (**2a**, **2g**, **Z_2a** and **Z_2g**) compounds have a singlet signal at δ 6.97–7.07 ppm due to the presence of two protons of NH_2 group of sulfonamide which innervate the desired results [4]. The proton of azomethine group (CH=N) of compounds (**2a**-**2e**, **2g**) appears at δ 8.58–9.07 ppm [21]. The 2-azetidinone compounds (**Z_2a**-**Z_2e** and **Z_2g**) are characterized by showing doublet signal at δ 3.02–4.17 ppm and at δ 4.22–6.05 ppm, which can be assigned to the (CH-N) and (CH-Cl) protons, respectively and disappearing the azomethine signal that exists in Schiff bases (**2a**-**2e** and **2g**) [11,36]. The ^{1}H-NMR spectra of the 4-thiazolidinones and 4-selenazolidinones (**Z_2B**, **Z_2E**, **Z_2B'** and **Z_2E'**) are characterized by showing singlet signals at δ 3.03–3.67 ppm and at δ 3.25–3.74 ppm, which attributed to the (CH_2-S) and (CH_2-Se) protons respectively [21,37]. Also, singlet signal that appears at δ 4.92–6.03 can be attributed to the (CH-N) proton of these compounds [21]. The compounds (**2b**, **2c**, **2d**, **Z_2b**, **Z_2c**, **Z_2d**, **Z_2B** and **Z_2B'**) shows a singlet signal at δ 1.18–3.03 ppm due to methyl protons [4,21]. In addition, multiple signals that appear at δ 6.54–8.86 ppm can be attributed to aromatic rings of all the studied compounds [21,38]. Therefore, the ^{1}H-NMR result supports the formation of four- or five-membered rings.

The ^{13}C-NMR spectra of azetidine-2-ones, 1,3-thiazolidin-4-ones and 1,3-selenazolidin-4-ones show signals at the range δ 168.48–172.15 ppm, δ 167.87–170.68 ppm and signal at δ 167.86–173.82 ppm which attribute to cyclic carbonyl carbon (C=O), respectively [20-21]. The 2-azetidinone compounds are characterized by showing two signals at δ 56.46–68.98 and δ 45.71–62.47 ppm and which can be assigned to the C-Cl and C-N in lactam ring, respectively [11]. Also, the spectra of the thiazolidine-4-one or selenazolidin-4-one derivatives exhibited two signals at δ 56.17–58.47 and δ 31.22–35.66 ppm, which can be assigned to the 2-C and 5-C in 1,3-thiazo or 1,3-selenazolidin-4-one ring, respectively [21,39]. The ^{13}C-NMR spectra of the prepared compounds (**Z_2b**, **Z_2c**, **Z_2d**, **Z_2e**, **Z_2B**, **Z_2B'**, **Z_2E** and **Z_2E'**) show signals at the range δ 151.62–166.23 ppm is due to the imine functional group (C=N) in sulfonamide ring. Additionally, the compounds (**Z_2b**, **Z_2c**, **Z_2d**, **Z_2B**, and **Z_2B'**) show signals at δ 12.58–29.83 ppm that can be attributed to methyl groups [4]. Furthermore, the signals of aromatic carbons of these synthesized compounds are represented at δ 111.52–154.64 ppm [4]. The ^{13}C-NMR spectral data of the 2-azetidinones and thiazolidine-4-ones or selenazolidin-4-ones are in accord with the suggested structures.

EI-mass

The mass spectrum of all studied compounds detects the molecular ion peaks $[M]^+$ are in excellent acceptance with the suggested structures. The potential suggested ion fragments with the appearance of the result of fragmentation of these synthesized compounds are shown in Scheme 3, furthermore, the peaks intensity gives an idea about the stability of fragments primarily with the base peaks.

The mass spectrum of the compound **Z_2b** shows several fragments peaks at m/z 365, 225, 195, and m/z 148, and these peaks can be assigned to $[C_{18}H_{14}ClN_6O]^+$, $[C_9H_9N_2O_3S]^+$, $[C_9H_8ClN_2O]^+$ and $[C_9H_{10}NO]^+$ ions, respectively. The mass spectrum of the compound **Z_2B** shows five fragments peaks at m/z 364, 272, 250, 147 and m/z 105, and these peaks can be attributed to $[C_{15}H_{16}N_4O_3S_2]^{\bullet+}$, $[C_{12}H_{10}N_5OS]^+$, $[C_{10}H_{10}N_4O_2S]^{\bullet+}$, $[C_5H_{11}N_2OS]^+$ and $[C_3H_7NOS]^{\bullet+}$ ions, respectively. On the other hand, the mass spectrum of compound **Z_2B'** is characterized by the appearance of five fragmentation peaks at m/z 407, 303, 227, 199 and 134 which can be attributed to $[C_{18}H_{13}N_6OSe]^+$, $[C_9H_9N_2O_3SSe]^+$, $[C_9H_{10}NOSe]^+$, $[C_{10}H_9N_5]^{\bullet+}$ and $[C_8H_8NO]^+$ ions respectively. The base peaks at m/z 86 can be assigned to the $[C_4H_8NO]^+$ ion for most 2-azetidinone compounds. Successive degradation of the target compound and the appearance of different peaks due to various fragments

are good evidence for the molecular structure of the investigated compounds.

Biological Activity

The median lethal dose (LD_{50})

The lethal dose (LD_{50}) of the studied compounds (**Z_2E** and **Z_2E'**) *in-vivo* was determined in mice via intraperitoneally injecting dosages ranging from 500–750 mg/kg with equal spacing (concentrations) between doses. Our data revealed that LD_{50} values were 658.45 and 758.45 mg/kg for the compounds **Z_2E** and **Z_2E'**, respectively. The results may give an indication about the moderate toxicity effect of the studied compounds and clinical change observed in the mice after giving different doses. The toxic signs observed in injected mice may be manifested in some behaviors such as tremors, straight tail, salivation, urination, lacrimation, defecation, shortness of breath, excitation, muscle fasciculations, capillary bulge, convulsions and also the tortuous reflex in some treatments, and finally death at high toxic doses, Table 2 [40-41].

Antibacterial activity

The sensitivity of four human pathogenic microbes (two of Gram-positive bacteria: *S. aureus*, *Bacillus* and two of Gram-negative bacteria: *E. coli*, *P. aeruginosa*) to the new synthetic heterocyclic compounds (**Z_2B**, **Z_2B'**, **Z_2E** and **Z_2E'**) was tested and compared to that of the commercially available antibacterial antibiotic tetracycline. Our study confirmed that the thiazolidine-4-one and selenazolidin-4-one compounds had antibacterial activity (increases as the compound concentration increases) against the studied bacteria, also minimum inhibitory concentration MIC which can define as the lowest concentration of the compound in the medium which out visible growth of the test organisms in a concentration ranging from 1–500 mg/mL, as shown in Table 3–6.

In the present work, the antibacterial activity of the new synthetic compounds may be attributed to the fact that these two groups of bacteria differ by their cell wall component and their thickness. The ability of these new

Table 2. Toxicity results (LD_{50}) and toxic signs on mice

Test characterization	Results	
	Z_2E	**Z_2E'**
Doses range	500–650 = 150 mg/kg	500–750 = 250 mg/kg
First dose	500 mg/kg	500 mg/kg
Last dose	650 mg/kg	750 mg/kg
Up and down dose	50 mg/kg	50 mg/kg
Median lethal dose (LD_{50}) mg/kg	658.45 mg/kg	758.45 mg/kg
Effective dose (LD_{50} /10) mg/kg	65.845 mg/kg	75.84 mg/kg
No. of mice	8 (XOXXOXOO)	8 (XXOXOOXO)
Onset of toxic signs	5–16 min	5–24 min
Toxic signs	Rolling convulsions, excitation, salivation, choreoathetosis, tremors, death	Salivation, dyspnoea, convulsions, excitation, tremors, muscle fasciculation, death

Table 3. The inhibition zones (mm) against *Staphylococcus aureus*

Coms.	Diameter of inhibition zone (mm) *Staphylococcus aureus*						
	Concentration (mg/mL)						
	1	**5**	**25**	**125**	**250**	**500**	**MIC**
Z_2B	NI	13	14	29	33	37	5
Z_2B'	NI	NI	NI	NI	NI	15	500
Z_2E	NI	NI	NI	10	12	14	125
Z_2E'	NI	NI	17	18	21	23	25
Tetracycline*	NI	4	10	14	25	48	5

* Standard, NI = No Inhibition

Table 4. The inhibition zones (mm) against *Bacillus*

Coms.	Diameter of inhibition zone (mm) *Bacillus*						
	Concentration (mg/mL)						
	1	**5**	**25**	**125**	**250**	**500**	**MIC**
Z_2B	NI	11	18	40	45	50	5
Z_2B'	NI	NI	NI	12	15	16	125
Z_2E	NI	NI	NI	14	16	18	125
Z_2E'	NI	NI	18	20	21	26	25
Tetracycline*	5	11	14	22	30	50	1

* Standard, NI = No Inhibition

Table 5. The inhibition zones (mm) against *Pseudomonas aeruginosa*

Coms.	Diameter of inhibition zone (mm) *Pseudomonas aeruginosa*						
	Concentration (mg/mL)						
	1	**5**	**25**	**125**	**250**	**500**	**MIC**
Z_2B	NI	NI	10	11	12	22	25
Z_2B'	NI	NI	NI	12	12	13	125
Z_2E	NI	NI	NI	NI	30	40	250
Z_2E'	NI	NI	19	20	24	26	25
Tetracycline*	NI	6	8	17	30	52	5

* Standard, NI = No Inhibition

Table 6. The inhibition zones (mm) against *Escherichia coli*

Coms.	Diameter of inhibition zone (mm) *Escherichia coli*						
	Concentration (mg/mL)						
	1	**5**	**25**	**125**	**250**	**500**	**MIC**
Z_2B	NI	NI	10	10	14	20	25
Z_2B'	NI	NI	NI	NI	10	12	250
Z_2E	NI	NI	NI	20	25	29	125
Z_2E'	NI	13	20	20	20	24	5
Tetracycline*	NI	8	11	15	21	44	5

* Standard, NI = No Inhibition

compounds to cause the bacterial colonies to disintegrate probably results from their interference with the bacterial cell wall, thereby inhibiting the microbial growth [42]. Among the new synthetic heterocyclic compounds, **Z_2E'** was found to be more effective than the positive control (tetracycline) against Gram-negative bacteria (*E. coli*) with an inhibition zone (IZ) of 13, 20 and 20 mm at the concentration of 5, 25 and 125 mg/mL, respectively. This result may come from the fact that the membrane of Gram-negative bacteria is surrounded by an outer membrane containing lipopolysaccharides, which makes the compound able to combine with the lipophilic layer in order to enhance the permeability of the membrane to Gram-negative bacteria. In conclusion, the antibacterial activity of any compound may be related to the cell wall structure of bacteria due to the importance of this wall for bacterial survival. Thus, the ability of antibiotics to kill or inhibit the growth of bacteria may be through inhibition of a step in peptidoglycan synthesis by gram-positive bacteria [43-44].

In the case of antibacterial activity against Gram-positive bacteria (*S. aureus* and *Bacillus*), all compounds were found to have activity ranging between high and moderate. Our results indicated that the compound **Z_2B**

possessed the highest antibacterial activity against Gm+Ve (*S. aureus*) with an IZ of 13, 14, 29, and 33 mm at concentrations of 5, 25, 125, and 250 mg/mL, respectively. Also, the **Z_2B** compound showed more potent compared to the positive control IZ = 4–25 mm at the same concentration. On the other hand, our data pointed out that compound **Z_2B** showed a good antibacterial activity against Gm+Ve (*Bacillus*) with an IZ ranging from 11–45 mm as compared to tetracycline IZ = 11–30 mm at the concentrations 5–250 mg/mL.

All the thiazolidine-4-one or selenazolidin-4-one drugs are selective inhibitors of bacterial cell wall synthesis and therefore active against growing bacteria [44]. The biological activity of 4-thiazolidinone skeleton is believed to be associated with the chemical reactivity of the ring and on the substituents, especially in the nitrogen of 4-thiazolidinone ring [44]. Furthermore, the mechanism of action of sulfonamide is inhibition of the action of dihydropteroate synthase and blocking the net biosynthesis of folate coenzymes. Therefore, it represents bacteriostatic compounds [45].

The MIC of tested compounds in this study against the test organisms ranged between 1–500 mg/mL, Table 3–6. Antimicrobial agents with low activity against an organism had a high MIC while a highly active antimicrobial agent gave a low MIC. The most resistant microorganisms were *E. coli* and *P. aeruginosa*, whereas the most sensitive microorganisms were *S. aureus* and *Bacillus*. The lowest MIC value of 5 mg/mL was recorded on *S. aureus* and on *Bacillus* with compound **Z_2B**. The compound **Z_2E'** was more active as compared with its precursors and had the lowest MIC value of 5 mg/mL obtained on *E. coli* and on *P. aeruginosa*. However, the highest MIC value of 250 mg/mL was recorded on *E. coli* and on *P. aeruginosa* with compounds (**Z_2B'** and **Z_2E**), whereas the highest MIC values of 500 and 125 mg/mL were obtained on *S. aureus* and on *Bacillus* with compounds **Z_2B'** and **Z_2E**, respectively. The results of the present study suggest that the thiazolidine-4-one and selenazolidin-4-one compounds possess remarkable toxic activity against bacteria and may assume pharmacological importance [46].

Antioxidant activity

Reactive oxygen species (ROS) such as superoxide anions, hydrogen peroxide, hydroxyl, and nitric oxide radicals are generated during the bioorganic redox process and normal cellular metabolism. They play a significant role in oxidative stress related to the development and pathogenesis of life-limiting various diseases such as cancer, diabetes mellitus, arteriosclerosis, rheumatoid arthritis, and others [27].

The results in Table 7 and Fig. 1–4 indicated an increase in the antioxidant activity of the synthetic compounds and standard in the order of **Z_2d** < **Z_2B'** < **Z_2e** < **Z_2g** < **Z_2E'** < **Z_2b** < BHT with corresponding percentages values of 50.0, 53.0, 57.2, 57.7, 68.8, 73.0, and 82.3%, respectively. On the other hand, the lowest activity was observed for compounds **Z_2B**, **Z_2a**, **Z_2E**, and **Z_2c** with corresponding inhibition ratios 48.4, 47.4, 35.8,

Table 7. Antioxidant activity of prepared compounds, the values are the mean ± SD

Comp. symbol	Aj	At	Aj*	At*	AA%
BHT	0.582 ± 0.01	0.544 ± 0.011	0.456 ± 0.031	0.241 ± 0.016	82.3
Z_2a	0.527 ± 0.015	0.414 ± 0.023	0.456 ± 0.031	0.241 ± 0.016	47.4
Z_2b	0.479 ± 0.004	0.421 ± 0.019	0.456 ± 0.031	0.241 ± 0.016	73
Z_2c	0.474 ± 0.003	0.329 ± 0.028	0.456 ± 0.031	0.241 ± 0.016	32.6
Z_2d	0.573 ± 0.017	0.466 ± 0.008	0.456 ± 0.031	0.241 ± 0.016	50
Z_2e	0.561 ± 0.013	0.469 ± 0.014	0.456 ± 0.031	0.241 ± 0.016	57.2
Z_2g	0.463 ± 0.005	0.372 ± 0.018	0.456 ± 0.031	0.241 ± 0.016	57.7
Z_2B	0.540 ± 0.009	0.429 ± 0.012	0.456 ± 0.031	0.241 ± 0.016	48.4
Z_2B'	0.487 ± 0.007	0.386 ± 0.021	0.456 ± 0.031	0.241 ± 0.016	53
Z_2E	0.557 ± 0.013	0.419 ± 0.008	0.456 ± 0.031	0.241 ± 0.016	35.8
Z_2E'	0.459 ± 0.003	0.392 ± 0.014	0.456 ± 0.031	0.241 ± 0.016	68.8

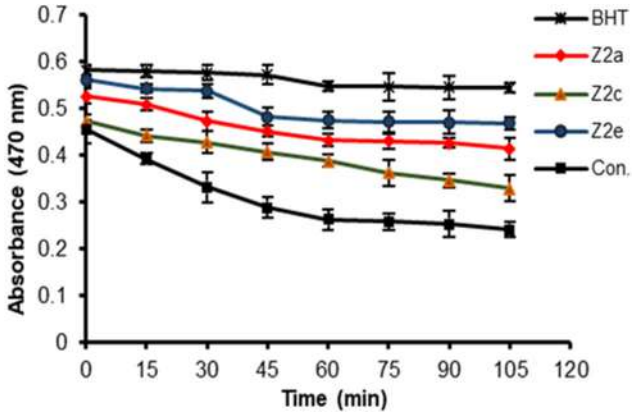

Fig 1. Antioxidant activity of compounds **Z_2a**, **Z_2c** and **Z_2e**

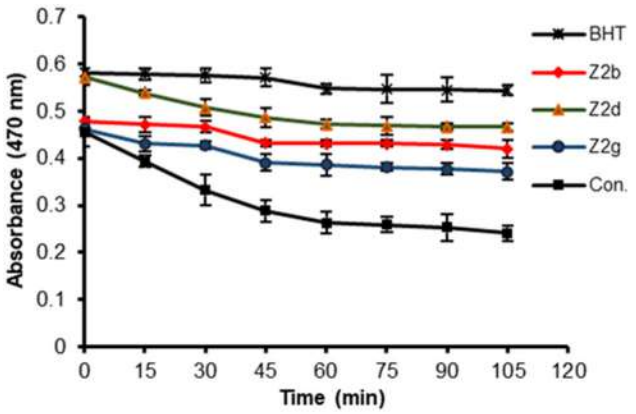

Fig 2. Antioxidant activity of compounds **Z_2b**, **Z_2d** and **Z_2g**

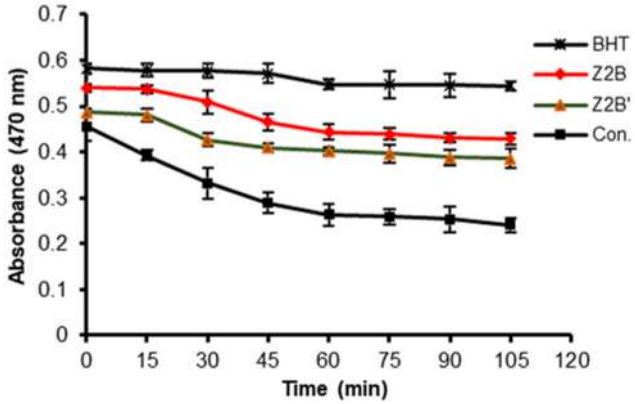

Fig 3. Antioxidant activity of compounds **Z_2B** and **Z_2B'**

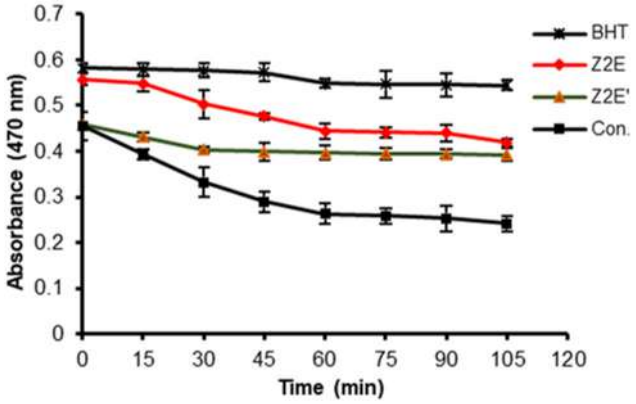

Fig 4. Antioxidant activity of compounds **Z_2E** and **Z_2E'**

and 32.6%, respectively. A possible explanation for the higher antioxidant activity of these compounds (**Z_2b**, **Z_2E'**, **Z_2g**, **Z_2e**, **Z_2B'** and **Z_2d**) might be due to the following reasons. First, since compounds **Z_2b** and **Z_2d** have an additional methyl group which increases the antioxidant activity, this activity may be correlated with the introduction of electron donor substituent which stabilizes the generated radical during oxidation [47]. Second, compounds **Z_2E'** and **Z_2B'** have Se-C moieties in 4-selenazolidinone ring which increase the antioxidant activity by the interaction with the active site of protein to form a new seleno-protein (Enz-Se) moiety in the active site [51]. Furthermore, the organoselenium compounds had the ability to catalyze the reduction of harmful peroxides by glutathione (GSH) and thereby protect the biomolecules against oxidative damage. Third, compounds (**Z_2b**, **Z_2g**, **Z_2e** and **Z_2d**) have a β-lactam ring which can act as a scavenger for radicals to prevent oxidative cellular damage and thus enhance antioxidant properties [48].

The finding that compound **Z_2b** possessed a strong protective effect is interesting and points to the potential use of this new compound as an agent to overcome oxidative stress that is associated with cellular metabolism and disease conditions [52]. The mechanism by which **Z_2b** protects the body's cells from oxidative damage may require further study and investigation.

Interestingly, the relative antioxidant effect of some β-lactam or 4-thiazo and 4-selenazolidinone antibiotics such as ampicillin on oxygen-reactive species (ROS) has been reported, and a possible therapeutic role for β-lactam agents in protecting host tissues from oxidative damage has been proposed. The keto lactam ring or thiazolidine ring is responsible for initiating the free radical scavenging activity due to its N-H and C=O moieties [49-50].

Notably, scientific studies have confirmed that compounds in general, including those that have antioxidant properties, may be subjected to metabolism *in vivo* through specialized enzymatic systems in the body, which often convert lipophilic chemical compounds into polar products that are easily secreted. Therefore, we expect that **Z_2d** and other new synthetic compounds enter different metabolic pathways in the body that may modify differently from their structure and/or toxicity, and this requires further research. Again, the exact possible mechanism via which compound **Z_2b** and the new other synthetic compounds protect against oxidative damage will be a matter of future studies and must be confirmed in a more controlled experimental design [27].

Cell cytotoxicity (anticancer) study

One of the first goals of researchers and scientists is to discover and develop a new anti-cancer drug that has good efficacy and does not cause any of the side effects of current chemotherapy drugs. Therefore, the need for a time-saving, low-cost, high-throughput drug efficacy testing system has led to the emergence of an *in vitro* model cytotoxicity testing on human cancer cell lines [50-51].

In this work, the cytotoxic effects of the synthesized compounds against breast cancer cell line (MCF-7) were evaluated using 5-fluorouracil (5-FU) as a reference cytotoxic drug. The IC_{50} and cell viability percent of MCF-7 cancerous at different concentrations ranging from 6.25–100 µg/mL are given in Table 8 and Fig. 5–7. The results showed that compound **Z_2E** was comparable to that of 5-FU (positive control), while compound **Z_2E'** (IC_{50} = 24.87 µg/mL) is a more cytotoxic agent than 5-FU (IC_{50} = 97.47 µg/mL), Table 8. It is evident that the tested compounds showed anticancer activity in all concentrations and the effects of these compounds were dose-dependent, *i.e.*, by increasing the concentration in the culture media; the percentage of cells viability is decreased (this means that the percentage of dead cells has increased). IC_{50} values ranged from 24.87 to 97.47 µg/mL. Also, we can note that the cytotoxic activity of compound **Z_2E'** was higher in cancerous cells when compared with the compound **Z_2E**,

Table 8. The IC_{50} values and the percent of cell viability of the tested compounds in breast cancer cell line MCF-7, the values are the mean ± SD

Coms.	Cell viability %						IC_{50} (µg/mL)
	Concentration (µg/mL)						
	6.25	12.5	25	50	75	100	
Z_2E	99.06 ± 0.83	98.68 ± 0.91	96.13 ± 1.15	94.10 ± 0.09	79.41 ± 0.52	34.35 ± 0.08	90.92
Z_2E'	98.84 ± 1.12	97.57 ± 1.09	49.11 ± 1.44	18.17 ± 2.01	17.48 ± 0.15	16.99 ± 0.02	24.87
5-Fluorouracil	83.13 ± 0.86	80.69 ± 1.07	72.76 ± 0.86	66.57 ± 1.06	58.93 ± 0.61	49.29 ± 0.06	97.47

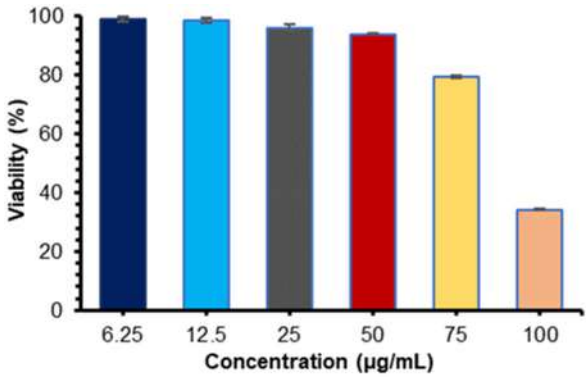

Fig 5. Anticancer activity of compound **Z_2E** at 6.25–100 µg/mL

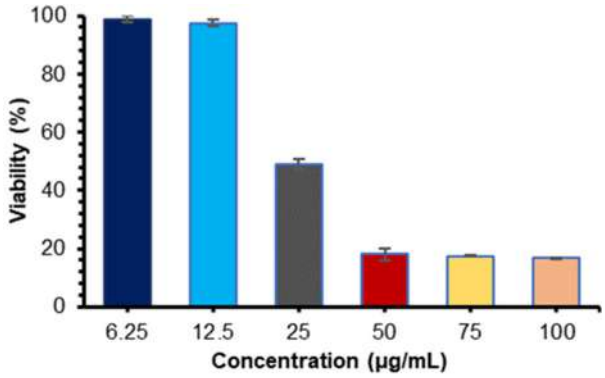

Fig 6. Anticancer activity of compound **Z_2E'** at 6.25–100 µg/mL

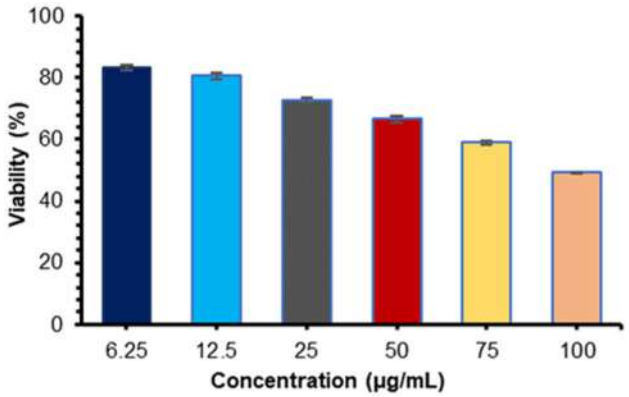

Fig 7. Anticancer activity of drug **5-Fluorouracil** at 6.25–100 µg/mL

especially at a concentration of 25 µg/mL.

Thiazolidine-4-one compounds revealed their pharmaceutical significance as anticancer agents. Numerous antitumor thiazolidinones are currently used to treat cancer, such as anthracyclines, bleomycin, mitomycin C, dactinomycin, and mithramycin. The major mechanism of action for these antitumor thiazolidinones is inhibition of cell wall synthesis, DNA intercalation or inhibition of DNA synthesis [51-52]. The presence of 4-thiazolidinone ring in the molecular structure of compounds **Z_2E** and **Z_2E'** is related to anticancer activity by inhibiting the transpeptidase enzyme, which catalyzes the cross-linking of the peptidoglycan strands in the cell wall phase of the cancer cell wall biosynthesis. The thiazolidinone or selenazolidinone ring can bind to the active site of the transpeptidase enzyme since its structure resembles that

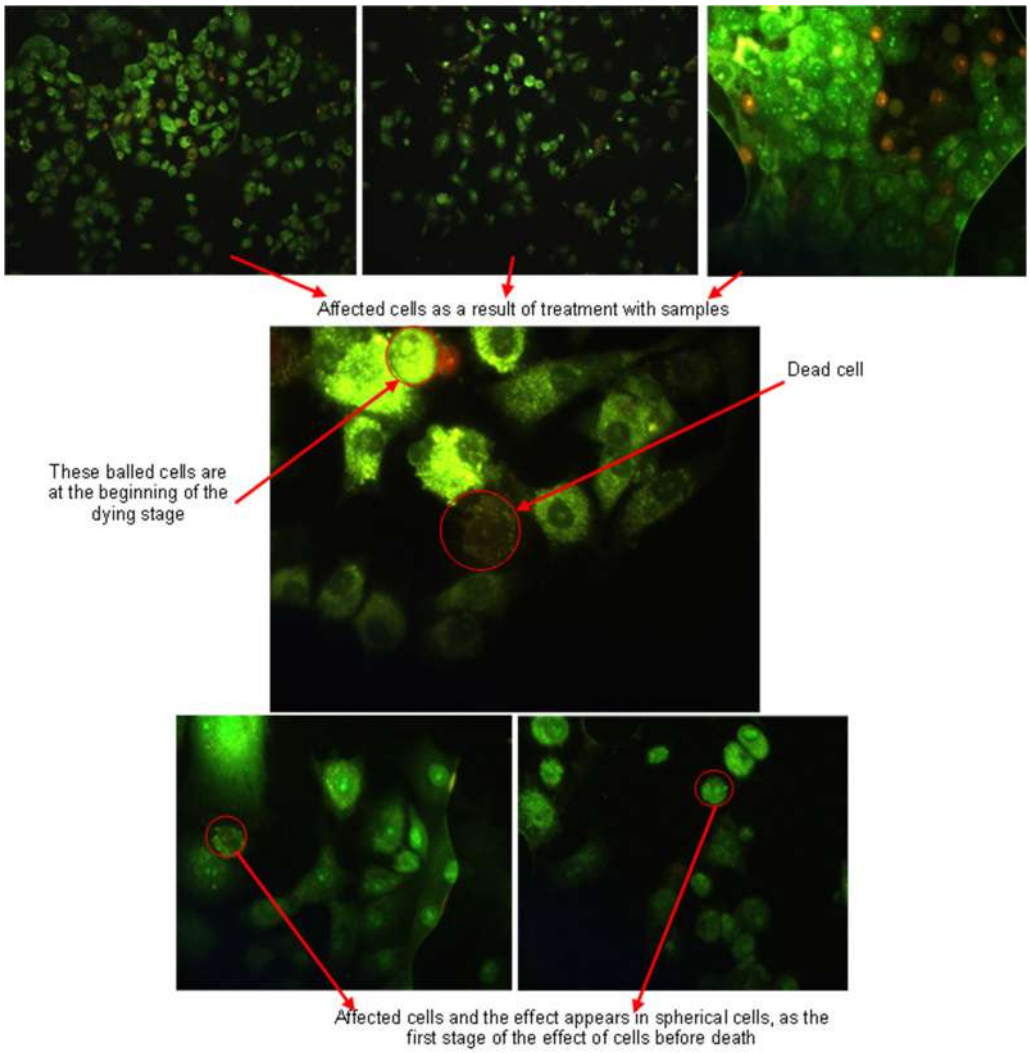

Fig 8. Anticancer activity of compound **Z_2E** at 75–100 µg/mL

of the substrate, which is the terminal D-ala-D-ala dipeptide of the pentapeptide of each monomer unit [47]. Note that D-ala-D-ala dipeptide of the substrate can exist in multiple conformations formed by rotation around the C-C single bonds but a thiazolidine-4-one molecule has a limited variety of conformation because of the rigidity of the five-membered ring [48]. Of the many conformations possible for the terminal dipeptide the one that binds to the enzyme resembles the structure of the thiazolidine-4-one ring, and thus, the two can compete for binding to the active site of the enzyme. The -C(O)-N bond of the thiazolidine-4-one or selenazolidin-4-one mimics the -C(O)-N of the peptide bond of the terminal dipeptide. Therefore, inhibition the formation of the cancer cell wall, which leads to cells death [46,49]. Banik et al. [50,52] also show that thiazolidine-4-ones with polyaromatic substituents induce tumor cell death in a variety of breast cancer cell lines. As well, the presence of (-S-C-N- and -Se-C-N-) moieties in the tested compounds is related to anticancer activity by the interaction with the active site of protein through hydrogen bonding bringing about the hindrance development of cells [50]. However, several novel classes of thiazolidine-4-ones and selenazolidin-4-ones have been shown to possess anticancer properties as well [52].

On the other hand, the present results clearly indicated that the compounds **Z_2E** and **Z_2E'** had an ability to induce apoptosis of MCF-7 Cells, as illustrated in Fig. 8–9. Acridine orange (AO) is a vital dye and will stain the nuclei of both live and dead cells to green while ethidium bromide (EB) will stain only cells that have lost membrane integrity to red. Thus, live cells will appear uniformly green while early apoptotic cells will have condensed or fragmented nuclei with bright green color. Late apoptotic cells will show condensed and fragmented orange chromatin. The results showed that increased the compound **Z_2E'** concentration resulted in gradual increases in orange and red staining accompanied by reductions in green staining of nuclei, indicating cell damage and apoptosis (Fig. 9). Therefore, a high concentration (100 µg/mL) of **Z_2E'** could cause serious membrane damage in around 84% of cells. Moreover, these results indicate that the apoptotic rate gradually increases with the **Z_2E** and **Z_2E'** concentrations and treatment time. It is verified that at around 25 µg/mL **Z_2E'** can induce half of the cells to undergo apoptosis at 48 h, consistent with the IC_{50} results.

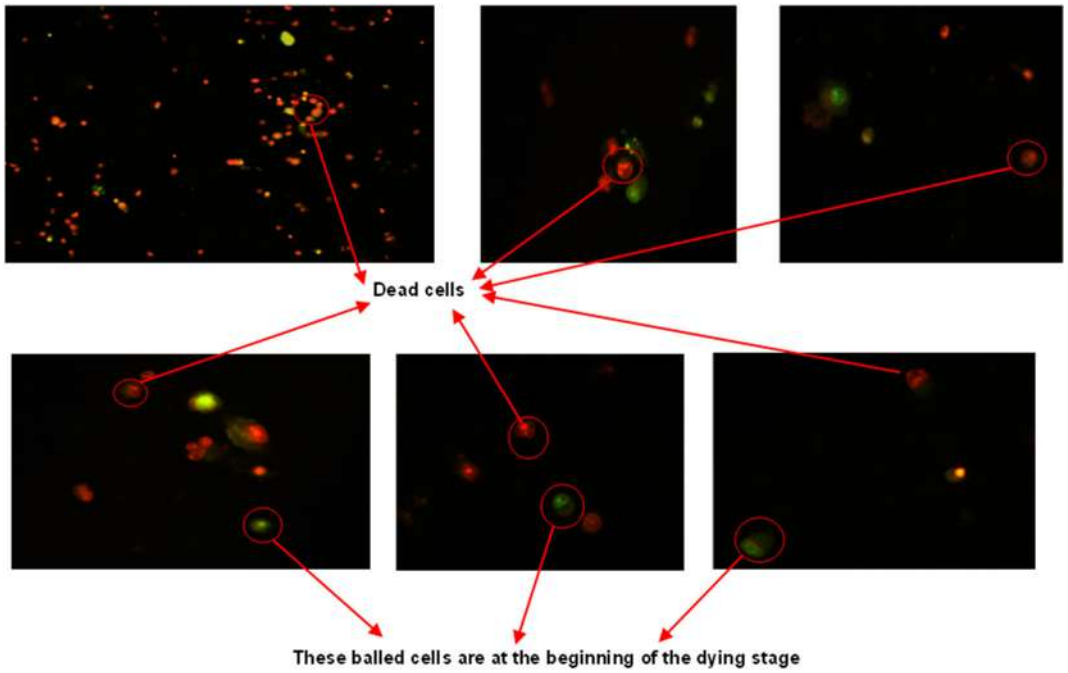

Fig 9. Anticancer activity of compound **Z_2E'** at 12.5–25 µg/mL

■ CONCLUSION

In this study new series of 2-azetidinone (**Z_2a**-**Z_2e**, **Z_2g**), thiazolidinone and selenazolidinone derivatives (**Z_2B**, **Z_2E**, **Z_2B'**, **Z_2E'**) have been designed and synthesized starting based on sulfonamide. The proposed structures of all the synthesized compounds were proved using spectral methods. The newly synthesized compounds were evaluated for their *in vitro* antibacterial, antioxidant, toxicity, and anticancer activities. Results of the LD_{50} test using Dixon's up and down method indicated that the compound containing selenium (**Z_2E'**) was less toxic than its analogs containing sulfur (**Z_2E**). Although their antimicrobial potential was good, **Z_2E'** compound was more active against Gram-negative bacteria with the lowest MIC value of 5 mg/mL. All compounds showed antioxidant activity, but **Z_2b** was the main compound that possesses strong activity as antioxidants (73%). *In vitro* MTT viability assay indicated that all tested compounds had cytotoxic effects on MCF-7 cells after 72 h of treatment. The results revealed that **Z_2E'** and **Z_2E** compounds possessed strong activity with good IC_{50} = 24.8 and 90.9, respectively at a higher rate than the standard compound 5-FU, IC_{50} = 97.47. These results support that **Z_2E'** has potential properties as a promising drug in several diseases such as breast cancer due to their numerous pharmacological and biological activities.

■ ACKNOWLEDGMENTS

The authors are highly thankful to the head of the Chemistry Department, College of Science, the University of Basrah for providing their kind support and facilities to accomplish the present research project within time.

■ REFERENCES

[1] Mansour, A.M., 2014, Selective coordination ability of sulfamethazine Schiff-base ligand towards copper (II): Molecular structures, spectral and SAR study, *Spectrochim. Acta, Part A*, 123, 257–266.

[2] Claudel, M., Schwarte, J.V., and Fromm, K.M., 2020, New antimicrobial strategies based on metal complexes, *Chemistry*, 2 (4), 849–899.

[3] Tačić, A., Nikolić, V., Nikolic, L., and Savić, I., 2017, Antimicrobial sulfonamide drugs, *Adv. Technol.*, 6 (1), 58–71.

[4] Al-Atbi, H.S., Al-Assadi, I.J., Al-Salami, B.K., and Badr, S.Q., 2020, Study of new azo-azomethine derivatives of sulfanilamide: Synthesis, characterization, spectroscopic, antimicrobial, antioxidant and anticancer activity, *Biochem. Cell. Arch.*, 20 (2), 4161–4174.

[5] Bytyqi-Damoni, A., Genç, H., Zengin, M., Demir, D., Gençer, N., and Arslan, O., 2020, Novel β-lactam compounds as activators for polyphenoloxidase, *ChemistrySelect*, 5 (25), 7671–7674.

[6] Elkanzi, N.A.A., 2013, Short review on synthesis of thiazolidinone and *β*-lactam, *World J. Org. Chem.*, 1 (2), 24–51.

[7] Martelli, G., and Giacomini, D., 2018, Antibacterial and antioxidant activities for natural and synthetic dual-active compounds, *Eur. J. Med. Chem.*, 158, 91–105.

[8] Piens, N., 2017, Synthesis of new β-lactam building blocks and their application in heterocyclic Chemistry, *Dissertation*, Faculty of Bioscience Engineering, Ghent University, Belgium.

[9] Elkanzi, N.A.A., and Mohamed, N.M.M., 2014, Synthesis and antimicrobial activity of β-lactams: Antibacterial activities and antifungal activities, *Heterocycl. Lett.*, 4 (1), 153–182.

[10] Salamanca, C.H., Yarce, C.J., Roman, Y., Davalos, A.F., and Rivera, G.R., 2018, Application of nanoparticle technology to reduce the anti-microbial resistance through β-lactam antibiotic-polymer inclusion nano-complex, *Pharmaceuticals*, 11 (1), 19.

[11] Bhalla, A., Bari, S.S., Berry, S., Bhalla, J., Vats, S., Mandal, S., and Khullar, S., 2015, Facile synthesis of novel monocyclic *trans*- and *cis*-3-oxy/thio/seleno-4-pyrazolyl-β-lactams, *ARKIVOC*, 2015 (7), 10–27.

[12] Patel, J.A., Mistry, B.D., and Desai, K.R., 2008, Conventional and microwave induced synthesis of various azetidinone and thiazolidinone derivatives from 3-[(1E)-1-aza-2-(2-chloro-7-methoxy-3-quinolyl)-vinyl]-4-(aryldiazenyl) phenol and their antimicrobial screening, *Indian J. Chem., Sect. B*, 47B (10), 1695–1700.

[13] Chaban, Z., Harkov, S., Chaban, T., Klenina, O., Ogurtsov, V., and Chaban, I., 2017, Recent advances in synthesis and biological activity evaluation of condensed thiazoloquinazolines: A review, *Pharmacia*, 64 (3), 52–66.

[14] Neri, R., and Bossmann, S.H., 2021, Isoselenocyanates: Synthesis and their use for preparing selenium-based heterocycles, *Synthesis*, 53 (12), 2015–2028.

[15] Nirwan, S., Chahal, V., and Kakkar, R., 2019, Thiazolidinones: Synthesis, reactivity, and their biological applications, *J. Heterocycl. Chem.*, 56 (4), 1239–1253.

[16] Trotsko, N., 2021, Antitubercular properties of thiazolidin-4-ones–A review, *Eur. J. Med. Chem.*, 215, 113266.

[17] Banerjee, B., and Koketsu, M., 2017, Recent developments in the synthesis of biologically relevant selenium-containing scaffolds, *Coord. Chem. Rev.*, 339, 104–127.

[18] Abd Al-khaliq, Z.M., 2015, Synthesis, characterization and antibacterial activity of new series of sulfamethoxazole derivatives, *Thesis*, College of Pharmacy, University of Al-Mustansiriyah, Baghdad, Iraq.

[19] Sahu, P.K., Kim, G., Yu, J., Ahn, J.Y., Song, J., Choi, Y., Jin, X., Kim, J.H., Lee, S.K., Park, S., and Jeong, L.S., 2014, Stereoselective synthesis of 4′-selenonucleosides via seleno-Michael reaction as potent antiviral agents, *Org. Lett.*, 16 (21), 5796–5799.

[20] Desai, N.C., Harsora, J.P., Monapara, J.D., and Khedkar, V.M., 2021, Synthesis, antimicrobial capability and molecular docking of heterocyclic scaffolds clubbed by 2-azetidinone, thiazole and quinoline derivatives, *Polycyclic Aromat. Compd.*, 0, 1–15.

[21] Ramachandran, S., Cheriyan, B.V., and Aanandhi, M.V., 2021, Activities of thiazolidine-4-one and azetidine-2-one derivatives-A review, *Res. J. Pharm. Technol.*, 14 (8), 4513–4516.

[22] Jarrahpour, A., Rezaei, S., Sinou, V., Latour, C., and Brunel, J.M., 2017, Synthesis of some novel 3-spiro monocyclic β-lactams and their antibacterial and antifungal investigations, *Iran. J. Sci. Technol., Trans. A: Sci.*, 41 (2), 337–342.

[23] Al-Masoudi, W.A., Al-Diwan, M.A., and Hassan, I.J., 2015, Synthesis, acute toxicity and modelling docking studies of azo compound derived from sulphonamide and pyrimidine derivative, *Pharma Chem.*, 7 (9), 1–5.

[24] Ahmad, M.F., 2018, *Ganoderma lucidum*: Persuasive biologically active constituents and their health endorsement, *Biomed. Pharmacother.*, 107, 507–519.

[25] Al-Fregi, A.A., Al-Fadhly, A.L., and Al-Salami, B.K., 2017, Synthesis, characterization and biological activity study of some new palladium(II) complexes containing amine or azomethine groups, *Eur. J. Chem.*, 8 (2), 155–161.

[26] Rusmana, D., Wahyudianingsih, R., Elisabeth, M., Balqis, B., Maesaroh, M., and Widowati, W., 2017, Antioxidant activity of Phyllanthus niruri extract, rutin and quercetin, *InaBJ*, 9 (2), 84–90.

[27] Al-Fartosy, A.J.M., 2011, Antioxidant properties of methanolic extract from *Inula graveolens* L., *Turk. J. Agric. For.*, 35 (6), 591–596.

[28] Al-Shammari, A.M., Al-Esmaeel, W.N., Al-Ali, A.A., Hassan, A.A., and Ahmed, A.A., 2019, Enhancement of oncolytic activity of Newcastle disease virus through combination with retinoic acid against digestive system malignancies, *Mol. Ther.*, 27 (4), 126–127.

[29] Sharma, A., and Puhar, A., 2019, Gentamicin protection assay to determine the number of intracellular bacteria during infection of human TC7 intestinal epithelial cells by *Shigella flexneri*, *Bio-Protoc.*, 9 (13), e3292.

[30] Liu, K., Liu, P.C., Liu, R., and Wu, X., 2015, Dual AO/EB staining to detect apoptosis in osteosarcoma cells compared with flow cytometry, *Med. Sci. Monit. Basic Res.*, 21, 15–20.

[31] Mahdi, I.S., Yousif, S.A., and Khammas, S.J., 2019, Synthesis and characterization of some new (tetrazole, thiazolidin-4-one) compounds derived from drugs and evaluation of their biological activities, *Int. J. Pharm. Qual. Assur.*, 10 (4), 720–727.

[32] Bhaskar, V.H., and Mohite, P.B., 2011, Synthesis analgesic, Anti-Inflammatory and antimicrobial activities of some 1-[5-(substituted phenyl)-4,5-dihydro-1*H*-pyrazol-3-yl]-5-phenyl-1*H*-tetrazole, *J. Optoelectron. Biomed. Mater.*, 3 (1), 7–16.

[33] Verma, V.A., Saundane, A.R., Meti, R.S., Shamrao, R., and Katkar, V., 2020, Synthesis, biological evaluation and docking studies of some new indolyl-pyridine containing thiazolidinone and azetidinone analogs, *Polycyclic Aromat. Compd.*, 42 (4), 1545–1559.

[34] Al-Rubaie, A.Z., Al-Masoudi, W.A., Hameed, A.J., Yousif, L.Z., and Graia, M., 2008, Synthesis, reaction and antiviral activity of 2,4-diaryl-1,3-selenazoles, *J. Korean Chem. Soc.*, 52 (1), 36–46.

[35] Alam, S., Hasan, P., Aneja, B., Ahmad, M.B., and Abid, M., 2016, $POCl_3$ mediated Staudinger reaction of imines with ketenes: Synthesis of monocyclic β-lactam and 1,3-oxazinone derivatives, *Rasayan J. Chem.*, 9 (2), 101–111.

[36] Xie, Y., Liu, J., and Li, J., 2011, Selective synthesis of novel 2-imino-1,3-selenazolidin-4-ones and 2-amino-1,3,4-selenadiazin-5-ones from isoselenocyanates, *Tetrahedron Lett.*, 52 (8), 932–935.

[37] Saini, N., Sharma, A., Thakur, V.K., Makatsoris, C., Dandia, A., Bhagat, M., and Sharma, P.C., 2020, Microwave assisted green synthesis of thiazolidin-4-one derivatives: A perspective on potent antiviral and antimicrobial activities, *Curr. Res. Green Sustainable Chem.*, 3, 100021.

[38] Rafique, J., Canto, F.S.R., Saba, S., Barbosa, F.A.R., and Braga, A.L., 2016, Recent advances in the synthesis of biologically relevant selenium-containing 5-membered heterocycles, *Curr. Org. Chem.*, 20 (2), 166–188.

[39] Sharp, D.J., Rogers, G.C., and Scholey, J.M., 2000, Microtubule motors in mitosis, *Nature*, 407 (6800), 41–47.

[40] Usui, K., Nishida, S., Sugita, T., Ueki, T., Matsumoto, Y., Okumura, H., and Sekimizu, K., 2016, Acute oral toxicity test of chemical compounds in silkworms, *Drug Discoveries Ther.*, 10 (1), 57–61.

[41] Thomba, D.U., Mirgane, S.R., Ambhure, R.U., Pawar, R.P., and Ameta, K.L., 2017, Synthesis and antimicrobial study of novel Schiff bases and metal complexes, *Biochem. Biophys.*, 3, 7–11.

[42] Sevgi, F., Bagkesici, U., Kursunlu, A. N., and Guler, E., 2018, Fe (III), Co (II), Ni (II), Cu (II) and Zn (II) complexes of Schiff bases based-on glycine and phenylalanine: Synthesis, magnetic/thermal properties and antimicrobial activity, *J. Mol. Struct.*, 1154, 256–260.

[43] Opoku-Temeng, C., Naclerio, G.A., Mohammad, H., Dayal, N., Abutaleb, N.S., Seleem, M.N., and Sintim, H.O., 2018, N-(1,3,4-oxadiazol-2-yl)benzamide analogs, bacteriostatic agents against methicillin-and vancomycin-resistant bacteria, *Eur. J. Med. Chem.*, 155, 797–805.

[44] Dhanya, S., and Aravind, A., 2015, Synthesis, characterization and evaluation of antioxidant activities of some new quinazolino-acetidinone derivatives, *J. Chem. Pharm. Res.*, 7 (12), 849–856.

[45] AL-Salami, B.K., AL-Khazragie, Z.K., and Al-Fregi, A.A., 2018, Synthesis, characterization, antimicrobial activity and antioxidant of azo Schiff bases containing sulfanilamide, *J. Global Pharma Technol.*, 10 (3), 952–962.

[46] Kuhn, D., Coates, C., Daniel, K., Chen, D., Bhuiyan, M., Kazi, A., Turos, E., and Ping Dou, Q., 2004, Beta-lactams and their potential use as novel anticancer chemotherapeutics drugs, *Front. Biosci.*, 9 (4), 2605–2617.

[47] Mohana, K.N., and Kumar, C.B.P., 2013, Synthesis and antioxidant activity of 2-amino-5-methylthiazol derivatives containing 1,3,4-oxadiazole-2-thiol moiety, *Int. Scholarly Res. Not.*, 2013, 620718.

[48] Singh, F.V., and Wirth, T., 2018, "Synthesis of Organoselenium Compounds with Potential Biological Activities" in *Organoselenium Compounds in Biology and Medicine: Synthesis, Biological and Therapeutic Treatments*, Eds. Jain V.K., and Priyadarsini K.I., The Royal Society of Chemistry, London, UK, 77–121.

[49] Eruygur, N., Koçyiğit, U.M., Taslimi, P., Ataş, M., Tekin, M., and Gülçin, İ., 2019, Screening the *in vitro* antioxidant, antimicrobial, anticholinesterase,

antidiabetic activities of endemic *Achillea cucullata* (Asteraceae) ethanol extract, *S. Afr. J. Bot.*, 120, 141–145.

[50] Bhattacharjee, M.K., 2016, "Antibiotics That Inhibit Cell Wall Synthesis" in *Chemistry of Antibiotics and Related Drugs*, Springer, Cham, Switzerland, 49–94.

[51] Al-Fartosy, A.J.M., and Ati, M.H., 2021, A predictive clinical markers to make prostate cancer and benign prostate hyperplasia easy diagnosis, *Biochem. Cell. Arch.*, 21 (2), 2939–2947.

[52] El-Desoky, S.I., Badria, F.A., Abozeid, M.A., Kandeel, E.A., and Abdel-Rahman, A.H., 2013, Synthesis and antitumor studies of novel benzo pyrano-1,2,3-selenadiazole and spiro[benzopyrano]-1,3,4-thiadiazoline derivatives, *Med. Chem. Res.*, 22 (5), 2105–2114.

Application of Poly(Ethyl Eugenyl Oxyacetate) Compounds as the Ions Carrier for Heavy Metals Separation and Separation of Fe and Ni in Ferronickel Using Liquid Membrane Transport Method

La Harimu[1*], Sabirin Matsjeh[2], Dwi Siswanta[2], Sri Juari Santosa[2], and Muhamad Jalil Baari[3]

[1]*Department of Chemistry Education, Faculty of Teacher Training and Education, Universitas Halu Oleo, Jl. Kampus Hijau Bumi Tridharma, Anduonou, Kendari 93132, Indonesia*

[2]*Department of Chemistry, Faculty of Mathematics and Natural Sciences, Universitas Gadjah Mada, Sekip Utara, Yogyakarta 55281, Indonesia*

[3]*Department of Chemistry, Faculty of Science and Technology, Universitas Sembilanbelas November Kolaka, Jl. Pemuda, Kolaka 93511, Indonesia*

**** Corresponding author:***

email: harim_l@yahoo.com

Received: January 24, 2022
Accepted: July 19, 2022

DOI: 10.22146/ijc.72486

Abstract: *Poly(ethyl eugenyl oxyacetate) (PEEOA) had been synthesized for separating heavy metals like Fe(III), Cr(III), Cu(II), Ni(II), Co(II), and Pb(II) by liquid membrane transport method. The effects of pH, ion carrier volume, stripping concentration, transport time, and metal ion concentration were investigated to obtain optimum conditions. Experimental results showed that optimum pH occurred at pH 4 for Fe(III) ions and pH 5 for others. Carrier volumes were optimum at 8.5 mL for Fe(III) and Pb(II) ions but 7.5 mL for others. The optimum concentrations of the stripping phase were 2 M for Fe(III) and Cu(II) ions, 1 M for Cr(III), Ni(II), Co(II) ions, and 0.5 M for Pb(II) ion. Transport times were optimum at 36 h for Fe(III) and Co(II) ions and 48 h for others. The optimum metal ion concentrations were 0.25 mM for Fe(III) and Cr(III) ions, while other ions were 0.1 mM. The response of PEEOA to Fe(III) ion was the best with selectivity order, Fe(III) > Cr(III) > Pb(II) > Cu(II) > Ni(II) > Co(II). PEEOA also could separate Fe and Ni in a ferronickel sample whose transport percents were 8.87 and 0.92%, respectively. Hence, PEEOA is reasonably effective as an ions carrier for separating metal ions individually or ionic mixture and also in a ferronickel compound.*

Keywords: *poly(ethyl eugenyloxyacetic acid); metal ion; transport; liquid membrane; ion carrier*

■ INTRODUCTION

The presence of heavy metals in a water environment and wastewater must be minimized. It directly relates to environmental sustainability and the health of surrounding organisms. The separation of metal ions from a particular mixture is challenging for scientists. It is affected by the similar tendency of metal ions to interact or bind with other substances. Thus, appropriate methods and selective ion carriers are required. A method that can separate and purify specified substances is liquid membrane transport due to its selectivity, efficiency, and relatively simple [1]. Macrocyclic and macromolecular compounds are mainly concerned by researchers with producing specific host-guest complexations and good separation selectivity.

Several studies in respect of metal ion separation using polymers as ion carriers in liquid membrane transport have been conducted by solvent extraction [2-3]. Chemical reactions among tested metal (solute) in the solvents extraction and liquid membrane transport are similar. However, the basic differences between those separating systems relate to the transport of the tested metal through a liquid membrane directly apart and the presence of the stripping phase. Whereas in

solvent extraction, the tested metal is still being extracted from the organic phase to the aqueous phase.

The phenomenon of the transport process in a liquid membrane shows that complex formation can be influenced by the physicochemical properties (permeability and selectivity) of the targeted ion, ion carrier, and solvent type in the membrane phase. In addition, the chemical composition of the membrane phase in both the source phase solution and the stripping phase also influences the amount of complex formation and transport percent. The selectivity of the membrane and its transport efficiency can be optimized by the macromolecular ion carrier design. It can be conducted through combinations of the ring size and its substituent groups [4-5]. Types of ion carriers lead to different complexation mechanisms. The molecular structure of the ion carrier and the chemical interactions involved in the complexation and transport process are the most decisive factors for membrane selectivity. Hence, it can be adjusted to obtain specific selectivity.

Alkaline and neutral ion carriers show poor selectivity for certain metal ions. Hence, research has been carried out using acidic compounds. Poly(eugenyl oxyacetate) or PEOA could separate Fe(III), Cr(III), Cu(II), Ni(II), Co(II), and Pb(II) using the solvent extraction method [6]. In the previous study, the PEOA compound also acted as a ligand to separate Fe(III), Cr(III), Cu(II), Ni(II), Co(II), and Pb(II) ions by transporting liquid membrane method [7].

Meanwhile, Poly(ethyl eugenyl oxyacetate) or PEEOA had been applied as a ligand to separate the Fe(III), Cr(III), Cu(II), Ni(II), Co(II), and Pb(II) ions using solvent extraction method [8]. The use of PEEOA as an ion carrier through liquid membrane transport for metal ions separation has not been reported. In this study, the performance of PEEOA was tested to separate Fe(III), Cr(III), Cu(II), Ni(II), Co(II), and Pb(II) ions using the liquid membrane transport method for seeking of a macromolecular compound with good separability and selectivity. The transported propensity of the targeted ion is generally carried out separately. However, this study was conducted in a solution with the presence of interfering ions to adjust the actual condition in the water environment. Investigations were carried out to analyze optimum pH, carrier/PEEOA volume, stripping concentration, transport time, and concentration of metal ions. In addition, the effectiveness of separating Fe and Ni ions in ferronickel samples was also analyzed.

■ EXPERIMENTAL SECTION

Materials

The materials used in this study are chloroform (Merck), NaOH (Merck), HCl (Merck), HNO_3 (Merck), $Fe(NO_3)_3{\cdot}9H_2O$ (Merck), $Cr(NO_3)_3{\cdot}6H_2O$ (Merck), $Ni(NO_3)_2{\cdot}6H_2O$ (Merck), $Co(NO_3)_2{\cdot}6H_2O$ (Merck), $Cu(NO_3)_2{\cdot}3H_2O$ (Merck), $Pb(NO_3)_2$ (Merck), demineralization water, and poly(ethyl eugenyl oxyacetate) or PEEOA. PEEOA was synthesized from a chemical reaction between polyeugenol and ethyl chloroacetate based on our previous study [8]. Structure characterizations had also conducted in that study. The structure of the PEEOA is displayed in Fig. 1.

Procedure

Transport of Fe(III), Cr(III), Ni(II), Co(II), Cu(II), and Pb(II) ions with PEEOA

The numbers of U tubes were filled with 7.5 mL of PEEOA with a concentration of 0.001 M in chloroform. Then, 10 mL of metal ion solutions were added to a side of the U tube as a source phase with a concentration of 0.1 mM in various pH (3, 4, and 5). Furthermore, as a stripping phase, 10 mL of HNO_3 1 M solution was poured on another side. U tube was closed and stirred with a magnetic stirrer for 24 h at room temperature. After completing the transport process, the solution on

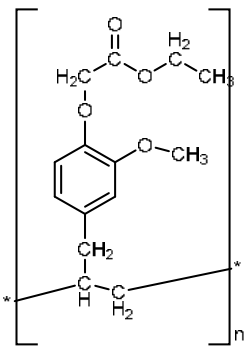

Fig 1. The structure of the PEEOA ion carrier

both sides of the U pipe was separated using a pipette. The concentration of metal ions in the source and stripping phases were analyzed using AAS. The optimum pH was used to optimize the ion carrier volume (7.5, 8.5, and 10 mL), the stripping concentration (0.5, 1, 2, and 4 M), transport time (12, 24, 36, and 48 h), and metal ion concentration (0.075, 0.1, 0.25, 0.5 mM). Transported efficiency or transport percent is calculated based on Eq. (1) as follows.

$$\%T = \frac{C_{Y,S}}{C_{Y,F}} \times 100 \quad (1)$$

where %T is transport percent, $C_{Y,S}$ is metal ion concentration on the stripping/targeted phase (mM), and $C_{Y,F}$ is the initial metal ion concentration in the source phase (mM).

Preparation of ferronickel samples

The ferronickel sample (0.16 g) was dissolved in 5 mL aqua regia (a mixture of concentrated HCl and HNO_3, 3:1) heated for 1 h. Then, the solution was moved to a room-temperature environment. After that, it was diluted with demineralization water up to 25 mL. The procedure of liquid membrane transport for Fe and Ni ions separation was similar to the treatment of pure metals. Fe and Ni contents before and after transport were measured by Atomic Absorption Spectrometer (AAS) Perkin Elmer 3110.

■ RESULTS AND DISCUSSION

PEEOA is a relatively neutral compound. This study uses it as an ion carrier to separate metal ions by liquid membrane transport. Complexation processes occur by forming a neutral complex with metal ions (M^{n+}) and anions (X^-) in the source phase. This separation takes place by symport mechanism. The transport force in the symport mechanism is the difference in metal ion concentration between the source and the stripping phases. Symport transport mechanism is more effective for metal ions in the form of M^+ and X^- with neutral ion carriers (I). The Symport mechanism between PEEOA ions carrier and the metal cation is displayed in Fig. 2.

Transport Parameters with PEEOA as Ions Carrier

The value of the transport percent was calculated from the change in the amount of transported metal ions that pass the membrane phase and the stripping phase. The performance of PEEOA ions to optimally separate Fe(III), Cr(III), Cu(II), Ni(II), Co(II), and Pb(II) ions using liquid membrane transport is affected by several parameters as follows.

Effect of pH

The separation of metal ions using PEEOA as ions carrier through the liquid membrane transport method is related to its capability for accommodating metal ions via interactions with lone pair of electrons on the ester groups. Adjusting pH in the source phase will precisely generate selectivity, and the transport process will take place properly [9]. The influence of pH values on the transport percents is displayed in Fig. 3.

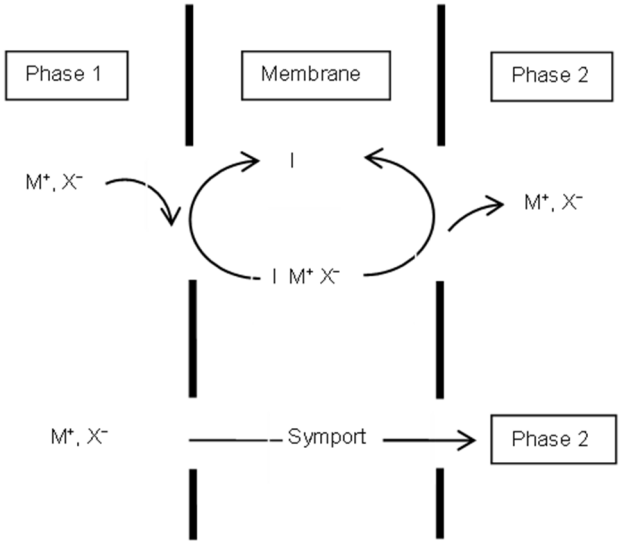

Fig 2. Transport mechanism of cation symport

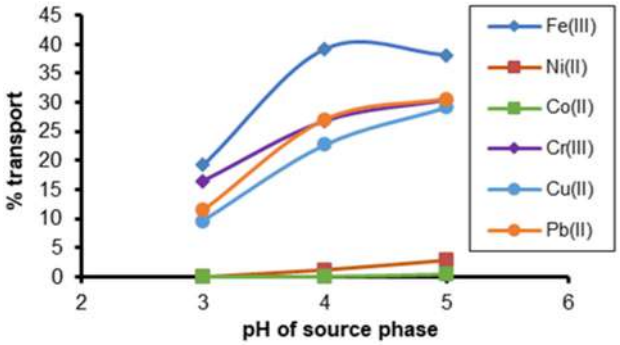

Fig 3. The relationship between the pH variations of the source phase and the transport percent at 0.1 mM of metal ion concentrations, 1 M of HNO_3, 1 mM of ion carrier concentration, and 36 h of transport time

Fig. 3 shows that the increase in pH generates the increment in the transport percent of metal ions from the source phase to the stripping phase through the membrane containing ion carriers. The highest percentage for transporting Fe(III) ions was 39.20% at pH 4. Then, it decreased at pH 5. This is probably caused by hydrolysis or precipitation of Fe(III) ions. Thus, the number of complexes between PEEOA and metal ions also becomes lower [8]. At pH 3, there is competition between Fe(III) ions with hydrogen ions. Optimum transport percents for Cr(III), Cu(II), Ni(II), Co(II), and Pb(II) are 30.36%, 29.22%, 2.95%, 0.54%, and 30.57%, respectively. These occur at pH 5. In this condition, all metal ions are still predominantly in the ionic state, for instance, Cr(III) as Cr^{3+}, $Cr(OH)^{2+}$, and $Cr(OH)_2^{+}$, Co(II) as Co^{2+}, Ni(II) as Ni^{2+}, Cu(II) as Cu^{2+}, and Pb(II) as Pb^{2+} when form complexes with PEEOA. Those metal ions tend to settle at higher pH [10].

Effect of PEEOA volume

The volume of PEEOA in organic solution will affect the number of moles of metal ions as well as the transport percent from the source phase to the stripping phase, as shown in Fig. 4.

Fig. 4 shows that increasing the volume of PEEOA in the organic phase will increase the amount of transported Fe(III) ions at 7.5 and 8.5 mL but decrease at 10 mL. Meanwhile, the optimum PEEOA volume for transporting other metal ions is 7.5 mL. The increasing volume of ions carrier will increase flux and permeability on the liquid membrane [11-12]. Hence, complex formation at the membrane interface is accelerated and increased. After that, it will be extracted to the stripping phase. Further addition of PEEOA volume even increases the thickness (viscosity) and the obstacle of the membrane. Thus, the transport percent of metal ions can decrease due to reducing ion activities at the membrane interface [10,13].

Effect of stripping phase concentration (HNO_3)

The effect of the stripping phase concentration in the liquid membrane transport was analyzed by varying the concentration of HNO_3 at ranges of 0.5, 1.0, 2.0, and 4.0 M. It was carried out at the optimum pH and PEEOA volume. The results show that the concentrations of the stripping phase affect transport percents (% transport), as shown in Fig. 5.

Fig. 5 shows that the optimum transport percent of Fe(III) ions is 43.25% when HNO_3 concentration is 2 M. While the transport percents of Cr(III), Ni(II), and Co(II) ions are optimum at 1.0 M HNO_3 with the values 33.42%, 6.87%, and 5.98%, respectively. Then, the optimum transport percents of Pb(II) and Cu(II) ions are 32.24% and 30.15% when the stripping concentration is 0.5 M. The increase in HNO_3 concentration until optimum concentration produces more hydrogen ions in the solution. These ions can break the complex formed at the interface of the membrane-stripping phase [14].

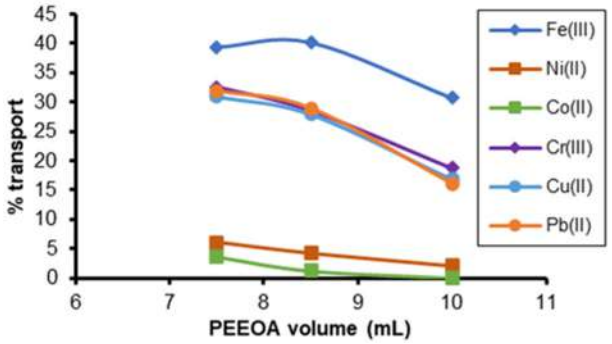

Fig 4. The influence of PEEOA volume on the transport percent at optimum pH, 0.1 mM of metal ion concentrations, 1 M of HNO_3, 1 mM of ion carrier concentration, and 36 h of transport time

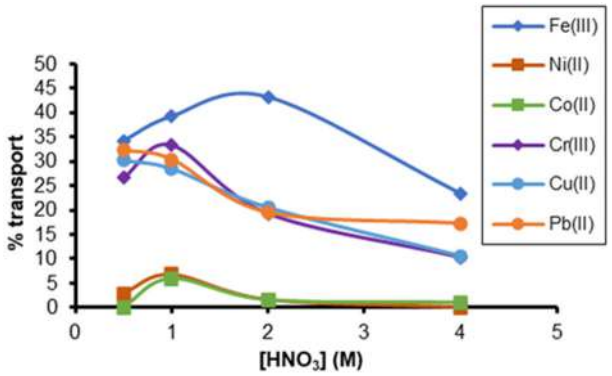

Fig 5. The influence of HNO_3 concentration on the transport percent (% transport) of metal ions at optimum pH and PEEOA volume, 0.1 mM of metal ion concentrations, 1 mM of ion carrier concentration, and 36 h of transport time

Therefore, ion carriers will return to the membrane-source phase to form complexes faster with metal ions [15]. However, hydrogen ions are significantly increased in the stripping solution after optimum conditions. Thus, the decomplexation process is more challenging to break because the process of releasing cation salts at the membrane-acceptor interface is obstructed. It will decrease the transport percent of metal ions to the stripping phase.

This analysis also informs a larger size of the metal ion needs a lower concentration of the HNO_3 solution. It is probably due to the large metal ion size at the Pb(II) and Cu(II) metal ions having greater decomplexation barriers at the membrane-acceptor interface. Table 1 displays bond energy data from computational simulation between metal ions and PEEOA. It informs that the charge and molecular size of the metal ion also affect the number of metal ions transported.

Table 1 shows that the Fe(III) ion has the highest metallic bonding energy, whereas the Pb(II) ion has the lowest energy. Computational simulation results for the reaction between the metal ions and PEEOA show that the highest bonding energy occurs between PEEOA and Cr(III) ions and the lowest bonding energy involves bonds between PEEOA and Co(II) ions. A different phenomenon occurs in Pb(II) ions with PEEOA. There is no stable bond structure between those species. Thus, theoretically, the Pb(II) ion will have a relatively more minor amount transported compared to the other tested metal ions. However, in reality, the transport percent of Pb(II) ions is higher than the Ni(II), Cu(II), and Co(II) ions. Several reasons may cause this. First, the Pb^{2+} ion with a larger ion size will be polarized to the PEEOA ion carrier. Hence, it is easier to escape in the stripping phase; second, small ions will have more water molecules in the hydration layer/cavities than large ions. Meanwhile, the adequate size of the hydrated ion in solution at the larger metal ion size will be small. As a result, the number of Pb(II) ions that may bind to PEEOA is higher; third, this relates to the size conformity between Pb(II) ions and PEEOA for interacting.

Effect of transport time

The transported rate of metal ions in the liquid membrane was measured by analysis of the transport process at various transport periods from 12, 24, 36, and up to 48 h under optimum pH, PEEOA concentration, and stripping concentration. This parameter also affects the transport percent of metal ions from the source phase to the stripping phase [16]. The results of this analysis are shown in Fig. 6.

Fig. 6 shows that an increase in the transport period will increase the metal ions transported from the

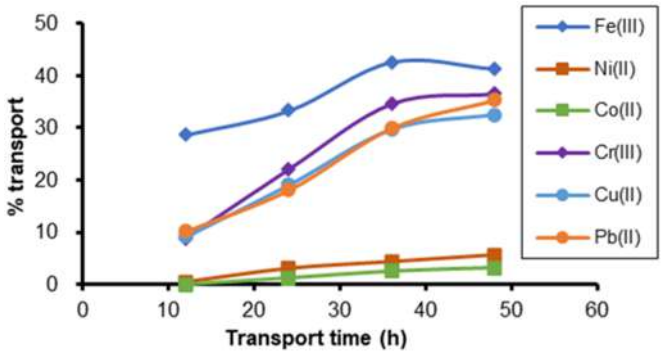

Fig 6. The influence of transport time on the transport percent of metal ions at optimum pH, PEEOA volume, and HNO_3 concentration, 0.1 mM of metal ion concentrations, 1 mM of ion carrier concentration, and 36 h of transport time

Table 1. Bond energy data from computational simulation between PEEOA and metal ions

No	Bond energy (kcal/mol)			
	Metal ion		PEEOA	PEEOA + metal ion
1	Fe(III)	1811.814		-10609.391
2	Cr(III)	1708.821	-14282.659	-10135.923
3	Ni(II)	1218.846		-10645.808
4	Co(II)	817.319		-10840.483
5	Cu(II)	887.024		-10619.235
6	Pb(II)	457.357		-

-: Cannot be determined

source phase to the stripping phase. This corresponds to the longer contact time between the PEEOA and the metal ion. The metal ions from the aqueous phase can form complexes at the interface of the aqueous phase and membrane phase, which will then be transported to the stripping or target phase. After passing optimum time, complexes slowly form because the equilibrium condition is almost reached [2].

The Fe(III) ion has an optimum transport time of 36 h, while the optimum transport time of Cr(III), Cu(II), Ni(II), Co(II), and Pb(II) ions is over 36 h. The formation rate of complex Fe(III) ions with PEEOA is faster. Fe(III) ions have higher reactivity, greater polarity, and smaller ionic radius to support complex formation with PEEOA ions. Thus, the transport time to the target phase is faster than other metal ions. In addition, there is a compatibility between the cavity size of carrier ions and the Fe(III) ions compared to other tested metal ions.

Effect of metal ion concentration

This analysis applied optimum pH, PEEOA volume, stripping concentration, and transport time from each metal ion which is displayed in Fig. 7.

Fig. 7 informs that the Fe(III) and Cu(II) ions are

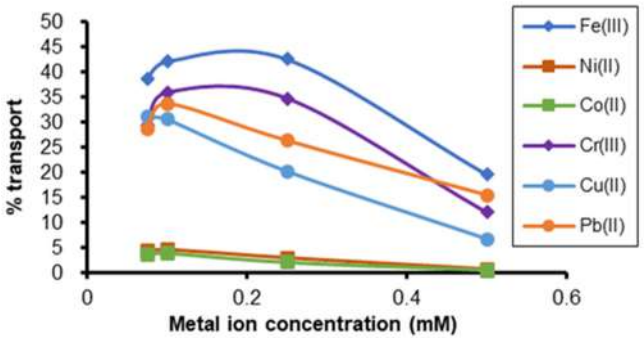

Fig 7. Effect of metal ion concentration (0.075, 0.1, 0.25, and 0.5 mM) on source phase to transport percent at optimum pH, PEEOA volume, HNO_3 concentration, and transport time

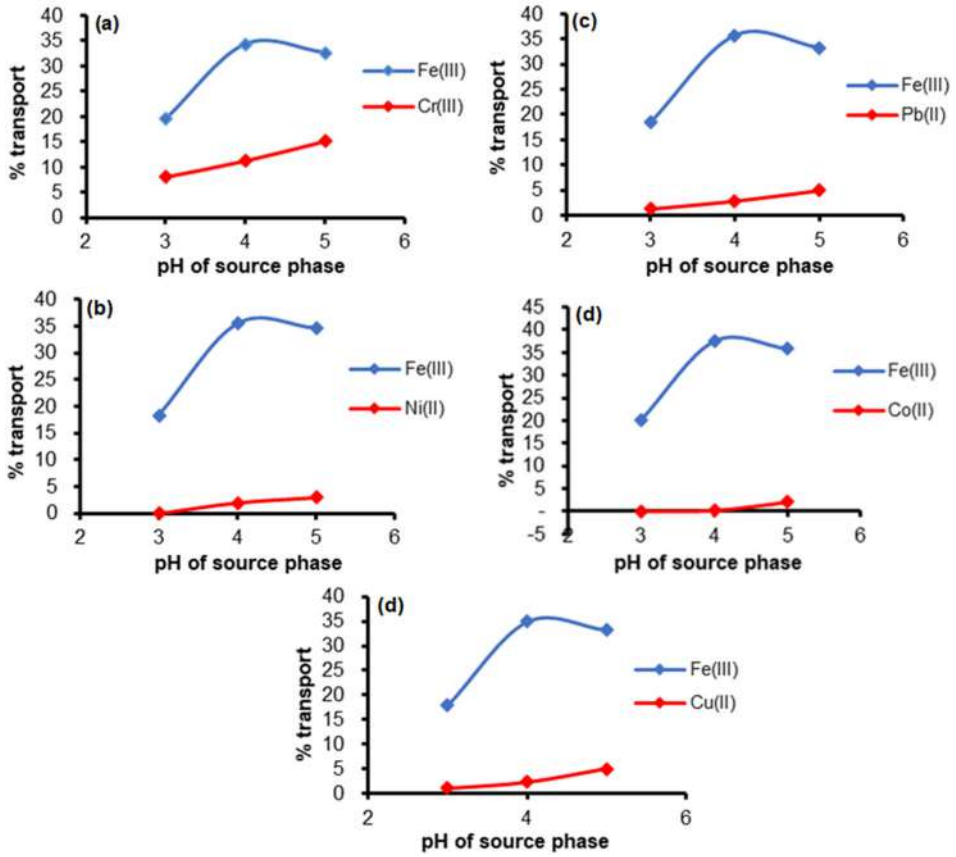

Fig 8. The effect of pH on transport percent in a mixture of Fe(III) + Cr(III) (a), Fe(III) + Ni(II) (b), Fe(III) + Pb(II) (c), Fe(III) + Co(II) (d), and Fe(III) + Cu(II) (e). Metal ion concentration was 0.1 mM, [HNO_3] = 2 M, ion carrier volume and concentration = 8.5 mL and 0.001 M, and transport time = 36 h

optimally transported at a concentration of 0.25 and 0.075 mM, respectively. The transport percentages are 42.64 and 31.20%. Meanwhile, the optimum concentration of Cr(III), Ni(II), Co(II), and Pb(II) ions is 0.1 mM with transport percents of 35.91, 4.74, 3.96, and 33.73%, respectively. Increasing metal ion concentration increases the number of metal ions transported in the target phase first. However, it even decreases above optimum concentration because equilibrium conditions have been reached [14]. In this condition, PEEOA cannot accommodate metal ions for the further transport process. The increase of metal ion concentration in solution after optimum conditions will reduce the diffusion permeability in the membrane [17].

Transport Competitions of Metal Ions

The selectivity and reactivity of PEEOA as Fe(III), Cr(III), Cu(II), Ni(II), Co(II), and Pb(II) ions carrier were analyzed from the mixture of two, three, and all-metal ions. Based on the optimization results of each metal ion separately, the Fe(III) ion has the best transport percent compared to the other tested metal ions. Therefore, Fe(III) ion was used as the main ion in the competition tests of metal transport.

Competition of Two Metals

These experiments compete Fe(III) ions with other metal ions that were conducted in various pH and transport times. The percent transport of metal ions depends on the type of metal ion and the used ion carrier [18]. Several simulations consist of Fe(III)-Cr(III), Fe(III)-Pb(II), Fe(III)-Ni(II), Fe(III)-Co(II), and Fe(III)-Cu(II). The amount of transported metal ions in various pH is presented in Fig. 8.

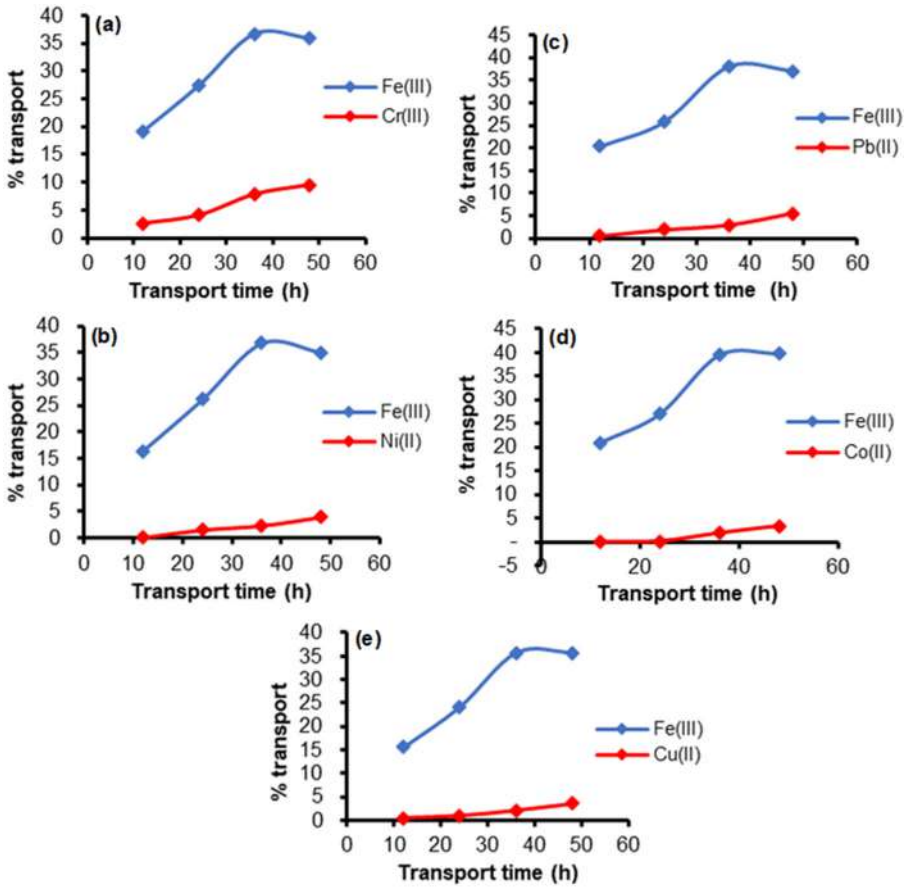

Fig 9. The effect of transport time on the transport percent in a mixture of Fe(III) + Cr(III) (a), Fe(III) + Ni(II) (b), Fe(III) + Pb(II) (c), Fe(III) + Co(II) (d), and Fe(III) + Cu(II) (e). Metal ion concentration = 0.1 mM, [HNO_3] = 2 M, ion carrier volume and concentration = 8.5 mL and 0.001 M, and transport time = 36 h

Fig. 8 shows that the presence of other metal ions in the solution sufficiently disrupts the ability of Fe(III) ions to be transported. The optimum condition for transporting Fe(III) ions occurs at pH 4 for all combinations. The amount of Fe(III) ions transported varies depending on the metal ion pair in the solution. The smallest percentage (34.26%) of transported Fe(III) ions occurred in the mixture of Fe(III) and Cr(III) ions. This is related to the acidity and polarity of Cr(III), which is almost identical to the Fe(III) ion. Thus, the ability to form complexes is also similar. Meanwhile, the velocity of each metal ion transported to the stripping phase in a mixture of two metal ions can be determined by variations of transport time using the optimum pH for Fe(III) ions transport. The results are shown in Fig. 9.

Fig. 9 shows that the increase in the transport time is accompanied by an increase in the transport percent of metal ions. This relates to the number of contacts between the metal ions in the source phase and the ion carriers at the membrane phase through the interface area. Then, complexes were formed. After that, these complexes diffuse across the membrane and are removed at the stripping phase. The presence of other ions as interference in the Fe(III) ion solution also affects the decrease in transport percent of Fe(III) ion in the stripping phase. The reduction of this transport percent is related to some active groups in the membrane phase forming complexes with interference ions [19].

Three Metals Competition

A competition analysis of three metals was carried out for three mixtures. It consists of Fe(III)-Cr(III)-Ni(II), Fe(III)-Cu(II)-Pb(II), and Fe(III)-Ni(II)-Co(II). The transport percents of Fe(III) ions in the stripping phase that are influenced by pH are shown in Fig. 10.

Fig. 10 shows the three types of simulated metal ions. The optimum Fe(III) ion transport percent occurred at pH 4. The most significant disturbance for transporting Fe(III) ions was found in the Fe(III)-Cr(III)-Ni(II) mixture. Cr(III) ions which are classified as hard acids, almost have similar acidity to Fe(III) ions which inflicts competition for complex formations. Besides that, increasing the number of metal ions will require more active sites to complex all metal ions in solution, while the number of active sites does not change. Therefore, the active site has a limited ability to complex all metal ions in solution.

Furthermore, competition of three metals in a system can retard the transport process of all metal ions, including Fe(III) ions. Fig. 11 shows that Fe(III) ions act

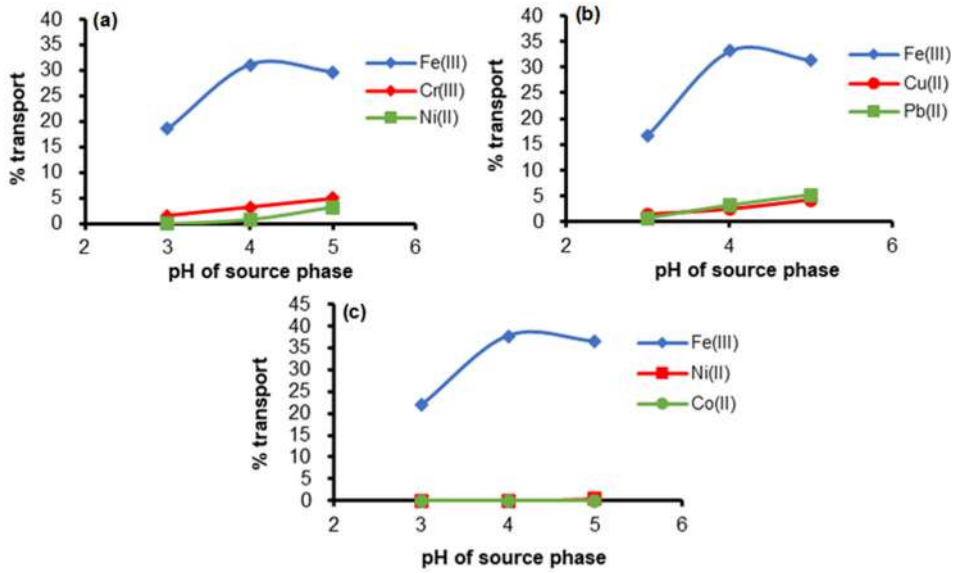

Fig 10. Transport percent of the system contained three metal ions in various pH. Fe(III) + Cr(III) + Ni(II) (a), Fe(III) + Cu(II) + Pb(II) (b), Fe(III) + Ni(II) + Co(II) (c). Metal ion concentration = 0.1 mM, [HNO_3] = 2 M, ion carrier volume and concentration = 8.5 mL and 0.001 M, and transport time = 36 h

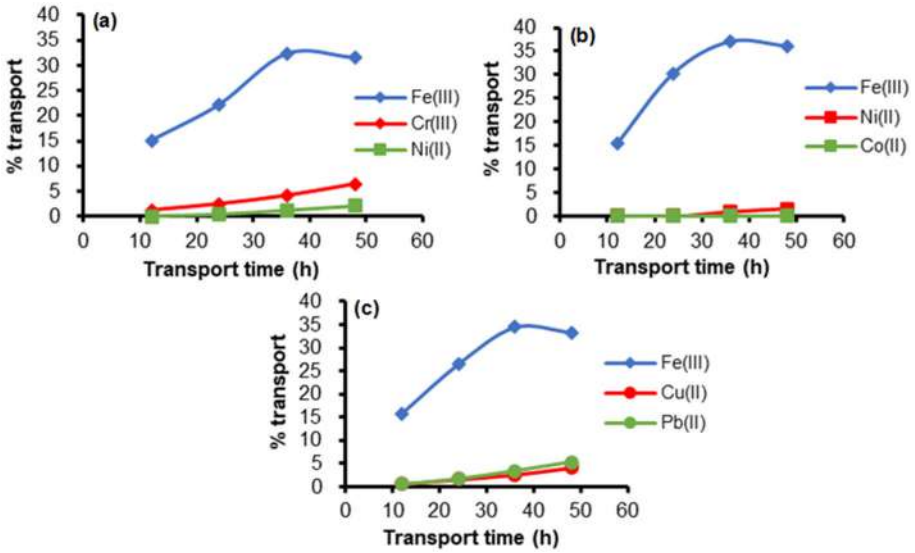

Fig 11. Transport percent of the system contained three metals in various transport times. Fe(III) + Cr(III) + Ni(II) (a), Fe(III) + Ni(II) + Co(II) (b), Fe(III) + Cu(II) + Pb(II) (c). Metal ion concentration = 0.1 mM, [HNO_3] = 2 M, ion carrier volume and concentration = 8.5 mL and 0.001 M

as the primary ion, while other metal ions act as interference. Adding metal ions in the source phase can reduce the number of transported Fe(III) ions in the stripping phase.

All Tested Metal Ion Competition

Competition of all tested metal ions was also conducted in optimum pH and transport time. The transport percents of each ion in the mixture at various pH are shown in Fig. 12.

Fig. 12 shows that the optimum conditions for Fe(III) metal ions in the mixture occurred at pH 4. This condition is similar to the system with two and three metal ions but has a lower transport percent. The presence of six metal ions will increase the viscosity of the solution and the concentration polarization. Thus, the activity of each metal ion is limited. As a result, the flux of ions in the ion-carrying solution is reduced [20]. In addition, the limited ion-carrying active site inflicts not all metal ions in the solution forming a complex. The ions' speed can be described by varying the transport time. The transport percent of each ion using PEEOA in different transport times is presented in Fig. 13.

Fig.13 shows that increasing the transport times increases the number of metal ions transported even though the percentage of each metal ion decreases with the

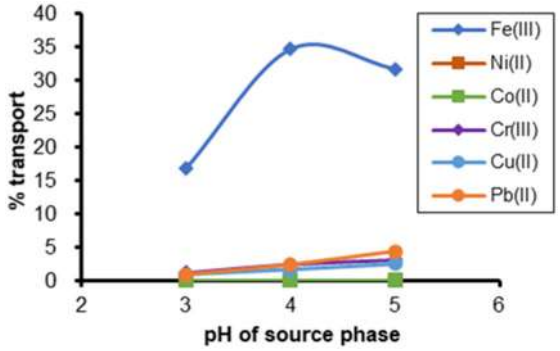

Fig 12. The effect of pH on the transport percent in the system contained all tested metals

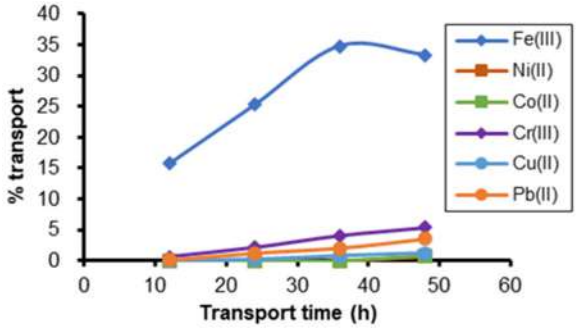

Fig 13. The effect of transport time on the transport percent in the system contained all tested metals

increasing the number of metal ions in the mixture. The expanding number of metal ions in the mixed solution decreases the activity of each metal ion. In this

condition, the number of active sites carrying ions remains, whereas the number of metal ions increases. Consequently, not all metal ions in the solution form complexes such as Ni(II) and Co(II) ions. Besides that, the transport percent of Pb(II) ion also significantly decreased after being in the mixture of metal. This probably relates to the size of Pb(II) ions which are relatively larger than other metal ions. As a result, its ability to form complexes with ion carriers reduces due to competition among metal ions in the solution. The presence of other metal ions in a solution containing Fe(III) ions (two, three, and a mixture of all tested metal ions) did not change the selectivity for the Fe(III) ion. But, it only reduced the amount of transported Fe(III) ions in the stripping phase.

Separation of Fe Ion from Ni Ion in Ferronickel Sample

In this study, PEEOA was also tested on a ferronickel sample from PT Aneka Tambang Pomalaa, Kolaka, Southeast Sulawesi. The main content of this ferronickel is Fe and Ni. It also contains chromium, cobalt, and some anions such as sulfide and phosphate.

The experiment was conducted to separate Fe(III) and Ni(II) ions in the ferronickel sample using a liquid membrane transport method under optimum conditions for transporting Fe(III) ions. The solution used was prepared from ferronickel concentrate, which has been diluted 50, 100, and 200 times respectively. The concentration of the ion carrier is 0.001 mM at pH 4. Then, ion carrier volume, stripping concentration, and transport time are 8.5 mL, 2.0 M, and 36 h, respectively. The transport efficiencies of the Fe(III) and Ni(II) ions before and after the transport process are presented in Table 2.

Table 2 shows that separating iron and nickel from ferronickel at different concentrations using PEEOA ion carriers with a concentration of 0.001 mM also has different transportability. A higher concentration of iron and nickel in ferronickel reduces the ability of PEEOA to transport Fe(III), while the Ni(II) ion is not transported for all concentrations. Concentrations of Fe(III) and Ni(II) ions in the stripping phase reduce compared to pure metals due to the presence of other ions as the mixtures in the ferronickel sample. The presence of phosphate and sulfur in ferronickel will compete with PEEOA ion carriers to bind Fe(III) or Ni(II) ions. Reactivity parameters explain phosphate is more reactive compared to PEEOA. Thus, it will reduce the ability of PEEOA to form complexes with Fe(III) and Ni(II) ions.

Table 2. The transport efficiency of liquid membrane on the separation of Fe and Ni from ferronickel concentrate using PEEOA as ion carrier

Metal ion	Concentration in source phase before transported ($\times 10^{-4}$ M)	Concentration in source phase (Cfs) after transported ($\times 10^{-4}$ M)	Concentration in the stripping phase (Cfp) after transport ($\times 10^{-4}$ M)	% Cfs	% Cfp
Fe	4.93	4.42	0.09	89.76	1.79
	2.60	1.85	0.11	85.42	5.27
	1.26	1.03	0.11	81.63	8.87
Ni	3.80	3.49	0	91.87	0
	1.66	1.61	0	96.70	0
	1.04	0.99	0.01	95.55	0.92
	Metal ion concentration after transported (blank)				
Fe	4.93	4.59	0.022	93.17	0.46
	2.16	2.10	0	97.08	0
	1.26	1.26	0	100	0
Ni	3.80	3.63	0	95.67	0
	1.66	1.61	0	96.91	0
	1.04	1.03	0	99.01	0

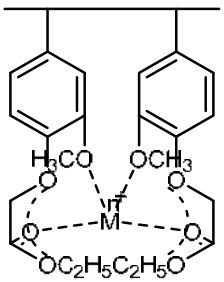

Fig 14. Approximation of complexed shape of PEEOA with metal ions (M = Fe(III), Cr(III), Ni(II), Co(II), Cu(II), and Pb(II) ions)

Separation of Fe(III) ion from Ni(II) ion in ferronickel using PEEOA shall be carried out at a ferronickel concentration of 0.126 mM for Fe(III) and 0.104 mM for Ni(II) (200 times of dilutions). Fe(III) and Ni(II) ions transport percentages are 8.87 and 0.92%, respectively. The ability of Fe(III) and Ni(II) to be transported in the stripping phase is affected by PEEOA as a carrier ion. This can be displayed from the experimental transport data with blanks or without ion carriers, but only using chloroform as a membrane phase that acts as an ion carrier. The results showed that both Fe(III) and Ni(II) ions are not transported in the stripping phase at all concentrations tested (≈0%). Complex formation between the metal ion and the PEEOA involves oxygen in the ether and carbonyl groups. Hence, the complex structure between the PEEOA and the metal ions is approximated in Fig. 14.

■ CONCLUSION

PEEOA has been used as an ions carrier to separate Fe(III), Cr(III), Cu(II), Ni(II), Co(II), and Pb(II) ions by liquid membrane transport method. Besides that, it could also separate Fe and Ni in the ferronickel sample. The best conditions for separating Fe(III) ions were pH 4 (single, mixed metal ions, and ferronickel sample). Increasing the volume of the ion carrier up to 8.5 mL will increase the number of transported Fe(III) ions. Meanwhile, other metal ions have been optimum at 7.5 mL. Optimum stripping concentration (HNO_3), transport time, and concentration of Fe(III) are 2 M, 36 h, and 0.075-0.25 mM, respectively. The order of metal selectivity is Fe(III) > Cr(III) > Pb(II) > Cu(II) > Ni(II) > Co(II). This propensity was almost similar to the extraction method. However, the transport percentages of metals are relatively lower than the extraction percentages in the solvent extraction method. Complex formations between Fe(III) ions and PEEOA in the transport process occur through interactions among oxygen atoms in the ether and carbonyl groups.

■ REFERENCES

[1] Minhas, F.T., Memon, S., Qureshi, I., Mujahid, M., and Bhanger, M.I., 2013, Facilitated kinetic transport of Cu(II) through a supported liquid membrane with calix[4]arene as a carrier, *C. R. Chim.*, 16 (8), 742–751.

[2] Cay, S., Sayin, S., and Engin, M.S., 2020, Calix[4]arene embedded polyamide supported liquid membrane for separation of heavy metals from aqueous solutions, *Turk. J. Agric. Food Sci. Technol.*, 8 (2), 387–391.

[3] El Batouti, M., Al-Harby, N.F., and Elewa, M.M., 2021, A review on promising membrane technology approaches for heavy metal removal from water and wastewater to solve water crisis, *Water*, 13 (22), 3241.

[4] Parhi, P.K., 2013, Supported liquid membrane principle and its practices: A short review, *J. Chem.*, 2013, 618236.

[5] Nguyen, B.N.T., Thoburn, J.D., Grommet, A.B., Howe, D.J., Ronson, T.K., Ryan, H.P., Bolliger, J.L., and Nitschke, J.R., 2021, Coordination cages selectively transport molecular cargoes across liquid membranes, *J. Am. Chem. Soc.*, 143 (31), 12175–12180.

[6] Harimu, L., Matsjeh, S., Siswanta, D., and Santosa, S.J., 2009, Synthesis Polieugenyl oxiacetic acid as a carrier to separate heavy metal ion Fe(III), Cr(III), Cu(II), Ni(II), Co(II) and Pb(II) using the extraction method, *Indones. J. Chem.*, 9 (2), 261–266.

[7] Harimu, L., Matsjeh, S., Siswanta, D., and Santosa, S.J., 2010, Separation of Fe(III), Cr(III), Cu(II), Ni(II), Co(II), and Pb(II) metal ions using poly(eugenyl oxyacetic acid) as an ion carrier by a

liquid membrane transport method, *Indones. J. Chem.*, 10 (1), 69–74.

[8] Harimu, L., Matsjeh, S., Siswanta, D., Santosa, S.J., and Sutapa, I.W., 2019, Synthesis of poly(ethyl eugenyl oxyacetate) as carrier for separation of heavy metal ions Fe(III), Cr(III), Cu(II), Ni(II), Co(II), and Pb(II) using liquid-liquid extraction method, *J. Phys.: Conf. Ser.*, 1341, 032003.

[9] Arous, O., Saoud, F., Amara, M., and Kerdjoudj, H., 2011, Efficient facilitated transport of lead and cadmium across a plasticized triacetate membrane mediated by D2EHPA and TOPO, *Mater. Sci. Appl.*, 2 (6), 615–623.

[10] Amini, M., Rahbar-Kelishami, A., Alipour, M., and Vahidi, O., 2018, Supported liquid membrane in metal ion separation: An overview, *J. Membr. Sci. Res.*, 4 (3), 121–135.

[11] Ferencz, A., Grosu, A.R., Al-Ani, H.N.A., Nechifor, A.C., Tanczos, S.K., Albu, P.C., Crăciun, M.E., Ioan, M.R., Grosu, V.A., and Nechifor, G., 2022, Operational limits of the bulk hybrid liquid membranes based on dispersion systems, *Membranes*, 12 (2), 190.

[12] Abejón, R., Rabadán, J., Garea, A., and Irabien, A., 2020, Comparison of supported ionic liquid membranes and polymeric ultrafiltration and nanofiltration membranes for separation of lignin and monosaccharides, *Membranes*, 10 (2), 29.

[13] Mohebali, S., Nazari, M., Rahbar-Kelishami, A., and Davoodi-Nasab, P., 2017, Performance of sunflower oil as green solvent for Cr(VI) extraction using supported liquid membrane, *Desalin. Water Treat.*, 64, 173–178.

[14] Mirea, C.M., Diaconu, I., Ruse, E., Serban, E.A., Clej, D.D., Popa, G.A., Popa, D.F., and Nechifor, G., 2016, The removal of heavy metals using the bulk liquid membrane technique, *Prog. Cryog. Isot. Sep.*, 19 (1), 45–54.

[15] Alguacil, F.J., 2019, Facilitated chromium(VI) transport across an ionic liquid membrane impregnated with Cyphos IL102, *Molecules*, 24 (13), 2437.

[16] Manikandan, G.N., Bogeshwaran, K., Jamuna, P., and Sandhya, S., 2014, A review on emulsion liquid membranes on heavy metal separation, *Int. J. ChemTech Res.*, 6 (9), 4328–4332.

[17] Albaraka, Z., 2019, Use of D2EHPA-mediated liquid membranes for heavy metal ions separation: A review, *Rev. Roum. Chim.*, 64 (2), 113–124.

[18] Verma, B., Balomajumder, C., Sabapathy, M., and Gumfekar, S.P., 2021, Pressure-driven membrane process: A review of advanced technique for heavy metals remediation, *Processes*, 9 (5), 752.

[19] Gubari, M.Q., Abdulkarim, A.A., and Alekseeva, N.V., 2021, Diffusion permeability of cation-exchange membrane in different solutions, *J. Ecol. Eng.*, 22 (8), 140–145.

[20] Nielen, W.M., Willott, J.D., Galicia, J.A.R., and de Vos, W.M., 2021, Effect of solution viscosity on the precipitation of PSaMA in aqueous phase separation-based membrane formation, *Polymers*, 13 (11), 1775.

GC-MS Based Metabolite Profiling and Antibacterial Activity of Torch Ginger (*Etlingera elatior*) Flowers Extract

Wahyu Haryati Maser[1*], Agus Purwoko[2], Nancy Dewi Yuliana[3], Linda Masniary Lubis[1], and Alfi Khatib[4]

[1]*Department of Food Technology, Faculty of Agriculture, Universitas Sumatera Utara, Jl. Dr. A. Sofian No. 3, Medan 20155, North Sumatera, Indonesia*

[2]*Department of Forestry, Faculty of Forestry, Universitas Sumatera Utara, Jl. Tri Darma Ujung No. 1, Medan 20155, North Sumatera, Indonesia*

[3]*Department of Food Science and Technology, Faculty of Agricultural Technology, IPB University, IPB Dramaga Campus, Bogor 16680, Indonesia*

[4]*Department of Pharmaceutical Chemistry, Faculty of Pharmacy, International Islamic University Malaysia, Kuantan 25200, Malaysia*

** **Corresponding author:***

tel: +62-81376340031
email: maser.wahyuharyati@usu.ac.id

Received: January 27, 2022
Accepted: April 26, 2022

DOI: 10.22146/ijc.72583

Abstract: *Torch ginger (*Etlingera elatior*) flowers are well known for their antibacterial effects against* Staphylococcus aureus*, however, the active compounds are still unknown. The purpose of this study was to conduct GC-MS-based metabolite profiling of torch ginger flower and identify compounds correlated with its* S. aureus *antibacterial activity using Orthogonal Projection to Latent Structure (OPLS). Using the well diffusion method, the antibacterial activity of ethanol extract, hexane, chloroform, and ethyl acetate fractions with a concentration of 80 mg/mL were investigated. The ethyl acetate fraction inhibited* S. aureus *growth the most (diameter of inhibition zone, DIZ 13.00–13.20 mm), while the hexane (DIZ 9.55–10.05 mm) and chloroform (DIZ 10.00–11.00 mm) fractions had moderate inhibitory activity, but the ethanol extract had no antibacterial effect. Using OPLS analysis, the GC-MS metabolite profile of all extracts and fractions was linked with the profile of antibacterial activity. This analysis revealed that Dodecanoic acid, 5-Tetradecene, and* n*-Hexadecanoic acid were identified as the compounds that were significantly connected with antibacterial activity.*

Keywords: *antibacterial activity;* Etlingera elatior*; GC-MS; metabolite profiling;* Staphylococcus aureus

■ INTRODUCTION

Torch ginger is a native plant of Indonesia. Torch ginger is a member of the Zingiberaceae family, the Etlingera genus, and the *Etlingera elatior* species [1]. It is widely used as a medicinal herb and an ingredient in local products such as soap, shampoo, and perfume [2]. Torch ginger, on the other hand, is not as widely used as other spices such as ginger, turmeric, and aromatic ginger. Torch ginger possesses antioxidant, anticancer, antibacterial, antihyperglycemic, and anti-inflammatory properties [3-4].

Staphylococcus aureus is one of the most common pathogenic bacteria in humans. Invasive *S. aureus* infection is becoming recognized progressively as a major cause of severe sepsis in developing countries, with death rates larger than in developed countries [5]. Furthermore, as resistance cases in *S. aureus* increase, these bacteria are becoming increasingly important major pathogens. As a result, efforts must be made to identify prospective antibiotic candidates, particularly from natural sources. According to some previous research, torch ginger blossom has an antibacterial effect

against *S. aureus* [3,6]. Testing the antibacterial activity of *S. aureus* on local torch ginger flower has been carried out by using the modification well diffusion method [7]. However, the identification of components of the antibacterial compound of *S. aureus* from local torch ginger flower has not yet been conducted. Therefore, this study aimed to conduct GC-MS metabolite profiling of torch ginger flower extract and to identify compounds that correlate with its antibacterial activity against growth using multivariate data analysis.

Metabolomics is a comprehensive analysis of components of an organism at a certain time or condition. It can be applied to study the correlation between bioactivity and metabolite profile which is ultimately used to identify the bioactive component in plants efficiently [8]. This method has been carried out by stratified sample extraction using a combination of solvents at the level of polarity [9]. One of the instruments that can be used for metabolomic analysis is Gas Chromatography-Mass Spectrometry (GC-MS). GC coupled to MS can be used to identify and elucidate the structure of compounds. The development of mass detection methods is one of the most widely used techniques for identifying compound structures. The ability to detect the atomic formula or specific functional group of an analyte has become a strong point for the use of MS in metabolomics [10]. Furthermore, GC-MS techniques have an advantage over LC-MS (Liquid Chromatography-Mass Spectrometry) techniques since GC-MS is considerably more repeatable than LC-MS according to the Electron Ionization (EI) approach that is typically used [11]. Several studies successfully identified bioactive metabolites from complex plant extracts using the GC-MS-based metabolomic method [12-14].

To extract information from the large amount of data generated from metabolomics study requires the use of multivariate data analysis. One multivariate data analysis method that can be used to observe a correlation between the metabolite profile of a complex plant extract with its activity is Orthogonal Projection to Latent Structure (OPLS) analysis. This analysis will group the samples based on their bioactivity in the form of an S-plot. In addition, the Y-related coefficient plot indicates metabolites significantly correlate with its bioactivity. Therefore, we used multivariate data analysis/OPLS to facilitate the identification of compounds correlated with antibacterial activity. The known antibacterial compound of the torch ginger flower can be further investigated for its use as an antibiotic drug and functional food that can prevent disease.

■ EXPERIMENTAL SECTION

Materials

The material used in this study was fresh torch ginger flower bud from Kabanjahe farmer Sumatera Utara, Indonesia. For future use, the voucher specimen was deposited and authenticated at the Herbarium Medanese, Universitas Sumatera Utara, Medan, Indonesia (voucher specimen: 6488/MEDA). Ethanol, *n*-hexane, chloroform, ethyl acetate, dimethyl sulfoxide (DMSO), chloramphenicol, MSTFA (*N*-Methyl-*N*-(trimethylsilyl)trifluoro-acetamide) (gas chromatography grade), and methoxyamine hydrochloride were purchased from Sigma-Aldrich. Pyridine was supplied by Merck. Methoxyamine HCl was supplied by Fisher Scientific (Acros Organics, Geel, Belgium), and liquid nitrogen was purchased from the MOX Company (Petaling Jaya, Malaysia). Nutrient agar media was supplied from Merck. *S. aureus* bacteria (ATCC 25923) was obtained from the Microbiology Laboratory, Faculty of Pharmacy, University of Sumatera Utara. All chemicals were of analytical grade.

Instrumentation

This study used GC-MS of Agilent 6890 and HP 5973 mass detector (Agilent Technologies, Santa Clara, USA), the centrifuge of Eppendorf 5415D (Eppendorf AG, Hamburg, Germany), and the rotary evaporator of Buchi (BÜCHI Labortechnik, Flawil, Switzerland).

Procedure

Samples preparation

Fresh torch ginger flower is sorted, washed, peeled, dried in an oven dryer at 50 °C for 12 h, then crushed into a powder using a food processor and filtered with a 30 mesh filter. Extraction was carried out on 50 g torch ginger flour with 80% ethanol by sonication for 1 h and

followed by centrifugation at 2000 rpm for 30 min. The extract was filtered and the filtrate was collected and dried using a rotary evaporator at 40 °C. The dried extract was subjected to partition liquid-liquid fractionation with *n*-hexane, chloroform, and ethyl acetate. All fractions were dried using a rotary evaporator at a temperature of 40 °C. The extraction and fractionation processes were carried out in 5 replications; thus, 20 samples were obtained in total.

Antibacterial analysis

The antibacterial activity on extraction result was carried out by a modified well diffusion method [15]. The extract and fraction were dissolved in DMSO with a concentration of 80 mg/mL. Next, 500 mL of sterilized NA media were poured into a 25 ± 2 mL Petri plate. The Petri plate containing the media was then allowed to stand for 1 h until it solidified. In this media, three wells of 6 mm diameter were made. A total of 60 µL extract was poured into the well, and other wells were used for positive control and negative control. DMSO:ethanol (6:2) was used as a negative control, and chloramphenicol was used as a positive control (2.50 mg/mL). *S. aureus* with a concentration culture test of 10^6 CFU/mL has been likened to the Mac Farland turbidity standard solution. It was taken, scratched into the media, and incubated at 37 °C for 48 h. Antibacterial activity was calculated based on DIZ (diameter of inhibition zone). The tests were carried out in 5 replications.

GC-MS analysis

Samples derivatization and GC-MS analysis method were referred to [13] method. The extracts (25 mg) were added by 50 µL pyridine in a 2 mL centrifuge tube and sonicated for 10 min at 30 °C. Next, 100 mL of methoxyamine HCl (20 mg/mL pyridine) was added and vortex. It was then incubated for 2 h at 60 °C. Next, 300 mL of MSTFA was added and re-incubated for 30 min at 60 °C. The sample is filtered, transferred into a tube, closed tightly and covered with aluminum foil, and left overnight at room temperature.

Samples were analyzed using the Agilent GC-MS system. A 1 µL sample was injected into the GC-MS system consisting of Agilent 6890 chromatography gas and HP 5973 mass selective detector. The GC column used was a 5% DB-5MS phenyl methyl siloxane column with an inner diameter (ID) of 250 µm and a thickness of 0.25 µm. The initial temperature was set at 50 °C for 3 min and rose to 315 °C for 10 min at a speed of 10 °C/min. Helium gas was used as a carrier gas with a speed of 1 mL/min. The temperature of the injector and ion source was set at 330 and 250 °C, respectively. The mass spectra were obtained using a full scan and monitoring mode with a mass scanning range of 50 to 550 m/z after 7 min of solvent delay.

The spectra for each chromatogram peak were compared with those in the NIST08 database and the retention time (RT) of the primary and secondary metabolites. Chromatogram and mass spectra were processed using Agilent ChemStation, Automated Mass Spectral Deconvolution and Identification System (AMDIS), and Agilent's Deconvoluted Reporting Software (DRS). The data processing approach was used after GC-MS analysis. The main purpose of data processing is to extract all related information from the raw data and turn it into a data matrix. This procedure involves noise filtering, binning data, automatic peak detection, and chromatographic alignment without the need for internal standards (ISs). The XCMS package in version R 2.15.1 was applied to align the GC-MS chromatogram with the following values: xcms Set (fwhm = 30, step = 0.1, Method = bin) and group (bw = 10) and used to extract all information from the data raw and summarize it in Excel sheet format.

OPLS analysis

OPLS analysis was conducted using SIMCA v.13.01. Two plots were used to interpret the OPLS data; S-plot and a Y-related coefficient plot. A significant correlation is indicated by the value of the Y-related coefficient that is greater than 0.50. The scaling method used the Pareto method because it gives each variant variable numerically the same as the standard deviation [16].

■ RESULTS AND DISCUSSION

Antibacterial Activity

The result of the antibacterial activity test of the extracts and fractions of torch ginger flower showed that

the fraction with the highest activity was ethyl acetate fraction (EF) (DIZ 13.00–13.20 mm), while ethanol extract (EE) showed no inhibitory activity (Fig. 1). The results were in agreement with those of Anzian et al. [17], who reported that oil extracts of torch ginger (*Etlingera elatior* Jack) flower using subcritical carbon dioxide (CO_2) exhibited very strong antibacterial activity against *S. aureus* (14.50 ± 2.21 mm). Research by Susanti et al. [18] showed that the 10 µL concentration of torch ginger flower essential oil could provide 6 mm inhibition in *S. aureus* bacteria. According to Ghasemzadeh et al. [3], Kelantan torch ginger flower extract at a concentration of 10 mg/mL gave 8.40 mm inhibitory power, while Johor torch ginger flower extract gave 4.00 mm inhibitory power, and Pahang torch flower ginger extract gave 9.20 mm inhibitory power. A previous report showed that the chloroform extract had an inhibitory value of 3.78 mm at a concentration of 500 mg/mL [7]. Differences in torch ginger flower source, extraction method, and solvent used can affect the concentration of secondary metabolites in the plants, consequently, influencing their antibacterial activity [3,19].

Metabolites Profiles

A metabolite profile was obtained from chromatograms resulting from GC-MS analysis of 602 metabolite profiles from the retention time of ethanol extract, hexane, chloroform, and ethyl acetate fractions. The compounds were detected by comparing their fragmentation pattern and mass spectra to those in the National Institute of Standards and Technology's mass spectral database (NIST14.L). The most abundant compounds in hexane fractions were 1-Dodecanol, Dodecanoic acid, and Cyclododecane. Meanwhile, the main compounds in chloroform fractions were 1-Dodecanol, Hexadecanoic acid, and Malonic acid. Dodecanoic acid, and (E)-5-Tetradecene were the major compounds of ethyl acetate fractions (Fig. 2). The EFs were the fraction that had the highest antibacterial inhibitory activity. The EFs of torch ginger contained 19 compounds, with Dodecanoic acid (18.60%) being the most abundant (Table 1). The (E)-5-Tetradecene, 1-Tetradecyl acetate, Cyclotetradecane, Tetradecanoic acid, Cyclotetradecane, *n*-Hexadecanoic acid, Tricosane, Dodecanoic acid, and Dodecyl ester were similar to the

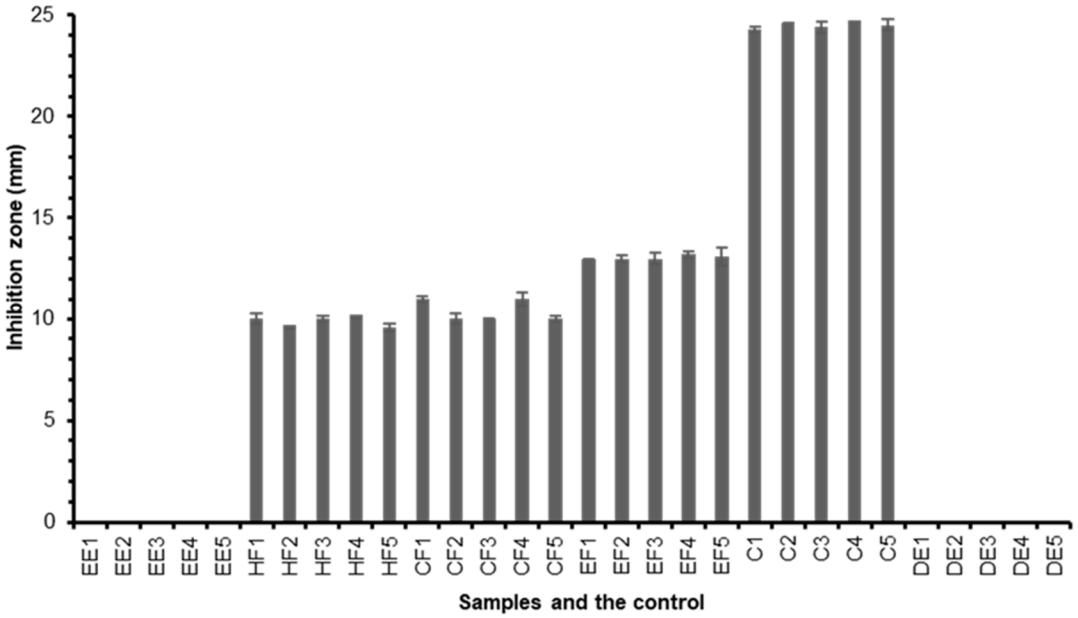

Fig 1. Antibacterial profile of torch ginger extract and fractions against *S. aureus* at 80 mg/mL concentration, 2.50 mg/mL of chloramphenicol (positive control), and DMSO:ethanol (6:2) as a negative control. EE = Ethanol Extract, HF = Hexane Fraction, CF = Chloroform Fraction, EF = Ethyl acetate Fraction, C = Chloramphenicol, and DE = DMSO:ethanol. The DIZ value was the average from two replication with a standard deviation

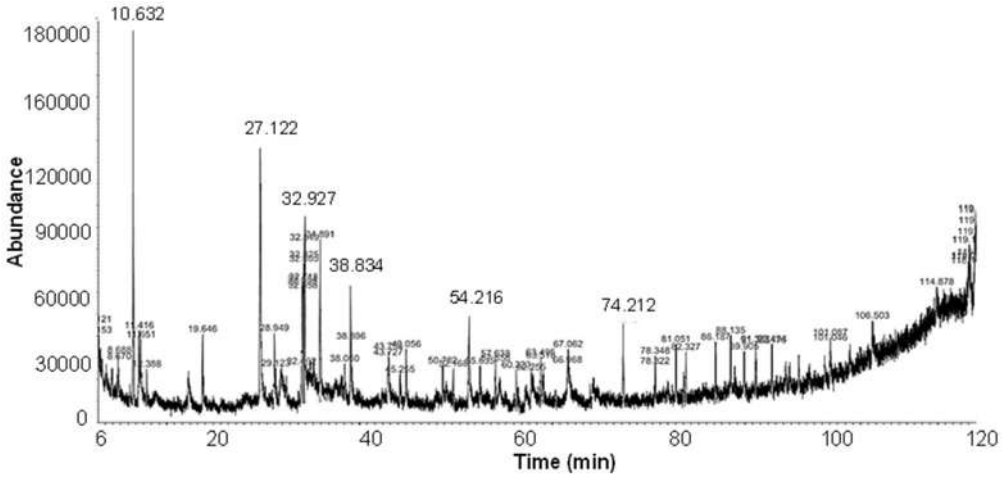

Fig 2. Chromatogram of ethyl acetate fraction from torch ginger

Table 1. Chemical composition of ethyl acetate fraction from torch ginger analyzed by GC-MS analysis

No	RT	Compound	Area %	MW	Structure	Precursor ion	$[M-H]^{+/-}$ product ion (m/z)	Ref. (NIST14.L Library)	Ref.
1	12.39	7-Oxooctanoic acid	0.78	158.19	$C_8H_{14}O_3$	159.00	117.10; 75.10	92728	-
2	27.12	(E)-5-Tetradecene	12.80	196.37	$C_{14}H_{28}$	196.00	55.10; 69.00; 83.10	61866	[20]
3	28.95	2,4-Di-tert-butylphenol	2.34	206.32	$C_{14}H_{22}O$	206.30	191.30; 57.30	70632	-
4	32.93	Dodecanoic acid	18.60	200.32	$C_{12}H_{24}O_2$	200.00	55.10; 60.10; 73.20; 128.90	64983	[2,17,20]
5	34.89	1-Tetradecyl acetate	6.71	256.42	$C_{16}H_{32}O_2$	252.40	55.10; 83.00; 97.30	117423	[2]
6	38.84	Cyclotetradecane	3.20	196.38	$C_{14}H_{28}$	196.30	55.10; 83.10;	61850	[20,21]
7	43.73	Tetradecanoic acid	0.14	228.37	$C_{14}H_{28}O_2$	228.00	55.10; 73.00;	91416	[2,18,20]
8	46.06	Cyclotetradecane	1.61	196.38	$C_{14}H_{28}$	196.50	55.10; 83.20	61849	[20,21]
9	52.17	Methyl hexadecanoate	1.19	270.50	$C_{17}H_{34}O_2$	271.40	87.30; 74.00; 87.30; 55.30; 227.30	130818	-
10	54.22	n-Hexadecanoic acid	3.60	256.42	$C_{16}H_{32}O_2$	256.10	73.10; 60.00	117418	[18,20]
11	55.63	Ethyl hexadecanoate	0.37	284.50	$C_{18}H_{36}O_2$	284.00	69.00; 55.00; 88.10; 100.90	144307	-
12	60.33	Myo-Inositol	0.01	180.16	$C_6H_{12}O_6$	193.10	73.20	273399	-
13	63.49	Ethyl linolate	1.11	308.50	$C_{20}H_{36}O_2$	308.00	67.20; 95.00	167365	-
14	67.06	Cyclobutenylbenzene	0.55	130.19	$C_{10}H_{10}$	131.00	131.00; 55.10; 117.00	41663	-
15	78.35	Tricosane	1.06	324.60	$C_{23}H_{48}$	324.20	57.10; 71.00; 85.00	155900	[20]
16	81.05	Dodecyl dodecanoate	1.91	340.60	$C_{22}H_{44}O_2$	334.20	201.20; 57.10; 71.20	182653	[18]
17	82.33	Hexacosane	1.69	366.70	$C_{26}H_{54}$	366.50	57.10; 71.20; 85.10	219427	-
18	86.19	8-Hexylpentadecane	0.96	296.57	$C_{21}H_{44}$	295.60	57.10; 71.20; 85.10	155894	-
19	89.90	Octacosane	1.70	394.76	$C_{28}H_{58}$	394.40	57.10; 71.20; 85.10	235613	-

previous reports [2,17-18,20-21].

We identified several compounds in extracts and fractions of torch ginger, have also been previously reported such as Dodecanoic acid [2,17,20], *n*-Hexadecanoic acid [18,20], 1-Dodecanol [2,17,20], Tetradecene [20], 1-Decanol [17-18], Tetradecanoic acid [2,18,20], 1-Tetradecyl acetate [2], Acetic acid [22], Dodecene [22], 1,3-Propanediol [22], Cyclododecane [20], 9-Tetradecen-1-ol [18,20], Propanedioic acid [20], 13-Octadecenoic acid [20], 9,12-Octadecadienoic acid [20], Tricosane [20], Dodecane [20], and 1-Tetradecanol [18]. Hexane, chloroform, and ethyl acetate fractions containing some of these compounds have inhibitory activity against *S. aureus*. These compounds have been reported to have antibacterial activities, such as Dodecanoic acid (dilution factor of 1:10) against *S. aureus* (15 ± 1.41 mm) and *Streptococcus pneumoniae* (15 ± 0.00 mm), *Mycobacterium tuberculosis* spp. (14 ± 1,41 mm) [23]. Moreover, *n*-Hexadecanoic acid was suspected as an antibacterial compound in

Pentanisia prunelloides against Gram-positive bacteria (*Bacillus subtilis*, *S. aureus*) and Gram-negative bacteria (*Escherichia coli*, *Klebsiella pneumoniae*) [24]. 1-Dodecanol and 1-Decanol were also reported to have activity against *S. aureus* (MIC 6.25 μg/mL, 50 μg/mL, respectively) and *P. acnes* (MIC 3.13 μg/mL, 25 μg/mL, respectively) [25]. In addition, Tetradecanoic acid-solid lipid nanoparticles (TAS) were also known to have an antibacterial activity where the viable colonies of *Salmonella* CVCC541 bacteria in cells were reduced by 95.83% after TAS treatment [26].

Furthermore, Acetic acid had good activity against clinical and type strains of *P. aeruginosa* at concentrations as low as 0.17%, while 0.31% inhibits MSSA and *A. baumannii* [27]. Kim et al. [28] reported the antibacterial activity of 1,3-Propanediol against *E. coli* (MIC 16%) and *S. aureus* (MIC 16%) bacteria. Moreover, Tricosane was active against Gram-positive: *B. subtilis* CICC 20034; *Flavobacterium SHL45* CICC 51823, Gram-negative: *E. coli* CICC 23845; *P. fluorescens* (*SHL5* CICC 20066, *SHL7* CICC 21620), and Yeast: *S. cerevisiae* (*Ja64* CICC 1346; *Tokay* CICC 1388; *Y-8* CICC 1390) with inhibition zones ranging from 8.03 to 15.97 mm at a concentration of 20 mg/mL [29]. Kubo et al. [30] have reported that 1-Tetradecanol was able to inhibit the growth of *Propionibacterium acnes*, *Brevibacterium ammoniagenes*, and *Streptococcus mutans*.

Orthogonal Projection to the Least Square (OPLS) Analysis of Metabolites Profile and Antibacterial Activity

In OPLS analysis, the X data matrix was the metabolite profile in each extract, and fractions correlated with its antibacterial activity as the Y data matrix. The metabolite profile data used the retention time generated from the GC-MS chromatogram of all extracts and fractions, while the antibacterial activity data used the inhibition zone diameter data of extracts and fractions against *S. aureus* bacteria. Using OPLS analysis, these X and Y data were used to determine the correlation of metabolite profiles and antibacterial activity of extracts and fractions.

To interpret the results of the OPLS analysis, S-plot and Y-related coefficient plot were used. The S-plot was used to classify the retention time of extracts and fractions based on the characteristics given by the Y data matrix. The separation of all retention times between those with low and high activity made it easier to identify retention times for further bioactive components using Y-related coefficients. Fig. 3 shows the S-plot of active and inactive retention times. The more positive the X value, the higher activity can be predicted. In Fig. 3, the retention time of 32.93 min showed the greatest X value, so the most active retention time can be expected. The compound at that retention time was Dodecanoic acid.

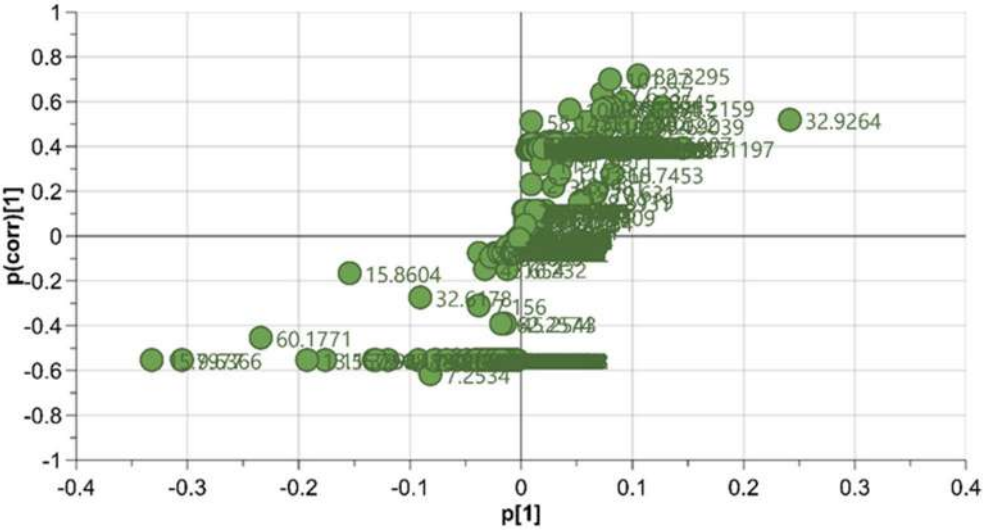

Fig 3. S-plot of extracts and fractions. The more positive the X value, it can be predicted the higher activity

This compound was found in high concentrations in ethyl acetate and hexane fractions. In contrast, the retention times of 15.80 and 60.18 min were the smallest and most predictable as compounds with no antibacterial activity. These compounds predominated in the ethanol extract, which was composed of Glycerol and Myo-Inositol. Glycerol has been reported in torch ginger as well [31]. Additionally, Myo-Inositol has also been found in *Orthosiphon aristatus* (Blume) Miq. (Lamiaceae) [32]. Glycerol and Myo-Inositol are sources of nutrients essential for microbial growth [33].

Furthermore, to determine the high positive correlation value of Y data matrix data with the peak of all retention time, Y-related coefficients were used. A significant correlation is indicated by the Y-related coefficient, which is more than 0.50 [16]. Fig. 4 shows the Y-related coefficient plot, with the highest value found at 32.93 min retention time of 0.81. In addition, there are two retention times with the Y-related coefficient near 0.50. The retention times are 27.12 and 54.22 min, respectively.

Investigation of the retention times of 32.93, 27.12, and 54.22 min resulted in the identification of the compounds of Dodecanoic acid, (E)-5-Tetradecene, and *n*-Hexadecanoic acid, respectively (Fig. 5). This identification was made by comparing the fragmentation pattern and molecular weight to mass spectra available in the NIST14.L and the literature [34-35]. Dodecanoic acid showed peak (intensity %): m/z 55.10 (100%), m/z 60.10 (98.41%), m/z 73.20 (92.89%),

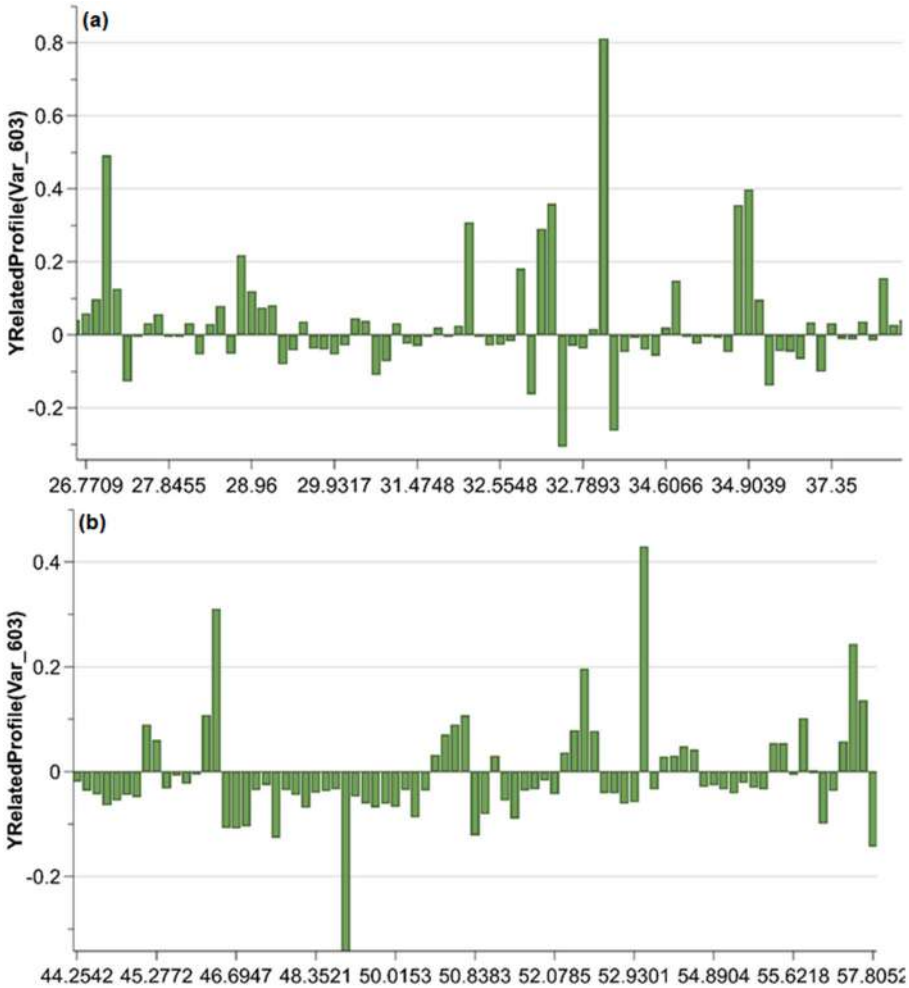

Fig 4. The values of the OPLS Y-related coefficient plot, (a) The plot runs from 26.77 to 37.35 min; (b) The plot runs from 44.25 to 57.80 min

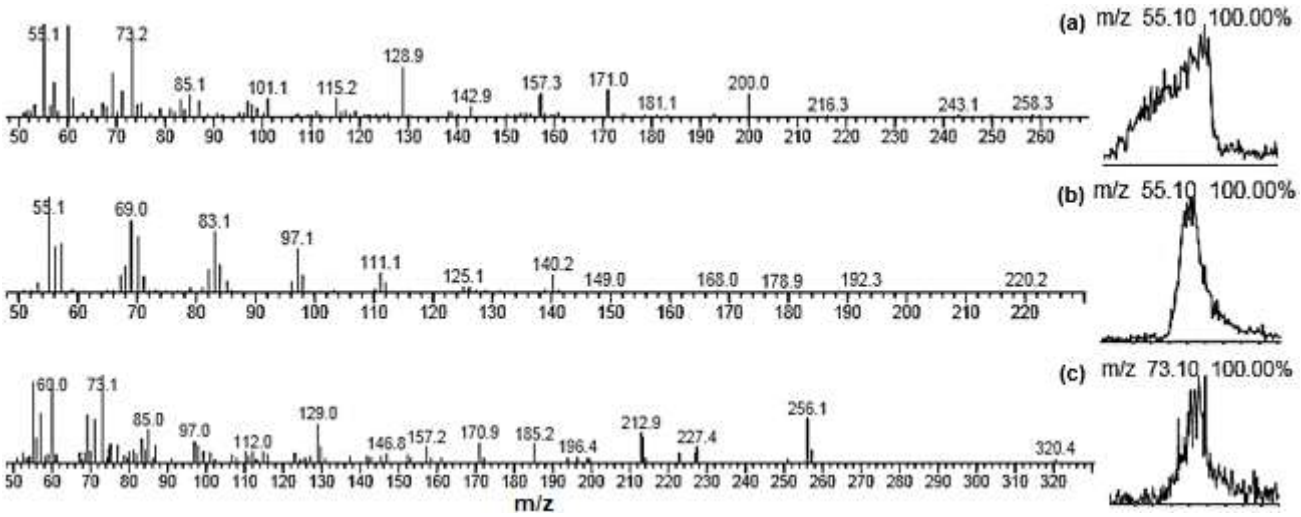

Fig 5. MS fragmentation pattern for retention times of (a) 32.93 min, (b) 27.12 min, and (c) 54.22 min

m/z 128.90 (53.86%), m/z 69.20 (46.78%), while in the literature it had peak (intensity %): m/z 55.10 (100%), m/z 43.00 (92%), m/z 73.00 (90%), m/z 60.00 (85%), m/z 129.00 (30%), m/z 85.00 (30%) [35]. (E)-5-Tetradecene showed peak (intensity %): m/z 55.10 (100%), m/z 69.00 (75.72%), m/z 83.10 (63.86%), m/z 70.20 (59.14%), m/z 57.20 (51.41%), while in the literature for 1-Tetradecene had peak: m/z 55, m/z 41, m/z 43, m/z 83, m/z 57, m/z 69, m/z 97, m/z 168 [34]. *n*-Hexadecanoic acid showed peak (intensity %): m/z 73.10 (100%), m/z 60.00 (93.86%), m/z 55.20 (92.04%), m/z 57.00 (56.69%), m/z 69.20 (55.05%), while in the literature it had peak (intensity %): m/z 73 (100%), m/z 129 (30%), m/z 97 (12%), m/z 256 (12%), m/z 213 (11%) [36].

E. elatior plant extract with *n*-hexane has been reported to have antibacterial activity of *C. gloeosporiodes,* which is identified as Dodecanoic acid, β-Sitosterol, and Stigmasterol [37]. In addition, essential oil components of the Etlingera genus such as Dodecanoic (lauric) acid, Decanoic (capric) acid, aldehydes of Dodecanal, monoterpenes of α-Pinene, β-Pinene, and sesquiterpene of (E)-Caryophyllene have been reported to have antibacterial, antifungal, and antiviral activities [38]. There have been no reports of Tetradecene's antibacterial activity, whereas *n*-Hexadecanoic acid has been extensively described as having antimicrobial activities [39]. In a previous study [40], *Plectranthus amboinicus* leaves extract showed inhibitory activity on *Bacillus subtilis*, Methicillin-resistant *S. aureus*, *Pseudomonas aeruginosa*, *Escherichia coli*, and *Candida albicans* which was correlated with the occurrence of more *n*-Hexadecanoic acid bioactive compounds. Dodecanoic acid and *n*-Hexadecanoic acid are free fatty acids (FFA) whose main antibacterial action is cell membranes, where they interfere with oxidative phosphorylation and the electron transport chain [38]. FFAs are reported to have a non-specific action mode and broad activity spectrum that can be applied in various medicine, food preservation, and agriculture, making them attractive as antibacterial agents where the use of conventional antibiotics is prohibited [38].

■ CONCLUSION

Antibacterial activity tests on the growth of *Staphylococcus aureus* showed the greatest inhibition (DIZ) in the ethyl acetate fraction (13.00–13.20 mm) and followed by chloroform (DIZ 10.00–11.00 mm) and hexane (DIZ 9.55–10.05 mm) fractions of torch ginger (*Etlingera elatior*) flower with a concentration of 80 mg/mL. The result of the OPLS analysis showed that the component at a retention time of 32.93 min correlated significantly with the growth of *S. aureus* bacteria (Y related coefficient value of 0.81). The compound was identified as Dodecanoic acid. Furthermore, (E)-5-Tetradecene and *n*-Hexadecanoic acid compounds were also discovered to be strongly connected to their activity

(Y related coefficient value near to 0.50). Dodecanoic acid and *n*-Hexadecanoic acid compounds have also been reported to have antimicrobial activity, but not (E)-5-Tetradecene. Purification of the (E)-5-Tetradecene compound can be done in further research to confirm its antibacterial activity.

■ ACKNOWLEDGMENTS

The authors are very thankful to the *Lembaga Penelitian* Universitas Sumatera Utara for funding this research (TALENTA USU No: 2590/UN5.1.R/PPM/2018).

■ AUTHOR CONTRIBUTIONS

WHM participated in doing research, AP participated in writing the script, NDY contributed to the analysis of OPLS and revised the manuscript, LML contributed to the extraction of the sample, and AK conducted GCMS analysis. All authors agreed to the final version of this manuscript.

■ REFERENCES

[1] Lutfia, A., Munir, E., and Yurnaliza, Y., 2020, Molecular identification of endophytic fungi from torch ginger (*Etlingera elatior*) antagonist to phytopathogenic fungi, *Biodiversitas*, 21 (6), 2681–2689.

[2] Anzian, A., Rashidah, S., Nazamid, S., Che Wan Sapawi, C.W.N., and Meor Hussin, A.S., 2017, Chemical composition and antioxidant activity of torch ginger (*Etlingera elatior*) flower extract, *Food Appl. Biosci. J.*, 5 (1), 32–49.

[3] Ghasemzadeh, A., Jaafar, H.Z.E., Rahmat, A., and Ashkani, S., 2015, Secondary metabolites constituents and antioxidant, anticancer and antibacterial activities of *Etlingera elatior* (Jack) R.M.Sm grown in different locations of Malaysia, *BMC Complementary Altern. Med.*, 15, 335.

[4] Juwita, T., Puspitasari, I.M., and Levita, J., 2018, Torch ginger (*Etlingera elatior*): A review on its botanical aspects, phytoconstituents and pharmacological activities, *Pak. J. Biol. Sci.*, 21 (4), 151–165.

[5] Nickerson, E.K., Wuthiekanun, V., Wongsuvan, G., Limmathurosakul, D., Srisamang, P., Mahavanakul, W., Thaipadungpanit, J., Shah, K.R., Arayawichanont, A., Amornchai, P., Thanwisai, A.T., Day, N.P., and Peacock, S.J., 2009, Factors predicting and reducing mortality in patients with invasive *Staphylococcus aureus* disease in a developing country, *Plos One*, 4 (8), e6512.

[6] Wijekoon, M.M.J.O., Bhat, R., Karim, A.A., and Fazilah, A., 2013, Chemical composition and antimicrobial activity of essential oil and solvent extracts of torch ginger inflorescence (*Etlingera elatior* Jack.), *Int. J. Food Prop.*, 16 (6), 1200–1210.

[7] Maser, W., Rusmarilin, H., and Yuliana, N., 2017, Aplikasi metabolomik berbasis HPLC untuk mengidentifikasi waktu retensi komponen antibakteri *Stapylococcus aureus* pada ekstrak bunga kecombrang (*Etlingera elatior*), *ALCHEMY Jurnal Penelitian Kimia*, 13 (2), 241–251.

[8] Yuliana, N.D., Khatib, A., Verpoorte, R., and Choi, Y.H., 2011, Comprehensive extraction method integrated with NMR metabolomics: A new bioactivity screening method for plants, adenosine A1 receptor binding compounds in *Orthosiphon stamineus* Benth, *Anal. Chem.*, 83 (17), 6902–6906.

[9] Maser, W.H., Yuliana, N.D., and Andarwulan, N., 2015, Rapid identification of antibacterial compounds from Turkey berry by HPLC-based metabolomics, *J. Liq. Chromatogr. Relat. Technol.*, 38 (12), 1230–1235.

[10] Gathungu, R.M., Kautz, R., Kristal, B.S., Bird, S.S., and Vouros, P., 2020, The integration of LC-MS and NMR for the analysis of low molecular weight trace analytes in complex matrices, *Mass Spectrom. Rev.*, 39 (1-2), 35–54.

[11] Jorge, T.F., Mata, A.T., and António, C., 2016, Mass spectrometry as a quantitative tool in plant metabolomics, *Philos. Trans. R. Soc., A*, 374 (2079), 20150370.

[12] Javadi, N., Abas, F., Hamid, A.A., Simoh, S., Shaari, K., Ismail, I.S., Mediani, A., and Khatib, A., 2014, GC-MS-based metabolite profiling of *Cosmos caudatus* leaves possessing alpha-glucosidase inhibitory activity, *J. Food Sci.*, 79, C1130–C1136.

[13] Murugesu, S., Ibrahim, Z., Ahmed, Q.U., Nik Yusoff, N.I., Uzir, B.F., Perumal, V., Abas, F., Saari,

K., El-Seedi, H., and Khatib, A., 2018, Characterization of α-glucosidase inhibitors from *Clinacanthus nutans* Lindau leaves by gas chromatography-mass spectrometry-based metabolomics and molecular docking simulation, *Molecules*, 23 (9), 2402.

[14] Tan, D.C., Kassim, N.K., Ismail, I.S., Hamid, M., and Ahamad Bustamam, M.S., 2019, Identification of antidiabetic metabolites from *Paederia foetida* L. twigs by gas chromatography-mass spectrometry-based metabolomics and molecular docking study, *Biomed Res. Int.*, 2019, 7603125.

[15] Balouiri, M., Sadiki, M., and Ibnsouda, S.K., 2016, Methods for *in vitro* evaluating antimicrobial activity: A review, *J. Pharm. Anal.*, 6 (2), 71–79.

[16] Weisenhorn, E.M.M., van 't Erve, T.J., Riley, N.M., Hess, J.R., Raife, T.J., and Coon, J.J., 2016, Multi-omics evidence for inheritance of energy pathways in red blood cells, *Mol. Cell. Proteomics*, 15 (12), 3614–3623.

[17] Anzian, A., Muhialdin, B.J., Mohammed, N.K., Kadum, H., Marzlan, A.A., Sukor, R., and Meor Hussin, A.S., 2020, Antibacterial activity and metabolomics profiling of torch ginger (*Etlingera elatior* Jack) flower oil extracted using subcritical carbon dioxide (CO_2), *Evidence-Based Complementary Altern. Med.*, 2020, 4373401.

[18] Susanti, D., Awang, N.A., Qaralleh, H., Sheikh Mohamed, H.I., and Attoumani, N., 2013, Antimicrobial activity and chemical composition of essential oil of Malaysian *Etlingera elatior* (Jack) RM Smith flowers, *J. Essent. Oil Bear. Plants*, 16 (2), 294–299.

[19] Kumar, V., Ahluwalia, V., Saran, S., Kumar, J., Patel, A.K., and Singhania, R.R., 2021, Recent developments on solid-state fermentation for production of microbial secondary metabolites: Challenges and solutions, *Bioresour. Technol.*, 323, 124566.

[20] Maimulyanti, A., and Prihadi, A.R., 2015, Chemical composition, phytochemical and antioxidant activity from extract of *Etlingera elatior* flower from Indonesia, *J. Pharmacogn. Phytochem.*, 3 (6), 233–238.

[21] Sukandar, D., Fitriyanti, M., Amelia, E.R., Riyadhi, A., and Azizah, R.N., 2017, Characterization of Chemical Constituent and Antibacterial Activity of Honje Fruit Skin (*Etlingera elatior*), *Proceedings of the International Conference on Science and Technology (ICOSAT 2017)*, 21–24.

[22] Abdelwahab, S.I., Zaman, F.Q., Mariod, A.A., Yaacob, M., Ahmed Abdelmageed, A.H., and Khamis, S., 2010, Chemical composition, antioxidant and antibacterial properties of the essential oils of *Etlingera elatior* and *Cinnamomum pubescens* Kochummen, *J. Sci. Food Agric.*, 90 (15), 2682–2688.

[23] Anzaku, A., Akyala, J., Juliet, A., and Obianuju, E., 2017, Antibacterial activity of lauric acid on some selected clinical isolates, *Ann. Clin. Lab. Res.*, 5 (2), 1–5.

[24] Yff, B.T., Lindsey, K.L., Taylor, M.B., Erasmus, D.G., and Jäger, A.K., 2002, The pharmacological screening of *Pentanisia prunelloides* and the isolation of the antibacterial compound palmitic acid, *J. Ethnopharmacol.*, 79 (1), 101–107.

[25] Kubo, I., Muroi, H., Masaki, H., and Kubo, A., 1993, Antibacterial activity of long-chain alcohols: The role of hydrophobic alkyl groups, *Bioorg. Med. Chem. Lett.*, 3 (6), 1305–1308.

[26] Meng, K., Chen, D., Yang, F., Zhang, A., Tao, Y., Qu, W., Pan, Y., Hao, H., and Xie, S., 2020, Intracellular delivery, accumulation, and discrepancy in antibacterial activity of four enrofloxacin-loaded fatty acid solid lipid nanoparticles, *Colloids Surf., B*, 194, 111196.

[27] Fraise, A., Wilkinson, M., Bradley, C., Oppenheim, B., and Moiemen, N., 2013, The antibacterial activity and stability of acetic acid, *J. Hosp. Infect.*, 84 (4), 329–331.

[28] Kim, S.H., Yun, Y., and An, S., 2018, A study on synergistic antibacterial activity of cosmetic ingredients, *J. Soc. Cosmet. Sci. Korea*, 44 (1), 1–7.

[29] Tao, C., Wu, J., Liu, Y., Liu, M., Yang, R., and Lv, Z., 2018, Antimicrobial activities of bamboo (*Phyllostachys heterocycla cv. Pubescens*) leaf

essential oil and its major components, *Eur. Food Res. Technol.*, 244 (5), 881–891.

[30] Kubo, I., Muroi, H., and Kubo, A., 1995, Structural functions of antimicrobial long-chain alcohols and phenols, *Bioorg. Med. Chem.*, 3 (7), 873–880.

[31] Srey, C., 2015, Chemical study of *Etlingera elatior* (Zingiberaceae)-rhizome and its α-glucosidase and α-amylase inhibitory activities, *Thesis*, Prince of Songkla University, Thailand.

[32] Arifullah, M., Vikram, P., Chiruvella, K.K., Shaik, M.M., and Ripain, I.H.B.A., 2014, A review on Malaysian plants used for screening of antimicrobial activity, *Annu. Res. Rev. Biol.*, 4 (13), 2088–2132.

[33] You, R., Wang, L., Shi, C., Chen, H., Zhang, S., Hu, M., and Tao, Y., 2020, Efficient production of myo-inositol in *Escherichia coli* through metabolic engineering, *Microb. Cell Fact.*, 19 (1), 109.

[34] Matloub, A.A., Hamed, M.A., and El Souda, S., 2014, Chemo-protective effect on hepato-renal toxicity and cytotoxic activity of lipoidal matter of *Atriplex lindleyi* Moq, *Int. J. Pharm. Pharm. Sci.*, 6 (8), 187–196.

[35] Bakr, R.O., Mohamed, S.A., and Waly, N.E., 2017, Phytochemical and biological investigation of *Eugenia uniflora* L. cultivated in Egypt, *J. Pharmacogn. Phytother.*, 9 (5), 57–66.

[36] Song, S.H., Park, D.H., Bae, M.S., Choi, C.Y., Shim, J.H., Yoon, G., Cho, Y.C., Oh, D.S., Yoon, I.S., and Cho, S.S., 2018, Ethanol extract of *Cudrania tricuspidata* leaf ameliorates hyperuricemia in mice via inhibition of hepatic and serum xanthine oxidase activity, *Evidence-Based Complementary Altern. Med.*, 2018, 8037925.

[37] Punnawich, Y., Montree, I., Warin, I., and Kan, C., 2009, Antifungal effects of Thai medicinal plants against *Collectotrichum gloeosporioides* Penz., *Philipp. Agric. Sci.*, 92 (3), 265–270.

[38] Desbois, A.P., and Smith, V.J., 2010, Antibacterial free fatty acids: Activities, mechanisms of action and biotechnological potential, *Appl. Microbiol. Biotechnol.*, 85 (6), 1629–1642.

[39] Willie, P., Uyoh, E.A., and Aikpokpodion, P.O., 2021, Gas chromatography-mass spectrometry (GC-MS) assay of bio-active compounds and phytochemical analyses in three species of Apocynaceae, *Pharmacogn. J.*, 13 (2), 383–392.

[40] Swamy, M.K., Arumugam, G., Kaur, R., Ghasemzadeh, A., Yusoff, M.M., and Sinniah, U.R., 2017, GC-MS based metabolite profiling, antioxidant and antimicrobial properties of different solvent extracts of Malaysian *Plectranthus amboinicus* leaves, *Evidence-Based Complementary Altern. Med.*, 2017, 1517683.

Gold Nanoparticle Capped Citrate as a Ligand for Chromium(III) Ion: Optimization and Its Application in Contaminated Tap Water

Eman Turky Shamkhy[1*] and Amjed Mirza Oda[2]

[1]*Department of Basic Science, College of Dentistry, University of Baghdad, Iraq*

[2]*Department of Chemistry, College of Sciences, University of Babylon, Babylon 51002, Iraq*

* ***Corresponding author:***

tel: +964-7714627857
email: Emanturky.832017@gmail.com

Received: January 30, 2022
Accepted: April 1, 2022

DOI: 10.22146/ijc.72651

Abstract: *Citrate-capped gold nanoparticle (GNP) was used as a ligand for chromium chelating, and chromium ions reaction led to GNP aggregation. The color change of GNP by aggregation in the presence of chromium is a simple and rapid colorimetric test for these ions in an aqueous solution. GNP capped citrate was prepared by the citrate method and characterized by TEM, and its particle size was 20 nm. Also, the surface plasmon resonance (SPR) peak was 520 nm. In the presence of chromium ions, the color of GNP at 520 nm was shifted to 650 nm because of aggregation to give a signal as a ratio of $A_{650/520}$ more than one and proportional with chromium concentration directly. The optimum conditions were studied to obtain the high signal represented by the volume of GNP, reaction kinetic of A_{650} with time, selectivity, and interferences of Zn(II), Fe(III), Fe(II), Sn(II), Ni(II), Ca(II), Al(III), Sr(II), Cu(II), Mn(II), Co(II), Mg(II), Ag(I), and Pb(II) ions. The calibration curve is linear in the range of 100–500 ppb, and the regression was 0.9951 and applied on tap water chromium ions in the same range in the regression of 0.95. This method was simple, rapid reaction, consumed low volumes of sample, and had low detection limits. It can be recommended as a new method for chromium (III) detection in aqueous solutions.*

Keywords: *citrate; chromium(III); nanoparticle; gold capped; tap water*

■ INTRODUCTION

The entering of heavy metal wastes as a result of increased industrial use through numerous channels generates very effective harm to the environment and humankind. Lead, copper, iron, zinc, nickel, cobalt, cadmium, chromium, mercury, gold, and silver are all heavy metals that are not biodegradable. Heavy metal uptake from the surrounding environment via the food chain results in the presence and enrichment of higher species tens of thousands of times, and human ingestion via the food chain could result in chronic poisoning. In vivo, high Cr absorptions can cause fibroproliferative disease, airway hypersensitivity, nasal cancer, lung cancer, and other cancers. Exposure to Cr can produce different point mutations in DNA, chromosomal damage, and oxidative alterations in proteins in addition to adduct formation. Because each form of Cr has a different level of toxicity, the health impacts of each are varied [1-3]. Dispersive liquid-liquid microextraction and dried-droplet laser ablation ICP-MS [4], carbon composite-PVC based membrane coated platinum electrode, amperometric enzyme-based sensor [5], flame atomic absorption spectrometry [6], fluorine-doped graphite pencil electrode [7], and nano-Au/TiO_2 photocatalysis reduction with low-cost instrumentation requirements, as well as simple operation and quick results [8], and immunochromatographic assay were rapid and simple detection of chromium ion [9].

The wide range of uses for metal nanoparticles in sensing, catalysis, electronics, and photonics has a huge interest [10]. GNPs are of special interest because of their good biocompatibility, conductivity, and high surface-to-volume ratio, which have made them useful in environmental monitoring and biological sensing [11]. GNPs are commonly employed in electroanalysis [12], biosensors [13], colorimetric detection [14], and other applications. It is straightforward and quick to use

a colorimetric detection approach based on monitoring the color change caused by GNP aggregation or corrosion. Also, heavy metal ions have been detected using this technology extensively [15-16].

In this research, simple colorimetric detection of chromium ions was demonstrated good sensing at trace concentration. The procedure was based on the GNP aggregation to give a clear signal and shift from red to blue midnight color. GNP was synthesized by the citrate method and characterized by TEM, and the detection was optimized according to the volume of GNP and aggregation dependence time. Also, the selectivity and interferences were studied, and a calibration curve of pure and tap water was established.

■ EXPERIMENTAL SECTION

Materials

Gold(III) chloride trihydrate ($HAuCl_4 \cdot 3H_2O$) and sodium citrate were sourced from Sigma-Aldrich. Salts of Cu^{2+}, Ag^{+}, Ca^{2+}, Cd^{2+}, Zn^{2+}, Mg^{2+}, Sn^{2+}, Fe^{2+}, Fe^{3+}, Al^{3+}, Sr^{2+}, and Ni^{2+} were purchased from Thompson baker, India. Acetic acid and chromium salt were supplied from GCC.

Instrumentation

Transmission electron microscopy (TEM) measurements were carried out using a Zies transmission electron microscope operating at 100 kV. A drop of the GNP solution was placed on a copper grid and air-dried before the measurement. The UV-visible absorption spectra were obtained using a PerkinElmer Lambda 25 spectrophotometer.

Procedure

Synthesis of GNP

GNP capped citrate with a diameter of 20 nm was prepared by reducing 1 mM of $HAuCl_4$ by sodium citrate (1%) according to [17-18] with slight modification. Briefly, 10 mL of $HAuCl_4$ was heated nearing boiling temperature, and 1 mL of citrate solution was added rapidly. The solution was stirred continuously, and the yellow color of gold ions was fainted to colorless. Then blue sky color is appeared and darkens into dark blue, turning to cherry red color after 15 min of heating. Mixing was continued till cooling to room temperature, and the dark red mixture was filtered with a 0.22 μM Millipore membrane filter, then GNP solution was used for detection freshly.

Optimization of chromium ions detection

Several experiments were done to optimize the final conditions for chromium detection by GNP. Firstly, the reaction of chromium ions with GNP capped citrate is limited and sensitive to acetic acid addition, where at a certain volume, the aggregation is triggered and changes the color. Therefore, acetic acid 1% (v/v) is used in the following additions (5, 10, 15, 20, 25, and 30 μL) to 300 μL of GNP, and the color change was monitored for 15 min, where no change in color is the volume that GNP is stable. The color is stable at 25 μL and enough to give a final change in color after the addition of 200 ppb chromium ions. Also, the development of color was monitored after the addition of chromium ions (200 ppb), and the absorbance at 650 was measured with time for 10 min to establish a stable signal. GNP volume was studied in the various volume of GNP (100, 200, 300, 400, 500, and 600 μL) to validate the high signal as $A_{650/520}$ in the detection of chromium ions (200 ppb). The effect of selectivity and interferences ions were Zn(II), Fe(III), Fe(II), Sn(II), Ni(II), Ca(II), Al(III), Sr(II), Cu(II), Mn(II), Co(II), Mg(II), Ag(I), and Pb(II) ions, where the volume of GNP and acetic acid were 200 μL and 25 μL, respectively, the ions were 500 ppb, and the final volume was 1 mL. All these experiments were measured at room temperature and for 10 min, and the absorbance was recorded as $A_{650/520}$.

■ RESULTS AND DISCUSSION

In Fig. 1, the UV-visible absorption spectrum of GNP is shown, where the SPR band was discovered to be located at 520 nm. The Au SPR absorption is ascribed to this band. The location of this band was consistent within 2 nm four times of GNP preparations. The shape and size of the GNP were determined using TEM techniques. The TEM picture showed three scales and described all samples with a spherical and narrow distribution of GNP. The particles were spherical or semispherical in shape and had an average size of 20 nm, as shown in Fig. 2. The cherry red of GNP is clear and has

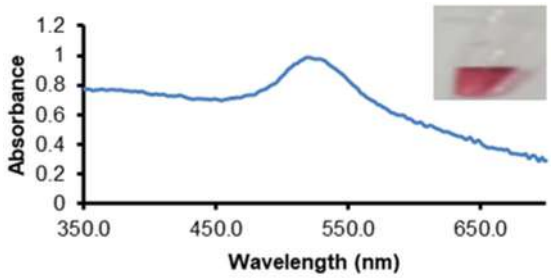

Fig 1. The absorption spectra of GNP (Inset: the red solution of prepared GNP)

good stability for 1 week, which is prepared by the citrate method many times in the same color and absorption values.

At 520 nm, GNPs with less than 60 nm have extraordinarily high extinction coefficients. Furthermore, the various aggregation phases of GNPs can cause significant color variations. These unique optical properties make GNP a suitable color-reporting candidate for signaling molecular recognition events and enable trace concentration detection. As a result, colorimetric assays based on GNP aggregation are well established as a simple and sensitive detection method. The GNPs are aggregated by an analyte of cross-linking molecules that have several binding sites for molecules immobilized on the GNP surface in the majority of these experiments [19]. This phenomenon is the base of chromium detection in aqueous solutions by GNP color change, and it is important to optimize the clear signal for a visual test. The test depends on the deep red color of GNP at the level that is visual to the naked eye, so the effect of dilution on GNP solution is studied, where the tolerance is not exceeded five times dilution. The concentration of GNP was determined and found to equal to 10.9 nM from Beer-Lambert law via UV-vis spectroscopy and based on as reported, where the extension coefficient was 8.78×10^8 M^{-1} cm^{-1} at λ_{max} 520 nm and the size was 20 nm [20]. The as-prepared GNP can be diluted to give a good signal and easily detected by the eyes. In our experiments, the dilution was 5 times applied for all experiments. In Fig. 3, the calibration curve is plotted according to the high extension coefficient as reported above, and the relationship is in a good straight line with a high correlation coefficient equal to 0.9956.

GNP stability solution is monitored for any alteration in color under storage, and we recommend it be used for not more than one weak. The storage of GNP was done in the ambient condition in our lab, and the

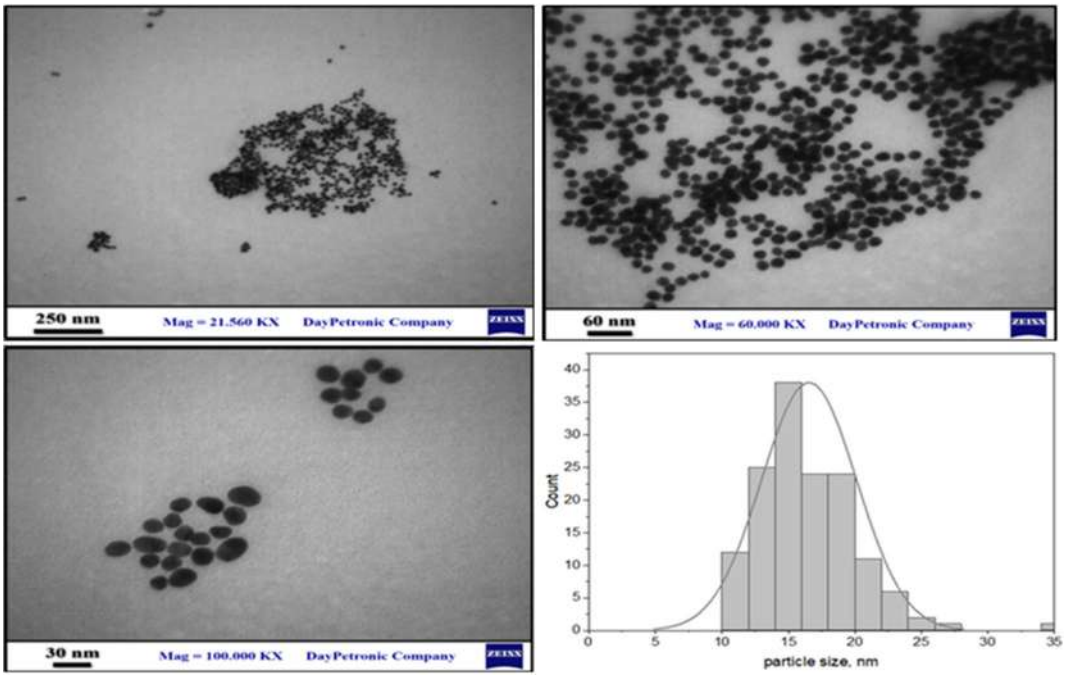

Fig 2. TEM images of GNP in different scales as prepared by citrate method and the size distribution

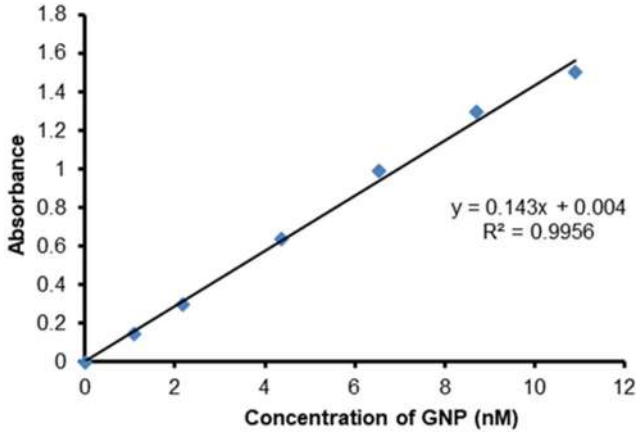

Fig 3. Correlation between GNP concentration and absorbance at 520 nm

absorbance was tested every day as absorbance at 520 nm in a UV-vis spectrophotometer. The result is not shown, but the data of absorbance was stable and changed by only 20%. This is due to self-aggregation or formation of clusters in the preparation and should be monitored with time as reported [21].

Optimization of GNP Detection

Effect of time

The color change of citrate-capped GNP is sensitive to the presence of chromium ions. This reaction depends on the aggregation of gold nanoparticles capped citrate, where the latter is the ligand probe for chromium ion masking [22]. The reaction is working on, and a fast reaction needs a second to change color from red to blue but to reach a stable blue color needing time to give a stable absorbance. The change of color is monitored by measuring the absorbance at 650 nm with time from 0–10 min to determine the optimum time and constant absorbance with time. The kinetics of aggregation was studied for A_{650} as a signal for aggregation. It was increased in steeping slope. For 3 min, the absorbance was stable, and then a plateau appeared in the range of 3–10 min. In our results, we found the rapid test by this simple procedure as the change in color is fast and indicates the presence of chromium(III) ions in aqueous solutions. The results appear in Fig. 4, which is shown the absorbance at 650 nm of gold nanoparticles solution (after aggregation) related to time in seconds. Our findings on this kinetics are agreed upon by other researchers who worked on the kinetics of gold nanoparticle aggregation [23].

Effect of GNP volume

This part aims to optimize the volume of GNP for a high detection signal in the presence of a constant concentration of chromium ions. The procedure was done by measuring the signal as A_{650}/A_{520} of the samples by adding various volumes of gold nanoparticles and chromium ions at 500 ppb. The highest signal of GNP in various volumes to detect chromium ions was 200 µL and then diluted with distilled water for a final volume of 1 mL. As the GNP volume was changed, the signal was different due to GNP capped citrate working as a ligand and aggregating around chromium ion to give the highest signal. At a low volume of GNP, the change in

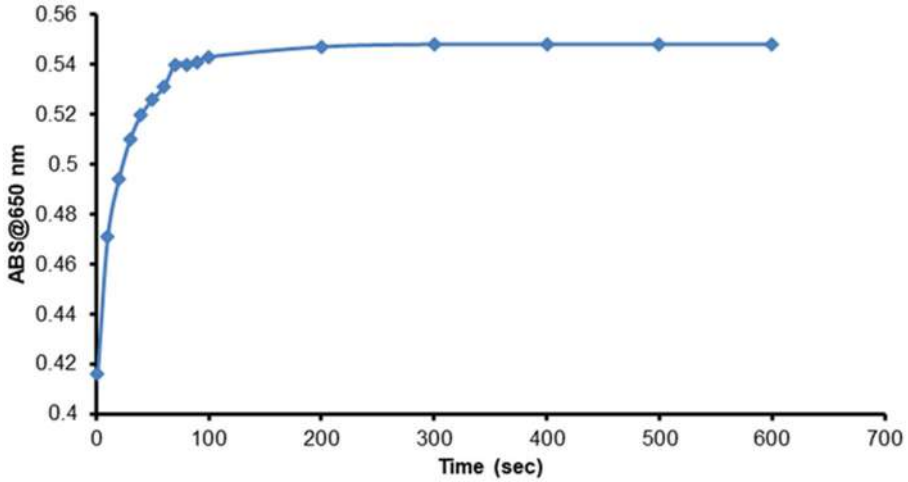

Fig 4. The kinetic plot of GNP as a function of time (200 ppb of chromium, 200 µL of GNP, and total volume is 1 mL)

color into the blue is not representing all chromium ions attaching because the ratio of reaction is low, and many chromium ions were free without reaction leading to low aggregation. Whereas at a high volume of GNP, all chromium ions are attached. But the excess of non-aggregated GNP affected the signal value, especially at A_{520}, where a high value made the final signal of absorbance ratio A_{650}/A_{520} low. We found that 200 µL of GNP as a volume is the best, where the signal was high and a low-noise red color. In Fig. 5, the volume of GNP added to chromium ions solution was effective on the signal of detection (A_{650}/A_{520}). The distinctive color was clear and gave a high signal in the form of A_{650}/A_{520}, as shown compared to other signals resulting from different GNP volumes.

Effect of acetic acid

The important factor in the color change was the addition of acetic acid (1% v/v), and we found that the trigger was this acid. In the preliminary experiment, in the absence of acetic acid, there is no change in color though chromium ion was added. Thus, this detection is very limited by acetic acid, and changing its addition was a reactive stimuli factor for detection. When the addition was less than 25 µL, there was no change in color, which gave the false-negative signal. In contrast, more than this volume, the color change into blue (aggregation by acid) despite no chromium ions being added, and this is the false-positive signal due to the salting out of GNP. Also, acetic acid could aid in the stability of GNP in an aqueous solution to keep surface charge high and zeta potential. Acetic acid gives high dispersion as the carboxylic moieties make the protection of surface [24]. There is no visual change in GNP solution at 25 µL of 1% acetic acid. It was stable for 30 min, and there was no change in absorption or wavelength. The blue color appeared in the acidified GNP solution after the addition of chromium ions, where the absorption changed and the bathochromic shift at 650 nm. The role of acetic acid as a trigger in detection is working for the acceleration of aggregation, especially when chromium ions are found [25]. In Fig. 6, the UV-vis absorption spectra red and blue line of acidified GNP solution before and after chromium ions addition, respectively, and the stacked photograph picture is the GNP before (right) and after chromium addition (left).

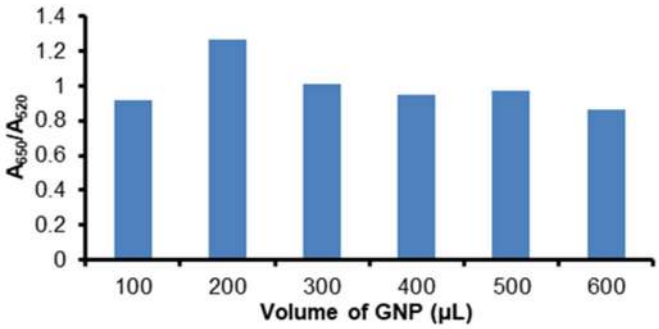

Fig 5. Effect of volume change of GNP on signal A_{650}/A_{520} in chromium detection (200 ppb)

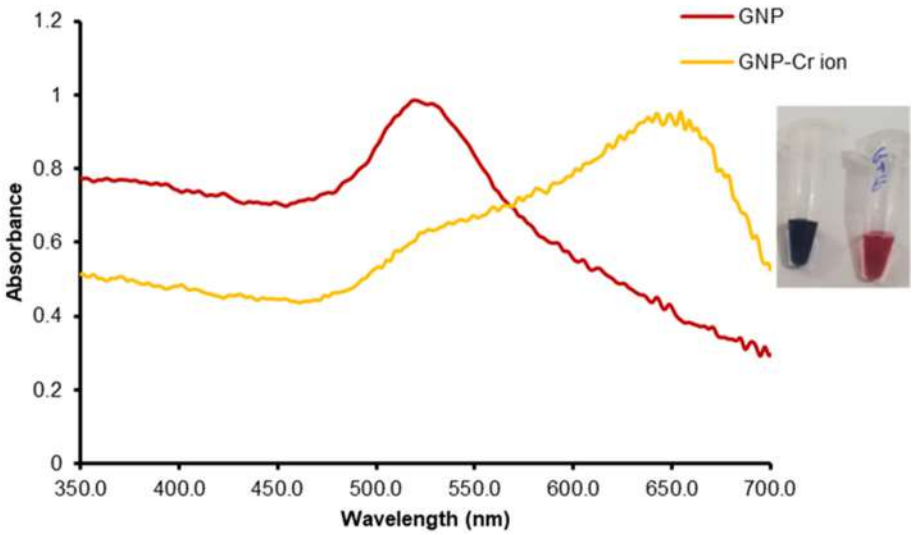

Fig 6. UV-vis spectra of GNP solution before and after detection of chromium ions

To show that citrate-capped GNP is selective for chromium ions, we studied the interaction of other ions on the signal of GNP ratio A_{650}/A_{520}. Like these ions Zn(II), Fe(III), Fe(II), Sn(II), Ni(II), Ca(II), Al(III), Sr(II), Cu(II), Mn(II), Co(II), Mg(II), Ag(I) and Pb(II) and each ions concentration was 500 ppb and chromium ions were 200 ppb. Experimentally, there is no color change of GNP with these ions compared to chromium ions. The color stays red, the signal is strong for chromium ions, and the blue color is clear visually. In Fig. 7, the representation results of selectivity of GNP toward chromium ion to give a high signal compared to other ions, and the difference is very large. All ions under study have not interacted with GNP, and their color is unchanged visually. Also, the signal of other ions is near the GNP blank with red color. This is explained that the high absorbance ratio of chromium-GNP was affected by the aggregation of GNP. In contrast, in the presence of other ions, the value of A_{650}/A_{520} was low, indicating well-dispersed forms of citrate-capped GNP. Therefore, chromium ions must selectively interact with a specific site on the surface of GNP [26].

The selectivity of this procedure is examined to detect the interference of coexisting ions. Metal ions such as ions Zn(II), Fe(III), Fe(II), Sn(II), Ni(II), Ca(II), Al(III), Sr(II), Cu(II), Mn(II), Co(II), Mg(II), Ag(I) and Pb(II) challenge this detection technique [27]. Each type of metal ion has a concentration of 500 ppb. The chromium ion concentration is chosen to be 200 ppb. All ions are added to the same solution to the GNP solution to study the interference effect of all ions on the color of GNP. The signal is almost stable for 30 min, and no color change in the absence of chromium ions. Also, the spectrum of GNP with ions is similar to the negative signal. According to the spectra in Fig. 8, the absorption at 520 nm is not changed despite the presence of interferences of ions and no difference in peak location of citrate-capped GNP and GNP with interference ions. After adding chromium ions, the absorption peak decreased at 520 nm and increased at 650 nm considerably, as reported [28]. That is an indication of interferences from all ions understudy that did not affect the signal of GNP. In Fig. 9, the $A_{650/520}$ ratio for chromium ions is greater than one. Its value exceeds the signal of A_{650}/A_{520} that belongs to GNP with or without interfered ions, where this is a very good result to estimate chromium according to this method. Also, we found the signal induction is strong in the presence of other ions as an indication that the interference ions do not affect chromium ions detection, and this method is hard resisting the interferences [29]. The signal as A_{650}/A_{520} of GNP in the presence and absence of chromium ions interfered with the ions under study is shown in Fig. 9.

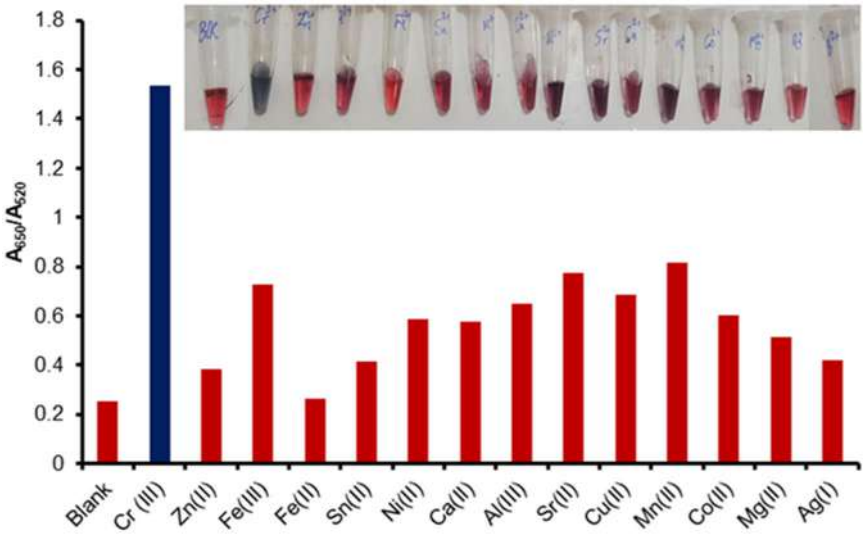

Fig 7. Ratio A_{650}/A_{520} of the chromium ions selectivity against other studied ions. Chromium ions concentration is 200 ppb, and the other ions are 500 ppb, and the stacked picture is the visual color of blank GNP (first left), chromium ions (second left), and all ions on the right

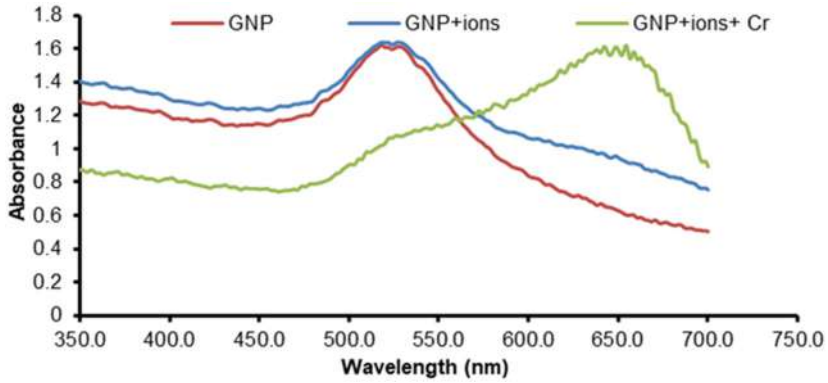

Fig 8. UV-vis spectra of GNP, GNP-interfered ions, and GNP-interfered ions after chromium ions addition. The ions are Zn(II), Fe(III), Fe(II), Sn(II), Ni(II), Ca(II), Al(III), Sr(II), Cu(II), Mn(II), Co(II), Mg(II) and Pb(II)

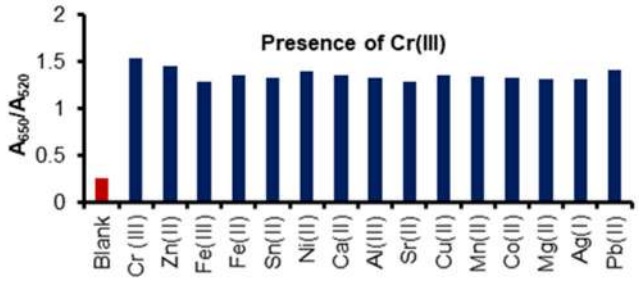

Fig 9. Signal A_{650}/A_{520} of GNP and GNP in the presence of interference ions

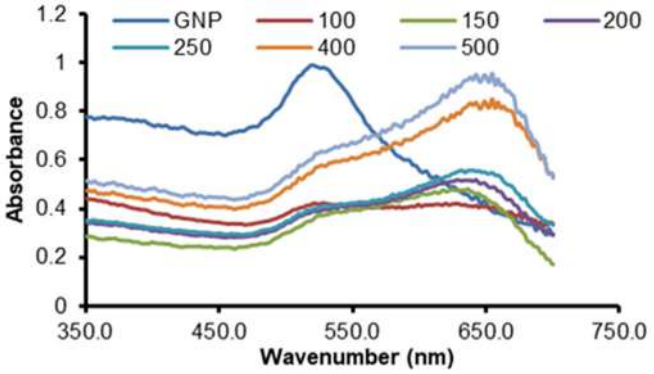

Fig 10. UV-vis spectra of GNP before and after adding standard concentrations of chromium ions

Calibration

Chromium was quantified by GNP capped citrate, where the absorption ratio of A_{650}/A_{520} was used to monitor the color change of GNP by adding various concentrations of chromium ions in the range of 100–500 ppb. We found a related signal to the changing of concentration chromium ions. As the chromium ions concentration increased, the color of the GNP solution changed from red to dark midnight blue. The understudy concentrations were 100–500 ppb, where the absorbance at 650 nm increased, whereas the peak at 520 nm decreased, as shown in Fig. 10. The absorption spectra of GNP before reaction and after reaction with chromium ions have appeared and shifted from 520 nm to 650 nm in each spectrum. The absorption ratio A_{650}/A_{520} was used as a signal, and it is different in sensitivity and proportional to chromium concentration. In this study, the calibration is ranged from 100 to 500 ppb within the linear range of the calibration curve with high regression equal to 0.9951, and the detection limit was 50 ppb was calculated according to the

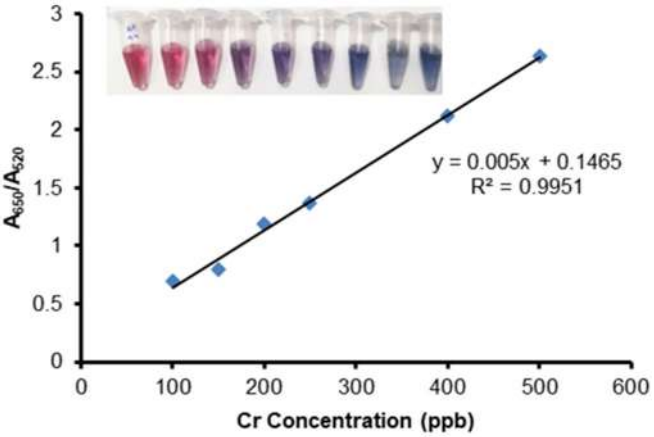

Fig 11. Calibration curve of chromium ions according to A_{650}/A_{520} of GNP, and the stacked picture is a color change of GNP

S/N = 3 rule [30]. The calibration curve of chromium ion concentration change was proportional to the signal A_{650}/A_{520}, which is illustrated in Fig. 11.

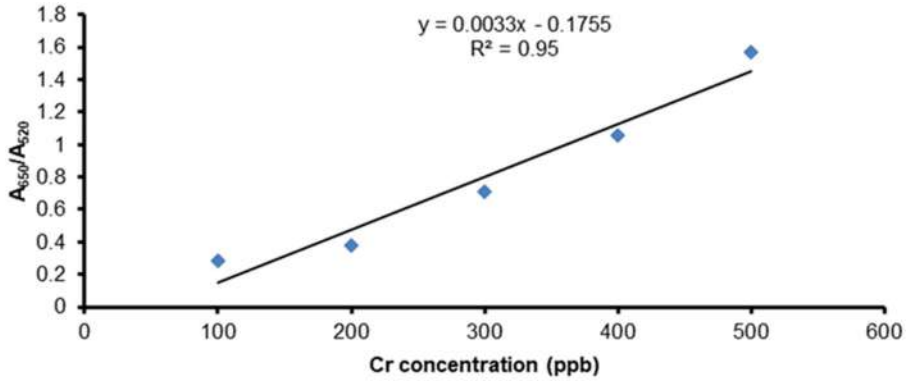

Fig 12. The application of chromium ions detection by GNP as a calibration curve

The detection application is applied on real tap water to specify the accuracy in color change and compare it with experimental calibration. The concentration of chromium ions in the range of 100–500 ppb was prepared as a sample in tap water, and GNP color change was recorded as A_{650}/A_{520}. The range of detection for chromium ions in tap water with good regression (0.95) and good signal to detect in tap water is shown in Fig. 12.

■ CONCLUSION

GNP capped citrate was prepared at particle size about 20 nm by citrate method and stable for one week and can be prepared three repeats without SPR peak change. This method is simple and rapid for chromium ions detection using GNP as a ligand. The change in color absorption decreased at 520 nm and increased at 650 nm, where the signal was more reasonable as A_{650}/A_{520}. The aggregation is affected by acetic acid addition, which accelerates the color change, and the signal A_{650}/A_{520} was affected by the volume of GNP. The signal A_{650}/A_{520} of chromium ions was not affected in the presence of Zn(II), Fe(III), Fe(II), Sn(II), Ni(II), Ca(II), Al(III), Sr(II), Cu(II), Mn(II), Co(II), Mg(II), Ag(I) and Pb(II), to be selective and less interfere chromium ions in aqueous solution. The A_{650}/A_{520} was proportional with chromium concentration, and the range was 100–500 ppb with 50 ppb as a detection limit. Also, it was applicable in tab water in the same concentration range. This method was very beneficial for chromium(III) ion detection in the lab or polluted sample, and it can be immobilized on paper lateral force test to get a more powerful and easy test.

■ REFERENCES

[1] Li, Y.T., Becquer, T., Dai, J., Quantin, C., and Benedetti, M.F., 2009, Ion activity and distribution of heavy metals in acid mine drainage polluted subtropical soils, *Environ. Pollut.*, 157 (4), 1249–1257.

[2] Nguyen, H.D., Nguyen, T.T.L., Nguyen, K.M., Tran, T.A.T., Nguyen, A.M., and Nguyen, Q.H., 2015, Determination of ppt level chromium(VI) using the gold nano-flakes electrodeposited on platinum rotating disk electrode and modified with 4-thiopyridinium, *Am. J. Anal. Chem.*, 6 (5), 457–467.

[3] Liu, X., Xiang, J.J., Tang, Y., Zhang, X.L., Fu, Q.Q., Zou, J.H., and Lin, Y., 2012, Colloidal gold nanoparticle probe-based immunochromatographic assay for the rapid detection of chromium ions in water and serum samples, *Anal. Chim. Acta*, 745, 99–105.

[4] Villaseñor, Á., Greatti, C., Boccongelli, M., and Todolí, J.L., 2017, A dried droplet calibration approach for the analysis of solid samples through laser ablation - inductively coupled plasma mass spectrometry, *J. Anal. At. Spectrom.*, 32 (3), 587–596.

[5] Han, X., Li, C., and Yong, D., 2019, Microbial electrode sensor for heavy-metal ions, *Sens. Mater.*, 31 (12), 4103–4111.

[6] Bhatt, R., Bhatt, R., and Padmaja, P., 2018, DTPA capped gold and silver nanofluids-facile synthesis and their application as chromium sensors, *Sens. Actuators, B*, 258, 602–611.

[7] Ly, S.Y., and Kim, M.J., 2009, Diagnostic assay of

chromium (VI) in the ex vivo fluid of the urine of a smoker using a fluorine-doped handmade sensor, *J. Clin. Lab. Anal.*, 23 (2), 82–87.

[8] Peng, G., He, Q., Lu, Y., Huang, J., and Lin, J.M., 2017, Flow injection microfluidic device with on-line fluorescent derivatization for the determination of Cr(III) and Cr(VI) in water samples after solid-phase extraction, *Anal. Chim. Acta*, 955, 58–66.

[9] Paek, S.H., Lee, S.H., Cho, J.H., and Kim, Y.S., 2000, Development of rapid one-step immuno chromatographic assay, *Methods*, 22 (1), 53–60.

[10] Hussein, M.A., Ganash, A.A., and Alqarni, S.A., 2019, Electrochemical sensor-based gold nanoparticle/poly(aniline-co-o-toluidine)/graphene oxide nanocomposite modified electrode for hexavalent chromium detection: a real test sample, *Polym.-Plast. Technol. Mater.*, 58 (13), 1423–1436.

[11] He, M.Q., Yu, Y.L., and Wang, J.H., 2020, Biomolecule-tailored assembly and morphology of gold nanoparticles for LSPR applications, *Nano Today*, 35, 101005.

[12] Bagheri, N., Mazzaracchio, V., Cinti, S., Colozza, N., Di Natale, C., Netti, P.A., Saraji, M., Moscone, D., and Arduini, F., 2021, Electroanalytical sensor based on gold-nanoparticle-decorated paper for sensitive detection of copper ions in sweat and serum, *Anal. Chem.*, 93 (12), 5225–5233.

[13] Liu, M., Yu, X., Chen, Z., Yang, T., Yang, D., Liu, Q., Du, K., Li, B., Wang, Z., Li, S., Deng, Y., and He, N., 2017, Aptamer selection and applications for breast cancer diagnostics and therapy, *J. Nanobiotechnol.*, 15 (1), 81.

[14] Bothra, S., Kumar, R., and Sahoo, S.K., 2015, Pyridoxal derivative functionalized gold nanoparticles for colorimetric determination of zinc(II) and aluminium(III), *RSC Adv.*, 5 (118), 97690–97695.

[15] Priyadarshini, E., and Pradhan, N., 2017, Metal-induced aggregation of valine capped gold nanoparticles: An efficient and rapid approach for colorimetric detection of Pb^{2+} ions, *Sci. Rep.*, 7 (1), 9278.

[16] Wang, Y., Wang, L., Su, Z., Xue, J., Dong, J., Zhang, C., Hua, X., Wang, M., and Liu, F., 2017, Multipath colourimetric assay for copper(II) ions utilizing MarR functionalized gold nanoparticles, *Sci. Rep.*, 7 (1), 41557.

[17] Leng, W., Pati, P., and Vikesland, P.J., 2015, Room temperature seed mediated growth of gold nanoparticles: Mechanistic investigations and life cycle assessment, *Environ. Sci.: Nano*, 2 (5), 440–453.

[18] Herizchi, R., Abbasi, E., Milani, M., and Akbarzadeh, A., 2016, Current methods for synthesis of gold nanoparticles, *Artif. Cells Nanomed. Biotechnol.*, 44 (2), 596–602.

[19] Bansal, S.A., Kumar, V., Karimi, J., Singh, A.P., and Kumar, S., 2020, Role of gold nanoparticles in advanced biomedical applications, *Nanoscale Adv.*, 2 (9), 3764–3787.

[20] Kim, D.K., Hwang, Y.J., Yoon, C., Yoon, H.O., Chang, K.S., Lee, G., Lee, S., and Yi, G.R., 2015, Experimental approach to the fundamental limit of the extinction coefficients of ultra-smooth and highly spherical gold nanoparticles, *Phys. Chem. Chem. Phys.*, 17 (32), 20786–20794.

[21] Epanchintseva, A.V., Poletaeva, J.E., Pyshnyi, D.V., Ryabchikova, E.I., and Pyshnaya, I.A., 2019, Long-term stability and scale-up of noncovalently bound gold nanoparticle-siRNA suspensions, *Beilstein J. Nanotechnol.*, 10, 2568–2578.

[22] Chang, C.C., Chen, C.P., Wu, T.H., Yang, C.H., Lin, C.W., and Chen, C.Y., 2019, Gold nanoparticle-based colorimetric strategies for chemical and biological sensing applications, *Nanomaterials*, 9 (6), 861.

[23] Zhang, Z., Ye, X., Liu, Q., Liu, Y., and Liu, R., 2020, Colorimetric detection of Cr^{3+} based on gold nanoparticles functionalized with 4-mercapto benzoic acid, *J. Anal. Sci. Technol.*, 11 (1), 10.

[24] Ejeta, S.Y., and Imae, T., 2021, Selective colorimetric and electrochemical detections of Cr(III) pollutant in water on 3-mercaptopropionic acid-functionalized gold plasmon nanoparticles, *Anal. Chim. Acta*, 1152, 338272.

[25] Iglesias, E., 2020, Gold nanoparticles as colorimetric sensors for the detection of DNA bases and related compounds, *Molecules*, 25 (12), 2890.

[26] Kim, K.M., Nam, Y.S., Lee, Y., and Lee, K.B., 2018, A highly sensitive and selective colorimetric Hg^{2+} ion probe using gold nanoparticles functionalized with polyethyleneimine, *J. Anal. Methods Chem.*, 2018, 1206913.

[27] Salimi, F., Kiani, M., Karami, C., and Taher, M.A., 2018, Colorimetric sensor of detection of Cr(III) and Fe(II) ions in aqueous solutions using gold nanoparticles modified with methylene blue, *Optik*, 158, 813–825.

[28] Jin, W., Huang, P., Chen, Y., Wu, F., and Wan, Y., 2015, Colorimetric detection of Cr^{3+} using gold nanoparticles functionalized with 4-amino hippuric acid, *J. Nanopart. Res.*, 17 (9), 358.

[29] Jian-feng, G., Chang-jun, H., Mei, Y., Dan-qun, H., Jun-jie, L., Huan-bao, F., Hui-bo, L., and Ping, Y., 2016, Colorimetric sensing of chromium(VI) ions in aqueous solution based on the leaching of protein-stabled gold nanoparticles, *Anal. Methods*, 8 (27), 5526–5532.

[30] Karami, C., Arkan, E., and Arabi, M.S., 2019, Detection of chromium(III) in drinking water with modified gold nanoparticle, *Desalin. Water Treat.*, 165, 197–202.

Supplementary Data

This supplementary data is a part of paper entitled "Sesquiterpenoids from the Stem Bark of *Lansium domesticum* Corr. Cv. Kokossan and Their Cytotoxic Activity against MCF-7 Breast Cancer Cell Lines".

Table of Contents

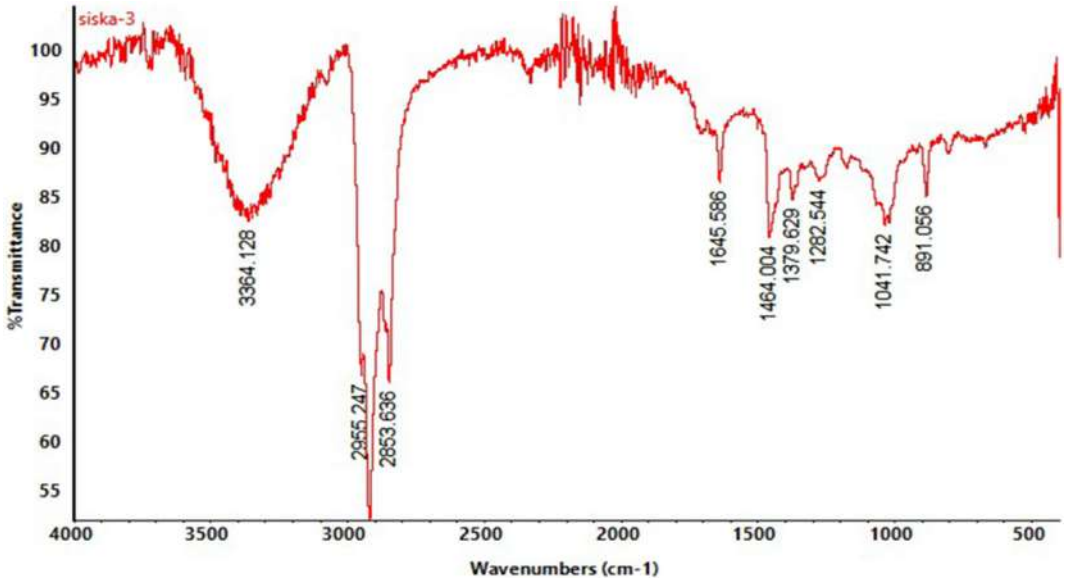

Fig S1. FT-IR spectrum of **1**

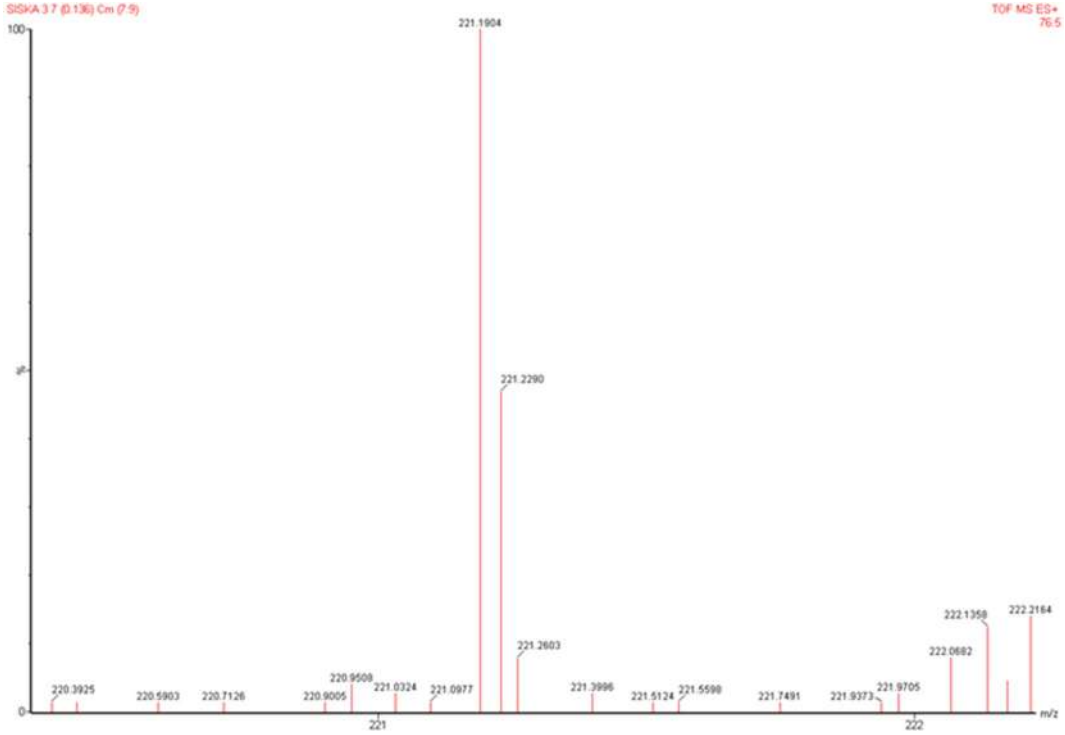

Fig S2. HR-TOFMS spectrum of **1**

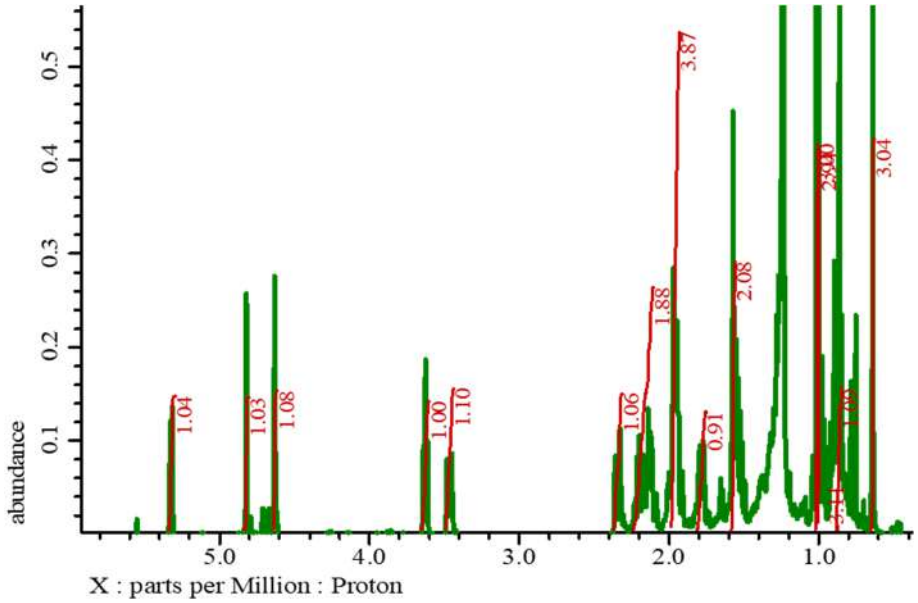

Fig S3. ^{1}H-NMR spectra of **1** (500 MHz in $CDCl_3$)

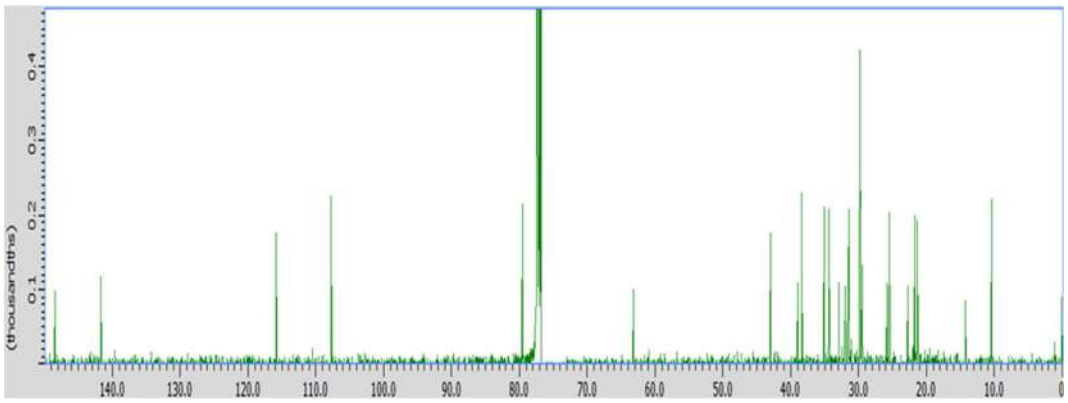

Fig S4. ^{13}C-NMR spectrum of **1** (125 MHz in CDCl3)

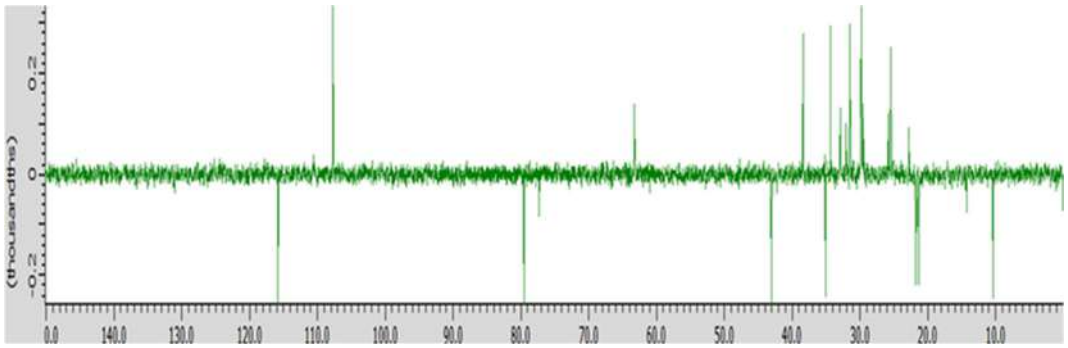

Fig S5. DEPT- 135° spectrum of **1** (125 MHz in CDCl3)

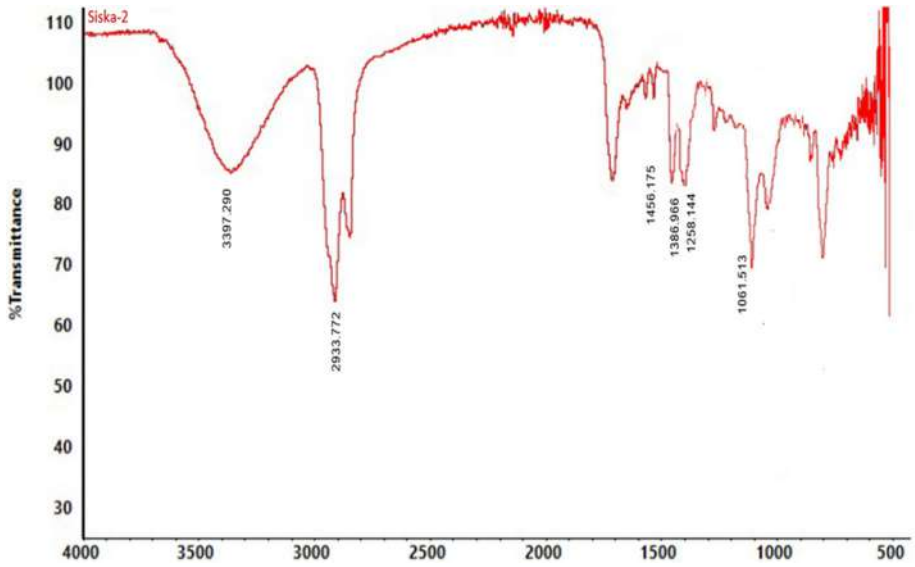

Fig S6. FTIR spectrum of **2**

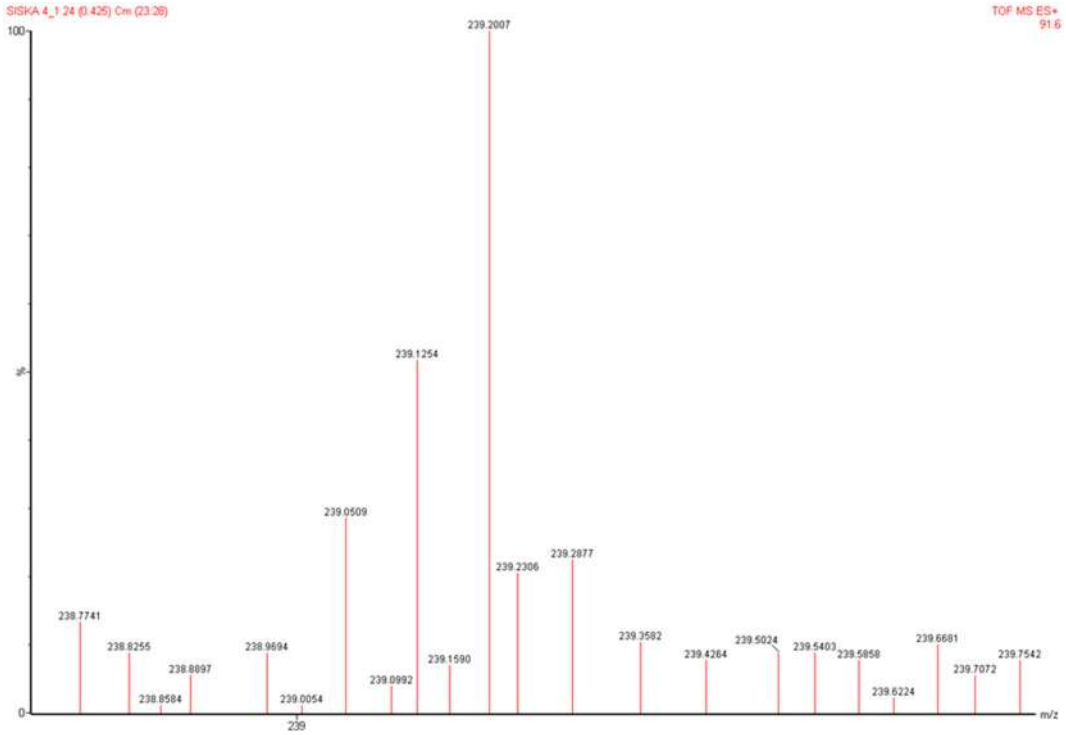

Fig S7. HRTOF-MS spectrum of **2**

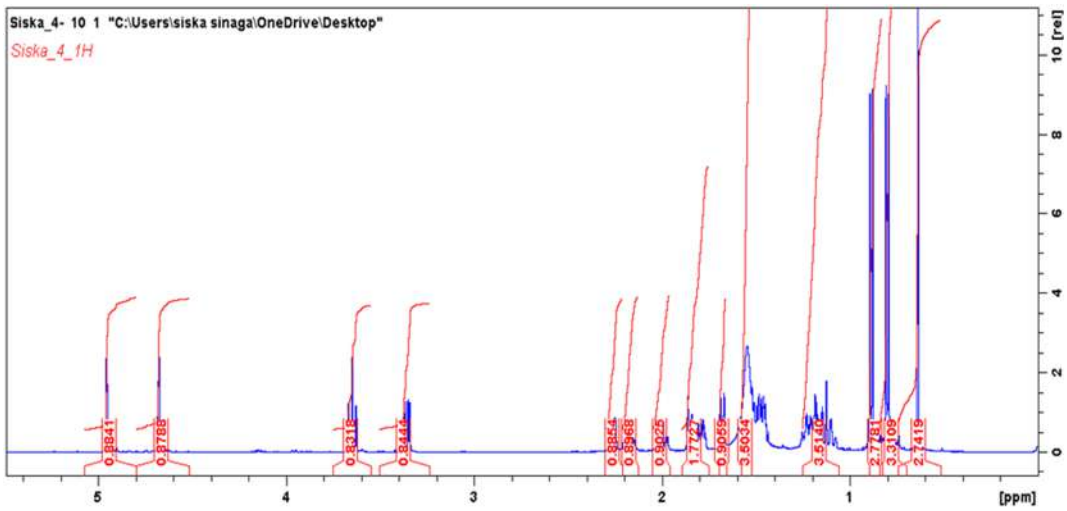

Fig S8. ^{1}H-NMR spectra of **2** (500 MHz in CDCl3)

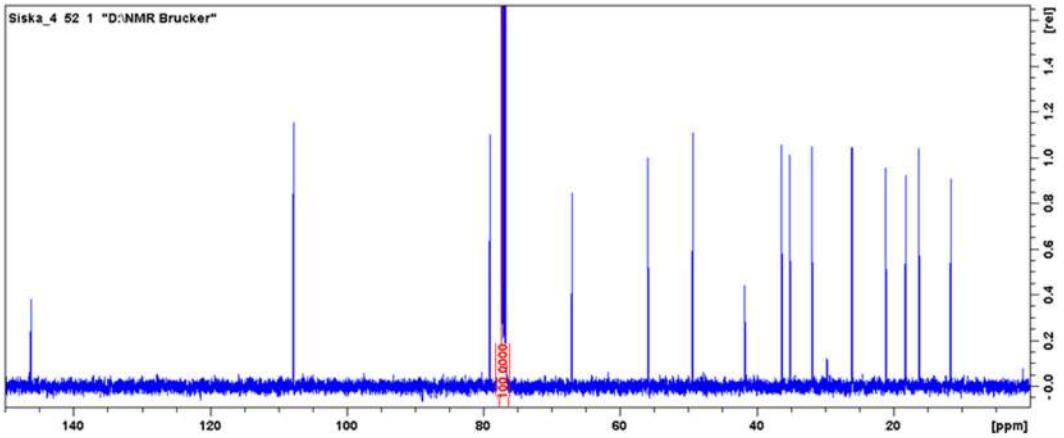

Fig S9. ^{13}C-NMR spectrum of **2** (125 MHz in CDCl3)

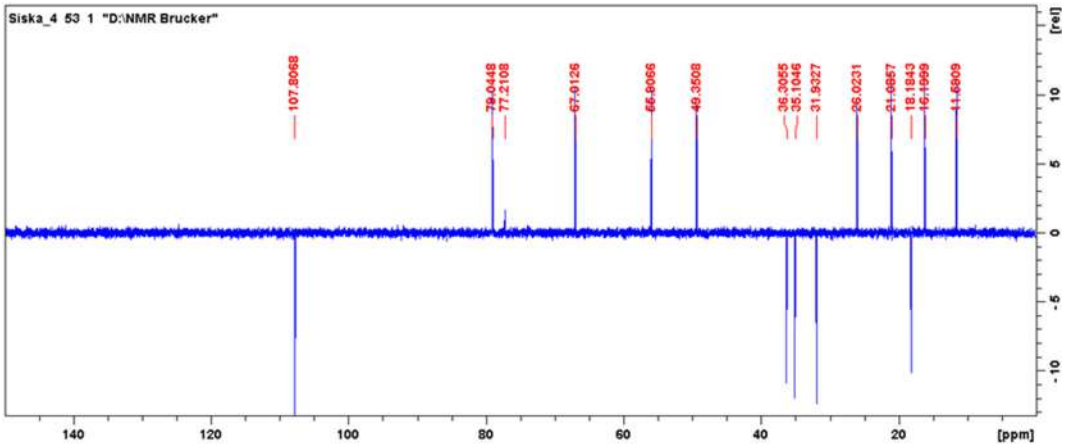

Fig S10. DEPT- 135° spectrum of **2** (125 MHz in CDCl3)

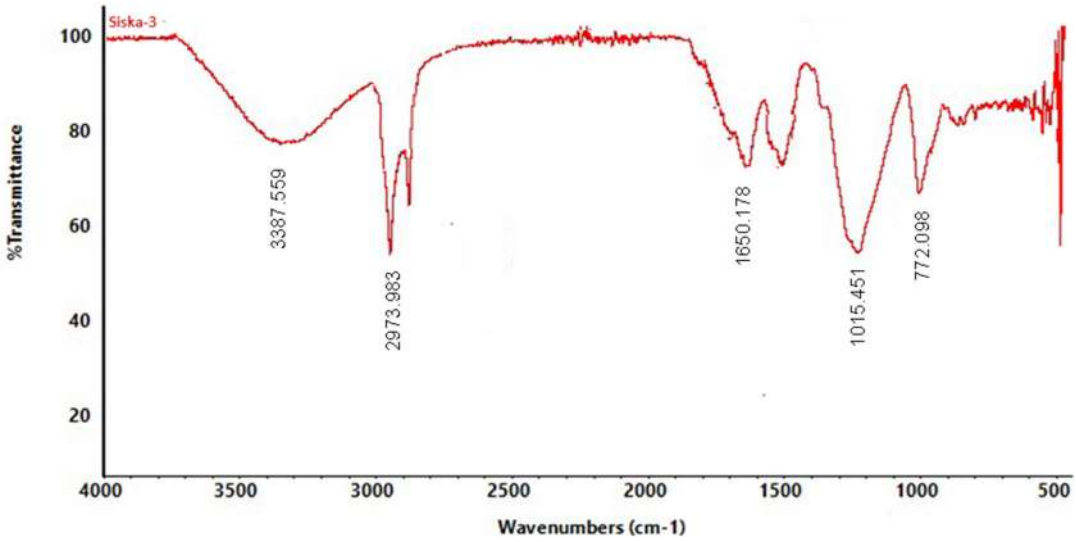

Fig S11. FTIR spectrum of **3**

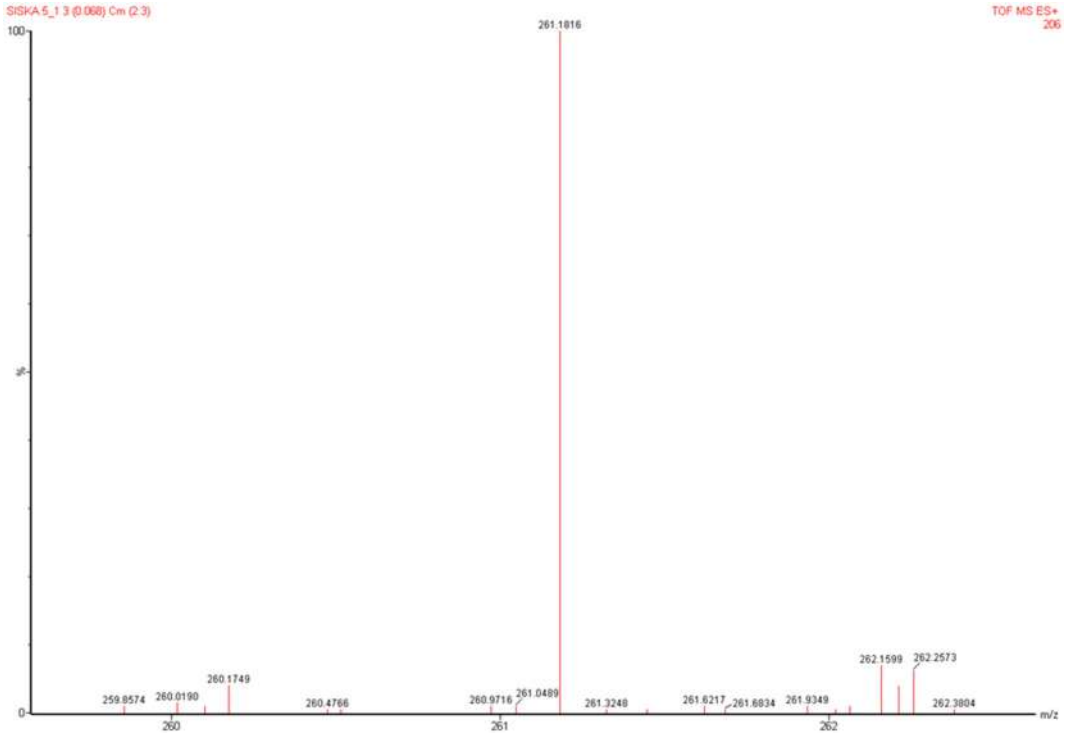

Fig S12. HR-TOFMS spectrum of **3**

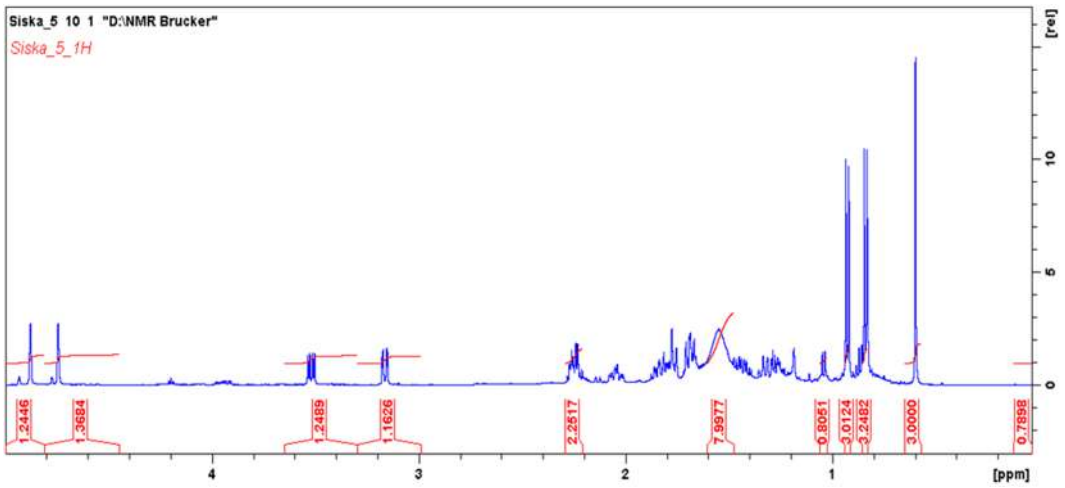

Fig S13. ^{1}H-NMR spectra of **3** (500 MHz in $CDCl_3$)

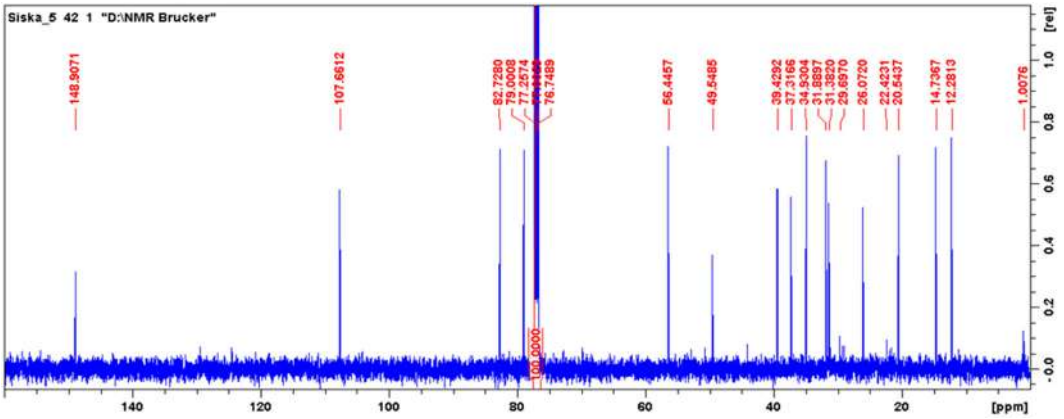

Fig S14. ^{13}C-NMR spectrum of **3** (125 MHz in $CDCl_3$)

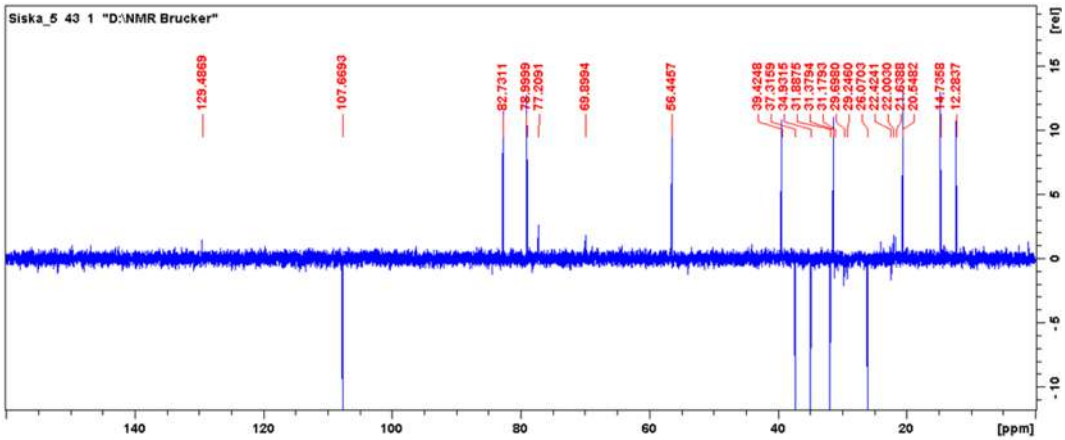

Fig S15. DEPT 135° spectrum of **3** (125 MHz in $CDCl_3$)

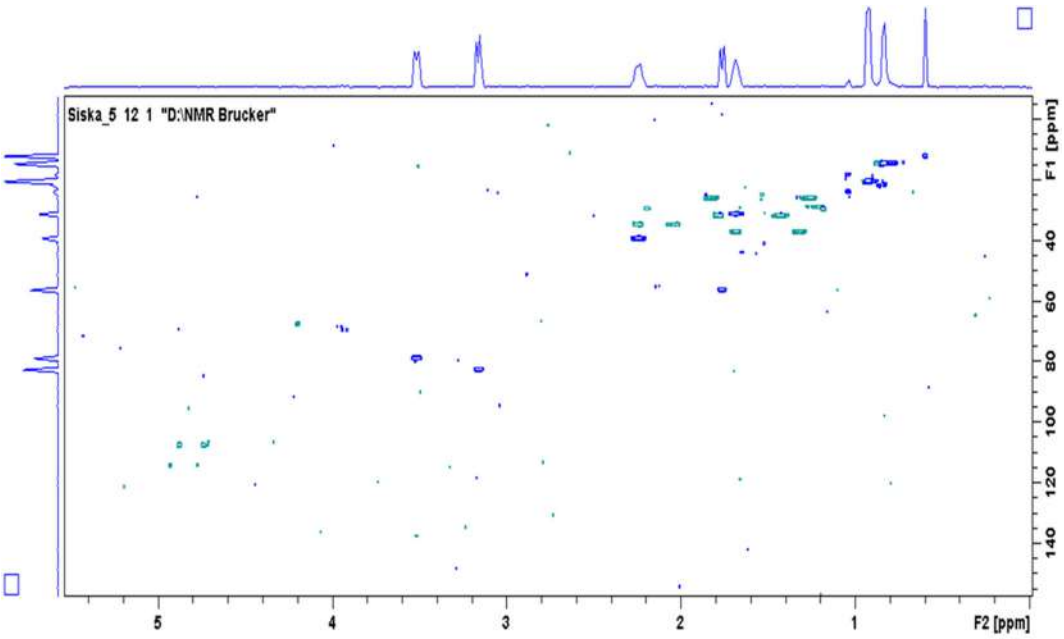

Fig S16. HSQC spectrum of **3**

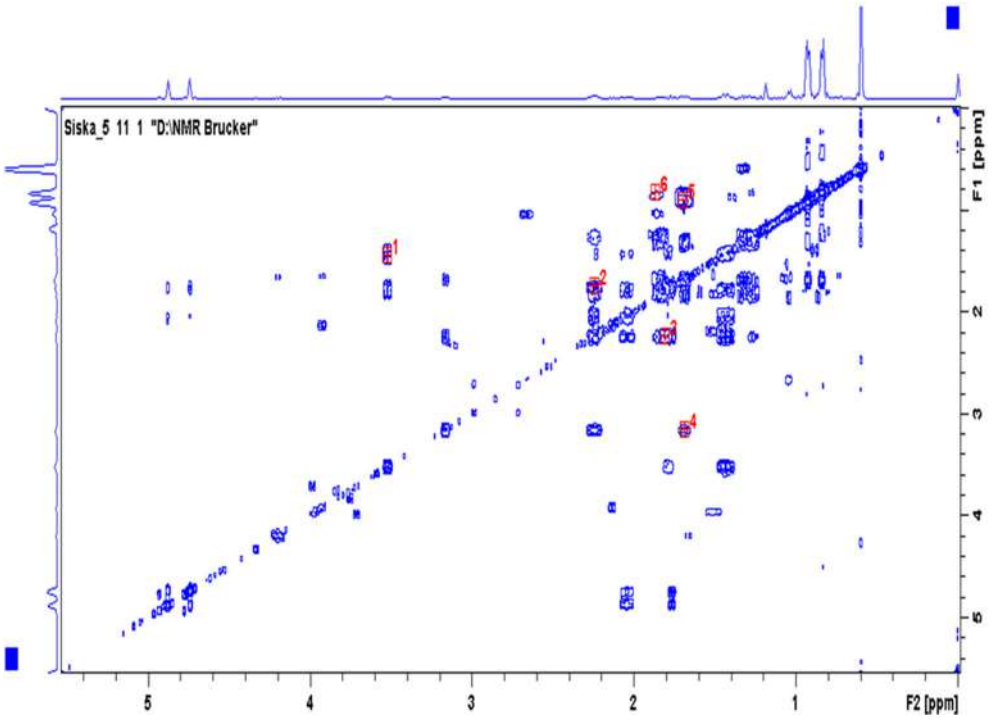

Fig S17. ^{1}H-^{1}H-COSY spectra of **3**

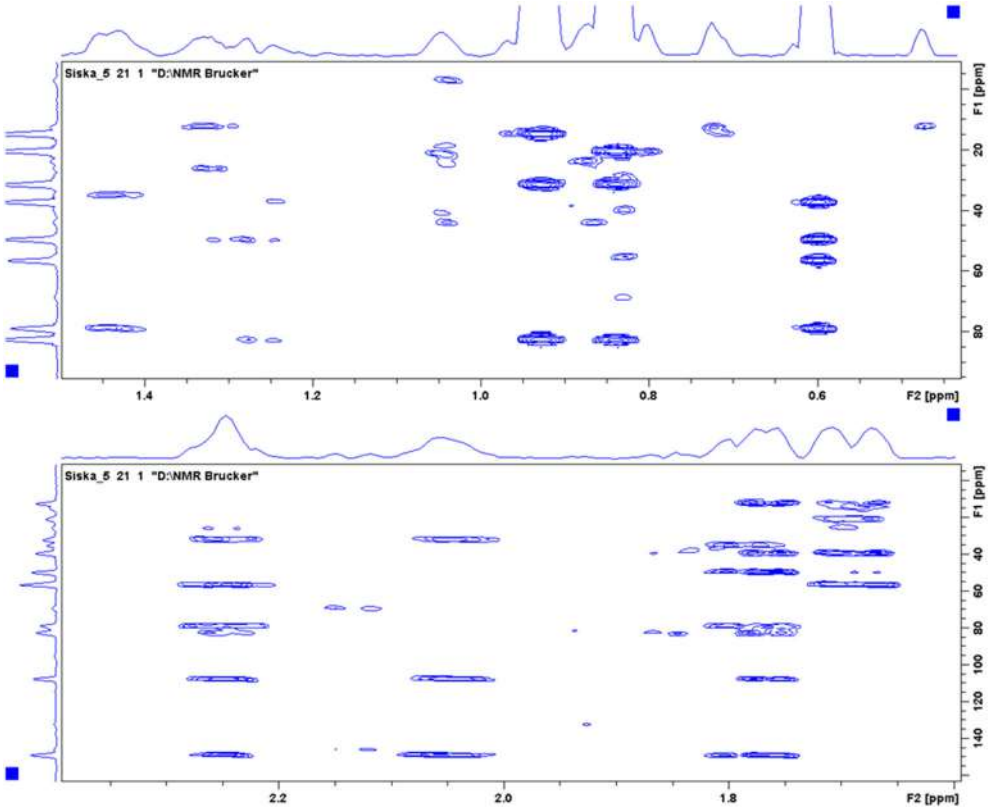

Fig S18. HMBC spectrum of **3**

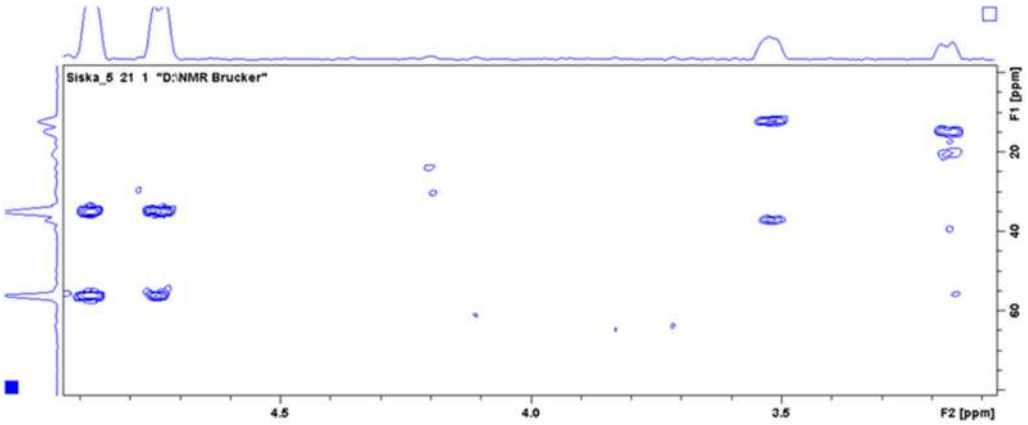

Fig S18. HMBC spectrum of **3** (*Continued*)

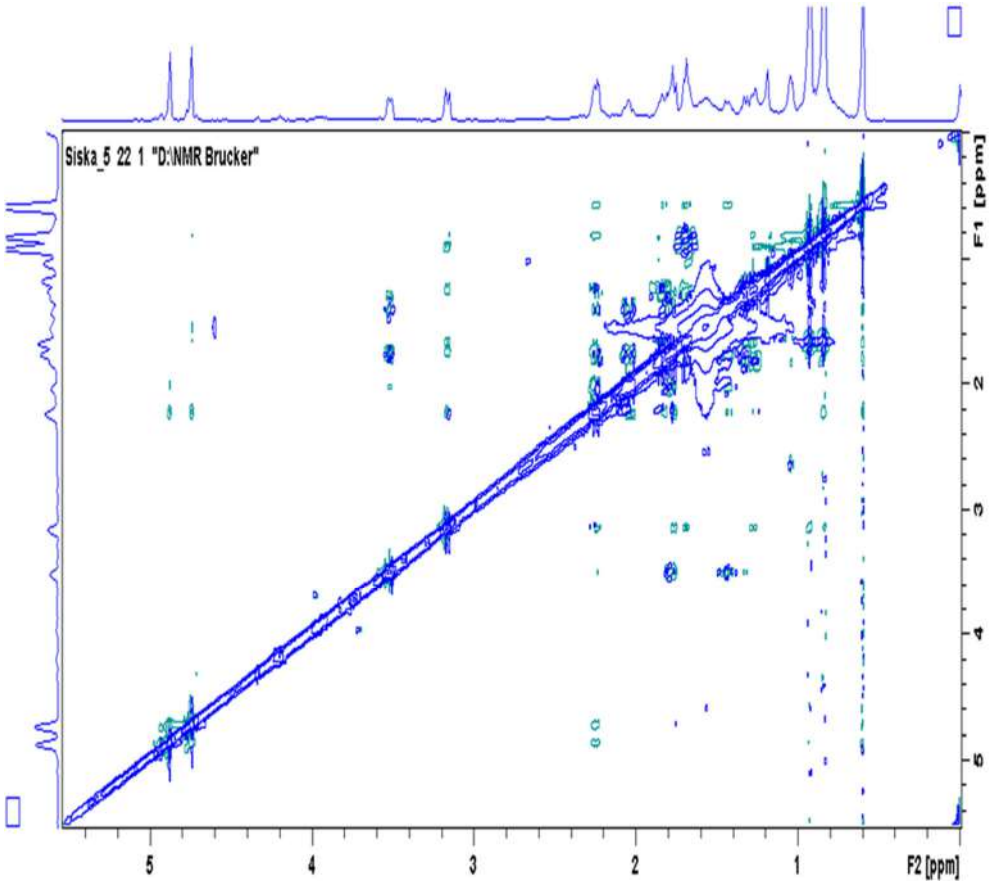

Fig S19. NOESY spectra of **3**

Sesquiterpenoids from the Stem Bark of *Lansium domesticum* Corr. Cv. Kokossan and Their Cytotoxic Activity against MCF-7 Breast Cancer Cell Lines

Siska Elisahbet Sinaga[1], Tri Mayanti[1], Al Arofatus Naini[1], Desi Harneti[1], Nurlelasari Nurlelasari[1], Rani Maharani[1,2], Kindi Farabi[1], Unang Supratman[1,2*], Sofa Fajriah[3], and Mohamad Nurul Azmi[4]

[1]*Department of Chemistry, Faculty of Mathematics and Natural Sciences, Universitas Padjadjaran, Jl. Raya Bandung-Sumedang Km. 21, Jatinangor, Sumedang 45363, Indonesia*

[2]*Central Laboratory of Universitas Padjadjaran, Jl. Raya Bandung-Sumedang Km. 21, Jatinangor, Sumedang 45363, Indonesia*

[3]*Research Center for Raw Materials for Medicine and Traditional Medicine, National Research and Innovation Agency (BRIN), Tangerang Selatan, Banten 15314, Indonesia*

[4]*School of Chemical Sciences, Universiti Sains Malaysia, 11800 Minden, Penang, Malaysia*

* ***Corresponding author:***

tel: +62-22-7794391
email: unang.supratman@unpad.ac.id

Received: February 2, 2022
Accepted: May 13, 2022

DOI: 10.22146/ijc.72742

Abstract: *The* n*-hexane fraction from the stem bark of* Lansium domesticum *Corr. Cv. Kokosan afforded 3 sesquiterpenoids, namely eudesm-4(15),7-dien-1β-ol (**1**), eudesm-4(15)-ene-1β,6α-diol (**2**), and octahydro-4-hydroxy-3a-methyl-7-methylene-a-(1-methylethyl)-1*H*-indene-1-methanol (**3**). These three compounds were discovered in the* Lansium *genus for the first time. Their chemical structures were determined based on data generated from various spectroscopic methods, including one- and two-dimensional NMR, as well as mass spectroscopy. Sesquiterpenoid compounds (**1**-**3**) have also been evaluated on MCF-7 breast cancer cell lines and the compound **1** showed the strongest activity with an IC_{50} value of 17.97 μg/mL while compounds **2** and **3** showed moderate and weak activity with IC_{50} values of 121.65 and 201.57 μg/mL, respectively. The implication of the findings of these compounds is as an illustration that one of these sesquiterpenoids has potential as an anticancer with the presence of double bond which played important role in the cytotoxic activity that can be studied for new drug discovery.*

Keywords: *cytotoxic activity;* Lansium domesticum *Corr. Cv. Kokosan; MCF-7 cell lines; sesquiterpenoid*

■ INTRODUCTION

Sesquiterpenoids are secondary metabolites of the terpenoid class that have important roles in the biological systems used by humans [1]. Sesquiterpenoids, generally found in higher plants as a volatile oil, are derived from the acyclic derivative of the initial compound, namely farnesyl pyrophosphate (FPP) derived from three isoprene units as the precursors. The FPP has a long chain structure and three double bonds, so it can form various cyclic formations with more flexibility such as monocyclic, tricyclic and tetracyclic [2]. Sesquiterpenoids have a C-15 framework and diverse structures due to the presence of functional groups and substituents [3]. In addition, sesquiterpenoids have also various biological activities such as anti-inflammatory, antibacterial, antioxidant, antitumor, and antimalarial [4]. The previous studies reported that aromadendrane-type sesquiterpenoids displayed antifeedant, antifouling, antimicrobial, antiviral, insect repellent, and cytotoxic activities [5]. Sesquiterpenoids are widely found in the Meliaceae family. The genera of the Meliaceae family which contain sesquiterpenoids are Trichilia [6-7], Capadessa [8], *Dysoxylum* [9], *Aglaia* [10], and *Lansium* [11-13]. Several sesquiterpenoids were isolated from Meliaceae family with good activity against MCF-7 breast cancer cells such as 10β-hydroxy-4α,4β-dimethyl-5α*H*,7α*H*-

eudesm-3-one and spatunelol. These two compounds were isolated from the stem bark of *D. parasiticum* with IC_{50} values for MCF-7 of 12.17 and 23.79 μM, respectively [14]. The other sesquiterpenoids isolated from the stem bark of plants from the Meliaceae family (*Aglaia harmsiana*) have good cytotoxic against MCF-7, namely; β-caryophyllene oxide, senecrassidiol; 4β,10α-dihydroxy aromadendrane; 4α,10α-dihydroxyaromadendrane with the IC_{50} values of 0.62, 1.32, 8.41, and 2.8 μM, respectively [15-16].

Lansium domesticum Corr. is a species and seasonal plant that belongs to the *Lansium* genus. *L. domesticum* Corr., which grows in tropical regions, especially in Southeast Asia, such as Philippines, Malaysia, Thailand, and Indonesia [17]. Previous research on this species reported that this species has compounds that have been isolated as follows: triterpenoids, onoceranoid-type onoceradiendione, limonoids, glycoside [18], and sesquiterpenoids. In Indonesia, this species has three cultivars and *Lansium domesticum* Corr. Cv. Kokosan is one of its cultivars which was observed to study the cytotoxicity of the Indonesian *Lansium* plant against MCF-7 breast cancer cell lines. We revealed the isolation, structure elucidation, and cytotoxic evaluation of an oppositane sesquiterpene and two eudesmane-type sesquiterpenoids **1**-**3**.

■ EXPERIMENTAL SECTION

Materials

The stem bark of Kokosan was gathered from Pangandaran Botanical Garden, Pangandaran, West Java Province, Indonesia, in March 2021. The plant was determined at Laboratory Plant Taxonomy, Faculty of Mathematics and Natural Sciences, Universitas Padjadjaran, Jatinangor, West Java and the voucher specimen has been deposited at the Laboratory. Organic solvents including ethanol, *n*-hexane, ethyl acetate, methanol, *n*-butanol, methylene chloride, and acetone were purchased from Kristata Gemilang Company, Bandung in technical quality and distilled.

Instrumentation

The IR spectra were obtained by Perkin Elmer Spectrum 100 FTIR spectrometer (Shelton, Connecticut, USA) using a NaCl plate. The mass spectra were recorded with Waters Q-TOF Xevo mass spectrometer instrument (Waters, Milford, Massachusetts, USA). The NMR spectra of all compounds were recorded on the JEOL JNM-ECX500R/S1 spectrometer (Tokyo, Japan) at 500 MHz for ^{1}H and 125 MHz for ^{13}C with TMS as an internal standard. The column chromatography was conducted on silica gel 60 (70–230 and 230–400 mesh, Merck, Darmstadt, Germany). The TLC analyses were implemented with silica GF_{254} (Merck, 0.25 mm) using various solvent systems and spot detection was attained by spraying with 10% of H_2SO_4 in EtOH, followed by heating and irradiating under ultraviolet-visible light (254 and 365 nm).

Procedure

Extraction and isolation

The dried bark Kokosan (3.18 kg) was macerated with ethanol (20 L) at room temperature (25 °C). The extract was evaporated by a rotary evaporator at 40 °C under reduced pressure to acquire the concentrated ethanol extract (300 g). Then, this residue was dissolved in water and partitioned successively with *n*-hexane (8 L) to yield 124 g, ethyl acetate (7 L) 54 g, and *n*-butanol (1.5 L) 15 g. This separation was monitored by thin layer chromatography and compound detection was carried out using 10% H_2SO_4 stain in ethanol and heated. Then, the *n*-hexane extract (124 g) was fractionated by vacuum liquid chromatography on silica gel G60 using 10% gradient elution of *n*-hexane:EtOAc:MeOH to acquire 12 (A-L) subfractions. Fraction B (15.2 g) was further fractionated by vacuum liquid chromatography using 2% gradient elution of *n*-hexane:EtOAc to afford eight fractions. Fraction B5a (4.37 g) was separated using column chromatography on silica gel (230–400 mesh) eluted with *n*-hexane:DCM:EtOAc (7.5:0.5:0.1) to afford compound **1** (10.5 mg). The B6 fraction (0.69 g) was separated using column chromatography on silica gel (230–400 mesh) eluted with using 5% gradient elution of *n*-hexane:EtOAc to afford 3 fractions (B.6a-B.6c). Fraction B6a (98.5 mg) was separated using column chromatography on octadecyl silane (ODS) eluted with methanol:water (5:5) to obtain compound **2** (10.2 mg) and **3** (9.3 mg).

Eudesm-4(15),7-dien-1β-ol (1). Pale yellow oil, IR ν_{max} 3364; 2955; 1645; 1464; 1379;1282; 1041 cm^{-1}. ^{1}H-NMR ($CDCl_3$, 500 MHz) and ^{13}C-NMR ($CDCl_3$, 125 MHz) data are shown in Table 1. HR-TOFMS *m/z* found 221.1904 $[M+H]^+$ (calculated for $C_{15}H_{24}O$, *m/z* 220.1905).

Eudesm-4(15)-ene-1β,6α-diol (2). White powder, IR ν_{max} 3397; 2933; 1456; 1386;1061 cm^{-1}. ^{1}H-NMR ($CDCl_3$, 500 MHz) and ^{13}C-NMR ($CDCl_3$, 125 MHz) data are shown in Table 1. HR-TOFMS *m/z* found 239.2007 $[M+H]^+$ (calculated for $C_{15}H_{26}O_2$, *m/z* 239.2011).

5-Octahydro-4-hydroxy-3r-methyl-7-methylene-r-(1-methylethyl)-1H-indene-1-methanol (3). Colorless oil, IR ν_{max} 3387; 2973;1650; 772 cm^{-1}. ^{1}H-NMR ($CDCl_3$, 500 MHz) and ^{13}C-NMR ($CDCl_3$, 125 MHz) data are shown in Table 1. HR-TOFMS *m/z* found 261.1816 $[M+Na]^+$, (calculated for $C_{15}H_{26}O_2Na$, *m/z* 261.1831).

Cytotoxic activity test by the MTT assay

Cell viability was assessed by MTT reagent (Thermo Fisher Scientific, Uppsala, Sweden) based on the reduction of resazurin (blue), which works as a function of redox potential. Actively respiring cells convert the water-soluble MTT to an insoluble purple formazan. The formazan is then solubilized and its concentration is determined by optical density. In the initial step, MCF-7 cell cultures that were 80% confluent were washed with 1 mL 1X PBS twice. Cells were added with 1 mL of trypsin EDTA and then incubated for 3 min until the cells were released. Then, the cells were transferred into a Falcon tube containing 5 mL of culture medium and centrifuged at 1,200 rpm for 4 min. The supernatant was discarded and cells were resuspended with 1 mL of culture medium. then, cells were counted using a haemocytometer and planted in 96 well plates with a series number for the standard curve (6 times replications) and 3 times repetitions for the treatment then added 100 µL of the medium, incubated at 37 °C for 24 h, 5% CO_2.

The medium was replaced with 180 µL of new medium and added 20 µL of compound **1**-**3** (1, 10, 100, 250, and 500 ppm) with co-solvent with various percentages of DMSO (0.5–2.5%) in PBS (Uppsala, Sweden). incubated at 37 °C for 24 h, 5% CO_2. After that, cells were added with MTT 20 µL, incubated for at 37 °C for 3 h, 5% CO_2. The absorbance was determined at 570 nm and the IC_{50} value was appointed with the equation given below based on the comparison of the percentage of cytotoxicity to untreated cells. In this trial, the used control positive was Doxorubicin. Based on the literature [14], all assays and analyses were respectively run in duplicate and all averaged so that a plot of % cytotoxicity versus sample concentration was used to calculate the concentration indicating 50% cytotoxicity (IC_{50}).

■ RESULTS AND DISCUSSION

The *n*-hexane extract from the stem bark of the Kokosan was separated and purified using the column chromatography method repeatedly, to produce three sesquiterpene compounds **1**-**3**.

Compound **1**, pale yellow oil, with the yield of 0.2% (10.5 mg) from B5a fraction (4.37 g), was elucidated by interpreting peaks of the IR spectrum (Fig. S1) which appeared at 3364 (hydroxyl group), 2955 (C-H sp^3) 1645 (olefinic bond), 1645 (C=C double bonds), 1464 and 1379 (*gem*-dimethyl), and 1041 cm^{-1} (C-O stretching). The structural formula was established with HR-TOF-MS (Fig. S2) which showed the molecular ion peak of 221.1904 $[M+H]^+$ and the calculated mass of $C_{15}H_{24}O$ *m/z* 220.1827. The prediction was supported by NMR data. The ^{1}H-NMR spectrum (Fig. S3) showed the presence of one tertiary methyl at δ_H 0.64 ppm (CH_3-14), *gem*-dimethyl at δ_H 0.99 ppm (CH_3-12 and CH_3-13) as well as two olefinic protons at 4.63 and 4.82 ppm (CH_2-15). The ^{13}C-NMR spectrum (Fig. S4) showed 15 signals of carbons and the classification of these signals based on their chemical shifts and DEPT 135° (Fig. S5) as three methyls, four methylenes, three methines (one oxygenated methine), one quaternary carbon, and four olefinic carbons (including two quaternary carbons, one methylene and one methine). Based on the structure elucidation of compound **1**, there were 4 degrees of

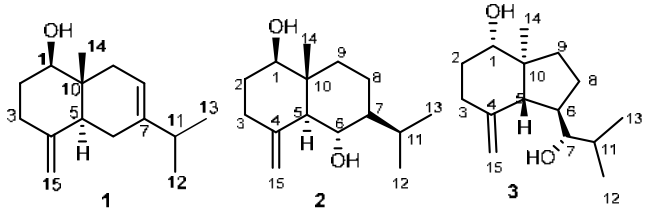

Fig 1. Structures of sesquiterpenoids **1**-**3**

unsaturation consisting of 2 double bonds and bicyclic skeleton, each consisting of six carbons. This compound showed the presence of an isopropyl group at C-7 and a methyl group at C-10 which was a characteristic of eudesmane-type sesquiterpene compounds [1] and was supported by previous report [19]. Compound **1** was determined as the known compound eudesm-4(15),7-dien-1β-ol (**1**) and the structure of this compound can be seen in Fig. 1 number 1. This compound was isolated from the genus *Lansium* for the first time.

Compound **2** was acquired as a white powder with melting point of 118–120 °C in 10.36% yield (10.2 mg) from B6a fraction (98.5 mg). The IR spectrum (Fig. S6) showed the absorption band of the hydroxyl group (3397 cm^{-1}), C-H sp^3 (2933 cm^{-1}), *gem*-dimethyl (1456 and 1386 cm^{-1}), and C-O stretching (1061 cm^{-1}). The structural formula was established with HR-TOFMS (Fig. S7) which showed molecular ion peak of *m/z* 239.2007 $[M+H]^+$ and the calculated mass of $C_{15}H_{26}O_2$ *m/z* 238.1933. The ^{1}H-NMR spectrum (Fig. S8) showed the presence of one tertiary methyl at δ_H 0.65 ppm (CH_3-14), *gem*-dimethyl at 0.89 and 0.80 ppm (CH_3-12 and CH_3-13) and also two olefinic protons at δ_H 4.68 and 4.95 ppm (-CH_2-15). The ^{13}C-NMR spectrum (Fig. S9) showed 15 signals of carbons and the classification of these signals based on their chemical shifts and DEPT 135° (Fig. S10) as three methyls, four methylenes, five methines (two oxygenated methine), one quaternary carbon, and two olefinic carbons (including one quaternary carbons, and one methylene).

The structure elucidation of compound **2** showed that there were 3 degrees of unsaturation consisting of 1 double bond and bicyclic moiety, each consisting of six carbons, similar to compound **1**. This compound showed the presence of an isopropyl group at C-7 and a methyl group at C-10 which was a characteristic of eudesmane-type sesquiterpenoid [1] and was supported by the previous report [20]. The position of the functional group was proved by the correlation of HSQC (Fig. S9). This compound was isolated from the genus *Lansium* for the first time and its structure can be seen in Fig. 1 number 2.

Compound **3** was acquired as a colorless oil in 9.44% yield (9.3 mg) from B6a fraction (98.5 mg). The IR spectrum (Fig. S11) showed the absorption band of the hydroxyl group (3387 cm^{-1}), C-H sp^3 (2973 cm^{-1}), and C=C double bond (1650 cm^{-1}). The structural formula was established with HR-TOFMS (Fig. S12) which showed molecular ion peak of 261.1816 $[M+Na]^+$ and the calculated mass of $C_{15}H_{26}O_2Na$ *m/z* 261.1933. This prediction was supported by NMR data. The ^{1}H-NMR spectrum (Fig. S13) showed the presence of one tertiary methyl at δ_H 0.60 ppm (CH_3-14), *gem*-dimethyl at 0.92 and 0.84 ppm (CH_3-12 and CH_3-13) as well as two olefinic protons at 4.74 and 4.88 ppm (CH_2-15). The ^{13}C-NMR spectrum (Fig. S14) showed 15 signals of carbons and the classification of these signals based on their chemical shifts and DEPT 135° (Fig. S15) as three methyls, four methylenes, five methines (two oxygenated methines), one quaternary carbon, and two olefinic carbons (including one quaternary carbon and one methylene). This compound had 3 degrees of unsaturation consisting of 1 double bond and bicyclic skeleton.

The ^{1}H-NMR, ^{13}C-NMR and DEPT spectra were supported by spectral data from HSQC (Fig. S16) where the spectral matching pattern was appropriate and the chemical shift can be seen in Table 1. Apart from being compared to the literature, compound **3** was reviewed through the ^{1}H-^{1}H COSY correlation (Fig. S17) where there was a relationship between H_1-H_2-H_3 and the continuous relationship between H_5-H_6-H_8-H_9 and H_6-H_7-H_{11}-$H_{12,13}$ (Fig. 2). These correlations showed the presence of rings A and B (bicyclic bonds) with the presence of an isobutanol group attached to the B ring. This compound had a different skeleton from compound **2**, where the skeleton of compound **2** had bicyclic each six carbons whereas compound **3** had six carbon (ring A) and five-carbon (ring B) showed by the relationship of spectrum ^{1}H-^{1}H COSY (H_5-H_6-H_8-H_9 and H_6-H_7-H_{11}-$H_{12,13}$) (Fig. 2). This data supported that this compound is an opposite sesquiterpenoid- type and was proved by the HMBC correlation (Fig. S18).

The tertiary methyl (CH_3-14) (δ_H 0.60) was correlated to C-9 (δ_C 37.3), C-10 (δ_C 49.5), C-5 (δ_C 56.4), and C-1 (δ_C 79.0). Then, the correlation of CH_3-13 (δ_H 0.84) to C-12 (δ_C 20.6), C-11 (δ_C 31.3), C-7 (δ_C 82.7), and

the correlation of CH_3-12 (δ_H 0.92) to C-13 (δ_C 14.8), C-11 (δ_C 31.3), C-7 (δ_C 82.7) showed that C-13 and C-12 are *gem*-dimethyl group attached to C-11 and indicated that the partial structure of **3** contains isobutanol group which bound to C-6, cyclopentane ring and C-7 has a hydroxyl group. The correlation of methylene protons at δ_H 1.24 and 1.84 (H-8) to C-9 (δ_C 37.3), C-10 (δ_C 49.5), C-7 (δ_C 82.7), and C-6 (δ_C 39.4) and methylene protons at δ_H 1.31 and 1.69 (H-9) to C-8 (δ_C 37.3), C-6 (δ_C 39.4), C-10 (δ_C 49.5), C-5 (δ_C 56.4), C-1 (δ_C 79.0 showed the oxygenated C with hydroxyl group) indicated that the compound **3** contained cyclopentane ring at C-5, C-6, C-8, C-9 and C-10 in the presence of isobutanol group located at C-6.

Another partial skeleton was determined by the strong correlation of methine proton at δ_H 1.77 (H-5) to C-6 (δ_C 39.4), C-4 (δ_C 148.9) C-10 (δ_C 49.5), C-7 (δ_C 82.7), C-3 (δ_C 34.9), C-1 (δ_C 79.0), C-14 (δ_C 12.3), and C-15 (δ_C 107.6), indicated that H-5 was between cyclopentane and another part of the skeleton. This correlation showed that this skeleton indicated a double bond at C-4 (δ_C 148.9) and C-15 (δ_C 107.6). This conjecture was confirmed by the proton H-15 at δ_H 4.88 and 4.74 (H-15) to C-4 (δ_C 148.9), C-3 (δ_C 34.9), and C-5 (δ_C 56.4) which showed the double bond attached to C-4, which was adjacent to C-3 and C-5.

The other correlation of methylene protons were at δ_H 2.04 and 2.23 ppm (H-3) to C-4, C-5, C-15, C-2, and C-1 and at δ_H 1.41 and 1.78 ppm (H-2) to C-1, C-3, C-10, C-4, and C-1. The data correlations proved that methylene CH_2 (2) and CH_2 (3) were next to each other and in the same cyclic as evidenced by the HMBC correlation, that this cyclic was composed of six carbons (C-1, C-2, C-3, C-4, C5 and C-10), cyclohexane (ring A), wherein C-5 and C-10 were bridges to ring B (cyclopentane). In ring A, there was a carbon that was oxygenated by a hydroxyl group, located in C-1 (δ_C 79.0) and there was a double bond between carbon C-4 and C-15. The relative stereochemistry of compound **3** was

Table 1. NMR data of compounds **1**-**3** ($CDCl_3$ at 500 MHz for ^1H and 125 MHz for ^{13}C)

Position Carbon	Compounds					
	1		**2**		**3**	
	δ_C (mult.)	δ_H (∑H, mult., *J* = Hz)	δ_C (mult.)	δ_H (∑H, mult., *J* = Hz)	δ_C (mult.)	δ_H (∑H, mult., *J* = Hz)
1	79.6 (d)	3.62 (1H, t, 11.7)	79.0 (d)	3.38 (1H, dd, 11.6, 4.7)	79.0 (d)	3.53 (1H, dd, 11.0, 5.0)
2	31.5 (t)	1.83 (2H, m)	31.9 (t)	1.82 (2H, m)	31.9 (t)	1.41 (1H, m)
						1.78 (1H, m)
3	34.3 (t)	2.35 (2H, m)	35.1 (t)	2.3 (2H, m)	34.9 (t)	2.04 (1H, m)
						2.23 (1H, m)
4	148.4 (s)	-	146.2 (s)	-	148.9 (s)	-
5	43.0 (d)	1.72 (1H, m)	55.9 (d)	1.7 (1H, m)	56.4 (d)	1.77 (1H, m)
6	25.6 (t)	1.95 (2H, m)	67.0 (d)	3.68 (1H, t, 9.8)	39.4 (d)	2.24 (1H, m)
7	141.7 (s)	-	49.3 (d)	1.26 (1H, m)	82.7 (d)	3.17 (1H, dd, 2.5, 9.5)
8	115.8 (d)	5.31 (1H, dd, 5.4, 2.1)	18.2 (t)	1.5 (2H, m)	26.1 (t)	1.25; 1.84 (m)
9	38.4 (t)	1.90 (2H, m)	36.3 (t)	1.88 (2H, dt, 12.4, 2.9)	37.3 (t)	1.31 (1H, m)
						1.69 (1H, m)
10	38.9 (s)	-	41.7 (s)	-	49.5 (s)	-
11	35.1 (d)	2.16 (1H, m)	26.0 (d)	2.2 (1H, m)	31.3 (d)	1.77 (1H, m)
12	21.7 (q)	0.99 (3H, d, 6.8)	21.1 (q)	0.89 (3H, d, 7.0)	20.6 (q)	0.92 (3H, d, 7.0)
13	21.3 (q)	0.99 (3H, d, 6.8)	16.2 (q)	0.80 (3H, d, 7.0)	14.9 (q)	0.84 (3H, d, 7.0)
14	10.4 (q)	0.63 (3H, s)	11.5 (q)	0,65 (3H, s)	12.4 (q)	0.60 (3H, s)
15	107.8 (t)	4.62 (1H, d, 1.5)	107.8 (d)	4.68 (1H, d, 1.1)	107.7 (t)	4.88 (1H, d, 1.5)
		4.83 (1H, d, 1.5)		4.95 (1H, d, 1.1)		4.74 (1H, d, .5)

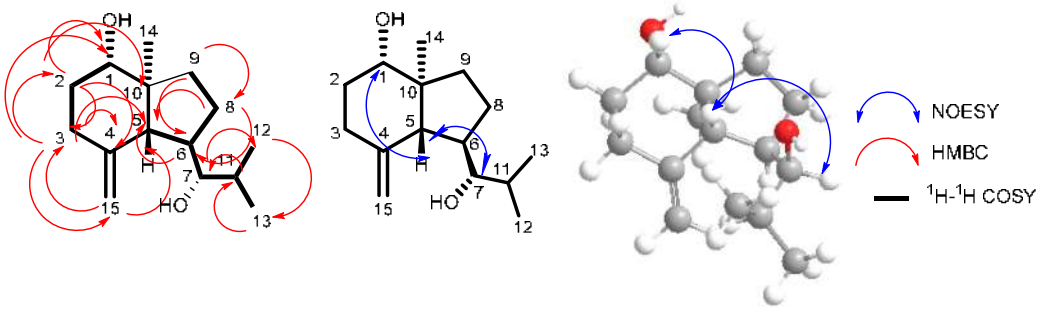

Fig 2. Selected HMBC, ^{1}H-^{1}H-COSY and NOESY correlations of compound **3**

Table 2. The cytotoxic activity of compounds **1**-**3** against MCF-7 breast cancer cell lines

Compounds	IC_{50} (µg/mL)
Eudesm-4(15),7-dien-1β-ol (**1**)	17.97
Eudesm-4(15)-ene-1β, 6α-diol (**2**)	121.65
Octahydro-4-hydroxy-3r-methyl-7-methylene-r-(1-methylethyl)-1H-indene-1methanol (**3**)	201.57
Doxorubicin (+)	0.17

supported by NOESY correlations (Fig. S19). The results displayed that the correlation of H-5 (β-oriented) with H-1 and H-7, and hydroxyl group at C-1 and C-7 was α-oriented. Whereas H-14 and H-6 have no correlation with H β-oriented, so they have α-configuration. Compound **3** has a different cyclicity from compounds **1** and **2** (Fig. 1), detailed examination of the NMR spectral data and comparison with those reported [20] for compound **3** identified that the structure of this compound is octahydro-4-hydroxy-3a-methyl-7-methylene-a-(1-methyl ethyl)-1*H*-indene-1methanol (**3**), similar to compounds eudesm-4(15),7-dien-1β-ol (**1**), and eudesm-4(15)-ene-1β, 6α-diol (**2**). The three compounds have many similarities in the proton shift NMR and C-NMR data which can be seen in Table 2, this compound is also the first to be isolated from the genus *Lansium*. The structure of compound **3** can be seen in Fig. 1 and the correlation between HMBC, ^{1}H-^{1}H COSY and the determination of its configuration through NOESY can be seen in Fig. 2.

The cytotoxic activity of the sesquiterpenoids **1**-**3** was carried out against the MCF-7 cancer cell according to a method described [21-22]. The used positive control was doxorubicin (0.17 µg/mL) and the results are shown in Table 2. Among all sesquiterpenoid compounds, eudesm-4(15),7-dien-1β-ol (**1**) showed the highest cytotoxic activity, while octahydro-4-hydroxy-3a-methyl-7-methylene-a-(1-methylethyl)-1*H*-indene-1-methanol (**3**) showed the lowest activity. The IC_{50} value indicated that the presence of an olefinic group at C-7 of compound **1** significantly increased cytotoxic activity compared to compound **2** which has lost one of the olefinic group at C-7 and underwent the addition of a hydroxyl group at C-6. This conversion reduced cytotoxic activity as well as compound **3** which had lower IC_{50} than that of compound **2** apart from the loss of olefinic group and addition of hydroxyl group. Compound **3** also underwenr a structural change from cyclohexane substituted with isopropyl group to cyclopentane substituted 2-methylpropanol at C-6. Therefore, changes in ring shape and substituents of this compound may reduce the IC_{50} value. These three compounds were also compared with the new eudesman 10β-hydroxy-4α,4β-dimethyl-5αH,7α*H*-eudesm-3-one compound which was successfully isolated by Naini et al. [14] from *Dysoxylum parasiticum* which had a higher IC_{50} value with the presence of a ketone group at C-3 and only one hydroxyl group was substituted at C-10 while compounds **1**-**3** have a methyl group at C-10. The significant probability of the presence of a π electron can increase the IC_{50} value. These results indicated that the hydroxyl and olefinic groups played several critical structural features in the cytotoxic activity of eudesmane-type sesquiterpenoids.

■ CONCLUSION

Three eudesmane-type sesquiterpenoid, eudesm-4(15),7-dien-1β-ol (**1**), eudesm-4(15)-ene-1β,6α-diol (**2**), and octahydro-4-hydroxy-3a-methyl-7methylene-a-(1-methylethyl)-1*H*-indene 1-methanol (**3**) were successfully isolated from the *n*-hexane extract of the stem bark of Kokosan. All compounds (**1**-**3**) were reported from the genus *Lansium* for the first time and were evaluated for their cytotoxic activity against MCF-7 breast cancer cell lines. Among the eudesm-type sesquiterpenoids, compound **1** showed the highest activity while compound **3** showed the lowest activity. The different values of IC_{50} were caused by the different functional groups of the skeleton eudesm-type. The presence of hydroxyl group decreased the IC_{50} value and the presence of olefinic group increased the IC_{50} value. The hydroxyl group and the olefinic group played some important structural features for cytotoxic activity in eudesmane-type sesquiterpenoid, one of these sesquiterpenoids had the potential as an anticancer breast that can be developed as a target molecule through a mechanism that can be studied for new drug discovery.

■ ACKNOWLEDGMENTS

This research was financially supported by *Lembaga Pengelola Dana Pendidikan, Indonesia* (LPDP), Indonesia (No: 20200811683229 for Siska Elisahbet Sinaga) and by Universitas Padjadjaran, Academic Leadership Grant No: 1504/UN6.3.1/PT.00/2022 for Unang Supratman.

■ REFERENCES

[1] Chappell, J., and Coates, R.M., 2010, "Sesquiterpenes" in *Comprehensive Natural Products II*, vol. 1. Eds. Mandler, L., and Liu, H.W., Elsevier, Kidlington, United Kingdom, 609–641.

[2] Talapatra, S.K., and Talapatra, B, 2015, *Chemistry of Plant Natural Products: Stereochemistry, Conformation, Synthesis, Biology, and Medicine*, Springer-Verlag, Berlin Heidelberg.

[3] Gong, D.Y., Chen, X.Y., Guo, S.X., Wang, B.C., and Li, B., 2021, Recent advances and new insights in biosynthesis of dendrobine and sesquiterpenes, *Appl. Microbiol. Biotechnol.*, 105 (18), 6597–6606.

[4] Zhao, W.Y., Yan, J., Liu, T.T., Gao, J., Huang, H.L., Sun, C.P., Huo, X.K., Deng, S., Zhang, B.J., and Ma, X.C., 2020, Natural sesquiterpenoid oligomers: A chemical perspective, *Eur. J. Med. Chem.*, 203, 112622.

[5] Jaeger, R., and Cuny, E., 2016, Terpenoids with special pharmacological significance: A review, *Nat. Prod. Commun.*, 11 (9), 1373–1390.

[6] Nangmo, K.P., Tsamo, T.A., Zhen, L., Mkounga, P., Akone, S.H., Tsabang, N., Müller, W.E.G., Marat, K., Proksch, P., and Mkengfack, A.E., 2018, Chemical constituents from leaves and root bark of *Trichilia monadelpha* (Meliaceae), *Phytochem. Lett.*, 23, 120–126.

[7] Hou, L., Tang, G.H., Zhang, Y., Hao, X.J., Zhao, Q., and He, H.P., 2013, A new carotane sesquiterpene from *Walsura robusta*, *Chin. J. Nat. Med.*, 11 (1), 84–86.

[8] Fu, L.R., Ma, Q.Y., Huang, S.Z., Dai, H.F., Guo, Z.K., Yu, Z.F., and Zhao, Y.X., 2014, Terpenoids and their anti-feedant activity from *Cipadessa cinerascens*, *J. Asian Nat. Prod. Res.*, 16 (11), 1054–1059.

[9] Nugroho, A.E., Sugiura, R., Momota, T., Hirasawa, Y., Wong, C.P., Kaneda, T., Hadi, A.H.A., and Morita, H., 2015, Dysosesquiflorins A and B, sesquiterpenoids from *Dysoxylum densiflorum*, *J. Nat. Med.*, 69 (3), 411–415.

[10] Huang, P.Q., Deng, J.W., Li, Y., Liao, Z.B., Zhao, E., Tian, Y.C., Tu, Y.D., Li, D.L., Jin, J.W., Zhou, C.X., Wu, R.H., and Gan, L.S., 2022, Terpenoids from the twigs and leaves of *Aglaia elaeagnoidea* and their chemotaxonomic significance, *Biochem. Syst. Ecol.*, 103, 104427.

[11] Fadhilah, K., Wahyuono, S., and Astuti, P., 2021, Fractions and isolated compounds from *Lansium domesticum* fruit peel exhibited cytotoxic activity against T-47D and HepG2 cell lines, *Biodiversitas*, 22 (9), 3743–3748.

[12] Fadhilah, K., Wahyuono, S., and Astuti, P., 2020, A bioactive compound isolated from duku (*Lansium domesticum* Corr) fruit peels exhibits cytotoxicity against T47D cell line, *F1000Res.*, 9, 3.

[13] Fadhilah, K., Wahyuono, S., and Astuti, P., 2020, A

sesquiterpene aldehyde isolated from ethyl acetate extract of *Lansium Domesticum* fruit peel, *Indones. J. Pharm*., 3 (2), 394–398.

[14] Naini, A.A., Mayanti, T., Nurlelasari, Harneti, D., Maharani, R., Safari, A., Hidayat, A.T., Farabi, K., Lesmana, R., Supratman, U., and Shiono, Y., 2022, Cytotoxic sesquiterpenoids from *Dysoxylum parasiticum* (Osbeck) Kosterm. stem bark, *Phytochem. Lett.*, 47, 102–106.

[15] Milawati, H., Sukmawati, W., Harneti, D., Maharani, R., Nurlelasari, N., Hidayat, A.T., Darwati, D., Supratman, U., and Shiono, Y., 2020, Cytotoxic sesquiterpenoids from the stem bark of *Aglaia harmsiana* (Meliaceae), *Indones. J. Chem*., 20 (6), 1448–1454.

[16] Milawati, H., Harneti, D., Maharani, R., Nurlelasari, N., Hidayat, A.T., Azmi, M.N., Shiono, Y., and Supratman, U., 2019, Caryophyllene-type sesquiterpenoids from the stembark of *Aglalia harmsiana* and their cytotoxic activity against MCF-7 breast cancer cells, *Molekul*, 14 (2), 126–132.

[17] Lubis, M.F., Hasibuan, P.A., Syahputra, H., and Astyaka, R., 2022, A Review on phytochemicals and pharmacological activities as ethnomedicinal uses of duku (*Lansium domesticum* Corr.), *Open Access Maced. J. Med. Sci*., 10 (F), 57–65.

[18] Mayanti, T., Apriantini Y.P., Soidah, S., Sianturi, J., Darneti, D., Julaeha, E., Sumiarsa, D., Nurlelasari, and Maharani, R., 2018, Antibacterial triterpenoids from the barks and leaves of *Lansium domesticum* Corr cv. Kokossan (Meliaceae), *J. Chem.*, 12 (1), 54–58.

[19] Soares, L.R., de Queiroz e Silva, A.C., Freire, T.V., Garcez, F.R., and Garcez, W.S., 2012, Sesquiterpenos de sementes de *Guarea guidonia* (Meliaceae), *Quim. Nova*, 35 (2), 323–326.

[20] Zhang, H.J., Tan, G.T., Santarsiero, B.D., Mesecar, A.D., Van Hung, N., Cuong, N.M., Soejarto, D.D., Pezzuto, J.M., and Fong, H.H.S., 2003, New sesquiterpenes from *Litsea verticillata*, *J. Nat. Prod*., 66 (5), 609–615.

[21] Xu, M., McCanna, D.J., and Sivak, J.G., 2015, Use the viability reagent PrestoBlue in comparison with alamarBlue and MTT to assess the viability of human corneal epithelial cells, *J. Pharmacol. Toxicol. Methods*, 71, 1–7.

[22] Azizi, K., Hamedi, A., Azarpira, N., Shahini, M., and Pasdaran, A., 2021, A new cytotoxic sesquiterpene lactone from *Euphorbia microsphaera* Boiss against human breast cancer (MCF-7) and human fibrosarcoma (HT1080) cells, *Toxicon*, 202, 60–66.

Molecular Dynamics Simulation of a tRNA-Leucine Dimer with an A3243G Heteroplasmy Mutation in Human Mitochondria Using a Secondary Structure Prediction Approach

Iman Permana Maksum[1*], Ahmad Fariz Maulana[1], Muhammad Yusuf[1,2], Rahmaniar Mulyani[1], Wanda Destiarani[1], and Rustaman Rustaman[1]

[1]*Department of Chemistry, Faculty of Mathematics and Natural Sciences, Universitas Padjadjaran, Jl. Raya Bandung-Sumedang km 21, Jatinangor 45363, West Java, Indonesia*

[2]*Research Centre for Molecular Biotechnology and Bioinformatics, Universitas Padjadjaran, Jl. Raya Bandung-Sumedang km 21, Jatinangor 45363, West Java, Indonesia*

* ***Corresponding author:***

tel: +62-82240839482
email: iman.permana@unpad.ac.id

Received: February 3, 2022
Accepted: April 20, 2022

DOI: 10.22146/ijc.72774

Abstract: *Mitochondrial DNA mutations, such as A3243G, can affect changes in the structure of biomolecules, resulting in changes in the structure of Leucine transfer Ribose Nucleic Acid to form a dimer. Dimer structure modeling is needed to determine the properties of the structure. However, the lack of a structure template for the transfer of Ribose Nucleic Acid (tRNA) is challenging for the modeling of mutant structures of tRNA, especially mitochondrial tRNA that are susceptible to mutation. Therefore, this study predicted the structure of mitochondrial leucine tRNA and its stability through a knowledge-based method and molecular dynamics. Structural modeling and initial assessment were performed using RNAComposer and MolProbity, HNADOCK, and Discovery studios to form the dimer structure. Molecular dynamics simulations for stability analysis were performed using Amber and AmberTools20 software, showing that the conformational energy of the mutant leucine tRNA dimer structure was lower than the native structure. Moreover, the Root Mean Square Deviation (RMSD) of monomer native leucine tRNA was lower than the mutant, indicating that the dimer structure of mutant leucine tRNA is more stable than usual, and the normal leucine tRNA is more stable than the mutant.*

Keywords: *A3243G; molecular dynamics; mitochondrial DNA; structure prediction*

■ INTRODUCTION

The mitochondrion is a cytoplasmic organelle in which respiration (aerobic metabolism) occurs in eukaryotic cells. The primary function of mitochondria is to produce chemical energy in Adenosine triphosphate (ATP) [1]. Unlike other organelles, mitochondria contain nucleotides that encode 22 tRNA and two ribosomal RNA (rRNA) essential for protein synthesis [2]. Transcription occurs via three multi-subunit complexes, namely RNA polymerase I, II, and III. RNA polymerase enzyme type III is specialized for the transcription of transfer RNA (tRNA) and other non-coding RNAs such as 5S rRNA, small RNA (snRNA), microRNA (miRNA), and 7 Spliced Leader RNA (SL-RNA) [3]. Unfortunately, mitochondria DNA (mtDNA) repair mechanisms are not as effective as nuclear DNA, making mtDNA more susceptible to free radical damage. In addition, the lack of proofreading activity means that replication errors cannot be corrected, thereby a higher mutation rate of mtDNA than core DNA [4], leading to molecular damage, hence mitochondrial disease. One such mitochondrial disease that occurs due to this mutation is Maternally Inherited Diabetes and Deafness (MIDD), caused by a point mutation of A3243G that changes base A to G at position 3243 of the leucine tRNA gene [5].

This mutation also causes cataracts and can be detected by PCR-amplification of specific allele (PASA),

Polymerase Chain Reaction-Restriction Fragment Length Polymorphism (PCR-RFLP), and Electrochemical Biosensor. It has been demonstrated that the A3243G mutation is present in 20 of 57 patients, eleven patients with type 2 diabetes and cataracts, five patients with type 2 diabetes mellitus, and four patients with cataracts [5-6]. Interestingly, A3243G was found in patients with pure cataracts, a non-neuromuscular disease, and could be a potential biomarker because of impaired ATP metabolism due to mutations in the respiratory complex. Another secondary mutation that also occurs in the genome carrying A3243G is T10609C, which was found in type-2 diabetes mellitus (T2DM) patients but has also been reported to be associated with Leber Hereditary Optic Neuropathy (LHON) disease in a Kuwait family, 11 and C10676G found in cataract patients [7].

Maksum et al. reported six mutations in mtDNA in patients with T2DM and cataracts. Among the mutations, m.9053G>A was located at respiration complex protein, ATPase6, and found unrelated to neuromuscular diseases, e.g., myopathy and deafness. ATPase6 is a proton translocation channel in the mitochondrial matrix that triggers a change in the catalytic site of F1 for ATP synthesis through the rotation of the F0 ring. This mutation often coexists with the A3243G mutation [8].

Changes in the nucleotides cause the formation of mutated tRNA dimers. Wittenhagen and Kelley [9] reported that the A3243G mutation induces significant changes in the tRNA structure due to dimer formation in the D-loop system. Polyacrylamide gel electrophoresis (PAGE) revealed two bands, one band parallel to the native structure and the other with a movement parallel to the dimer structure. However, PAGE is limited in providing information on the number of nucleotides and the structure of either the native leucine tRNA or the dimer.

Current 3D RNA structure information is limited [10]. Experimental methods such as X-ray crystallography, Nuclear Magnetic Resonance (NMR), and electron microscopy can determine the 3D RNA structure in high or low resolution but are expensive and time-consuming. The rapid development of RNA sequencing technology has made experimental methods no longer the primary choice for determining the 3D RNA structure in high resolution. Hence, computational structure prediction is necessary [11]. Moreover, 3D structural modeling is essential because much can be learned from the visual RNA structure, such as the RNA backbone, considering its role as a stabilizer, the location of intermolecular bonds, and activation of conformational changes that coincide with RNA-protein interactions [12].

A secondary structure prediction approach was adopted in this study because the secondary structure of tRNA is no more complex than the tertiary structure of tRNA and is a good starting point for structural and functional analysis [13]. Furthermore, with automation in tertiary structure modeling, secondary structures can lead to tertiary structures using knowledge-based methods [14]. The secondary structure assessment was performed with online tRNAScan-SE software and the tertiary structure assessment with MolProbity software [12,15].

■ COMPUTATIONAL METHODS

The software used was Amber20, AmberTools20, VMD, and Discovery Studio. The webserver used was tRNAScan-SE (http://lowelab.ucsc.edu/tRNAscan-SE/), RNA Composer (http://rnacomposer.cs.put.poznan.pl/) and MolProbity (http://www.biochem.duke.edu). The nucleotide sequence encoding the leucine

Procedure

Modeling of the tRNALeu structure

The gene sequences of mtDNA encoding tRNA-Leucine obtained from the National Center for Biotechnology Information (NCBI) webserver were translated into nucleotide RNA sequences using notepad++ software by converting T to U and saved in a fasta format. The mutated nucleotide was obtained by copying the data from the native sequence, then converting the 14th sequence nucleotide from A to G in notepad++ software and saved as the mutant A3243G in fasta format. The nucleotide sequence of the native tRNA was used to predict the 2D structure using tRNAScan software, then 3D modeling was performed using RNAComposer software.

Model analysis and assessment

The obtained 3D structure was uploaded to the

MolProbity web tool (http://molprobity.biochem.duke.edu), which removes the hydrogen in the uploaded structure, then adds it back for analysis.

tRNA structure refinement

The tRNA structure was repaired using QRNAS software, which minimizes the structure energy [16], then reassessed by the MolProbity web tool, and its clash score value was re-analyzed.

RNA-RNA molecular docking

Molecular docking was performed in two ways. The mutant leucine tRNA structure was uploaded to the HNADOCK web tool [17] (http://huanglab.phys.hust.edu.cn/hnadock/), and the ten best structures were visualized to select a structure that adopts the G14 bond. The second dimer was adjusted to the position of the monomer in the mutant leucine tRNA dimer using the Discovery Studio software by utilizing molecule alignment.

Molecular dynamics (MD) simulations

MD simulations were performed using Amber20, and the formed structure was included in LEaP. Then, water and an Mg^{2+} ion were added, and the system was minimized, involving water and the whole system. The trajectories obtained from the MD results were analyzed with AmberTools20 to obtain root-mean-square deviation (RMSD), root-mean-square fluctuation (RMSF), hydrogen bonds, and dihedral angles.

Hydrogen bond analysis

Hydrogen bonds were analyzed using the cpptraj program from the AmberTools20 software package. Cut-off is set at the default setting (3 Å)

■ RESULTS AND DISCUSSION

Structural Modeling

The nucleotide sequence encoding the leucine tRNA structure in human mitochondria is 3230 to 3304. Three nucleotides (CCA) were added to the 3' end because the tRNA undergoes post-transcription, which involves adding CCA nucleotides to the aminoacylation site via the CCA enhancing enzyme [18]. For the mutant sequence, the native and 14th sequences were changed from A to G because the A3243G mutation can affect the leucine tRNA sequence by changing the nucleotides at position 14 from A14 to G14 [4].

Sequences of the native tRNA were copied to the tRNAscan-SE site (http://lowelab.ucsc.edu/tRNAscan-SE/) to predict the secondary structure, which resembled a cloverleaf (Fig. 1) and is like the general tRNA secondary structure [19]. The score was 100.9 bits, which is above 55 bits. Therefore the predicted structure is a functional tRNA structure [15].

The 3D structure for the native and mutant was predicted using RNAComposer with secondary structure notation. Before modeling, changes were made to form a mutant leucine tRNA structure. For the native leucine tRNA, the secondary structure notation used notation from the tRNAScan-SE web tool, in which the brackets were changed to dots in the 13th and 24th sequences for the leucine tRNA mutant structure, as the A3243G mutation forms a dimer tRNA structure with the intermolecular interaction bonds in the GGGCCC sequence [9]. The predicted native tRNA has the general tRNA letter "L" shape [18], whereas the mutant leucine tRNA has a more obtuse angle (Fig. 2).

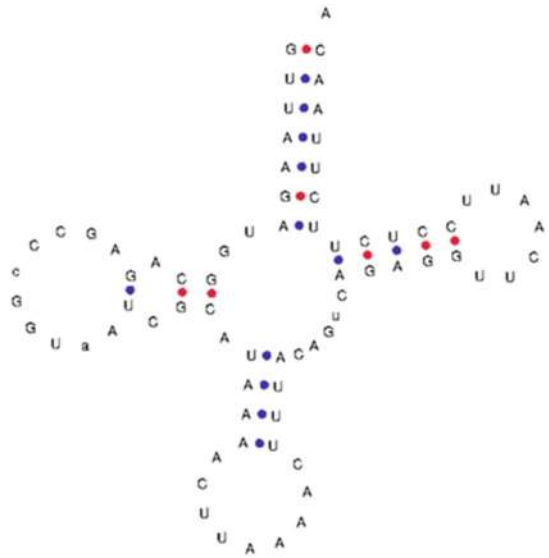

Fig 1. Secondary structure of leucine tRNA predicted by tRNAScan-SE. The secondary structure contains a pair of Watson-Crick and non-canonical bases. The non-canonical base pair is on nucleotide A12 which does not appear to be paired with nucleotide C25. The red and blue dots represent two and three hydrogen bonds, respectively

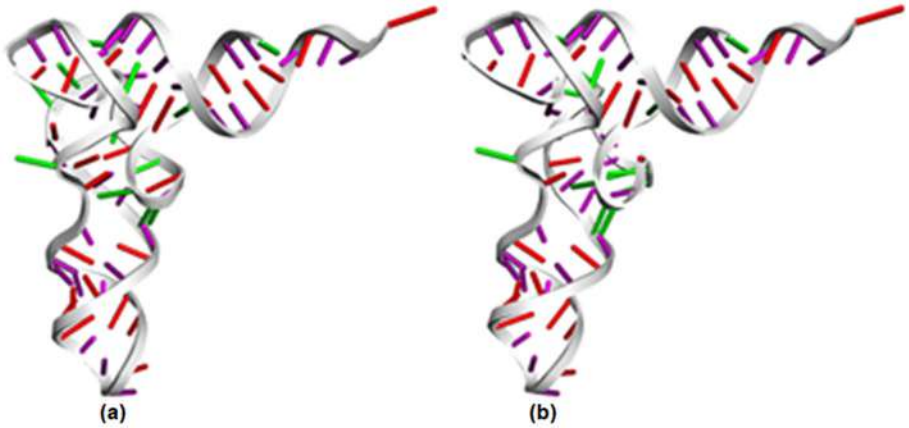

Fig 2. The native (a) and mutant (b) leucine tRNA structures were predicted by RNAComposer. The native structure is 'L' shaped, whereas the mutant structure has a more obtuse angle

Table 1. The number of models used to form a single structure of the native (a) and mutant (b) leucine tRNA. Different models were used for native and mutant tRNAs, especially the loop

(a)

No	Part name	Sequence	Model	Homology (%)
1	Stem D1	1–7 & 68–74	2R8S	64.29
2	Stem D2	10–11 & 26–27	3SJ2	100
3	Stem D3	29–32 & 42–45	3U5H	75
4	Stem D4	51–55 & 63-67	2CT8	80
5	Loop L1	27–29, 45–51, & 67–68	1QTQ	65.5
6	Loop L2	11–13 & 24–26	4FE5	83.33
7	Loop L3	13–24	3AMT	66.67
8	Loop L4	32–42	1EHZ	54.55
9	Loop L5	55–63	3TRA	100
10	Single Strand	74–78	1EHZ	100

(b)

No	Part name	Sequence	Model	Homology (%)
1	Stem D1	1–7 & 68–74	2R8S	64.29
2	Stem D2	10–11 & 26–27	3SJ2	100
3	Stem D3	29–32 & 42–45	3U5H	75
4	Stem D4	51–55 & 63–67	2CT8	80
5	Loop L1	7–10, 27–29, 45–51, & 67–68	1QTQ	62.50
6	Loop L2	11–26	3U5D	31.25
7	Loop L3	32–42	1EHZ	54.55
8	Loop L4	55–63	3TRA	100
9	Single Strand	72–76	1EHZ	100

The RNAComposer web tool searches for other structure fragments with the same secondary structure as the secondary structure input, showing ten fragments of native leucine tRNA and nine fragments of the mutant leucine tRNA (Table 1). Therefore, the free energy of both tRNAs is similar, with the native tRNA structure having total energy of –1356 kcal/mol and –1368 kcal/mol for the mutant tRNA structure.

3D molecules were assessed using the MolProbity web tool to determine whether there were any

overlapping atoms [20]. Before the assessment, tRNA was repaired using QRNA software, indicating that the minimized structure at the 200th iteration (for the native leucine tRNA structure) and 100th (for the mutant leucine tRNA structure) is the best dimer structure (Table 2). The Bad Backbone Conformation value is red because the predicted model is made from other parts of the RNA connected to form a new complete tRNA structure. Therefore, many conformations are incompatible with the database used by MolProbity.

Molecular Docking

Molecular docking using the HNADOCK web tool [17] involves the same two structures to form a dimer structure. The first structure formed was the mutant leucine tRNA dimer structure, with HNADOCK recommending ten molecular docking results for consideration (Table 3).

Of the ten recommended structures, apart from being selected according to their ranking, structures that have intermolecular bonds involving the 5'-GGGCCC nucleotides in the sequence 13 to 18 are also selected. Of the ten observed models, none involve the whole 5'-GGGCCC nucleotide [9]. However, a model involves several nucleotides that match the location where the dimer structure is formed, namely the second model with a docking score of –249.66. This structure has intermolecular hydrogen bonds involving: G14: N2-G19: O4', G15: N2-G19: O6, G15: N1-G19: O6, C17: C5'-U21: O2, G15: N2-G20, C18: O2'-A59 (Fig. 3).

The dimer of the native tRNA was predicted using Discovery Studio software utilizing a molecule overlay of the position of each monomer involved. This modeling yielded a dimer structure of the native tRNA monomer involving nucleotide A14 (Fig. 4).

Molecular Dynamics Simulations

Molecular dynamics simulations start from topology arrangement, equilibrium, and production. In the topology arrangement, several force fields are entered,

Fig 3. The dimer structure from the molecular docking. The selected dimer structures have intermolecular hydrogen bonds involving nucleotide G14

Table 2. Structural repair QRNAS analysis. The native tRNA has a clash score value of 4.83, and the mutant tRNA has a clash score value of 10.05. The green color indicates that the structure matches the database used by MolProbity, and yellow indicates outliers based on the MolProbity database. In contrast, red indicates many outliers based on the MolProbity database

	Native	Mutant
Clashscore, all atoms	4.83	10.05
Probably Wrong sugar puckers	1.28%	1.28%
Bad backbone conformation	26.32%	23.68%
Bad bonds	0%	0%
Bad angles	0.07%	0.04%

Table 3. A summary of the ten best leucine dimer tRNA molecular docking results. The ranking that is formed is sorted based on the docking score, starting from the easiest to form to those that are difficult to form

Ranking	1	2	3	4	5	6	7	8	9	10
Docking score (kcal/mol)	–265.64	–249.66	–240.52	–231.18	–223.87	–223.67	–221.42	–220.05	–219.48	–216.49
RMSD ligand (Å)	54.01	52.74	38.92	51.73	64.09	60.67	63.07	58.90	53.93	60.48

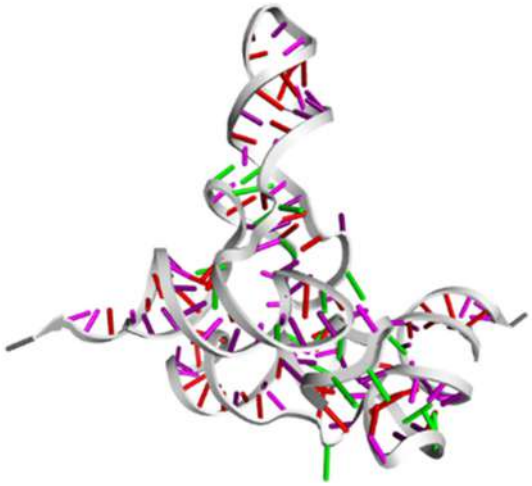

Fig 4. Dimer structure of native tRNA. The structural position is based on the monomer positions of the tethering molecules between the mutant tRNAs

OL3 for RNA and TIP3P for water. RMSD analysis was performed using the cpptraj program available on AmberTools20 to determine the equilibrium that occurs during the production process, the quality of the biomolecular simulations, and the part where the two structures being compared have the same conformation. This assessment is also used in predicting protein structures to compare the similarities between the structure of a computer prediction and the X-ray or NMR method [21]. The monomeric structures of native and direct mutant leucine tRNAs display contrasting differences in their RMSD values (Fig. 5).

From Fig. 5, the native tRNA RMSD value is lower than the mutant tRNA, indicating that the mutant tRNA has more significant structural aberration than the native tRNA. The mutant leucine tRNA has RMSD values ranging from 0 to 20.6 Å with a mean of 17.1 Å, while the native leucine tRNA has RMSD values of 0 s, d 14.7 Å with a mean value of 11.69 Å. Both structures show the RMSF value, which has the same pattern but different parts, namely in the 14 to 28 nucleotide range (Fig. 6(a)) and the nucleotide range 44 to 69 (Fig. 6(b)). The range of nucleotides is part of D and T, where the intermolecular bonds are located.

There are slight differences in results between the two simulated structures. Overall, the mutant leucine tRNA dimer had a more excellent mean RMSD value than the native leucine tRNA dimer due to the molecular mass of tRNA being lighter than protein. This mass allows the tRNA structure to move more quickly than the protein structure, resulting in a more considerable RMSD value. In addition to the RMSD value, the RMSF value (Fig. 7) was also visualized to observe the magnitude of the deviation from each nucleotide.

From Fig. 7, both structures have high and highly volatile RMSF values, indicating that the flexibility of the two dimer structures is very high, thus allowing for a very contrasting structural change compared to the initial structure before the simulations.

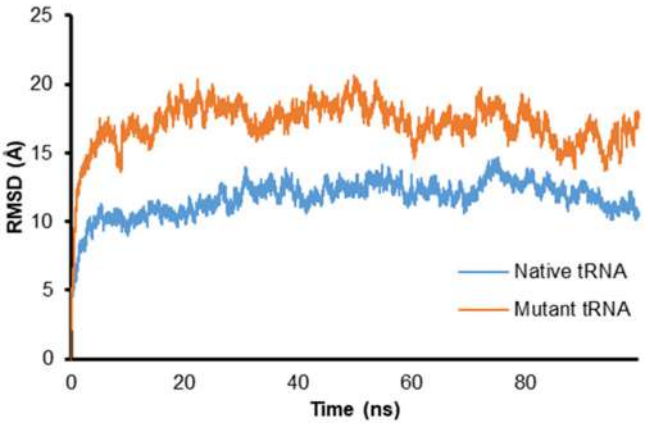

Fig 5. Comparison of the two RMSD values for native and mutant leucine tRNAs. The native leucine tRNA is blue, and the mutant leucine tRNA is orange

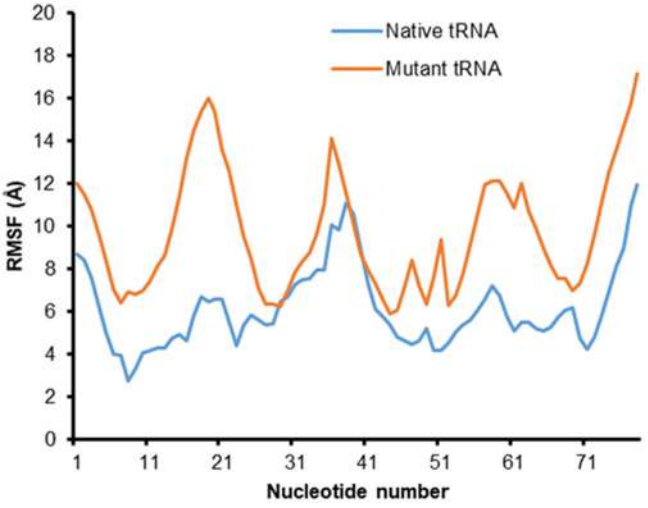

Fig 6. RMSF values for the tRNA structures. The native tRNA is marked in blue, while the mutant tRNA is marked in orange

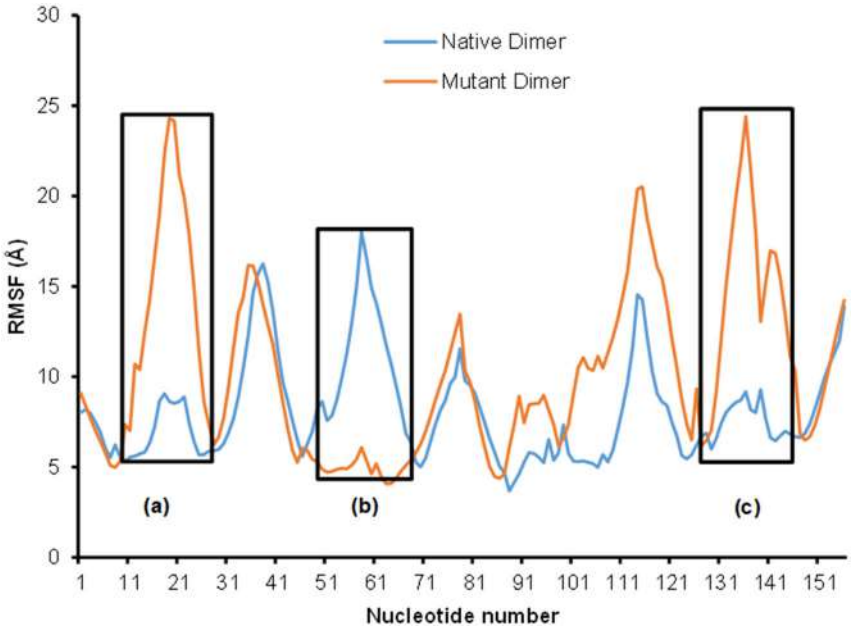

Fig 7. RMSF values for the dimeric structure of the native and mutant leucine tRNA. The RMSF value of the mutant leucine tRNA is shown in orange, while the RMSF value of the native dimer structure is shown in blue

At the RMSF value of the native leucine tRNA dimer structure, there are two positions where the RMSF value of the native leucine tRNA dimer structure is smaller than the mutant leucine tRNA (Fig. 7(a) and Fig. 7(c)), that is, the location of the formation of intermolecular interactions. For the RMSF value of the mutant leucine dimer tRNA, there is one position where the RMSF value of the mutant leucine dimer tRNA structure is smaller than the native leucine tRNA (Fig. 7(b)), where the T part becomes impermeable for the formation of intermolecular interactions. The RMSD value of the intermolecular interaction site can be determined. Another RMSD analysis can be performed on the part that has intermolecular hydrogen bond interactions. For the dimer structure of the mutant leucine tRNA, the nucleotides to be observed were 57, 58, 59, 97, 98, and 99. For the dimer structure of the native leucine tRNA, the nucleotides to be observed were 13, 15, 18, 19, 20, 96, 98, 99, 100, 136, and 137.

From Fig. 8, the RMSD value for the mutant leucine tRNA dimer is lower than that of the native leucine tRNA dimer, suggesting that the intermolecular interactions of the mutant leucine tRNA dimer are more stable than the native leucine tRNA dimer. In addition, the stability of

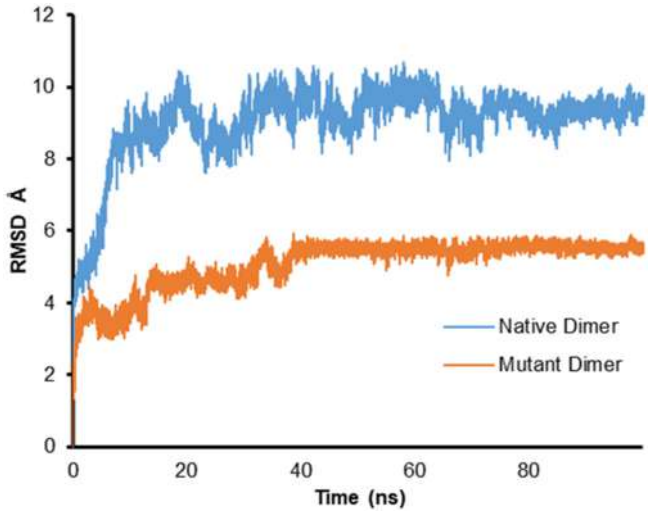

Fig 8. Comparison of the values of the two intermolecular interaction zones of the two dimers. The blue color is the RMSD value for the native dimer structure, and the orange color is the RMSD value for the mutant dimer structure

the mutant leucine tRNA dimer structure is supported by the value of free energy that occurs during the simulations. For the mutant leucine tRNA dimer, the free energy is –333.037 kcal/mol and –310.648 kcal/mol for the native leucine tRNA dimer.

Table 5. Mutant dimer tRNA nucleotide pair during simulations. This interaction is an intermolecular interaction of the mutant dimer structure

Nucleotide pair	Percentage (%)
C58–G20	38.44
U21–C58	22.90
U99–A59	17.29
G20–A59	16.59
C64–A23	14.13
G20–U57	13.35

The mutant tRNA dimer has six hydrogen bonds that contribute to intermolecular interactions (Table 5).

The number of hydrogen bonds indicates that the mutant leucine tRNA dimer has stronger intermolecular interaction bonds than the native tRNA dimer. Therefore, based on the RMSD value in the intermolecular interaction zone and a large number of intermolecular hydrogen bonds, the mutant dimer structure will be more stable.

■ CONCLUSION

Structural models of the native and mutant leucine tRNAs were predicted in stages from primary to tertiary by assessing the secondary structure. The dimer structure of the mutant leucine tRNA was more stable based on the conformational energy and RMSD values for the intermolecular interactions, with more intermolecular hydrogen bonds than the native leucine tRNA dimer.

■ ACKNOWLEDGMENTS

The authors wish to thank Universitas Padjadjaran for the financial support of this research in the form of an Academic Leadership Grant (ALG) 2020 [1427/UN6.3.1/LT/2020].

■ AUTHOR CONTRIBUTIONS

Ahmad Fariz Maulana experimented, Muhammad Yusuf and Rustaman conducted the method improvement, Iman Permana Maksum, Wanda Destiarani, and Rahmaniyar Mulyani wrote and revised the manuscript. All authors agreed to the final version of this manuscript.

■ REFERENCES

[1] Nelson, D.L., and Cox, M.M., 2013, *Lehninger Principles of Biochemistry*, 6th Ed., W.H. Freeman & Company, New York.

[2] Li, L.H., Kang, T., Chen, L., Zhang, W., Liao, Y., Chen, J., and Shi, Y., 2014, Detection of mitochondrial DNA mutations by high-throughput sequencing in the blood of breast cancer patients, *Int. J. Mol. Med.*, 33 (1), 77–82.

[3] Ramsay, E.P., and Vannini, A., 2017, Structural rearrangements of the RNA polymerase III machinery during tRNA transcription initiation, *Biochim. Biophys. Acta, Gene Regul. Mech.*, 1861 (4), 285–294.

[4] Dianov, G.L., Souza-Pinto, N., Nyaga, S.G., Thybo, T., Stevnsner, T., and Bohr, V.A., 2001, Base excision repair in nuclear and mitochondrial DNA, *Prog. Nucleic Acid Res. Mol. Biol.*, 68, 285–97.

[5] Maksum, I., Natradisastra, G., Nuswantara, S., and Ngili, Y., 2013, The effect of A3243G mutation of mitochondrial DNA to the clinical features of type-2 diabetes mellitus and cataract, *Eur. J. Sci. Res.*, 96 (4), 591–599.

[6] Maksum, I.P., Farhani, A., Rachman, S.D., and Ngili, Y., 2013, Making of the A3243G mutant template through site directed mutagenesis as positive control in PASA-mismatch three bases, *Int. J. PharmTech Res.*, 5 (2), 441–450.

[7] Destiarani, W., Mulyani, R., Yusuf, M., and Maksum, I.P., 2020, Molecular dynamics simulation of T10609C and C10676G mutations of mitochondrial *ND4L* gene associated with proton translocation in type 2 diabetes mellitus and cataract patients, *Bioinf. Biol. Insights*, 14, 1177932220978672.

[8] Maksum, I.P., Saputra, S.R., Indrayati, N., Yusuf, M., and Subroto, T., 2017, Bioinformatics study of m.9053G>A mutation at the *ATP6* gene in relation to type 2 diabetes mellitus and cataract diseases, *Bioinform. Biol. Insights*, 11, 1177932217728515.

[9] Wittenhagen, L.M., and Kelley, S.O., 2002, Dimerization of a pathogenic human mitochondrial tRNA, *Nat. Struct. Biol.*, 9 (8), 586–590.

[10] Popenda, M., Szachniuk, M., Antczak, M., Purzycka, K.J., Lukasiak, P., Bartol, N., Blazewicz, J., and Adamiak, R.W., 2012, Automated 3D structure

composition for large RNAs, *Nucleic Acids Res.*, 40 (14), e112.

[11] Kaufmann, M., Klinger, C., and Savelsbergh, A., 2017, *Functional Genomics: Methods and Protocols*, 3rd Ed., Humana Press, New York, USA.

[12] Jain, S., Richardson, D.C., and Richardson, J.S., 2015, Computational methods for RNA structure validation and improvement, *Methods Enzymol.*, 558, 181–212.

[13] Baba, N., Elmetwaly, S., Kim, N., and Schlick, T., 2016, Predicting large RNA-like topologies by a knowledge-based clustering approach, *J. Mol. Biol.*, 428 (5 Pt A), 811–821.

[14] Antczak, M., Popenda, M., Zok, T., Sarzynska, J., Ratajczak, T., Tomczyk, K., Adamiak, R.W., and Szachniuk, M., 2016, New functionality of RNAComposer: An application to shape the axis of miR160 precursor structure, *Acta Biochim. Pol.*, 63 (4), 737–744.

[15] Chan, P.P., and Lowe, T.M., 2019, "tRNAscan-SE: Searching for tRNA Genes in Genomic Sequences" in *Gene Prediction. Methods in Molecular Biology,* vol 1962, Eds. Kollmar, M., Humana Press, New York, USA, 1–14.

[16] Stasiewicz, J., Mukherjee, S., Nithin, C., and Bujnicki, J.M., 2019, QRNAS: Software tool for refinement of nucleic acid structures, *BMC Struct. Biol.*, 19 (1), 5.

[17] He, J., Wang, J., Tao, H., Xiao, Y., and Huang, S.Y., 2019, HNADOCK: A nucleic acid docking server for modeling RNA/DNA-RNA/DNA 3D complex structures, *Nucleic Acids Res.*, 47 (W1), W35–W42.

[18] Lorenz, C., Lünse, C.E., and Mörl, M., 2017, tRNA modifications: Impact on structure and thermal adaptation, *Biomolecules*, 7 (2), 35.

[19] Turner, P., McLennan, A., Bates, A., and Mike, W., 2018, *Molecular Biology*, 3rd Ed., Academic Cell, Cambridge Massachusetts, USA.

[20] Williams, C.J., Headd, J.J., Moriarty, N.W., Prisant, M.G., Videau, L.L., Deis, L.N., Verma, V., Keedy, D.A., Hintze, B.J., Chen, V.B., Jain, S., Lewis, S.M., Arendall, W.B., Snoeyink, J., Adams, P.D., Lovell, S.C., Richardson, J.S., and Richardson, D.C., 2018, MolProbity: More and better reference data for improved all-atom structure validation, *Protein Sci.*, 27 (1), 293–315.

[21] Sargsyan, K., Grauffel, C., and Lim, C., 2017, How molecular size impacts RMSD applications in molecular dynamics simulations, *J. Chem. Theory Comput.*, 13 (4), 1518–1524.

Heavy Metals Concentration in Muscle Tissue of Threatened Sharks (*Rhizoprionodon acutus*, *Sphyrna lewini,* and *Squallus hemipinnis*) from Binuangeun, Lebak Banten, Indonesia

Suratno Suratno[1,2], Dwi Siswanta[2], Satriyo Krido Wahono[1], and Nurul Hidayat Aprilita[2*]

[1]*Research Center for Food Technology and Processing (PRTPP), National Research and Innovation Agency (BRIN), Jl. Jogja-Wonosari Km 31.5, Playen, Gunungkidul, Yogyakarta 55861, Indonesia*

[2]*Department of Chemistry, Faculty of Mathematics and Natural Sciences, Universitas Gadjah Mada, Sekip Utara, Yogyakarta 55281, Indonesia*

** **Corresponding author:***

email: nurul.hidayat@ugm.ac.id

Received: February 4, 2022
Accepted: June 26, 2022

DOI: 10.22146/ijc.72795

Abstract: *Metals accumulation in threatened sharks' meat represents a global health issue. The objective of the current study was to measure the concentration of six metals (Li, Ti, Ni, Cd, As, and Pb) using ICP-MS in threatened sharks' meat of* Rhizoprionodon acutus, Squalus hemipinnis, *and* Sphyrna lewini *from Binuangeun Fish Auction in Lebak, Banten, Indonesia. The results showed that the concentration of Ni, Li, Cd, and Pb was below the acceptable levels for food sources for human consumption, except for As concentration (more than 30 fold higher). This study showed high levels of Ti concentration in all threatened sharks' meat. Overall, this study shows that an accumulation of Ti in sharks' meat should be considered a risk to the health of seafood consumers.*

Keywords: *heavy metals;* Rhizoprionodon acutus*;* Sphyrna lewini*;* Squalus hemipinnis*; Binuangeun*

■ INTRODUCTION

Elasmobranchii can be found in many habitats and at various depths. They show a variety of foraging strategies and tactics, including planktonic filter-feeding and predatory species. *Elasmobranchii* (sharks and rays) seek the meat of cartilaginous fish used to make shark fin soup dishes throughout Southeast Asia in many regions, including Indonesia [1]. Sharks are commonly consumed in shark fin soup, filets (fresh meat), and liver oil in many countries such as Australia [2], Brazil [3], China [1], Japan [4], and South Korea [5]. Metal accumulation is an essential parameter in determining the food safety of shark meat due to the many harmful effects of metals [5-6]. Since shark meat has long been an important food source, much research has been done on heavy metal concentrations to ensure food safety [2,4,7-10].

Sharks can accumulate heavy metals such as Pb, Hg, Cd, and As when they ingest prey through the food web [11] and the feeding behavior of each species [12]. Because sharks exhibit characteristics associated with low metabolic rates and high longevity [13], they are more susceptible to the accumulation of these metals [2]. Heavy metals from shark meat can cause harmful effects on humans if consumed frequently in large amounts [14].

Sharks are secondary products in the Binuangeun Fish Auction that mainly focus on pelagic fishes (tuna, skipjack tuna, and mackerel tuna) and are dominantly caught by gillnet and longline fishing [15]. Types of sharks and rays recorded landed at Binuanguen Fish Auction in Banten such as *A. marmoratus*, *C. falciformis*, *C. longimanus*, *C. brevipinna*, *C. melanopterus*, *A. pelagicus*, *Squalus hemipinnis*, *I. oxyrinchus*, *C. sealei*, *R. acutus*, *H. griseus*, *S. lewini*, *R. australiae*, *R. penggali*, *Mobula* sp., *T. lymma*, *R. javanica*, and *N. caeruleopunctata* [15]. Sharks are sold directly at the Binuangeun Fish Auction and are commonly consumed as fishmeal without processing (salted, smoked, or

dried). *Rhizoprionodon acutus* and *Squalus hemipinnis* are listed as vulnerable in The IUCN Red List of Threatened Species, while *Sphyrna lewini* is a critically endangered species [16-18]. Previous studies have demonstrated the ability of *Elasmobranchii* to accumulate high levels of metals such as As on *S. lewini* muscle tissues from the Gulf of California [19]; Cd and Pb on *R. acutus* from the Persian Gulf area [20], and Kuala Terengganu Malaysia [21]; Cd and As on *S. lewini* from Trinidad-Tobago [22].

The metal concentration in shark meat consumed in Indonesian areas is limited, especially from the Southern Java Sea. In this study, we evaluated the concentration of heavy metals (As, Cd, Pb, Ni, Li, and Ti) in three threatened shark species (*R. acutus*, *S. lewini*, and *S. hemipinnis*) that landed at Binuangeun Fish Auction, Banten, Indonesia. We also examined correlations between metal concentrations and biological aspects such as total length (TL) and total weight (TW) and metal-metal correlation in each species of sharks. By measuring metal concentrations in sharks and comparing them with national and international standards, risks to human health can be assessed, and it is possible to know the pollution status of *Elasmobranchii* from the Binuangeun area. Current findings may be helpful to future researchers.

■ EXPERIMENTAL SECTION

Materials

Sharks were purchased at Binuangeun Fish Auction in Lebak Banten, Indonesia (latitude: -6.838101°, longitude: 105.883637°) in September 2019. A total of sixteen *R. acutus*, eight *S. lewini,* and six *S. hemipinnis* were measured the morphometric with a rolling meter for the total length (TL) and digital balance for the total weight (TW) and directly frozen (-20 °C) before further analysis. In the laboratory, approximately 50 g of sharks' muscle was filleted from the dorsal area, collected in plastic bags, and kept in a freezer (-20 °C) until further analysis. Nitric acid 65% Merck (Darmstadt, Germany), mixed standard stock solutions (containing 100 mg/L of each element) were provided by Merck (Darmstadt, Germany). All reagents used were of analytical reagent grade, and the solutions were prepared using ultra-pure water (Milli-Q).

Instrumentation

Dried sample preparation using oven (Heraeus Instrument), volumetric flash 25 mL, glass funnel, petri dish, spatula, mortar and pestle, and a microwave digestion system (Multiwave 5000 Anton Paar with 41 rotor vessels). The metal concentration analysis using ICP-MS ICAP-RQ Thermo. All glassware was soaked in 10% of HNO_3 for 24 h and rinsed three-time using deionized water before being used.

Procedure

Sample preparation

Shark muscles were dried in an oven at 60 °C for 24 h for metals analysis and moisture content. Dried samples were homogenized using mortar and pestle. Digestion procedures were developed according to the procedures from Anton Paar [23] with modifications on temperature, the volume of acid, and time for digestion.

Metals analysis

Approximately 0.2 g (triplicate) of homogenized dried sharks' muscle samples were digested using Multiwave 5000 microwave digestion. Each sample was mixed with 5 mL of HNO_3 and heated gradually from room temperature to 100 °C in 10 min and held for 5 min, increased to 175 °C in 8 min, and held for 15 min to complete digestion processes. Samples were cooled to room temperature, deionized water was added to digested samples, and diluted until 25 mL using a volumetric flask. Blank digestion was also carried out the same as the sample digestion process consisting of 5 mL HNO_3. Heavy metals analysis was based on a previous study by Murugesan et al. [24]. Total concentration of 6 metals (arsenic [^{75}As], cadmium [^{111}Cd], lead [^{208}Pb], lithium [^{7}Li], nickel [^{60}Ni] and titanium [^{48}Ti]) were analyzed using ICP-MS. Analysis was carried out in Kinetic Energy Discrimination (KED) mode, the ^{140}Ce.^{16}O/^{140}Ce ratio of 0.017%, plasma power of 1550 W, auxiliary flow of 0.8 L/min, and nebulizer flow of 0.985 L/min. The digested solutions (blanks, samples, and Certified Reference Materials (CRMs)) were measured

three times for each sample (Relative Standard Deviation (RSD) < 5%). The final concentration of metals was reported as μg/g wet weight. Wet weight concentration is calculated by multiplying the dry weight concentration with the moisture content factor. The accuracy and precision were verified using CRM DORM-4 provided by the National Research Council of Canada (NRCC) (n = 3).

Statistical analysis

Statistical correlation and graphical plot were based on the open-source R program (package R.4.1.2 for Windows) [25]. The normality data was first confirmed by conducting a Kolmogorov-Smirnov test. Pearson's correlation coefficient analysis determines the significant relationship between total length/total weight and metals concentration in each species. Two-tailed p-value < 0.05 and p-value < 0.01 were considered significant.

■ RESULTS AND DISCUSSION

Metals Concentration on Each Species of Sharks

The morphometrics of sharks analyzed in this study is shown in Table 1. The results of heavy metal concentration (μg/g wet weight) analysis in the meat of *R. acutus*, *S. hemipinnis*, and *S. lewini* are shown in Table 2. The *R. acutus* and *S. hemipinnis* samples were mature based on the size described in the IUCN report [17-18], while *S. lewini* size shows in the juvenile stage [16]. The highest concentrations of As were found in the meat of *R. acutus* (9.60 ± 8.01 μg/g) and *S. hemipinnis* (9.57 ± 3.95 μg/g), and the lowest values were found in *S. lewini* (3.93 ± 1.08 μg/g). The highest concentrations of Ti were found in *S. lewini* (0.619 ± 0.398 μg/g). Pb concentrations were up to ten times higher in *R. acutus* (0.060 ± 0.037 μg/g) than in *S. lewini* (0.006 ± 0.008 μg/g). Ni concentrations were observed equally in *R. acutus* and *S. lewini* (0.037 ± 0.044 μg/g and 0.037 ± 0.019 μg/g, respectively). Li concentrations were found around 0.009–0.018 μg/g in all shark meat. Cd concentrations were observed only on *R. acutus* (0.004 ± 0.001 μg/g), while *S. hemipinnis* and *S. lewini* below LOD. Measurement of CRM (DORM-4) shows promising results with a range from 81.28–107.73% of the recovery (Li: 100.41%; Ni: 81.28%; As: 92.52%; Cd: 81.60% and Pb: 107.73%, respectively), indicating the digestion method suitable to apply on shark muscle samples.

In this study, the concentration of As showed a significantly higher concentration in demersal sharks (*S. hemipinnis*) [18] than in pelagic sharks (*R. acutus* and *S. lewini*) [16-17]. The As concentration in *R. acutus* is lower than the previous study reported by Kim et al. [5] from Jeju island, the Republic of Korea, and by Boldrocchi et al. [26] from Djibouti, Indian Ocean areas, but shows a higher concentration of As compared to study reported by Muhammed and Muhammed [22] from Trinidad and Tobago areas. The As concentration in *S. lewini* is threefold lower than the previous study reported by Berges-Tiznado et al. [19] and Boldrocchi et al. [26] from Djibouti, Indian Ocean areas. Differences in these findings in this species may be related to differences in As availability at different sites and biological parameters involved in As metabolism (length, age, weight, reproductive stage) [19]. Feeding behavior and the food sources of the shark species were other factors that metals can uptake in shark metabolism [19] and trophic position on the food web [27]. *S. lewini* has been classified as a general opportunistic predator [16],

Table 1. Total body length, body weight, and sex of sampled sharks

Scientific name	Common name	N	Total weight (g)	Total length (cm)	Sex	IUCN status
Rhizoprionodon acutus	Milk shark	16	195–450	34.5–46.8	M: 11 F: 5	Vulnerable [17]
Squalus hemipinnis	Indonesian shortnose spurdog shark	6	485–1190	49.5–62.3	M: 1 F:5	Vulnerable [18]
Sphyrna lewini	Hammerhead shark	8	825–1335	56.4–68.0	M:4 F:4	Critically endangered [16]

Table 2. The concentration of metals (μg/g wet weight) in sharks' species from Binuangeun, Lebak, Banten, Indonesia. The average concentration is shown in brackets

Species	Li	Ti	Ni	Cd	As	Pb
R. acutus	0.004–0.108 (0.018)	0.048–0.579 (0.295)	0.001–0.139 (0.037)	0.002–0.006 (0.004)	1.57–23.49 (9.60)	0.009–0.140 (0.060)
S. hemipinnis	0.005–0.018 (0.009)	0.287–0.604 (0.384)	< LoD	< LoD	3.73–13.50 (9.57)	0.003–0.063 (0.036)
S. lewini	0.08–0.023 (0.014)	0.310–1.570 (0.619)	0.011–0.062 (0.037)	< LoD	3.00–5.85 (3.93)	0.001–0.021 (0.006)

LoD: limit of detection

directly relating to the abundance of prey in the study area [19,28]. Another factor is the migratory pattern of the shark while in the juvenile and adult stages or during the nurseries stage [29-30].

Pb, Cd, and Ni concentration in *R. acutus* and *S. lewini* from Binuangeun show a lower trend than the previous result on Ong and Gang [21] from Kuala Terengganu, Malaysia, Boldrocchi et al. [27] from Djibouti, Indian Ocean areas, and Adel et al. [20] from the Persian Gulf. This study's Cd, Ni, and Pb concentrations were lower than Hauser-Davis et al. [31] on blue sharks (*Prionace glauca*) from the Western North Atlantic Ocean. The concentration of Cd and Pb in *S. lewini* reported by Mohammed and Mohammed [22] from Trinidad and Tobago shows a higher concentration in all muscles (hypaxial muscle, epaxial muscle, and dorsal fin) compared to this study. These metals have been the most studied in life because their effects can severely alter metabolic processes and even lead to death at low concentrations [32-33]. This study reported new data related to metals on *S. hemipinnis* because there is no publication about metal accumulation in Indonesian sprout nose dogfish from Indonesia. The concentration of Cd and Pb on demersal sharks in this study was lower than the study reported by Bilbao et al. [10] from Macaronesian Archipelago.

Unfortunately, there are no studies of titanium accumulation by sharks in the study area. The concentration of Ti in this study was shown to be lower compared to the study reported by Hauser-Davis et al. [31] on *P. glauca* from the Western North Atlantic Ocean and Ju et al. [34] on megamouth sharks (*Megachasma pelagios*) from Taiwan. However, higher than a study reported by Bouchoucha et al. [35] from the Western Mediterranean Sea on commercial fishes. Ju et al. [34] reported that a high concentration of Ti on *M. pelagios* is probably because of the feeding habits of planktivorous compared to carnivorous sharks. Titanium has been reported to be associated with marine microalgae (diatoms and dinoflagellates) in high concentrations (more than 1,000 μg/g dry weight) [36]. Titanium (Ti) is a contaminant of increasing concern, exhibiting increased bioavailability in aquatic environments in recent decades due to increased use in personal care products (toothpaste, conditioner, shampoo, and conditioner) in the form of TiO_2 nanoparticles [37]. Some previous studies had reported Ti could be biomagnified through food webs and bioaccumulated in several aquatic organisms [38-43]. The International Agency for Research on Cancer has already classified titanium as "possibly carcinogenic to humans" (Group 2B) because it may pose significant risks to human health [44]. Future assessments will be conducted to clarify the accumulation of Li and Ti on marine fishes. The concentration of metals varies according to the habitats, feeding behavior, and species-specific [4-5,10,45].

Metals Correlation on Each Species

We observed specific metal-metal correlation in sharks meat shows different responses due to species-specific metabolism, and no significant correlation was observed between total length or total weight and concentration of metals in the meat of all shark species. Total weight of *R. acutus* was shown significantly positive correlation ($p < 0.001$) with total length ($r^2 = 0.91$). A significant negative correlation ($p < 0.001$) was

observed between Ti-Cd (r^2 = -0.79) and As-Cd (r^2 = -0.69, $p < 0.01$) on *R. acutus*. A significant positive correlation ($p < 0.05$) on *R. acutus* was observed between Li-Ti (r^2 = 0.43), Li-As (r^2 = 0.51), Li-Pb (r^2 = 0.59), Ti-As (r^2 = 0.49), Ti-Pb (r^2 = 0.45) and As-Pb (r^2 = 0.50). A significant negative correlation ($p < 0.05$) on *R. acutus* was observed between Li-Cd (r^2 = -0.47) and Cd-Pb (r^2 = -0.52). *S. hemipinnis* and *S. lewini* were observed a significant positive correlation ($p < 0.001$) on TW-TL (r^2 = 0.94) and TW-TL (r^2 = 0.99), respectively.

Biplot PCA grouping of samples on threatened sharks from the Binuangeun area using the concentration of metals, TW, and TL as factors shows separation from *R. acutus* to *S. hemipinnis* and *S. lewini* (Fig. 1). *R. acutus* negatively correlates with Li, As, and Pb but positively correlates with Cd. *S. hemipinnis* and *S. lewini* show a positive correlation with Ti concentration, indicating that those sharks accumulate higher titanium than *R. acutus*. PCA can show factors correlating to metal accumulation in each species of threatened sharks from the Binuangeun area.

The multivariate analysis (PCA) can identify the differences in metals among shark species. Variable food sources could explain the variability in each species in their habitat [13,19]. The metals pattern of PCA is useful because it normalizes data, minimizes the effects of individual element concentrations, and more clearly divides samples into two or more groups based on species or sex identities. In this study, linear regression analysis did not reveal a significant relationship between shark length/weight and metal concentration in each species. However, length/metals or weight/metals relationships have been reported in the previous study [5,46]. We observed a significant relationship between habitat (coastal/pelagic sharks vs. deep-water/benthic sharks) and metal concentration. Titanium concentration showed a significant positive relationship with total length and weight (Pearson correlation, (TW) r = 0.40, p = 0.028, n = 28; (TL) r = 0.43, p = 0.016, n = 28) if analysis based on habitat (coastal/pelagic vs demersal/deep-water), while lead showed a significant negative relationship with TW and TL (TW r = -0.58, p = 0.0016, n = 25; TL r = -0.61, p = 0.0008, n = 25). In habitat, many factors influence the uptake of metals in sharks, such as a variety of food diets [2,19], the abundance of food sources [19], anthropogenic activities [7,26], and different trophic positions while juvenile stage vs. adult stage [27,29].

Heavy metals concentration such as Cd and Pb except As were lower than the permissible limit ([As] = 0.25 μg/g, [Cd] = 0.10 μg/g and [Pb] = 0.20 μg/g) from National Agency of Drug and Food Control (NADFC) or BPOM [47] or JECFA/WHO [48]. The concentration is of As in *S. lewini* four times (3.93 μg/g) higher than the NADFC permissible guideline, while in *R. acutus* (9.60 μg/g) and *S. hemipinnis* (9.57 μg/g), more than 38 fold than the rules. The TL of *S. lewini* did not exceed 70 cm, and it is evident that samples consist mainly of juveniles [16], but *R. acutus* and *S. hemipinnis* showed

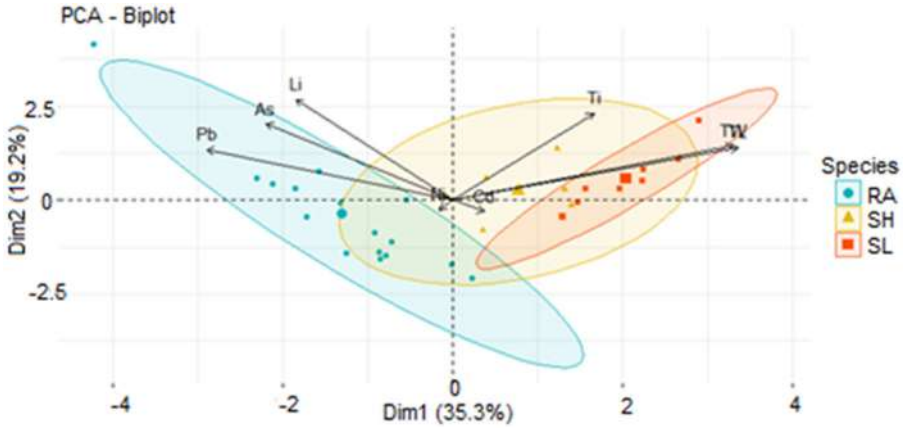

Fig 1. Biplot PCA metals concentration in threatened sharks from Binuangeun, Lebak, Banten, Indonesia. RA = *R. acutus*; SH = *S. hemipinnis*; SL = *S. lewini*

mainly adult samples [17-18,49]. In the shark fishery, small sizes are preferred for meat due to the low concentration of urea (the way it decomposes affects the smell and taste of meat), low commercial price, and other potentially toxic elements [19]. As in shark meat (commonly marine fish), the concentration of arsenic is primarily in the form of an organic compound (85 to 90%) and will secrete from the human body by urinary excretion [50]. Even though inorganic As is the dominant species in freshwaters and marine, it will rapidly bio transform to organic As such as methyl arsenate or dimethyl arsenate by an aquatic organism. The organic arsenic is bioaccumulated in biota and biomagnified through the food web, but the concentration of inorganic As does not increase through trophic levels [19,26-27]. The consumption of shark's meat in Binuangeun areas must be considered the As concentration level because arsenic correlates to Li and Ti, especially on *R. acutus* (Fig. 1). However, whether the same biomagnification pattern of As is different species or different adult-juvenile populations is still unknown. This is evidence that more studies are required to elucidate whether arsenic is increasing in the aquatic food web, including all the shark species from Binuangeun areas.

■ CONCLUSION

This study showed a significant concentration of metals in threatened sharks' meat from Binuangeun Fish Auction, Lebak, Banten, Indonesia. The concentration of total As in milk shark and dogfish shark meat was found to be higher compared to a scalloped hammerhead shark. The presence of a high concentration of Ti in *S. lewini* and *S. hemipinnis* through this study requires investigation regarding the form of Ti that accumulated in sharks' meat.

■ ACKNOWLEDGMENTS

The authors would like to thank Rian Hidayatullah for assisting during the sampling. This research was funded by the Ministry of Research and Technology/National Research and Innovation Agency (KEMRISTEK/BRIN) through the Doctoral Dissertation Research contract no: 2269/UN1/DITLIT/DIT-LIT/PT/2021. The authors also acknowledge the National Research and Innovation Agency (BRIN), Gunungkidul, Yogyakarta, for facilitating ICPMS.

■ AUTHOR CONTRIBUTIONS

Conceptualization, S.S. and N.A.; sample analysis, S.S.; statistical analysis, S.S. and D.S.; writing-original draft preparation, S.S.; writing-review and editing, S.S., N.A. and S.W. All authors have read and agreed to the published version of the manuscript.

■ REFERENCES

[1] Dent, F., and Clarke, S., 2015, State of the global market for shark products, *FAO Fisheries and Aquaculture Technical Paper No. 590*, FAO, Rome, 187.

[2] Pethybridge, H., Cossa, D., and Butler, E.C.V., 2010, Mercury in 16 demersal sharks from southeast Australia: Biotic and abiotic sources of variation and consumer health implications, *Mar. Environ. Res.*, 69 (1), 18–26.

[3] Mársico, E.T., Machado, M.E.S., Knoff, M., and São Clemente, S.C., 2007, Total mercury in sharks along the Southern Brazilian coast, *Arq. Bras. Med. Vet. Zootec.*, 59 (6), 1593–1596.

[4] Endo, T., Kimura, O., Ohta, C., Koga, N., Kato, Y., Fujii, Y., and Haraguchi, K., 2016, Metal concentrations in the liver and stable isotope ratios of carbon and nitrogen in the muscle of silvertip shark (*Carcharhinus albimarginatus*) culled off Ishigaki Island, Japan: Changes with growth, *PLoS One*, 11 (2), e0147797.

[5] Kim, S.W., Han, S.J., Kim, Y., Jun, J.W., Giri, S.S., Chi, C., Yun, S., Kim, H.J., Kim, S.G., Kang, J.W., Kwon, J., Oh, W.T., Cha, J., Han, S., Lee, B.C., Park, T., Kim, B.Y., and Park, S.C., 2019, Heavy metal accumulation in and food safety of shark meat from Jeju island, Republic of Korea, *PLoS One*, 14 (3), e0212410.

[6] Escobar-Sánchez, O., Galván-Magaña, F., and Rosíles-Martínez, R., 2010, Mercury and selenium bioaccumulation in the smooth hammerhead shark, *Sphyrna zygaena* Linnaeus, from the Mexican Pacific Ocean, *Bull. Environ. Contam. Toxicol.*, 84 (4), 488–491.

[7] Adel, M., Oliveri Conti, G., Dadar, M., Mahjoub, M., Copat, C., and Ferrante, M., 2016, Heavy metal concentrations in edible muscle of white cheek shark, *Carcharhinus dussumieri* (elasmobranchii, chondrichthyes) from the Persian Gulf: A food safety issue, *Food Chem. Toxicol.*, 97, 135–140.

[8] Adel, M., Copat, C., Saeidi, M.R., Conti, G.O., Babazadeh, M., and Ferrante, M., 2018, Bioaccumulation of trace metals in banded Persian bamboo shark (*Chiloscyllium arabicum*) from the Persian Gulf: A food safety issue, *Food Chem. Toxicol.*, 113, 198–203.

[9] Kim, S.J., Lee, H.K., Badejo, A.C., Lee, W.C., and Moon, H.B., 2016, Species-specific accumulation of methyl and total mercury in sharks from offshore and coastal waters of Korea, *Mar. Pollut. Bull.*, 102 (1), 210–215.

[10] Lozano-Bilbao, E., Lozano, G., Gutiérrez, Á.J., Rubio, C., and Hardisson, A., 2018, Mercury, cadmium, and lead content in demersal sharks from the Macaronesian islands, *Environ. Sci. Pollut. Res.*, 25 (21), 21251–21256.

[11] Barrera-García, A., O'Hara, T., Galván-Magaña, F., Méndez-Rodríguez, L.C., Castellini, J.M., and Zenteno-Savín, T., 2012, Oxidative stress indicators and trace elements in the blue shark (*Prionace glauca*) off the east coast of the Mexican Pacific Ocean, *Comp. Biochem. Physiol., Part C: Toxicol. Pharmacol.*, 156 (2), 59–66.

[12] Turoczy, N.J., Laurenson, L.J.B., Allinson, G., Nishikawa, M., Lambert, D.F., Smith, C., Cottier, J.P.E., Irvine, S.B., and Stagnitti, F., 2000, Observations on metal concentrations in three species of shark (*Deania calcea*, *Centroscymnus crepidater*, and *Centroscymnus owstoni*) from Southeastern Australian waters, *J. Agric. Food Chem.*, 48 (9), 4357–4364.

[13] McMeans, B.C., Borgå, K., Bechtol, W.R., Higginbotham, D., and Fisk, A.T., 2007, Essential and non-essential element concentrations in two sleeper shark species collected in arctic waters, *Environ. Pollut.*, 148 (1), 281–290.

[14] Bosch, A.C., O'Neill, B., Sigge, G.O., Kerwath, S.E., and Hoffman, L.C., 2016, Heavy metals in marine fish meat and consumer health: A review, *J. Sci. Food Agric.*, 96 (1), 32–48.

[15] Oktaviany, S., Kurniawan, W., Sjafrie, N.D.M., Triyono, T., and Suratno, S., 2019, Pendataan dan Aspek Biologi Ikan Hiu dan Pari Apendik CITES dan Terancam Punah di Indonesia, *Final Report*, Research Center for Oceanography-LIPI, Jakarta, Indonesia.

[16] Rigby, C.L., Dulvy, N., Carlson, J., Fernando, D., Fordham, S., Jabado, R.W., Liu, K.M., Marshall, A., Pacoureau, N., Romanov, E., Sherley, R.B., and Winker, H., 2019, *Sphyrna lewini*, *IUCN Red List Threatened Species*, 2019, e.T39385A2918526.

[17] Rigby, C.L., Harry, A.V., Pacoureau, N., Herman, K., Hannan, L., and Derrick, D., 2020, *Rhizoprionodon acutus*, *IUCN Red List Threatened Species*, 2020, e.T41850A68642326.

[18] Dulvy, N.K., Bineesh, K.K., Cheok, J., Dharmadi, Finucci, B., Sherman, C.S., and VanderWright, J., 2020, *Squalus hemipinnis*, *IUCN Red List Threatened Species*, 2020, e.T161410A124480327.

[19] Bergés-Tiznado, M.E., Vélez, D., Devesa, V., Márquez-Farías, J.F., and Páez-Osuna, F., 2021, Arsenic in tissues and prey species of the scalloped hammerhead (*Sphyrna lewini*) from the SE Gulf of California, *Arch. Environ. Contam. Toxicol.*, 80 (3), 624–633.

[20] Adel, M., Mohammadmoradi, K., and Ley-Quiñonez, C.P., 2017, Trace element concentrations in muscle tissue of milk shark, (*Rhizoprionodon acutus*) from the Persian Gulf, *Environ. Sci. Pollut. Res.*, 24 (6), 5933–5937.

[21] Ong, M.C., and Gan, S.L., 2017, Assessment of metallic trace elements in the muscles and fins of four landed elasmobranchs from Kuala Terengganu Waters, Malaysia, *Mar. Pollut. Bull.*, 124 (2), 1001–1005.

[22] Mohammed, A., and Mohammed, T., 2017, Mercury, arsenic, cadmium and lead in two commercial shark species (*Sphyrna lewini* and C*araharinus porosus*) in Trinidad and Tobago, *Mar. Pollut. Bull.*, 119 (2), 214–218.

[23] Anton Paar, 2020, High-throughput Digestion of

Food and Other Organic Samples with Rotor 41HVT56, *Application Reports*, Anton Paar GmbH, Graz, Austria.

[24] Murugesan, S., Surekar, B., Mandal, S., Pandey, B., and Oulkar, D., 2020, Determination of trace heavy metals in spices using single quadrupole ICP-MS, *Application Note 44476*, Thermo Fischer Scientific.

[25] R Core Team, 2021, *R: A Language and Environment for Statistical Computing*, R Foundation for Statistical Computing, Viena, Austria.

[26] Boldrocchi, G., Monticelli, D., Omar, Y.M., and Bettinetti, R., 2019, Trace elements and POPs in two commercial shark species from Djibouti: Implications for human exposure, *Sci. Total Environ.*, 669, 637–648.

[27] Boldrocchi, G., Spanu, D., Mazzoni, M., Omar, M., Baneschi, I., Boschi, C., Zinzula, L., Bettinetti, R., and Monticelli, D., 2021, Bioaccumulation and biomagnification in elasmobranchs: A concurrent assessment of trophic transfer of trace elements in 12 species from the Indian Ocean, *Mar. Pollut. Bull.*, 172, 112853.

[28] Bergés-Tiznado, M.E., Márquez-Farías, F., Lara-Mendoza, R.E., Torres-Rojas, Y.E., Galván-Magaña, F., Bojórquez-Leyva, H., and Páez-Osuna, F., 2015, Mercury and selenium in muscle and target organs of scalloped hammerhead sharks *Sphyrna lewini* of the SE gulf of California: Dietary intake, molar ratios, loads, and human health risks, *Arch. Environ. Contam. Toxicol.*, 69 (4), 440–452.

[29] Coiraton, C., Amezcua, F., and Ketchum, J.T., 2020, New insights into the migration patterns of the scalloped hammerhead shark *Sphyrna lewini* based on vertebral microchemistry, *Mar. Biol.*, 167 (5), 58.

[30] Coiraton, C., and Amezcua, F., 2020, *In utero* elemental tags in vertebrae of the scalloped hammerhead shark *Sphyrna lewini* reveal migration patterns of pregnant females, *Sci. Rep.*, 10 (1), 1799.

[31] Hauser-Davis, R.A., Rocha, R.C.C., Saint'Pierre, T.D., and Adams, D.H., 2021, Metal concentrations and metallothionein metal detoxification in blue sharks, *Prionace glauca* L. from the Western North Atlantic Ocean, *J. Trace Elem. Med. Biol.*, 68, 126813.

[32] Storelli, M.M., Giacominelli-Stuffler, R., and Marcotrigiano, G., 2002, Mercury accumulation and speciation in muscle tissue of different species of sharks from Mediterranean Sea, Italy, *Bull. Environ. Contam. Toxicol.*, 68 (2), 201–210.

[33] Storelli, M.M., Ceci, E., Storelli, A., and Marcotrigiano, G.O., 2003, Polychlorinated biphenyl, heavy metal and methylmercury residues in hammerhead sharks: Contaminant status and assessment, *Mar. Pollut. Bull.*, 46 (8), 1035–1039.

[34] Ju, Y.R., Chen, C.F., Chen, C.W., Wang, M.H., Joung, S.J., Yu, C.J., Liu, K.M., Tsai, W.P., Vanson Liu, S.Y., and Dong, C., 2021, Profile and consumption risk assessment of trace elements in megamouth sharks (*Megachasma pelagios*) captured from the Pacific Ocean to the east of Taiwan, *Environ. Pollut.*, 269, 116161.

[35] Bouchoucha, M., Chekri, R., Leufroy, A., Jitaru, P., Millour, S., Marchond, N., Chafey, C., Testu, C., Zinck, J., Cresson, P., Mirallès, F., Mahe, A., Arnich, N., Sanaa, M., Bemrah, N., and Guérin, T., 2019, Science of the Total Environment Trace element contamination in fish impacted by bauxite red mud disposal in the Cassidaigne canyon (NW French Mediterranean), *Sci. Total Environ.*, 690, 16–26.

[36] Buettner, K.M., and Valentine, A.M., 2012, Bioinorganic chemistry of titanium, *Chem. Rev.*, 112 (3), 1863–1881.

[37] Corsi, I., Bergami, E., and Grassi, G., 2020, Behavior and bio-interactions of anthropogenic particles in marine environment for a more realistic ecological risk assessment, *Front. Environ. Sci.*, 8, 60.

[38] Shi, W., Han, Y., Guo, C., Zhao, X., Liu, S., Su, W., Zha, S., Wang, Y., and Liu, G., 2017, Immunotoxicity of nanoparticle $nTiO_2$ to a commercial marine bivalve species, *Tegillarca granosa*, *Fish Shellfish Immunol.*, 66, 300–306.

[39] Cunha, R.L.D.D., and de Brito-Gitirana, L., 2020, Effects of titanium dioxide nanoparticles on the intestine, liver, and kidney of *Danio rerio*, *Ecotoxicol. Environ. Saf.*, 203, 111032.

[40] López-Mayán, J.J., del-Ángel-Monroy, S., Peña-Vázquez, E., Barciela-Alonso, M.C., Bermejo-

Barrera, P., and Moreda-Piñeiro, A., 2022, Titanium dioxide nanoparticles assessment in seaweeds by single particle inductively coupled plasma – Mass spectrometry, *Talanta*, 236, 122856.

[41] Oya-Silva, L.F., Vicari, T., Rodrigo Disner, G., Lirola, J.R., Klingelfus, T., Gonçalves, H.D.L.S., Leite, T.P.B., Calado, S.L.D.M., Voigt, C.L., Silva de Assis, H.C., and Cestari, M.M., 2021, Tissue-specific genotoxicity and antioxidant imbalance of titanium dioxide nanoparticles ($NPTiO_2$) and inorganic lead (PbII) in a neotropical fish species, *Environ. Toxicol. Pharmacol.*, 82, 103551.

[42] Baharlooeian, M., Kerdgari, M., and Shimada, Y., 2021, Ecotoxicological effects of TiO_2 nanoparticulates and bulk Ti on microalgae *Chaetoceros muelleri*, *Environ. Technol. Innovation*, 23, 101720.

[43] Auguste, M., Lasa, A., Pallavicini, A., Gualdi, S., Vezzulli, L., and Canesi, L., 2019, Exposure to TiO_2 nanoparticles induces shifts in the microbiota composition of *Mytilus galloprovincialis* hemolymph, *Sci. Total Environ.*, 670, 129–137.

[44] IARC Working Group on the Evaluation of Carcinogenic Risks to Humans, 2010, *Carbon Black, Titanium Dioxide and Talc*, *IARC Monographs on the Evaluation of Carcinogenic Risks to Humans, No. 93*, International Agency for Research on Cancer, Lyon, France.

[45] Hauser-Davis, R.A., Pereira, C.F., Pinto, F., Torres, J.P.M., Malm, O., and Vianna, M., 2020, Mercury contamination in the recently described Brazilian white-tail dogfish *Squalus albicaudus* (Squalidae, Chondrichthyes), *Chemosphere*, 250, 126228.

[46] Shipley, O.N., Lee, C.S., Fisher, N.S., Sternlicht, J.K., Kattan, S., Staaterman, E.R., Hammerschlag, N., and Gallagher, A.J., 2021, Metal concentrations in coastal sharks from The Bahamas with a focus on the Caribbean Reef shark, *Sci. Rep.*, 11 (1), 218.

[47] National Agency of Drug and Food Control of the Republic of Indonesia (BPOM), 2018, *Batas Maksimum Cemaran Logam Berat dalam Pangan Olahan*, Regulation of the Drug and Food Control Agency No. 5, Jakarta, Indonesia.

[48] Joint FAO/WHO Food Standards Programme, Codex Alimentarius Commission, 2016, *Codex Alimentarius: Working Document for Information and Use in Discussions Related to Contaminants and Toxin in GSCTFF*, Codex Committee on Contaminants in Foods, 2016 (CF/10 INF/1), World Health Organization: Food and Agriculture Organization of the United Nations, Rome.

[49] Fahmi, F., and Sentosa, A.A., 2017, Biology and fisheries aspects of western longnose spurdog, *Squalus edmundsi* from the Eastern Indian Ocean, Indonesia, *Biodiversitas*, 18 (4), 1714–1722.

[50] Taylor, V., Goodale, B., Raab, A., Schwerdtle, T., Reimer, K., Conklin, S., Karagas, M.R., and Francesconi, K.A., 2017, Human exposure to organic arsenic species from seafood, *Sci. Total Environ.*, 580, 266–282.

Supplementary Data

This supplementary data is a part of a paper entitled "Total Synthesis of a Reversed-Bacicyclin Using a Combination of Solid- and Solution-Phase Methods".

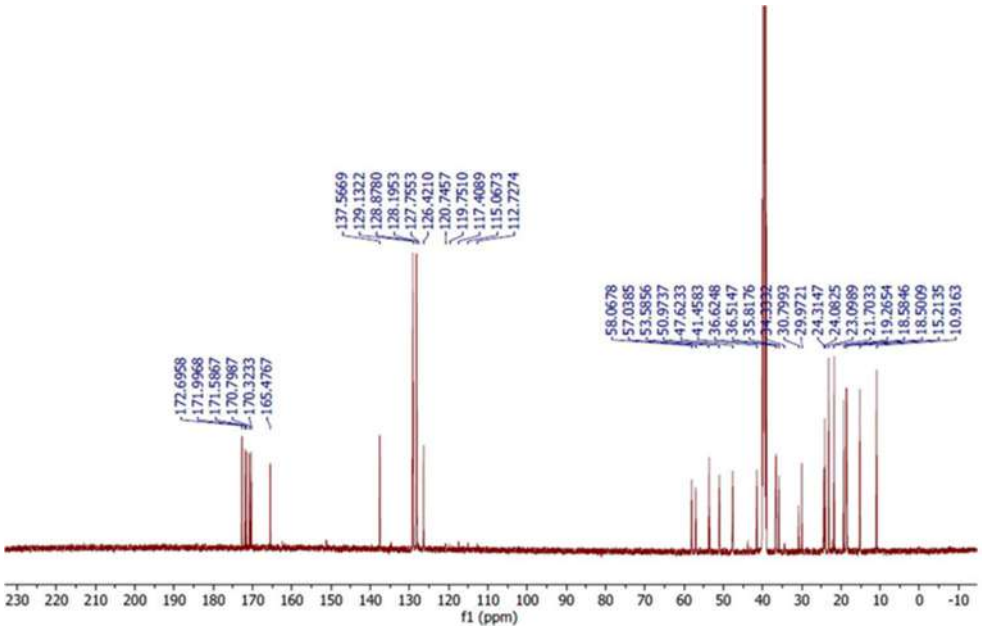

Fig S1. ^{13}C-NMR (125 MHz, DMSO-d6) spectra of linear bacicyclin

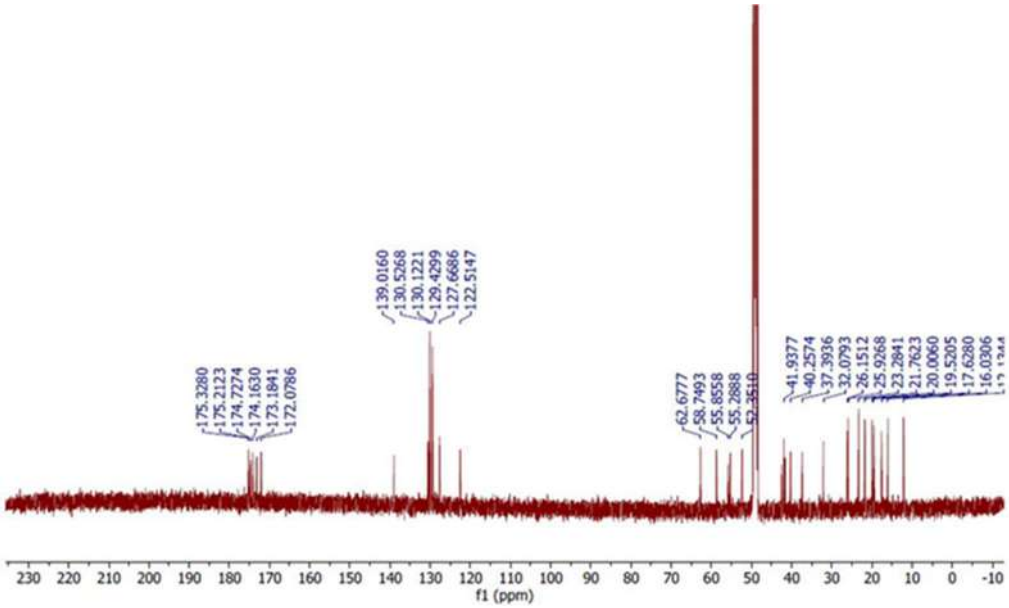

Fig S2. ^{13}C-NMR (125 MHz, CD_3OD) spectra of bacicyclin

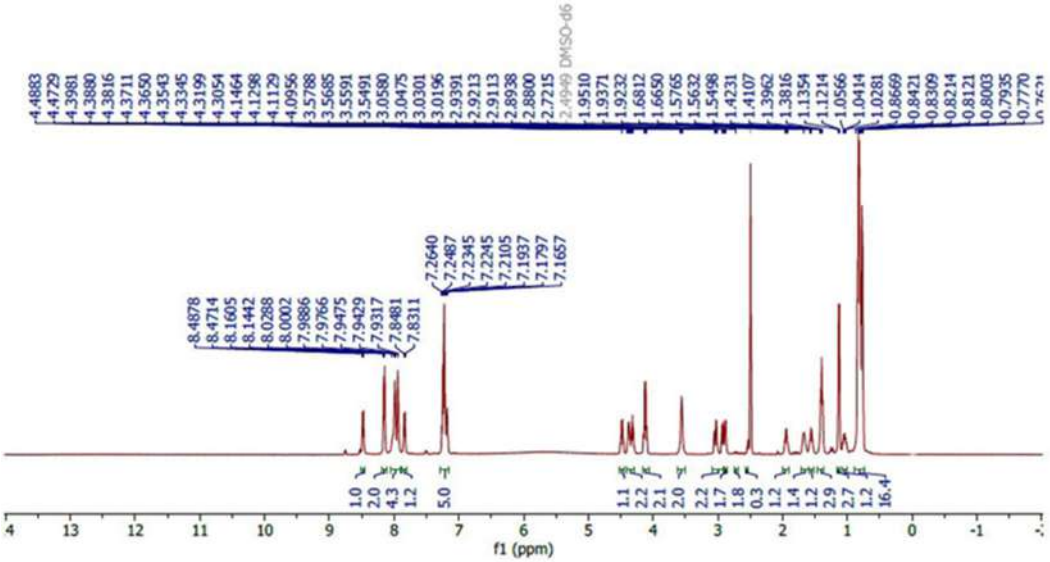

Fig S3. ^{1}H-NMR (500 MHz, DMSO-d*6*) spectra of linear bacicyclin

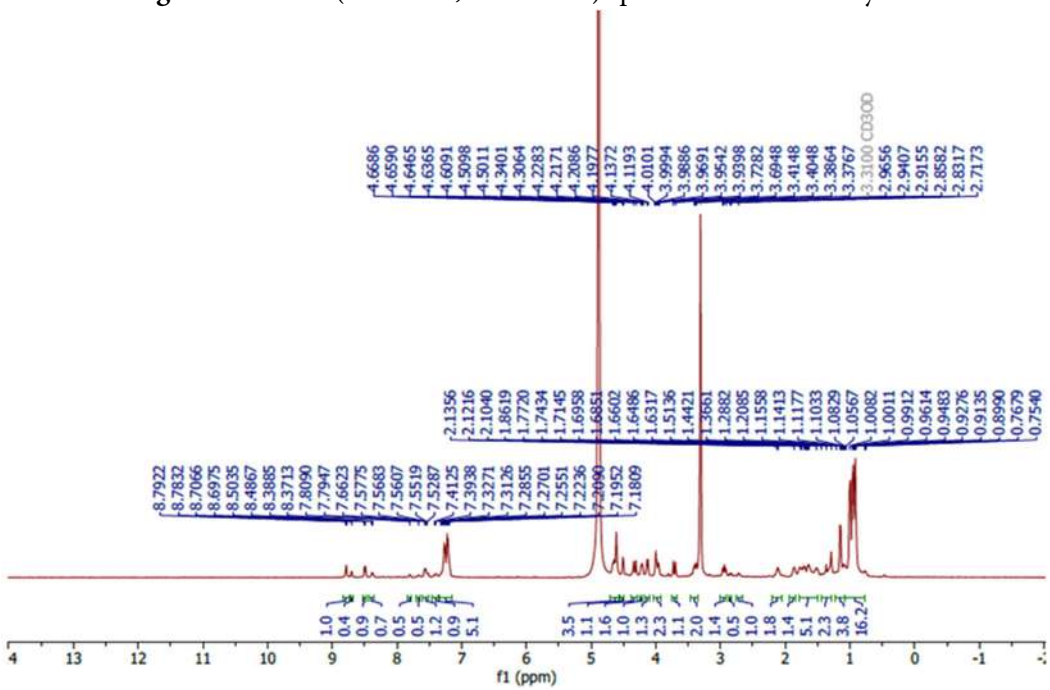

Fig S4. ^{1}H-NMR (500 MHz, CD_3OD) spectra of bacicyclin

Total Synthesis of a Reversed-Bacicyclin Using a Combination of Solid- and Solution-Phase Methods

Rani Maharani[1,2,3*], Anastasya Firdausi[1], Tri Mayanti[1,3], Desi Harneti[1,3], Nurlelasari Nurlelasari[1,3], Safri Ishmayana[1], Kindi Farabi[1,2,3], Unang Supratman[1,2,3], and Ace Tatang Hidayat[1,2,3]

[1]*Department of Chemistry, Faculty of Mathematics and Natural Sciences, Universitas Padjadjaran, Jl. Raya Bandung-Sumedang Km. 21, Jatinangor, Sumedang 45363, Indonesia*

[2]*Central Laboratory of Universitas Padjadjaran, Jl. Raya Bandung-Sumedang Km. 21, Jatinangor, Sumedang 45363, Indonesia*

[3]*Study Center of Natural Product and Synthesis, Universitas Padjadjaran, Jl. Raya Bandung-Sumedang Km. 21, Jatinangor, Sumedang 45363, Indonesia*

* ***Corresponding author:***

tel: +62-81290184903
email: r.maharani@unpad.ac.id

Received: February 10, 2022
Accepted: June 14, 2022

DOI: 10.22146/ijc.72956

Abstract: *Bacicyclin is a cyclic hexapeptide with antibacterial activity against* Enterococcus faecalis *and* Staphylococcus aureus *with minimum inhibition concentration (MIC) values of 8 and 12 μM, respectively. Studies on a reversed sequence of bacicyclin were conducted to investigate how the reversed peptide sequence affects its biological properties. A reversed-bacicylin, cyclo-(Gly-Leu-Val-Ile-Ala-Phe), was successfully synthesized by constructing the linear precursor on 2-chlorotrityl chloride resin using a Fmoc-based strategy. The HATU/HOAt reagent was applied in all peptidic bond formations, and the desired linear hexapeptide (82% yield) was cleaved off the resin using a mixture of trifluoroacetic acid:dichloromethane (2:8). The linear peptide was cyclized using 1-[bis(dimethylamino)methylene]-1*H*-1,2,3-triazolo[4,5-b]pyridinium-3-oxidehexa-fluorophosphate (HATU) as a coupling agent and diisopropylethylamine (DIPEA) as the base in a very dilute solution (0.001 M) in dichloromethane, then purified by octadecyl silica gel (ODS) column chromatography to obtain the reversed-bacicyclin (43.7% yield). The purity of the cyclic product was analyzed using analytical RP-HPLC (t_R = 20.01 min), and characterized by HR-TOF-MS, ^{1}H-NMR, and ^{13}C-NMR. The biological activity of the reversed-bacicyclin is much lower compared to bacicyclin, indicating that the amino acid sequence of the cyclopeptide dictates the antibacterial activity. This finding gives additional information on the relationship between peptide sequence and biological properties.*

Keywords: *bacicyclin; solid-phase peptide synthesis; cyclisation; cyclic hexapeptide; antibacterial peptide*

■ INTRODUCTION

Peptides, in particular cyclic peptides, have attracted much attention over the last few decades [1] because they exhibit unique advantages over linear peptides, such as their high affinity, fixed geometry and rigid structure, metabolic stability, and defined conformation. Cyclic peptides are a promising source of new drug candidates as they possess interesting biological activities, including antibiotic, antifungal [2], Cushing's disease [3], and anti-inflammatory [4]. Bacicyclin [cyclo-(D-Phe-D-Ala-Ile-Val-Ile-Gly)] (**1**) (Fig. 1) is a cyclic hexapeptide first isolated by Wiese et al. [5] from a marine *Bacillus* sp. strain (BC028). It shows antibacterial activity against the clinically relevant *Enterococcus faecalis* and *Staphylococcus aureus* with MIC values of 8 and 12 μM, respectively [5]. Structurally, its cyclic structure and the presence of D-configured residues make bacicyclin resistant to proteases, thus, it has potential as a drug

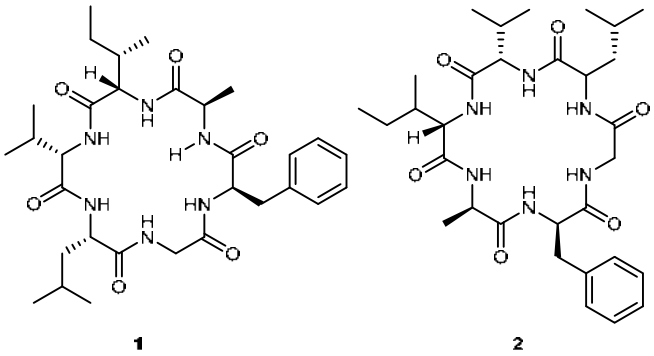

Fig 1. Structure of bacicyclin (**1**) and reversed-bacicylin (**2**)

candidate. Chen et al. [6] successfully synthesized bacicyclin and its analogs using a combination of solid- and solution-phase methods. However, synthetic bacicylin and analogs showed no significant antibacterial properties with an IC_{50} > 128 μM. The difference in antibacterial properties between the synthetic bacicylin and its natural product was caused by the different conformation and purities.

According to Damjanovic et al. [7], cyclic peptides with the same amino acid composition but different sequences exhibit different structural behavior in solution, which may change their activities. Rezai et al. [8] and Claro et al. [9] describe how cyclic peptides interact with the biological membrane and show that the interaction depends on the sequence, which dictates the conformation of the cyclic peptide. Therefore, it is interesting to compare the biological activities of peptides with the same amino acid composition but different sequences. Herein, we report the total synthesis of a bacicyclin isomer with a reversed sequence, cyclo-(Gly-Leu-Val-Ile-D-Ala-D-Phe) (**2**) (Fig. 1).

Most cyclic peptides are prepared via solid-phase peptide synthesis (SPPS) of the linear precursor, continued by macrocyclization on-resin or in solution [10]. The efficiency of the solution and on-resin cyclization were compared extensively by Sewald and colleagues [11] for the synthesis of cyclopeptides and cyclohexapeptides. The results showed that better method was achieved when cyclization was performed in solution-phase (9–36%) than on-resin (1–22%). A combination of solid- and solution-phase methods are commonly used for the synthesis of many cyclic peptides such as wollamide A, B, desotamide B [12], and their analogs [13-14]. This method was also used in the current synthesis, with SPPS and a Fmoc strategy performed to synthesize the linear precursor and cyclization conducted in solution-phase. The cyclization of a linear peptide with six residues is challenging [14], but the presence of two D amino acids facilitates the cyclization of the linear peptide, so D-Phe was located at the C-terminus and Gly at the N-terminus for cyclization [15]. The antibacterial properties of the synthesized reversed-bacicyclin against *S. aureus* and *E. faecalis* were then evaluated.

■ EXPERIMENTAL SECTION

Materials

The chemicals used were 2-chlorotrityl chloride resin, dimethylformamide (DMF), dichloromethane (DCM), 1-[bis(dimethylamino)methylene]-1*H*-1,2,3-triazolo[4,5-b]pyridinium-3-oxide hexafluorophosphate (HATU), *n*-hexane *N*,*N*-diisopropylethylamine (DIPEA), 1-hydroxy-7-azabenzotriazole (HOAt), piperidine, ethyl acetate, and trifluoroacetic acid. All amino acid residues, Fmoc-D-Phenylalanine, Fmoc-D-Alanine, Fmoc-L-Isoleucine, Fmoc-L-Valine, Fmoc-L-Leucine, Fmoc-L-Glycine, and 2-chlorotrityl chloride (0.972 mmol/g) were purchased from GL-biochem Ltd., Shanghai, China.

Instrumentation

Analysis of the linear and cyclic hexapeptides was performed on a Waters 2998 Photodiode Array Detector (PDA) with a wavelength of 210, 240, and 254 nm and LiChrospher 100 C-18 column (5 μm) for RP-HPLC. Acetonitrile (A) and deionized water (B) were used as the mobile phase with gradient elution and the addition of 0.1% trifluoroacetic acid (TFA) (vol/vol), with a flow rate of 1.0 mL/min and column temperature 25 °C for 30 min. The peptides were characterized by ^{1}H- and ^{13}C-NMR spectra using an Agilent ^{1}H-NMR 500 MHz and ^{13}C-NMR 125 MHz with deuterated solvent. The mass spectra were obtained from Waters HR-ToF-MS Lockspray, and the absorbance of loaded resin was measured on a UV-Vis Spectrophotometer (TECAN Infinite Pro 200).

Procedure

Synthesis of linear hexapeptides, a precursor of reversed-bacicyclin

The synthesis was performed on 2-chlorotrityl chloride resin (400 mg, 0.4 mmol), which was swollen in dichloromethane (10 mL) for 15 min at room temperature. Fmoc-D-Phe-OH (210 mg, 0.7 mmol) was loaded onto the resin in a mixture of dichloromethane (5 mL) and DIPEA (210 µL, 1.2 mmol). To measure the loading resin absorbance, 20% piperidine in DMF (3 mL) was added to 0.8 mg Fmoc-D-Phe-resin in an Eppendorf tube and left for 1 h, followed by sonification for 5 min before the absorbance was measured at 290 nm. Then, the resin was capped by adding 10 mL of MeOH:DCM:DIPEA (15:80:5) twice before the addition of 20% piperidine in DMF (5 mL) for 2 × 5 min to eliminate the Fmoc group, yielding a free amino group on the resin. Fmoc-D-Phe-NH_2 was coupled with the second residue, Fmoc-D-Ala-OH, using a combination of HATU (222.4 mg, 0.5 mmol) and HOAt (79.6 mg, 0.5 mmol) as a coupling agent and DIPEA (271.7 µL, 2.1 mmol) as a base in DMF (5 mL) for 4 h at room temperature. The Fmoc group was removed from Fmoc-D-Phe-D-Ala-Fmoc using 20% piperidine in DMF (5 mL) for 2 × 5 min to afford the resin-D-Phe-D-Ala-NH_2. This cycle of coupling and Fmoc deprotection was repeated with subsequent Fmoc-protected amino acids to obtain the resin-D-Phe-D-Ala-Ile-Val-Leu-Gly-NH_2. Finally, the peptide was cleaved from the resin using 20% TFA in dichloromethane (10 mL) for 2 × 20 min. After the collection of filtrate and subsequent TFA evaporation, the crude peptide was repeatedly washed with dichloromethane and dried under a vacuum. The linear peptide was injected into an analytical RP-HPLC (5–40% acetonitrile in water for 20 min, flow rate 1 mL/min, λ 240 nm) and characterized using HR-ToF-MS, ^{1}H-NMR (500 MHz, DMSO-d_6), and ^{13}C-NMR (125 MHz, DMSO-d_6).

Linear hexapeptide (precursor of reversed-bacicyclin): White solid; (91.3 mg, 82% yield); ^{1}H-NMR (500 MHz, DMSO-d_6, δ, ppm) 4.09 (m, CH-α, 2H), 4.38 (t, J = 8.4 Hz, CH- α, 1H), 4.12 (dd, J = 10.8;6.2 Hz, CH-α, 1H), 3.57 (d, J = 8.4 Hz, CH-α, 1H), 4.31 (m, J = 8.8 Hz, CH-α, 1H), 4.48 (q, J = 11.4; 4.2 Hz, CH-α, 1H), 8.48 (d, NH, 1H), 8.02 (d, NH, 1H), 7.94 (d, NH, 1H), 8.16 (d, NH, 1H), 7.83 (d, NH, 1H), 1.42 (s, NH_2, 2H), 1.57 (m, H-β/β' Leu, 2H), 1.64 (m, H-γ Leu, 1H), 0.81 (d, J = 7.8 Hz, H-δ Leu, 3H), 0.82 (d, J = 7.7 Hz, H-δ' Leu, 3H), 1.70 (m, H-β Val, 1H), 0.86 (d, J = 6.4 Hz, H-γ Val, 3H), 0.88 (d, J = 6.4 Hz, H-γ' Val, 3H), 1.97 (m, H-β Ile, 1H), 0.79 (d, H-γ Ile, 2H), 1.01 (d, H-γ' Ile, 3H), 0.76 (d, H-δ Ile, 3H), 1.13 (d, J = 8.4 Hz, H-β Ala, 3H), 3.06/2.93 (m, H-β/β' Phe, 2H), 7.26 (m, H-Bz-o, 2H), 7.22 (m, H-Bz-m, 2H), 7.16 (m, H-Bz-p Phe, 2H).^{13}C-NMR (125 MHz, DMSO-d_6, δ, ppm) 171.9 (C=O Gly), 172.7 (C=O Leu), 170.7 (C=O Val), 170.3 (C=O Ile), 171.5 (C=O Ala), 165.4 (C=O Phe), 41.4 (C-α Gly), 50.9 (C-α Leu), 58.0 (C-α Val), 57.0 (C-α Ile), 47.6 (C-α Ala), 53.5 (C-α Phe), 39.1 (C-β/β' Leu), 24.3 (C-γ Leu), 23.0 (C-δ Leu), 21.7 (C-δ' Leu), 30.7 (C-β Val), 18.5 (C-γ/γ' Val), 35.8 (C-β Ile), 15.2 (C-γ Ile), 29.9 (C- γ' Ile), 10.9 (C-δ), 18.5 (C-β Ala), 36.5 (C-β/β' Phe). HR-TOF-MS m/z 619.3892 $[M+H]^+$ (calcd. $C_{31}H_{51}N_6O_7$ 619.3894).

Synthesis of cyclic hexapeptides

The linear hexapeptide (30 mg, 0.05 mmol) was dissolved in DMSO (500 µL, 6.4 mmol), then dichloromethane (50 mL) before the addition of HATU (6 equiv. 110.7 mg, 0.3 mmol) and DIPEA (12 equiv. 75.3 µL, 0.6 mmol). The reaction mixture was stirred for 48 h at room temperature (monitored by TLC), then evaporated under vacuum to yield the crude cyclic product as a dark-yellow oil which was extracted between ethyl acetate (50 mL) and brine solution (3 × 30 mL). The organic fractions were combined and evaporated to give crude peptides as a bright-yellow solid, which were purified by reversed-phase ODS column chromatography (MeOH:H_2O = 5:5–6:4) to obtain the desired product (15.6 mg; yield 52%).

Reversed-Bacicyclin (**2**): White solid; 43.7% yield. ^{1}H-NMR (500 MHz, CD_3OD, δ, ppm) and ^{13}C-NMR (125 MHz, CD_3OD, δ, ppm) data can be seen in Table 1. HR-TOF-MS m/z $[M+H]^+$ 601.3713 (calcd. $C_{31}H_{49}N_6H_6$ 601.3714).

Antimicrobial assays

The antimicrobial activity of the test peptides was assessed by the disc method described by Mustafa et al.

[16] with some modifications. Briefly, agar plates were inoculated with *Escherichia coli* (Gram-negative bacteria), *Enterococcus faecalis*, *Staphylococcus aureus* (Gram-positive bacteria) and *Candida albicans* (fungi), then sterile paper discs saturated with the test peptides were placed on top of the agar and incubated at 37 °C for 16–18 h before the resulting inhibition zones were measured.

The microdilution method described by Mustafa et al. [16] with some modifications was also performed to evaluate the antibacterial activity of the test peptides against *S. aureus* and *E. faecalis*. Briefly, the peptides were dissolved in 2% DMSO at a concentration of 1 µg/mL to prepare a series of serial dilutions (1000; 500; 250; 125; 62.5; 31.25; 15.62; 7.81; 3.90; 1.95; 0.97 and 0.48 ppm). The sample solutions, amoxicillin, and 2% DMSO were placed in a 96-well microplate and incubated at 37 °C for 18 h before the absorbance was measured at 600 nm to calculate the MIC values.

■ RESULTS AND DISCUSSION

The synthesis procedure of reversed-bacicyclin is shown in Scheme 1. The linear hexapeptide was prepared via an SPPS method using 2-chlorotrityl chloride (2-CTC) resin because the resin can suppress diketopiperazine formation due to the bulky size of the chlorotrityl group and provide a mild acidic cleavage condition. The synthesis was initiated by the loading of the first residue, Fmoc-D-Phe-OH, onto the resin to obtain 0.45 mmol/g, which was categorized as good (0.3–0.6 mmol/g) [17-18]. The unreacted sites were then capped using MeOH:DIPEA:DCM (15:5:85), and the Fmoc group was deprotected with 20% piperidine in DMF to obtain a free amino group. The product was then coupled with Fmoc-D-Ala-OH using HATU/HOAt as the coupling reagent, and DIPEA as the base before the peptide was elongated by the attachment of subsequent L-isoleucine, L-valine, L-leucine, and glycine residues and final Fmoc deprotection to give the linear hexapeptidyl resin-D-Phe-D-Ala-Ile-Val-Leu-Gly-NH_2 (**2**).

The linear hexapeptide was cleaved from the resin using 20% TFA in DCM to yield a high purity linear product for macrocyclization. The HPLC chromatogram showed a single peak with a retention time of 7.140 min (Fig. 2), and the molecular ion peaks at *m/z* 619.3892 $[M+H]^+$ and $[2M+H]^+$ 1237.8109 in the HR-TOF-MS spectra confirmed the successful synthesis of the desired hexapeptide (Fig. 3). The ^{1}H- and ^{13}C-NMR of the linear precursor revealed five amide NH at

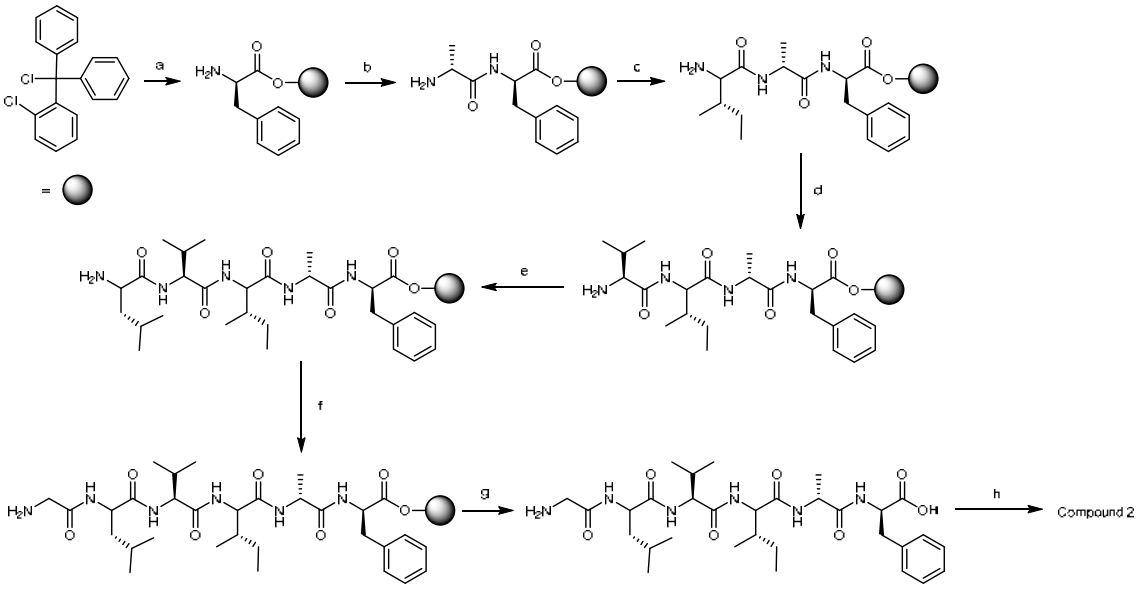

(a) (1) Fmoc-D-Phe-OH, DIPEA in dichloromethane, 8 h, rt, 20% piperidine in DMF, (2) MeOH DIPEA:DCM (15:5:80) 2 × 20 min, rt, (b) (1) Fmoc-D-Ala-OH, HATU/HOAT, in DMF, 4 h, rt, (2) 20% piperidine in DMF, (c) (1) Fmoc-L-Ile-OH HATU/HOAT, in DMF, 4 h, rt, (2) 20% piperidine in DMF, (d) (1) Fmoc-L-Val-OH, HATU/HOAT, in DMF, 4 h, rt, (2) 20% piperidine in DMF, (e) (1) Fmoc-L-Leu-OH, HATU/HOAT, in DMF, 4h rt, (2) 20% piperidine in DMF, (f) (1) Fmoc-L-Gly-OH, HATU/HOAT, in DMF, 4 h, rt, (2) 20% piperidine in DMF, (g) 20% TFA in DCM, 2 × 20 min, rt, (h) HATU, DIPEA in DCM, 10^{-3} M, 48 h, rt

Scheme 1. Fmoc-based SPPS and solution-phase macrocyclization of reversed bacicyclin

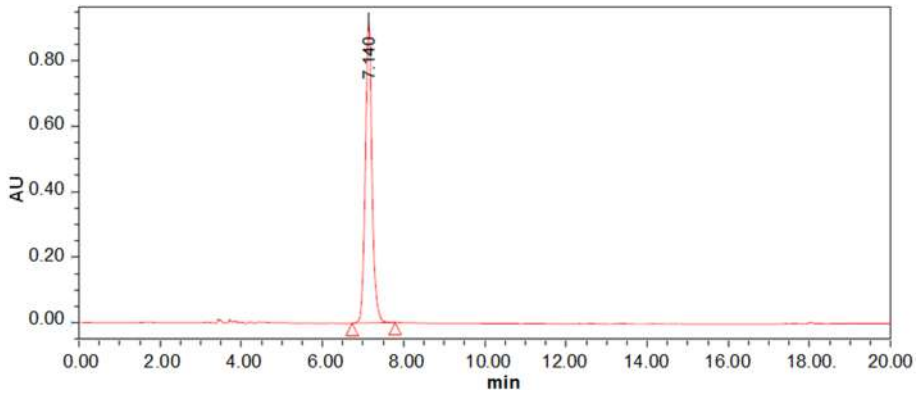

Fig 2. HPLC spectra of linear hexapeptide (precursor of bacicyclin) in acetonitrile:H_2O (5–40% linear gradient) at a flow rate of 1 mL/min, and λ 240 nm

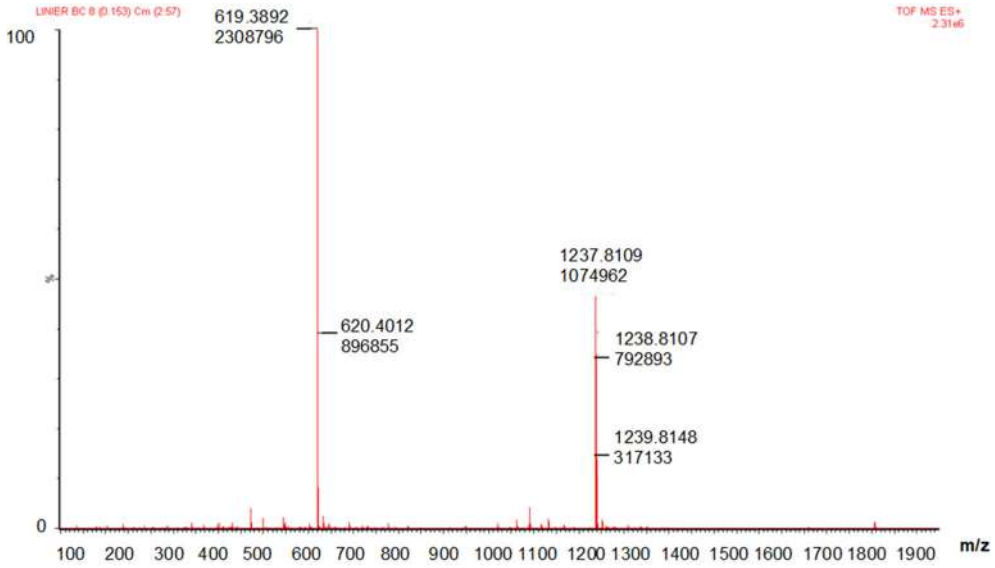

Fig 3. MS spectra of the linear hexapeptide

8.48 (d, 1H), 8.02 (d, 1H), 7.94 (d, 1H), 8.16 (d, 1H), and 7.83 (d, 1H), six α-protons at the chemical shifts of 4.09 (1H), 4.38 (1H), 4.12 (1H), 3.57 (1H), 4.31 (1H), and 4.48 (1H) ppm, one NH_2 proton at the chemical shift of 1.42 (s, 2H) ppm, six carbonyls at the chemical shifts of 165.4 (Gly), 172.7 (Leu), 170.7 (Val), 170.3 (Ile), 171.5 (Ala), and 171.9 (Phe) ppm and six α-carbons at the chemical shifts of 41.4, 50.9, 58.0, 57.0 47.6, and 53.5 ppm. Taken together, these data confirm the peptidic structure of the linear hexapeptide and 82% yield without any further purification required.

The linear hexapeptide was less soluble in DCM, DMF, acetonitrile, and other organic solvents but dissolved well in DMSO. Therefore, to avoid difficulties with DMSO removal, a minimal amount of DMSO was used to dissolve the peptide. Macrocyclization was firstly trialed in a dilute solution of 0.001 M in dichloromethane following the protocol of Ma and colleagues [19], but the linear peptide was still detected in the MS spectra. Therefore, the amount of HATU (6 equiv.) was increased, and the addition of DIPEA was stopped until it reached 12 equivalent. The reaction was completed in 48 h, yielding approximately 53% of the desired compound. The reaction was monitored by TLC (*n*-hexane:isopropanol (7:3) and peptide dimerization was avoided by conducting the macrocyclization reaction at a very dilute peptide concentration (less than 1 mM).

The success of the cyclization relies on the ring size

and the residues present in the peptide sequence, with side reactions, such as racemization, occurring if the linear peptide consists of less than seven amino acid residues [20]. However, the presence of amino acids such as proline, D-configured amino acids, the thiazole or oxazole ring, and an achiral amino acid such as glycine can increase cyclization success [21]. To minimize racemization, thus diastereomer formation during cyclization, the cyclic target was disconnected at the site between D-phenylalanine at the C-terminus and glycine at the N-terminus, which can also reduce steric resistance during the macrocyclic process.

HPLC analysis of the crude product showed that the cyclic peptide was the major product without any remaining linear starting material in the reaction mixture. The mixture was then concentrated and extracted with sodium chloride solution and evaporated using a rotary evaporator. Crude bacicyclin was purified by a flash column chromatography using MeOH:H_2O (gradient: 6:4-5:5) as the eluent, yielding 15.6 mg of compound **2** as white solid (52%). The purity of peptide **2** was checked by analytical RP-HPLC (Fig. 4; retention time = 20.01 min), and it was characterized by HR-TOF-MS, ^{1}H-NMR, ^{13}C-NMR, and IR. The mass spectra of HR-TOF-MS showed the correct molecular ion peak of the desired cyclic peptide with *m/z* 601.3713 $[M+H]^+$ (calcd. *m/z* 601.3714) and *m/z* 623.3525 $[M+Na]^+$ (calcd. *m/z* 623.3526) (Fig. 5).

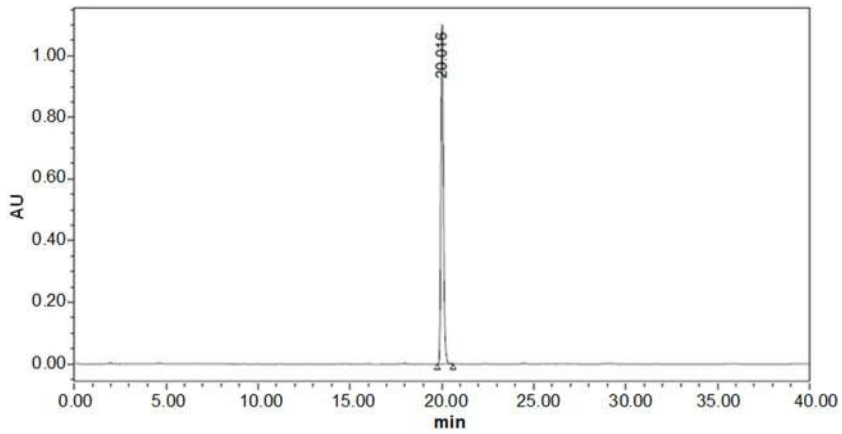

Fig 4. Analytical RP-HPLC chromatogram of reversed-bacicyclin 2 in acetonitrile:water (5–40% linear gradient) at a flow rate of 1 mL/min and λ 240 nm

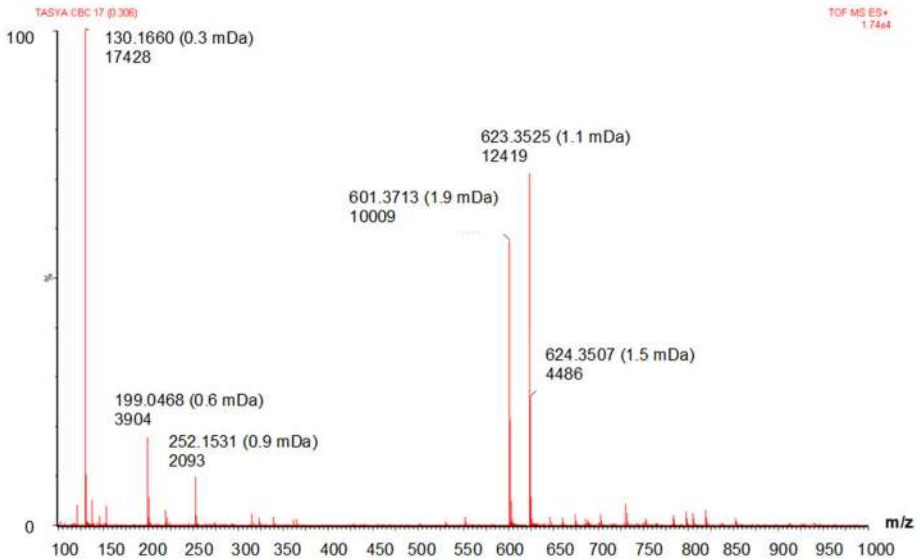

Fig 5. MS spectra of reversed-bacicyclin 2

Table 1. ^{1}H-NMR and ^{13}C-NMR spectra data of reversed-bacicyclin and comparison with bacicyclin spectral data by Wiese and colleagues

Amino acid residues	δ_C **1** [5] (CD_3OD, 150 MHz)	δ_C **2** (CD_3OD, 125 MHz)	δ_H **1** [5] (CD_3OD, 600 MHz)	δ_H **2** (synthesized) (CD_3OD, 500 MHz)
Gly				
CO	179.1	175.3		
α	41.4	41.2	3.36, t (*J* = 8.4 Hz)	3.38, t (*J* = 8.5 Hz)
Leu				
CO	171.5	172.0		
α	52.7	53.2	3.8, t (*J* = 8.4 Hz)	3.88, t (*J* = 8.5 Hz)
β/β'	41.8	41.9	1.58, m	1.60, m
γ	26.2	25.9	1.62, m	1.67, m
δ	22.5	23.2	0.91, d (*J* = 7.8 Hz)	0.99, d (*J* = 7.8 Hz)
δ'	21.6	21.7	0.96, d (*J* = 7.7 Hz)	1.08, d (*J* = 7.7 Hz)
Val				
CO	175.5	175.2		
α	60.6	62.6	4.21, dd (*J* = 10.8; 6.2 Hz)	4.22, dd (*J* = 10.5; 6.3 Hz)
β	31.8	32.0	1.98, m	1.86, m
γ	19.5	19.5	0.89, d (*J* = 6.4 Hz)	0.96, d (*J* = 6.4 Hz)
γ'	18.9	17.6	0.88, d (*J* = 6.6 Hz)	0.92, d (*J* = 6.8 Hz)
Ile				
CO	173.2	173.2		
A	58.9	58.7	4.19, d (*J* = 8.5 Hz)	4.19, d (*J* = 8.5 Hz)
B	36.1	37.3	2.03, m	2.13, m
Γ	12.1	12.1	0.84	0.85
γ'	27.5	26.1	1.28	1.28
Δ	14.6	16.1	0.86	0.86
Ala				
CO	173.4	174.1		
A	49.9	50.1	4.30, q (*J* = 9.0 Hz)	4.3, q (*J* = 8.8 Hz)
B	18.1	18.1	1.17, d (*J* = 8.4 Hz)	1.15, d (*J* = 8.5 Hz)
Phe				
CO	173.9	174.7		
A	56.8	55.8	4.3, q (*J* = 11.4; 4.2 Hz)	4.3, q (*J* = 11.0; 4.2 Hz)
β/ β'	29.1	28.1	3.31/3.05, m	3.20/3.16, m
Bz-I	128.9	139.0		
Bz-o	112.3	122.5	7.22, m	7.29, m
Bz-m	119.4	127.6	6.98, m	7.18, m
Bz-p	124.6	129.4	7.18, m	7.27, m

The ^{1}H-NMR and ^{13}C-NMR spectra of **2** and the linear peptide were different, with the absence of the chemical shift at 1.42 ppm of the free amine ($-NH_2$) proton of glycine in the ^{1}H-NMR spectra confirming cyclization (Table 1). The absence of NH_2 proton and the presence of NH amide signals in ^{1}H-NMR are commonly observed when the linear peptide is completely converted into a cyclic peptide [22-23]. Moreover, the successful formation of an amide bond between the amino group of glycine and carboxyl group

of D-phenylalanine was proven by the presence of the deshielding carbonyl signal of Phe at 175.3 ppm. Overall, the ^{13}C-NMR spectra displayed six amide-type carbonyls (δ 175.3, 172.0, 175.2, 173.1, 174.1, 174.7 ppm), five α-methine carbons (δ 53.2, 62.6, 58.7, 50.1, 55.8 ppm), α-methylene carbon (41.2), seven methyl groups (23.2, 21.7, 19.5, 17.6, 12.1, 16.1, 18.1 ppm), and three methylene groups (41.9, 37.3, 28.1 ppm). The NMR spectral data of **2** was similar to the NMR data obtained by Wiese et al. [5] for bacicyclin (Table 1).

The antimicrobial activities of the linear and cyclic peptides of **2** were assessed, showing that the linear and cyclic peptides of the reversed-bacicyclin **2** inhibited the growth of gram-negative *E. coli* with weak antibacterial activity at a concentration of 2000 ppm. The peptides also exhibited moderate antibacterial activity against *S. aureus* and *E. faecalis* but were not as effective as the natural product [5] or synthetic bacicylin [6], indicating that reversing the peptide structure affected the biological properties of the peptide.

■ CONCLUSION

Reversed-bacicyclin (cyclo-Gly-Leu-Val-Ile-D-Ala-D-Phe) has been successfully synthesized in a two-step process, achieving an overall yield of 43.7%. However, the biological properties of the reversed peptide were different to the natural product. This finding gives additional information on the relationship between peptide sequence and biological properties.

■ ACKNOWLEDGMENTS

The authors would like to thank the research grants of thesis magister-DIKTI-Indonesia (1827/UN6.3.1/LT/2020) and Academic Leadership Grant (ALG) Universitas Padjajaran, Indonesia (1427/UN6.3.1/LT/2022) for financial support.

■ AUTHOR CONTRIBUTIONS

RM, AF, and ATH designed the research. AF and KF conducted the research. TM, DH, N, and US helped in the purification step, RM and SI wrote the manuscript. All authors agreed to the final version of this manuscript.

■ REFERENCES

[1] Ha, K., Monbaliu, J.C.M., Williams, B.C., Pillai, G.G., Ocampo, C.E., Zeller, M., Stevens, C.V., and Katritzky, A.R., 2012, A convenient synthesis of difficult medium-sized cyclic peptides by Staudinger mediated ring-closure, *Org. Biomol. Chem.*, 10 (40), 8055–8058.

[2] Zhong, C., Liu, T., Gou, S., He, Y., Zhu, N., Zhu, Y., Wang, L., Liu, H., Zhang, Y., Yao, J., and Ni, J., 2019, Design and synthesis of new *N*-terminal fatty acid modified-antimicrobial peptide analogues with potent in vitro biological activity, *Eur. J. Med. Chem.*, 182, 111636.

[3] Sawicka-Gutaj, N., Owecki, M., and Ruchala, M., 2018, Pasireotide-mechanism of action and clinical applications, *Curr. Drug Metab.*, 19 (10), 876–882.

[4] Noh, H.J., Hwang, D., Lee, E.S., Hyun, J.W., Yi, P.H., Kim, G.S., Lee, S.E., Pang, C., Park, Y.J., Chung, K.H., Kim, G.D., and Kim, K.H., 2015, Anti-inflammatory activity of a new cyclic peptide, citrusin XI, isolated from the fruits of *Citrus unshiu*, *J. Ethnopharmacol.*, 163, 106–112.

[5] Wiese, J., Abdelmohsen, U.R., Motiei, A., Humeida, U.H., and Imhoff, J.F., 2018, Bacicyclin, a new antibacterial cyclic hexapeptide from *Bacillus* sp. strain BC028 isolated from *Mytilus edulis*, *Bioorg. Med. Chem. Lett.*, 28 (4), 558–561.

[6] Chen, Q., Wu, M., Chang, Q., and Zhao, X., 2021, Total synthesis and modification of Bacicyclin (1), a new marine antibacterial cyclic hexapeptide, *Tetrahedron Lett.*, 63, 152705.

[7] Damjanovic, J., Miao, J., Huang, H., and Lin, Y.S., 2021, Elucidating solution structures of cyclic peptides using molecular dynamics simulations, *Chem. Rev.*, 121 (4), 2292–2324.

[8] Jwad, R., Weissberger, D., and Hunter, L., 2020, Strategies for fine-tuning the conformations of cyclic peptides, *Chem. Rev.*, 120 (17), 9743–9789.

[9] Claro, B., Peón, A., González-Freire, E., Goormaghtigh, E., Amorín, M., Granja, J.R., Garcia-Fandiño, R., and Bastos, M., 2021,

Macromolecular assembly and membrane activity of antimicrobial *D*, *L*-α-Cyclic peptides, *Colloids Surf., B*, 112086.

[10] Farah, H.I., Supratman, U., Hidayat, A.T., and Maharani, R., 2022, An overview of the synthesis of biologically active cyclodepsipeptides, *ChemistrySelect*, 7 (1), e202103470.

[11] Malesevic, M., Strijowski, U., Bächle, D., and Sewald, N., 2004, An improved method for the solution cyclization of peptides under pseudo-high dilution conditions, *J. Biotechnol.*, 112 (1-2), 73–77.

[12] Tsutsumi, L.S., Tan, G.T., and Sun, D., 2017, Solid-phase synthesis of cyclic hexapeptides wollamides A, B and desotamide B, *Tetrahedron Lett.*, 58 (27), 2675–2680.

[13] Tsutsumi, L.S., Elmore, J.M., Dang, U.T., Wallace, M.J., Marreddy, R., Lee, R.B., Tan, G.T., Hurdle, J.G., Lee, R.E., and Sun, D., 2018, Solid-phase synthesis and antibacterial activity of cyclohexapeptide wollamide B analogs, *ACS Comb. Sci.*, 20 (3), 172–185.

[14] Chen, Y.X., Liu, C., Liu, N., Wu, Y., Zhao, Q.J., Hu, H.G., Li, X., and Zou, Y., 2018, Total synthesis and antibacterial study of cyclohexapeptides desotamide B, wollamide B and their analogs, *Chem. Biodivers.*, 15 (1), e1700414.

[15] Bodanszky, M., 2012, *Principles of Peptide Synthesis*, Springer Science & Business Media, Berlin, Germany.

[16] Mustafa, Y.F., Khalil, R.R., and Mohammed, E.T., 2020, Antimicrobial activity of aqueous extracts acquired from the seeds of two apples' cultivars, *Syst. Rev. Pharm.*, 11 (2), 382–387.

[17] Chan, W.C., and White, P., 1999, *Fmoc Solid Phase Peptide Synthesis: A Practical Approach*, Oxford University Press, Oxford, UK.

[18] Behrendt, R., White, P., and Offer, J., 2016, Advances in Fmoc solid-phase peptide synthesis, *J. Pept. Sci.*, 22 (1), 4–27.

[19] Ma, C., Chen, M., Chu, W., Tao, J., Kong, D., Zhang, M., and Feng, W., 2019, A practical and total synthesis of pasireotide: Synthesis of cyclic hexapeptide via a three-component condensation, *Molecules*, 24 (11), 2185.

[20] White, C.J., and Yudin, A.K., 2011, Contemporary strategies for peptide macrocyclization, *Nat. Chem.*, 3 (7), 509–524.

[21] Humphrey, J.M., and Chamberlin, A.R., 1997, Chemical synthesis of natural product peptides: Coupling methods for the incorporation of noncoded amino acids into peptides, *Chem. Rev.*, 97 (6), 2243–2266.

[22] Napitupulu, O.I., Sumiarsa, D., Subroto, T., Nurlelasari, N., Harneti, D., Supratman, U., and Maharani, R., 2019, Synthesis of cyclo-PLAI using a combination of solid-and solution-phase methods, *Synth. Commun.*, 49 (2), 308–315.

[23] Kurnia, D.Y., Maharani, R., Hidayat, A.T., Al-Anshori, J., Wiani, I., Mayanti, T., Harneti, D., and Supratman, U., 2021, Total synthesis of xylapeptide B [Cyclo-(L-Leu-L-Pro-N-Me-Phe-L-Val-D-Ala)], *J. Heterocycl. Chem.*, 59 (1), 131–136.

Distribution of Heavy Metals in Sediments and Soft Tissues of the *Cerithidea obtusa* from Sepang River, Malaysia

Kumar Krishnan[1*], Elias Saion[2], Chee Kong Yap[3], Prakash Balu[4], Wan Hee Cheng[1], and Mee Yoke Chong[5]

[1]*Faculty of Health and Life Sciences, Inti International University, Persiaran Perdana BBN, Nilai 71800, Negeri Sembilan, Malaysia*

[2]*Department of Physics, Faculty of Science, University Putra Malaysia, Serdang 43400, Selangor, Malaysia*

[3]*Department of Biology, Faculty of Science, University Putra Malaysia, Serdang 43400, Selangor, Malaysia*

[4]*Department of Biotechnology, Vels Institute of Science, Technology and Advanced Studies (VISTAS), PV Vaithiyalingam Rd, Velan Nagar, Krishnapuram, Pallavaram, Chennai, Tamil Nadu 600117, India*

[5]*Matrix Global School, Pt 12652, Sendayan Merchant Square, Persiaran 1 Sendayan Utama, Pusat Dagangan Sendayan, 71950 Bandar Sri Sendayan, Seremban, Negeri Sembilan, Malaysia*

* ***Corresponding author:***

tel: +603-7982000
email: kumar.krishnan@newinti.edu.my

Received: February 11, 2022
Accepted: May 11, 2022

DOI: 10.22146/ijc.72991

Abstract: *The main purpose of the research was to analyze the distribution of Arsenic (As), Cadmium (Cd), Copper (Cu), Iron (Fe), Nickel (Ni), Cobalt (Co), Mangan (Mn), and Zinc (Zn) in soft tissues, shells, and associated surface sediments of* Cerithidea obtusa *(*C. obtusa*) mangrove snails collected from Sungai Besar Sepang. The concentration of iron (Fe) was found to be the highest in relation to other toxic elements in sediments, soft tissues, and shells of* C. obtusa. *The concentrations of Cu and Zn in soft tissues of* C. obtusa *were found to exceed the concentrations in sediments, indicating bioaccumulation of these metals. Metal pollution was assessed with the Enrichment Factor (EF), Geoaccumulation Index (I_{geo}), and Pollution Factor (CF). EF, I_{geo}, and CF were 0.34 to 22.41, -3.37 to 2.65, and 0.14 to 9.42, respectively. The results indicate that sediments in Sungai Besar Sepang are contaminated with As and Zn. According to the bivalve bioaccumulation results, the soft tissues of* C. obtusa *act as a macro-concentrator for Cu and Zn. As a result, it is suggested that ongoing monitoring of releases of heavy metals from anthropogenic sources and stricter environmental protection measures should be implemented.*

Keywords: *enrichment; bio-accumulation; trace elements; neutron activation analysis*

■ INTRODUCTION

Mollusks are invertebrates found in oceans, rivers, lakes, or even on land [1]. Mollusks are easily obtained from their habitat due to their wide distribution and abundance [2]. Mollusks have the great advantage of being able to be used as bioindicators based on minerals absorbed from their habitat environment [3]. Since these mollusks are one of the important food sources for various living things of beings, it is important to avoid these mollusks being exposed to harmful toxic compounds [4]. The toxic content of mollusks is elevated because of phytoplankton feeding or sediment filtration [5]. As reported in other studies, mollusks have been shown to store high levels of heavy metals in their tissues and shell and adapt to changing environmental conditions [6-7]. Consequently, these heavy metals are partially or fully used for the growth of shells and soft tissues of mollusks [8]. Recently, the accumulation of heavy metals in the shell and soft tissues of mollusks has received much attention [9]. The number of heavy metals in the shells and soft tissues of mollusks and in sediments can be used to assess the degree of

contamination levels [3]. The type of diet they consume and how they live has an impact on their ability to deposit heavy metals into the shells and tissues of mollusks. These mollusks live by feeding or filtering sediment, exposing them to heavy metals consumed directly from the sediment. Therefore, thorough research is needed to determine the potential of this species to accumulate and store this toxic element in its shell and soft tissues from sediments in its natural habitat [10]. Numerous researches have been conducted to propose environmental analyses using elements found in sand and mollusks [3].

The purpose of this study was to determine the distribution of heavy metals in the shell and soft tissues of the *Cerithidea obtusa* mollusk, as well as sediments from their habitat. Furthermore, to investigate the potential application of this capability for pollution biomonitoring in research areas, as well as to compare heavy metal levels in the study environment with those in other parts of the world.

■ EXPERIMENTAL SECTION

Study Sites and Samples Collection

The research area of this study focused on the mouth of Sungai Sepang Besar (Sepang Besar River), which flows into the Straits of Malacca in Sepang District, Selangor Malaysia, at GPS coordinate: N 02° 56' 16.9" and E 101° 45' 9.4" as shown in Fig. 1. The study region has a tropical environment all year, with temperatures ranging from 27 to 34 °C and a moderately humid atmosphere. The amount of cloud cover is modest, and November is the wettest month, albeit rainfall is rare. Sepang District had rapid and significant growth from 1995 to 2015, owing to its proximity to Malaysia's administrative capital, Putrajaya. As a result, an expansion of urban growth has been found to impact Sungai Sepang Besar's ecosystems. The reserve forests and mangrove regions in Sepang District are quite modest, with mangrove forests covering around 546.7 hectares along the rivers Sungai Sepang Kecil and Sungai Sepang Besar. It has fish, crabs, and shrimp, which are all biodiversity components of the mangrove environment. Under the Sepang Local Plan 2025, the mangrove regions are designated as Level 1 Environmentally Sensitive Areas (ESA) (Sepang 2017) [11-12].

Bivalve mollusks (*C. obtusa*) were selected to assess the bioaccumulation of heavy metals in their shell and soft tissues because of their wide dispersion and abundance in the study area. This species has been identified in the same manner as in previous studies. Only commercially recognized normal sizes for each species were compiled to avoid changes in metal content related to its size or reproductive stage [13-14]. For this study, 40–50 individual snails of similar length (3.5 to 5.0 cm) and mangrove sediments weighing approximately 500–600 g were randomly collected at a depth of 3.0-5.0 cm by scraping the surface layer with a plastic spoon [15-16]. At the laboratory, all samples were rinsed off with tap water to remove the soil attached to the snails and placed in a clean plastic bag with a label. As shown in Fig. 2(a) and 2(b), the soft tissue is then removed from the shell by fine-crushing the shell without damaging the soft tissue. Each sedimentary, shell,

Fig 1. Map of Sepang Besar River

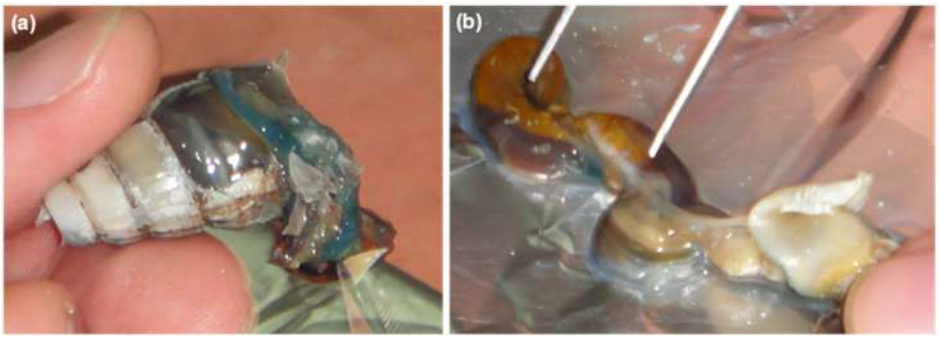

Fig 2. (a) Removing the shell, (b) Soft tissue

and tissue sample was packaged in a polyethylene plastic bag and stored in an icebox [17]. To remove moisture, sediments, shells, and soft tissues are dried in an oven at 85 °C for at least 72 h until a dry weight is produced. With glass mortar, each sediment sample, soft tissue, and shell of *C. obtusa* were individually crushed into a powder form. Then the powder is filtered through an opening made of stainless steel of 63 μm. Samples were stored in plastic pillboxes after being stirred vigorously and ready for further analysis [18].

Instrumentation

Neutron activation analysis (NAA) method was used to determine the concentration of elements. The powdered samples were separated into four subsamples of 150 and 200 mg each and stored individually in heat-sealed polyethylene vials for short and long radiation. Half-lives and gamma energies from radionuclides, along with a comparison approach, were used to determine element concentrations [19-20]. IAEA SL–1 (Lake Sediment)) and SRM 1566b/SRM 2976 were used as multi-element comparators for sediment and soft tissue bivalve mollusk, respectively.

For quality assurance, blank samples, standard reference material, IAEA-SL-1, and SRM 1566b/SRM 2976 were all irradiated simultaneously in the pneumatic transport facility at the 750 kW (MINT TRIGA) research reactor with a thermal neutron flux of 4.0 $Tcm^{-2}s^{-1}$. The samples were radiated for 1 min and then counted for 5 and 20 min after cooling for 20 min and 24 h, respectively, under brief radiation. For extended radiation, the samples were irradiated for 6 h and then counted for 1 h after cooling for 3–4 and 21–28 days, respectively. The distance between the detector and the sample was kept between 12 cm (short radiation) and 2 cm (long radiation). A calibrated high-resolution HPGe detector was used to count radiated samples. The components present in the sample, as well as their concentration, were identified using the specific energy of delayed gamma rays. All the countings were done in conditions where the dead time was less than 10% [19].

Prior to the use of an Atomic Absorption Spectroscopy (AAS), a sediment sample of approximately 500 mg was digested in a 4:1 mixture of nitric acid and perchloric acid in powder form (BDH Analar grade). For the first hour, all digestive tubes were placed in a digestion block at 40 °C and then digested entirely at 140 °C for at least 3 h [8]. Forty milliliters of double distilled water was added to dilute the resultant solution. The solution was then filtered into a polyethylene container using a WhatmanTM No. 1 filter. The concentrations of the elements were determined using a Perkin Elmer Model Analyst 800 and an air-acetylene AAS in three replicates on all of the samples [8].

Procedure

The status of enrichment of heavy metals in sediments can be assessed using pollution tools such as enrichment factor, contamination factor, and geo-accumulation index. On the other hand, the bioaccumulation factor was used for the bioaccumulation of sediment-associated organic compounds or metals into the tissues of ecological.

Enrichment factor (EF)

The EF was used to assess the size of anthropogenic

metal inputs. Metals in sediment with values ranging between 0.5 and 1.5 have a lithospheric or crustal origin, whereas values greater than 1.5 (EF > 1.5) have an anthropogenic origin [21]. Eq. (1) is used to determine the EF:

$$EF = \frac{(M/Fe)_{sample}}{(M/Fe)_{shale}} \quad (1)$$

where M and Fe are the metal concentrations in the sample and shale be averaged [22-23]. The EF values were interpreted as shown in Table 1.

Geo-accumulation index (I_{geo})

Müller created the geo-accumulation index (I_{geo}), which is a reliable instrument for calculating a system's contaminated condition [24]. It can be calculated using Eq. (2):

$$I_{geo} = \log_2\left[\left(C_N/1.5B_N\right)\right] \quad (2)$$

where C_N denotes the metal concentration in the sample, and B_N denotes the average shale background metal concentration [25]. The background matrix correction factor of 1.5 is used to minimize variance owing to lithogenic influences. Muller divided the I_{geo} value into seven categories, as shown in Table 2 [26].

Contamination factor (CF)

The amount of metal contamination in sediment is frequently described as a contamination factor (CF). It calculates the amount of pollution caused by pollutants in an ecological system and can be calculated by using Eq. (3):

$$CF = \left(\frac{C_N}{B_N}\right) \quad (3)$$

where C_N denotes the metal content in the sample and B_N denotes the background metal concentration in typical shale [25]. The CF readings were interpreted as shown in Table 3 [27].

Table 1. Pollution classification of the enrichment factor (EF)

	Range	Status
Enrichment Factor (EF)	1	no enrichment
	3–5	minor enrichment
	5–10	moderately severe enrichment
	10–25	severe enrichment
	25–50	very severe enrichment, and
	> 50	extremely severe enrichment

Table 2. Pollution classification of the geo-accumulation index (I_{geo})

	Range	Status
Geo-accumulation (I_{geo})	< 0	virtually unpolluted
	0–1	unpolluted to moderately polluted
	1–2	moderately polluted
	2–3	moderately to highly polluted
	3–4	strongly polluted
	4–5	strongly to severely polluted
	> 5	extremely contaminated

Table 3. Pollution classification of the contamination factor (CF)

	Range	Status
Contamination Factor (CF)	CF < 1	low contamination
	1 ≤ CF ≤ 3	moderate contamination
	3 ≤ CF ≤ 6	considerable contamination
	CF > 6	very high contaminations

Biota-sediment accumulation factor (BSAF)

For selected metals, the BSAF was estimated using Eq. (4) [28]:

$$BSAF = \frac{C_x}{C_s} \quad (4)$$

where C_x and C_s are the mean metal concentrations in various snail parts (tissues and shell) and in sediment, respectively. BSAF values can be classified into three groups, as indicated in Table 4 [29].

Statistical analysis

All of the findings were statistically analyzed with SPSS version 22.0. The difference between groups (i.e., sample locations) and the association between environmental parameters and accumulation were determined using Pearson's correlation coefficient test. MS Excel was used to calculate the mean and standard deviation (SD).

■ RESULTS AND DISCUSSION

The concentrations of eight elements were determined from four replicates across all samples and certified reference material (CRM), as shown in Table 5. The recovery percentage for all elements of the SL-1 and SRM 1566b CRMs of the IAEA ranges from 81.2% to 144.6% and 84.6% to 145%, respectively. The determined values corresponded well to their certified values.

The mean concentration of the target element in sediment, soft tissue, and shell of *C. obtusa*, along with their standard deviation, are presented in Table 6. The concentration of metals for this study was calculated based on the average values of all the analyzed samples and the standard error (SE) of total metal concentrations (in mg/kg dry weight basis). A total of eight elements were identified and quantified using the Instrumentation Neutron Activation Analysis (INAA) and alternative technique, i.e., the AAS method. The mean concentration of elements in the sediments was Fe > Mn > Zn > Ni > As > Cu > Co. Fe was found most abundant among all monitored toxic elements at trace levels in sediment. The mean concentration of elements in sediments is higher, suggesting the tendency of studied elements to accumulate in sediments as well as the role of sediments as a receptor of heavy metals. This is consistent with the studies in Qeshm Island, Persian Gulf of United Arab Emirates [30], and Sepang River, Malaysia [31-32]. Based on the results, the high concentration of elements in sediments can be due to the impact of a common resource (natural or anthropogenic) in the study area. Sediment quality guides and other studies results are provided in Table 7. The comparison of the results of the sediment sample of this study against the relevant guide suggests that the

Table 4. Pollution classification of the BSAF

	Range	Status
Biota-Sediment Accumulation Factor (BSAF)	> 2	macroconcentrators
	1–2	microconcentrators
	< 1	deconcentrators

Table 5. Mean of measured and certified values of CRM (mg/kg dry weight)

	SL-1			SRM1566b/SRM2976		
	Standard value	Measured value	Recovery (%)	Standard value	Measured value	Recovery (%)
Fe	67400	68716	102.0	205.8	278.6	135.4
As	27.6	22.4	81.2	7.65	6.47	84.6
Mn	3460	3178.1	91.9	18.5	16.61	89.8
Zn	223	257.3	115.4	1424	1386.4	97.4
Co	19.8	21.3	107.6	0.371	0.538	145.0
Cd	1.3	1.88	144.6	0.82	0.85	103.7
Ni	26	28.15	108.3	0.93	0.86	92.5
Cu	11	11.13	101.2	71.6	70.1	97.9

Table 6. Concentrations of heavy metals (mg/kg dry weight) in sediment, soft tissue, and shell of *C. obtusa*

		min	max	average	Std. dev.
Fe	Assoc.sediments	21874	25674	23659	1910
	Soft tissues	224	4822	2230	2236
	shell	286.64	345.32	315.9	41.5
As	Assoc.sediments	14.57	18.34	16.95	1.68
	Soft tissues	9.46	16.41	12.06	3.03
	shell	0.453	0.602	0.552	0.068
Mn	Assoc.sediments	123.45	152.39	137.68	12.15
	Soft tissues	53.85	184.08	134.55	70.49
	shell	9.35	15.23	12.33	2.58
Zn	Assoc.sediments	85.08	101.35	91.78	7.24
	Soft tissues	67.72	110.51	92.34	18
	shell	8.26	10.39	9.29	0.87
Co	Assoc.sediments	5.68	6.59	7.33	0.72
	Soft tissues	0.91	8.19	4.06	3.74
	shell	0.13	0.58	0.31	0.24
Cd	Assoc.sediments	nd	nd	nd	nd
	Soft tissues	0.640	0.904	0.773	0.132
	shell	0.311	0.336	0.327	0.014
Ni	Assoc.sediments	17.23	28.20	22.72	5.48
	Soft tissues	17.97	18.42	18.19	0.22
	shell	11.98	17.78	14.88	2.90
Cu	Assoc.sediments	11.11	11.19	11.14	0.04
	Soft tissues	90.59	103.88	97.24	9.40
	shell	1.73	2.50	2.11	0.54

nd – not detected

Table 7. Comparison of Mn, As, Zn, Fe, Cu, Ni, and Cd concentrations (mg/kg dry weight basis) with other studies and guideline

Guideline	Mn	Cu	As	Zn	Cd	Ni	Fe	Ref.
NOAA Guidelines								
ERL (Effects Range Low)	na	34	8.2	150	1.2	20.9	na	[44]
ERM (Effects Range Median)	na	270	70	410	9.6	51.6	na	
Canadian Guideline								
TEL (Threshold Effect Level)	na	18.7	7.24	124	0.7	15.9	na	[43]
PEL (Probable Effect Level)	na	108	41.6	271	4.2	42.8	na	
USEPA standards limits harbor sediments		25–50	3–8	90–200	6	20–50		[41]
(Mean current study)	137.68	11.14	16.95	91.78	-	22.7	23659	
Sepang River, Malaysia	na	77.17±0.25		246.38±0.22	1.15±0.04	26.05±0.08	na	[42]
Peninsular Malaysia	na	1.63–150.81		23.70–609.20	1.63–150.81	2.41–36.29	na	[31]
Qeshm Island, Persian Gulf	na	31.58–127.86		61.80–159.22	0.11–0.16	27.35–109.46	na	[30]

na – not available

concentration of other measurable elements was lower compared to the presented guide except for As and Ni. Also, in the sediment sample, As and Ni has been larger than ERL, TEL, and USEPA standards. These findings

show that human activities such as urban, residential, and industrial wastewater, agriculture, shipping and transportation, coastal activities (i.e., marinas, jetties, ports, and harbors), and mining operations may have an impact on this area with high As and Ni concentrations. These findings are consistent with those of prior investigations [30,33]. Quick environmental changes altered the components in water, whereas sediments preserved the history of environmental changes [34].

The abundance order of target elements in soft tissue and shell of *C. obtusa* was found as Fe > Mn > Cu > Zn > Ni > As > Co > Cd and Fe > Ni > Mn > Zn > Cu > As > Cd > Co respectively. The heavy metal concentrations in the shells show a similar pattern of accumulation when compared with soft tissues of *C. obtusa*. The levels of As, Mn, Zn, Co, and Cu in the shells of *C. obtusa* were significantly lower than in the soft tissues. The accumulation of the studied elements except for the Ni, Co, and Cd in the soft tissue was far higher than that in the shell. This accumulation was obtained with a significant difference for Fe, Cu, Zn, and Mn compared to the shell. Different elements have various roles and functions, which lead to differences in the accumulation of elements in the tissues of the mollusk. The higher values of Cu and Zn in soft tissues can be due to the tendency of *C. obtusa* to accumulate these essential elements for cell growth and metabolism. In mollusks, Zn is used in the structure of many enzymes and the synthesis of hematocyanin [35]. Cu's role in the metabolism of molecular oxygen in mollusks is biochemically similar to, if not identical, that of Fe because the oxygen-carrying pigment of mollusk's blood is Cu-containing cuproprotein, hemocyanin, rather than hemoglobin [36]. Furthermore, Cd binds to low-molecular-weight proteins called metallothionein, which reduces its toxicity [37]. So, by applying the mechanism of detoxification, the soft tissue of oysters can accumulate more contents of this element [38] suggesting that mollusks may accumulate a portion of absorbed heavy metals in their shell. This issue can be a part of the detoxification process of over-absorbed essential elements and unnecessary elements in mollusks.

Several environmental indicators (EF, I_{geo}, and CF) were monitored to determine the pollutant level in the sediments. Table 8 shows the mean of the EF, I_{geo}, and CF of target elements in sediment, as well as their standard deviation. The Sepang river site was extremely severely enriched with As (10 < EF < 25) and minor enriched with Zn (3 < EF < 5), according to the results of enrichment factor data shown in Table 8. The study area was extremely heavily contaminated with As (CF > 6) and moderately contaminated with Zn (CF = 1–3), based on the contamination factor. According to Hakanson, Mn, Fe, Co, Cd, and Ni had low contamination in all investigated heavy metals (CF < 1). The geo-accumulation index (I_{geo}) showed that the mangrove environment of Sungai Besar Sepang was polluted with As but relatively unpolluted (I_{geo} < 0) for other elements in this study which is consistent with findings from prior studies in the area [32]. Bioaccumulation is the process of a chemical migrating from the external environment into the organism through all possible exposure channels, which is evaluated by a BSAF [39]. In this regard, the soft tissue

Table 8. The calculated value of enrichment factor (EF), geoaccumualtion index (I_{geo}), and contamination factor (CF)

	Enrichment Factor (EF)				Geo-accumulation (I_{geo})				Contamination Factor (CF)			
	min	max	average	Std dev	min	max	average	Std dev	min	max	average	Std dev
Fe	-	-	-	-	-1.95	-1.72	-1.84	0.12	0.39	0.46	0.42	0.03
As	20.83	22.34	22.41	0.89	2.43	2.76	2.65	0.17	8.09	10.19	9.42	1.06
Mn	0.33	0.35	0.34	0.01	-3.53	-3.23	-3.37	0.15	0.13	0.16	0.14	0.02
Zn	3.13	3.17	3.12	0.03	-0.30	-0.05	-0.19	0.13	1.22	1.45	1.31	0.12
Co	0.58	0.58	0.70	0.07	-2.72	-2.51	-2.36	0.18	0.23	0.26	0.29	0.03
Ni	0.53	0.59	0.80	0.14	-2.87	-2.47	-2.16	0.36	0.21	0.27	0.34	0.07
Cu	0.48	0.41	0.44	0.03	-3.02	-3.01	-3.01	0.01	0.19	0.19	0.19	0.00

shows larger BSAF values than the shell, indicating the greater tendency of elements to accumulate in the soft tissue than in the shell. Based on data presented in Table 9, the Cu and Zn concentrations in the soft tissue of *C. obtusa* are several times greater than their concentration in the sediments. This suggests the ability of the soft tissue to accumulate metals several times as large as the environment. The soft tissue of the studied *C. obtusa* acts as a macroconcentrator for the elements of Cu and Zn, and its shell functions similarly for Cd, according to the classification presented for the BSAF factor, which is similar to the findings of similar bivalve and which have presented *C. obtusa* as a macroconcentrator of metals [40]. The lower values of the BSAF factor for elements such as Co, Ni, and As in the soft tissue can be due to the fact that they are not biologically needed, which corresponds to the other study findings on bivalve mollusks [30]. The concentration of elements in the oyster shell is less influenced by the physicochemical conditions of the environment. The lower values of coefficient variation indicate greater accuracy in determining the biomonitor organism for the studied metals. According to the studies [3], the lower coefficient of variation for the concentration of metals in a particular tissue suggests the accuracy and validity of that tissue being used as a biomonitor of metals. Thus, this factor can be effective in choosing a living organism as a biomonitor.

Table 9. BSAF of shell and soft tissue of *C. obtusa* in the whole area investigated

		min	max	average	Std dev
Fe	muscle	0.01	0.19	0.10	0.09
	shell	0.01	0.01	0.01	-
As	muscle	0.65	0.89	0.71	0.13
	shell	0.03	0.03	0.03	-
Mn	muscle	0.44	1.21	0.98	0.40
	shell	0.08	0.10	0.09	0.01
Zn	muscle	0.80	1.09	1.01	0.15
	shell	0.12	0.09	0.10	0.01
Co	muscle	0.16	1.24	0.55	0.55
	shell	0.02	0.09	0.04	0.03
Ni	muscle	1.04	0.81	0.65	0.20
	shell	0.70	0.78	0.53	0.13
Cu	muscle	8.15	8.69	9.32	0.59
	shell	0.16	0.22	0.19	0.03

Table 10. Relations between the heavy metals concentrations in sediment and those in the soft tissue and shell of *C. obtusa*

Fe	sediment	Soft tissues	shell
sediment	1		
Soft tissues	0.994**	1	
shell	0.356	0.449	1

As	sediment	Soft tissues	shell
sediment	1		
muscle	0.294	1	
shell	0.857	0.550	1

Mn	sediment	Soft tissues	shell
sediment	1		
Soft tissues	-0.241	1	
shell	-0.990**	0.316	1

Zn	sediment	Soft tissues	shell
sediment	1		
muscle	-0.609	1	
shell	0.039	0.246	1

Co	sediment	Soft tissues	shell
sediment	1		
Soft tissues	0.692	1	
shell	0.156	-0.550	1

Cu	sediment	Soft tissues	shell
sediment	1		
muscle	0.488	1	
shell	0.401	0.995**	1

Cu	sediment	Soft tissues	shell
sediment	1		
muscle	0.488	1	
shell	0.401	0.995**	1

Correlation is significant at the 0.01 level

The Pearson's correlation coefficients in Table 10 illustrate the correlation of metals between soft tissues, the shell of *C. obtusa*, and sediments. The concentration of all the heavy metal (except for Mn and Zn) in surface sediments were positively and strongly correlated with respective heavy metals in soft tissues and the shell of *C. obtusa*. The correlations of Fe, As, Co, Ni, and Cu concentrations in soft tissue and habitat sediments showed the ability of bivalve mollusks to reflect their individual metal levels in their environment. For As, Ni, and Cu, the shells revealed substantial relationships with the surface sediments. This showed that the *C. obtusa* shell could be used as a biomonitor for the three metals.

■ CONCLUSION

The variations in metal distribution could be attributed to variances in tissue physiology as well as metal handling, storage, and detoxification procedures, according to the current findings. Cu and Zn concentrations in soft tissues were substantially greater than in sediments. According to the pollution index, the area is severely enriched with As and Zn, possibly as a result of anthropogenic activity near the sampling point. *C. obtusa* soft tissues are macroconcentrators and could be employed as biomonitors for metal buildup. As a result, our findings are useful for future ecotoxicological investigations aiming at establishing *C. obtusa* as a good heavy metal biomonitor and bioindicator species. Stricter environmental protection measures should be implemented to control the discharge of heavy metals from anthropogenic sources. In order to preserve sustainable development in the Sungai Besar Sepang river, it is also critical to raise public knowledge about maritime environmental preservation.

■ ACKNOWLEDGMENTS

The authors wish to acknowledge the financial support via the Research Grant Scheme (Seed Grant no: INTI-FHLS-10-03-2021) provided by INTI International University, Nilai, Malaysia.

■ AUTHOR CONTRIBUTIONS

Elias B. Saion and Yap CK are the team leader who proposed the work and designed the experiment. Kumar Krishnan, Cheng WH, Prakash Balu, and Chong MY executed the experiments and analyzed the results, manuscript writing, revised and verified the manuscript and the results obtained from the experiment. All authors read and approved the manuscript. All playing roles as the main contribution to this study due to their expertise and knowledge.

■ REFERENCES

[1] Ratih, S.A., Pertiwi, M.P., and Rostikawati, R.T., 2021, Mollusk diversity in the intertidal zone of Menganti Beach, Kebumen, Central Java, *Depik*, 10 (1), 23–29.

[2] Triacha, Z.I.E.C., Pertiwi, M.P., and Rostikawati, R.T., 2021, Keanekaragaman echinodermata di pantai Cibuaya Ujung Genteng, Jawa Barat, *JID*, 22 (1), 9–18.

[3] Yap, C.K., Sharifinia, M., Cheng, W.H., Al-Shami, S.A., Wong, K.W., and Al-Mutairi, K.A.A., 2021, Commentary on the use of bivalve mollusks in monitoring metal pollution levels, *Int. J. Environ. Res. Public Health*, 18 (7), 3386.

[4] Telesca, L., Peck, L.S., Sanders, T., Thyrring, J., Sejr, M.K., and Harper, E.M., 2019, Biomineralization plasticity and environmental heterogeneity predict geographical resilience patterns of foundation species to future change, *Global Change Biol.*, 25 (12), 4179–4193.

[5] Rosa, M., Ward, J.E., and Shumway, S.E., 2018, Selective capture and ingestion of particles by suspension-feeding bivalve mollusks, *A review*, *J. Shellfish Res.*, 37 (4), 727–746.

[6] Yap, C.K., Cheng, W.H., Karami, A., and Ismail, A., 2016, Health risk assessments of heavy metal exposure via consumption of marine mussels collected from anthropogenic sites, *Sci. Total Environ.*, 553, 285–296.

[7] Yap, C.K., Chew, W., Cheng, H., Okamura, H., Harino, H., Peng, S.H.T., Ismail, M.S., and Leow, C.S., 2019, Higher bioavailability and contamination by copper in the edible mussels, snails and horseshoe crabs at Kampung Pasir Puteh: Evidence of an industrial effluent receiving site at Pasir Gudang area, *Adv. Bioequivalence Bioavailability*, 2 (5), 000548.

[8] Yap, C.K., 2017, From mussel watch monitoring to health risk assessment: A public health concern, *GSL J. Public Health Epidemiol.*, 1, 103.

[9] Alkan, N., Alkan, A., Demirak, A., and Bahloul, M., 2020, Metals/metalloid in marine sediments, bioaccumulating in macroalgae and a mussel, *Soil Sediment Contam.*, 29 (5), 569–594.

[10] Yap, C.K., Ariffin, N., Nulit, R., Ibrahim, M.H., Peng, S.H.T., Yap, C.W., and Ng, W.K., 2019, The potential of digestive caecum in mudflat snail Telescopium telescopium as a possible cadmium source for industrial application, *EC Gastroenterol. Dig. Syst.*, 6 (9), 752–756.

[11] Yasin, M.Y., Noor, N.M., Yusoff, M.M., Abdullah, J., and Noor, N.M., 2021, SPOT imagery observation on mangrove changes using NDVI density analysis: The case of Sepang Besar River, Malaysia, *Arab World Geogr.*, 23 (2-3), 217–228.

[12] Yasin, M.Y., Yusoff, M.M., and Noor, N.M., 2019, Urban sprawl assessment using time series LULC and NDVI variation: A case study of Sepang Malaysia, *Appl. Ecol. Environ. Res.*, 17 (3), 5583–5602.

[13] Yap, C.K., 2018, Selected organs of marine mussels as accurate biomonitors of metal bioavailability and contamination in the coastal waters: Challenges, *EC Pharmacol. Toxicol.*, 6 (7), 528–534.

[14] Liu, J., Wu, H., Feng, J., Li, Z., and Lin, G., 2014, Heavy metal contamination and ecological risk assessments in the sediments and zoobenthos of selected mangrove ecosystems, South China, *CATENA*, 119, 136–142.

[15] Asimiea, O.A., and Gobo, A.E., 2012, Nematod speciation along the New Calabar and Bonny River systems of the Niger Delta, Nigeria, *J. Emerging Trends Eng. Appl. Sci.*, 3 (5), 765–769.

[16] Ra, K., Kim, J.K., Hong, S.H., Yim, U.H., Shim, W.J., Lee, S.Y., Kim, Y.O., Lim, J., Kim, E.S., and Kim, K.T., 2014, Assessment of pollution and ecological risk of heavy metals in the surface sediments of Ulsan Bay, *Korea*, *Ocean Sci. J.*, 49 (3), 279–289.

[17] Liu, Q., Liao, Y., and Shou, L., 2018, Concentration and potential health risk of heavy metals in seafoods collected from Sanmen Bay and its adjacent areas, China, *Mar. Pollut. Bull.*, 131 (Pt A), 356–364.

[18] Krishnan, K., Saion, E.B., Yap, C.K., Chong, M.Y., and Nadia, A. S, 2022, Determination of trace elements in sediments samples by using neutron activation analysis, *J. Exp. Biol. Agric. Sci.*, 10 (1), 21–31.

[19] Kumar, K., Saion, E., Halimah, M.K., Yap, C., and Hamzah, M.S., 2014, Rare earth element (REE) in surface mangrove sediment by instrumental neutron activation analysis, *J. Radioanal. Nucl. Chem.*, 301 (3), 667–676.

[20] Benarfa, A., Begaa, S., Messaoudi, M., Hamlat, N., and Sawicka, B., 2020, Elemental composition analysis of *Pistacia lentiscus* L., leaves collected from Mitidja plain in Algeria using instrumental neutron activation analysis (INAA) technique, *Radiochim. Acta*, 108 (10), 821–828.

[21] Mir, S.I., Karim, M.A., Ali, M.I., and Ramli, N.I., 2017, Assessment of heavy metal contents in surface sediment of the Tungguk River surrounding the industrial complex of Gebeng City, *BRC*, 3 (1), 362–371.

[22] Khodami, S., Surif, M., Wan Omar, W.M., and Daryanabard, R., 2017, Assessment of heavy metal pollution in surface sediments of the Bayan Lepas area, Penang, Malaysia, *Mar. Pollut. Bull.*, 114 (15), 615–622.

[23] Barbieri, M., 2016, The importance of enrichment factor (EF) and geoaccumulation index (Igeo) to evaluate the soil contamination, *J. Geol. Geophys.*, 5 (1), 1000237.

[24] Müller, G., 1979, Schwermetalle in den sedimenten des Rheins: Veranderungen seitt 1971, *Umschau*, 79, 778–783.

[25] Turekian, K.K., and Wedepohl, K.H., 1961, Distribution of the elements in some major units of the earth's crust, *Geol. Soc. Am. Bull.*, 72 (2), 175–192.

[26] Müller, G., 1981, Die schwermetallbelastung der sedimente des neckars und seiner nebenflusse: Eine bestandsaufnahme, *Chem.-Ztg.*, 105, 157–164.

[27] Hakanson, L., 1980, An ecological risk index for aquatic pollution control. A sedimentological approach, *Water Res.*, 14 (8), 975–1001.

[28] Kobkeatthawin, T., Sirivithayapakorn, S., Nitiratsuwan, T., Muenhor, D., Loh, P.S., and Pradit, S., 2021, Accumulation of trace metal in sediment and soft tissue of *Strombus canarium* in a tropical remote island of Thailand, *J. Mar. Sci. Eng.*, 9 (9), 991.

[29] Yunus, K., Zuraidah, M.A., and John, A, 2020, A review on the accumulation of heavy metals in coastal sediment of Peninsular Malaysia, *Ecofeminism Clim. Change*, 1 (1), 21–35.

[30] Nourozifard, P., Mortazavi, S., Asad, S., and Hassanzadeh, N., 2020, Using *Saccostrea cucullata* as a biomonitor of heavy metals (Cu, Pb, Zn, Cd, Ni, and Cr) in water and sediments of Qeshm Island, Persian Gulf, *ECOPERSIA*, 8 (3), 181–190.

[31] Zulkifli, S.Z., Mohamat-Yusuff, F., Arai, T., Ismail, A., and Miyazaki, N, 2010, An assessment of selected trace elements in intertidal sediments collected from the Peninsular Malaysia, *Environ. Monit. Assess.*, 169 (1), 457–472.

[32] Syaizwan, Z.Z., Siti, A.R., Ferdaus, M.y., and Ahmad, I., 2014, Geochemical fractionations of heavy metals in sediments of Sepang Besar River, Malaysia, *Acta Biol. Malays.*, 3 (1), 1–9.

[33] Yap, C.K., Mohd Ruszaidi, S., Cheng, W.H., and Tan, S.G, 2010, Heavy metal concentrations in the mangrove snail, Nerita lineata and surface sediments collected from Klang River Estuary, Selangor, Malaysia, *J. Sustainability Sci. Manage.*, 5 (1), 1–12.

[34] Abbasi, S., Soltani, N., Keshavarzi, B., Moore, F., Turner, A., and Hassanaghaei, M., 2018, Microplastics in different tissues of fish and prawn from the Musa Estuary, Persian Gulf, *Chemosphere*, 205, 80–87.

[35] Larsson, J., Smolarz, K., Świeżak, J., Turower, M., Czerniawska, N., and Grahn, M., 2018, Multibiomarker analysis of pollution effect on resident populations of blue mussels from the Baltic Sea, *Aquat. Toxicol.*, 198, 240–256.

[36] Vernon, E.L., and Jha, A.N., 2019, Assessing relative sensitivities of marine and freshwater bivalves following exposure to copper: Application of classical and novel genotoxicological biomarkers, *Mutat. Res., Genet. Toxicol. Environ. Mutagen.*, 842, 60–71.

[37] Chen, X., Wang, Z., Zhu, G., Nordberg, G.F., Ding, X., and Jin, T., 2018, The Association between renal tubular dysfunction and zinc level in a Chinese population environmentally exposed to cadmium, *Biol. Trace Elem. Res.*, 186 (1), 114–186.

[38] Hertika, A.M.S., Kusriani, K., Indrayani, E., Yona, D., and Putra, R.B.D.S., 2019, Metallothionein expression on oysters (*Crassostrea cuculata* and *Crassostrea glomerata*) from the southern coastal region of East Java, *F1000Research*, 8, 56.

[39] Savoca, D., and Pace, A., 2021, Bioaccumulation, biodistribution, toxicology and biomonitoring of organofluorine compounds in aquatic organisms, *Int. J. Mol. Sci.*, 22 (12), 6276.

[40] Yap, C.K., and Cheng, W.H., 2013, Distributions of heavy metal concentrations in different tissues of the mangrove snail *Nerita lineata*, *Sains Malays.*, 42 (5), 597–603.

[41] Samara, F., Elsayed, Y., Soghomonian, B., and Knuteson, S.L., 2016, Chemical and biological assessment of sediments and water of Khalid Khor, Sharjah, United Arab Emirates, *Mar. Pollut. Bull.*, 111 (1-2), 268–276.

[42] Ramsie, S.A., Zulkifli, S.Z., Mohamat-Yusuff, F., and Ismail, A., 2014, Geochemical fractionations of heavy metals in sediments of Sepang Besar River, Malaysia, *Acta Biol. Malays.*, 3 (1), 1–9.

[43] Sundaray, S.K., Nayak, B.B., Lin, S., and Bhatta, D., 2011, Geochemical speciation and risk assessment of heavy metals in the river estuarine sediments-A case study: Mahanadi basin, *J. Hazard. Mater.*, 186 (2-3), 1837–1846.

[44] Long, E.R., MacDonald, D.D., Smith, S.L., and Calder, F.D., 1995, Incidence of adverse biological effects within ranges of chemical concentrations in marine and estuarine sediments, *Environ. Manage.*, 19 (1), 81–97.

The Prediction of Pharmacokinetic Properties of Compounds in *Hemigraphis alternata* (Burm.F.) T. Ander Leaves Using pkCSM

Yeni Yeni* and Rizky Arcinthya Rachmania

Department of Pharmacy, Universitas Muhammadiyah Prof. DR. HAMKA, Jl. Delima II/IV, Jakarta 13460, Indonesia

* ***Corresponding author:***

tel: +62-81219612608
email: yeni@uhamka.ac.id

Received: February 18, 2022
Accepted: May 16, 2022

DOI: 10.22146/ijc.73117

Abstract: *The inflammatory process aids in healing and maintains the body's balance. Untreated acute inflammation can cause organ disease, which can lead to a chronic inflammatory phenotype.* Hemigraphis alternata *is a plant that has anti-inflammatory activity. The compounds contained in* H. alternata *leaves have been predicted to have an affinity for receptors involved in the inflammatory process. A large number of drug candidates were withdrawn from preclinical trials due to their poor pharmacokinetic profiles. Drug compounds must cross the barriers that exist in the body to reach their biological targets so that they can generate a biological effect. The pharmacokinetic features of 22 components in* H. alternata *leaves were predicted in order to search for inflammatory medication candidates with suitable pharmacokinetic profiles. The pkCSM, a strategy for predicting and optimizing the pharmacokinetic properties of small molecules based on distance-based graph signatures was used in this work. The pkCSM employed 20 predictors separated into four groups: absorption, distribution, metabolism, and excretion. Based on the prediction findings, there are five substances with the best pharmacokinetic features, 8a-methyl-3,4,4a,5,6,7-hexahydro-2*H*-naphthalene-1,8-dione, (*E*)-3,7,11,15-tetramethylhexadec-2-en-1-ol, 2-methylenecholestan-3-ol, 5-(hydroxymethyl) furan-2-carbaldehyde and 2,3-dihydro-2,5-dimethyl-5*H*-1,4-dioxepin.*

Keywords: Hemigraphis alternata*; pharmacokinetic profiles; pkCSM*

■ INTRODUCTION

Inflammation is the body's defensive reaction to potentially hazardous impulses such as viruses or chemicals that induce cell injury. It triggers inflammatory cells and signaling pathways. The inflammation process is critical in the recovery process because it allows aberrant bodily homeostasis to be restored. Acute inflammation that is not effectively managed can aggravate organ disease and eventually develop into a chronic inflammatory phenotype [1-3].

Hemigraphis alternata possesses anti-nociceptive, anti-inflammatory, and anti-diarrheal effects. In mice, ethyl acetate and methanol extracts of *H. alternata* leaves were found to exhibit anti-inflammatory and non-toxic effects [4]. This plant's leaves contain 22 secondary metabolites (Fig. 1) [5]. These substances exhibit anti-inflammatory effects against cyclooxygenase-1 (COX-1) and 5-lipoxygenase (5-LOX) receptors [6-7].

The interaction of pharmacokinetic characteristics, toxicity, and potency significantly impacts a drug's efficacy. A compound's pharmacokinetic profiles are determined to assess its absorption, distribution, metabolism, and excretion (ADME) features [8]. The preliminary evaluation of ADME features will assist pharmaceutical researchers in selecting the best medication candidates for development and rejecting drug candidates with a poor likelihood of success [9]. Creating novel drug candidates is a challenging, time-consuming, and expensive procedure. In developing novel medications, *in silico* computational model plays an essential role. Its use reduces the amount of time and resources needed for the rational design of novel medication candidates. Pharmaceutical advancements have raised the necessity for more accurate methodologies to predict the pharmacokinetic features of novel drug candidates. Because of the improvement of

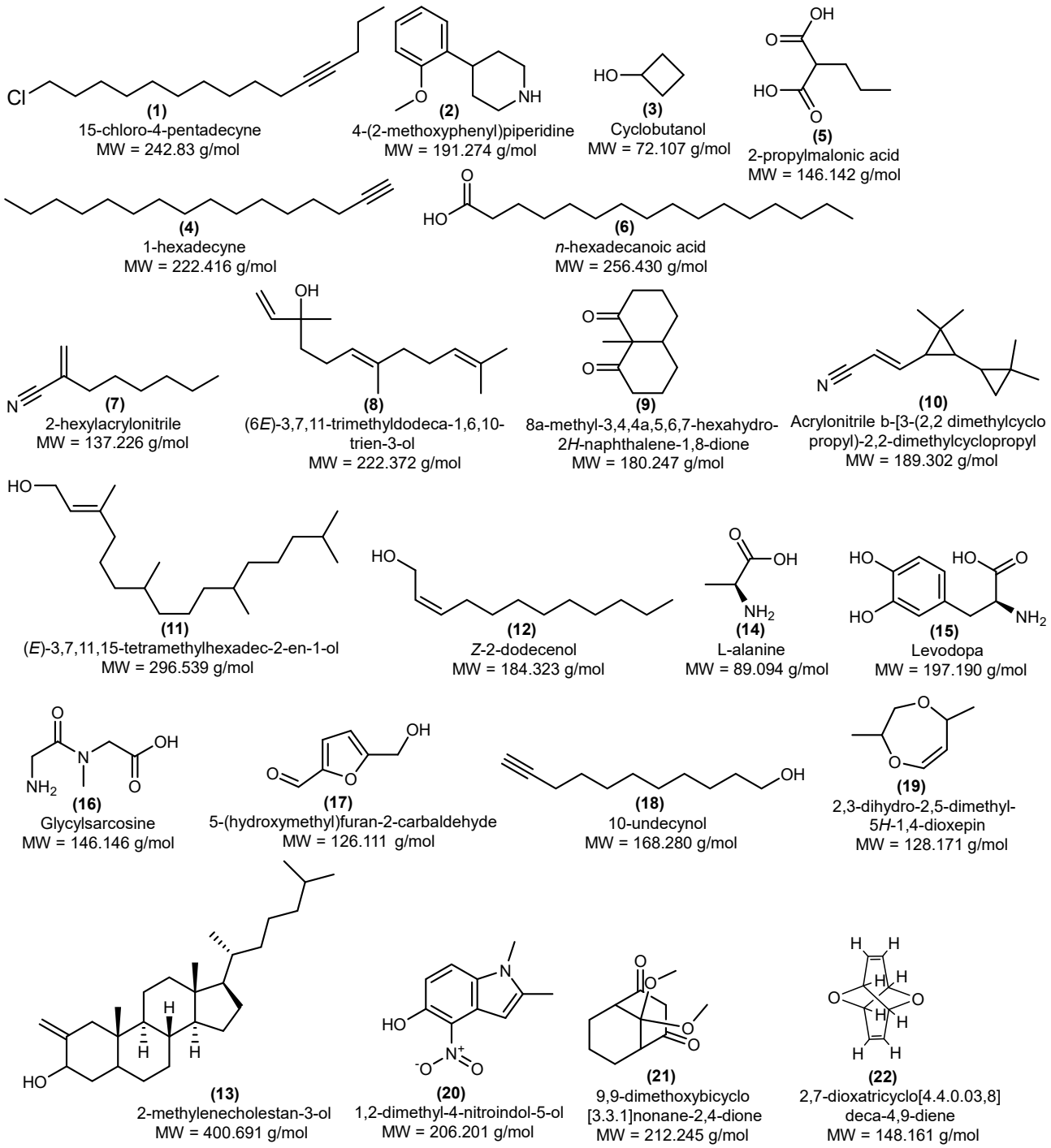

Fig 1. The compounds contained in *H. alternata* leaves [6-7]

computer algorithms and massive information databases, computational prediction tools are increasingly routinely employed in the procedure for drug discovery. Furthermore, *in silico* technologies have been employed to discover various drugs that are now used in the treatment of disorders [10-13].

The pkCSM is a tool that can characterize the pharmacokinetic profile of compounds comprehensively. The concept used to predict the predictors by this tool is graph-based structural

signatures which train the prediction algorithm by encoding the pattern of distances between atoms. Graphical modeling results from an understandable and well-established mathematical description of chemical entities. Different predictors, including molecular structure and chemistry, may be retrieved using pkCSM [14-16]. Despite the diversity in the size of the data set and the distribution of experimental values, the pkCSM model was able to establish a strong correlation with experimental results through regression analysis of the ADME predictors [8]. The mission of *in silico* ADME prediction is to accurately forecast the *in vivo* pharmacokinetic features of prospective therapeutic compounds in humans using only virtual structures. In this work, *in silico* analysis was used to estimate the pharmacokinetic features of 22 chemicals found in *H. alternata* leaves.

■ EXPERIMENTAL SECTION

Materials

PubChem (pubchem.ncbi.nlm.nih.gov) provided the SMILES format of 22 chemicals found in the leaves of *H. alternata*. The SMILES translator, cactus in https://cactus.nci.nih.gov can be used to get compounds that do not have the SMILES format in PubChem.

Instrumentation

The pharmacokinetic characteristics of 22 chemicals in the leaves of *H. alternata* were estimated using pkCSM (http://biosig.unimelb.edu.au/pkcsm/prediction).

Procedure

The application of pkCSM is based on general compound qualities (molecular properties, toxicophores, and pharmacophores), as well as distance-based graph signatures. In pkCSM, there are 20 predictors that describe the pharmacokinetic properties of a compound. The predictors were divided into the absorption of 7 predictors, distribution of 4 predictors, metabolism of 7 predictors, and excretion of 2 predictors (Table 1) [8,17-18].

In this study, virtual screening was carried out to obtain several compounds that had good ADME. The findings of the ADME predictor, which has a numerical value with specific constraints, are used in virtual screening. Caco-2 permeability (A2), intestinal absorption

Table 1. Distribution of ADME predictors in pkCSM [8]

Pharmacokinetic parameter	Predictor (code)	Unit	Requirement value
Absorption	Water solubility (A1)	log mol/L	-
	Caco-2 permeability (A2)	log Papp in 10^{-6} cm/s	> 0.9
	Intestinal absorption (human) (A3)	% Absorbed	> 30%
	Skin permeability (A4)	log Kp	≥ -2.5
	P-glycoprotein substrate (A5)	Yes/No	-
	P-glycoprotein I inhibitor (A6)	Yes/No	-
	P-glycoprotein II inhibitor (A7)	Yes/No	-
Distribution	VDss (human) (D1)	log L/kg	≥ -0.15
	Fraction unbound (human) (D2)	Fu	-
	BBB permeability (D3)	log BB	≥ -1
	CNS permeability (D4)	log PS	≥ -3
Metabolism	CYP2D6 substrate (M1)	Yes/No	-
	CYP3A4 substrate (M2)	Yes/No	-
	CYP1A2 inhibitor (M3)	Yes/No	-
	CYP2C19 inhibitor (M4)	Yes/No	-
	CYP2C9 inhibitor (M5)	Yes/No	-
	CYP2D6 inhibitor (M6)	Yes/No	-
	CYP3A4 inhibitor (M7)	Yes/No	-
Excretion	Total clearance (E1)	log mL/min/kg	Higher is better
	Renal OCT2 substrate (E2)	Yes/No	-

(human) (A3), skin permeability (A4), the human volume of distribution at steady state (VDss) (D1), Blood-Brain Barrier (BBB) permeability (D3), Central Nervous System (CNS) permeability (D4), and total clearance were the predictors (E1) [19].

Initially, test compounds were selected based on predictors of Caco-2 permeability (A2), intestinal absorption (human) (A3), skin permeability (A4), VDss (human) (D1), BBB permeability (D3), and CNS permeability (D4). The compounds that meet the requirements will be re-screened based on the highest total clearance (E1) value [8].

■ RESULTS AND DISCUSSION

The use of pkCSM is a strategy for estimating and improving the pharmacokinetic characteristics of small compounds based on distance-based graph signatures. The use of pkCSM extends the cutoff scanning idea to depict molecular and chemical structures in order to characterize and predict their pharmacokinetic features [8].

Water solubility is an essential aspect in a drug's pharmacological reaction following oral delivery. Drugs with strong water solubility will have good absorption and bioavailability qualities. Drug absorption and bioavailability can boost plasma drug concentrations at the target location, allowing it to fulfill therapeutic actions [20].

Caco-2 cells are a kind of colorectal cancer cell line [21]. In preclinical studies, the Caco-2 model was utilized to predict medication gastrointestinal permeability. Based on the properties of the human small intestine, this model expresses enterocytes, transporters, cytochrome P450 enzymes and microvilli [22]. A compound's Caco-2 permeability is high if its Papp is more than 8×10^{-6} cm/s.

The gut is the primary location of oral medication absorption. The skin serves as a barrier between the interior and exterior environments of the body. Skin qualities and traits can vary and influence medication distribution and toxicity [23]. The skin permeability constant log Kp (cm/h) expresses a compound's likelihood to be skin permeable.

P-glycoprotein (P-gp) is an ATP-binding cassette (ABC) transporter that acts as a biological barrier in cells by eliminating toxins and xenobiotics. The ability of a chemical to block the transport of P-gp I and P-gp II is referred to as P-gp I/II inhibitor. P-gp-mediated transport modification has important pharmacokinetic consequences for P-gp substrates. Inhibiting P-gp I or P-gp II might provide therapeutic benefits or result in contraindications [8].

VDss (human) is calculated by dividing all drugs inside the body by drug concentration in plasma in a stable state. This state happens when the system receives a consistent rate of medication infusion into the plasma, and all drug concentrations in the body remain constant [24]. The capacity of medicine to bind proteins in the blood can have an impact on its efficacy. The greater the proportion of the drug that is not bound to protein (fraction unbound), the more effectively the medication will cross or diffuse through the cell membrane [8].

Increased permeability of the BBB, a physical and biochemical barrier that plays a role in the protection of cerebral homeostasis, can alter the pathological development of ischemic tissue [25-26]. The value of the blood-brain permeability surface area product can be used to estimate a pharmacological compound's capacity to reach the CNS (log PS). This value was achieved through *in situ* brain perfusion with the chemical directly injected into the carotid artery without any systemic distribution impact that may skew brain penetration [8].

Cytochrome P450 is a detoxifying enzyme present in the liver. In general, cytochrome P450 is involved in drug metabolism. However, P450 inhibitors can significantly affect medication pharmacokinetics. As a result, it is critical to determine if the provided molecule is a CYP2D6/CYP3A4 substrate expected to be processed by P450. Cytochrome P450 oxidizes xenobiotics so that they can be excreted. Many medications are inactivated by cytochrome P450, whereas others might be activated by it. These enzyme inhibitors have the potential to interfere with medication metabolism and are thus not recommended. Therefore, it is critical to evaluate the compound's capacity to inhibit cytochrome P450 (isoforms CYP1A2/CYP2C19/CYP2C9/CYP2D6/CYP3A4). A substance is termed a cytochrome P450 inhibitor if the

concentration required to achieve 50% inhibition is less than 10 M [8].

The amount of drug removed from plasma in the vascular compartment per unit time is referred to as drug clearance. Total clearance is the result of all body clearances. Total clearance indicates drug removal from the core compartment without regard for the process mechanism [27]. The renal uptake transporter Organic Cation Transporter 2 (OCT2) is crucial for the disposition of drugs and renal clearance. When used with OCT2 inhibitors, OCT2 substrates might have negative side effects [8].

In the results of the prediction of absorption properties obtained compounds 3, 6, 9, 11, 13, 17, 19, 20, 21, and 22, which are in accordance with the requirements (Table 2). Meanwhile, the compounds that

Table 2. The prediction results of absorption properties 22 compounds contained in *H. alternata* using pkCSM

No	Compound	MW	A1	A2	A3	A4	A5	A6	A7
1	15-chloro-4-pentadecyne	242.830	-7.634	1.402	92.577	-2.420	No	No	No
2	4-(2-methoxyphenyl)piperidine	191.274	-1.835	1.385	91.872	-2.283	No	No	No
3	Cyclobutanol	72.107	0.092	1.463	98.450	-3.027	Yes	No	No
4	1-hexadecyne	222.416	-7.801	1.382	92.797	-2.225	No	No	No
5	2-propylmalonic acid	146.142	-1.323	0.667	74.589	-2.735	No	No	No
6	*n*-hexadecanoic acid	256.430	-5.562	1.558	92.004	-2.717	No	No	No
7	2-hexylacrylonitrile	137.226	-3.861	1.357	94.383	-1.278	No	No	No
8	(6*E*)-3,7,11-trimethyldodeca-1,6,10-trien-3-ol	222.372	-5.176	1.498	91.887	-1.477	No	No	No
9	8a-methyl-3,4,4a,5,6,7-hexahydro-2*H*-naphthalene-1,8-dione	180.247	-2.187	1.605	97.468	-2.814	No	No	No
10	Acrylonitrile β-[3-(2,2-dimethylcyclopropyl)-2,2-dimethylcyclopropyl	189.302	-4.729	1.382	95.941	-1.606	No	No	No
11	(*E*)-3,7,11,15-tetramethylhexadec-2-en-1-ol	296.539	-7.554	1.515	90.710	-2.576	No	No	Yes
12	*Z*-2-dodecenol	184.323	-4.816	1.474	91.684	-1.529	No	No	No
13	2-methylenecholestan-3-ol	400.691	-5.818	1.208	95.328	-2.733	No	No	Yes
14	L-alanine	89.094	-2.887	0.466	81.091	-2.738	No	No	No
15	Levodopa	197.190	-2.890	-0.289	47.741	-2.735	Yes	No	No
16	Glycylsarcosine	146.146	-2.699	0.545	68.130	-2.735	No	No	No
17	5-(hydroxymethyl)furan-2-carbaldehyde	126.111	-0.590	1.172	95.848	-3.416	No	No	No
18	10-undecynol	168.280	-3.892	1.476	93.273	-1.448	No	No	No
19	2,3-dihydro-2,5-dimethyl-5*H*-1,4-dioxepin	128.171	-0.757	1.621	97.700	-2.878	No	No	No
20	1,2-dimethyl-4-nitroindol-5-ol	206.201	-2.799	0.903	92.210	-2.622	No	No	No
21	9,9-dimethoxybicyclo[3.3.1]nonane-2,4-dione	212.245	-1.452	1.237	100	-3.221	No	No	No
22	2,7-dioxatricyclo[4.4.0.03,8]deca-4,9-diene	148.161	-1.632	1.563	100	-3.097	No	No	No

Note: = The compounds that satisfy the requirement values, MW = Molecular Weight (g/mol), A1 = Water solubility, A2 = Caco2 permeability, A3 = Intestinal absorption (human), A4 = Skin Permeability, A5 = P-glycoprotein substrate, A6 = P-glycoprotein I inhibitor, A7 = P-glycoprotein II inhibitor

meet the requirements for distribution and excretion properties are compounds 1, 2, 4, 7, 8, 9, 11, 12, 13, 17, 18, and 19 (Table 3). Therefore, the compounds 9 (8a-methyl-3,4,4a,5,6,7-hexahydro-2*H*-naphthalene-1,8-dione), 11 ((*E*)-3,7,11,15-tetramethylhexadec-2-en-1-ol), 13 (2-methylenecholestan-3-ol), 17 (5-(hydroxymethyl) furan-2-carbaldehyde) and 19 (2,3-dihydro-2,5-dimethyl-5*H*-1,4-dioxepin) can be used as anti-inflammatory drug candidates that have good ADME because these compounds are intersection which meet the requirements of absorption, distribution and excretion predictors. Prediction of the metabolism properties of these 22 compounds provides information about the possibility of these compounds being metabolized in the liver. There are 2 compounds from 5 virtual screening compounds that are predicted to be metabolized in the liver. Compound 11 is a CYP3A4 substrate (M2) and a CYP1A2 inhibitor (M3), while compound 13 is a CYP3A4

Table 3. The prediction results of distribution and excretion properties 22 compounds contained in *H. alternata* using pkCSM

No	Compound	D1	D2	D3	D4	E1	E2
1	15-chloro-4-pentadecyne	0.534	0.062	0.917	-1.257	0.557	No
2	4-(2-methoxyphenyl)piperidine	1.122	0.462	0.502	-2.260	0.880	No
3	Cyclobutanol	0.047	0.762	-0.031	-2.820	0.448	No
4	1-hexadecyne	0.631	0.067	0.956	-1.364	1.870	No
5	2-propylmalonic acid	-0.936	0.588	-0.060	-3.023	0.444	No
6	*n*-hexadecanoic acid	-0.543	0.101	-0.111	-1.816	1.763	No
7	2-hexylacrylonitrile	0.260	0.414	0.571	-1.976	0.550	No
8	(6*E*)-3,7,11-trimethyldodeca-1,6,10-trien-3-ol	0.370	0.234	0.652	-2.093	1.739	No
9	8a-methyl-3,4,4a,5,6,7-hexahydro-2*H*-naphthalene-1,8-dione	0.191	0.564	0.447	-2.813	1.266	No
10	Acrylonitrile β-[3-(2,2-dimethylcyclopropyl)-2,2-dimethylcyclopropyl	0.531	0.271	0.609	-1.923	0.120	No
11	(*E*)-3,7,11,15-tetramethylhexadec-2-en-1-ol	0.468	0	0.806	-1.563	1.686	No
12	*Z*-2-dodecenol	0.358	0.275	0.713	-1.902	1.781	No
13	2-methylenecholestan-3-ol	-0.145	0	0.808	-1.411	0.546	No
14	L-alanine	-0.534	0.473	-0.412	-3.405	0.370	No
15	Levodopa	-0.105	0.604	-0.843	-3.032	0.430	No
16	Glycylsarcosine	-0.680	0.538	-0.614	-3.183	0.217	No
17	5-(hydroxymethyl)furan-2-carbaldehyde	-0.146	0.744	-0.361	-2.914	0.614	No
18	10-undecynol	0.300	0.353	0.721	-1.957	1.713	No
19	2,3-dihydro-2,5-dimethyl-5*H*-1,4-dioxepin	-0.007	0.692	0.014	-2.842	0.569	No
20	1,2-dimethyl-4-nitroindol-5-ol	0.209	0.207	-0.263	-2.106	0.537	No
21	9,9-dimethoxybicyclo[3.3.1]nonane-2,4-dione	0.015	0.617	-0.217	-2.909	0.198	No
22	2,7-dioxatricyclo[4.4.0.03,8]deca-4,9-diene	0.558	0.678	-0.01	-3.357	0.135	No

Note: = The compounds that satisfy the requirement values, D1 = VDss (human), D2 = Fraction unbound (human), D3 = BBB permeability, D4 = CNS permeability, E1 = Total Clearance, E2 = Renal OCT2 substrate

Table 4. The prediction results of metabolism properties 22 compounds contained in *H. alternata* using pkCSM

No	Compound	M1	M2	M3	M4	M5	M6	M7
1	15-chloro-4-pentadecyne	No	Yes	Yes	No	No	No	No
2	4-(2-methoxyphenyl)piperidine	No	No	No	No	No	No	No
3	Cyclobutanol	No	No	No	No	No	No	No
4	1-hexadecyne	No	Yes	Yes	No	No	No	No
5	2-propylmalonic acid	No	No	No	No	No	No	No
6	*n*-hexadecanoic acid	No	Yes	No	No	No	No	No
7	2-hexylacrylonitrile	No	No	No	No	No	No	No
8	(6*E*)-3,7,11-trimethyldodeca-1,6,10-trien-3-ol	No	No	No	No	No	No	No
9	8a-methyl-3,4,4a,5,6,7-hexahydro-2*H*-naphthalene-1,8-dione	No	No	No	No	No	No	No
10	Acrylonitrile β-[3-(2,2-dimethylcyclopropyl)-2,2-dimethylcyclopropyl	No	No	No	No	No	No	No
11	(*E*)-3,7,11,15-tetramethylhexadec-2-en-1-ol	No	Yes	Yes	No	No	No	No
12	*Z*-2-dodecenol	No	No	No	No	No	No	No
13	2-methylenecholestan-3-ol	No	Yes	No	No	No	No	No
14	L-alanine	No	No	No	No	No	No	No
15	Levodopa	No	No	No	No	No	No	No
16	Glycylsarcosine	No	No	No	No	No	No	No
17	5-(hydroxymethyl)furan-2-carbaldehyde	No	No	No	No	No	No	No
18	10-undecynol	No	No	No	No	No	No	No
19	2,3-dihydro-2,5-dimethyl-5H-1,4-dioxepin	No	No	No	No	No	No	No
20	1,2-dimethyl-4-nitroindol-5-ol	No	No	Yes	No	No	No	No
21	9,9-dimethoxybicyclo[3.3.1]nonane-2,4-dione	No	No	No	No	No	No	No
22	2,7-dioxatricyclo[4.4.0.03,8]deca-4,9-diene	No	No	No	No	No	No	No

Note: = The selected compounds, M1 = CYP2D6 substrate, M2 = CYP3A4 substrate, M3 = CYP1A2 inhibitor, M4 = CYP2C19 inhibitor, M5 = CYP2C9 inhibitor, M6 = CYP2D6 inhibitor, M7= CYP3A4 inhibitor

substrate (M2) (Table 4). The basic structures of the five drugs projected to have favorable pharmacokinetic characteristics differ. However, several of them share the same substituents. Compounds 9, 11, 13, and 19 all contain methyl substituents. Compounds 11, 13, and 17 all contain hydroxyl substituents. In this study, the screening process was based on predictors which had a limited value to determine whether or not the pharmacokinetic profile of a compound was good. The predictors included Caco-2 permeability (A2), intestinal absorption (human) (A3), skin permeability (A4), VDss (human) (D1), BBB permeability (D3) and CNS permeability (D4). The results of the virtual screening were then sorted based on the highest total clearance value (E1) log mL/min/kg, in this study ≥ 0.54.

■ CONCLUSION

There are five chemicals in *Hemigraphis alternata* leaves that are projected to have the best pharmacokinetic qualities, 8a-methyl-3,4,4a,5,6,7-

hexahydro-2*H*-naphthalene-1,8-dione, (*E*)-3,7,11,15-tetramethylhexadec-2-en-1-ol, 2-methylenecholestan-3-ol, 5-(hydroxymethyl) furan-2-carbaldehyde and 2,3-dihydro-2,5-dimethyl-5*H*-1,4-dioxepin. These compounds met the most absorption, distribution, and excretion predictors requirements compared to other compounds.

■ ACKNOWLEDGMENTS

Universitas Muhammadiyah Prof. DR. HAMKA's Research and Development Institute was especially helpful in performing the research.

■ AUTHOR CONTRIBUTIONS

YY and RAR conducted the experiment, YY conducted the conceptualization, methodology, formal analysis, writing, review, and editing, and RAR conducted data curation and writing-original draft preparation.

■ REFERENCES

[1] Chen, L., Deng, H., Cui, H., Fang, J., Zuo, Z., Deng, J., Li, Y., Wang, X., and Zhao, L., 2018, Inflammatory responses and inflammation-associated diseases in organs, *Oncotarget*, 9 (6), 7204–7218.

[2] Antonelli, M., and Kushner, I., 2017, It's time to redefine inflammation, *FASEB J.*, 31 (5), 1787–1791.

[3] Serhan, C.N., Gupta, S.K., Perretti, M., Godson, C., Brennan, E., Li, Y., Soehnlein, O., Shimizu, T., Werz, O., Chiurchiù, V., Azzi, A., Dubourdeau, M., Gupta, S.S., Schopohl, P., Hoch, M., Gjorgevikj, D., Khan, F.M., Brauer, D., Tripathi, A., Cesnulevicius, K., Lescheid, D., Schultz, M., Särndahl, E., Repsilber, D., Kruse, R., Sala, A., Haeggström, J.Z., Levy, B.D., Filep, J.G., and Wolkenhauer, O., 2020, The atlas of inflammation resolution (AIR), *Mol. Aspects Med.*, 74, 100894.

[4] Rahman, S.M.M., Atikullah, M., Islam, M.N., Mohaimenul, M., Ahammad, F., Islam, M.S., Saha, B., and Rahman, M.H., 2019, Anti-inflammatory, antinociceptive and antidiarrhoeal activities of methanol and ethyl acetate extract of *Hemigraphis alternata* leaves in mice, *Clin. Phytosci.*, 5 (1), 16.

[5] Ming, W.K., 2019, Bioassay-guided purification and identification of chemical constituents from *Hemigraphis alternata*, *Dissertation*, Monash University, Malaysia.

[6] Yeni, Y., Rachmania, R.A., and Mochamad, D.Y.M., 2021, Affinity of compounds in *Hemigraphis alternata* (Burm.F.) T. Ander leaves to cyclooxygenase 1 (COX-1): *In silico* approach, *Proceedings of the 4th International Conference on Sustainable Innovation 2020–Health Science and Nursing (ICoSIHSN 2020)*, Atlantis Press, 552–555.

[7] Yeni, Y., Rachmania, R., and Yanuar, M.D., 2021, *In silico* study of compounds contained in *Hemigraphis alternata* leaves against 5-LOX for anti-inflammatory, *Indones. J. Pharm. Sci. Technol.*, 8 (1), 34–41.

[8] Pires, D.E.V., Blundell, T.L., and Ascher, D.B., 2015, pkCSM: Predicting small-molecule pharmacokinetic and toxicity properties using graph-based signatures, *J. Med. Chem.*, 58 (9), 4066–4072.

[9] Boobis, A., Gundert-Remy, U., Kremers, P., Macheras, P., and Pelkonen, O., 2002, *In silico* prediction of ADME and pharmacokinetics: Report of an expert meeting organised by COST B15, *Eur. J. Pharm. Sci.*, 17 (4-5), 183–193.

[10] Brogi, S., Ramalho, T.C., Kuca, K., Medina-Franco, J.L., and Valko, M., 2020, Editorial: *In silico* methods for drug design and discovery, *Front. Chem.*, 8, 612.

[11] Chandrasekaran, B., Abed, S.N., Al-Attraqchi, O., Kuche, K., and Tekade, R.K., 2018, "Computer-Aided Prediction of Pharmacokinetic (ADMET) Properties" in *Dosage Form Design Parameters: Advances in Pharmaceutical Product Development and Research*, vol. II, Academic Press, Cambridge, United States, 731–755.

[12] Shaker, B., Ahmad, S., Lee, J., Jung, C., and Na, D., 2021, *In silico* methods and tools for drug discovery, *Comput. Biol. Med.*, 137, 104851.

[13] de Souza Neto, L.R., Moreira-Filho, J.T., Neves, B.J., Maidana, R.L.B.R., Guimarães, A.C.R., Furnham, N., Andrade, C.H., and Silva, F.P., 2020, *In silico* strategies to support fragment-to-lead optimization in drug discovery, *Front. Chem.*, 8, 93.

[14] Mvondo, J.G.M., Matondo, A., Mawete, D.T., Bambi, S.M.N., Mbala, B.M., and Lohohola, P.O., 2021, *In silico* ADME/T properties of quinine derivatives using SwissADME and pkCSM Webservers, *Int. J. Trop. Dis. Health*, 42 (11), 1–12.

[15] Pires, D.E., Kaminskas, L.M., and Ascher, D.B., 2018, "Prediction and Optimization of Pharmacokinetic and Toxicity Properties of the Ligand" in *Computational Drug Discovery and Design*, Eds. Gore, M., and Jagtap, U., pp. 271–284, Humana Press, New York, United States.

[16] Udrea, A.M., Gradisteanu Pircalabioru, G., Boboc, A.A., Mares, C., Dinache, A., Mernea, M., and Avram, S., 2021, Advanced bioinformatics tools in the pharmacokinetic profiles of natural and synthetic compounds with anti-diabetic activity, *Biomolecules*, 11 (11), 1692.

[17] Udrea, A.M., Puia, A., Shaposhnikov, S., and Avram, S.P., 2018, Computational approaches of new perspectives in the treatment of depression during pregnancy, *Farmacia*, 66 (4), 680–687.

[18] Domínguez-Villa, F.X., Durán-Iturbide, N.A., and Ávila-Zárraga, J.G., 2021, Synthesis, molecular docking, and *in silico* ADME/Tox profiling studies of new 1-aryl-5-(3-azidopropyl) indol-4-ones: Potential inhibitors of SARS CoV-2 main protease, *Bioorg. Chem.*, 106, 104497.

[19] Mansour, M.A., AboulMagd, A.M., and Abdel-Rahman, H.M., 2020, Quinazoline-Schiff base conjugates: *In silico* study and ADMET predictions as multi-target inhibitors of coronavirus (SARS-CoV-2) proteins, *RSC Adv.*, 10 (56), 34033–34045.

[20] Tripathy, D., Nayak, B.S., Mohanty, B., and Mishra, B., 2019, Solid dispersion: A technology for improving aqueous solubility of drug, *J. Pharm. Adv. Res.*, 2 (7), 577–586.

[21] Henriques, J., Falé, P.L., Pacheco, R., Florêncio, M.H., and Serralheiro, M.L., 2018, Phenolic compounds from *Actinidia deliciosa* leaves: Caco-2 permeability, enzyme inhibitory activity and cell protein profile studies, *J. King Saud Univ., Sci.*, 30 (4), 513–518.

[22] Awortwe, C., Fasinu, P.S., and Rosenkranz, B., 2014, Application of Caco-2 cell line in herb-drug interaction studies: Current approaches and challenges, *J. Pharm. Pharm. Sci.*, 17 (1), 1–19.

[23] Pecoraro, B., Tutone, M., Hoffman, E., Hutter, V., Almerico, A.M., and Traynor, M., 2019, Predicting skin permeability by means of computational approaches: Reliability and caveats in pharmaceutical studies, *J. Chem. Inf. Model.*, 59 (5), 1759–1771.

[24] Berezhkovskiy, L.M., 2007, The connection between the steady state (V_{ss}) and terminal (V_{β}) volumes of distribution in linear pharmacokinetics and the general proof that $V_{\beta} \geq V_{ss}$, *J. Pharm. Sci.*, 96 (6), 1638–1652.

[25] Guo, T., Wang, Y., Guo, Y., Wu, S., Chen, W., Liu, N., Wang, Y., and Geng, D., 2018, 1, 25-D_3 protects from cerebral ischemia by maintaining BBB permeability via PPAR-γ activation, *Front. Cell. Neurosci.*, 12, 480.

[26] Ju, F., Ran, Y., Zhu, L., Cheng, X., Gao, H., Xi, X., Yang, Z., and Zhang, S., 2018, Increased BBB permeability enhances activation of microglia and exacerbates loss of dendritic spines after transient global cerebral ischemia, *Front. Cell. Neurosci.*, 12, 236.

[27] Bhosle, V.K., Altit, G., Autmizguine, J., and Chemtob, S., 2017, "Basic Pharmacologic Principles" in *Fetal and Neonatal Physiology*, 5th Ed., Eds. Polin, R.A., Abman, S.H., Rowitch, D.H., Benitz, W.E., and Fox, W.W., Elsevier, Philadelphia, United States, 187–201.

Optimizing Rice Husk Silica Mass and Sonication Time for a More Efficient and Environmentally Friendly Synthesis of SBA-15

Suyanta Suyanta* and Mudasir Mudasir

Department of Chemistry, Faculty of Mathematics and Natural Sciences, Universitas Gadjah Mada, Sekip Utara, Yogyakarta 55281, Indonesia

* ***Corresponding author:***

email: suyanta_mipa@ugm.ac.id

Received: February 25, 2022
Accepted: May 4, 2022

DOI: 10.22146/ijc.73258

Abstract: *By optimizing rice husk silica mass and sonication time, SBA-15 was successfully synthesized in a more efficient and environmentally friendly way. The solution of Pluronic P-123 was mixed with the solution containing NaOH and various masses of rice husk silica (4–12 g), followed by sonication for a certain time (30–150 min). The mixture was filtered and washed with distilled water and ethanol until neutral, then dried at 110 °C for 2 h and calcined at 500 °C for 6 h. The results showed that the optimal mass of rice husk silica was 8 g, while the optimal sonication time was 30 min. The product has a cylindrical pore shape with good crystallinity and pore structure regularity. The specific surface area (S_{BET}), the pore diameter (D_{BJH}), the specific pore volume (V_{BJH}), and the wall thickness (W_T) of the product were 601 $m^2\ g^{-1}$, 4.76 nm, 0.88 mL g^{-1}, and 5.02 nm, respectively. These results are not considerably different from the porosity of SBA-15, synthesized previously using conventional hydrothermal techniques from various silica sources. In addition, it is also comparable to the porosity of SBA-15 produced from TEOS by sonochemical methods as well as with commercial SBA-15.*

Keywords: *rice husk silica; SBA-15; optimization; mass; sonication time*

■ INTRODUCTION

The mesoporous silicate family, which includes Santa Barbara Amorphous No. 15 (SBA-15), folded sheet mesoporous material No. 16 (FSM-16), and the M4IS family (Mobil Composition of Matter No. 41, MCM-41; Mobil Composition of Matter No. 48, MCM-48; and Mobil Composition of Matter No. 50, MCM-50) has attracted the attention of researchers to the point where it now occupies a superposition in materials science because of its potential to be applied in various fields. As a material having a regular pore structure with a diameter of 2–50 nm, it can minimize crystal formation, inhibit nanoparticle aggregation, stabilize the position, and improve the special surface of the material. Therefore, it can be used in various surface-related applications, such as catalysis [1-3], gas separation [4-7], drug delivery [8-9], energy storage [10-11], membranes [12-13], and sensors [14-15]. According to their pore size, mesoporous silicates can provide access to relatively large molecules and enhance diffusion. This is an advantage when compared to micro materials such as zeolites [16]. SBA-15 was originally synthesized by Zhao et al. [17] using a poly(ethylene oxide)-poly(propylene oxide)-poly(ethylene oxide) template commercially known as Pluronic P-123. SBA-15 has a two-dimensional hexagonal pore shape similar to MCM-41, but it has tiny mesopores on the pore walls that link parallel mesopores [18-19]. As a result, SBA-15 outperforms MCM-41 in terms of adsorbent and catalyst applications. Furthermore, the SBA-15 family has thicker pore walls, resulting in superior thermal and hydrothermal stability than the M41S and FSM-16 families [20-22].

In general, commercial materials such as tetraethyl orthosilicate (TEOS) [23-25] and sodium silicate [26-27] are utilized as silica precursors in the production of SBA-15, which are, of course, relatively expensive. Several natural materials have been used as a source of silica in the synthesis of SBA-15, including sugarcane bagasse [28], brickyard ash [29], coal gangue [30], oil palm ash [31], and rice husk ash [32-34], to reduce production

costs. Rice husk ash is the most potent natural material because it contains more than 90% of SiO_2 [35-37]. Moreover, rice is widely grown in Asian countries such as China, India, Pakistan, Cambodia, Indonesia, Laos, Malaysia, Myanmar, Philippines, Thailand, Vietnam, etc. [38], giving large opportunity to use the rice husk ash as the source of silica in the synthesis of SBA-15. According to Barrera et al. [39], the silica/surfactant ratio has a significant impact on the mechanism of mesoporous development in the synthesis of SBA-15. Other report suggests that a low silica/surfactant ratio causes the mesoporous material to be difficult to create, but a high ratio causes the structure's regularity to be compromised [40]. Therefore, it is quite clear that the silica/surfactant ratio is one of the important key factors in the successful synthesis of SBA-15. However, to the best of our knowledge, the report that deals with the optimization of the silica/surfactant ratio, especially in cases where rice husk silica is used as the source of silica, is rarely found. Therefore, in order to obtain the best ratio of silica/surfactant in the more efficient synthesis of SBA-15 from rice hush ash, it is quite challenging to conduct research on the optimization of the silica/surfactant ratio.

SBA-15 is typically synthesized using the hydrothermal technique [23-34], which involves heating the reactants with air in a closed container (autoclave). The hydrothermal approach is less cost-effective and does not adhere to the green chemistry principle since it takes a long time and a lot of energy to complete the reaction. Several studies have used alternative methods to synthesize SBA-15, such as the sonochemical approach, which involves the use of ultrasonic waves [41-45]. Ultrasonic waves can cause chemical reactions in liquids by causing micro-cavitation bubbles to develop. High temperatures and pressures can be produced by burst bubbles, allowing chemical reactions to take place [46]. Because it consumes less time and energy, the sonochemical approach is considered as more cost-effective and supports green chemistry principles.

The sonication time affects product quality in the synthesis of several materials; for example, the thermal stability of the product in the synthesis of polystyrene/montmorillonite nanocomposites [47], the morphology and dispersion of the product in the synthesis of cellulose nanocrystals [48], the specific surface area of the product in the synthesis of micron-sized vermiculite particles [49], the properties of the product in the synthesis of methylcellulose-montmorillonite films [50], and so on. In case of SBA-15 synthesis, Chaeronpanich et al. [51] has reported that increasing sonication time could increase the specific surface area, specific pore volume, and pore diameter of the product. Unfortunately, there is still no report that focuses on the optimization of sonication time in the synthesis of SBA-15 using rice husk silica as a precursor. The information about the effect of sonication time on the efficiency of the SBA-15 synthesis is essential to reduce the time and energy required for the synthesis.

Therefore, based on the above-mentioned ideas, we report the results of our systematic study on the optimization of the rice husk silica to surfactant ratio (Pluronic P-123) as well as the optimization of the sonication time to obtain a more efficient and environmentally friendly SBA-15 synthesis method. Optimization of the ratio of rice husk silica to Pluronic P-123 was carried out by varying the mass of rice husk silica for a certain number of Pluronic P-123 surfactants. The characterization data of SBA-15 synthesized in this study were compared to SBA-15 synthesized previously using conventional hydrothermal techniques from various silica sources. More specifically, the data was also compared with SBA-15 produced from TEOS by sonochemical methods as well as with commercial SBA-15.

■ EXPERIMENTAL SECTION

Materials

The rice husk was taken from the rice huller in the districts of Klaten, Central Java, Indonesia. Chemicals used in this study were purchased from Merck (Germany), i.e., Pluronic P-123 (M-Clarity™ quality level = MQ100, MW: 5800 g/mol), HCl (37%), NaOH (100%), toluene (99.5%), ethanol (96%). All of the chemicals are analytical reagent grade and used without further purification. Distilled water was used in all experiments.

Instrumentation

Ultrasonic emission is performed using a Bransonic 220 ultrasonic instrument (Taiwan) with a frequency of 48 kHz and a heating power of 100 W at a room temperature (25 to 32 °C). X-ray diffraction (XRD) patterns were recorded at room temperature using Cu K powder irradiated at = 0.154 nm on an X-ray diffractometer, Shimadzu 6000 (Japan). A Shimadzu FTIR Prestige-21 (Japan) was used to measure a Fourier-transform infrared (FTIR) spectroscopic spectra, which were acquired in the transmittance mode in the range of 4000–400 cm^{-1} at room temperature using the KBr disc pellets. The nitrogen adsorption-desorption isotherm was measured at liquid nitrogen temperature using a Quantachrome NovaWin2 version 2.2 (USA). Samples were outgassed overnight at 250 °C before measurement. Using adsorption data at a relative pressure (P/P_0) of 0.03 to 0.1, the Brunauer–Emmett–Teller (BET) surface area is calculated using the multipoint BET method. At a relative pressure of 0.95, isotherms were used to calculate a mesoporous volume. The Barrett-Joyner-Halenda (BJH) approach was used to calculate the average mesoporous diameter based on the nitrogen isotherm adsorption branch. The pore size distributions were calculated using the BJH model. Transmission electron microscopy (TEM) JEOL JEM-1400 (USA) was used to examine the features of the SBA-15 pores.

Procedure

Extraction of silica from rice husk

Rice husk (2 kg) was washed with water, dried in the sun, and then burned to ashes in the open air. This ash (100 g) is placed in 125 mL of concentrated HCl which has been diluted to 500 mL with distilled water. To make rice husk silica, the mixture was agitated at 60 °C for 3 h, then filtered with Whatman 42 filter paper, rinsed with distilled water, dried at 120 °C for 24 h, then calcined at 600 °C for 6 h. FTIR and XRD were used to characterize the product.

Synthesis of SBA-15 with variations in the mass of rice husk silica

To make a sodium silicate solution, 4 g of rice husk silica, and 10 g of NaOH were added to the distilled water (100 mL). The mixture was agitated for 2 h at 80 °C, and then incubated for 12 h. Pluronic P-123 (4 g) was dissolved in 100 mL of 1.6 M HCl, then heated to 45 °C while stirring to dissolve it. The sodium silicate solution (100 mL) was added to the Pluronic P-123 solution (100 mL), then was sonicated for 60 min and heated at 60 °C for 1 h. After filtering the mixture with Whatman 42 filter paper, it was rinsed with distilled water and ethanol until the pH was neutral. The resulting solid was dried at 110 °C for 2 h, then calcined at 500 °C for 6 h to produce a white powder denoted as SBA-15 (4 g, 60 min). The same procedure was done 4 times with different amounts of rice husk silica (6, 8, 10, and 12 g, respectively). The resulting material was denoted as SBA-15 (6 g, 60 min), SBA-15 (8 g, 60 min), SBA-15 (10 g, 60 min), and SBA-15(12 g, 60 min), respectively. The methods of FTIR, XRD, GSA, and TEM were used for characterization of the product.

Synthesis of SBA-15 with variations in sonication time

The procedure of SBA-15 synthesis above was carried out four times, each time with the optimal mass of rice husk silica and a sonication time of 30, 90, 120, and 150 min, respectively. The materials were labeled as SBA-15 (X g, 30 min), SBA-15 (X g, 90 min), SBA-15 (X g, 120 min), and SBA-15 (X g, 150 min), respectively, where X represents the optimal mass of rice husk silica.

■ RESULTS AND DISCUSSION

Rice Husk Silica

The silica extracted from rice husk is in the form of a white powder, which matches nicely the properties and color of commercial silica [52]. The FTIR spectra of rice husk silica and commercial silica (for comparison) are presented in Fig. 1. It is easily seen that the two spectra are closely resemble one each other, indicating the success of silica extraction from rice husk. Table 1 gives some distinctive bands for siloxane groups (Si–O–Si) and silanol groups (Si–OH) in the rice husk silica.

The XRD patterns for both rice husk silica and commercial silica (Fig. 2) reveal broad peaks around 23°, which are typical of amorphous silica [52], suggesting that the extraction of silica from rice husks has been

successfully carried out. This XRD pattern data supports the FTIR spectra, suggesting the success of silica extraction form rice husk.

SBA-15 Synthesized by Varying the Volume of Sodium Silicate

FTIR spectra analysis

The FTIR spectra of SBA-15 produced with varying amounts of sodium silicate and those of commercial SBA-15 are given in Fig. 3. Both spectra show multiple characteristic absorption bands for mesoporous silicates dominated by siloxane (Si–O–Si) and silanol (Si–OH) groups, similar to the spectra of rice husk silica. Furthermore, due to Si–O stretching vibration on the silanol group, absorption exhibits around 970 cm^{-1} [55]. The broad peak at 3460 cm^{-1} belongs to the remaining absorbed water molecules in the samples overlapped with the O–H bond stretching vibration of the silanol groups [56]. The bending vibration of the O–H of water appears at wavenumber 1635 cm^{-1} [54,57]. The strong characteristic peak of siloxane (Si–O–Si) appears at 1082 cm^{-1} [53]. The rocking vibration of the Si–O bond is observed at 490 cm^{-1} [53]. On the basis of these data, it can be stated that the use of sodium silicate solution with a mass of 4, 6, 8, 10 and 12 g in this study has resulted in a material containing a –Si–O–Si– network and a Si–OH group.

The spectra of SBA-15 (4 g, 60 min) and SBA-15 (12 g, 60 min) show a lower absorption intensity, indicating that the formation of the –Si–O–Si– network and the Si–OH group in the two samples is not flawless. This is most likely caused by a very low or very high-mass ratio of silica to surfactant in these two samples. The formation of the –Si–O–Si– network and the –Si–OH group can be hampered by a silica/surfactant ratio that is either too small or too large [39]. On the other hand, the samples of SBA-15 (6 g, 60 min), SBA-15 (8 g, 60 min), and SBA-15 (10 g, 60 min) exhibit relatively high absorption intensities, indicating that the –Si–O–Si– network and

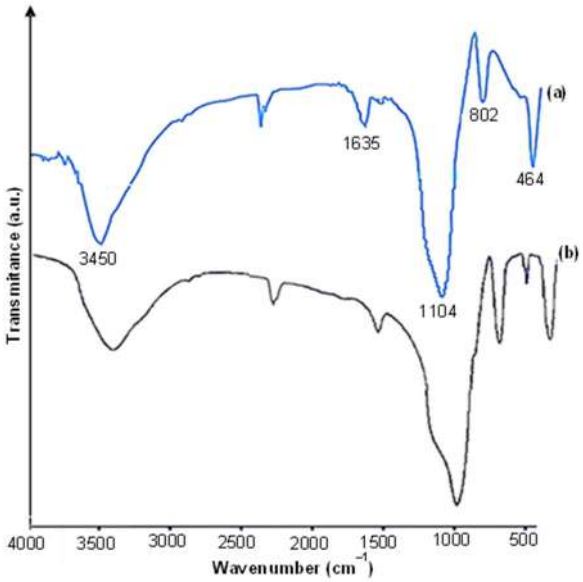

Fig 1. FTIR spectra of rice husk silica (a) and commercial silica (b)

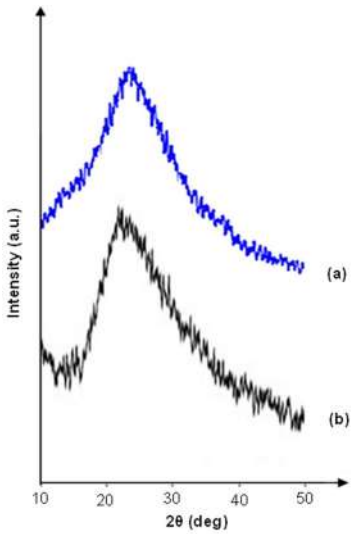

Fig 2. XRD diffractograms of rice husk silica (a) and commercial silica (b)

Table 1. Important FTIR absorption bands of rice husk silica and their interpretation

No	Wavenumber	Interpretation	Reference
1	464 cm^{-1}	Rocking vibration of Si–O bond	[53]
2	802 cm^{-1}	Symmetric stretching vibration of Si–O–Si	[53]
3	1104 cm^{-1}	Asymmetric stretching vibration of Si–O–Si	[53]
4	1635 cm^{-1}	Bending vibration of the O–H of water	[54]
5	3448 cm^{-1}	O–H Vibrations of silanol groups and adsorbed water	[54]

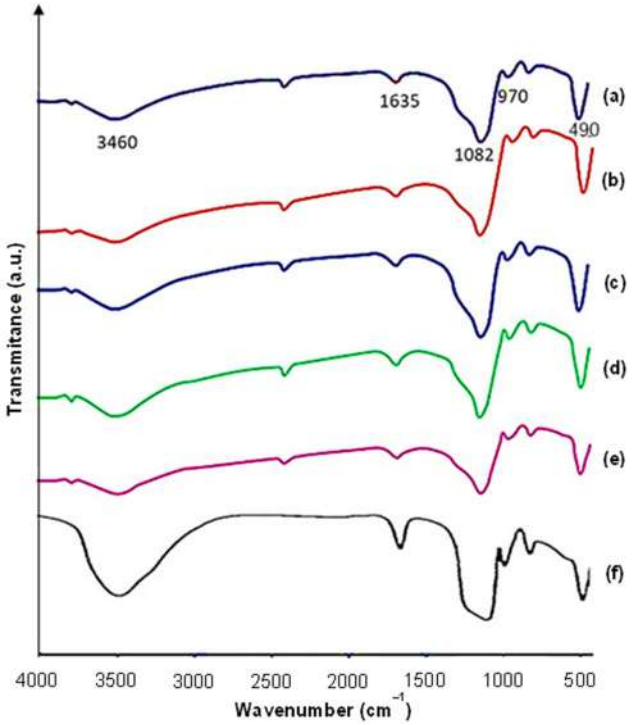

Fig 3. The FTIR spectra of: (a) SBA-15 (4 g, 60 min), (b) SBA-15 (6 g, 60 min), (c) SBA-15 (8 g, 60 min), (d) SBA-15 (10 g, 60 min), and (e) SBA-15 (12 g, 60 min), and (f) commercial SBA-15

–Si–OH are well-formed. Because FTIR spectra only provide information on the functional groups present in a material, FTIR alone is insufficient to draw a conclusion about the appropriate mass of rice husk silica in the synthesis of SBA-15. Therefore, more diverse characterization data generated by other analytical methods are necessary.

XRD pattern analysis

Fig. 4 shows the effect of rice husk silica mass used in the synthesis on the number, diffraction angle, and intensity of diffractogram peaks. The diffractogram of commercial SBA-15 is also presented as a reference. The peaks of [100] are found in all of the diffractograms, which are typical of 2D hexagonal formations. The peak number for diffractogram of SBA-15 (4 g, 60 min) is limited to only one peak, [100] with quite low intensity. This is probably due to insufficient amount of silica present in the sample, preventing the creation of micelles that serve as the hexagonal structural template [39]. On the other hand, each diffractogram of SBA-15 (6 g, 60 min), SBA-15 (8 g, 60 min), SBA-15 (10 g, 60 min), and commercial SBA-15 contains three peaks ([100], [110], and [200]), whereas the SBA-15 (12 g, 60 min) diffractogram exhibits two peaks ([100] and [110]). The presence of additional peaks in the diffractograms, especially peaks [110] and [200], suggests the occurrence of mesoporous regularity growth in the samples [39].

The diffraction angle of [100] peak gets bigger in the order of SBA-15 (4 g, 60 min) < SBA-15 (6 g, 60 min) < SBA-15 (8 g, 60 min) < SBA-15 (10 g, 60 min), but gets smaller at SBA-15 (12 g, 60 min). The diffraction angle is inversely proportional to the interplanar spacing (d_{100}), where the d_{100} decreases as the diffraction angle increases. So, it can be concluded that the use of more rice husk silica, from 4 to 10 g, d_{100} gives rise to a smaller d-spacing, but the use 12 g results in a bigger d-spacing. The similar trends have also been reported by Mendelez-Ortiz et al. [57]. The value of d_{100} can be used to obtain the lattice parameters a_o (where $a_o = 2d_{100}/\sqrt{3}$), which can

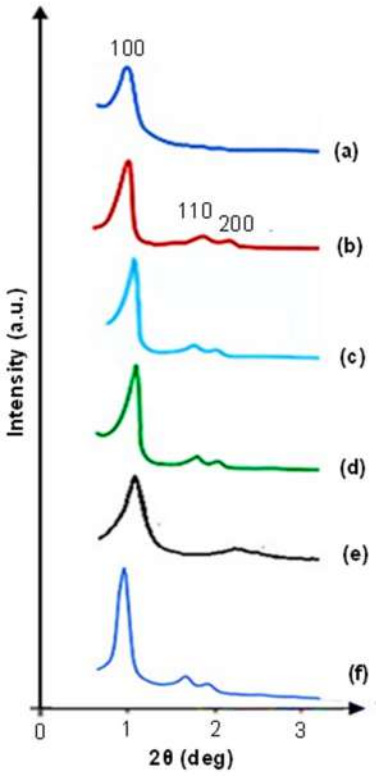

Fig 4. The XRD diffractogram of: (a) SBA-15 (4 g, 60 min), (b) SBA-15 (6 g, 60 min), (c) SBA-15 (8 g , 60 min), (d) SBA-15 (10 g, 60 min), and (e) SBA-15 (12 g, 60 min), and (f) commercial SBA-15

then be used to calculate the pore wall thickness (W_T) using the equation $W_T = a_0 - D_{BJH}$, where D_{BJH} is the average pore diameter acquired from the GSA data.

The peak intensity, especially the main peak [100] indicates the crystallinity of SBA-15 [58]. Fig. 4 demonstrates that the crystallinity of each sample produced in this study is still lower than that of commercial SBA-15. For the synthesized samples, the peak intensity [100] rose as the mass of rice husk silica used increased (from 4, 6, 8, and 10 g), but reduced when 12 g was used. This shows that the crystallinity of SBA-15 grew as the mass of rice husk silica used increased but declined as the mass of rice husk silica used climbed too high. A similar thing has been documented by other studies [39]. Based on the discussion on the FTIR spectra and XRD diffractogram, it can be stated that SBA-15 materials which have high crystallinity and relatively good hexagonal structure regularity are SBA-15 (6 g, 60 min), SBA-15 (8 g, 60 min), and SBA-15 (10 g, 60 min). These three samples were further analyzed quantitatively using a GSA to determine their porosity.

Gas adsorption analysis

The adsorption-desorption isotherms of the SBA-15 (6 g, 60 min), SBA-15 (8 g, 60 min), and SBA-15 (10 g, 60 min) samples are shown in Fig. 5 together with the isotherm of commercial SBA-15 for the purpose of comparison. According to the IUPAC classification, all four curves are classified as type IV, which is typical of mesoporous materials [59-60]. Generally, these isotherms exhibit a similar trend, which has five stages. There is a considerable increase in the volume of N_2 adsorbed at a relative pressure of 0.03 to 0.1, indicating the presence of single-layer N_2 adsorption on the surface of SBA-15, including external and internal surfaces. This stage is used as the basis for measuring the pore surface area using the BET method. Furthermore, the adsorption curve rises at a relative pressure of roughly 0.4, indicating the presence of multilayer N_2 adsorption across the entire surface. Because of the condensation of N_2 in the capillaries included in SBA-15, the adsorption curve dramatically increased at a relative pressure of about 0.4–0.7. The curve is nearly gentle at relative pressures above 0.6, indicating that only a little quantity of N_2 is adsorbed. Only the exterior

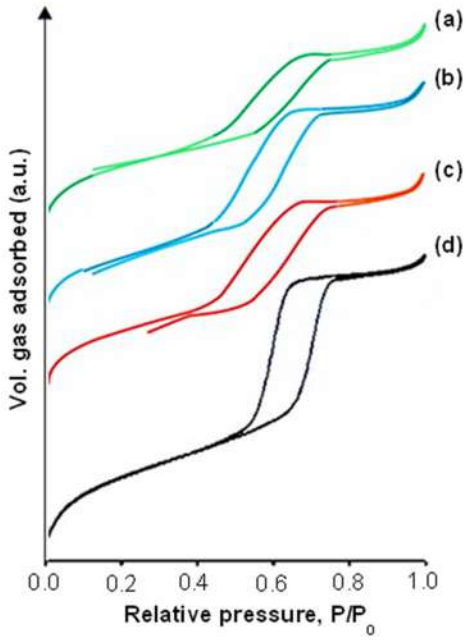

Fig 5. The adsorption-desorption isotherms of: (a) SBA-15 (6 g, 60 min), (b) SBA-15 (8 g, 60 min), (c) SBA-15 (10 g, 60 min), and (d) commercial SBA-15

surface of SBA-15 can still adsorb nitrogen molecules at this point. The short slope of the curve at this point illustrates the limited exterior surface area of the materials. Finally, due to the adsorption of N_2 in the interparticle region, the re-adsorption curve increases slightly for relative pressures close to 1.

A formation of hysteresis loop when the pressure is reduced, suggesting that the volume of desorbed gas does not equal the volume of adsorbed gas. This can happen as a result of the previously described capillary condensation. The hysteresis loop in the three samples of SBA-15 in this study is type H1 which is characteristic of mesoporous materials with one-dimensional cylindrical channels open on both sides [61]. For all the samples, type IV isotherms with steep H1 hysteresis loops at relative pressure P/P_0 of 0.4–0.8 can be observed, implying the formation of a uniform large mesopore. The bigger the pore diameter, the further right the inflection location, whereas the sharpness of the curve after the inflection reflects the uniformity of the mesoporous size distribution [62]. Furthermore, at this stage, the height of the curve is proportional to the pore volume of the materials. From Fig. 5, it is observed that

the distribution of mesoporous size is relatively uniform but the uniformity is slightly lower compared to commercial SBA-15.

The porosity of the SBA-15 (6 g, 60 min), SBA-15 (8 g, 60 min), and SBA-15 (10 g, 60 min) samples are shown in Table 2 together with the porosity of commercial SBA-15 for the purpose of comparison. The porosity data of the four samples (Table 2) reveal that the S_{BET} and V_{BJH} trends follow the crystallinity trend, according to the order Commercial SBA-15 > SBA-15 (8 g, 60 min) > SBA-15 (10 g, 60 min) > SBA-15 (6 g, 60 min). The crystallinity trend, however, does not appear to be related to both of the D_{BJH} as well as the W_T trend.

Fig. 6 shows that the commercial SBA-15 has a narrow pore size distribution with the highest intensity of about 5 nm, while the samples SBA-15 (6 g, 60 min), SBA-15 (8 g, 60 min), and SBA-15 (10 g, 60 min) had relatively wide pore size distributions with the highest intensity of about 4.3, 4.1, and 3.5 nm, respectively. This is supported by the XRD diffractogram in Fig. 4, which shows that the commercial SBA-15 diffractogram contains three peaks with the highest intensity when compared to other samples. Among the three samples synthesized with variations in the mass of rice husk silica, SBA-15 (10 g, 60 min) was the most homogeneous sample, characterized by a narrower curve with higher peaks. As for the samples of SBA-15 (6 g, 60 min) and SBA-15 (8 g, 60 min), the pore size distribution was more varied, with short and wide peaks. The pore diameter with the highest intensity on each curve is slightly different when compared to the average pore diameter of each sample in Table 2. This is because the average pore diameter covers all the pores in each sample.

Based on the porosity data in Table 2 and the pore size distribution in Fig. 6, it is evident that each synthesized sample has its own advantages in certain parameters, and no sample excels in all parameters. Although the SBA-15 (6 g, 60 min) sample has the biggest pore diameter and thickest pore wall, it has the smallest specific surface area and specific pore volume. Although the SBA-15 (6 g, 60 min) sample has the biggest

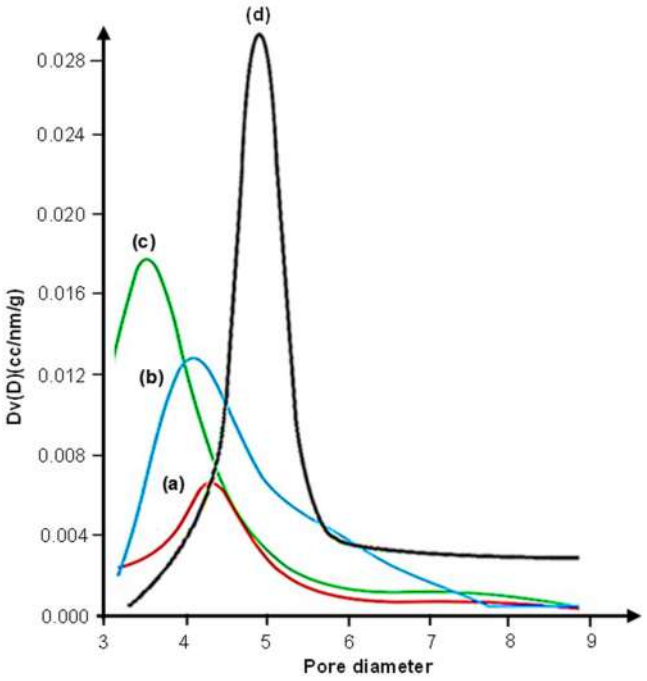

Fig 6. Pore size distribution of (a) SBA-15 (6 g, 60 min), (b) SBA-15 (8 g, 60 min), (c) SBA-15 (10 g, 60 min), and (d) Commercial SBA-15 samples

Table 2. The porosity of SBA-15 (6 g, 60 min), SBA-15 (8 g, 60 min), SBA-15 (10 g, 60 min), and commercial SBA-15

Sample	S_{BET} (m^2/g)	D_{BJH} (nm)	V_{BJH} (mL/g)	d_{100} (nm)	a_0 (nm)	W_T (nm)
SBA-15 (6 g, 60 min)	325	4.79	0.37	9.58	11.66	6.87
SBA-15 (8 g, 60 min)	652	3.98	0.65	8.89	10.27	6.29
SBA-15 (10 g, 60 min)	626	3.52	0.56	8.27	9.55	6.03
Commercial SBA-15	660	6.21	0.98	10.63	12.28	6.07

S_{BET} : specific surface area, BET
D_{BJH} : pore diameter, BJH adsorption
V_{BJH} : specific pore volume
d_{100} : interplanar spacing
a_o : lattice parameter, for hexagonal = $2d_{100}/\sqrt{3}$
W_T : silica wall thickness, for hexagonal $W_T = a_0 - D_{BJH}$

specific surface area and specific pore volume, the pore diameter is smaller and the pore walls are thinner than the SBA-15 (6 g, 60 min) sample. Moreover, although the SBA-15 (10 g, 60 min) sample has a narrower pore size distribution, it has flaws in several other characteristics. Nevertheless, the SBA-15 (8 g, 60 min) sample has been chosen as the one out of the three with the best accumulative porosity properties. The reasons for this choice are that the sample has the largest specific surface area and specific pore volume, while the pore diameter and pore wall thickness were not significantly different from that of the SBA-15 (6 g, 60 min) sample. In addition, the pore size distribution was better than that of the SBA-15 (6 g, 60 min) sample although it is not as good as that of the SBA-15 (10 g, 60 min) sample. For further experiments, we have only focused on the study of the effect of sonication time on the effectiveness of the synthesis of SBA-15 using an 8 g rice husk silica.

Effect of Sonication Time on the Synthesis Efficiency of SBA-15

FTIR spectra analysis

The FTIR spectra of SBA-15 produced with varying sonication times and those of commercial SBA-15 were presented in Fig. 7. This figure revealed distinctive absorptions for the siloxane and silanol groups, which were nearly identical to those shown in Table 1. The high intensity of these absorptions indicated the successful formation of –Si–O–Si– and Si–OH groups in all variations of sonication time. The spectra of the six FTIR appeared to be identical to one another, with no new absorption band shifts or substantial wavenumber shifts. The difference may be seen in the intensity of the absorption band, particularly at wavenumbers around 1096 cm^{-1}. The intensity of the absorption band decreased little as the sonication time increased from 30 to 150 min. So it can be stated that the sonication time of 30 min resulted in the formation of the most perfect –Si–O–Si– network, whereas extending the sonication time resulted in damage to portions of the –Si–O–Si– network.

Fig. 8 show the effect of sonication time on the number, diffraction angle, and intensity of the diffractogram peaks. The diffractogram of commercial

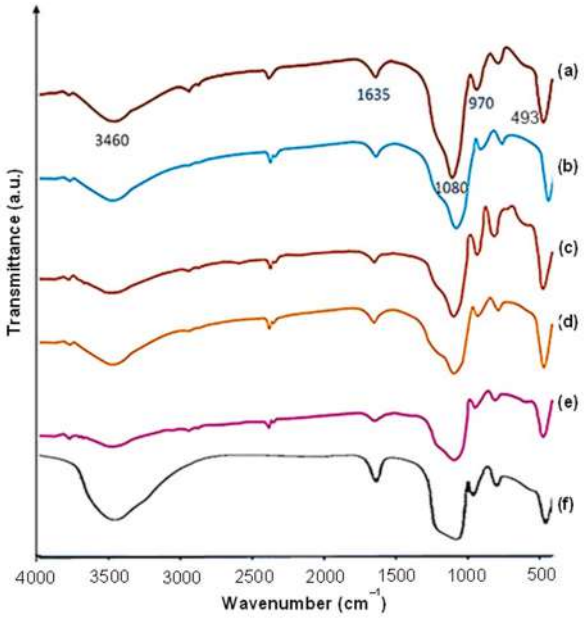

Fig 7. The FTIR spectra of: (a) SBA-15 (8 g, 30 min), (b) SBA-15 (8 g, 60 min), (c) SBA-15 (8 g, 90 min), (d) SBA-15 (8 g, 120 min), (e) SBA-15 (8 g, 150 min), and (f) commercial SBA-15

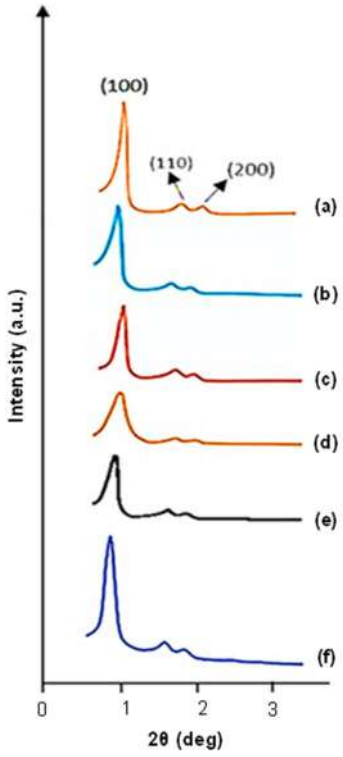

Fig 8. The XRD diffractogram of: (a) SBA-15 (8 g, 30 min), (b) SBA-15 (8 g, 60 min), (c) SBA-15 (8 g, 90 min), (d) SBA-15 (8 g, 120 min), and (e) SBA-15 (8 g, 150 min)

SBA-15 is also presented as a reference. The existence of three diffractogram peaks, [100], [110], and [200], was seen in all diffractograms, showing that the mesoporous silicate SBA-15 could be produced with any sonication time utilized in this investigation.

The 2θ of these diffractograms are 1.04, 0.99, 1.020, 0.97, and 0.96 for the sonication time of 30, 60, 90, 120, and 150 min, respectively. It is clear that except for the increase in sonication time from 60 to 90 min, where the peak changed to the right, the diffractogram's peak location shifted to the left as the sonication time was increased. The d_{100} samples can be obtained quantitatively using Bragg's Equation [63]: $\lambda = 2d_{100}\sin\theta$, where λ = wavelength of X-ray (0.154 nm), and θ = diffraction angle. So, we find the d_{100} are 8.47, 8.89, 8.62, 9.06, and 9.18 nm for sonication times of 30, 60, 90, 120, and 150 min, respectively. In general, increasing the sonication time increases the d_{100}, except for increasing the sonication time from 60 to 90 min. Mendelez-Ortiz et al. [57] reported similar results, where the value of d_{100} generally increased with increasing reaction time.

Fig. 8 indicates a drop in peak intensity [100] as sonication time is increased from 30 to 60, 90, and 120 min, but an increase when sonication time is raised to 150 min. This indicates that the crystallinity of SBA-15 varies, as evidenced by fluctuations in the [100] peak intensity. The highest peak intensity was produced if the sonication time was decreased to 30 min, which was getting closer to the intensity of commercial SBA-15. Table 3 shows the results quantitatively compared to commercial SBA-15, wherewith the sonication times of 30, 60, 90, 120, and 150 min, the relative crystallinities were 87.51, 74.81, 60.63, 35.64, and 43.26%, respectively. It was mean that with increasing sonication time, there is a trend of decrease in relative crystallinity. This is in line with the findings of On et al. [64], who found that a long sonication period might produce hydrolysis, which damages the pore wall and reduces pore size.

The higher energy received by the SBA-15 material, which is created together with the longer sonication time, can also cause damage to the pore structure. However, it appears that silicate anions formed by hydrolysis and exposed to sonication energy can polymerize again to form siloxane groups, resulting in a considerable increase in crystallinity when 150 min of sonication time. Perhaps, there is competition between the hydrolysis and deconstruction of siloxane groups by energy exposure on the one hand, with the polymerization process of silicate anions forming new siloxane groups on the other. Several earlier studies [65-67] also found that increasing sonication time or hydrothermal duration increased or decreased product crystallinity in the synthesis of various materials.

According to the FTIR spectra and XRD diffractogram analysis, the samples of SBA-15 (8 g, 30 min), SBA-15 (8 g, 60 min), and SBA-15 (8 g, 90 min) show outstanding crystallinity and usually high hexagonal structure regularity. These three samples were quantitatively evaluated using a gas sorption analyzer to determine the porosity.

Gas adsorption analysis

The adsorption-desorption isotherms of the SBA-15 (8 g, 30 min), SBA-15 (8 g, 60 min), and SBA-15 (8 g, 90 min) samples are shown in Fig. 9 together with the isotherm of commercial SBA-15 for the purpose of comparison. The curves of all samples exhibit a type IV isotherm which is characteristic for mesoporous materials. In general, the isotherm curves in this figure are not different to the type IV curve of Fig. 5. However, Fig. 9(a) reveals a distinct difference, in which the inflection point shifts to the right, and both the slope and height of the curve increase. It is indicating that the material has a larger pore diameter, more uniform mesopore, and a higher pore volume. In addition, the

Table 3. The relative crystallinity of SBA-15 synthesized with variation of sonication time compared to commercial SBA-15

Sample	Intensity (counts)	Relative crystallinity (%)*
Commercial SBA-15	2009	100
SBA-15 (8 g, 30 min)	1758	87.51
SBA-15 (8 g, 60 min)	1503	74.81
SBA-15 (8 g, 90 min)	1218	60.63
SBA-15 (8 g, 120 min)	716	35.64
SBA-15 (8 g, 150 min)	869	43.26

* compared to commercial SBA-15

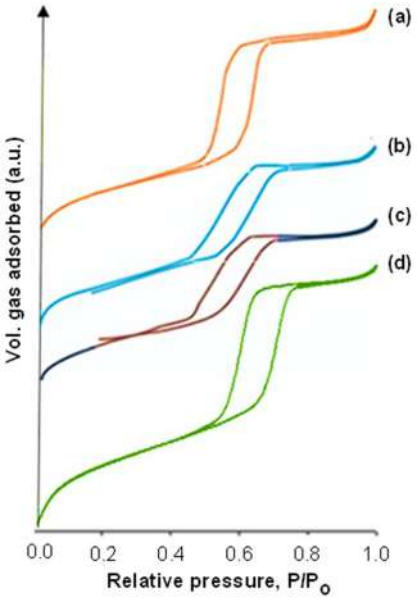

Fig 9. The adsorption-desorption isotherm of (a) SBA-15 (8 g, 30 min), (b) SBA-15 (8 g, 60 min), (c) SBA-15 (8 g, 90 min), and (d) commercial SBA-15

appearance of curve 9(a) more closely resembles the isothermal curve of commercial SBA-15 (Fig. 9(d)). This indicated that the sample has a diameter, volume, and uniformity of pores that are closer to the commercial SBA-15 as shown in Table 4 and Fig. 11.

The porosity of the four materials (Table 4) shows that the order of the specific surface area (S_{BET}) from large to small is Commercial SBA-15 > SBA-15 (8 g, 90 min) > SBA-15 (8 g, 60 min) > SBA-15 (8 g, 30 min). It is clear that the SBA-15 materials increase in specific surface area with increasing sonication time. A similar case was also reported by Chaeronpanich [51]. However, the difference in specific surface area in the present study is not significant, and each has a fairly large surface area (> 600 m^2/g). The order of pore diameters from large to small is Commercial SBA-15 > SBA-15 (8 g, 30 min) > SBA-15 (8 g, 90 min) > SBA-15 (8 g, 60 min). The order of the specific pore volumes from largest to smallest is Commercial SBA-15 > SBA-15 (8 g, 30 min) > SBA-15 (8 g, 60 min) > SBA-15 (8 g, 90 min). The order of pore wall thickness from thick to thin is Commercial SBA-15 > SBA-15 (8 g, 60 min) > SBA-15 (8 g, 90 min) > SBA-15 (8 g, 30 min). Among the synthesized SBA-15, the S_{BET} trends follow the crystallinity trend, which peaked in the SBA-15 (8 g, 30 min) sample. The crystallinity trend, on the other hand, does not appear to be linked to the D_{BJH}, V_{BJH}, and W_T trend.

The pore size distributions of SBA-15 synthesized with varying of sonication time and those of commercial SBA-15 are given in Fig. 10. The pore size distribution of SBA-15 (8 g, 30 min) (Fig. 10(a)) is similar to the pore size distribution of commercial SBA-15 (Fig. 10(d)), both having peaked at a pore diameter of about 5 nm. However, Fig. 10(d) is sharper with a higher peak intensity, which indicates that the uniformity of commercial SBA-15 is still higher than that of SBA-15 (8 g, 30 min). On the other hand, the pore size distributions of SBA-15 (8 g, 60 min) (Fig. 10(c)) and SBA-15 (8 g, 90 min) (Fig. 10(d)) are relatively wide, having peaked at 4.5 and 4 nm, respectively, with diameters ranging from 3 to 7 nm. Among the three synthesized materials, SBA-15 (8 g, 30 min) material has the highest pore volume at the same pore diameter, as demonstrated by the height

Table 4. The porosity of SBA-15 (8 g, 30 min), SBA-15 (8 g, 60 min), and SBA-15 (8 g, 90 min), and Commercial SBA-15

Sample	S_{BET} (m^2/g)	D_{BJH} (nm)	V_{BJH} (mL/g)	d_{100} (nm)	a_0 (nm)	W_T (nm)
SBA-15 (8 g, 30 min)	601	4.76	0.88	8.47	9.78	5.02
SBA-15 (8 g, 60 min)	635	3.98	0.65	8.89	10.27	6.29
SBA-15 (8 g, 90 min)	652	4.32	0.61	8.62	9.95	5.63
Commercial SBA-15	660	6.21	0.98	10.63	12.28	6.07

SBET : specific surface area, BET
D_{BJH} : pore diameter, BJH adsorption
V_{BJH} : specific pore volume
d_{100} : interplanar spacing
a_o : lattice parameter, for hexagonal = $2d_{100}/\sqrt{3}$
W_T : silica wall thickness, for hexagonal $W_T = a_0 - D$

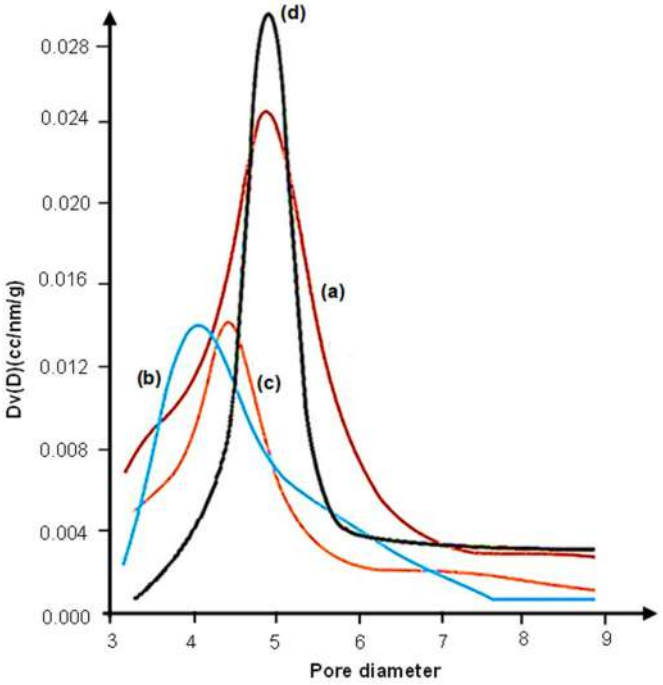

Fig 10. Pore size distribution of (a) SBA-15 (8 g, 30 min), (b) SBA-15 (8 g, 60 min), (c) SBA-15 (8 g, 90 min), and (d) Commercial SBA-15 samples

of its curve, which generally exceeds the other two curves. For the same pore diameter, SBA-15 (8 g, 30 min) has a longer pore length than SBA-15 (8 g, 60 min) and SBA-15 (8 g, 90 min).

Each sample of SBA-15 synthesized with this variation of sonication time has advantages in certain parameters, according to the porosity data in Table 4, but no sample is superior in all parameters. The most regular pore structure, as well as the largest pore diameter and specific pore volume, is found in sample SBA-15 (8 g, 30 min), however, it has the smallest specific surface area and thinnest pore wall. The pore structure of sample SBA-15 (8 g, 60 min) is fairly regular, with the thickest pore wall but the smallest pore diameter. The sample SBA-15 (8 g, 90 min) exhibited a higher specific surface area but a less uniform pore structure and the smallest specific pore volume. Overall, SBA-15 (8 g, 30 min) is the best of the three samples because it has the most regular pore structure, the largest pore diameter and specific pore volume, and takes the least amount of sonication time. Although not the best, the surface area and pore wall thickness of this sample were not substantially different from the others.

TEM analysis

The TEM image of SBA-15 (8 g, 30 min) and commercial SBA-15 (as a reference) are presented in Fig. 11. The TEM image of SBA-15 (8 g, 30 min) sample (Fig. 11(a)) reveals a significant degree of pore regularity although it is not as good as commercial SBA-15 (Fig. 11(b)). According to Fig. 11, the typical pore diameter and pore wall thickness of this material is around 5 and 5.5 nm, respectively. These results match well to those obtained by XRD and GSA data, indicating that the pore diameter and pore wall thickness of this material was 4.76 and 5.02 nm, respectively. For commercial SBA-15, TEM images show the pore diameter and wall thickness of 6.5 and 5 nm, respectively. This is also close to the results obtained from XRD and GSA data, which are 6.21 and 6.07 nm, respectively.

Table 5 compares the porosity of SBA-15 (8 g, 30 min) produced in this study to those achieved by other researchers employing a hydrothermal technique and a variety of silica sources [17-19,35-37], and also to the commercial SBA-15. The SBA-15 prepared in this work, i.e. SBA-15 (8 g, 30 min) which requires a shorter synthesis time and a less expensive silica source, is shown to be comparable to both those previously published in a

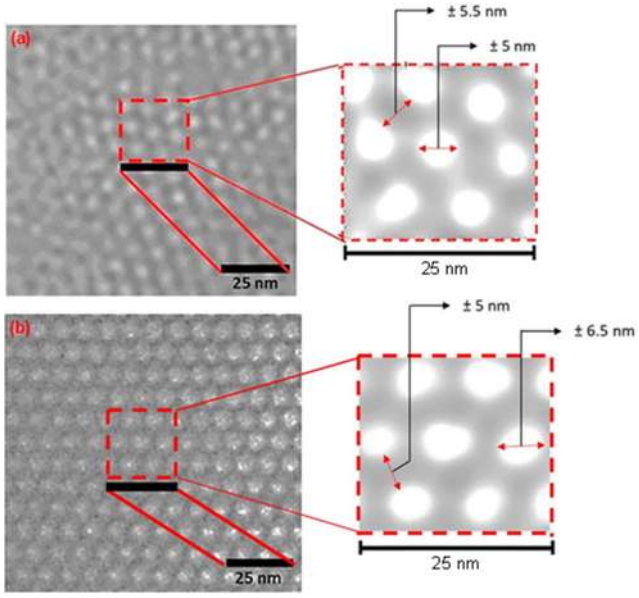

Fig 11. The TEM image of (a) SBA-15 (8 g, 30 min) and (b) commercial SBA-15

Table 5. the porosity of SBA-15 produced in the present research along with those obtained by other workers and the commercial SBA-15

Synthesis time (min)	Method	Silica source	S_{BET} (m^2 g^{-1})	D_{BJH} (nm)	V_{BJH} (cm^3/g)	Reference
1200	hydrothermal	TEOS	700	7	0.98	68
180	hydrothermal	TEOS	795	7.89	1.289	69
1440	hydrothermal	TEOS	948	5.5	1.3	70
4320	hydrothermal	TEOS	835	6.7	0.7	71
2880	hydrothermal	Rice husk silica	310	6.85	0.43	72
1440	hydrothermal	TEOS	558	6.5	0.8	73
1440	hydrothermal	Rice husk silica	656	11.73	1.092	74
1440	hydrothermal	Sodium silicate solution	869	5.7	1.24	75
1440	hydrothermal	TEOS	674	3.92	0.66	76
1440	hydrothermal	TEOS	1000	4.99	1.250	77
*	hydrothermal	TEOS	660	6.21	0.98	Commercial SBA-15
30	Sonochemical	Rice husk silica	601	4.76	0.88	This study

* There is no information

Table 6. the porosity of SBA-15 produced in the present research along with those obtained from many studies using the sonochemical method and TEOS as silica source, and the commercial SBA-15

Synthesis time (min)	Method	Silica source	S_{BET} (m^2 g^{-1})	D_{BJH} (nm)	V_{BJH} (cm^3/g)	Reference
60	Sonochemical	TEOS	562	4.7	0.65	78
120	Sonochemical	TEOS	606	4.9	0.74	78
180	Sonochemical	TEOS	618	4.6	0.72	78
240	Sonochemical	TEOS	570	4.4	0.62	78
60	Sonochemical	TEOS	760	6.5	0.76	42
*	Hydrothermal	TEOS	660	6.21	0.98	Commercial SBA-15
30	Sonochemical	Rice husk silica	601	4.76	0.88	This study

* There is no information

variety of publications as well as commercial SBA-15. As shown in Table 6, the porosity of SBA-15 (8 g, 30 min) obtained in this work is also comparable to the results of several works that use sonochemical method and TEOS as a silica source. Our results are generally comparable to those previously reported by some researchers [38-43], although we use non-commercial silica, extracted from rice husk. The successful use of low-cost materials such as rice husk silica with shorter synthesis times is promising and challenging for the future commercial synthesis of low-cost SBA-15.

■ CONCLUSION

SBA-15 has been successfully synthesized from rice husk silica utilizing a sonochemical method. The optimization of mass ratio of rice husk silica to surfactant (Pluronic P-123) and the sonication time has led to the more efficient and eco-friendly synthesis method. It has been observed that the amount of rice husk silica used and the sonication time have a significant impact on crystallinity, S_{BET}, D_{BJH}, V_{BJH}, W_T, and pore size distribution of the SBA-15 products. In general, the best results has been obtained from using 8 g of rice husk silica and a 30 min sonication time. The product has a specific surface area of 601 m^2 g^{-1}, a wall thickness of 5.02 nm, an average pore diameter of 4.76 nm, a specific pore volume of 0.88 mL g^{-1}, and a narrow pore size distribution (3–6.5 nm). The characteristics of the synthesized SBA-15 in this study are quite comparable to those of SBA-15 synthesized by using

commercial silica materials (TEOS) and the hydrothermal method, which consumes much more time and energy. In addition, the characteristics of SBA-15 synthesized in this study are also quite comparable to those of commercial SBA-15. Therefore, the synthesis method developed in this study is recommended to be used for further synthesis of SBA-15 because it is more efficient and environmentally friendly. The obtained SBA-15 from this study is potentially applied in the catalysis processes as well as in the adsorption study of hazardous pollutants such as heavy metals and dyes.

■ ACKNOWLEDGMENTS

The first author thanks and acknowledges financial support from the Universitas Gadjah Mada (UGM) Faculty of Mathematics and Natural Sciences through a BPPTNBH research grant with the contract number 87/J01.1.28/PL.06.02/2020. Thanks also to Wahyu Nugroho, A.Md., S.Si., and Kristiana Fajariatri, A.Md., S.Si., who have helped with this research.

■ REFERENCES

[1] Sun, L.B., Liu, X.Q., and Zhou, H.C., 2015, Design and fabrication of mesoporous heterogeneous basic catalysts, *Chem. Soc. Rev.*, 44 (15), 5092–5147.

[2] Sabbaghi, A., Lam, F.L.Y., and Hu, X.J., 2015, High Zr-loaded SBA-15 cobalt catalyst for efficient NO*x* reduction in lean-burn exhaust, *Appl. Catal., A*, 508, 25–36.

[3] Lai, Y.T., Chen, T.C., Lan, Y.K., Chen, B.S., You, J.H., Yang, C.M., Lai, N.C., Wu, J.H., and Chen, C.S., 2014, Pt/SBA-15 as a highly efficient catalyst for catalytic toluene oxidation, *ACS Catal.*, 4 (11), 3824–3836.

[4] Jiang, W.J., Yin, Y., Liu, X.Q., Yin, X.Q., Shi, Y.Q., and Sun, L.B., 2013, Fabrication of supported cuprous sites at low temperatures: an efficient, controllable strategy using vapor-induced reduction, *J. Am. Chem. Soc.*, 135 (22), 8137–8140.

[5] Buonomenna, M.G., Golemme, G., Tone, C.M., De Santo, M.P., Ciuchi, F., and Perrotta, E., 2013, Amine-functionalized SBA-15 in poly(styrene-*b*-butadiene-*b*-styrene) (SBS) yields permeable and selective nanostructured membranes for gas separation, *J. Mater. Chem. A*, 1 (38), 11853–11866.

[6] Yin, Y., Tan, P., Liu, X.Q., Zhu, J., and Sun, L.B., 2014, Constructing a confined space in silica nanopores: an ideal platform for the formation and dispersion of cuprous sites, *J. Mater. Chem. A*, 2 (10), 3399–3406.

[7] Yin, Y., Zhu, J., Liu, X.Q., Tan, P., Xue, D.M., Xing, Z.M., and Sun, L.B., 2016, Simultaneous fabrication of bifunctional Cu(I)/Ce(IV) sites in silica nanopores using a guests-redox strategy, *RSC Adv.*, 6 (74), 70446–70451.

[8] Vavsari, V.F., Ziarani, G.M., and Badiei, A., 2015, The role of SBA-15 in drug delivery, *RSC Adv.*, 5 (111), 91686–91707.

[9] Karnopp, J.C.F., Cardoso, T.F.M., Gonçalves, D., Carollo, A.R.H., de Castro, G.R., Duarte, A.P., and Martines, M.A.U., 2020, Preparation of the Rutin-SBA-16 drug delivery system, *J. Biomater. Nanobiotechnol.*, 11 (1), 1–13.

[10] Wang, J., Yang, M., Lu, Y., Jin, Z., Tan, L., Gao, H., Fan, S., Dong, W., and Wang, G., 2016, Surface functionalization engineering driven crystallization behavior of polyethylene glycol confined in mesoporous silica for shape-stabilized phase change materials, *Nano Energy*, 19, 78–87.

[11] Angioni, S., Villa, D.C., Cattaneo, A.S., Mustarelli, P., and Quartarone, E., 2015, Influence of variously functionalized SBA-15 fillers on conductivity and electrochemical properties of PBI composite membranes for high temperature polymer fuel cells, *J. Power Sources*, 294, 347–353.

[12] Pizzoccaro-Zilamy, M.A., Huiskes, C., Keim, E.G., Sluijter, S.N., van Veen, H., Nijmeijer, A., Winnubst, L., and Luiten-Olieman, M.W.J., 2019, New generation of mesoporous silica membranes prepared by a Stöber-solution pore-growth approach, *ACS Appl. Mater. Interfaces*, 11 (20), 18528–18539.

[13] Yang, J., Lin, G.S., Mou, C.Y., and Tung, K.L., 2020, Mesoporous silica thin membrane with tunable pore size for ultrahigh permeation and precise

molecular separation, *ACS Appl. Mater. Interfaces*, 12 (6), 7459–7465.

[14] Taweekarn, T., Wongniramaikul, W., Limsakul, W., Sriprom, W., Phawachalotorn, C., and Choodum, A., 2020, A novel colorimetric sensor based on modified mesoporous silica nanoparticles for rapid on-site detection of nitrite, *Microchim. Acta*, 187 (12), 643.

[15] Hassan, H.M., Ab Rahman, N.B., and Jalil, M.N., 2016, Mesoporous silica electrochemical sensors for the detection of ascorbic acid and uric acid, *Malays. J. Anal. Sci.*, 20 (2), 351–357.

[16] Linares, N., Silvestre-Albero, A.M., Serrano, E., Silvestre-Albero, J., and García-Martínez, J., 2014, Mesoporous materials for clean energy technologies, *Chem. Soc. Rev.*, 43 (22), 7681–7717.

[17] da Silva, F.C.M., Costa, M.J.S., da Silva, L.K.R., Batista, A.M., and da Luz, G.E., 2019, Functionalization methods of SBA-15 mesoporous molecular sieve: A brief overview, *SN Appl. Sci.*, 1 (6), 654.

[18] Selvakannan, P.R., Mantri, K., Tardio, J., and Bhargava, S.K., 2013, High surface area Au–SBA-15 and Au–MCM-41 materials synthesis: Tryptophan amino acid mediated confinement of gold nanostructures within the mesoporous silica pore walls, *J. Colloid Interface Sci.*, 394, 475–484.

[19] Costa, J.A.S., de Jesus, R.A., Santos, D.O., Mano, J.F., Romão, L.P.C., and Paranhos, C.M., 2020, Recent progresses in the adsorption of organic, inorganic, and gas compounds by MCM-41-based mesoporous materials, *Microporous Mesoporous Mater.*, 291, 109698.

[20] Gobara, H.M., 2016, Synthesis, mechanisms and different applications of mesoporous materials based on silica and alumina, *Egypt. J. Chem.*, 59 (2), 163–194.

[21] Zhang, H., Tang, C., Lv, Y., Sun, C., Gao, F., Dong, L., and Chen, Y., 2012, Synthesis, characterization, and catalytic performance of copper-containing SBA-15 in the phenol hydroxylation, *J. Colloid Interface Sci.*, 380 (1), 16–24.

[22] dos Santos, S.M.L., Nogueira, K.A.B., de Souza Gama, M., Lima, J.D.F., da Silva Júnior, I.J., and de Azevedo, D.C.S., 2013, Synthesis and characterization of ordered mesoporous silica (SBA-15 and SBA-16) for adsorption of biomolecules, *Microporous Mesoporous Mater.*, 180, 284–292.

[23] Schwanke, A.J., Favero, C., Balzer, R., Bernardo-Gusmão, K., and Pergher, S.B.C., 2018, SBA-15 as a support for nickel-based catalysts for polymerization reactions, *J. Braz. Chem. Soc.*, 29 (2), 328–333.

[24] Adrover, M.E., Pedernera, M., Bonne, M., Lebeau, B., Bucalá, V., and Gallo, L., 2020, Synthesis and characterization of mesoporous SBA-15 and SBA-16 as carriers to improve albendazole dissolution rate, *Saudi Pharm. J.*, 28 (1), 15–24.

[25] Thahir, R., Wahab, A.W., La Nafie, N., and Raya, I., 2019, Synthesis of high surface area mesoporous silica SBA-15 by adjusting hydrothermal treatment time and the amount of polyvinyl alcohol, *Open Chem.*, 17 (1), 963–971.

[26] Juárez-Serrano, N., Berenguer, D., Martínez-Castellanos, I., Blasco, I., Beltrán, M., and Marcilla, A., 2021, Effect of reaction time and hydrothermal treatment time on the textural properties of SBA-15 synthesized using sodium silicate as a silica source and its efficiency for reducing tobacco smoke toxicity, *Catalysts*, 11 (7), 808.

[27] Lázaro, A.L., Rodríguez-Valadez, F.J., López, J.J.M., and Espejel-Ayala, F., 2020, SBA-15 synthesis from sodium silicate prepared with sand and sodium hydroxide, *Mater. Res. Express*, 7, 045503.

[28] Norsurayaa, S., Fazlenaa, H., and Norhasyimia, R., 2016, Sugarcane bagasse as a renewable source of silica to synthesize Santa Barbara Amorphous-15 (SBA-15), *Procedia Eng.*, 148, 839–846.

[29] Nguyen, Q.N.K., Yen, N.T., Hau, N.D., and Tran, H.L., 2020, Synthesis and characterization of mesoporous silica SBA-15 and ZnO/SBA-15 photocatalytic materials from the ash of brickyards, *J. Chem.*, 2020, 8456194.

[30] Wang, J., Fang, L., Cheng, F., Duan, X., and Chen, R., 2013, Hydrothermal synthesis of SBA-15 using sodium silicate derived from coal gangue, *J. Nanomater.*, 2013, 352157.

[31] Razak, H., Abdullah, N., Setiabudi, H.N., Yee, C.S., and Ainirazali, N., 2019, Refluxed synthesis of SBA-15 using sodium silicate extracted from oil palm ash for dry reforming of methane, *Mater. Today: Proc.*, 19, 1363–1372.

[32] Rodrigues, J.J., Fernandes, F.A.N., and Rodrigues, M.G.F., 2018, Co/Ru/SBA-15 catalysts synthesized with rice husk ashes as silica source applied in the Fischer-Tropsch synthesis, *Braz. J. Pet. Gas*, 12 (3), 169–179.

[33] Liou, T.H., Tseng, Y.K., Liu, S.M., Lin, Y.T., Wang, S.Y., and Liu, R.T., 2021, Green synthesis of mesoporous graphene oxide/silica nanocomposites from rice husk ash: Characterization and adsorption performance, *Environ. Technol. Innovation*, 22, 101424.

[34] Watthanachai, C., Ngamcharussrivichai, C., and Pengprecha, S., 2018, Synthesis and characterization of bimodal mesoporous silica derived from rice husk ash, *Eng. J.*, 23 (1), 25–34.

[35] Fernandes, L.J., Calheiro, D., Sánchez, F.A.L., Camacho, A.L.D., de Campos Rocha, T.L.A., Moraes, C.A.M., and de Sousa, V.C., 2017, Characterization of silica produced from rice husk ash: Comparison of purification and processing methods, *Mater. Res.*, 20 (Suppl. 2), 512–518.

[36] Hossain, S.K.S., Mathur, L., and Roy, P.K., 2018, Rice husk/rice husk ash as an alternative source of silica in ceramics: A review, *J. Asian Ceram. Soc.*, 6 (4), 299–313.

[37] Xu, K., Sun, Q., Guo, Y., and Dong, S., 2013, Effects on modifiers on the hydrophobicity of SiO_2 films from nano-husk ash, *Appl. Surf. Sci.*, 276, 796–801.

[38] Laborte, A.G., Velasco, M.L., Wang, H., Behura, D., Pagnchak, M.R., Singh, H.N., Wardana, I.P., Vilayvong, S., and Shah, H., 2017, Release and adoption of improved cultivars in South and Southeast Asia: Rice, *The 9th ASAE International Conference: Transformation in Agricultural and Food Economy in Asia*, Bangkok, Thailand, 11-13 January 2017, 1455–1469.

[39] Barrera, D., Villarroel-Rocha, J., Marenco, L., Oliva, M.I., and Sapag, K., 2011, Non-hydrothermal synthesis of cylindrical mesoporous materials: Influence of the surfactant/silica molar ratio, *Adsorpt. Sci. Technol.*, 29 (10), 975–988.

[40] Yang, Q.Y., Zhu, H., Tian, L., Xie, S.H., Pei, Y., Li, H., Li, H.X., Qiao, M.H., and Fan, K.N., 2009, Preparation and characterization of Au-In/APTMS-SBA-15 catalysts for chemoselective hydrogenation of crotonaldehyde to crotyl alcohol, *Appl. Catal., A*, 369 (1-2), 67–76.

[41] Mollakarimi Dastjerdi, N., and Ghanbari, M., 2020, Ultrasound-promoted green approach for the synthesis of multisubstituted pyridines using stable and reusable SBA-15@ADMPT/$H_5PW_{10}V_2O_{40}$ nanocatalyst at room temperature, *Green Chem. Lett. Rev.*, 13 (3), 192–205.

[42] Prabhu, A., Sudha, V., Pachamuthu, M.P., Sundaravel, B., and Bellucci, S., 2022, Ultrasonic synthesis of Al-SBA-15 nanoporous catalyst for *t*-butylation of ethylbenzene, *J. Nanomater.*, 2022, 2512223.

[43] Li, J.Z., and Bai, X.F., 2017, Ultrasonic synthesis of Pd/SBA-15 catalyst for Suzuki-Miyaura coupling, *Adv. Eng. Res.*, 136, 454–457.

[44] Sun, S., Wang, S., Wang, P., Wu, Q., and Fang, S., 2015, Ultrasound assisted morphological control of mesoporous silica with improved lysozyme adsorption, *Ultrason. Sonochem.*, 23, 21–25.

[45] Ramos, J.M., Wang, J.A., Flores, S.O., Chen, L., Arellano, U., Noreña, L.E., González, J., and Navarrete, J., 2021, Ultrasound-assisted hydrothermal synthesis of V_2O_5/Zr-SBA-15 catalysts for production of ultralow sulfur fuel, *Catalysts*, 11 (4), 408.

[46] Yusof, N.S.M., Babgi, B., Alghamdi, Y., Aksu, M., Madhavan, J., and Ashokkumar, M., 2016, Physical and chemical effects of acoustic cavitation in selected ultrasonic cleaning applications, *Ultrason. Sonochem.*, 29, 568–576.

[47] Alshabanat, M., Al-Arrash, A., and Mekhamer, W., 2013, Polystyrene/montmorillonite nanocomposites: study of the morphology and effects of sonication time on thermal stability, *J. Nanomater.*, 2013, 650725.

[48] Shojaeiarani, J., Bajwa, D., and Holt, G., 2020, Sonication amplitude and processing time influence the cellulose nanocrystals morphology and dispersion, *Nanocomposites*, 6 (1), 41–46.

[49] Ali, F., Reinert, L., Lévêque, J.M., Duclaux, L., Muller, F., Saeed, S., and Shah, S.S., 2014, Effect of sonication conditions: solvent, time, temperature and reactor type on the preparation of micron sized vermiculite particles, *Ultrason. Sonochem.*, 21 (3), 1002–1009.

[50] Jokar, A., Azizi, M.H., Esfehani, Z.H., and Abbasi, S., 2017, Effects of ultrasound time on the properties of methylcellulose-montmorillonite films, *Int. Nano Lett.*, 7 (1), 59–68.

[51] Chaeronpanich, M., Nanta-ngern, A., and Limtrakul, J., 2007, Short-period synthesis of ordered mesoporous silica SBA-15 using ultrasonic technique, *Mater. Lett.*, 61 (29), 5153–5156.

[52] Banoth, S., Babu, V.S., Raghavendra, G., Rakesh, K., and Ojha, S., 2021, Sustainable thermochemical extraction of amorphous silica from biowaste, *Silicon*, 2021, s00240-021-01293-z.

[53] Yener, H.B., and Helvacı, Ş.Ş., 2015, Effect of synthesis temperature on the structural properties and photocatalytic activity of TiO_2/SiO_2 composites synthesized using rice husk ash as a SiO_2 source, *Sep. Purif. Technol.*, 140, 84–93.

[54] Ma, X., Zhou, B., Gao, W., Qu, Y., Wang, L., Wang, Z., and Zhu, Y., 2012, A recyclable method for production of pure silica from rice hull ash, *Powder Technol.*, 217, 497–501.

[55] Zemnukhova, L.A., Panasenko, A.E., Artem'yanov, A.P., and Tsoy, E.A., 2015, Dependence of porosity of amorphous silicon dioxide prepared from rice straw on plant variety, *BioResources*, 10 (2), 3713–3723.

[56] Palanivelu, R., Padmanaban, P., Sutha, S., and Rajendran, V., 2014, Inexpensive approach for production of high-surface-area silica nanoparticles from rice hulls biomass, *IET Nanobiotechnol.*, 8 (4), 290–294.

[57] Meléndez-Ortiz, H.I., Puente-Urbina, B., Castruita-de Leon, G., Mata-Padilla, J.M., and Garcia-Uriostegui, L., 2016, Synthesis of spherical SBA-15 mesoporous silica. Influence of reaction conditions on the structural order and stability, *Ceram. Int.*, 42 (6), 7564–7570.

[58] González, J., Wang, J.A., Chen, L., Manríquez, M., Salmones, J., Limas, R., and Arellano, U., 2018, Quantitative determination of oxygen defects, surface Lewis acidity, and catalytic properties of mesoporous MoO_3/SBA-15 catalysts, *J. Solid State Chem.*, 263, 100–114.

[59] Alavi, S., Hosseini-Monfared, H., and Siczek, M., 2013, A new manganese(III) complex anchored onto SBA-15 as efficient catalyst for selective oxidation of cycloalkanes and cyclohexene with hydrogen peroxide, *J. Mol. Catal. A: Chem.*, 377, 16–28.

[60] Hashemikia, S., Hemmatinejad, N., Ahmadi, E., and Montazer, M., 2015, Optimization of tetracycline hydrochloride adsorption on amino modified SBA-15 using response surface methodology, *J. Colloid Interface Sci.*, 443, 105–114.

[61] Gonzalez, G., Sagarzazu, A., Cordova, A. Gomes, M.E., Salas, J., Contreras, L., Noris-Suarez, K., and Lascano, L., 2018, Comparative study of two silica mesoporous materials (SBA-16 and SBA-15) modified with a hydroxyapatite layer for clindamycin controlled delivery, *Microporous Mesoporous Mater.*, 256, 251–265.

[62] Andrade, G.F., Gomide, V.S., da Silva Júnior, A.C., Goes, A.M., and de Sousa, E.M.B., 2014, An in situ synthesis of mesoporous SBA-16/hydroxyapatite for ciprofloxacin release: in vitro stability and cytocompatibility studies, *J. Mater. Sci.: Mater. Med.*, 25 (11), 2527–2540.

[63] Sheng, Y., Tang, X., Peng, E., and Xue, J., 2013, Graphene oxide based fluorescent nanocomposites for cellular imaging, *J. Mater. Chem. B*, 14 (4), 512–521.

[64] On, T.D., Zaidi, S.M.J., and Kaliaguine, S., 1998, Stability of mesoporous aluminosilicate MCM-41 under vapor treatment, acidic and basic conditions, *Microporous Mesoporous Mater.*, 22 (1-3), 211–224.

[65] Shirvanimoghaddam, K., Balaji, K.V., Yadav, R., Zabihi, O., Ahmadi, M., Adetunji, P., Naebe, M.,

2021, Balancing the toughness and strength in polypropylene composites, *Composites, Part B*, 223, 109121.

[66] Ramirez Mendoza, H., Jordens, J., Valdez Lancinha Pereira, M., Lutz, C., and Van Gerven, T., 2020, Effects of ultrasonic irradiation on crystallization kinetics, morphological and structural properties of zeolite FAU, *Ultrason. Sonochem.*, 64, 105010.

[67] Chagas, J.S., Almeida, J.N.S., Pereira, A.C.L., Medeiros, E.S., Silva Guedes de Lima, B.A., Ferreira e Santos, A.S., Oliveira, J.E., and Mattoso, L.H.C., 2019, Effect of sonication time interval on the size and crystallinity degree of cellulose nanocrystals, *Proceedings of the 18th Brazilian Material Research Society Meeting*, Rio de Janeiro, Brazil, 22-26 September 2019.

[68] Thielemann, J.P., Girgsdies, F., Schlögl, R., and Hess, C., 2011, Pore structure and surface area of silica SBA-15: Influence of washing and scale-up, *Beilstein J. Nanotechnol.*, 2, 110–118.

[69] Deryło-Marczewska, A., Zienkiewicz-Strzałka, M., Skrzypczyńska, K., Świątkowski, A., and Kuśmierek, K., 2016, Evaluation of the SBA-15 materials ability to accumulation of 4-chlorophenol on carbon paste electrode, *Adsorption*, 22 (4), 801–812.

[70] Mayani, S.V., Mayani, V.J., and Kim, S.W., 2014, SBA-15 supported Fe, Ni, Fe-Ni bimetallic catalysts for wet oxidation of bisphenol-A, *Bull. Korean Chem. Soc.*, 35 (12), 3535.

[71] Pérez-Vidal, H., Lunagómez, M.A., Pacheco, J.G., Torres-Torres, J.G., De la Cruz-Romero, D., Cuauhtémoc-López, I., and Beltramini, J.N., 2018, Co/SBA-15 modified with TMB in the degradation of phenol, *J. Appl. Res. Technol.*, 16 (5), 422–436.

[72] Lin, D., Huang, Y., Yang, Y., Long, X., Qin, W., Chen, H., Zhang, Q., Wu, Z., Li, S., Wu, D., Hu, L., Zhang, X., 2018, Preparation and characterization of highly ordered mercapto-modified bridged silsesquioxane for removing ammonia-nitrogen from water, *Polymers*, 10 (8), 819.

[73] Schwanke, A.J., Favero, C., Balzer, R., Bernardo-Gusmão, K., and Pergher, S.B.C., 2018, SBA-15 as a support for nickel-based catalysts for polymerization reactions, *J. Braz. Chem. Soc.*, 29 (2), 328–333.

[74] Liou, T.H., and Liou, Y.H., 2021, Utilization of rice husk ash in the preparation of graphene-oxide-based mesoporous nanocomposites with excellent adsorption performance, *Materials*, 14 (5), 1214.

[75] Mansour, S., Akkari, R., Chaabene, S.B., and Zina, M.S., 2020, Effect of surface site defects on photocatalytic properties of $BiVO_4/TiO_2$ heterojunction for enhanced methylene blue degradation, *Adv. Mater. Sci. Eng.*, 2020, 6505301.

[76] Kruatim, J., Jantasee, S., and Jongsomjit, B., 2016, Improvement of cobalt dispersion on Co/SBA-15 and Co/SBA-16 catalysts by ultrasound and vacuum treatments during post-impregnation step, *Eng. J.*, 21 (1), 17–28.

[77] Ruchomski, L., Pikula, T., Kamiński, D., Słowik, G., and Kosmulski, M., 2022, Synthesis and characterization of a novel composites derived from SBA-15 mesoporous silica and iron pentacarbonyl, *J. Colloid Interface Sci.*, 608, 2421–2429.

[78] Palani, A., Wu, H.Y., Ting, C.C., Vetrivel, S., Shanmugapriya, K., Chiang, A.S.T., and Kao, H.M., 2010, Rapid temperature-assisted sonochemical synthesis of mesoporous silica SBA-15, *Microporous Mesoporous Mater.*, 131 (1-3), 385–392.

Supplementary Data

This supplementary data is a part of a paper entitled "Triterpenoids from Stem Bark of *Dysoxylum excelsum* and Their Cytotoxic Activity against MCF-7 Breast Cancer Cells".

Table of Contents

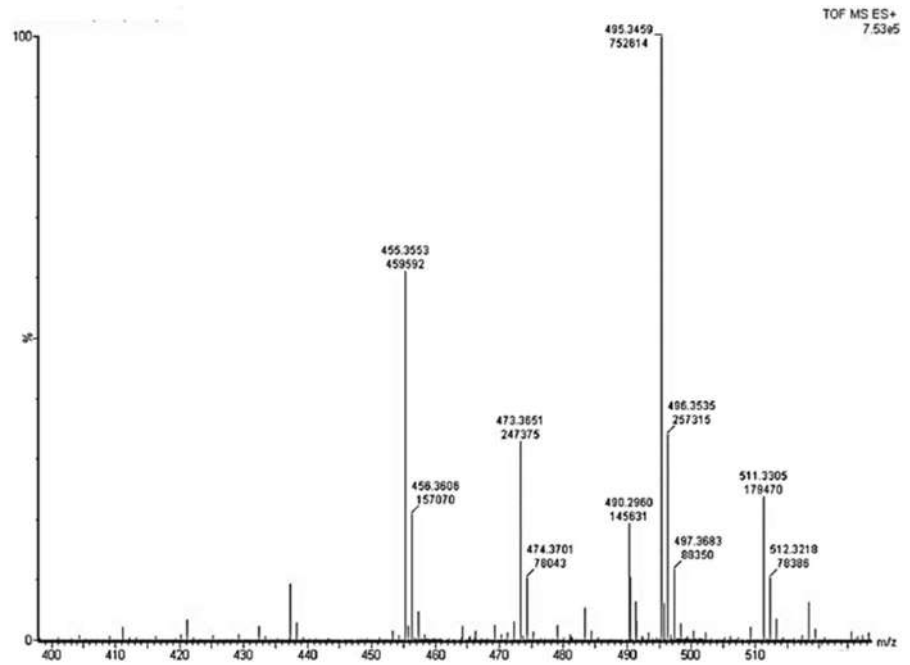

Mass	Calc. Mass	mDa	PPM	DBE	i-FIT	i-FIT (Norm)	Formula
495.3459	495.3450	0.9	1.8	6.5	422.7	1.1	C30 H48 O4 Na

Fig S1. HRTOFMS spectrum of compound **1** ($[M+Na]^+$)

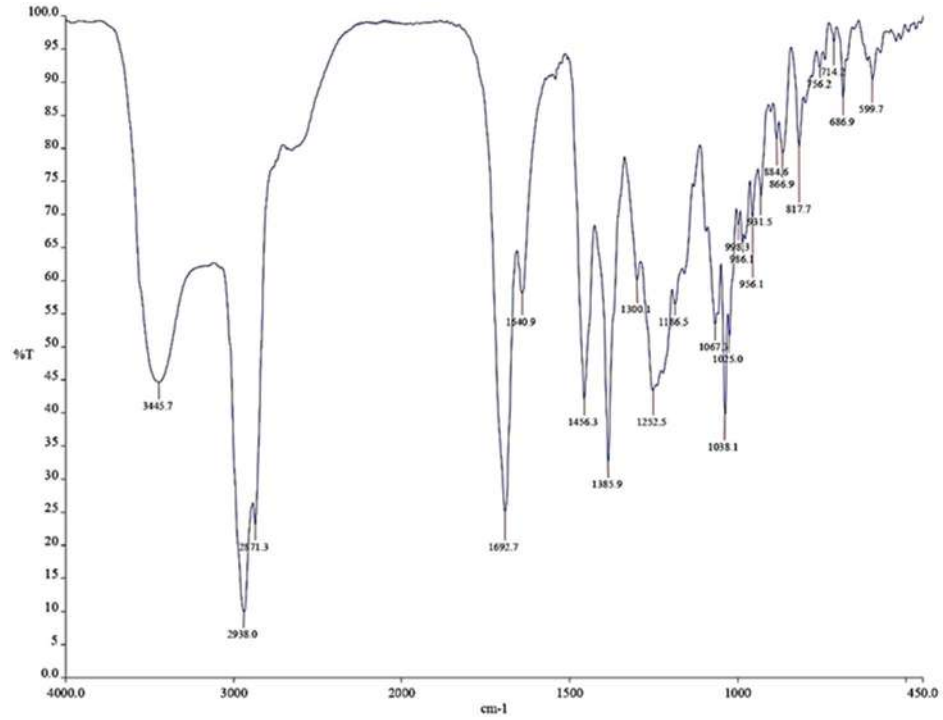

Fig S2. IR (KBr disc) spectrum of compound **1**

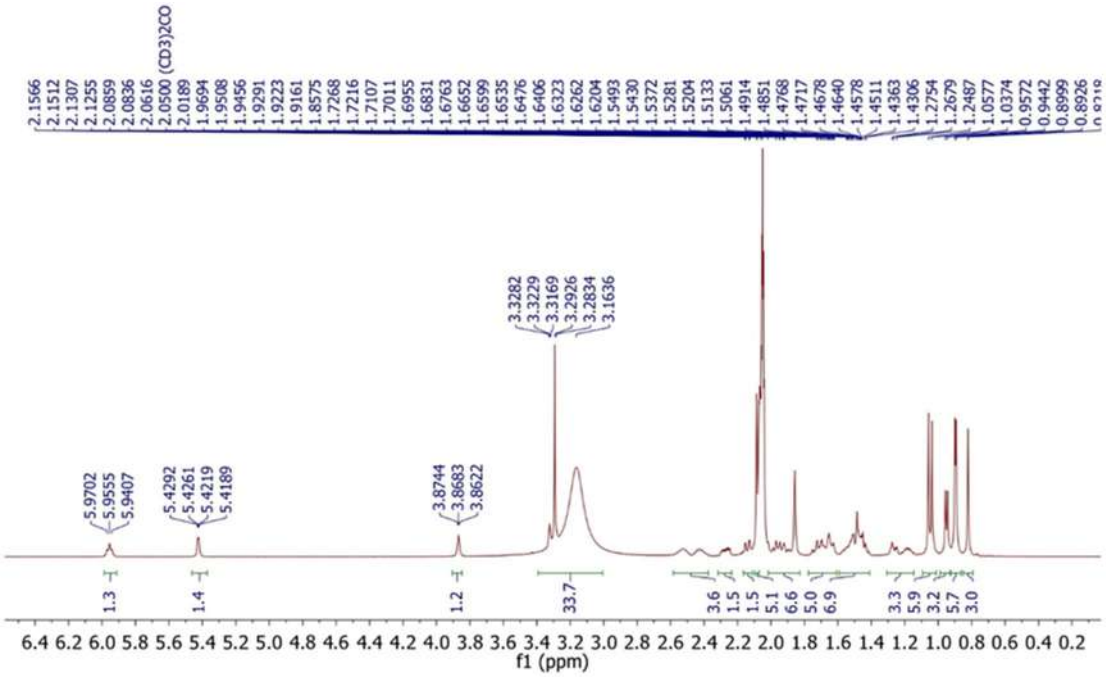

Fig S3. ^{1}H-NMR spectrum of compound **1** in $(CD_3)_2CO$ (500 MHz)

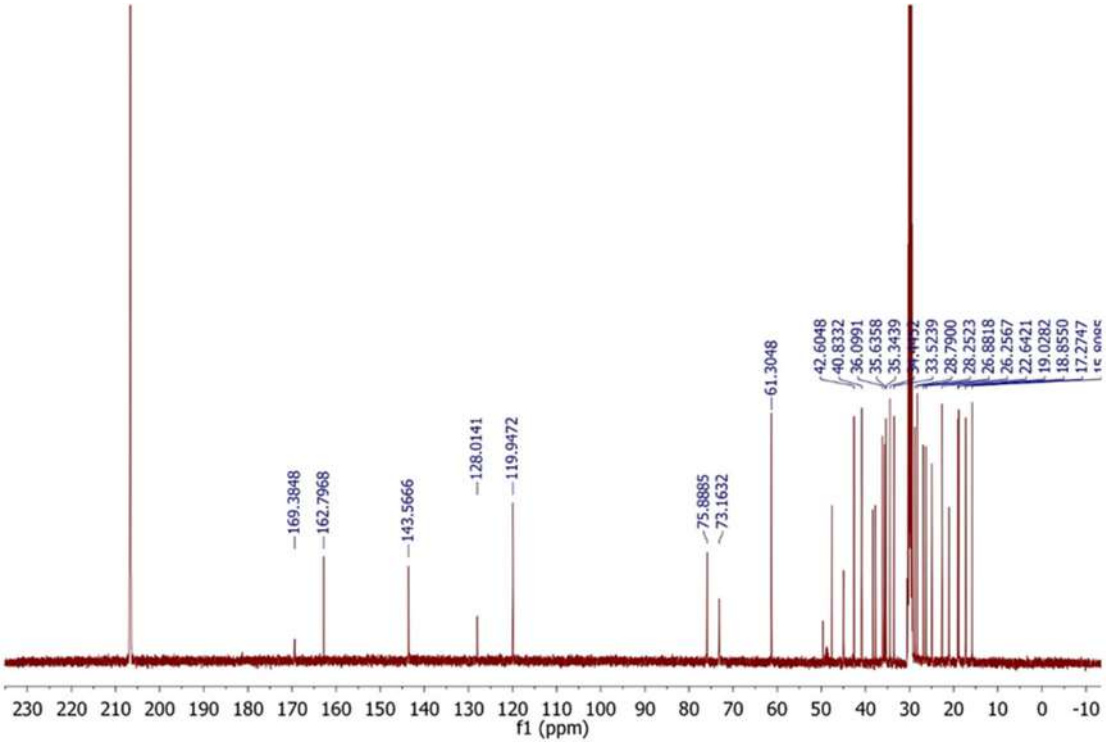

Fig S4. ^{13}C-NMR spectrum of compound **1** in $(CD_3)_2CO$ (125 MHz)

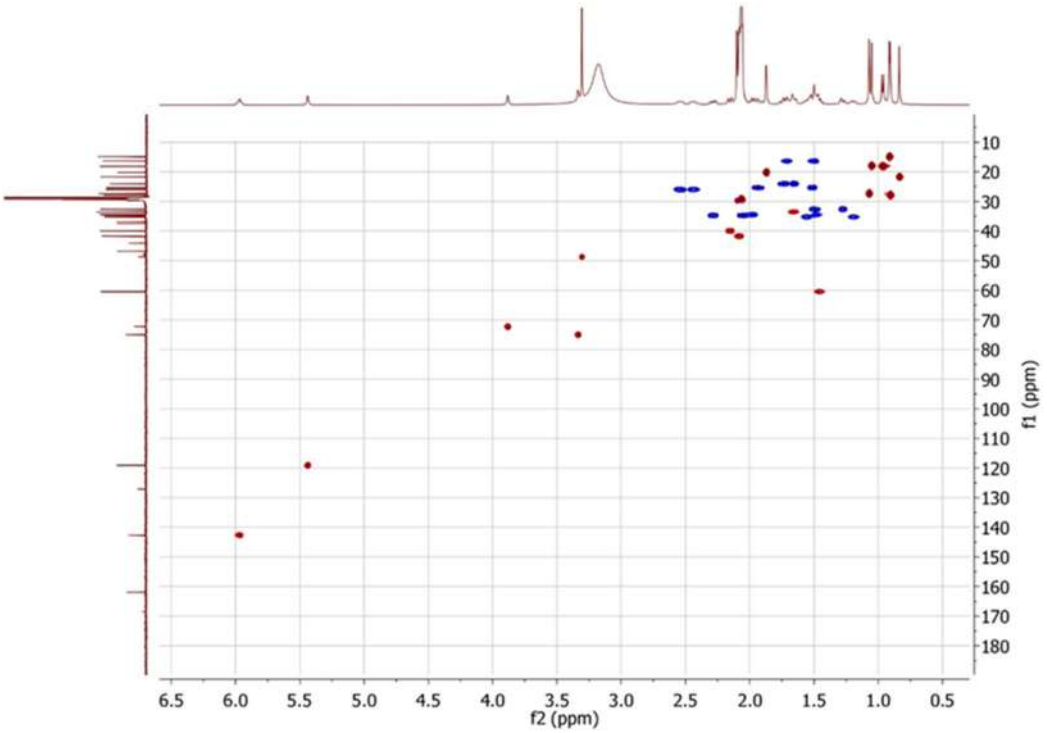

Fig S5. HSQC spectrum of compound **1** in $(CD_3)_2CO$

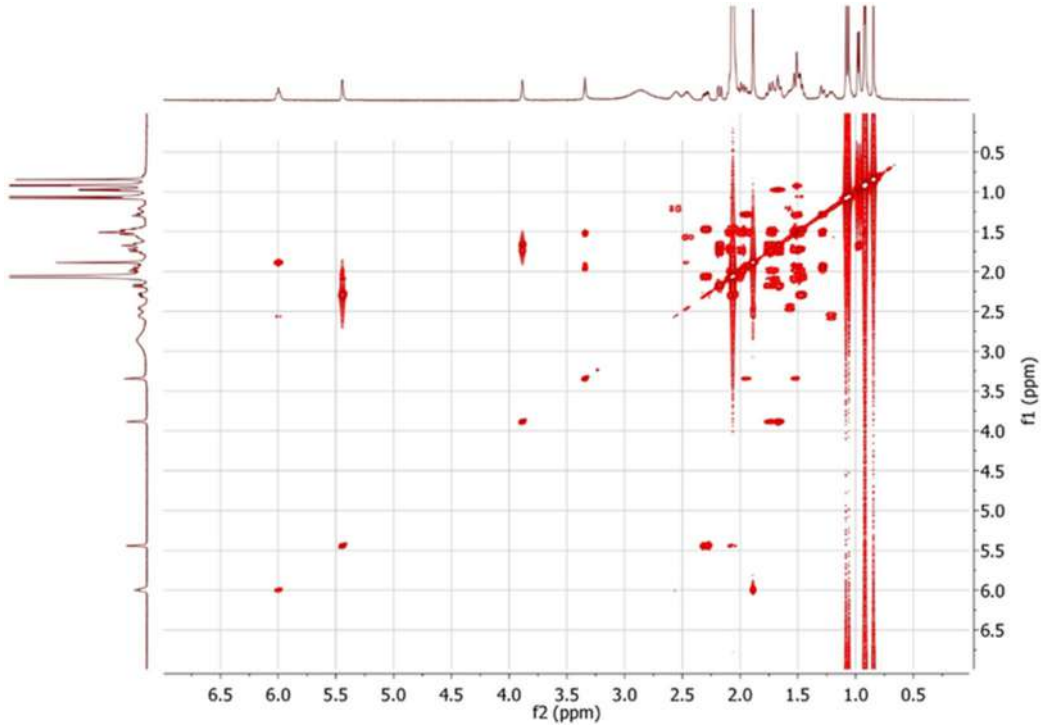

Fig S6. ^1H-^1H COSY spectrum of compound **1** in $(CD_3)_2CO$

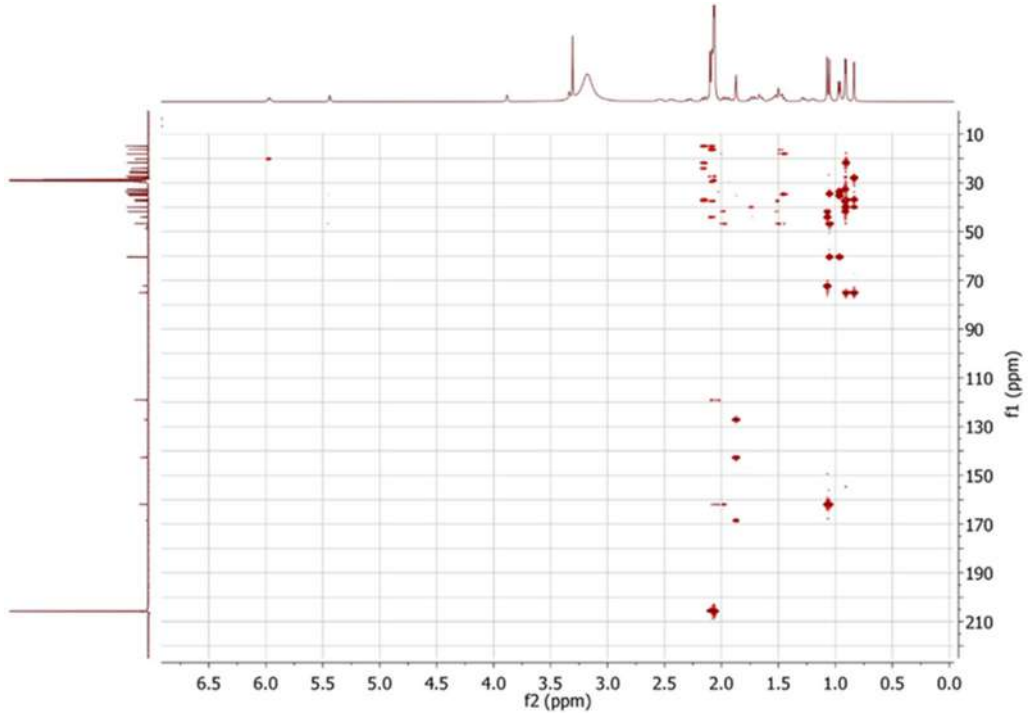

Fig S7. HMBC spectrum of compound **1** in $(CD_3)_2CO$

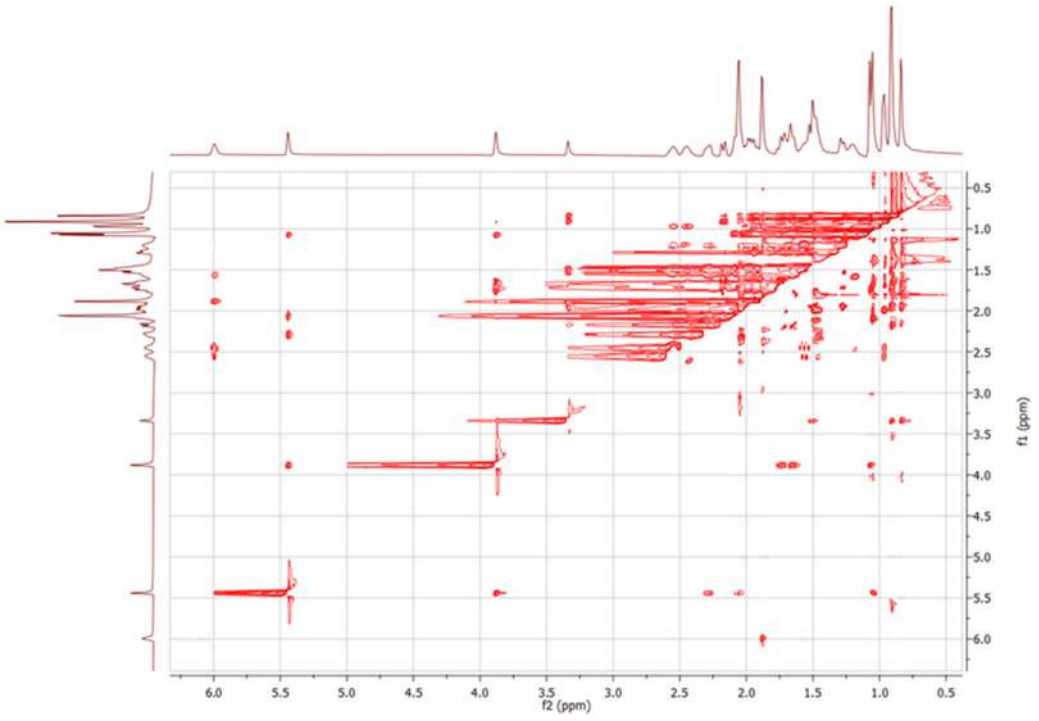

Fig S8. ROESY spectrum of compound **1** in $(CD_3)_2CO$

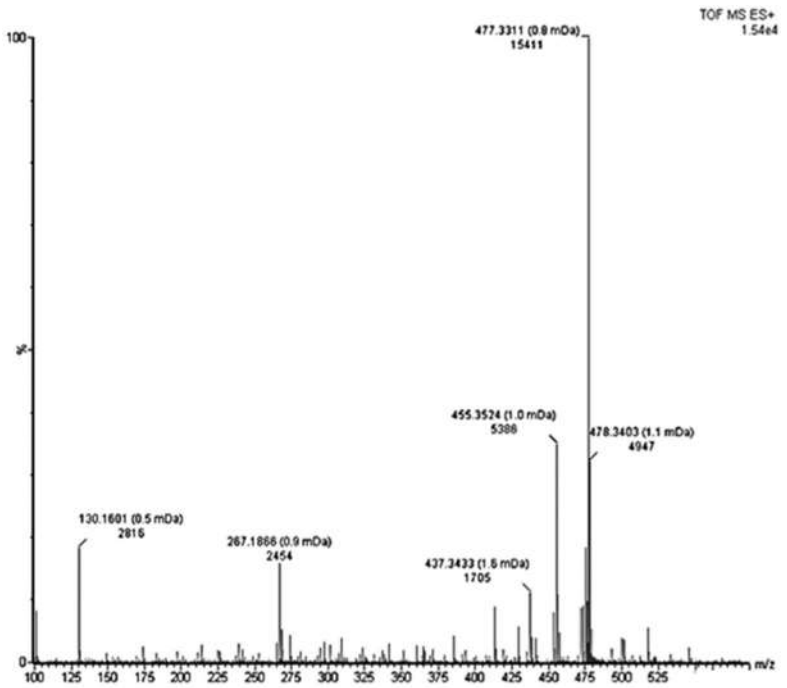

Mass	Calc. Mass	mDa	PPM	DBE	i-FIT	i-FIT (Norm)	Formula
477.3311	477.3345	-3.4	-7.1	7.5	236.2	0.0	C30 H46 O3 Na

Fig S9. HRTOFMS spectrum of compound **2** ([M+Na]$^+$)

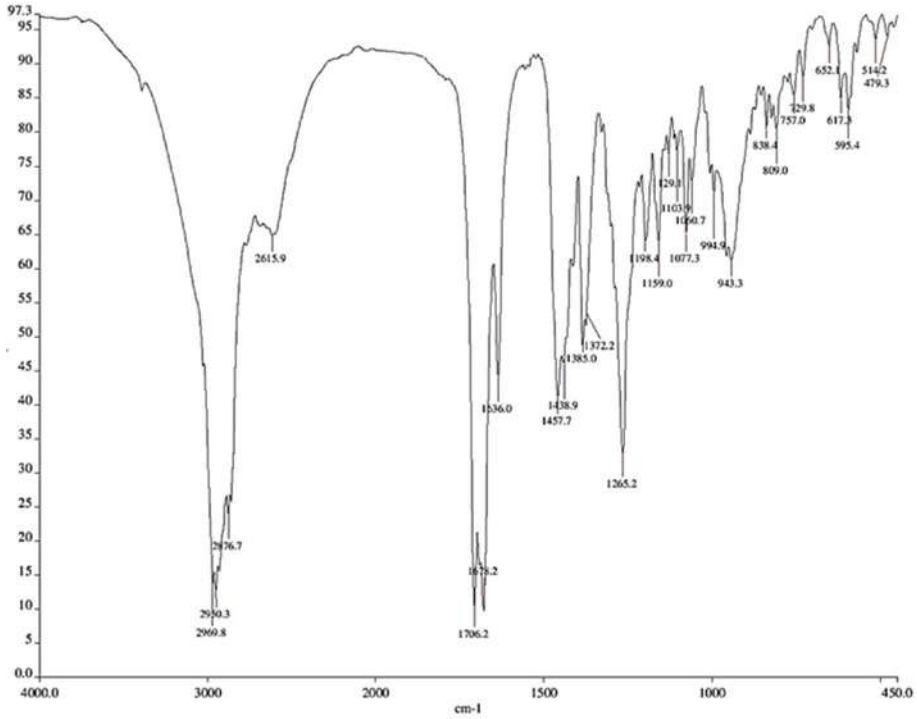

Fig S10. IR (KBr disc) spectrum of compound **2**

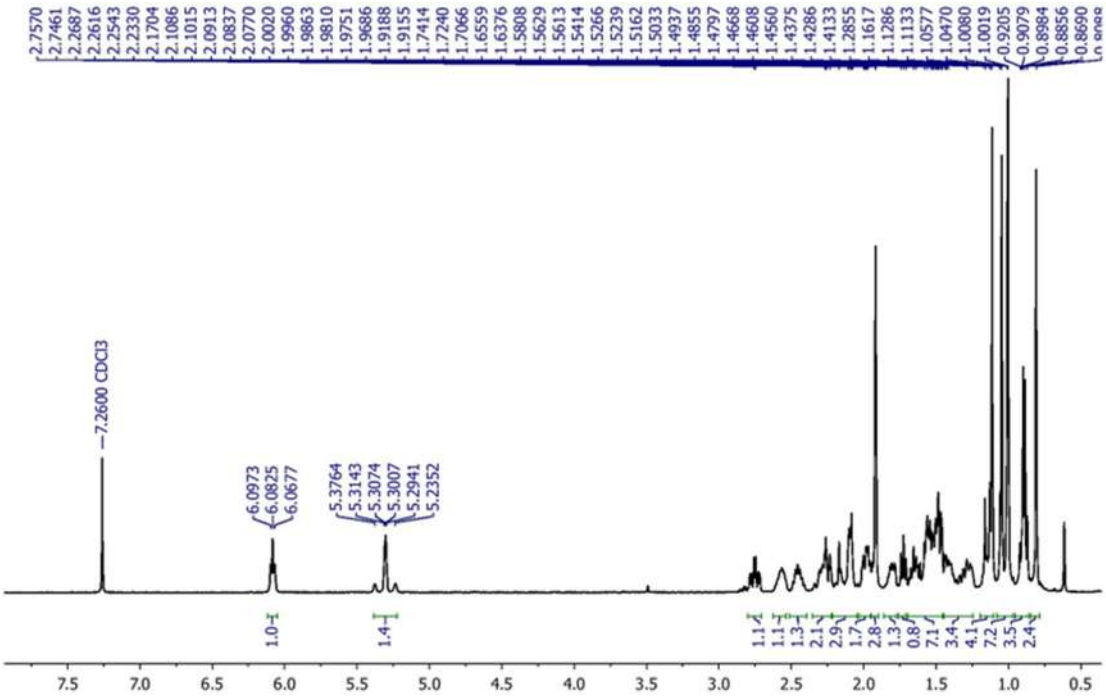

Fig S11. ^{1}H-NMR spectrum of compound **2** in $CDCl_3$ (500 MHz)

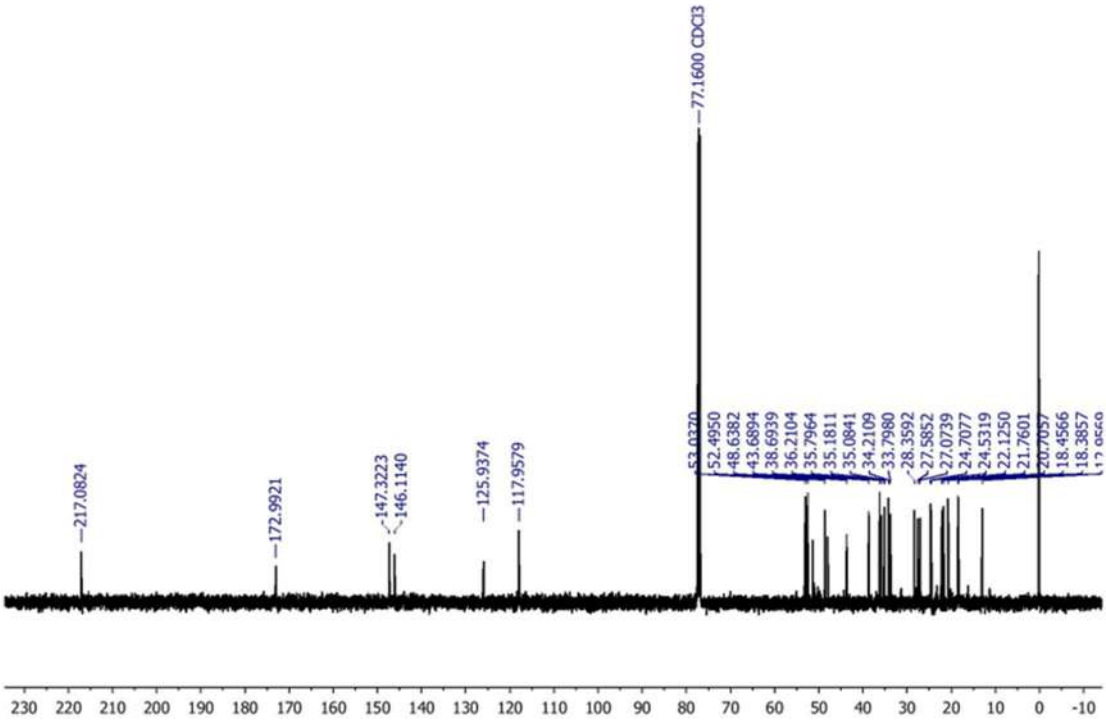

Fig S12. ^{13}C-NMR spectrum of compound **2** in $CDCl_3$ (125 MHz)

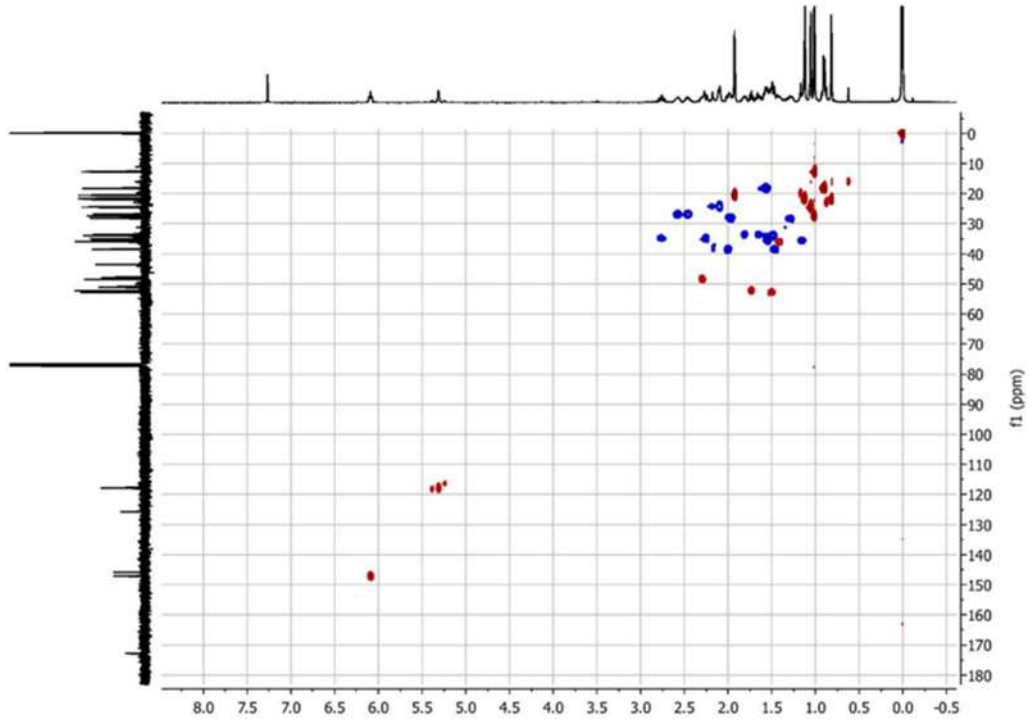

Fig S13. HSQC spectrum of compound **2** in $CDCl_3$

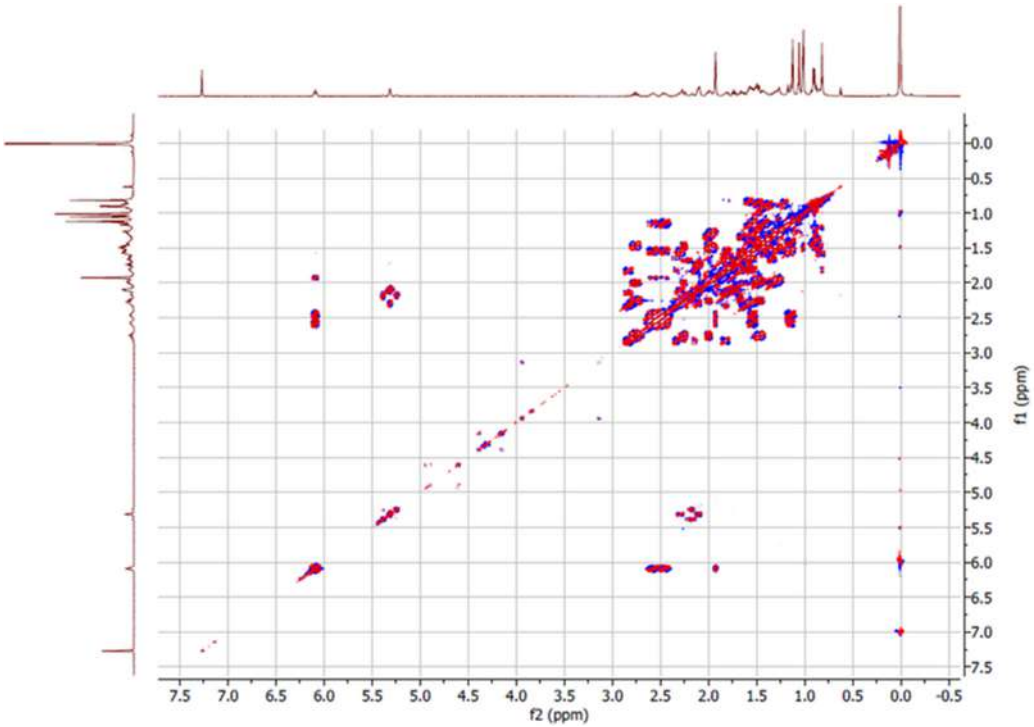

Fig S14. ^{1}H-^{1}H COSY spectrum of compound **2** in $CDCl_3$

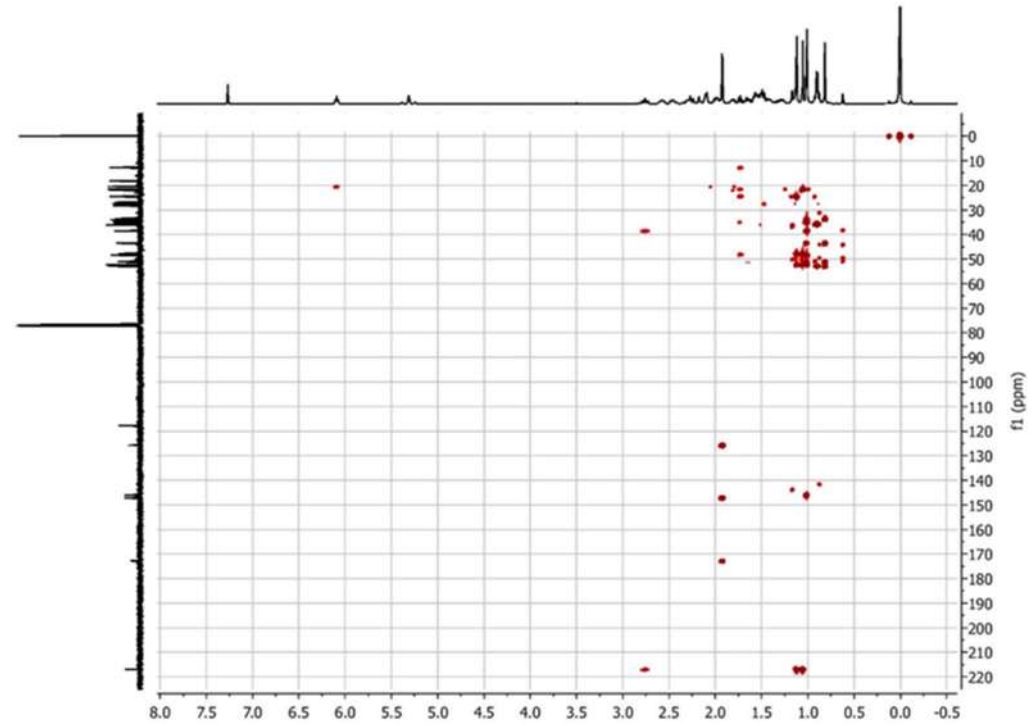

Fig S15. HMBC spectrum of compound **2** in $CDCl_3$

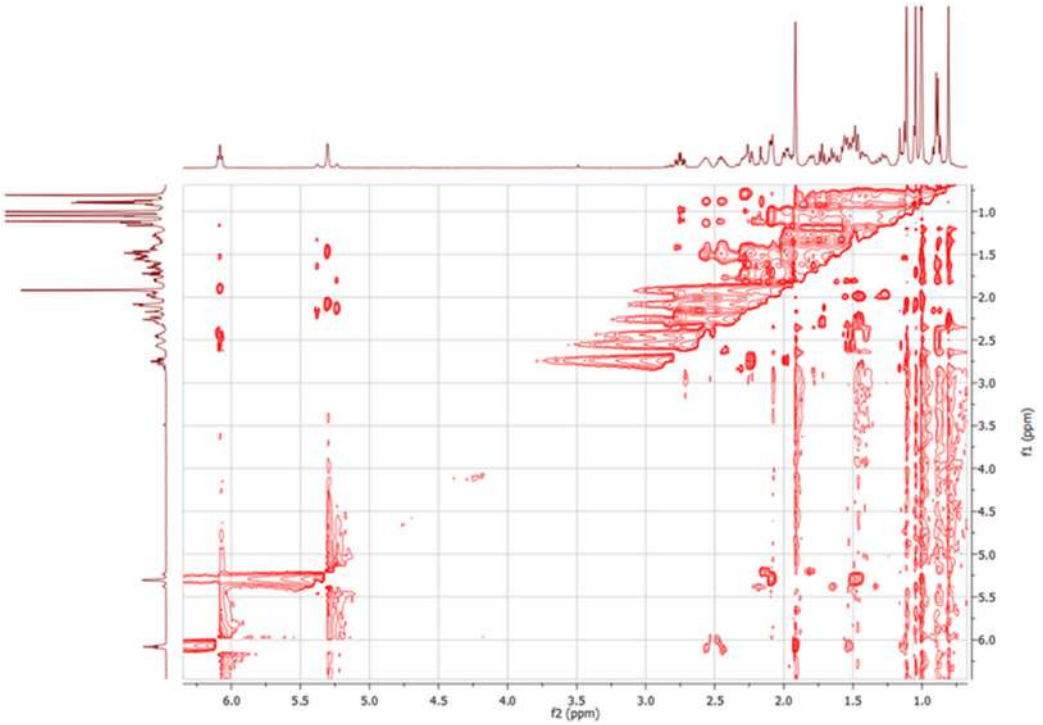

Fig S16. ROESY spectrum of compound **2** in $CDCl_3$

Table S1. IC_{50} values of compound **1**

Var	Concentration (µg/mL)				IC_{50} (µg/mL)	IC_{50} (µM)
	7.81	15.63	31.25	62.50		
1	36.30	36.30	55.26	96.52	24.04	50.93
2	25.06	30.81	47.28	93.51	29.95	63.45
3	20.49	19.00	45.60	97.51	32.20	68.22
Average IC_{50} ± std deviation						60.87 ± 8.93

Table S2. IC_{50} values of compound **2**

Var	Concentration (µg/mL)				IC_{50} (µg/mL)	IC_{50} (µM)
	7.81	15.63	31.25	62.5		
1	25.71	28.50	40.95	96.9	30.78	67.80
2	17.92	23.27	42.92	96.69	32.55	71.70
3	9.21	14.75	36.87	96.02	35.91	79.10
Average IC_{50}±std deviation						72.86 ± 5.74

Triterpenoids from Stem Bark of *Dysoxylum excelsum* and Their Cytotoxic Activity against MCF-7 Breast Cancer Cells

Sylvia Rachmawati Meilanie[1], Tri Mayanti[1], Nurlelasari Nurlelasari[1], Desi Harneti Putri Huspa[1], Rani Maharani[1], Achmad Zainuddin[1], Darwati Darwati[1], Euis Julaeha[1], Unang Supratman[1,2], and Jamaludin Al Anshori[1*]

[1]*Department of Chemistry, Faculty of Mathematics and Natural Sciences, Universitas Padjadjaran, Jl. Raya Bandung-Sumedang Km. 21, Jatinangor, Sumedang 45363, Indonesia*

[2]*Central Laboratory of Universitas Padjadjaran, Jl. Raya Bandung-Sumedang Km. 21, Jatinangor, Sumedang 45363, Indonesia*

* ***Corresponding author:***

tel: +62-81320535955
email: jamaludin.al.anshori@unpad.ac.id

Received: March 16, 2022
Accepted: May 31, 2022

DOI: 10.22146/ijc.73616

Abstract: *The diversity of structures of triterpenoids provides a variety of interesting pharmacological effects, one of them being anticancer. Sources of triterpenoids are found in* Dysoxylum excelsum*, it is still rarely studied, and it potentially contains triterpenoids with cytotoxic activity. Therefore, the research aimed to isolate the triterpenoids from the stem bark of* D. excelsum *and determine their cytotoxic efficacy against the breast cancer cells of MCF-7. The dried stem bark of* D. excelsum *was macerated using methanol and then fractionated with* n*-hexane and ethyl acetate to obtain the corresponding fractions. Two triterpenoids, 3α,7α-dihydroxyapotirucalla-14,24-Z-dien-26-oic acid (**1**) and masticadienonic acid or 3-oxo-tirucalla-7,24-Z-dien-26-oic acid (**2**) were isolated in the first place from the* Dysoxylum *genus. Compounds **1** and **2** were assayed for their cytotoxic potency anti- MCF-7 using the MTT assay and gave moderate IC_{50} values of 60.87 and 72.86 μM, respectively. Based on their analogs, partial structure modification of the compounds might increase the activity; thus, they can be further utilized as better lead compounds for anticancer drugs candidate.*

Keywords: Dysoxylum excelsum*; triterpenoids; Meliaceae; cytotoxic; MCF-7 breast cancer*

■ INTRODUCTION

Of the known Meliaceae family, around 200 species of the *Dysoxylum* genus are distributed widely in India, China, Australia, and Southeast Asia, including Indonesia [1-2]. Diverse compound groups of this genus, for instance, alkaloids [3-4], limonoids [5-7], steroids [8], sesquiterpenoids [9-11], diterpenoids [12-14], triterpenoids [15-19], and triterpenoid glycosides [20] mostly have been elucidated. Furthermore, numerous bioactive compounds such as central nervous system depressants, anti-respiratory syncytial virus, antifeeding, antitumor triterpenoid glycosides [20], anti-inflammatory [3,17,21-22], antirheumatic, and cardiac-active alkaloids [5], cytotoxic [23-28], antimicrobial [2,18-29], and antibacterial [30-31] have been isolated from *Dysoxylum* plants.

D. excelsum Blume is a plant with a tall tree distributed in Asia, yet it has been barely investigated on its chemical constituents and cytotoxic activity [32]. In the previous finding, Zainuddin et al. [33] isolated a tirucallane skeleton-type of triterpenoid, masticadienolic acid, from a similar natural source as we reported here. A potent cytotoxic property against the breast cancer cells of MCF-7 was exhibited by masticadienolic acid (IC_{50} 3.5 μm). To obtain prospective lead compound models as cancer drug candidates, exploration of other cytotoxic compounds in this species needs to be done. Perhaps, it might further inspire the

development of synthetic cancer drugs based on their structure-activity relationship (SAR).

In this article, we reported the isolation and structural elucidation of two triterpenoids, 3α,7α-dihydroxyapotirucalla-14,24-*Z*-dien-26-oic acid (**1**) and masticadienonic acid or 3-oxo-tirucalla-7,24-*Z*-dien-26-oic acid (**2**) which have been reported for the first-ever in the *D. excelsum*. Furthermore, compounds **1**-**2** were *in vitro* assayed cytotoxic potential against the breast cancer cells of MCF-7 using a microtetrazolium (MTT) assay.

■ EXPERIMENTAL SECTION

Materials

The stem bark of *D. excelsum* was obtained from Bogor Botanical Garden, Bogor, West Java, Indonesia, in June 2016. Its taxonomy was determined in the Laboratory of Bogoriense Herbarium, Indonesia (collect. No III. F. 67).

Instrumentation

A Perkin-Elmer spectrum-100 FTIR was employed to record the IR spectra on a KBr Disk. The high-resolution mass was analyzed with a QTOF MS of Waters Xevo. Comprehensive NMR spectra, together with ^{1}H-^{1}H COSY, HSQC, HMBC, and ROESY experiments, were measured on a 500 MHz NMR spectrometer of Agilent with a DD2 console system using a TMS internal standard. Column chromatography matrix was using silica gel 60 with the mesh size of 70–230 and 230–400 (Merck) and chromatorex ODS (Fuji Silysia Chemical, Japan), while a TLC plate was based on aluminium silica gel-coated with fluorescent indicator F_{254} (Merck, 0.25 mm. To visualize the TLC spots, a staining agent of 10% ethanolic H_2SO_4 (v/v) was sprayed and subsequently heated and irradiated under UV/Vis light at 254 and 365 nm.

Procedure

Preparation of extracts

The air-dried stem bark of *D. excelsum* (2.7 kg) was ground and entirely macerated with MeOH (5 L) at ambient temperature (± 25 °C) for 3 days. The filtrated methanolic extract was then concentrated under a rotary vacuum at a temperature of ± 40 °C. After evaporation of the solvent at vacuo, the crude methanolic extract (300 g) was suspended in water (400 mL) and then successively partitioned with *n*-hexane (3 × 100 mL) and EtOAc (3 × 100 mL) to yield the corresponding extract of 16.2 and 102.7 g, respectively.

Isolation of triterpenoids

The EtOAc fraction (102.7 g) was separated on a vacuum-liquid chromatography (VLC) loaded with dry silica gel 60 (230–400 mesh) and eluted gradient using *n*-hexane and EtOAc (10:0–0:10, v/v) to result in 10 fractions (A-J). Fraction C (6.37 g) was then purified on a column chromatography (silica gel 70–230 mesh, eluent *n*-hexane:EtOAc (10:0–8:2, v/v)) to obtain 16 fractions (C1-C16). Further purification was employed for the subfraction of C14 (362.8 mg) using a silica gel 60 column chromatography (eluent *n*-hexane:EtOAc (10:0–5:5, v/v) to yield **2** (109.9 mg). On the other hand, fraction E (15.15 g) was separated on a VLC column packed with dry silica gel 60 (eluent *n*-hexane:EtOAc (10:0–3:7, v/v) to afford 9 fractions (E1-E9). Extra purification of the E8 fraction (127.0 mg) was accomplished on silica gel 60 column chromatography with eluent of *n*-hexane:EtOAc (10:0–0:10, v/v) to give 12 subfractions (E8a-E8l). Finally, the compound **1** (12.9 mg) was obtained from the subfraction of E8f (36.6 mg), after additional purification on ODS column chromatography (eluent MeOH:MeCN:H_2O (7:2:1, v/v/v).

Determination of cytotoxic activity using MTT assay

Initially, the MCF-7 breast cancer cells were attached and cultivated into 96-well plates at 3×10^4 cells cm^{-3} density and then incubated for 24 h. Afterwards, various concentrations of samples dissolved in DMSO were added to the well plates. Later, six desirable concentrations were prepared at buffered pH of 7.30–7.65 (phosphoric buffer solution). The well plates of negative control contained only DMSO, and positive control of doxorubicin was also prepared. Once a 48-h incubation period was finished, the assay was quenched by MTT reagent [3-(4,5-dimethylthiazol-2-yl)-2,5-diphenyl tetrazolium bromide]. An MTT-quencher dissolved in SDS (sodium dodecyl sulfate) was then dropped to the plates for further 2–4 h incubation, followed by final incubation for another 24 h. Upon

scanning of a microplate reader at 450 nm, the optical density of the samples was obtained. Based on the linear regression of the corrected percentage live of cells (%) versus the tested concentration of compounds (μg/mL), the IC_{50} values were computed. Each assay was conducted three times, and their analysis results were reported as averaged IC_{50} values with relative standard deviation.

■ RESULTS AND DISCUSSION

Compound **1** was isolated as a white crystal. The molecular formula calculated by HRTOFMS ($[M+Na]^+$) was found as $C_{30}H_{48}O_4$ with *m/z* 495.3459, calcd. 495.3450. Based on the MS result supported by NMR data (Table 1), the unsaturation degree of compound **1** was confirmed at seven. The IR spectrum revealed the moieties of hydroxyl at 3445 cm^{-1}, an α,β-unsaturated carbonyl at 1692 cm^{-1}, and olefinic carbon at 1640 cm^{-1}. The ^{1}H-NMR spectrum (Table 1) discovered methyl signals as six singlets at δ_H/ppm 0.82, 0.89, 0.90, 1.04, 1.06, and 1.86, and one doublet at δ_H/ppm 0.95 (3H, d, *J* = 6.5 Hz, H-21). Two olefinic methines at δ_H/ppm 5.42 (1H, dd, *J* = 1.5, 3.6 Hz, H-15) and 5.95 (1H, t, *J* = 7.4 Hz, H-24), as well as two oxymethine signals at δ_H/ppm 3.32 (1H, t, *J* = 3.0 Hz, H-3) and 3.87 (1H, t, *J* = 3.1 Hz, H-7), were also assigned. In addition, the ^{13}C-NMR data showed 30 varied chemical shifts of carbon (Table 1). Being supported by the HSQC data, the carbon signals were representing seven methyls at δ_C/ppm 15.8 (C-19), 18.9 (C-18), 19.0 (C-21), 21.1 (C-27), 22.6 (C-29), 28.3 (C-30), and 28.8 (C-28), eight methylenes at δ_C/ppm 17.3 (C-11), 24.9 (C-6), 26.3 (C-2), 26.9 (C-23), 33.5 (C-1), 35.3 (C-12), 35.6 (C-16), and 36.1 (C-22), eight methines at δ_C/ppm 34.4 (C-20), 40.8 (C-5), 42.6 (C-9), 61.3 (C-17), 73.2 (C-7), 75.9 (C-3), 120.0 (C-15), and 143.6 (C-24), six quarternary carbons at δ_C/ppm 37.7 (C-4), 38.4 (C-10), 45.0 (C-8), 47.6 (C-13), 128.0 (C-25), 162.8 (C-14), and one carbonyl at δ_C/ppm 169.4 (C-26). Therefore, the ^{1}H- and ^{13}C-NMR data implied the presence of a triterpenoid tetracyclic skeleton in **1** (Fig. 1). To prove the existence of the skeleton (A, B, C, and D) in structure **1**, spectra of ^{1}H–^{1}H COSY and HMBC were recorded (Fig. 2). The correlations between H_1-H_2-H_3, H_5-H_6-H_7, H_9-H_{11}-H_{12}, H_{15}-H_{16}-H_{17}-H_{20}, and H_{21}-H_{20}-H_{22}-H_{23} were observed in the ^{1}H–^{1}H COSY spectrum of **1**, thus supporting the occurrence of triterpenoid tetracyclic structure in **1**. Additionally, the HMBC correlations of the methyl protons to their nearby carbons supported the interpretation of proton signals of the six singlets of methyl and one of secondary methyl. All anticipated correlations (CH_3-18 → C-13, 12, 14, 17; CH_3-19 → C-10, 1, 5, 9; and CH_3-30 → C-8, 7, 9, 14) revealed strong cross-peaks. An olefinic moiety was discovered by the HMBC correlations of H-16 to C-14 at δ_C/ppm 162.8 and C-15 at δ_C/ppm 120.0, and H-15 to C-13 at δ_C/ppm 47.6, C-16 at δ_C/ppm 35.6, and C-17 at δ_C/ppm 61.3. Similarly, the appearance of α,β-unsaturated carboxylic acid was also revealed by HMBC correlation signals of H-24 to C-27 at δ_C/ppm 21.1, C-22 at δ_C/ppm 36.1, and H-27 to C-24 at δ_C/ppm 143.6, C-25 at δ_C/ppm 128.0, C-26 at δ_C/ppm 169.4. Other correlations from CH_3-28, CH_3-29 to C-3 at δ_C/ppm 75.9, and from CH_3-30 to C-7 at δ_C/ppm 73.2, implied that hydroxy groups were located at C-3 and C-7, respectively. Furthermore, the presence of a side-chain structure of **1** was confirmed by the HMBC cross-peaks of CH_3-21 to C-17 at δ_C/ppm 61.3, C-20 at δ_C/ppm 34.4, and C-22 at δ_C/ppm 36.1. To resolve the relative stereochemical configuration of **1**, the analysis of coupling constants and the rotating-frame nuclear overhauser effect spectroscopy (ROESY) experiment were conducted (Fig. 3). The coupling constants of H-3 at δ_H/ppm 3.32 (t, *J* = 3.0 Hz) and H-7 at δ_H/ppm 3.87 (t, *J* = 3.1 Hz) proposed their orientation in an equatorial position and *β*-oriented [34-35]. Moreover, based on the ROESY spectrum, the correlations of H-3/CH_3-19/CH_3-29 and H-7/CH_3-30 further verified the *α*-configuration of the hydroxy moieties at C-3 and C-7. In addition, the ROESY correlations of CH_3-28/H-5 directed the *α*-configuration of CH_3-28. Correlations of H-9/CH_3-18 and CH_3-18/H-20 indicated the *α*-orientation of H-20, and the correlations of H-17/H-12*β* and H-12*β*/CH_3-21 designated *β*-orientation of CH_3-21 which was in agreement with those of apotirucallane-type triterpenoids. The configuration of the *Z* double bond among C-24 at δ_C/ppm 143.6 and C-25 at δ_C/ppm 128.0 was resolved by the ROESY correlation between H-24 at δ_H/ppm 5.95 (t, *J* = 7.4 Hz) and CH_3-27 at δ_H/ppm 1.86 (s) [2]. Overall, the structure of compound **1** had an

apotirucallane skeleton. Instead of the configuration of CH_3-21, most of the NMR data of **1** resembled previously reported chisopatens C, an apoeuphane triterpenoid [36]. Consequently, compound **1** was determined as 3*α*,7*α*-dihydroxyapotirucalla-14,24-*Z*-dien-26-oic acid (Fig. 1), which was isolated from this genus for the first ever. The configuration of the tirucallane-type and euphane-type triterpenoids is distinguished by H-21. The *β*-configuration is tirucallane-type, whereas the *α* one is euphane-type [37].

Table 1. ^{1}H and ^{13}C-NMR data of **1** in $(CD_3)_2CO$ and **2** in $CDCl_3$ (δ in ppm, 500 MHz for ^{1}H, and 125 MHz for ^{13}C)[a]

Position	**1**		**2**	
	δ_C	δ_H (ΣH, mult., *J*/Hz)	δ_C	δ_H (ΣH, mult., *J*/Hz)
1	33.5	1.26 (1H, dt, 3.0, 12.6)	38.7	1.46 (1H, td, 4.8, 14.3)
		1.49 (1H, td, 3.4, 10.5)		1.99 (1H, dt, 2.9, 13.5)
2	26.3	1.50 (1H, m)	35.1	2.73 (1H, dt, 3.6, 14.3)
		1.93 (1H, m)		2.75 (1H, td, 5.4, 14.5)
3	75.9	3.32 (1H, t, 3.0)	217.1	-
4	37.7	-	48.0	-
5	40.8	2.14 (1H, dd, 2.6, 12.8)	52.5	1.72 (1H, t, 8.7)
6	24.9	1.63 (1H, td, 3.5, 10.1)	24.5	2.09 (1H, m)
		1.72 (1H, dt, 2.6, 13.0)		2.16 (1H, m)
7	73.2	3.87 (1H, t, 3.1)	118.0	5.30 (1H, dd, 3.3, 6.6)
8	45.0	-	146.1	-
9	42.6	2.07 (1H, m)	48.6	2.30 (1H, m)
10	38.4	-	35.2	-
11	17.3	1.48 (1H, m)	18.5	1.56 (2H, m)
		1.69 (1H, m)		
12	35.3	1.48 (1H, m)	33.8	1.66 (1H, m)
		1.96 (1H, m)		1.81 (1H, m)
13	47.6	-	43.7	-
14	162.8	-	51.3	-
15	120.0	5.42 (1H, dd, 1.5, 3.6)	34.2	1.49 (2H, m)
16	35.6	2.02 (1H, m)	28.4	1.29 (1H, m)
		2.27 (1H, m)		1.95 (1H, m)
17	61.3	1.46 (1H, m)	53.0	1.50 (1H, m)
18	18.9	1.04 (3H, s)	22.1	0.81 (3H, s)
19	15.8	0.90 (3H, s)	12.9	1.00 (3H, s)
20	34.4	1.63 (1H, m)	36.2	1.41 (1H, m)
21	19.0	0.95 (3H, d, 6.5)	18.4	0.89 (3H, d, 6.4)
22	36.1	1.19 (1H, m)	35.8	1.16 (1H, m)
		1.56 (1H, m)		1.55 (1H, m)
23	26.9	2.43 (1H, m)	27.1	2.45 (1H, m)
		2.51 (1H, m)		2.50 (1H, m)
24	143.6	5.95 (1H, t, 7.4)	147.3	6.08 (1H, t, 7.4)
25	128.0	-	126.0	-
26	169.4	-	173.0	-
27	21.1	1.86 (3H, s)	20.7	1.92 (3H, s)
28	28.8	0.89 (3H, s)	21.8	1.11 (3H, s)
29	22.6	0.82 (3H, s)	24.7	1.05 (3H, s)
30	28.3	1.06 (3H, s)	27.6	1.01 (3H, s)

[a] the assignments were based on correlation experiments of ^{1}H-^{1}H COSY, HSQC, and HMBC

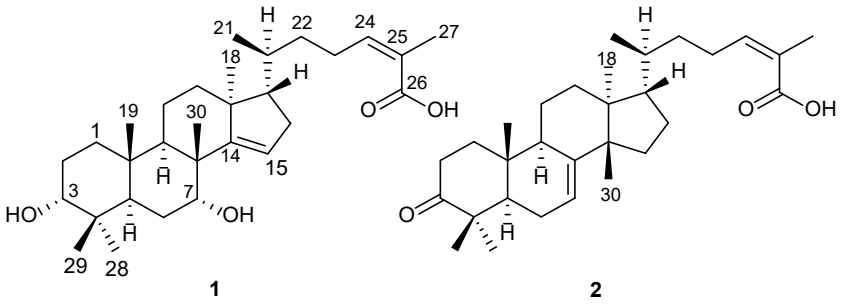

Fig 1. The structures of **1**-**2** isolated from *D. excelsum*

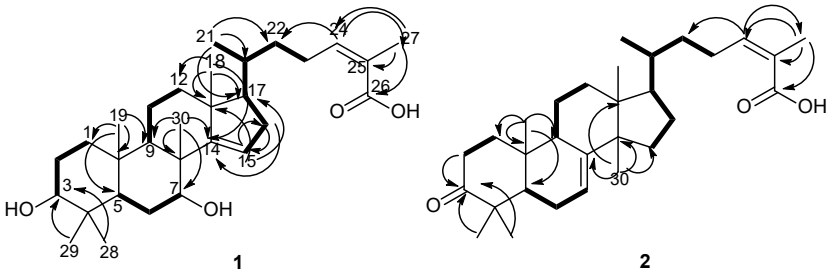

Fig 2. Key HMBC (⟶) correlations of **1**-**2**

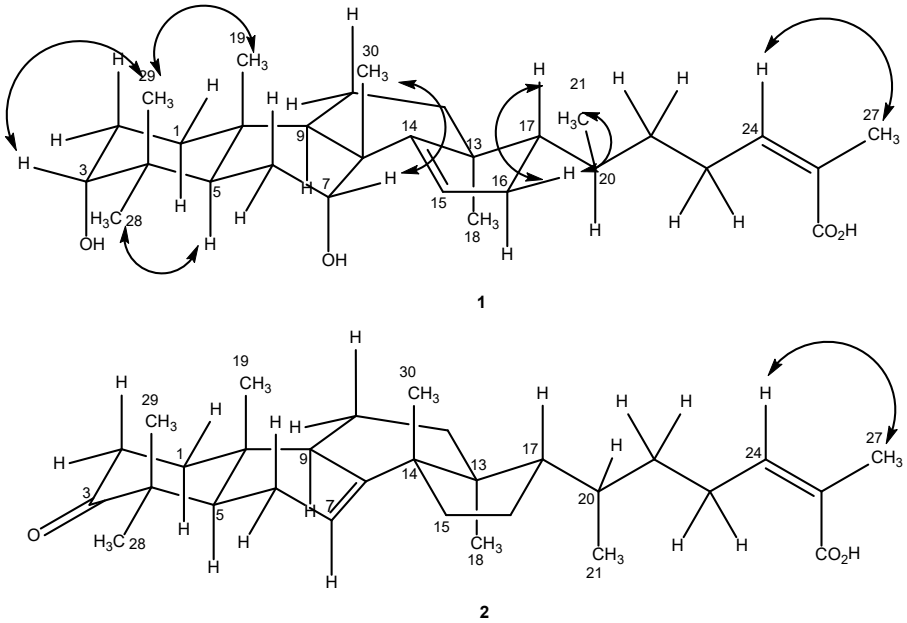

Fig 3. Key ROESY (⇢) correlations of **1**-**2**

Compound **2** was acquired as colorless needle-like crystals. The mass spectrum recorded by HRTOFMS ($[M+Na]^+$) showed the molecular formula as $C_{30}H_{46}O_3$ with *m/z* 477.3311, calcd. 477.3345. Being supported by NMR data (Table 1), the unsaturation of the compound was found by MS at eight degrees. Three main functional groups, i.e., a carbonyl ketone (1706 cm^{-1}), an α,β-unsaturated carbonyl (1678 cm^{-1}), and olefinic groups (1636 cm^{-1}) were revealed by the IR spectrum. The ^{1}H-NMR spectrum displayed nine proton signals consisting of six tertiary methyl moieties at δ_H/ppm 0.81, 1.00, 1.01, 1.05, 1.11, and 1.92, and one secondary methyl moiety at δ_H/ppm 0.89 (3H, d, *J* = 6.4 Hz, H-21), and two olefinic methines at δ_H/ppm 5.30 (1H, dd, *J* = 3.3, 6.6 Hz, H-7)

and 6.08 (1H, t, J = 7.4 Hz, H-24). On the otherside, the ^{13}C-NMR spectrometer identified 30 carbon signals (Table 1), consisted of seven methyls at δ_C/ppm 12.9 (C-19), 18.4 (C-21), 20.7 (C-27), 21.8 (C-28), 22.1 (C-18), 24.7 (C-29), and 27.6 (C-30), nine methylenes at δ_C/ppm 18.5 (C-11), 24.5 (C-6), 27.1 (C-23), 28.4 (C-16), 33.8 (C-12), 34.2 (C-15), 35.1 (C-2), 35.8 (C-22), and 38.7 (C-1), six methines at δ_C/ppm 36.2 (C-20), 48.6 (C-9), 52.5 (C-5), 53.0 (C-17), 118.0 (C-7), and 147.3 (C-24), six quarternary carbons at δ_C/ppm 35.2 (C-10), 43.7 (C-13), 48.0 (C-4), 51.3 (C-14), 126.0 (C-25), and 146.1 (C-8), and two carbonyl carbons at δ_C/ppm 173.0 (C-26), and 217.1 (C-3). The NMR evidence of compound 2 implied a tetracyclic triterpenoid skeleton (Fig. 1) emphasized by the ^{1}H–^{1}H COSY analysis (Fig. 2). The analysis revealed the correlations between H_1-H_2, H_5-H_6-H_7, H_9-H_{11}-H_{12}, H_{15}-H_{16}-H_{17}-H_{20}, and H_{21}-H_{20}-H_{22}-H_{23}-H_{24}. Based on the HMBC cross-peaks (Fig. 2), the occurrence of the carbonyl ketone at C-3 was supported by the correlation of H-28 at δ_H/ppm 1.11, H-29 at δ_H/ppm 1.05, and the methylene protons H-2 at δ_H/ppm 2.75 to the C-3 of carbonyl carbon at δ_C/ppm 217.1. The HMBC correlations of CH_3-19 at δ_H/ppm 1.00 to C-10 at δ_C/ppm 35.2, C-1 at δ_C/ppm 38.7, C-5 at δ_C/ppm 52.5, and C-9 at δ_C/ppm 48.6 verified the bonding of CH_3-19 to C-10, whereas the correlations between CH_3-30 at δ_H/ppm 1.01 and C-14 at δ_C/ppm 51.3, C-13 at δ_C/ppm 43.7, C-15 at δ_C/ppm 34.2, and C-8 at δ_C/ppm 146.1 confirmed the bonding of CH_3-30 to C-14. On the other side, the presence of HMBC correlation between CH_3-19 and C-9 at δ_C/ppm 48.6 confirmed another olefinic carbon at C-7/C-8 and olefinic of C-24/C-25. Overall, compound **2** has a similar α,β-unsaturated carboxylic acid group as confirmed in **1**. The relative configuration of **2** was further resolved by the ROESY experiment (Fig. 3). This evidence suggested that the structure of **2** has the skeleton-type of a tirucallane triterpenoid and resembles masticadienolic acid [33], and it was in agreement with masticadienonic acid [38]. Thus, compound **2** was determined as masticadienonic acid or 3-oxo-tirucalla-7,24-*Z*-dien-26-oic acid (Fig. 1).

An MTT assay to evaluate the cytotoxic potency of compounds **1**-**2** anti-MCF-7 was represented as IC_{50} values. The value will express how many substances are required to inhibit 50% of the biological process, thus revealing the activity degree of antagonist agents in pharmacological research [39]. In addition, the standard inhibitor of cancer (doxorubicin) [2] was also tested as the reference under the same condition. All the compounds (**1**-**2**) gave the IC_{50} values of 60.87 and 72.86 µM (Table 2 and Table S1, S2), respectively, which were classified as moderate cytotoxic [40]. In general, the resulted IC_{50} was roughly higher by two times than the positive control. Compound **2** exhibited weaker cytotoxic activity than **1,** which might be caused by the appearance of a carbonyl ketone moiety at C-3 that decreased the cytotoxicity [41]. Compound **1** did not show considerably better cytotoxic activity than **2**, which was suggested due to the occurrence of the hydroxyl moieties at C-3 and C-7 and the loss of olefinic moiety at C-7/C-8 [42]. Such analog compounds were reported to have various cytotoxicity. Two tirucallanes, 3β,16β,21α,25-tetrahydroxy-20,24-cyclotirucalla-7(8)-ene and 16β,21α,25-trihydroxy-20,24-cyclotirucalla-7(8)-en-3-one, displayed significant cytotoxic potency anti-MCF-7 and other cell lines with IC_{50} values of 6.64–10.55 and 8.90–12.08 µM, respectively [2]. Furthermore, five apotirucallanes exhibited moderate cytotoxic activities against MCF-7 at an IC_{50} range of 78.7–85.8 µM [23]. The SAR analysis showed that the occurrence of an aromatic heterocyclic such as pyrrole in the side chain combined with 3α-OH substituents influenced mostly the potent cytotoxicity [40].

Table 2. IC_{50} values of compounds **1** and **2** against the breast cancer cells of MCF-7

Compound	IC_{50} (µM) ± Stdv
1	60.87 ± 8.93
2	72.86 ± 5.74

Positive control: doxorubicin, IC_{50} = 35.67 µM

■ CONCLUSION

Two triterpenoids had been isolated from the stem bark of *D. excelsum*, 3*α*,7*α*-dihydroxyapotirucalla-14,24-*Z*-dien-26-oic acid (**1**) and masticadienonic acid or 3-oxo-tirucalla-7,24-*Z*-dien-26-oic acid (**2**) whereas compound **1** was found for the first time in the genus. The IC_{50} values of the compounds (**1**-**2**) against the

breast cancer cell lines of MCF-7 showed moderate cytotoxicity and were roughly two times less potent than the positive control of Doxorubicin. Compound **1** exhibited a lower IC_{50} value (60.87 μM) than **2** (72.86 μM) which might be due to the occurrence of a hydroxyl moiety at C-3. Such partial structure modification of the isolated compound with a side chain of aromatic heterocyclic and a hydroxy moiety at C-3 might increase the activity significantly. Thus, it can be further utilized as a more potential lead compound for anticancer drug candidates.

■ ACKNOWLEDGMENTS

The authors are grateful to Universitas Padjadjaran for ALG of Prof. Tri Mayanti (No: 2064/UN6.3.1/PT.00/2022).

■ AUTHOR CONTRIBUTIONS

TM, EJ, D conducted the experiment, US, DHPH, and N conducted the structure elucidation, and SRM, JAA, RM, and AZ wrote and revised the manuscript. All authors agreed to the final version of this manuscript.

■ REFERENCES

[1] Naini, A.A., Mayanti, T., Nurlelasari, N., Harneti, D., Maharani, R., Safari, A., Hidayat, A.T., Farabi. K., Lesmana, R., Supratman, U., and Shiono, Y., 2022, Cytotoxic sesquiterpenoids from *Dysoxylum parasiticum* (Osbeck) Kosterm. stem bark, *Phytochem. Lett.*, 47, 102–106.

[2] Saravanan, R., Arvind, D.P., and Sujana, K.A., 2014, *Dysoxylum* (Blume) – New generic record to Odisha, India, *Int. J. Adv. Res.*, 2 (8), 543–545.

[3] Kumar, V., Gupta, M., Gandhi, S.G., Bharate, S.S., Kumar, A., Vishwakarma, R.A., and Bharate, S.B., 2017, Anti-inflammatory chromone alkaloids and glycoside from *Dysoxylum binectariferum*, *Tetrahedron Lett.*, 58 (42), 3974–3978.

[4] Kumara, P.M., Zuehlke, S., Priti, V., Ramesha B.T., Shweta, S., Ravikanth, G., Vasudeva, R., Santhoshkumar, T.R., Spiteller, M., and Shaanker, R.U., 2012, *Fusarium proliferatum*, an endophytic fungus from *Dysoxylum binectariferum* Hook.f, produces rohitukine, a chromane alkaloid possessing anti-cancer activity, *Antonie van Leeuwenhoek*, 101 (2), 323–329.

[5] Zhou, B., Shen, Y., Wu, Y., Leng, Y., and Yue, J.M., 2015, Limonoids with 11β-hydroxysteroid dehydrogenase type 1 inhibitory activities from *Dysoxylum mollissimum*, *J. Nat. Prod.*, 78 (8), 2116–2122.

[6] Xu, J., Ni, G., Yang, S., and Yue, J., 2013, Dysoxylumins A–F: Six new limonoids from *Dysoxylum mollissimum* Bl, *Chin. J. Chem.*, 31 (1), 72–78.

[7] Tang, T., Liao, S.G., Na, Z., Li, Y., and Xu, Y.K., 2012, Dysoxylentin A, the first 21-nortriterpenoid bearing a 2-(propan-2-ylidenyl)furan-3(2*H*)-one, from *Dysoxylum lenticellatum*, *Tetrahedron Lett.*, 53 (9), 1183–1185.

[8] Yan, H.J., Wang, J.S., and Kong, L.Y., 2014, Cytotoxic steroids from the leaves of *Dysoxylum binectariferum*, *Steroids*, 86, 26–31.

[9] Liu, H.B., Zhang, C.R., Dong, S.H., Yang, S.P., Sun, Q., Geng, M.Y., and Yue, J.M., 2012, Sesquiterpenes from *Dysoxylum oliganthum* and *Dysoxylum excelsum*, *J. Asian Nat. Prod. Res.*, 14 (3), 224–234.

[10] Liu, W.X., Tang, G.H., He, H.P., Zhang, Y., Li, S.L., and Hao, X.J., 2012, Limonoids and triterpenoids from the twigs and leaves of *Dysoxylum hainanense*, *Nat. Prod. Bioprospect.*, 2 (1), 29–34.

[11] Dharmayani, N.K.T., Yoshimura, T., Hermawati, E., Juliawaty, L.D., and Syah, Y.M., 2020, Antibacterial and antifungal two phenolic sesquiterpenes from *Dysoxylum densiflorum*, *Z. Naturforsch., C: Biosci.*, 75, 1–5.

[12] Gu, J., Cheng, G.G., Qian, S.Y., Li, Y., Liu, Y.P., and Luo, X.D., 2014, Dysoxydensins A–G, seven new clerodane diterpenoids from *Dysoxylum densiflorum*, *Planta Med.*, 80 (12), 1017–1022.

[13] Zhang, P., Lin, Y., Wang, F., Fang, D., and Zhang, G., 2019, Diterpenes from *Dysoxylum lukii* Merr., *Phytochem. Lett.*, 29, 53–56.

[14] Zhao, J.X., Yu, Y.Y., Wang, S.S., Huang, S.L., Shen, Y., Gao, X.H., Sheng, L., Li, J.Y., Leng, Y., Li, J., and Yue, J.M., 2018, Structural elucidation and bioinspired total syntheses of ascorbylated

diterpenoid hongkonoids A-D, *J. Am. Chem. Soc.*, 140 (7), 2485–2492.

[15] Huang, R., Zhao, Y., Wang, Y., Zhou, L., Chen, Y.F., and Wang, J.F., 2017, Cytotoxic ring A-seco triterpenoids from the stem bark of *Dysoxylum lukii*, *J. Asian Nat. Prod. Res.*, 20 (9), 860–866.

[16] Yan, H., Wang, J., and Kong, L., 2014, Cytotoxic dammarane-type triterpenoids from the stem bark of *Dysoxylum binecteriferum*, *J. Nat. Prod.*, 77 (2), 234–242.

[17] Zou, Y.H., Liu, W.T., Zhang, J.X., and Xiang, D.C., 2017, Triterpenoids from the bark of *Dysoxylum hainanense* and their anti-inflammatory and radical scavenging activity, *Fitoterapia*, 121, 159–163.

[18] Yan, H.J., Si, H.L., Zhao, H.W., Chen, L., Yu, J.Q., Zhao, H.Q., and Wang, X., 2021, Four new cycloartane triterpenoids from the leaves of *Dysoxylum binectariferum*, *Phytochem. Lett.*, 41, 101–105.

[19] Wang, F., and Guan, Y., 2012, Cytotoxic nor-dammarane triterpenoids from *Dysoxylum hainanense*, *Fitoterapia*, 83 (1), 13–17.

[20] Fujioka, T., Sakurai, A., Mihashi, K., Kashiwada, Y., Chen, I.S., and Lee, K.H., 1997, Antitumor agents. 169. *Dysoxylum cumingianum* V. Cumingianosides P and Q, new cytotoxic triterpene glucosides with an apotirucallane-type skeleton from *Dysoxylum cumingianum*, *Chem. Pharm. Bull.*, 45 (1), 202–206.

[21] Kumar, V., Bharate, S.S., Bhurta, D., Gupta, M., Gandhi, S.G., Singh, D., Jaglan, S., Kumar, A., Vishwakarma, R.A., and Bharate, S.B., 2020, Evaluation of rohitukine-enriched fraction of *Dysoxylum binectariferum* Hook.f. (leaves) as anti-arthritic phytopharmaceutical candidate: Chemical standardization, in-vivo validation, formulation development and oral pharmacokinetics, *J. Ethnopharmacol.*, 254, 112758.

[22] Jiang, K., Chen, L.L., Wang, S.F., Wang, Y., Li, Y., and Gao, K., 2015, Antiinflammatory terpenoids from the leaves and twigs of *Dysoxylum gotadhora*, *J. Nat. Prod.*, 78 (5), 1037–1044.

[23] Hu, J., Song, Y., Li, H., Yang, B., Mao, X., Zhao, Y., and Shi, X., 2014, Cytotoxic and anti-inflammatory tirucallane triterpenoids from D*ysoxylum binectariferum*, *Fitoterapia*, 99, 86–91.

[24] Cao, P., Liang, G., Gao, X., Wang, X., and Li, Z., 2013, Three new nor-dammarane triterpenoids from *Dysoxylum hainanense* with particular cytotoxicity against glioma cell line, *Arch. Pharm. Res.*, 36 (3), 322–326.

[25] De Los Reyes, M.M., Oyong, G.G., Ng, V.A.S., Shen, C.C., and Ragasa, C.Y., 2016, Cytotoxic compounds from *Dysoxylum gaudichaudianum* (A. Juss.) Miq., *Int. J. Pharmacogn. Phytochem. Res.*, 8 (4), 663–667.

[26] Han, L.M., Zhao, J.X., Liu, H.C., Ni, G., Ding, J., Yang, S.P., and Yue, J.M., 2015, Limonoid and triterpenoids from *Dysoxylum mollissimum* var. *glaberrimum*, *J. Nat. Prod.*, 78 (4), 754–761.

[27] Ragasa, C.Y., Ng, V.A.S., De Los Reyes, M.M., Mandia, E.H., Oyong, G.G., and Shen, C.C., 2014, Chemical constituent and cytotoxic of the leaves of *Dysoxylum gaudichaudianum* (A. Juss.) Miq., *Pharma Chem.*, 6 (5), 182–187.

[28] Pham, N.K., Bui, H.T., Tran, T.H., Hoang, T.N.A., Vu, T.H., Do, D.T., Kim, Y.H., Song, S.B., To, D.C., and Nguyen, M.C., 2021, Dammarane triterpenes and phytosterols from *Dysoxylum tpongense* Pierre and their anti-inflammatory activity against liver X receptors and NF-κB activation, *Steroids*, 175, 108902.

[29] Gopalakrishnan, S., Lakshmi, S.Y.S., and Banu, F., 2015, Comparison of antimicrobial activities of silver nanoparticle synthesized from *Dysoxylum parasiticum*, *Indian J. Med. Healthcare*, 4 (2), 1–5.

[30] Dharmayani, N.K.T., Juliawaty, L.D., and Syah, Y.M., 2016, Three tetracyclic triterpenoic acids from *Dysoxylum densiflorum* and their antibacterial activities, *Nat. Prod. Commun.*, 11 (8), 1081–1083.

[31] Hu, J., Song, Y., Li, H., Mao, X., Zhao, Y., Shi, X., and Yang, B., 2014, Antibacterial and cytotoxic triterpenoids from the ethanol extract of *Dysoxylum densiflorum* (Blume) Miq., *Phytochem. Lett.*, 10, 219–223.

[32] Soepadmo, E., and Saw, L.G., 2002, *Tree Flora of Sabah and Sarawak*, Volume 3, 4th Ed., Sabah

Forestry Department, Forest Research Institute Malaysia (FRIM), Sarawak Forestry Department, Malaysia.

[33] Zainuddin, A., Meilanie, S.R., Darwati, D., Kurniawan, K., Nurlelasari, N., Herlina, T., Saputra, A.D., Al Anshori, J., and Mayanti, T., 2020, Cytotoxic triterpenoids from the stem barks of *Dysoxylum arborescens* and *Dysoxylum excelsum* against MCF-7 breast cancer cell, *Sains Malays.*, 49 (5), 989–994.

[34] Mehmood, A., Malik, A., Anis, I., Khan, P.M., Riaz, M., Makhmoor, T., and Choudhary, M.I., 2010, Highly oxygenated triterpenes from the roots of *Atropa acuminata*, *Nat. Prod. Lett.*, 16 (6), 371–376.

[35] Krasteva, I., Jenett-Siems, K., Kaloga, M., and Nikolov, S., 2009, 3-*O*-Sulfo-triterpenoid Saponins from *Gypsophila trichotoma* Wend, *Z. Naturforsch., B: Chem. Sci.*, 64 (3), 319–322.

[36] Supratman, U., Naibaho, W., Salam, S., Maharani, R., Hidayat, A.T., Harneti, D., Nurlelasari, N., and Shiono, Y., 2019, Cytotoxic triterpenoids from the bark of *Chisocheton patens* Blume (Meliaceae), *Phytochem. Lett.*, 30, 81–87.

[37] Wang, L.Y., Wang, N.L., Yao, X.S., Miyata, S., and Kitanaka, S., 2003, Euphane and tirucallane triterpenes from the roots of *Euphorbia kansui* and their in vitro effects on the cell division of *Xenopus*, *J. Nat. Prod.*, 66 (5), 630–633.

[38] Mulholland, D.A., and Nair, J.J., 1994, Triterpenoids from *Dysoxylum pettigrewianum*, *Phytochemistry*, 37 (5), 1409–1411.

[39] Kuete, V., and Efferth, T., 2015, African flora has the potential to fight multidrug resistance of cancer, *BioMed Res. Int.*, 2015, 914813.

[40] Naini, A.A., Mayanti, T., and Supratman, U., 2022, Triterpenoids from *Dysoxylum* genus and their biological activities, *Arch. Pharmacal Res.*, 45 (2), 63–89.

[41] Nugroho, A.E., Momota, T., Sugiura, R., Hanzawa, M., Yajima, E., Nagakura, Y., Yasuda, N., Hirasawa, Y., Wong, C.P., Kaneda, T., Hadi, A.H.A., Fukaya, H., and Morita, H., 2014, Dysotriflorins A–M, triterpenoids from *Dysoxylum densiflorum*, *Tetrahedron*, 70 (51), 9661–9667.

[42] Prakash, O., Ahmad, A., Tripathi, V.K., Tandon, S., and Pant, A.B., 2014, *In silico* assay development for screening of tetracyclic triterpenoids as anticancer agents against human breast cancer cell line MCF7, *PLoS ONE*, 9 (11), e111049.